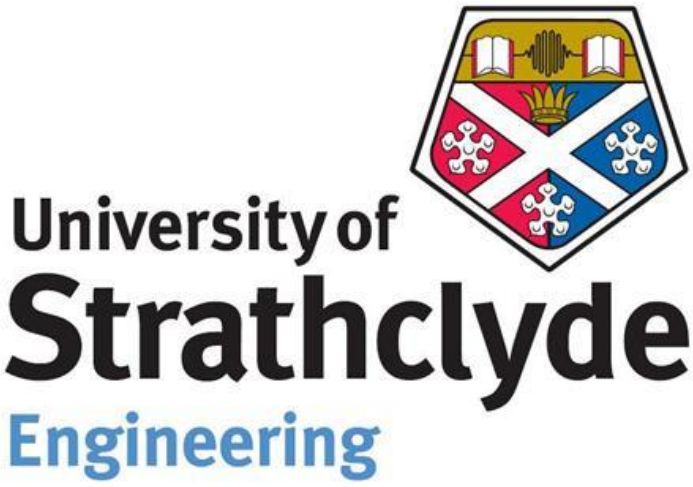

Characterisation and Modification of Residual Stress in Brazed Dissimilar Material Joints for a Future Fusion Divertor

David Easton

Partial Fulfilment of the Requirements for the Degree of

Doctor of Philosophy

Department of Mechanical and Aerospace Engineering

University of Strathclyde

June 2017

'This thesis is the result of the author's original research. It has been composed by the author and has not been previously submitted for examination which has led to the award of a degree.'

Author Signature: 

Date: 11/10/2017

Abstract

In a future nuclear fusion reactor, the critical divertor component will require dissimilar material joining of an armour and a structural material. Tungsten (armour) and copper or steel alloy (structural) have been identified as suitable candidates. A review of existing divertor designs and material combinations highlighted a requirement for further development of tungsten based dissimilar material joints and the associated residual stresses. An improvement in the residual stress state at the interface is seen as a way to improve the performance of the divertor under cyclic loading.

A method of beneficially modifying the residual stress state of vacuum brazed, fusion relevant, tungsten dissimilar material joints is presented in this thesis. Tungsten-copper and tungsten-316L stainless steel parts were successfully brazed using a eutectic gold-copper brazing alloy. A total of 30 dissimilar material brazed joints were successfully manufactured and analysed. The brazed parts have been characterised using a range of metallurgical and residual stress measurement techniques. The residual stress state has been predicted using finite element analysis. Temperature dependent thermo-mechanical material properties were experimentally determined for the gold-copper alloy to facilitate accurate finite element modelling. Good agreement between predicted and X-ray diffraction and Contour Method measured residual stresses for brazed tungsten-316L parts was obtained. The need for further research into the complex interfacial region, and translation of this region into a predictive model, was identified to improve correlation of predicted and measured residual stresses in brazed tungsten-copper parts.

Damaging tensile residual stresses in the brittle tungsten material were beneficially reduced in a brazed tungsten-316L part using thermal autofrettage. Reduction of high brazing induced tensile stresses was achieved both analytically and experimentally. This improvement in the residual stress distribution has promising applications in beneficially modifying real divertor dissimilar material tiles.

Acknowledgements

Firstly I would like to thank my supervisor Jim Wood for providing me with the opportunity to conduct my PhD in an interesting field. Your support throughout the duration of my research has been unwavering and hugely appreciated. The expert technical knowledge in such a varied range of disciplines has been an integral part of helping me steer my research in the direction I have gone. You gave me the freedom and confidence to explore what interested me, whilst providing knowledge advice and guidance all the way (even into your retirement!). For that I am hugely grateful.

I would also like to thank my second supervisor Alex Galloway for all of your support and advice throughout my PhD. I would also like to acknowledge my colleagues within the fusion materials group, Niall Hamilton, Mikael Robbie, and Yuxuan "Eric" Zhang. Your advice and support, particularly in the early days of my research, were invaluable and without which I have no doubts would have made the research experience much more challenging, and much less enjoyable.

A huge thank you is also due for my supervisors at Culham. In the early days the advice from Ioannis Katramados and Tom Barrett provided me with an excellent insight into the fusion engineering world. Extra special gratitude is owed to Chris Hardie. In addition to the guidance you provided since becoming involved with my research, the level of support in regards to my time at Culham performing testing is a huge factor in the output of my thesis. Your hosting made every trip to Culham an enjoyable one!

I would like to thank all of my colleagues at Strathclyde who helped me throughout the course of my work, including Fiona Sillars for her help in material characterisation and James Kelly for his support in the metallurgy lab. A special mention is also owed to my colleagues at AFRC, Ioannis, Gladys, Michael, Shan and Saber, for the thoughtful discussions and experimental support which helped me reach the finish line.

For his advice and support in all things residual stress, a special thank you is owed to Salah Rahimi. Your extremely helpful attitude, welcoming personality and willingness to devote your time to assist is appreciated massively.

Finally I would like to thank my friends and family for all of their support, which has been unwavering since the very beginning of my PhD. A special thank you is owed to my mum and

dad who have never failed to help me even during difficult periods of their own. Last but by no means least I would like to thank Carly for everything you have given me over the years. You may have no interest in dissimilar material residual stress states, but you soldiered on none the less and helped me when I most needed it. Thank you!

Table of Contents

List of Tables

List of Figures

List of Symbols

½ S2	X-ray elastic constant
A_c	Area of radiating object
c_i	Sensitivity coefficient
C_p	Specific heat capacity
C_p	Specific heat capacity
E	Youngs Modulus of Elasticity
E_{eff}	Effective elastic modulus (CSM method)
E_{tan}	Tangent (plastic) modulus
h	Displacement (CSM method)
k	Coverage factor
K	Stress intensity factor
L	Characteristic length
P	Force (CSM method)
q	Heat transfer coefficient
r	Polar coordinate
S	Stiffness (CSM method)
S1	X-ray elastic constant
T_c	Cold body temperature
T_h	Hot body temperature
U	Expanded uncertainty
$u(x_i)$	Standard uncertainty
u_c	Combined standard uncertainty
α	Coefficient of thermal expansion
ε	Strain
θ	Polar coordinate
ν	Poissons ratio
ϱ	Density
σ	Stefan-Boltzman constant
σ	Stress
σ_{yield}	Yield stress
ψ	Psi (X-ray coordinate)
φ	Phi (X-ray coordinate)
ω	Dundurs parameter

List of Abbreviations

AFM	Atomic force microscopy
AFRC	Advanced Forming Research Centre
AMRL	Advanced Material Research Laboratory
AuCu	Gold copper
CCFE	Culham Centre for Fusion Energy
CMM	Coordinate measuring machine
CSM	Continual stiffness method
CTE	Coefficient of thermal expansion
CuCrZr	Copper chrome zirconium
DBTT	Ductile brittle transition temperature
DEMO	Demonstration fusion power plant
DIC	Digital image correlation
DMA	Dynamic mechanical analyser
DSC	Digital scanning calorimetry
D-T	Deuterium - tritium
EBSD	Electron backscatter diffraction
EDM	Electrical discharge machining
EDS	Energy dispersive spectroscopy
ESPI	Electronic speckle pattern interferometry
ETMT	Electrothermal mechanical testing
FCC	Face centred cubic
FEA	Finite element analysis
FEM	Finite element modelling
FGM	Functionally graded material
FIB	Focussed Ion Beam
HEMJ	He-cooled modular divertor with multiple-jet cooling
HETS	High efficiency thermal shield
HHF	High heat flux
HIP	Hot isostatic pressing
HRP	Hot radial pressing
HV	Hardness (Vickers)
ICRH	Ion cyclotron resonance heating
ITER	International Thermonuclear Experimental Reactor

JET	Joint European Torus
LVDT	linear variable differential transformer
NBI	Neutral beam injection
NDE	Non-destructive evaluation
NIF	National Ignition Facility
ODS	Oxygen dispersion strengthened
OFHC	Oxygen free high conductivity
PFC	Plasma fainting component
PID	Proportional integral derivative
RAFM	Reduced activation ferritic martensitic
SAM	Scanning acoustical microscope
SEM	Scanning electron microscope
TAF	Thermal autofrettage
XCT	X-ray computer tomography
XEC	X-ray elastic constant
XRD	X-ray diffraction

1 Introduction

The ever growing requirement for a sustainable energy source in the near future is one of the most significant challenges mankind has to face. Nuclear fusion is a potential energy source which has a historic reputation of perennially being "50 years away" from realization. However in recent times significant progress has been made in transforming decades of research on nuclear fusion into a real power plant delivering energy to the grid.

A critical aspect still to be resolved in advance of a demonstration power plant (DEMO) is fulfilling the design requirements of the divertor component. The demands on the divertor materials extend far beyond what is encountered in current power plant technologies such as fission reactors. A requirement for dissimilar material joining of an armour like material to a high performance structural and heat removal material is clearly apparent. In the work presented in this thesis, characterisation of dissimilar material joining of fusion relevant materials has been investigated.

The objective of the work presented within this thesis is to successfully join divertor relevant materials and to improve said joints. The criteria for a successful joint presented henceforth is a full face bond with the absence of large defects, voids and brittle intermetallics. The focus for improving the performance of joint was through improvement of residual stress state. Whilst other parameters are crucial in determining component performance, such as mechanical strength, fracture toughness, surface condition and absence of cracks, residual stresses are defined as the key parameter for the purposes of this study. This reflects the requirements of the funding proposal for the CASE award which provided funding for the study.

In Chapter 2 of this work, the background of nuclear fusion is discussed. The demands of the materials within a fusion divertor component, and the requirement for continued research in the areas of dissimilar joints and associated residual stresses are presented.

In Chapter 3 an experimental brazing study is conducted. Dissimilar material joints consisting of tungsten, copper and 316L stainless steel were manufactured through vacuum furnace brazing using a eutectic gold-copper interlayer. Metallurgical characterisation of the fabricated dissimilar material parts was conducted using optical and scanning electron microscopy, elemental analysis, and micro-hardness and nano indentation. Non-destructive evaluation of the as-brazed parts was investigated.

In Chapter 4, thermo-mechanical properties of the gold-copper brazing alloy are experimentally determined. The temperature dependent material properties are required for analytical predictions of residual stress arising from the brazing process. In addition to conventional material property characterisation, the use of micro-mechanical methods was adopted to assess mechanical properties of the brazing alloy, and parent materials, in the as-brazed condition. Nano indentation and FIB milled micro cantilever beams were tested. Electrothermal mechanical testing and dynamic thermal mechanical analysis were utilised for obtaining temperature dependent mechanical properties of the as-received brazing alloy.
In Chapter 5 the residual stress state in brazed dissimilar material joints is discussed. Theoretical determination of the free edge stress state is based on material property relationships is predicted. The material properties generated in Chapter 4 are then implemented into a finite element model to predict the brazing induced residual stress state of the parts manufactured in Chapter 3. The effect of key material properties on the resulting stress state is explored.

In Chapter 6 the predicted residual stresses from Chapter 5 are compared with experimentally determined values. X-ray diffraction is used to measure biaxial surface residual stresses. A stress relaxation technique, the Contour Method, is applied to determine 2D maps of stress distributions across the entire brazed parts manufactured in Chapter 3.

In Chapter 7 a method of residual stress modification of dissimilar material brazed joints is presented. Thermal autofrettage is used with an aim to improve the residual stress distribution by beneficially reducing free edge tensile stresses in the brittle tungsten material. The effects thermal autofrettage process on residual stress are predicted using finite element analysis. The process is then applied on the real brazed parts followed by residual stress characterisation.

2 Background

2.1 Introduction to nuclear fusion technology

With the population of the planet predicted to grow for the foreseeable future, there is an ever increasing requirement for a stable, sustainable energy supply. By the middle of the century the world population will have grown to 9 billion and demand for energy will have more than doubled [1-3]. With over 4 million people die each year as a result of indoor biomass burning [4], environmentally friendly fusion energy could provide energy solutions to many millions of people in developing countries .

Nuclear fusion has is theorised to be capable of meeting this energy demand [5-7]. An important benefit of fusion power is that a fusion power plant would emit no greenhouse gasses [8], whilst remaining economically competitive with alternative energy sources [9, 10]. Fusion plants are also absent of any fissile materials, so the risk of proliferation for militaristic purposes is minimal [8]. Conceptual fusion plant studies show that fusion can be as little as 50% more expensive than fossil fuels, whilst costing approximately the same as renewable or nuclear fission energy [11]. Fusion energy will also provide a steady supply of energy required for a baseline energy source, compared with transient renewable sources. The role of nuclear fusion energy should complement development of renewable energy sources to help increase energy production efficiency, reduce pollution and combat climate change [11].

Whilst conventional nuclear power, nuclear fission, is also a strong candidate for a primary energy source in the future, nuclear fusion does present several advantages over fission. Considering the high profile incidents nuclear energy is often associated with, such as Fukishima and Chernobyl, the safety of any nuclear plant is of upmost concern. Conceptual nuclear fusion plants are shown to have no risk of loss of containment of radioactive material during plant energy loss [7]. A further significant benefit that nuclear fusion has compared to nuclear fission is the vastly reduced radioactive waste and irradiated structural material [7, 8]. For these reasons; clean, safe, cost effective, and steady supply, nuclear fusion presents a very promising prospect for future energy generation.

Research into developing nuclear fusion towards an economically viable power plant has made steady progress over a number of decades. Currently there are several large scale fusion reactor-like machines including National Ignition Facility (NIF) [12], Joint European Torus (JET) [13]

and Wendelstein 7-x (W7-x) [14]. Additionally, the largest fusion experiment in history, International Tokomak Experimental Reactor (ITER) [15], is currently being built with the aim of achieving the long sought after milestone of 10 times the power out of the machine compared to power supplied (i.e. Q=10) [16]. A future demonstration nuclear fusion power plant, DEMO, is under conceptual design with a plan of producing electricity via nuclear fusion in the next few decades [17, 18]. The focus of this thesis is on materials relevant to magnetic confinement fusion reactors, such as ITER and DEMO, as opposed to inertial confinement concepts such as NIF.

The concept of nuclear fusion is essentially replicating the process which occurs in stars such as our sun. Hydrogen atoms fuse and produce a helium atom and highly energetic neutron. This process requires extremely high temperatures and the immense pressure caused by the gravity of the sun [19]. Thankfully this process can be mimicked here on Earth in considerably shorter timescale using the reaction between two isotopes of hydrogen, namely deuterium (D) and tritium (T). The deuterium-tritium (D-T) reaction can be seen in Figure 2-1 [20]. The D-T fusion reaction result in an extremely high energy neutron being output alongside a helium atom. The goal of a fusion power plant is to harness the heat generated from this process to produce energy through conventional steam generation.

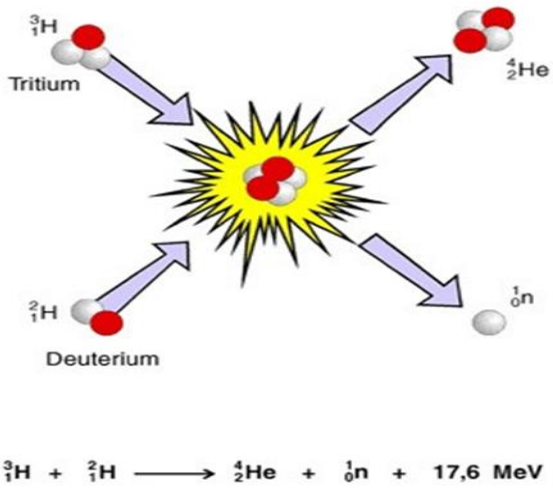

Figure 2-1 - Deuterium-tritium fusion reaction

This reaction requires temperatures greater than 100 million °C and a method for confining the extremely hot hydrogen plasma. One solution is to employ a tokamak type design, which is a means of magnetically confining the plasma using extremely powerful superconducting magnets. The tokamak (toroidal chamber with magnetic coils) was devised by Soviet physicists Sakharov and Tamm in 1951 [21]. A typical tokamak can be seen in Figure 2-2. The Lorentz force generated in the strong magnetic field acts on the plasma and can be manipulated to create a stable plasma at temperatures in excess of 100 million °C [22].

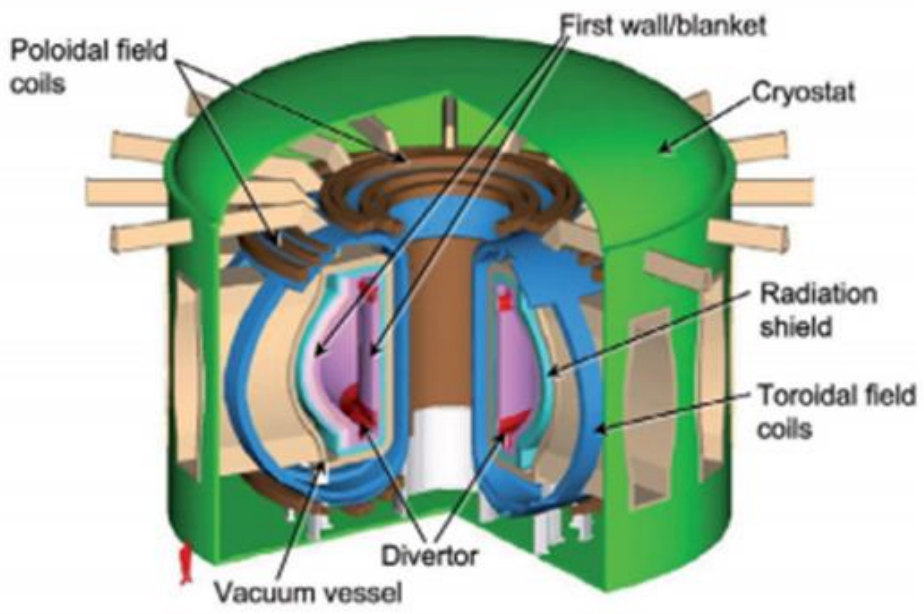

Figure 2-2 – Main features of magnetic confinement tokamak reactor [22]

The plasma is heated via a combination of current drive (Ohmic), ion cyclotron radiative heating (ICRH) and neutral beam injection (NBI) to c. 100 million °C. The plasma is controlled and stabilised using the toroidal and poloidal field coils comprised of liquid helium cooled niobium superconducting magnets [23]. The first wall (blanket) and divertor make up the plasma facing components (PFCs). Heat is extracted through the PFCs, which also act to shield sensitive components from the brunt of the neutron irradiation. The divertor, shown towards the bottom of the tokamak in Figure 2-2, is a critical component with extraordinary demands on material performance.

2.2 Divertor concepts and materials

The primary purpose of the divertor is to act as a high heat flux (HHF) component to extract heat from the plasma for energy generation. Additional requirements of the divertor are to act as an exhaust for helium and to remove dust and impurities to help maintain plasma operation [24].

The demands on the divertor component are extreme, and as such research into divertor materials and joining of different materials is a key focus of fusion research activity [25, 26].

The divertor is subjected to high thermal loads. For ITER, current divertor designs require a quasi-steady state heat flux of 10MW/m^2 with peak transient fluxes of up to 20MW/m^2 during

transient ELM (Edge Located Mode plasma disruption) events [27]. These requirements are exponentially higher than those of current fission reactors of approx. 0.5MW/m². Despite the small surface area of the divertor relative to the other PFCs, almost 15% of the total thermal fusion power is removed by the series of divertor cassettes [25].

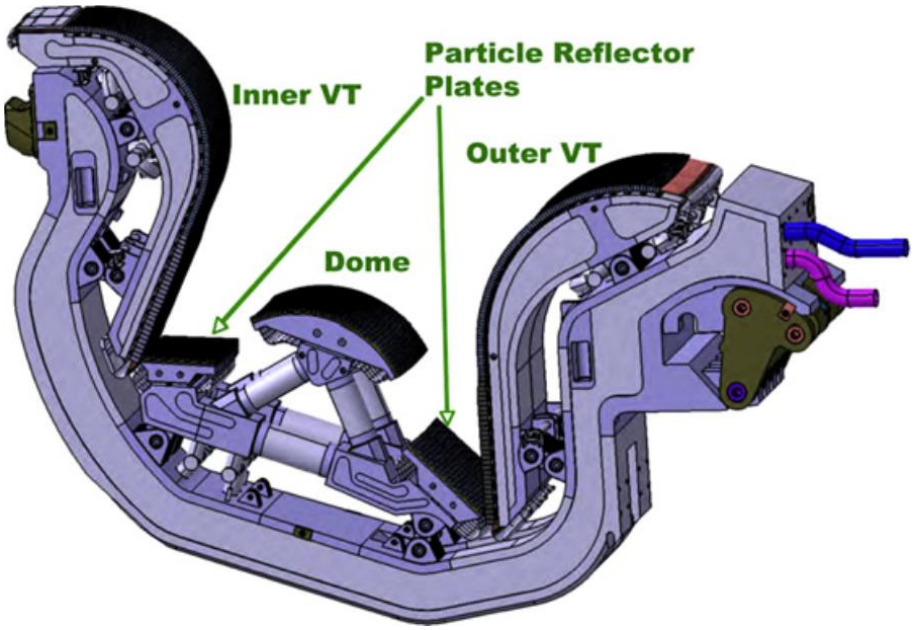

Figure 2-3 - ITER divertor component [28]

The divertor is subject to extremely high heat flux of 5-20MW/m², neutron sputtering damage, high operating temperatures and in excess of 300 thermal loading cycles at 20MW/m² [29]. Shown in Figure 2-3, the plasma facing surfaces consist of inner and outer vertical targets (VT), a central dome and particle reflector plates. Each of these surfaces require "armour" material. Additionally, the divertor has structural requirements and a need for high thermal extraction, and as such the requirements cannot be met by any single material [5, 10, 28, 30]. Divertor concept designs therefore use a combination of a plasma facing material called the "armour" material joined in some manner to a heat sink, structural material or combination of materials.

Tungsten has been identified as a suitable armour material due to its high thermal performance (highest melting point of any metal), erosion-corrosion resistance and relatively good neutron damage tolerance [31, 32]. The high melting temperature of tungsten (c. 3,400°C) is required as during peak thermal loads of 20MW/m² will result in surface temperatures in excess of 2,000°C [33]. In addition to the divertor, tungsten or tungsten alloys have been identified as potentially suitable candidates as the armour material for the blanket/first wall which covers the majority of the plasma facing surface area [32, 34]. One of the major concerns with tungsten as an armour material is the effect of neutron embrittlement at temperatures below 900°C [35]. Tungsten is an

inherently brittle material, with a ductile-brittle transition temperature (DBTT) of c. 500°C [32]. A brittle structural material is not desirable in terms of plant reliability, hence the need for a ductile structural material.

Whilst the design of a DEMO divertor remains fluid, it is not possible to determine exactly the likely operating parameters which will be considered when selecting materials. These parameters include service temperatures and the related magnitude of thermal loading on divertor tiles. However there are assumptions that can be made when assessing the likely failure and degradation mechanisms that will be pertinent to divertor design and operation.

The coolant temperature, for example, with a water cooled design the coolant temperature will be in order of 100°C. With steady state surface temperatures of the armour material in excess of 1000°C, a minimum temperature gradient of 900°C can then be found across the dissimilar material divertor tile. The location for the dissimilar material joint therefore has to be carefully selected such that each individual material is operating within appropriate conditions. Tungsten, for example, exhibits purely ductile behaviour above 900°C [26], so a joint where the structural part of the dissimilar joint is as high is possible is beneficial in regards to the fracture toughness of tungsten. However by increasing the dissimilar joint operating temperature, degradation mechanism such as creep become more critical in any interlayer and structural material. Careful consideration is required to ensure an appropriate trade off.
A helium cooled divertor can have an inlet cooling temperature of c. 700°C, allowing a high operating temperature for the tungsten material [26]. As described previously, this is beneficial in terms of avoiding brittle fracture of tungsten during operation. However the increased operating temperature will have undesirable effects on an interlayer material and structural material such as ODS steel, in particular with regards to creep damage.

Due to differences in thermal expansion between materials, upon cycling of the fusion reactor, a cyclic thermal stress is applied. Fatigue performance of the divertor, and in particular a dissimilar material joint, is therefore an important factor. The nature of the fatigue failure could be both high and low cycle fatigue, caused by continuous temperature fluctuations during quasi-steady state plasma conditions [36], and overall plant power up/down respectively.

Fatigue and creep are degradation mechanisms known to be strongly affected by the presence of residual stress [37]. It is therefore concluded that residual stress within the divertor component, and in particular the dissimilar material joint, is an extremely important consideration for divertor design.

2.2.1 Water-cooled flat tile and monoblock designs

There are multiple design variations for how to incorporate the armour and heat sink materials in the form of a divertor tile suitable for use in a DEMO like tokamak reactor. These include monoblock designs [33, 38], flat tile designs [25] and jet-impingement concepts. [39]. An example of a W/Cu/CuCrZr set up is shown in Figure 2-4 for both flat tile and monoblock configurations (recreated from KIT Fusion Summer School course notes [40]).

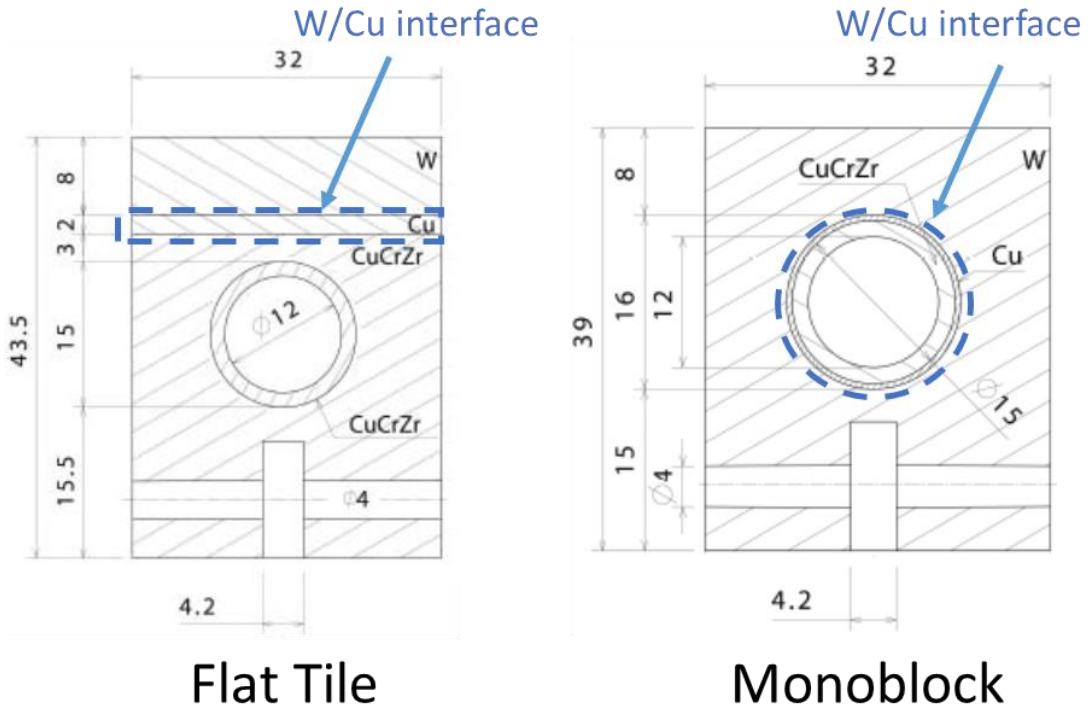

Figure 2-4 - Flat tile and monoblock divertor concepts [40]

The flat tile design consists of an 8mm thick tungsten armour section joined to the CuCrZr heat sink section in with a simple, flat interface. Whereas the monoblock design utilises a solid block of tungsten with a CuCrZr heat sink pipe bonded in the centre of the part.

The initial reference design for ITER divertor consisted of a carbon fibre composite (CFC) as the armour material in the form of a monoblock, with a CuCrZr heat sink material [25]. A transition to a full tungsten divertor, which is more applicable to a future DEMO design, was planned for a second divertor. However due to budget restrictions a full tungsten divertor is planned for initial use in ITER [41].

The current Japanese concept for a full tungsten divertor for ITER includes a tungsten monoblock with CuCrZr cooling tube [42]. A pure copper interlayer is used for bonding of tungsten to CuCrZr,. The pure copper is bonded with the tungsten monoblock with diffusion bonding, direct casting and hot isostatic pressing (HIPing), with different suppliers using different methods. The tungsten-copper part is then joined to the CuCrZr pipe by a brazing process using a 50μm thick Ni–Cu–Mn alloy (NiCuMan-37) brazing layer.

High-heat flux testing of ITER conceptual divertor concepts has been performed to demonstrate the suitability of tungsten-copper configurations to meet the ITER design requirements [43]. For this study tungsten was bonded to CuCrZr heat sink material using a pure copper interlayer. Acceptable test results were achieved for favourable operating conditions, however harsher conditions highlighted a need for continued development of balancing the combination of tungsten armour tile thickness with heat removal of the copper and CuCrZr.

Visca et. al [44] also assessed the performance of the ITER tungsten monoblock mock-up as shown in Figure 2-5. Instead of vacuum brazing, hot radial pressing (HRP) was used for the bonding of the tungsten tile to the CuCrZr, following preliminary step of direct casting of copper onto the tungsten material. Six mock-ups were manufactured in this method, with two been unaccepted due to not meeting the defined criteria of: defects under 4mm in size, no more than 10% total defect area, and a restriction on proximity of two or more small defects. As with Gavila [43], the HHF testing of HRP tungsten monoblocks found that the testing requirements were at the very limit of the performance of the mock-up. The need for better performance and improved quality of joints, and hence less unacceptance, highlights the need for further research of tungsten-copper dissimilar joints for a DEMO divertor.

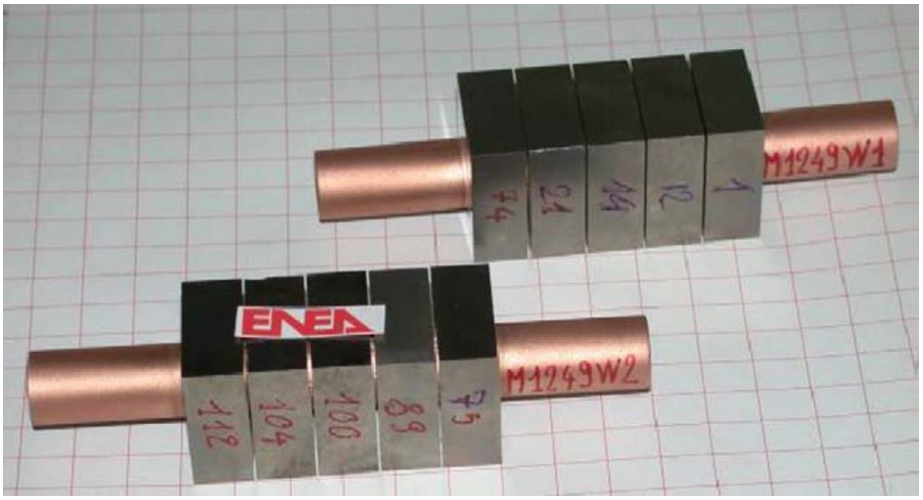

Figure 2-5 - ITER divertor mock-up for HHF testing with tungsten monoblack and CuCrZr heat sink pipe

The use of vacuum brazed tungsten-copper dissimilar material joints was investigated [45]. This consisted of a flat tile type design, with a tungsten tile, oxygen free high conductivity (OFHC) copper block and an oxygen dispersion strengthened (ODS) copper coolant pipe. Difficulty was found when joining the vastly dissimilar tungsten and copper. High residual stresses developed due to dissimilarity in CTE and elastic modulus.

2.2.2 Helium cooled divertor design

In order to transition from an ITER divertor to the more demanding thermal regime of the DEMO divertor, the transition from CuCrZr for the heat sink to advanced steels such as ODS or RAFM (reduced activation ferritic martensitic) steel has been suggested [46]. The dissimilar material interface of a monoblock design consisting of tungsten and F82H RAFM steel is shown in Figure 2-6.

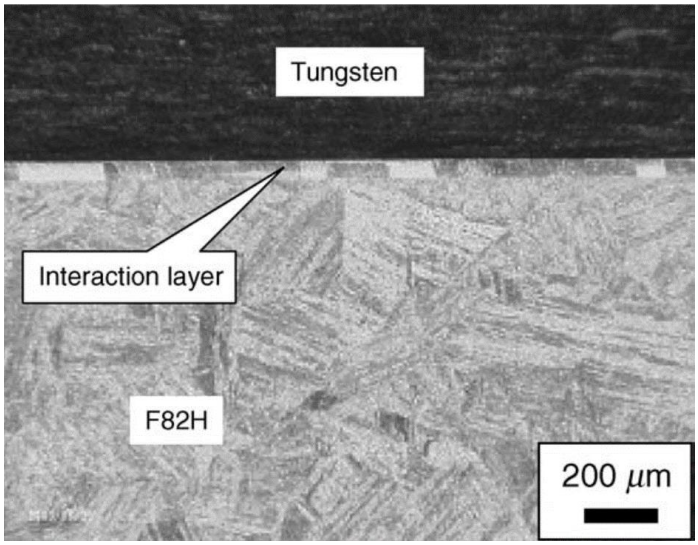

Figure 2-6 - HIPed tungsten and RAFM dissimilar joint [46]

The tungsten-RAFM steel dissimilar joint could then be incorporated into a full conceptual design for a DEMO ready divertor [26], shown in Figure 2-7.

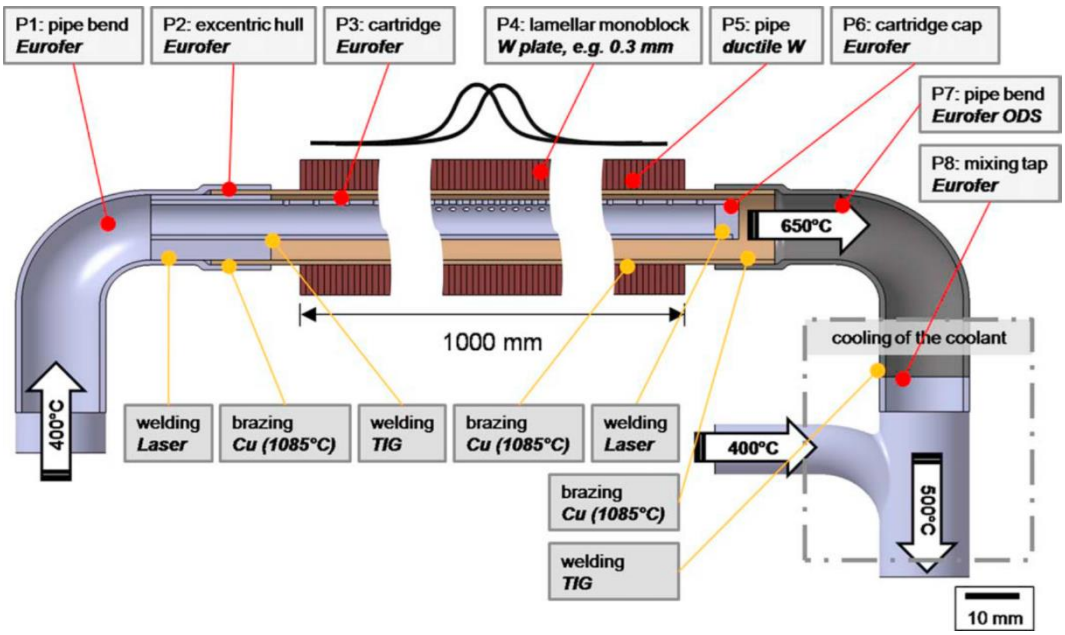

Figure 2-7 - Helium cooled divertor concept for DEMO [26]

The concept shown in Figure 2-7 contains a wide range of materials and requirements for dissimilar material joining. Tungsten, RAFM steel, ODS steel and copper are all present. Brazing, diffusion bonding, HRP and HIP have been shown to be potentially suitable joining methods (based on literature discussed in this section). However one restriction that exists is the need to avoid direct bonding of tungsten to steel, due to brittle intermetallic Fe compounds forming [26]. The use of a copper compliance layer exists in many divertor concepts [35]. Therefore there is an apparent appetite for continued research into dissimilar material joining of tungsten, copper and steel alloys.

2.2.3 HEMJ design

Jet-impingement type divertor tiles are strongly considered for DEMO applications. The HEMJ (He-cooled modular divertor with multiple-jet cooling) has been investigated in several studies [30, 47-50]. The HEMJ concept is shown in Figure 2-8.

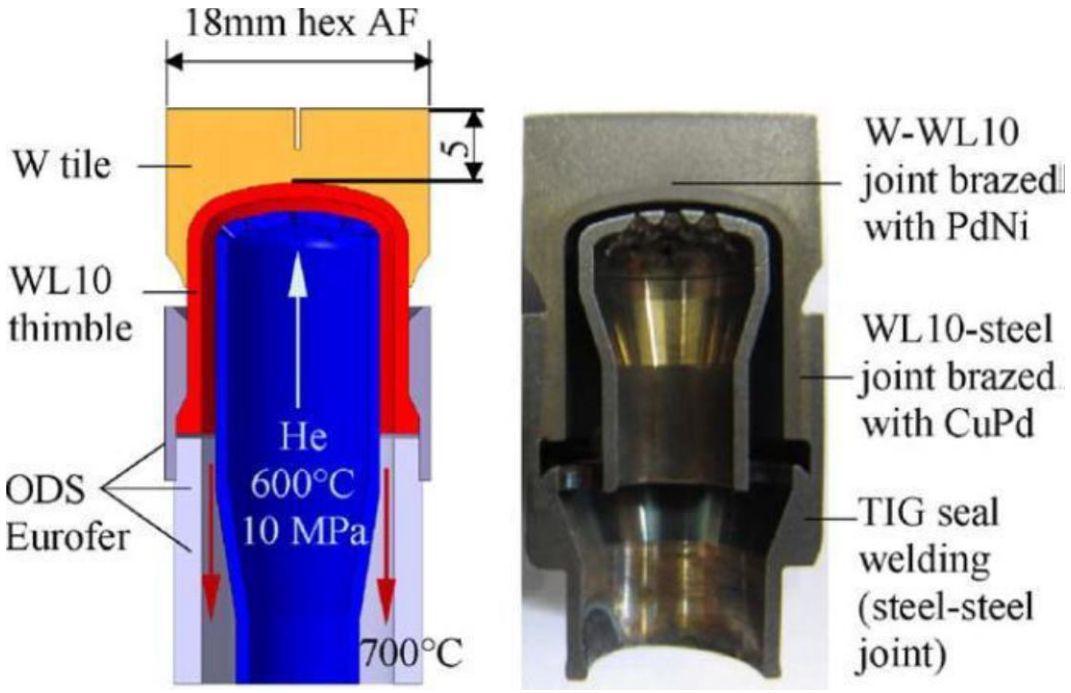

Figure 2-8 - HEMJ Divertor concept [50]

The HEMJ concept consists of a solid tungsten tile, or tungsten alloy such as WL10 (tungsten, 10% lanthanum), bonded to a tungsten thimble which in turn is bonded to a steel structure. Steel candidates include ODS steels and RAFM steels, such as EUROFER-97 and ODS EUROFER respectively [51].

A number of bonding techniques and joining/interlayer materials have been considered for the dissimilar material joining in the HEMJ concept. From Figure 2-8, brazing with palladium-nickel (PdNi) and copper-palladium (CuPd) was used for tungsten dissimilar material bonds, with TIG welding for steel-steel joining [50]. In a separate work by the same author, Norajitra et. al. experimentally fabricated and tested a number of thimble-tile joining options [48]. Vacuum brazing was utilised with copper-nickel interlayer (CuNi44) and nickel solder material interlayer (STEMET 1311). Joining of the thimble to the steel sleeve was achieved through a cobalt based brazing filler 971KHCP).

A critical shortcoming in the HEMJ design is the gap in the operational temperature window of the tungsten armour tile and structural steel materials [26]. Temperatures for which tungsten is no longer brittle exceed desirable temperatures for the steels considered. For optimal performance the tungsten should operate above 900°C, whereas ODS and RAFM steels should not exceed

650°C. This highlights the need for continued development of divertor concepts and research into advanced divertor materials.

2.2.4 Other divertor concepts

Ductilisation of tungsten has been investigated as a means to provide a bridge to the gap in operating temperatures of the armour and structural materials. This has been investigated through use of ductile tungsten laminate foils [52]. This material was shown to have favourable ductile characteristics [53], however the content of silver in the composition of the foil precludes it from fusion applications in its current development [52]. Recent research into the Ductilisation of tungsten through cold rolling shows promising results with obvious fusion divertor relevance [54].

Alternative divertor tile concepts include a high efficiency thermal shield device (HETS) [55] and a CuCrZr hexagonal heat sink concept [56]. Both of these concepts show promising thermal performance, although selection and development of armour materials and dissimilar material joining methods require further research.

2.3 Dissimilar material joining for divertor concepts

2.3.1 Diffusion bonding and HIPing

Dissimilar material joining of tungsten to fusion relevant structural materials has been studied in many sources of literature. Wang et al [57] produced tungsten-copper dissimilar material joints using a graded tungsten-copper alloy interlayer and amorphous tungsten-iron coatings. The direct bonding of tungsten to copper was avoided due to the high residual stresses that develop due to material property dissimilarity. The study concluded that good thermal shock resistance was obtained for the configuration, which could result in integration of this type of brazed and HRPed configuration into a divertor conceptual design.

The requirement of an interlayer between tungsten and copper was achieved through the use of vanadium [58]. HIPing was employed as the joining mechanism here. Successful bonding was achieved, however upon mechanical testing failure occurred in the bulk tungsten material. This was attributed to high thermally induced residual stresses in tungsten. This suggests that

understanding of the residual stress state, and reducing damaging residual stresses in tungsten, is required when dissimilarly bonding tungsten to copper.

An analytical study was conducted investigating the suitability of brazing for the joining of a tungsten alloy (WL10) to ODS steel for a DEMO divertor concept [59]. Different brazing configurations were investigated using FEM. It was found that both simple 90°, butt joints, and conical type joints, produced satisfactory results in terms of shear stress, ratcheting and plastic strain.

Dissimilar material joining of tungsten to copper through use of functional grading is perceived as an attractive solution with long term performance benefits [60].

2.3.2 Vacuum brazing

The joining of tungsten to RAFM steels through the use of vacuum brazing with a compliance interlayer has been achieved. As discussed in section 2.2, the use of pure copper as an interlayer between tungsten and steel is often cited. Alternative interlayer materials include titanium and iron based alloys [61] in addition to nickel-chromium based alloys [62]. Brazing induced residual stresses were observed in the braze interface region [62]. These residual stresses were partially relaxed due to the development of plastic strains. The potential susceptibility of fatigue and ratcheting under cyclic loading were identified as a cause for concern. The presence of elements including Fe and Ti can lead to the formation of brittle intermetallic compounds. A significant physicochemical interaction between parent materials and the interlayer materials was found, necessitating further research into the effects on the joint, particularly under irradiated conditions [61].

A nickel interlayer was used for a tungsten to ferritic steel brazed joint [63]. A successful braze with minimal bonding flaws or cracks was achieved. It was found that increased holding time at high temperature increased the tensile strength of the joint, however at a certain point (over 1 hour) there begins to form brittle tungsten nickel intermetallic compounds and hence degradation of mechanical strength. The brazed interface of tungsten and nickel is shown in Figure 2-9 .

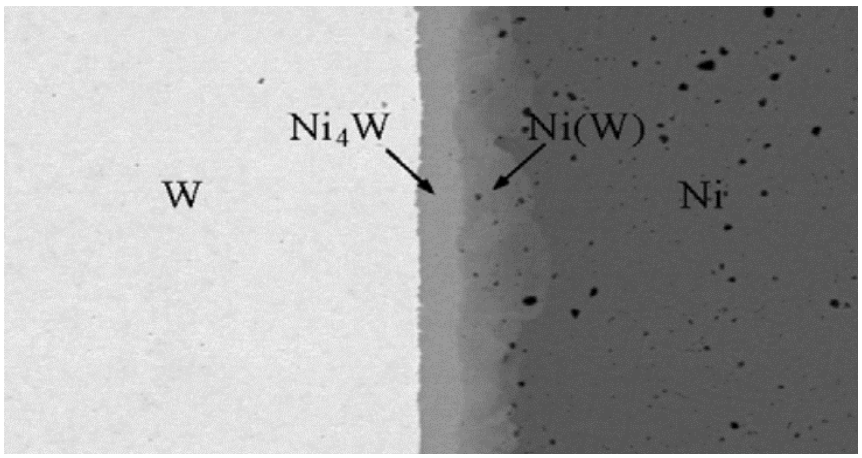

Figure 2-9 - Tungsten-nickel brazed interface with intermetallic compounds

2.4 Residual stress in dissimilar material joints

The presence of residual stress following dissimilar material joining, and subsequent effect on performance, was discussed briefly in section 2.3 for divertor relevant configurations. In this section the more general considerations for residual stress development following joining are discussed.

Residual stresses are those which exist in a part upon which no external forces are applied [37]. They arise from an incompatibility within a part, for example a large characteristic length scale scenario of geometrical misfit (for example an oversized part within a smaller cavity such as in shrink fitting) and steel thermal gradients, or from a localised effect such as differential phase transformation within an alloy [64]. In the case of dissimilar material joining as considered in this thesis, residual stresses arise from the incompatibility of thermal expansion/contraction due to differences in CTE and elastic modulus [65, 66].

The existence of residual stresses can degrade the performance of dissimilar material joints, and failure to account for them can result in unexpected, catastrophic failure [66]. The materials considered for armour (tungsten, WL10) and structural (steel, copper) materials in a divertor are by extremely dissimilar in nature, an inherent issue of the varied demands on the component.

Residual stresses are self-equilibrating elastic stresses and are classified over the characteristic length scale upon which they act [37]. Residual stresses are classified as one of three types:

- Type I – Macro stresses, continuum scale which are self-equilibrating over the length of a part and are not a function of local microstructural effects
- Type II – Micro scale stresses are microstructural dominated stresses that act on the length scale of several grains
- Type III – Micro scale stresses that act within a single grain at the atomic scale.

The stresses which are heavily influenced by dissimilar material joining are type I and type II in nature. Stresses of this order can be readily measured using experimental techniques such as Contour Method (Type I) a X-ray diffraction (Type I and II, or meso-scale) [67].

Cooling from high temperature dissimilar material joining can result in high interfacial stresses (with length scales typical of type I to type II stresses). When bonding a stiff, low CTE material such as tungsten, or a ceramic material, to a less stiff, higher CTE material such as copper or steel, high residual stresses are commonly encountered [66, 68].

The effect of high joining induced residual stresses can be negative and significant for the structural integrity of a dissimilar joint. A vanadium-ceramic joint with proposed application for a divertor was found to contain residual stresses of such magnitude that cracking of alumina occurs, and successful bonding could not be achieved [69]. Similar dissimilar interface cracking has been observed for titanium-molybdenum [70] and tungsten-copper [58] joints.

For a part such as the divertor which is subject to cyclic thermal loading, a mismatch in CTE will result in operational stress in addition to joining induced residual stress. The development of a crack was found for a CFC-copper joint [71]. In this instance, the presence of a ductile interlayer resulted in stress relieving at the crack tip. This suggests that for a tungsten-copper interface, if the cracking can be avoided in the brittle tungsten material then increased fatigue life could be obtained even in the presence of interfacial cracks.

The divertor will be subject to multiple degradation mechanisms including low and high cycle fatigue (induced through thermal loading), creep, radiation erosion, radiation embrittlement and corrosion [28, 72]. Each of these degradation mechanisms are known to be detrimentally affected by the presence of high magnitude residual stresses [37]. It is therefore an important to understand the presence of residual stresses within a divertor in order to predict the structural integrity of the component over its proposed operational lifetime.

Whilst the residual stress state will be altered at operating conditions, as compared with room temperature values which are more readily obtained, the existing residual stress state will still have an effect on component performance. The tungsten-interlayer interface for example, where cracking is postulated to be an issue, is more susceptible to cracking at lower temperatures. Therefore, the presence of residual stresses at temperatures below operating temperature (such as during heat up/cool down and maintenance operations), careful control of the residual stresses can avoid unexpected fractures. Research into the changes in residual stresses for a given divertor design and operation regime is required to determine the influence of residual stresses at operational temperatures.

Additionally, as evidenced in 2.3.2, the presence of residual stresses in dissimilar material divertor tiles are significant enough to cause fracture of test blocks during the manufacturing process. It is clear that fractures of this nature are not acceptable for full scale production components. This further emphasises the need to better understand, predict and control damaging residual stresses in dissimilar material divertor components.

2.5 Summary

In this chapter the requirement for dissimilar material joining of tungsten, copper and steel alloys has been determined. The divertor component of a fusion reactor is subject to extreme demands including thermal loading, neutron irradiation and cyclic performance requirements. No individual material as yet exists to satisfy these demands. Therefore current divertor component designs (such as ITER) or conceptual designs (such as DEMO) require bonding of an armour and structural/heat sink material.

Tungsten has been identified as a primary candidate for the armour material, with copper and steel alloys currently preferred for heat sink and structural requirements. There exist many concepts for a DEMO divertor, however all require dissimilar joining of these materials.

The dissimilarity of the materials under consideration is problematic in terms of practical fabrication of components. A significant disparity in properties such as CTE and elastic modulus results in high residual stresses during joining. Also the formation of brittle intermetallics is often observed. Combined these factors act to degrade the performance of dissimilar material joints. A requirement for further research into the development of tungsten based dissimilar material joints including understanding of residual stresses is clear to see.

3 Brazing Development and Metallurgical Characterisation

This work presented in this chapter investigates the development of the brazing procedure for bonding fusion relevant dissimilar materials and the metallurgy of the resulting brazed specimens. The primary joining technique used is vacuum furnace brazing. Other options that were considered are induction brazing (in vacuum) and hot isostatic pressing (HIPing).

This chapter shall focus on the bonding of tungsten to two materials that have potential applications in the divertor of a future fusion reactor, namely oxygen free high conductivity (OFHC) copper and 316L stainless steel. The primary brazing material used is a eutectic gold copper alloy with composition Au80%wt Cu20%wt. Also considered is the combination of 316L stainless steel-copper. The addition of the Cu-316L combination was to provide a specimen without the extreme differences in material properties that is present with copper and tungsten. This approach was employed to reduce the risk of obtaining no useful results from a possible failed braze of the two vastly dissimilar metals (tungsten and copper).

3.1 Introduction and materials

A future fusion reactor will have extreme and unique demands on material performance. The divertor component is a prime example of this. The divertor will have to withstand extraordinarily high thermal loads and neutron bombardment. The divertor of a demonstration thermonuclear fusion reactor (e.g. DEMO) will be subjected to unprecedented high thermal loads and high neutron fluence [73]. The first wall will experience thermal loads in excess of 3 MW/m^2 with peak loads on the divertor of 10 MW/m^2 and up to 20 MW/m^2 during transient occurrences known as ELMs [5, 7, 32, 73]. Temperatures in excess of 1000°C are expected in the armour tile [74].In order to ensure economic viability of fusion power and reduce the need for armour tile replacements it is necessary to have erosion of around 0.1mm/year [5]. It is necessary to ensure high heat transfer from the plasma to the coolant (water or helium)[10, 25, 30]. Materials that are capable of meeting these demands are few and far between. Currently no single material is capable of meeting all the demands of the divertor loading. Therefore the divertor shall be comprised of a variety of materials that in combination can meet these requirements [6, 32, 45, 75].

Tungsten has been identified as a likely candidate for the armour material due to its high melting point and high corrosion-erosion and neutron damage resistance [27, 31, 76-78].

Other materials including vanadium [79] and tungsten alloys containing relatively exotic elements, such as lanthanum, rhenium and yttrium are also considered in divertor concepts [77, 80]. However for the purposes of the work contained in this thesis only pure tungsten shall be considered. The reasoning for this was due to material availability, reducing complexity in an already little understood material system and the fact that pure tungsten on its own has promising applications within the fusion environment.

In this chapter two materials have been considered for the structural, or "heat sink", material, copper and 316L austenitic stainless steel.

Copper and many of its alloys are present in a multitude of divertor concepts [26]. The main reason for this is due to coppers very capable heat transfer properties. Copper and its alloys also has relatively good performance under radiation conditions although neutron embrittlement has been observed [25, 49].

Pure copper is considered primarily as a compliance layer between tungsten and either a copper alloy or steel. The alloy copper chrome zirconium (CuCrZr) is often considered. However there are additional complexities when brazing alloys like CuCrZr due to the risk of elements coming out of solution and preventing a barrier to brazing. Therefore as the purpose of the work presented within chapter is to successfully bond tungsten to a heat sink material for later metallurgical analysis and later residual stress analysis, pure copper was deemed the most appropriate material.

Two grades of copper were trialled in this chapter, commercial high purity CW-004 and oxygen free high conductivity (OFHC) copper. As shall be discussed later in the chapter only the OFHC variety was suitable for successfully brazing these materials.

The alternative heat sink material assessed in this work is 316L austenitic stainless steel. This is a molybdenum-bearing austenitic alloy demonstrating high toughness, creep resistance and corrosion resistance [26, 47]. 316L features in many potential DEMO divertor designs [26, 51, 77, 81] and is heavily utilised in ITER first wall components [27, 80, 82-84].

Reduced activation ferritic martensitic (RAFM) steels are another promising structural material for a fusion reactor [85-89]. The brazing of RAFM steels with tungsten have been investigated by colleagues at the University of Strathclyde and by the wider fusion technology community [90,

91]. Due the difficulty of obtaining sufficient quantities of RAFM steel, such as EUROFER, this material was discounted for this study.

3.2 Brazing process development

The dissimilar material joints were produced using the brazing technique. This is a process that involves heating the materials up with a joining alloy between them. The interlayer material is selected so as to be fully liquidus well below melting of the parent materials [92-94]. This ensures that the brazing interlayer material is fully melted and the parent materials are fully solid. The molten filler material is drawn to the surfaces of the parent materials to be joined by capillary action. Upon the cooling the filler material solidifies on the parent materials, joining the materials through atomic bonding.

The extent of the wetted area i.e. the degree of surface area bonded during brazing is dependent on a number of parameters including chemical composition of materials, contact angle, viscosity of molten filler material, atmospheric conditions and metallurgical reactions between the parent and filler metals [93].

Two variations of brazing were considered, namely vacuum furnace brazing and induction brazing. A vacuum or reduced atmosphere environment is required to prevent oxidization of the surfaces to be bonded during heating.

Vacuum brazing was performed commercially at Special Techniques Group, Culham [95]. The induction furnace brazing using a reduced atmosphere was performed at Strathclyde.

The AuCu brazing material is a eutectic alloy with a melting temperature of 910°C. The AuCu phase diagram is presented in Figure 3-1. The eutectic point for this binary system is with 80% wt balance of gold, as with the brazing alloy used. The face-centred tetragonal structure of AuCu, named AuCu I, undergoes a phase change at circa 300°C to longer ordered AuCu II. This phase change is regarded as phenomenologically similar to a martensitic transformation with volumetric change [96, 97] AuCu II then transforms to FCC structure at circa 400°C [96]. The material becomes fully liquidus at the eutectic temperature of 910°C. To ensure full melting of the material throughout the part brazing is usually performed at 30-50°C above the melting temperature [93]. Therefore for vacuum brazing temperatures ranged from 950°C to 1000°C for the trials in this study. Induction brazing is discussed in section 3.5.

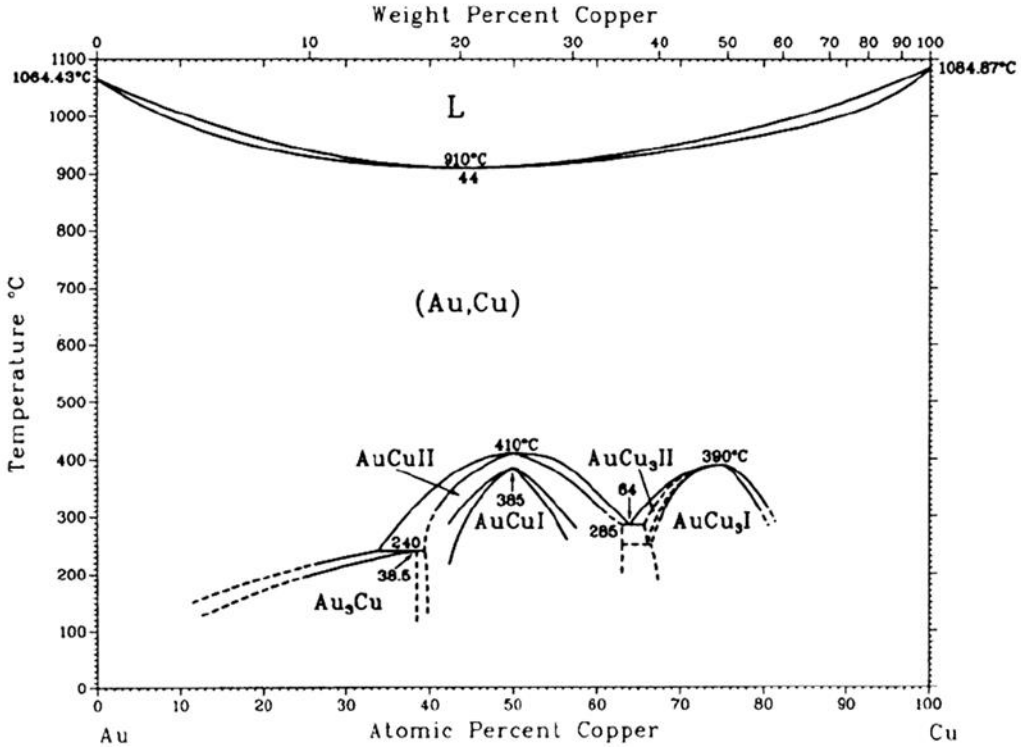

Figure 3-1 - Au Cu Phase Diagram [98]

Two dissimilar material sample geometries were manufactured. A smaller, characterisation sized set of samples were manufactured primarily for characterisation by optical and electron microscopy, micro-hardness, nano-indentation, FIB milling and elemental analysis. These samples have dimensions of 20.05mm length with 12.7mm diameter (consisting of 2 separate 10mm long, 12.7mm diameter parent materials and 0.05mm thick AuCu brazing foil joined in a butt joint configuration).

The second sample geometry was a longer specimen for the purposes of residual stress analysis. These dissimilar structures comprised of 2 parent materials with 25mm length, 0.05mm thick brazing alloy as before, joined in a butt joint configuration. The sample designs are presented in Figure 3-2.

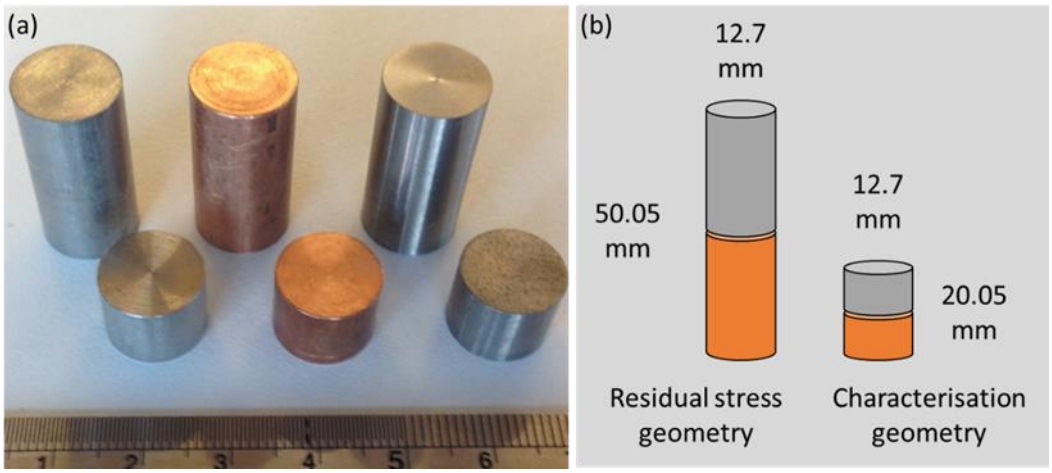

Figure 3-2 - (a) As-received parent materials from left to right 316L, OFHC Cu and W and (b) Brazed specimen geometry design

The characterisation samples were not considered to be dependent on consistent alignment. These samples were prepared by cleaning in an ultrasonic bath in an alcohol solvent. A disc of brazing alloy was then positioned on the surfaces to be joined. The two parts were then clamped with the AuCu foil between them.

The longer samples required attention for geometrical alignment. Angular and axial misalignment during brazing is known to significantly affect the residual and operational stress field in a dissimilar material component [99]. These parts used three ceramic rods located axially on the outside of the parts. These were tied using Niobium wire, and clamped securely on the ends. The wire and ceramic rods were then removed, leaving aligned, clamped parts ready to be placed in the vacuum furnace for brazing.

The rods were then removed to avoid material deposits on the outside of the part. This phenomenon was experienced during previous brazing experiments [91, 100]. These deposits could be detrimental to the outcome of the study in two ways. Firstly brazing alloy material migrating to the side of the sample results in a smaller volume of alloy in the interface of between the parent materials. This could leave voids or completely non bonded areas.

Secondly, these deposits would provide a stress concentration if fatigue testing is to be performed. This would necessitate surface machining of the parts. The vacuum chamber and clamping arrangements are displayed in Figure 3-3. Table 3-1 presents a summary of brazing trials conducted.

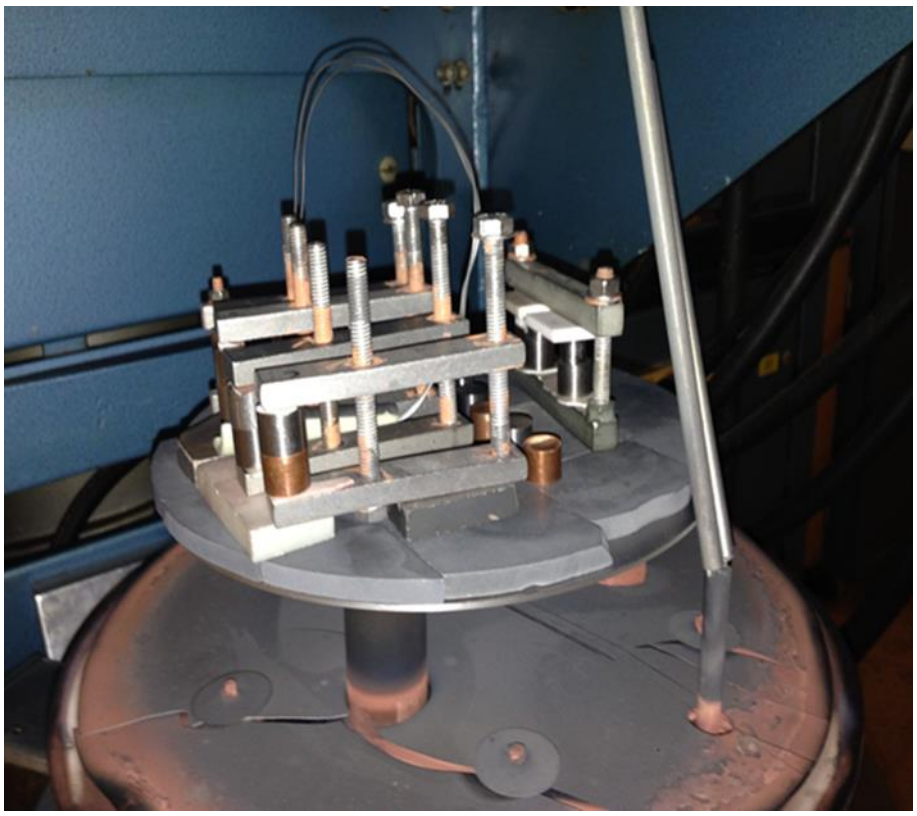

Figure 3-3 - Vacuum furnace chamber and clamped parts

Table 3-1 - Brazing trial summary

Brazing Trial	Vacuum Furnace	Brazing Alloy	Parent Materials	Brazing Temperature
1	Supplier A	Au80Cu19Fe1	OFHC Cu, W, 316L, EUROFER	1000°C
2	Supplier A	Au80Cu20	W, CW-004a Cu	930°C
3	Supplier A	Au80Cu20	W, CW-004a Cu	950°C
4	Supplier B	Au80Cu20	W, CW-004a Cu	950°C
5	Supplier A	Au80Cu20	W, OFHC Cu, 316L	950°C

3.2.1 Au80Cu19Fe1 - Collaborative brazing project

Initial brazing trials using Au80Cu19Fe1 were performed in collaboration with colleagues at the University of Strathclyde and Culham Centre for Fusion Energy (CCFE).

The brazing parameters and materials for this project are detailed as Trial 1 in Table 3-1. These trails have been reported in further detail in [90, 91]. The grade of AuCu brazing alloy used,

Au80Cu19Fe1, contained a small % wt balance of Fe to improve wetting and capillary flow characteristics.

All of the materials were cleaned thoroughly using firstly an ultrasonic alcohol bath, followed by a final cleaning with acetone. The samples were clamped together to minimize misalignment. The samples were then placed in the vacuum chamber. A vacuum of $1x10^{-4}$ to $1x10^{-5}$ millibar was drawn. The furnace was heated to the appropriate brazing temperature at a rate of about 10°C/min. The furnace dwelled at the brazing temperature for 5 minutes before slowly cooling over several hours to avoid thermal shock.

Bonding of the parent materials was achieved however there were significant flaws found within the bonded structures. W, Cu, 316L and EUROFER RAFM steel were considered for this study. Examples of such voids presented in Figure 3-4 and Figure 3-5.

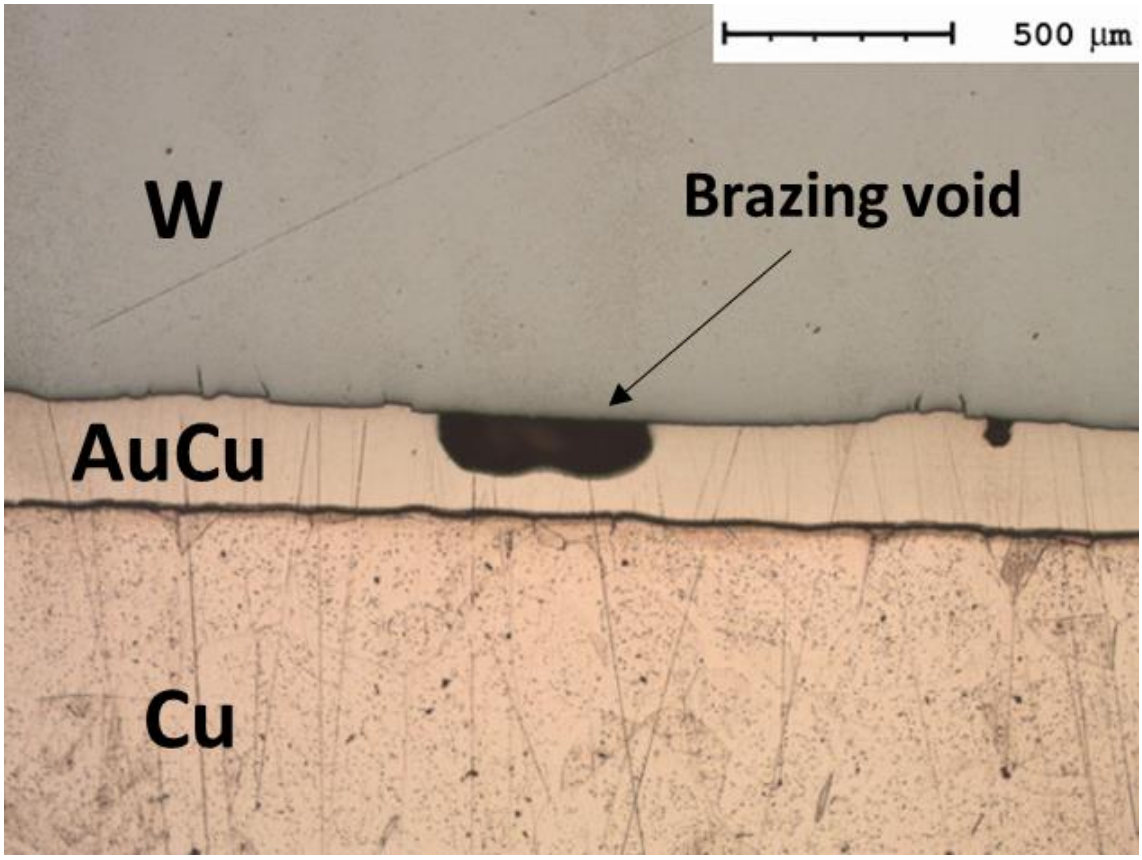

Figure 3-4 - W-Au80Cu19Fe1-Cu vacuum brazed joint demonstrating void in braze region at the W interface

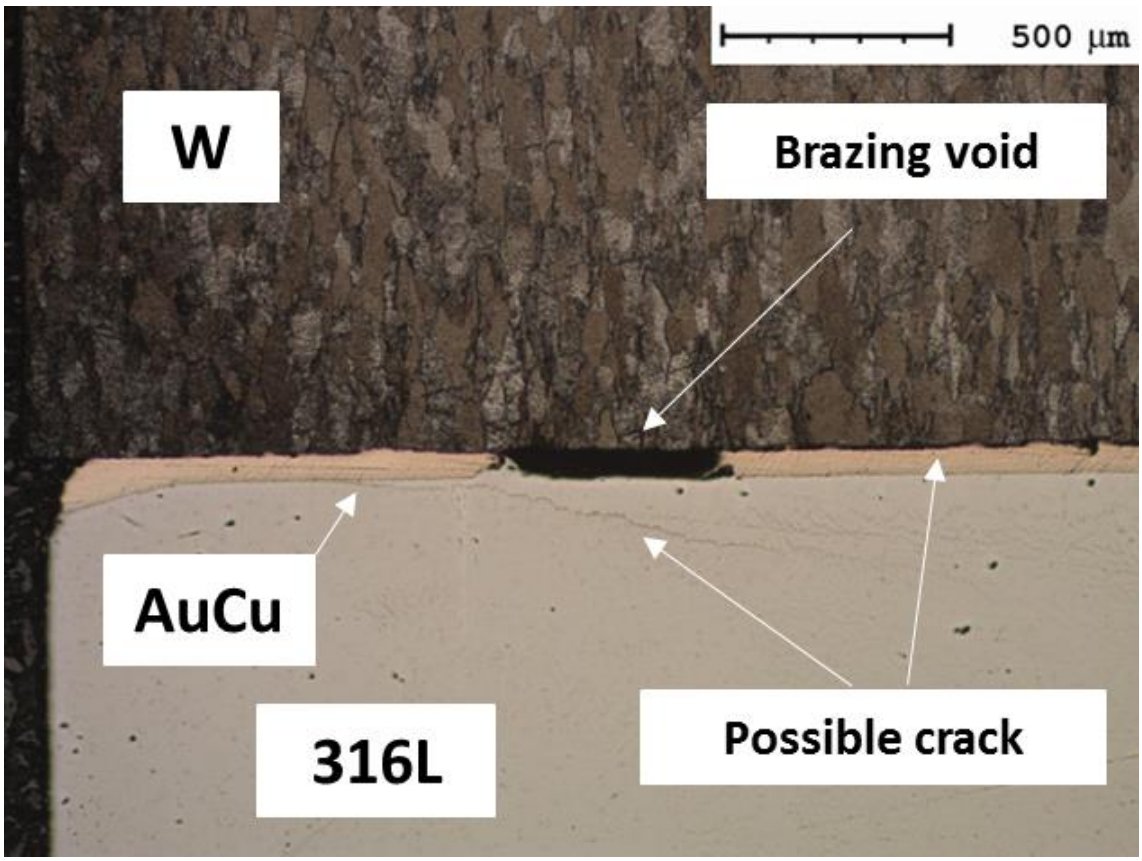

Figure 3-5 - From top to bottom - W-AuCuFe-316L vacuum brazed joint with void spanning the interface of W and 316L

There are large voids present in both the tungsten to copper and 316L specimens. It was observed that for certain material combinations the total bonded surface was as little as 10%.

In an attempt to eliminate flaws and voids in the braze interface alternative conditions were trialled. These included using a more complex counter-sunk geometry rather than the simple butt joint configuration shown in Figure 3-6.

The effect of gold plating the parent material bonding surfaces to attempt to increase the wetted area was also examined as shown in (b) and (d). There was no observable improvement in either wetted area or void reduction by gold coating the tungsten.

The complex geometry of including a recess in the copper did not result in improvement in bond quality. As shown in (c) there are still multiple cavities present within the interface. It was further observed that cracking occurred at the free edge at the interface with this configuration (Figure 5-15 in reference [91]). The dark shadow along the copper-AuCu interface was often observed in

this study and is postulated to be an effect from the grinding and polishing process, where uneven material removal at the interface occurs.

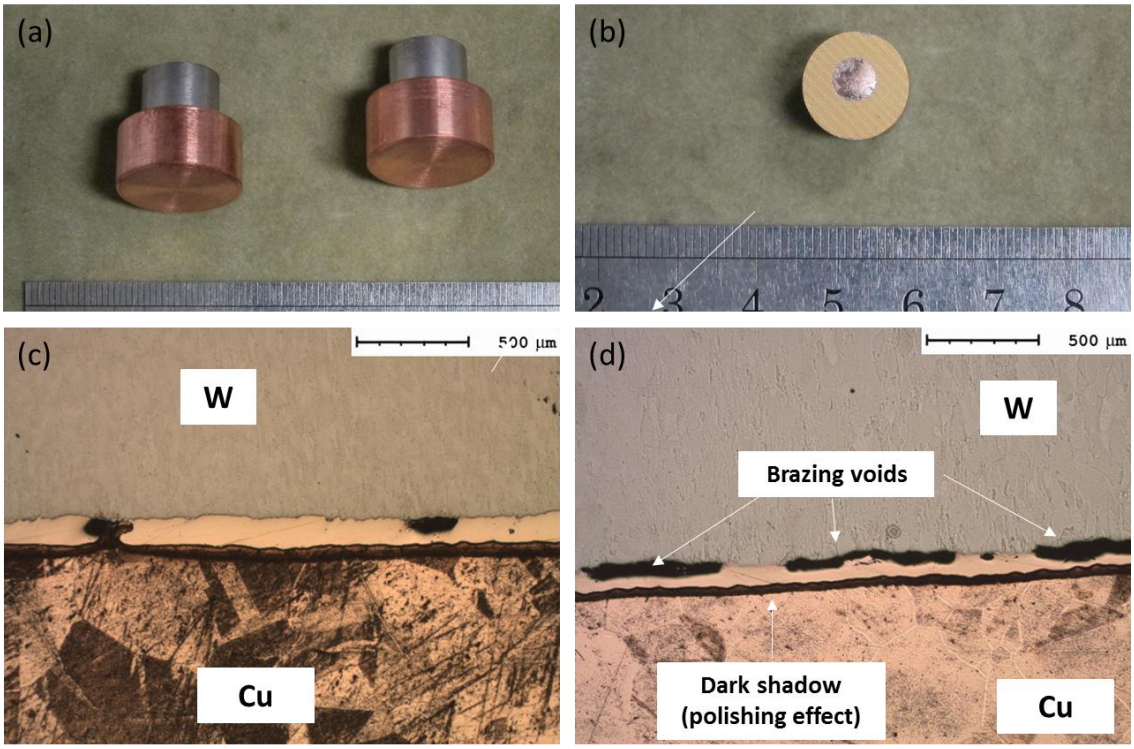

Figure 3-6 - (a) W-Cu part with countersink geometry, (b) Au coated W face with AuCuFe brazing alloy deposited, (c) Micrograph of W-AuCuFe-Cu countersink joint interface with voids, (d) Micrograph of interface of W with Au coating-AuCuFe-Cu brazed specimen

3.2.2 Au80Cu20 brazing alloy trials

A new grade of AuCu brazing alloy was employed for all following brazing trials. This grade has a chemical composition of 80%wt Au, 20%wt Cu.

In addition to a new brazing alloy, new parent materials were required to be sourced. Pure tungsten (>99%), cw-004 copper and 316L were procured in 12.7mm rod form. The material was cut to relevant length, 10 or 25mm for characterisation or residual stress geometries respectively, using electric discharge machining (EDM) wire cutting.

The second brazing trial, the first using the Au80Cu20 material, was conducted using a commercial vacuum furnace, as described in Table 3-1. The result of this experiment was unsuccessful bonding of the parent materials. The brazing temperature of 930C is 20C above the liquidus point of the material. It was believed that the lack of bonding could be due to insufficient

melting of the brazing alloy. Vacuum chamber conditions were kept constant with a heating rate of 10°C/min and vacuum pressure of $1x10^{-4}$ to $1x10^{-5}$ millibar.

The third brazing trial, Trial 3, was performed with the same conditions as Trial 2 with the exception of an increase in brazing temperature. The furnace was heated to 950°C and held at this temperature. The 20°C increase in temperature, now 40°C above the liquidus temperature of the eutectic AuCu. This is in agreement with standard brazing temperature selections [92]. Even at the higher temperature there was no risk of bulk melting of the parent materials, with copper having the lowest melting point circa 1085° C, still in excess of 100°C above the brazing temperature.

The results of Trial 3 proved to be unsuccessful in the same manner as Trial 2. A macroscopic image illustrating the failed bond on the surface can be observed in Figure 3-7. It can be seen that whilst the brazing alloy has bonded with the copper parent material, there is minimal contact with the tungsten. It is the authors understanding that this was caused by oxidation occurring in the interfacial region during heating to the brazing temperature. This is likely caused by oxygen or other impurity content present in the parent materials.

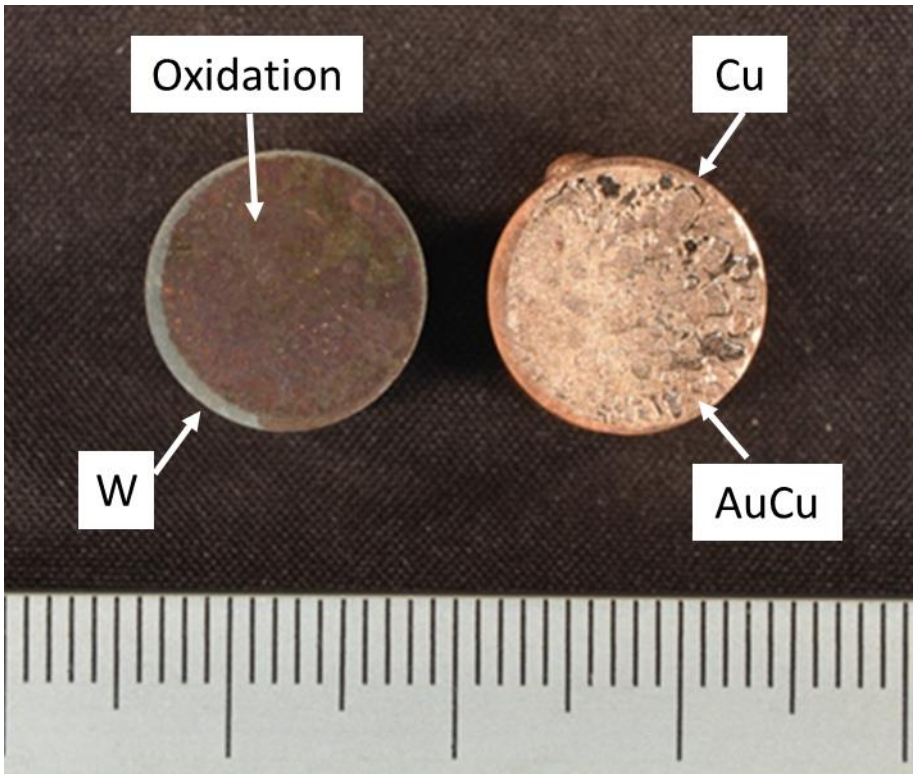

Figure 3-7 - Surface condition of W (left) and Cu (right) following unsuccessful bond during vacuum braze

As part of Trial 3, the effect of surface roughness on the quality of the bonded surface was investigated. Surface roughness is key parameter in brazing [92-94]. Following the unsuccessful brazing in Trial 2, it was believed that the surface condition of the materials could be the factor causing the lack of diffusion and other joining mechanisms between AuCu and W during brazing. A number of W-AuCu-Cu specimens were prepared for brazing. Three surface conditions were assessed:

1. As-machined
2. Manually prepared using 800 grit paper
3. Grit blasting on surfaces to be bonded using white fused alumina (F230 grade).

Figure 3-8 presents the surface condition of the W and Cu following grinding and grit blasting. It is known that increasing the roughness of a material to be brazed can result in increased capillary flow behaviour. The rougher surface also provides a greater area for bonding to occur, potentially increasing the mechanical strength of the joint.

The results of the surface trials were inconclusive as bonding did not occur for the prepared specimens. The effect of surface roughness on the metallurgy of the interfacial region of tungsten brazed joints is a recommended area for future research.

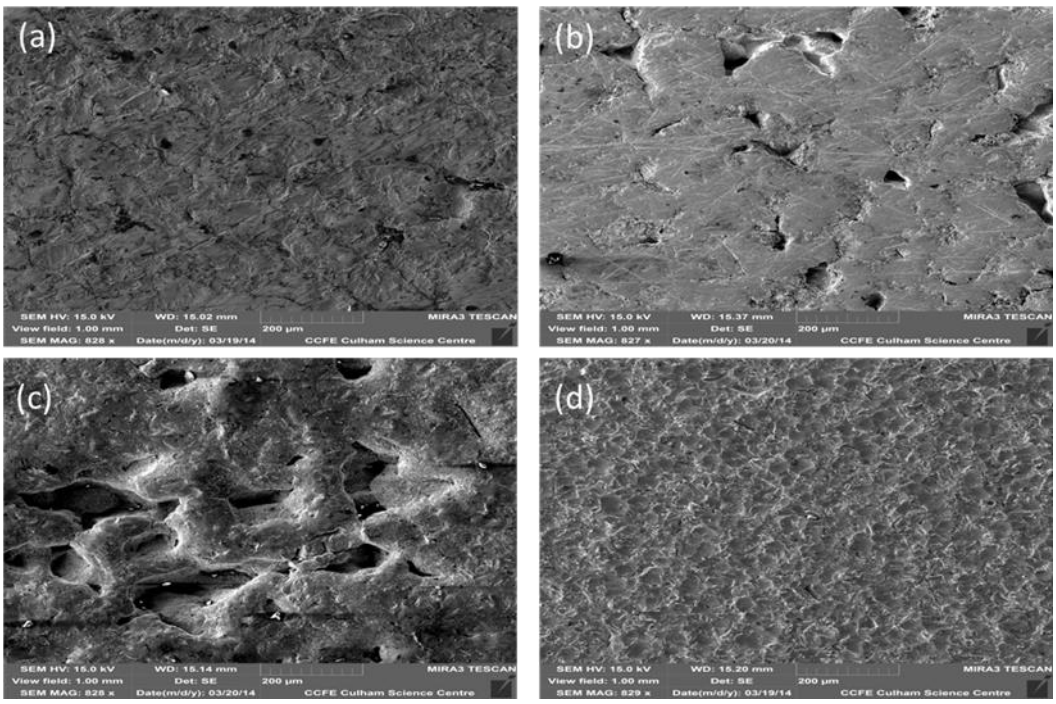

Figure 3-8 - SEM images at 830 magnification of (a) W as-EDM wire cut condition (b) W with 800 grit paper manual grind (c) W following grit blasting and (d) Cu following grit blast

Following the unsuccessful brazing Trail 3, an alternative commercial provider of vacuum furnace brazing was approached (Bodycote [101]). Brazing Trial 4 was essentially a repetition of Trial 3 at the alternative supplier. This trial also failed to produce successfully bonded W-Au80Cu20-Cu joints.

Temperature, vacuum chamber conditions and surface preparation had then been eliminated as sources of the barrier to a successful brazed joint. The parent materials were next considered.

Brazing Trial 4 was performed using OFHC copper, 316L and tungsten as the parent materials. Au80Cu20 was the brazing alloy. Brazing was performed at 950°C. This trial resulted in a successful bond of all materials as shown in Figure 3-9. Displayed are 6off characterisation specimens, 2 per combination (W-Cu, W-316L, 316L-Cu) and a number of residual stress analysis specimens. The characterisation specimens are examined in the following sections of this chapter. The residual stress analysis is discussed in Chapter 6 of this thesis.

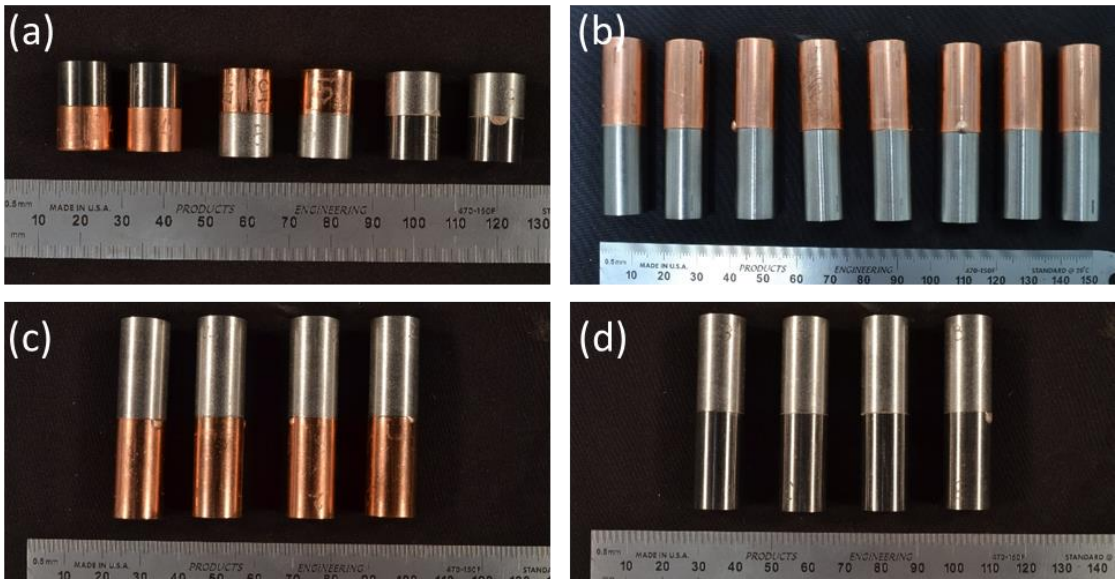

Figure 3-9 - Characterisation geometry vacuum brazed samples (a), Residual stress geometery AuCu vaccum brazed samples: (b) Cu-316L, (c) W-Cu, (d) W-316L

3.3 Vacuum brazing metallography

Having successfully manufactured a number of vacuum brazed characterisation style specimens, metallurgical analysis was performed. The purposes of the analysis were:

- Determine wetted regions of the interface to assess braze quality
- Inspect interface for flaws including voids and cracks
- Understand the microstructural evolution in the interfacial region following brazing
- Examine elemental composition of the interfacial region to determine the extent of diffusion occurring during joining

For the purposes of this thesis, a successful joint is defined as that which consists of a full face bond between both parent materials and brazing alloy, absence of large voids, and absence of brittle intermetallic compounds forming during brazing. As defined by ITER design documents, the wetted area should be in excess of 95% [102]. This criteria has been adopted here. Additional criteria such as strength and fracture toughness are not considered within the scope of this study.

The samples were prepared for metallurgical analysis using standard techniques [103]. The samples were sectioned using a precision cut-off saw (Streuers Accutom and Buehler Isomet 500). The sectioned parts were then mounted in a conductive epoxy. The surface of mounted parts were then prepared using a series of grinding papers, progressing from coarse to fine (120 grit to 2000 grit), on an automated machine. Finally the surfaces were polished using 9μm and 3μm diamond suspensions followed by 0.05μm colloidal silica. In certain instances the polished samples have been chemically or electro-chemically etched to reveal the microstructure more clearly.

Achieving a high quality of surface finish was a non-trivial challenge. Samples of 316L-Cu configuration were relatively straightforward. However the W-316L and particularly the W-Cu material combinations proved more difficult. There is an extreme differential in hardness properties between tungsten and the other parent materials. These are discussed later in the chapter. This results in a difference in the grinding/polishing characteristics of the materials. Tungsten takes considerably more effort to achieve a plane surface condition. Copper wears much quicker, and a sufficient surface finish is achieved comparatively quickly. Considering the two materials are bonded, this often resulted in an uneven surface condition. Copper will go through phases of plane condition, to unevenly scratched, due to a step in the distance between the grinding medium and the material surface in the region close to the interface.

In addition to the challenge of simultaneously preparing such dissimilar materials is the added complexity of the third material involved, the braze layer. It was often observed that the braze layer was recessed from the plane of the two parent materials. This results in a reduction in the quality of surface finish that can be achieved for the brazing layer. Large, deep scratches can be observed in the braze layer in the majority of prepared specimens. These flaws are tolerable for the purposes of optical light microscopy, SEM and EDS. However for the parts to be suitable for EBSD analysis, such as texture or plastic strain mapping, an improved preparation procedure would have to be devised. This could include extended periods of vibratory polishing

3.3.1 Base material microstructural evolution

Firstly the base materials were examined without consideration of the brazed region. The microstructure of tungsten in the as received and as brazed condition is presented in Figure 3-10 (a) and (b) respectively.

Prior to brazing the tungsten exhibits elongated grains in the rolling direction. Following brazing at 950°C the microstructure of the bulk tungsten is virtually unchanged. This is as expected considering the temperature is significantly below the recrystallization temperature of 1300-1500°C for tungsten [104]. The grains remain oriented with a strong texture in the rolling direction.

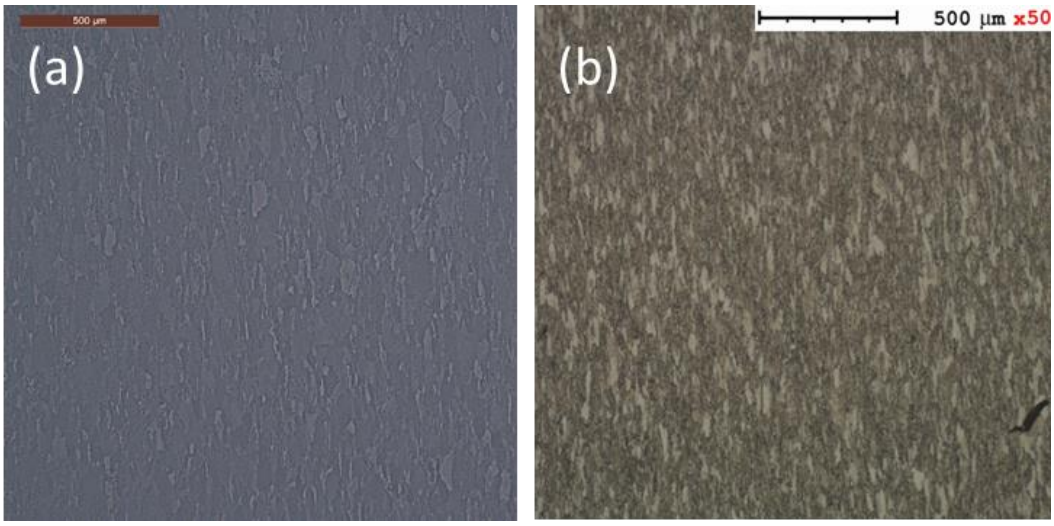

Figure 3-10 - W bulk microstructure in (a) as-received and (b) as-brazed condition

The microstructure evolution following brazing for OFHC copper is presented in Figure 3-11. The as-received copper shows no strong texture from the optical micrograph. The grain size is in the region of 20-50µm.

From Figure 3-11 (b) it can be observed that the copper underwent significant microstructural changes during the brazing process. The braze temperature of 950°C is much closer to the melting point of copper (circa 1085°C) than tungsten (circa 3400°C), so a more significant change in microstructure is to be expected as the copper is now in the fully annealed condition. The grain size has increased to over 100µm in large regions. It was observed that runaway grain growth occurred in several locations, with individual grains increasing to 1mm. These extremely large grains are visible upon inspection by the naked eye.
There is considerable twinning observed in the as-brazed copper. This is likely due to plastic deformation [105, 106] induced during the brazing process.

As the copper is in the annealed condition, subsequent heat treatment to improve mechanical properties would be required for any fusion applications such as in the divertor. This would also apply to copper alloys such as CuCrZr [107]. However for the purposes of this research only the as-brazed condition has been considered.

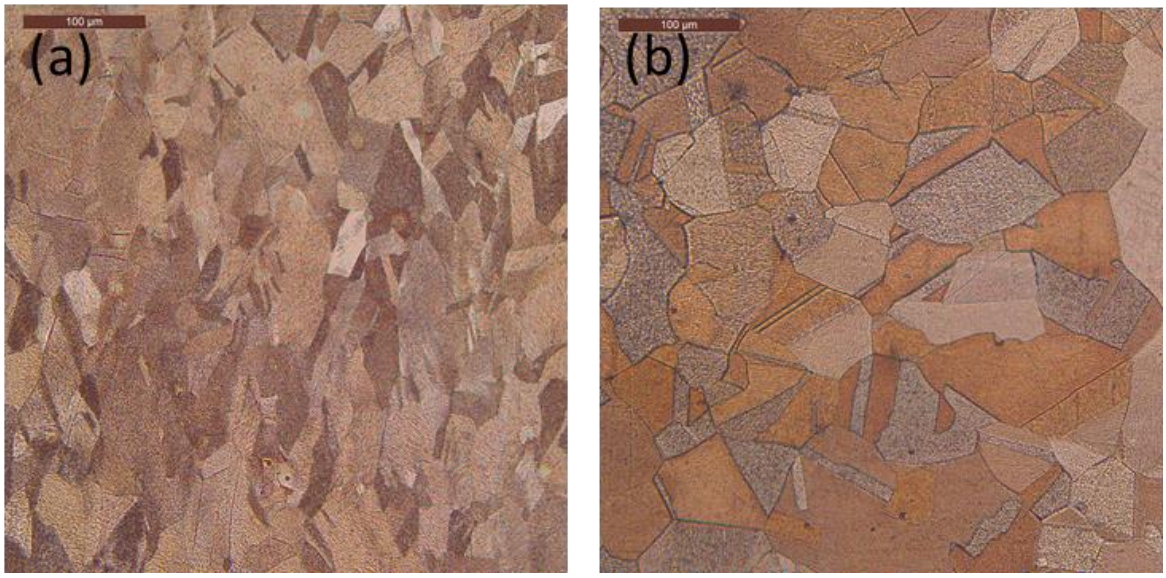

Figure 3-11 - Cu bulk microstructure in (a) as-received and (b) as-brazed condition (axial plane)

The temperature of brazing is sufficiently lower than the liquidus temperature of copper so as no melting of the copper should occur. However as can be seen in Figure 3-12 there is evidence of possible localized melting along the grain boundaries of the copper. The incipient melting at the grain boundaries is likely caused by higher concentrations of impurities at these regions.

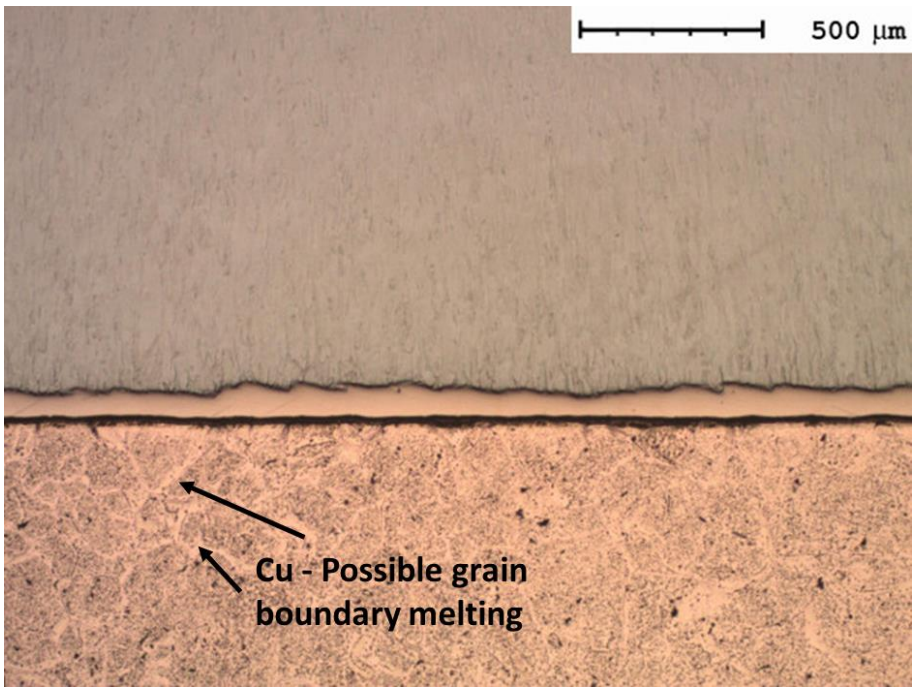

Figure 3-12 - Possible incipient grain boundary melting in Cu

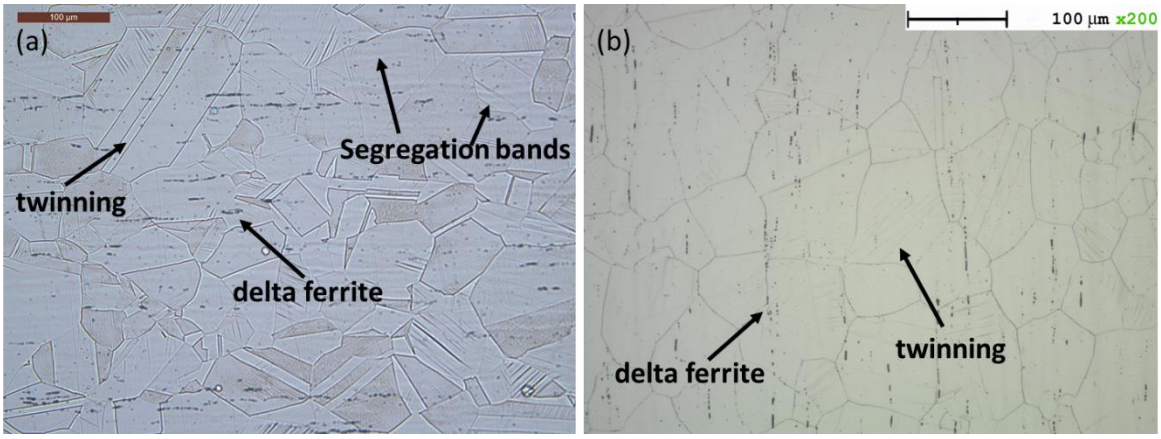

Figure 3-13 – 316L microstructure in (a) as-received and (b) as-brazed condition

The microstructure of the austenitic 316L is presented in Figure 3-13. The microstructure has been revealed using Oxalic acid with electrochemical etching. The grains are largely equiaxed with a grain size in the region of 100µm. Grain twinning is visible in the as-received and as-brazed material. Twinning is a common characteristic of austenitic steels such as 316L. There is no obvious increase in twinned grains in the proximity to the interface where plastic deformation is likely during brazing.

There are significant deposits of delta ferrite present in the microstructure. These deposits can be both beneficial and detrimental. The presence of a small percentage of delta ferrite can reduce fissuring in austenitic weld steels such as 316L [108]. However significant amounts of delta ferrite

can reduce corrosion resistance due to reduced composition content of Cr [109]. The quantity and distribution of delta ferrite is influenced not only by cooling rate, but also strongly affected by chemical composition [110]. These factors would have to be considered for getting the correct balance of delta ferrite to suit the demands of the steel in the fusion environment.

In addition to the dark delta ferrite concentrations there are also more subtle concentrations along the rolling direction. These are likely concentrations of segregated elements, namely Cr and Mo [111]. A chemical analysis in the referenced work showed variations in Cr balance of about 2% along the ridges.

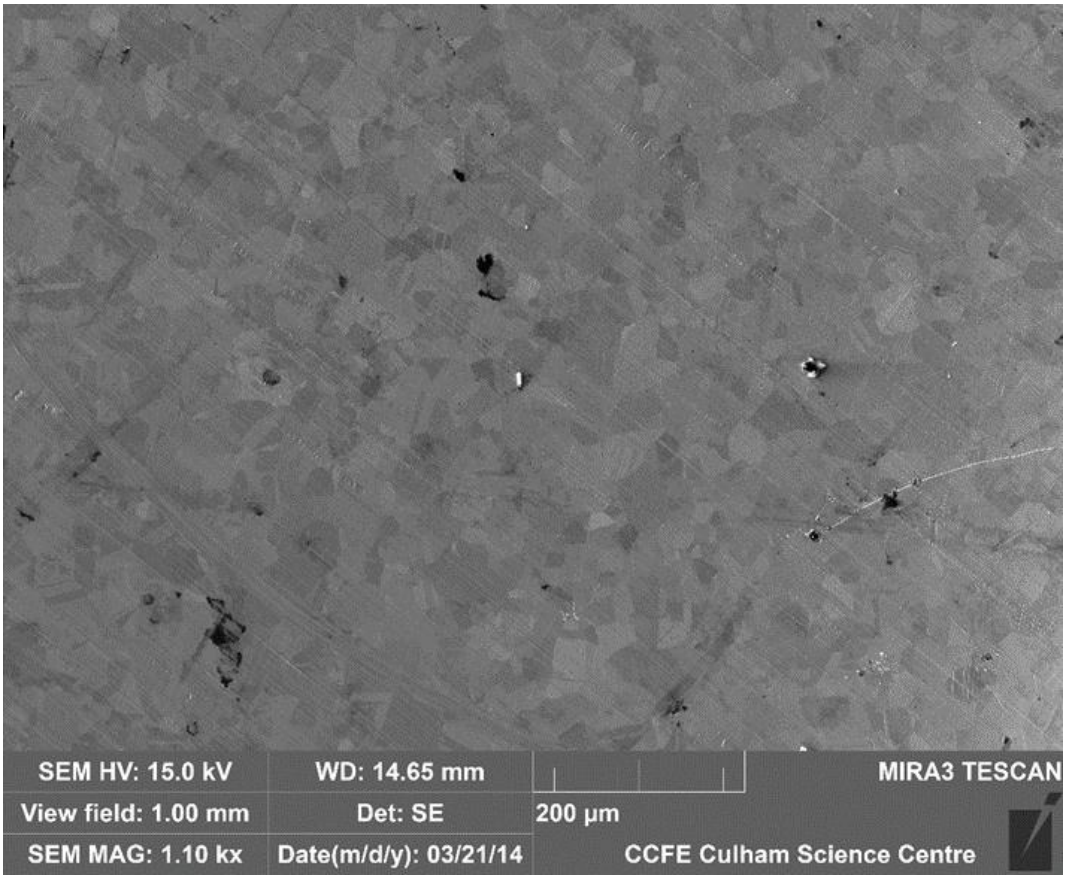

Figure 3-14 - Au80Cu20 brazing alloy in as-received condition

The microstructure of the as-received Au80Cu20 brazing alloy is presented in Figure 3-14, as viewed by SEM. It was found to be a significant challenge in preparing the 50µm thick AuCu foil for metallography analysis. The thin nature of the material made traditional mounting and polishing techniques unsuitable. Therefore the material was examined without any preparation using the secondary electron mode in an SEM. This approach was sufficient to display a microstructure which exhibits equiaxed grains. There is no apparent texture favouring the rolling or transverse directions.

The microstructure of the as-brazed AuCu material is not expected to share characteristics with the as-received material due it transitioning into a fully liquidus state during brazing, before re-solidifying. The microstructure of the AuCu alloy for each parent material combination has been analysed and is presented in the following sections. However revealing the grains of the alloy has proved a challenge due to the unresponsiveness of gold with many common etchants.

3.3.2 W-AuCu-Cu brazed interface metallography

The first material combination to be considered is the W-AuCu-Cu vacuum brazed specimen. The entire cross-section of the brazed interface is displayed in Figure 3-15. The image was captured using an Alicona Infinite Focus measurement microscope [112].

It can be stated with confidence that a high quality braze has been achieved for this material combination, using the metric of bonded area as a measure of quality. The wetted area of the brazing alloy covers the extent of the interface. This is critical for ensuring the maximum possible heat conduction from the tungsten armour material to the heat sink copper material. There is one small defect present towards the centre of the interface. This is potentially a void, or could be simply an artefact of the sample preparation. To determine this definitively non-destructive evaluation (NDE) is required. This type of analysis is discussed later in this chapter.
The dark spots present on the copper in Figure 3-15 are micro-indents resulting from hardness testing, and are not a microstructural feature of the material.

It is clear that the combination of the Au80Cu20 brazing alloy and OFHC copper, as opposed to Au80Cu19Fe1 alloy and 99.9% purity Cw-004 cooper, has resulted in the best possible braze for these materials. An added advantage is this approach requires no extra considerations such as gold coatings or complex geometries. This can be seen by comparing the lack of voids and un-wetted area in Figure 3-15 with the relatively largely flawed interface in Figure 3-6, or the completely un-bonded specimen in Figure 3-7.

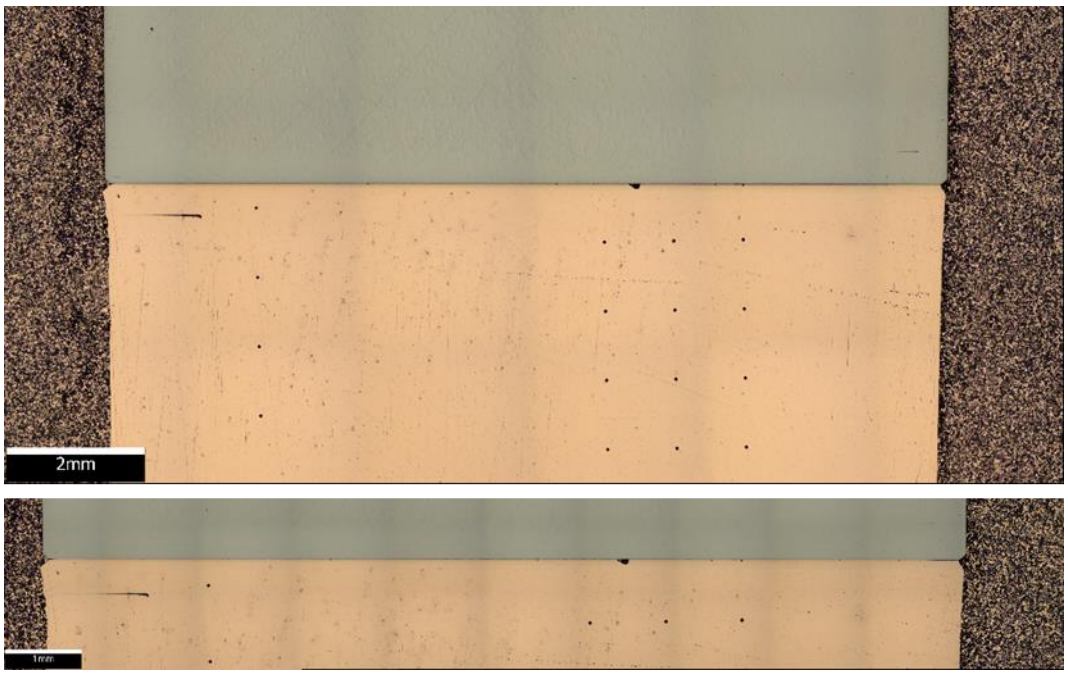

Figure 3-15 - W-AuCu-Cu brazed interface - entire cross section

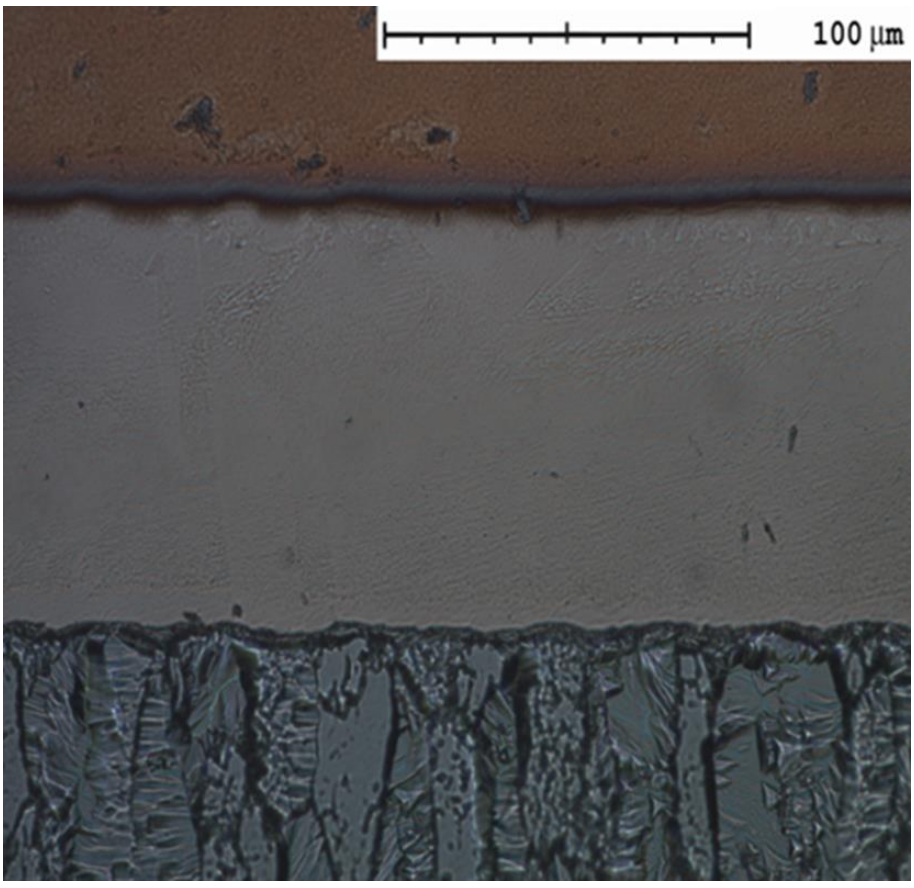

Figure 3-16 - Microstructure of W-AuCu-Cu brazed joint

The microstructure of the W-AuCu-Cu joint is presented in Figure 3-16. The thickness of the brazing alloy is observed to be in the range of 100-125µm. Considering the starting thickness of

50μm of the alloy in foil form it is clear that there has been volumetric expansion of the material. A contributing factor of this may be elemental diffusion of base material copper into the AuCu single phase alloy. A phase change causing volumetric expansion in the braze layer will also reduce the density of the material. Such a phase change is likely to occur through observation of the AuCu phase diagram Figure 3-1.

There is no optically visible migration of AuCu into the base tungsten material. This effect has been observed during a collaborative project with colleagues at the university [91]. An example of this is displayed in Figure 3-17. This is postulated to be caused by preferential diffusion of elements along grain boundaries. It has been shown that elements can diffuse up to 100 times faster along tungsten grain boundaries than through the grain itself [104, 113]. An alternative explanation could be small defects in forming in the parent tungsten material due to stresses caused by differential volumetric contraction on cooling from brazing temperature.

The absence of these "tendrils" in the W-AuCu-Cu brazed specimens presented in this chapter could be due to several reasons. If the migration of AuCu is caused by diffusion along grain boundaries, the absence of iron in the W-AuCu-Cu specimen in Figure 3-16 could be critical. Grain boundary diffusion in tungsten is dependent on the diffusing element, the absence of iron could have resulted in the lack of AuCu migration. The migration of AuCu along grain boundaries is will likely have an effect of intergranular cracking likelihood in addition to susceptibility to creep damage [114].

Alternatively, the absence of AuCu migration could be explained by a lack of micro-cracks observed in the base tungsten material.

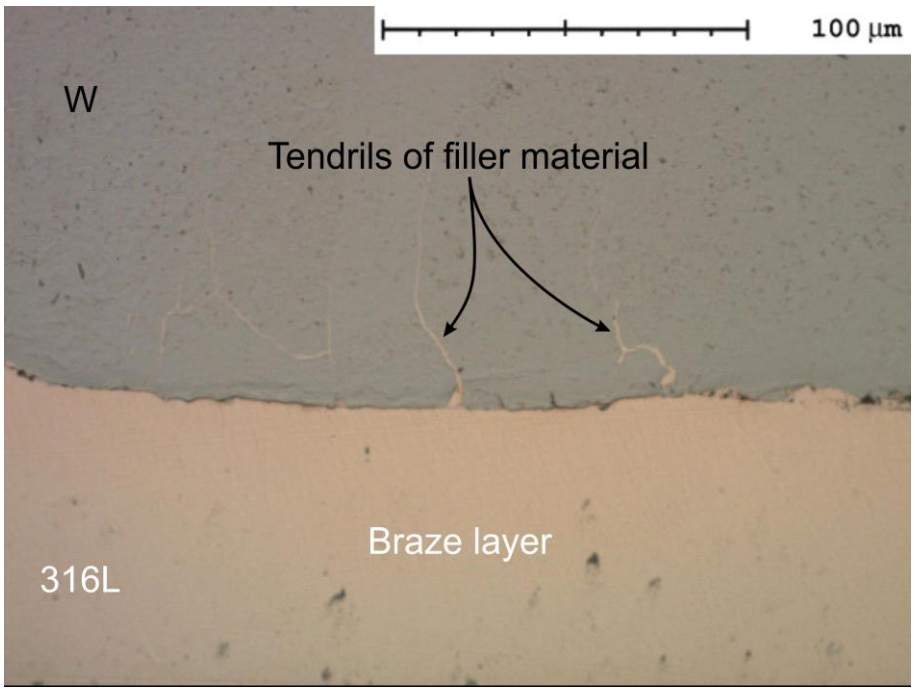

Figure 3-17 - AuCu migration into W [91]

Figure 3-18 – Optical microscope image of W-AuCu-Cu brazed interface - free edge location

The free edge region of the brazed W-AuCu-Cu specimen is presented in Figure 3-18. It is clear that there is misalignment of the parent materials. As the characterisation geometry specimens were only aligned and clamped simply this is hardly surprising. There is however a noticeable feature at the free edge as seen in the optical microscope image. There appears to be a darkened line originating from the free edge of the part along the W-AuCu interface for a length of several

hundred microns. Features of this nature had previously been observed and accounted for as being caused by a stepped height difference between materials. This is due to the harder tungsten wearing differently than the softer braze alloy and copper. Considering the location of the feature further analyses was required to validate or disprove this theory.

This feature was further investigated using SEM as shown in Figure 3-19. It is clear that the darkened region observed during optical microscopy was not merely an artefact of a difference in polishing behaviour. Instead, the SEM image displays a clear delamination of the AuCu from the tungsten material. This is likely to cause premature failure as the delamination, or crack, propagates under cyclic thermal loading experienced in a divertor. This is a known failure mechanism for bonded components subject to thermal loading [115].

It is not clear whether this type of flaw is caused purely by the misalignment of the parts, which in effect cause a bending moment to be applied to the edge region during cooling.

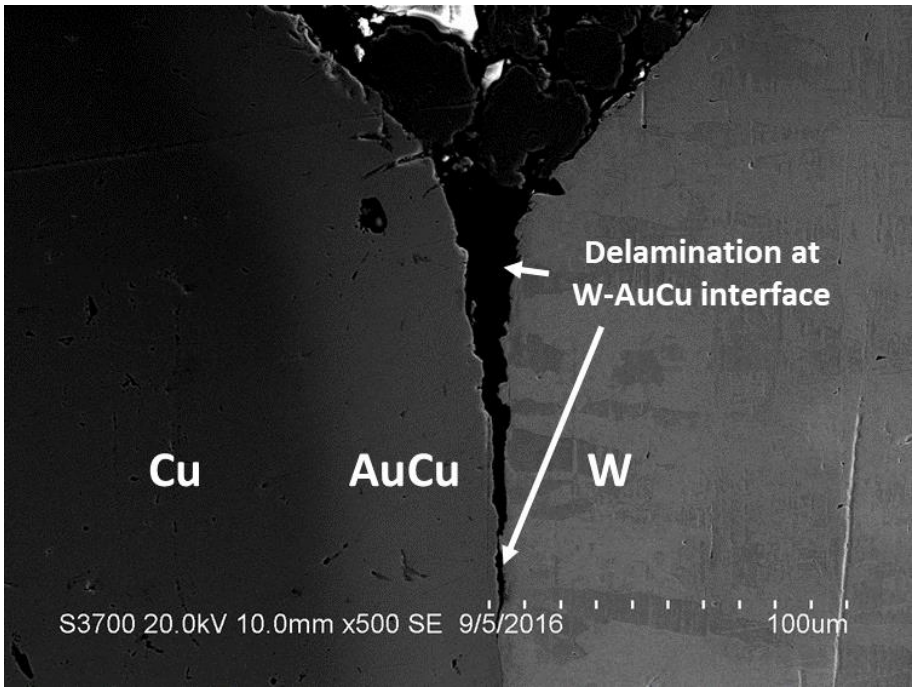

Figure 3-19 - SEM image of possible delamination at W-AuCu interface

A surface finishing technique such as edge grinding [116] or hard turning [117] could be applied to remove features such as small cracks or delamination occurring at the free edge of the interface. Beneficial modification of residual stress could be achieved through these methods.

The strength of a part containing a bonded interface is strongly influenced by the diffusion behaviour of the elements [118-120]. It is therefore crucial to understand the extent of elemental

diffusion across the brazed interface for the W-AuCu-Cu part. Energy-dispersive X-ray spectroscopy (EDS) elemental analysis has been performed using a Hitachi Field Emission SEM coupled with Oxford Instruments EDS detector [121]. Whilst not strictly quantitative in nature, EDS elemental distributions provide a useful insight into qualitative trends in the composition at the interfacial reion.

The location analysed across the brazed interface is presented in Figure 3-20 and the line spectrum results plotted in Figure 3-21. The elemental diffusion was investigated by performing a line spectrum scan consisting of 46 locations spaced 3µm apart. This covers a full cross section of the brazing alloy and portion of the parent material at either side of the braze interlayer.

It is apparent that there is very little diffusion of either gold or copper into the tungsten material. This can have a contributing effect on the likelihood of brittle failure at the W-AuCu interface. Contrastingly there is a very smooth transition from the copper into the AuCu interlayer. There is significant elemental transportation through diffusion such that the maximum measured concentration of gold anywhere on the braze layer is approximately 60%wt. This is significantly less than the initial balance of 80%wt.

The results of the EDS analysis are in strong agreement with studies conducted on similar specimens. Zhang and Easton [76, 90] conducted elemental analysis on a number of material combinations presented in this chapter. Zhang was using the Au80Cu19Fe1 brazing alloy will cause small deviations in results. The sharp transition from tungsten to brazing interlayer was demonstrated. The highly diffused copper – AuCu region is also apparent in this work.

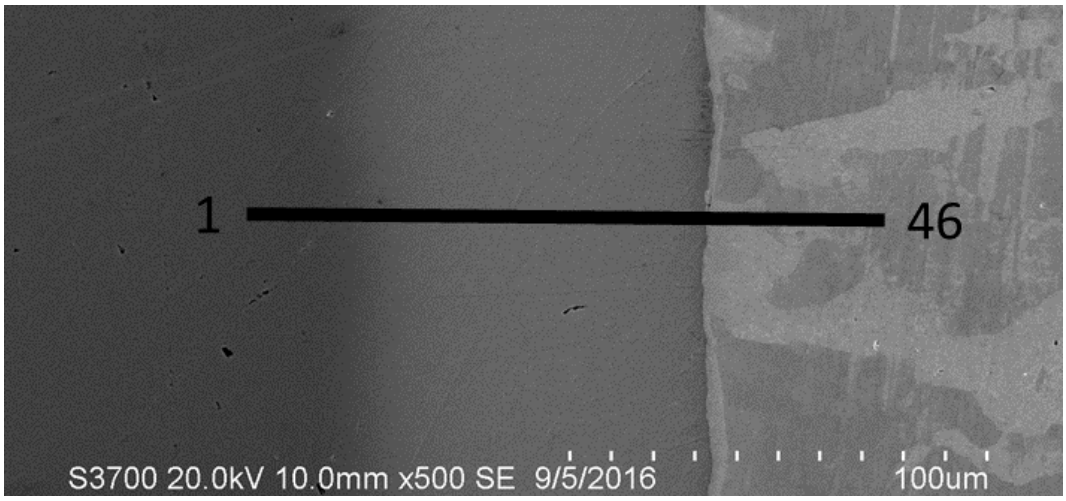

Figure 3-20 - Cu-AuCu-W interfacial region for EDS analysis

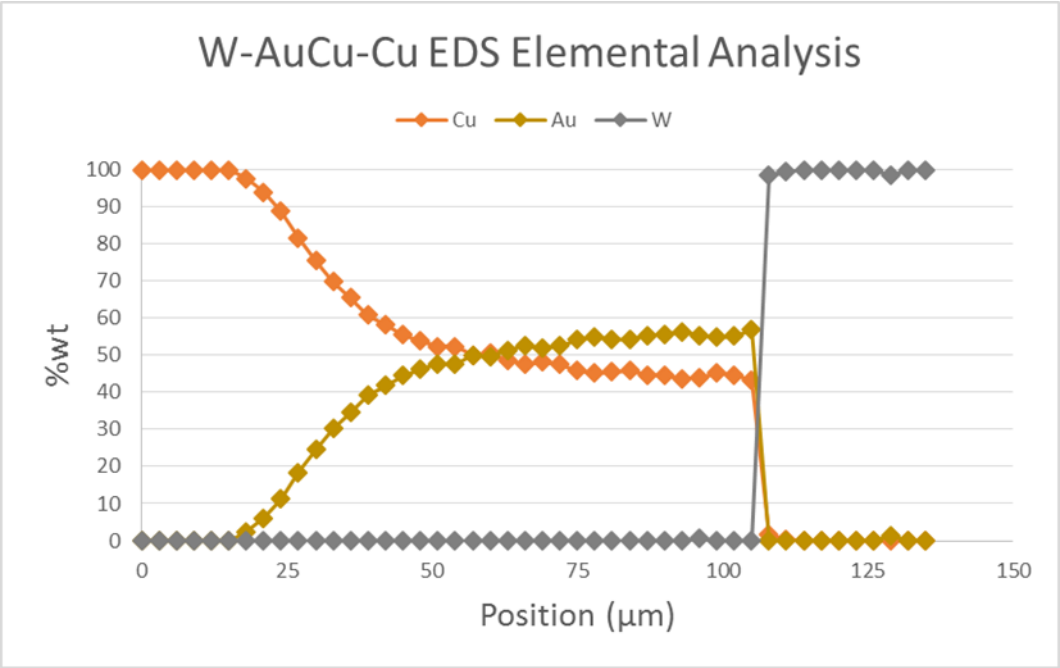

Figure 3-21 - W-AuCu-Cu EDS elemental analysis

3.3.3 W-AuCu-316L brazed interface metallography

A fully bonded W-AuCu-316L brazed joint has been successfully produced and been prepared for metallurgical analysis.

The interfacial region of the brazed tungsten and steel part is presented in Figure 3-22, with the tungsten towards the top of the image, 316L stainless steel at the bottom and the brazed AuCu layer sandwiched between the parent materials.

The brazing alloy appears to completely wet the surfaces of both parent materials, producing a high quality braze with minimal imperfections. This is comparable to the findings in section 3.3.2. There is a definite trend of improved wetting characteristics and reduction in flaws through the usage of Au80Cu20 compared to the poorer quality bonds achieved with Au80Cu19Fe1 brazing alloy [91]. The sole exception to this is a small cavity in the interior of the brazed interlayer. However even considering this there is still >95% fully bonded interface.

There is axial misalignment of approximately 100µm of the parent materials as observed with the W-AuCu-Cu combination. Whilst not believed to be important for characterisation purposed, such a misalignment would have a significant effect on joint performance.

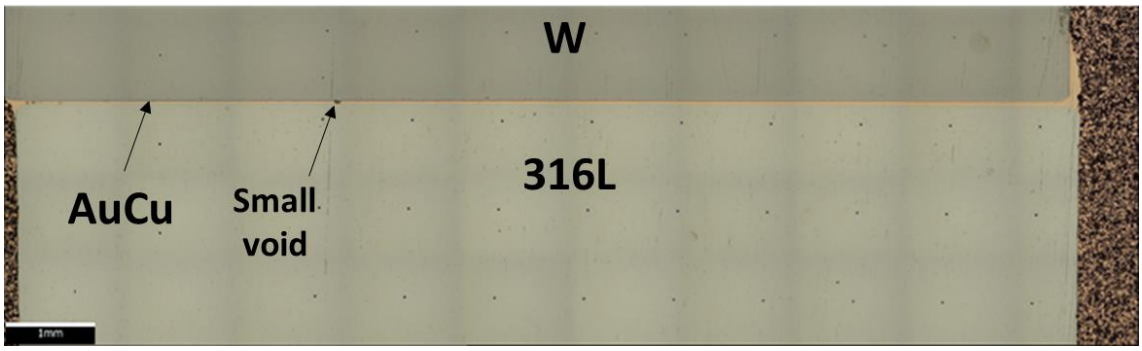

Figure 3-22 - W-AuCu-316L brazed interface - entire cross section

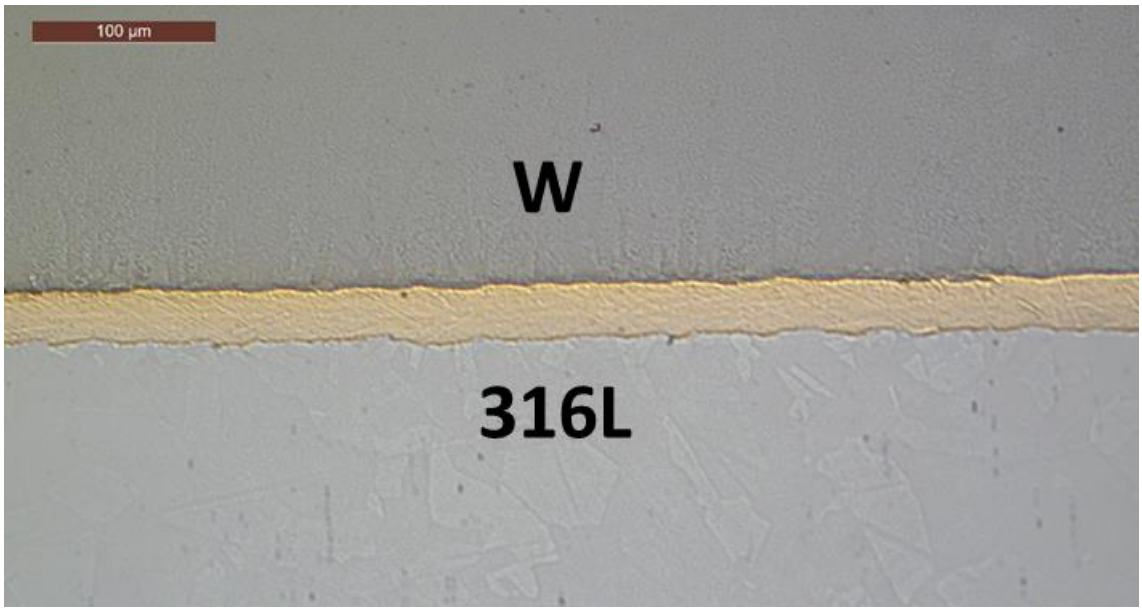

Figure 3-23 - Microstructure of W-AuCu-316L brazed joint

The microstructure of the interface region for the W-AuCu-316L specimen is presented in Figure 3-23. The thickness of the braze layer is measured to be approximately 50-60µm. This is significantly less than that observed for the tungsten – copper specimen (circa. 100µm), and is closer to the initial dimension of 50µm thickness for the brazing material in foil form. This can be explained partially by the lower level of diffusion of elements between AuCu and 316L. Additionally, there is more brazing material lost to the free edge of the W-AuCu-316L specimen. This is visible macroscopically in Figure 3-9 (a) where there is noticeable pooling of AuCu material on the exterior of the tungsten – steel part. The extent of pooling on the tungsten and copper part is much less.

This is further visible by examining the edge regions for the tungsten to copper and tungsten to steel joints shown in Figure 3-15 and Figure 3-22 respectively. Whereas there is pooling at the edge present with the steel part, the opposite is true for the copper part where there is a small

recess at the edge. As both parts are of equal dimensions, and contain the same volume of brazing alloy, this results in a larger volume of brazing alloy in the interior portion of the W-AuCu-Cu joint, creating a deeper interfacial region.

This has potentially serious effects on mechanical and thermal performance, as discussed previously interlayer thickness and edge characteristics are key parameters.

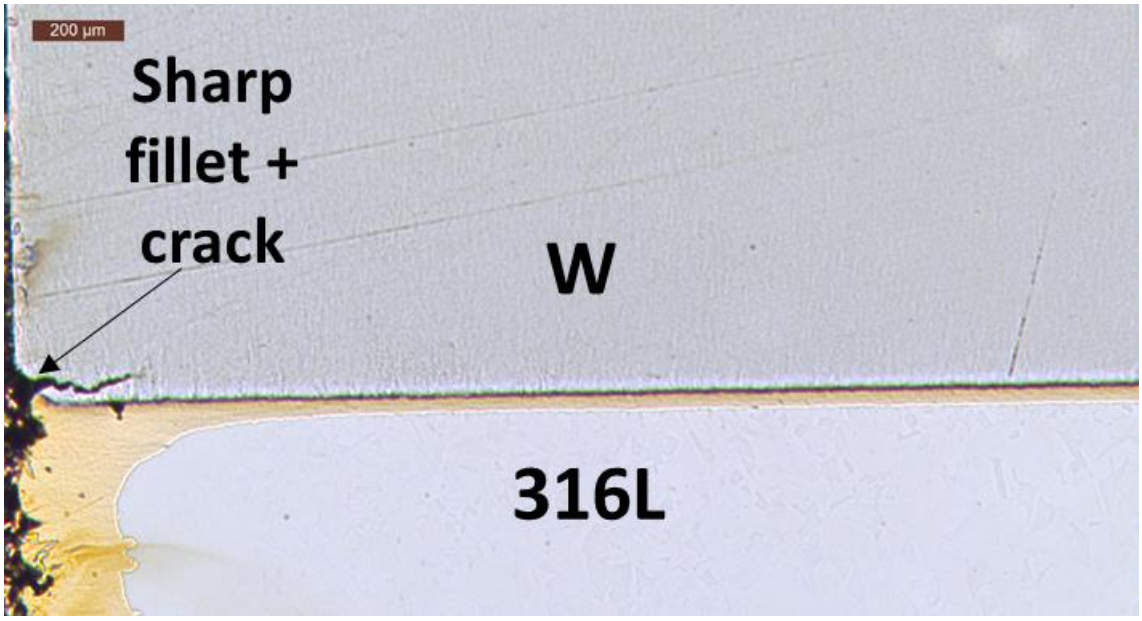

Figure 3-24 - Optical microscope image of W-AuCu-316L brazed interface - free edge location

The W-AuCu-316L edge region has been examined in closer detail (Figure 3-24). There is a large, obvious crack located at the tungsten and brazing alloy interface. The crack is located fully in the tungsten region which is intuitive due to the highly brittle nature of the material [32, 62, 104] and high theoretical elastic singularity at that location (Chapter 5). The crack appears to initiate at the corner of the interfaces between parent and braze materials, and propagates in excess of 200µm into the material. The fillet of the braze interlayer is common location for crack nucleation [93]. It is recommended that rounded fillets are achieved, whereas a sharp fillet is evident at the tungsten-braze interface. This is due to the tendency for brittle intermetallic concentrations to form here [93]. Higher concentrations of intermetallic compounds are found at the fillet due to the increased volume of the liquidus phase of a eutectic alloy at this location, from which the brittle intermetallics form. Whilst no brittle intermetallics have been observed in this work, or similar works [76, 90, 91], it is possible that there are micro segregations located at the fillet region which haven't been observed by EDS analysis.

The cracks at the free edge of the tungsten – steel joint are shown at higher magnification in Figure 3-25 (a) and (b). There are cracks present at both sides of the interface. Both are similar in nature, nucleating at the tungsten interface and penetrating to a depth of 100-200µm. Flaws in the same location were observed previously with the tungsten – copper combination, although delamination was the specific defect in that case, as opposed to a crack in the base metal.

The same crack locations in the tungsten have been examined using SEM (Figure 3-25 (c) and (d)). The SEM provides the advantage of increased depth perception as compared with the optical microscope image. This further clarifies that the defect is indeed a large crack, and not an artefact of the sample sectioning or mounting.

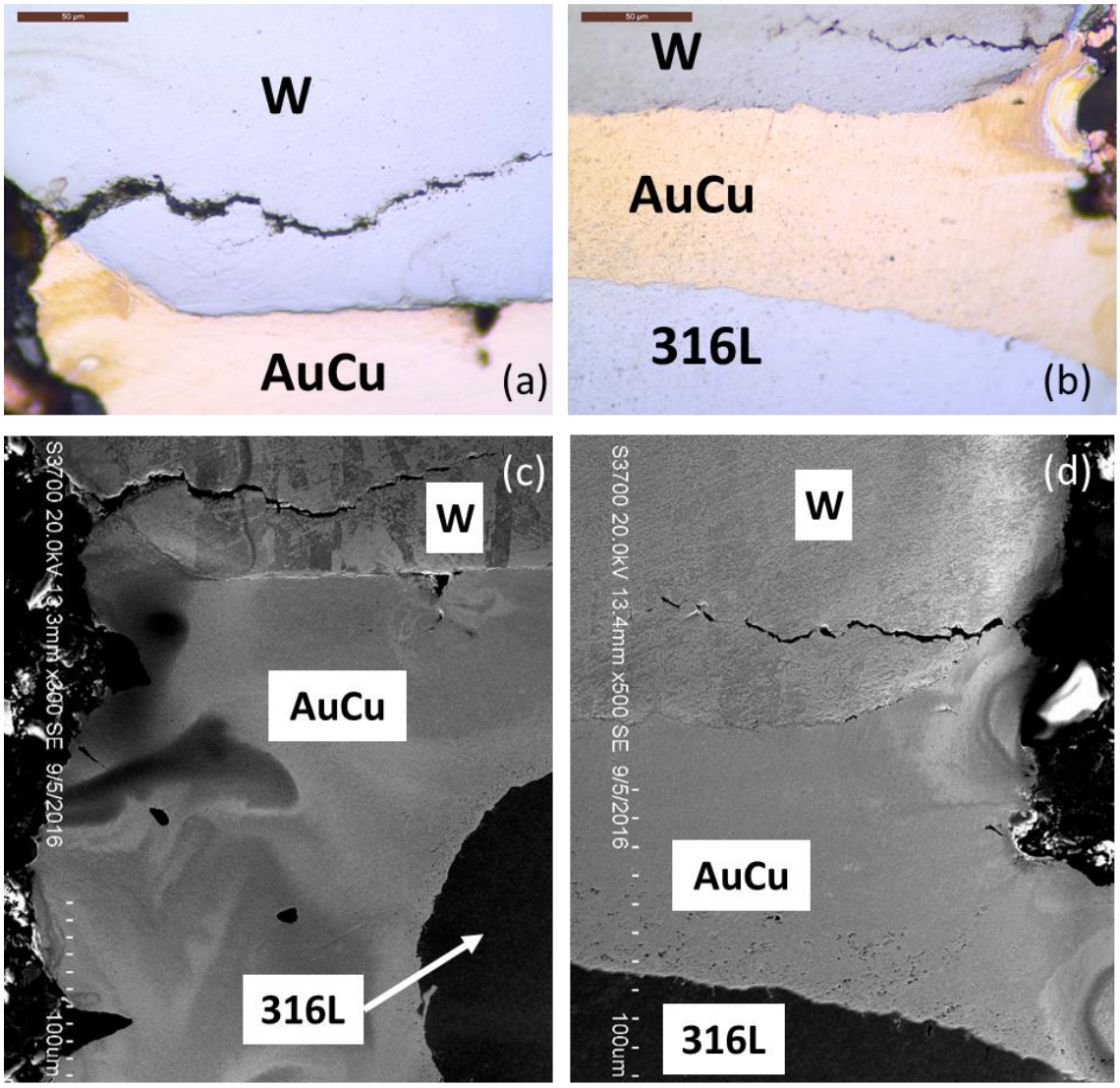

Figure 3-25 - Cracks at W interface in W-AuCu-316L joint. (a) and (b) optical images of cracks either side of the interface. (c) and (d) SEM images of the same cracks

These type of flaws are not acceptable for mechanical testing specimens, much less an actual divertor type component. Therefore further work is required to understand the presence of these edge cracks, and if they are solely caused by misalignment of the samples during brazing.

The exterior of a brazed W-AuCu-316L specimen has been examined in Figure 3-26. Only the exterior of this sample was available for inspection, as it required to be un-sectioned for residual stress analysis. A macroscopic image of the exterior interfacial region is presented in Figure 3-26. There appear to be thin, crack-like patterns on the tungsten material close to the interface. However this is not conclusive. This further leads to the recommendation that further research is required to characterise cracking behaviour at the interface of tungsten joints brazed with AuCu filler material.

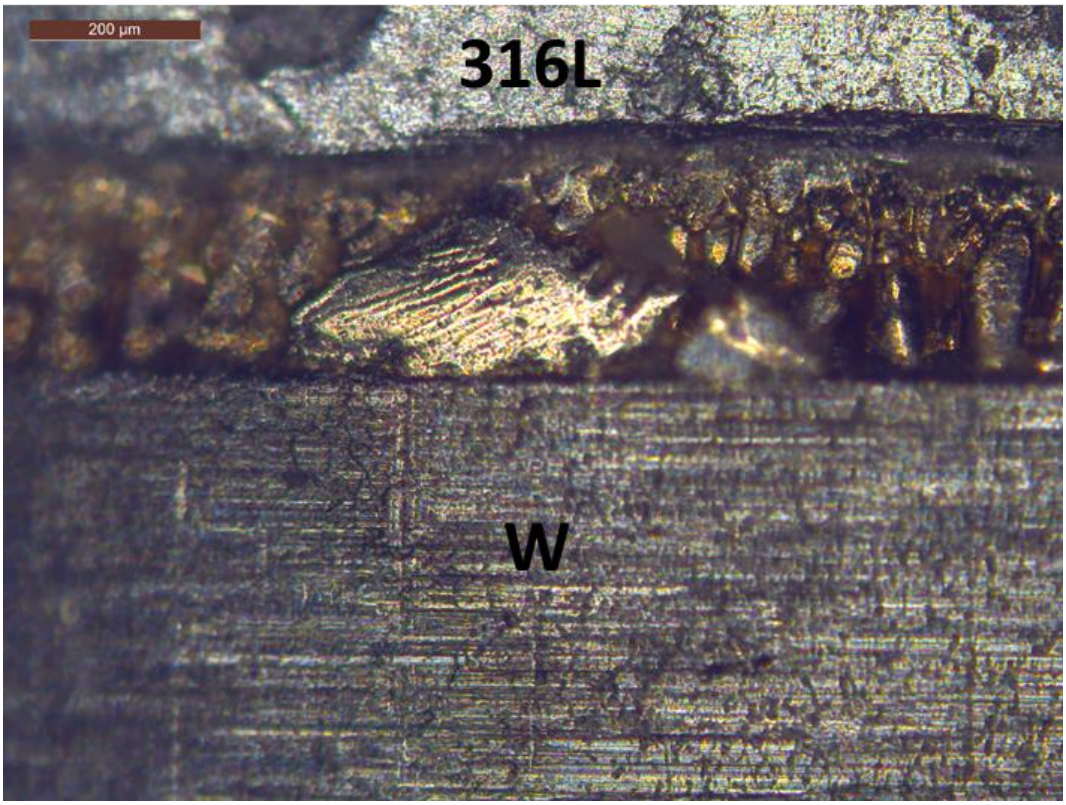

Figure 3-26 - Exterior of W-AuCu-316L brazed joint

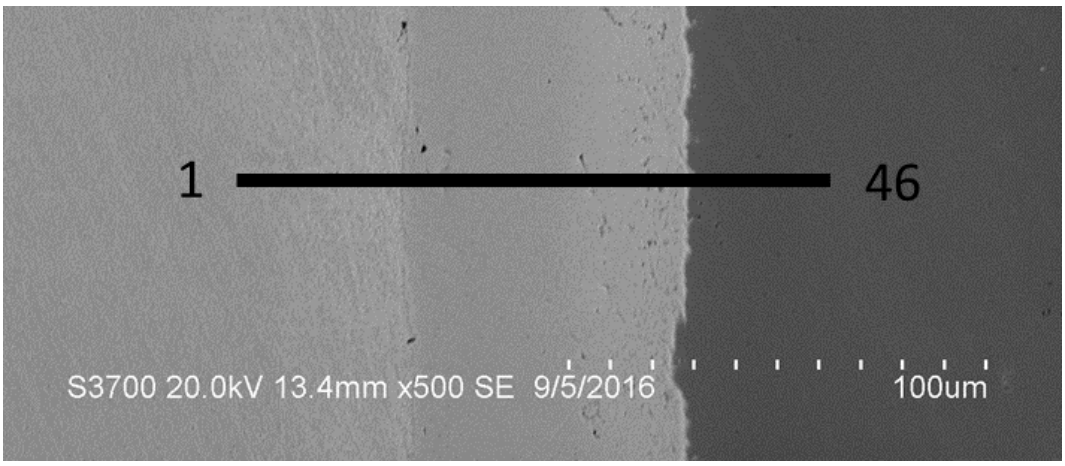

Figure 3-27 - W-AuCu-Cu interfacial region for EDS analysis

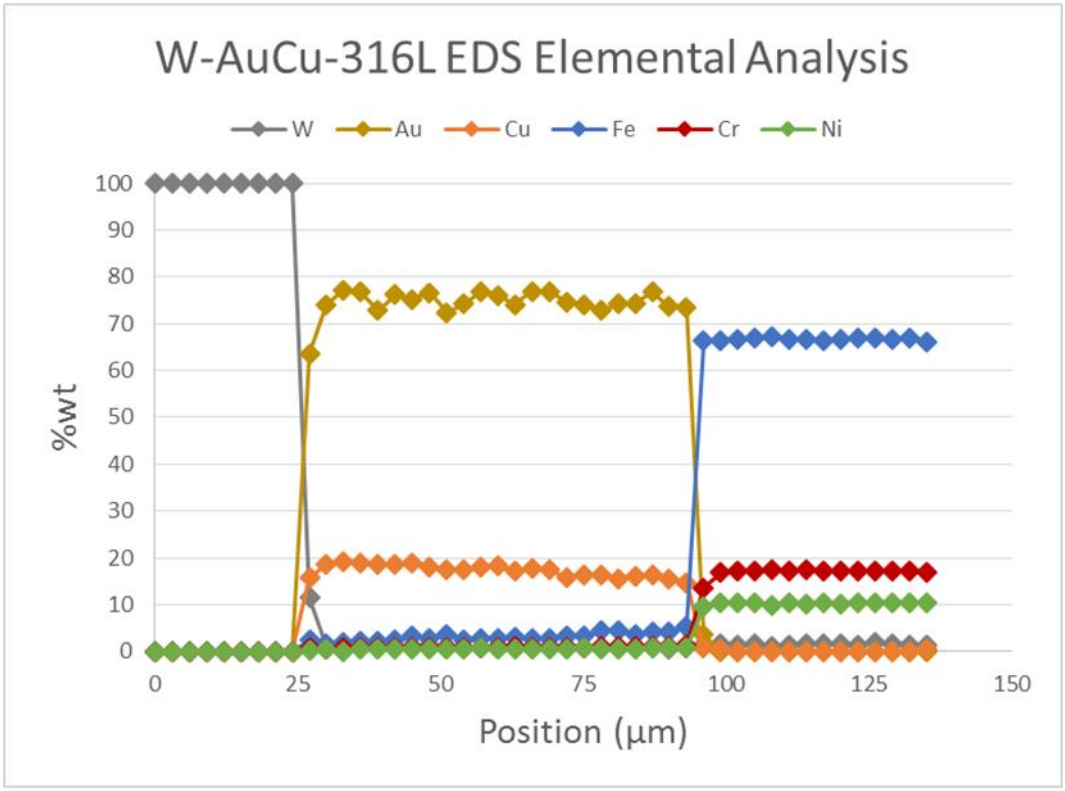

Figure 3-28 - W-AuCu-Cu EDS elemental analysis

The elemental diffusion behaviour of the W-AuCu-316L joint has been assessed through EDS analysis. The analysis location is presented in Figure 3-27 and the results shown in Figure 3-28.

A line profile was assessed using 46 points spaced approximately 3µm apart. There is minimal inter diffusion between tungsten and the AuCu material. This is consistent with the findings in section 3.3.2. There is marginally more diffusion of elements across the AuCu and 316L boundary. Most noticeably there is a small amount of copper and iron transported. However the degree of

diffusion is small, and the joint can be considered to have a sharp transition from parent material to brazing interlayer.
The balance of gold is significantly higher for this material combination with a value of 70-80%. Noticeably this sample is absent of a copper parent material. This is caused by the lack of diffusion of gold into the parent material, leaving the final composition of the brazing alloy much more aligned with the initial composition of 80% gold.

3.3.4 316L-AuCu-Cu brazed interface metallography

The final material combination for metallographic inspection is the brazed 316L-AuCu-Cu specimen. The purpose of this material combination was to provide somewhat of a control set of samples for which the complexities of brazing the extremely brittle and dissimilar tungsten (in terms of material properties) are not a contributing factor.

A cross section of the interface of the 316L-AuCu-Cu joint as captured by the Alicona Infinite Focus is presented in Figure 3-29.

There is a full face to face bond between both parent materials and the brazing alloy. There is a complete absence of any bonding imperfections. This is in contrast to both specimens containing tungsten, which exhibited a small void or cavity.

There is no obvious pooling or recessing of the braze alloy at the free edges of the interface. Axial misalignment of the parent materials is however visible.

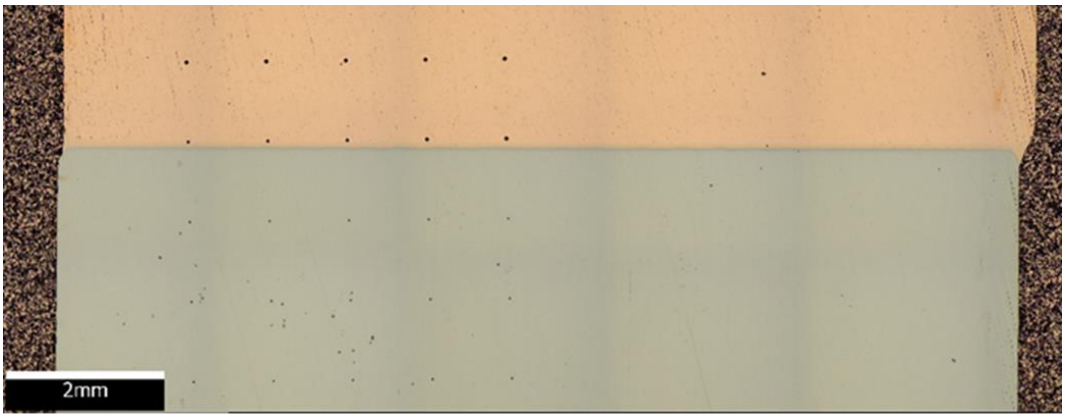

Figure 3-29 - Figure 21 - 316L-AuCu-Cu brazed interface - entire cross section

The microstructure of the 316L-AuCu-Cu specimen is presented in Figure 3-30. It observed that even at relatively high magnifications there are nothing of the nature of a defect or flaw.

It is not easily possible to determine the exact boundary between the copper base material and the AuCu alloy. This is consistent with previous observations of the Cu-AuCu interface [90]. This is due to the high diffusivity between copper and gold.

On the copper material there are dark spots due to pitting and are not of microstructural relevance.

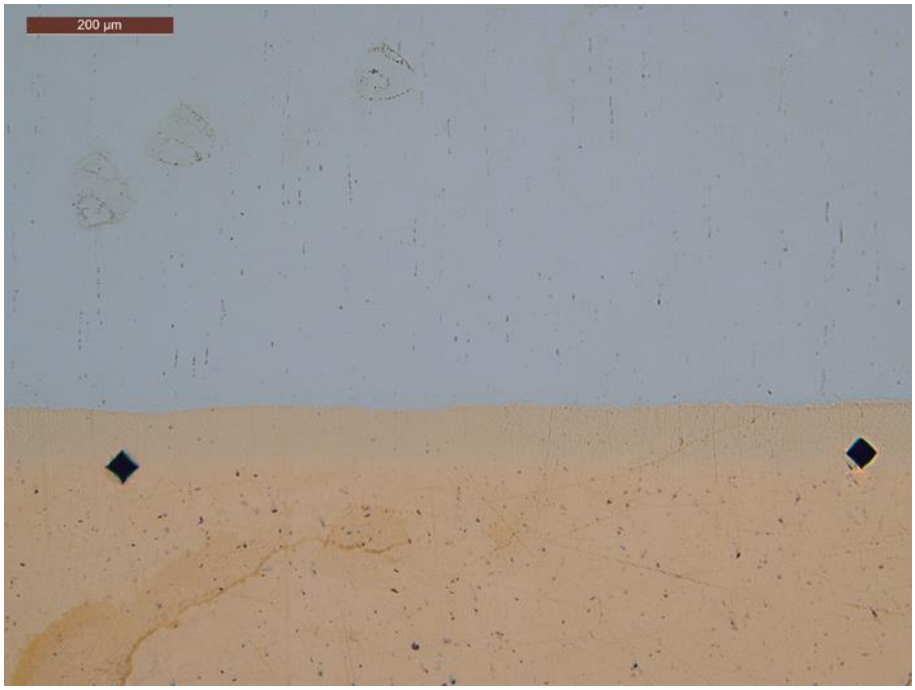

Figure 3-30 - Microstructure of 316L-AuCu-Cu brazed joint

The free edge region of the steel – copper specimen has been examined (Figure 3-31). There are no apparent flaws at the interface between either of the parent materials and brazing alloy. This could be considered a likely scenario due to the higher ductility of both 316L and copper in comparison to tungsten, in addition to lower discontinuity stresses (discussed in section 5.5.4) Figure 3-32 presents an SEM image of the steel – copper free edge to confirm the absence of any edge flaw such as cracks or delamination.

Figure 3-31 - Optical microscope image of 316L-AuCu-Cu brazed interface - free edge location

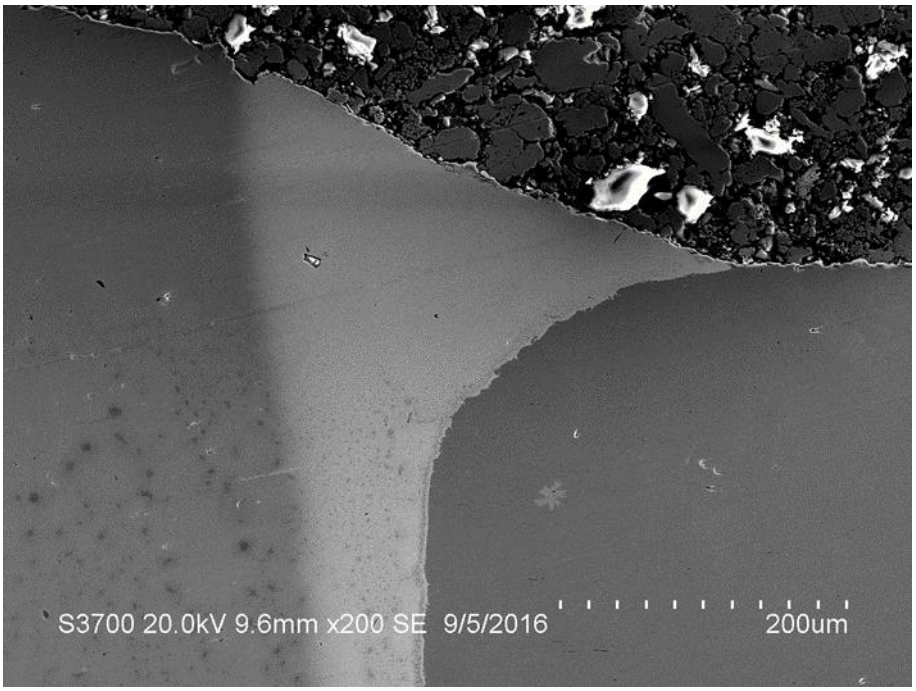

Figure 3-32 - SEM image showing the absence of interfacial defects in 316L-AuCu-Cu brazed joint

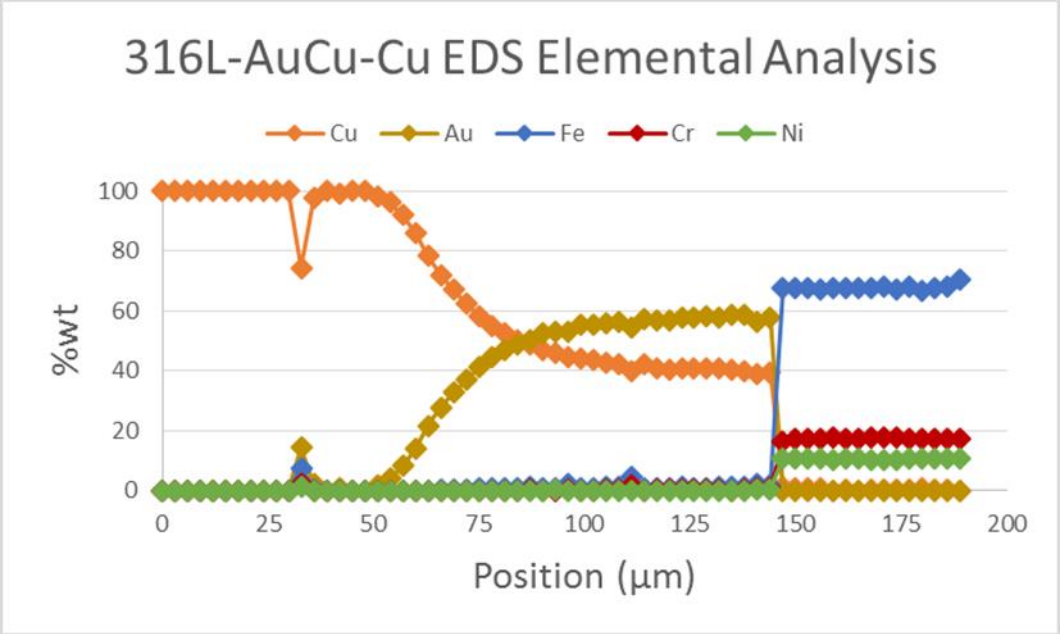

Figure 3-33 - 316L-AuCu-Cu EDS elemental analysis

The results of an elemental analysis across the 316L-AuCu-Cu interface are presented in Figure 3-33. The experimental set up was similar to that of previous analyses presented, with a line scan across the interface measured and a point spacing of 3µm.

The results for the interaction of both dissimilar material interfaces (Cu-AuCu and 316L-AuCu) are in line with EDS results presented in sections 3.3.2 and 3.3.3.

There is a very sharp transition between the 316L parent material and the AuCu alloy. The transition between copper and AuCu alloy is again very gradual and smooth by comparison. There is one location where 316L constituent elements are measured on the copper. However this is so far removed from the interface that diffusion cannot be considered as an explanation. The reason for the measurement is certainly a spec of material deposited during sample preparation. The balance of gold in the interlayer is similar to that of the tungsten – copper brazed specimen, due to a similar degree of diffusion of gold into the base copper material.

3.4 Nano and micro-hardness of brazed interfacial regions

The hardness of the materials at the interfacial region of the brazed specimens have been examined. Both nano-scale hardness using a nano-indenter and micro-hardness have been evaluated.

The distribution of hardness is a useful indicator of variations in chemical composition due to diffusion. Nano-hardness has the added benefit of being on a small enough scale that localized embrittlement due to intermetallic compounds would be detected if present [100, 118, 122].

Nano-indentation was performed using an Agilent Nanoindenter G200 with a Berkovich indenter tip and continuous stiffness (CSM) method [123, 124]. Micro hardness was measured using a DuraScan 70 G5 hardness tester using a Vickers hardness indenter with 0.1 kg load applied (HV 0.1 method).

It should be noted that access for the author to nano indentation equipment was limited, and therefore a single line scan consisting of a large quantity of indents was performed. It is recommended that future research implement additional instances of line scans for each material combination considered in order to remove uncertainty regarding the results.

3.4.1 W-AuCu-Cu brazed

The W-AuCu-Cu brazed interface is considered (Figure 3-34). A line profile beginning in the copper parent material, progressing through the brazed AuCu region, and finishing in the bulk tungsten was measured. A total of 45 locations were tested. Due to the sensitivity of the measurement on surface condition there were several measurements that did not return a valid result. The difficulty in preparing the tungsten and copper simultaneously was a considerable factor due to the difference in hardness.

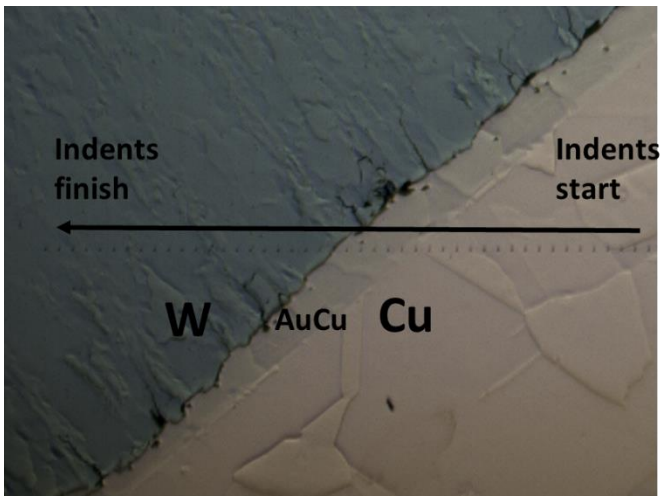

Figure 3-34 - W-AuCu-Cu brazed interface nano-indents

The results of the nano-indentation test are presented in Figure 3-35. The presented distance in mm is the true distance with respect to the normal of the interface. The locations were measured at a diagonal to allow for a higher point density in the interface, and the distance relative to the interface corrected using simple trigonometry. There is a quantifiably sizable difference in hardness properties between the two parent materials, which confirms validates the theory of an increased in polishing difficulty due to hardness differential.

There is a sharp transition in hardness from the tungsten into the AuCu alloy. The tungsten has a relatively constant hardness of around 7 GPa irrespective of distance from the interface. The hardness quickly transitions to a level of 4.5 GPa for the portion of the interlayer closest to the tungsten. This behaviour is expected due to the lack of diffusion between the materials that could arise to a smoother transitioning of hardness properties. The hardness relationship across the interface is in close correlation with the elemental composition examined previously.

The nano-hardness results are very similar in magnitude and distribution with those reported by Zhang [90] using the same parent materials with Au80Cu19Fe1 brazing alloy. This increases the confidence in the validity and repeatability of the results of the experiment.
There is a gradual reduction in hardness from the centre of the brazing interface to the copper parent material, with a drop from 4.5 GPa to 1.5 GPa. The hardness of 1.5 GPa remains constant as the distance into the copper increases. There is no apparent localized embrittlement in the braze region or the diffusion region of the parent materials. This would indicate that there are no significant brittle intermetallic compounds present for this combination of brazed materials.

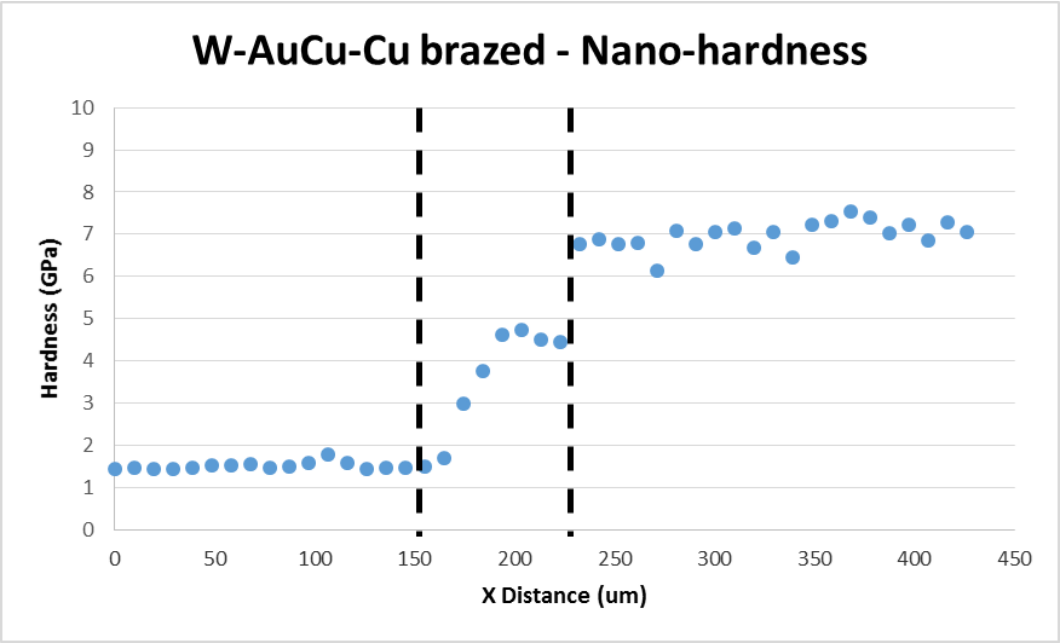

Figure 3-35 - Nano-hardness results - W-AuCu-Cu brazed

3.4.2 W-AuCu-316L brazed

The hardness profile of the W-AuCu-316L combination is now considered. An identical method was employed as per the tungsten – copper specimen. There is a noticeably more prominent surface texture present in the tungsten presented in Figure 3-36 compared with the tungsten in Figure 3-34. A variation in surface preparation is likely the cause for this disparity. There is also a clear height difference between the parent materials and the brazing alloy, highlighted by the darkened shadow along the interface. Both of these factors could lead to slight measurement inaccuracies.

The results for the nano-hardness test of W-AuCu-316L are presented in Figure 3-37. Again there is a clear sharp transition between the tungsten and brazing alloy. The values of hardness measured on the tungsten have a similar magnitude to those measured in the tungsten – copper sample of around 7 GPa. However the data is significantly noisier. The increase in surface texture of the tungsten is believed to be the cause of this.

There is a single extremely high hardness result recorded at the W-AuCu interface. The less damaging explanation of this is a measurement error due to the non-uniform surface profile at the interface. Alternatively, and of potentially detrimental consequence, the peak hardness could be a result of a brittle intermetallic region. It is believed that the former most likely holds true. There were no localized elemental variations as measured by EDS which would suggest the

presence of intermetallics for this material combination. There have also been no brittle intermetallic compounds encountered in similar W-Au80Cu19Fe1-316L parts [76, 90, 91].

There is a small variation in hardness across the length of the interface. The transition is limited in size as there is minimal diffusion of AuCu into 316L as compared with copper. The absolute magnitude of the hardness is therefore higher in the W-AuCu-316L specimen, with a value of 5-5.5 GPa. This increased hardness in comparison with the tungsten – copper specimen is due to the higher content of gold in the interlayer (80% compared to 60%). This increased volume fraction of higher hardness gold acts to increase the overall hardness of the interlayer.

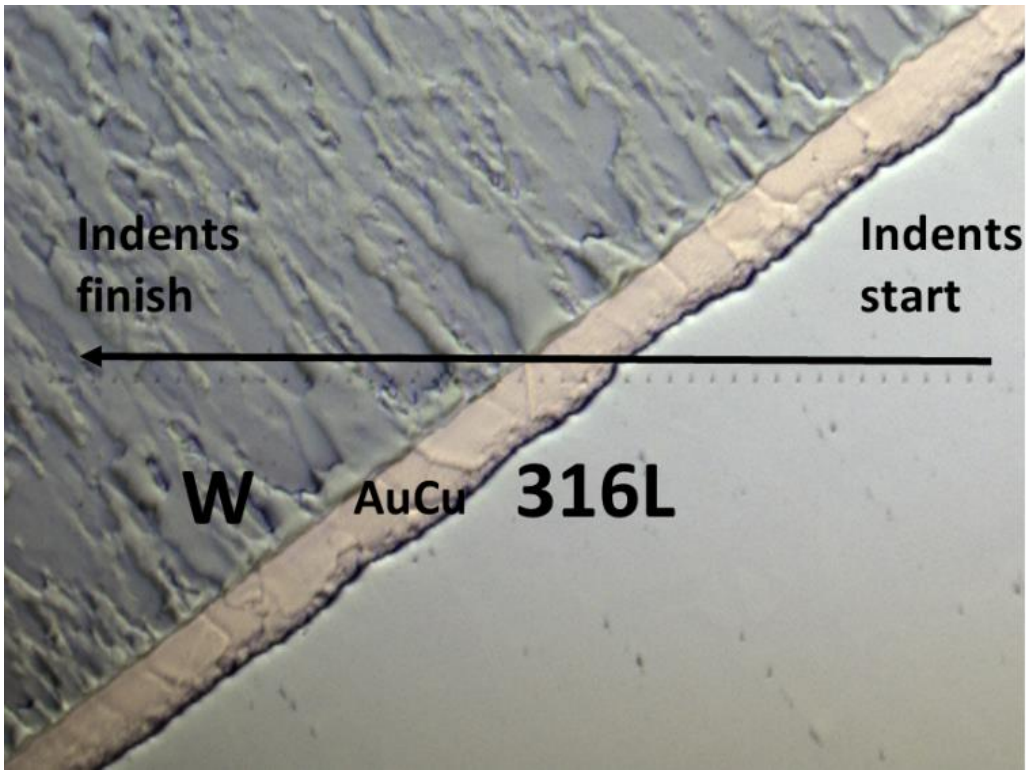

Figure 3-36 - W-AuCu-316L brazed interface nano-indents

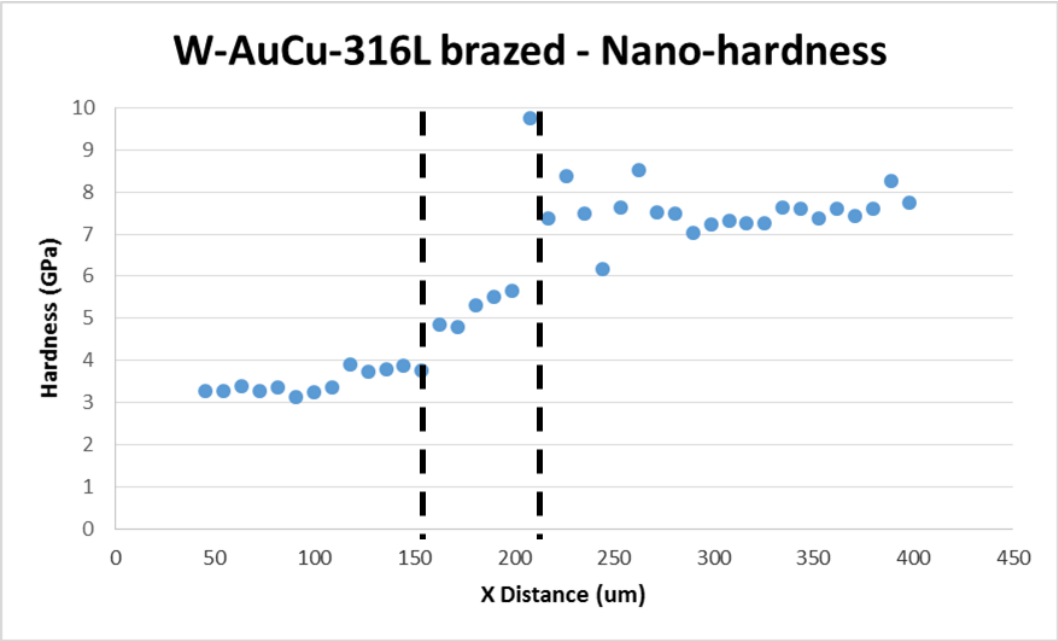

Figure 3-37 - Nano-hardness results - W-AuCu-316L brazed

There is a very shallow gradient in hardness reduction in the 316L, from about 4 GPa in the vicinity of the interface to 3.5 GPa distant from the interface. As there is no considerable observable diffusion of elements, this variation in hardness is attributed to localized strain hardening of the near-interfacial 316L following plastic deformation upon cooling from the brazing temperature.

The micro-hardness across the W-AuCu-316L interface has been measured and presented in Figure 3-38. The analysis area is significantly larger for micro scale hardness in comparison to nano scale. This has the advantage of giving information on the larger scale trends in material behaviour, but lacks the resolution required to be useful for the interfacial dimensions presented in this thesis.

The hardness of both parent materials remain constant within a range of about +/-25 HV. This falls within the expected experimental variance of the method. There is a sharp transition from one parent material to the other.

The hardness of the tungsten was in the range of 450 +/- 25 HV0.1. The hardness of the 316L was measured to be 185 +/- 25 HV0.1.

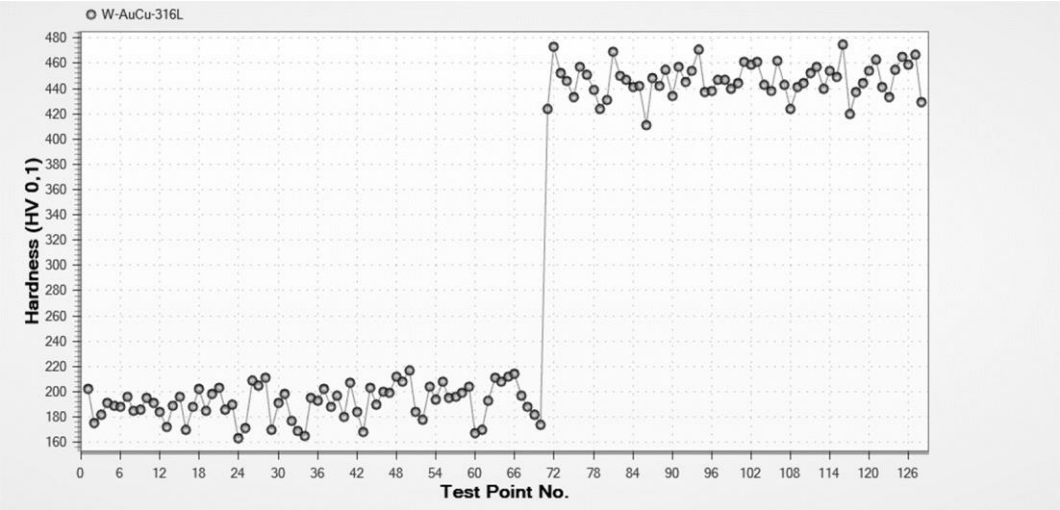

Figure 3-38 - Micro-hardness HV0.1 results W-AuCu-316L

3.4.3 316L-AuCu-Cu brazed

The nano-indentation locations and results for 316L-AuCu-Cu specimen are presented in Figure 3-39 and Figure 3-40 respectively.

The distribution of hardness across the interfacial region for this material combination are in close agreement with the elemental distributions. There is a gradual transition from the lower hardness copper into the AuCu interface. This is followed by an apparent sharp transition into 316L. Unfortunately several of the points close to the interface in 316L were not valid measurements. The experimental error is likely caused by the change in height from AuCu-316L. For an instrument as sensitive as the nano-indenter even a small change in height can introduce problems. The hardness of the AuCu is closer in value to the tungsten – copper result than the tungsten – steel results. Again this is caused by the increased diffusion of gold - copper in comparison to gold - steel.

The micro-hardness results are presented in Figure 3-41. Similarly to the W-316L results, it is difficult to determine any significant variation with respect to distance from the interface due to the increased length scale of the measurement area. There does however appear to be an increase from about 50 HV0.1 to 80 HV0.1 in the copper close to the interface, which would be consistent with the nano-hardness results.

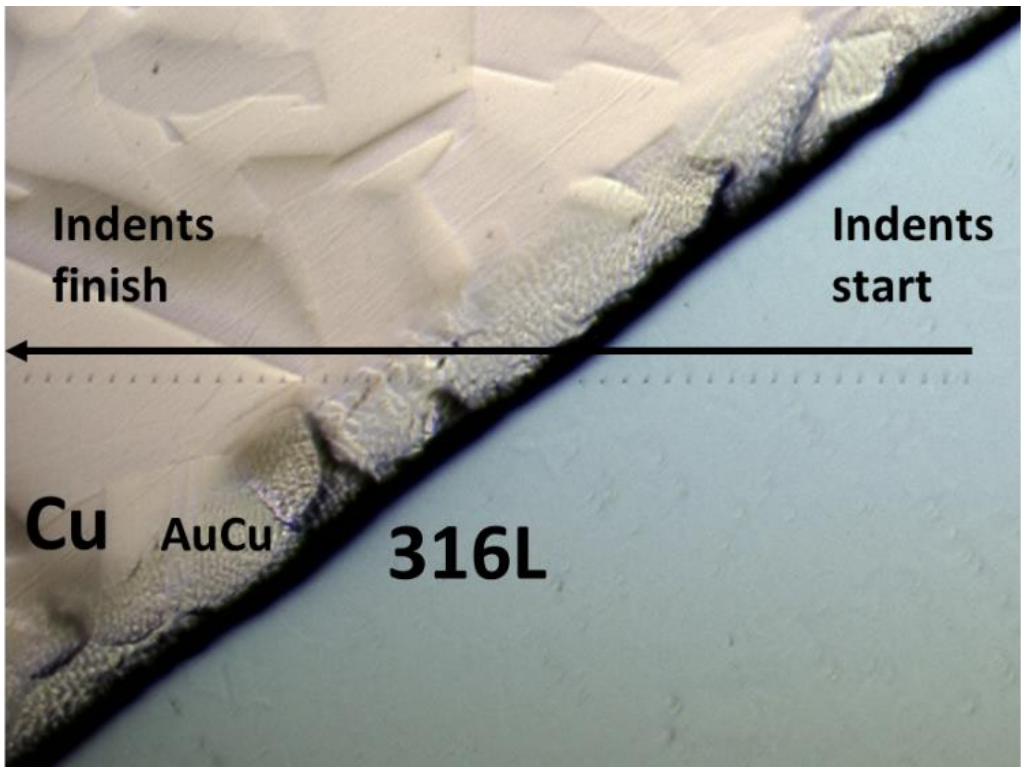

Figure 3-39 - 316L-AuCu-Cu brazed interface nano-indents

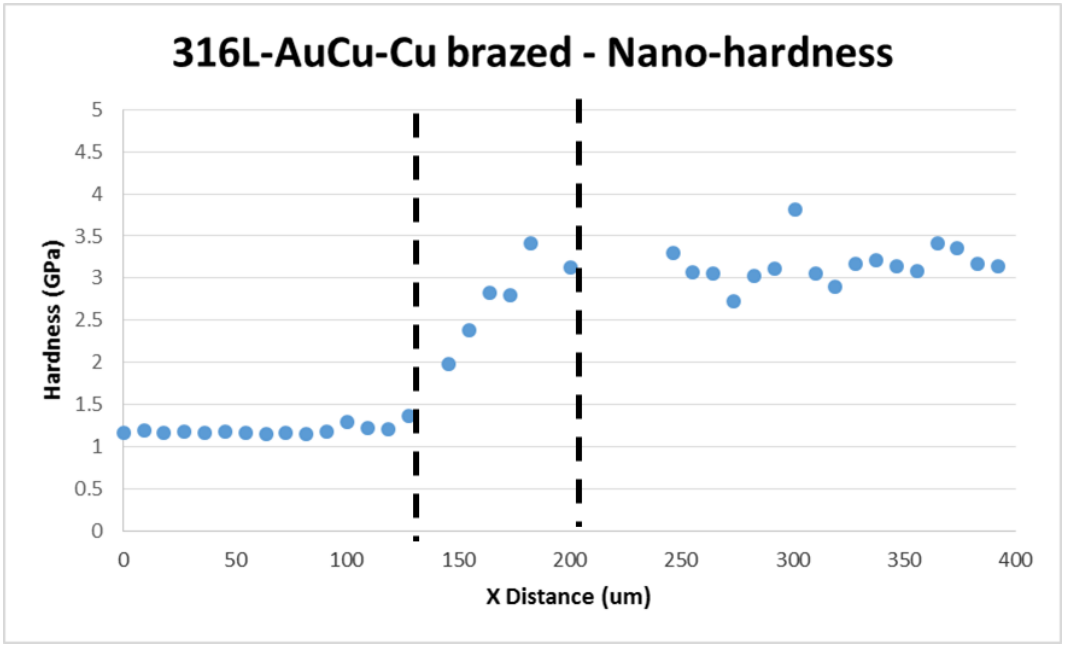

Figure 3-40 - Nano-hardness results - W-AuCu-316L brazed

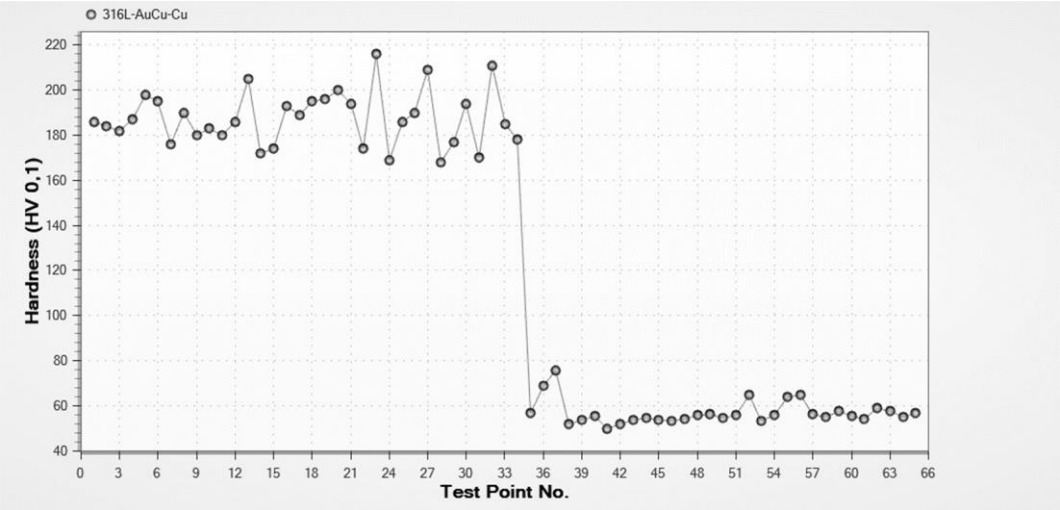

Figure 3-41 - Micro-hardness HV0.1 results 316L-AuCu-Cu

3.4.4 W-Cu HIPed with/without AuCu interlayer

In addition to W-Cu specimens being manufactured by brazing, a number of specimens were produced by hot isostatic pressing (HIPing). This majority of this work is not presented as part of this thesis and is covered elsewhere [125]. However the inclusion of nano-hardness data provides an interesting comparison with the brazed specimens.

W-Cu HIPed specimens were produced both with and without an AuCu interlayer. HIPing was performed at 900°C for 4 hours with an applied pressure of 150 MPa. The purpose was to further understanding of the W-Cu interaction as well as the W-AuCu interaction.

The interfacial area for the HIPed specimen without the interlayer is presented in Figure 3-42. The similar area on a HIPed specimen with the AuCu interlayer is presented in Figure 3-43. Both HIPing methods produced high quality, void free bonded interfaces.

The nano-hardness results for both parts are shown in Figure 3-44. In the parent materials distant from the interface, there is close agreement between the measured hardness. The base tungsten material measured about 7 GPa and the copper 1.5-2 GPa. This matches well with the brazed materials distant from the interface.

There is an abrupt change in hardness between the parent materials without an interlayer. This highlights the fact that there is very little inter diffusivity with W-Cu as well as W-AuCu. There is a localized peak at the interface in the tungsten, which similarly to the W-316L brazed specimen

can likely be explained due to the topographical change at the interface as opposed to intermetallic embrittlement.

Looking now at the HIPed W-AuCu-Cu specimen, containing the interlayer, and there appears to be improved smoothing of the transition of properties across the interface. This is apparent in Figure 3-45 which plots the brazed W-AuCu-Cu part (orange) alongside the HIPed specimen of same constituent parts (blue). There is a smooth, almost linear change from the low hardness of the copper to the high hardness of the tungsten.

If this gradual variation of material properties is attractive for future divertor designs, as opposed to a sharp transition, then HIPing could be considered as a promising bonding technique.

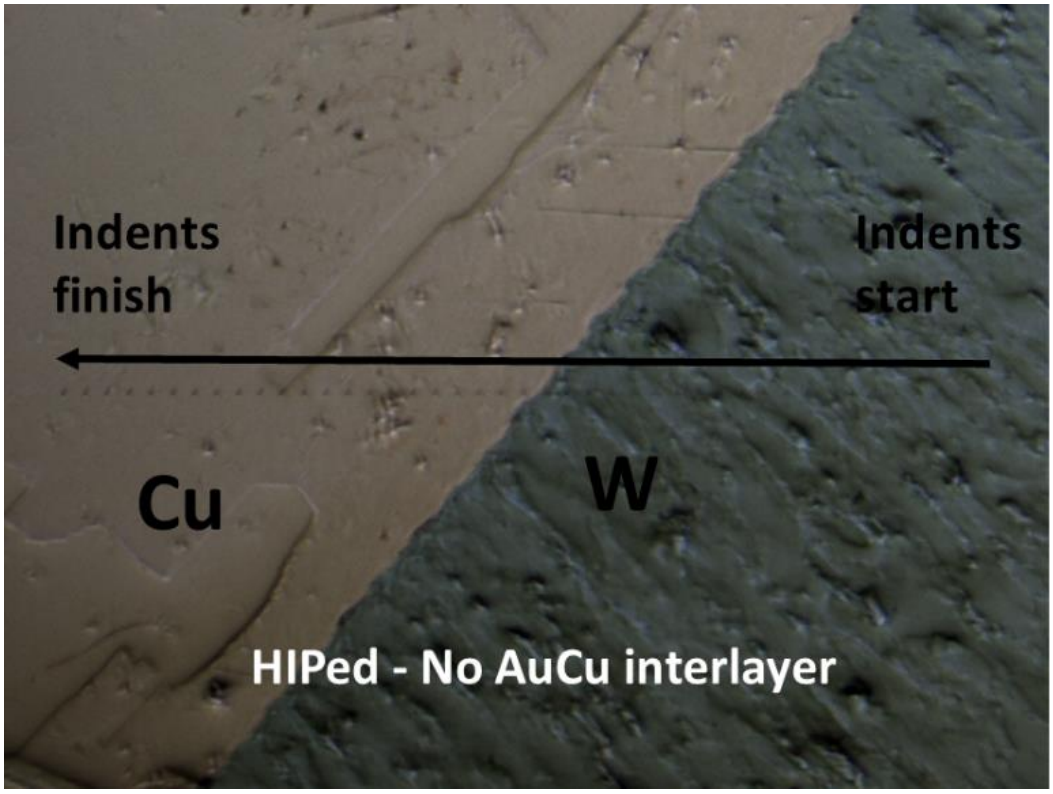

Figure 3-42 - HIPed W-Cu joint without AuCu interlayer - nano-indents

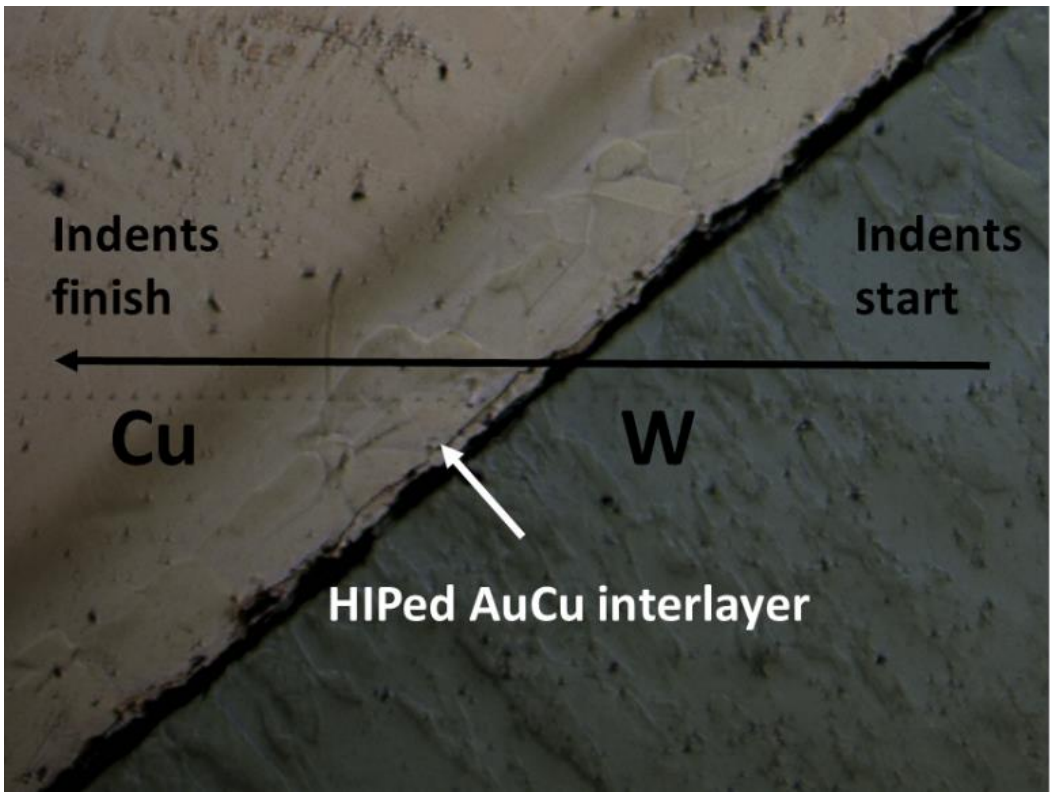

Figure 3-43 - HIPed W-Cu joint with AuCu interlayer - nano-indents

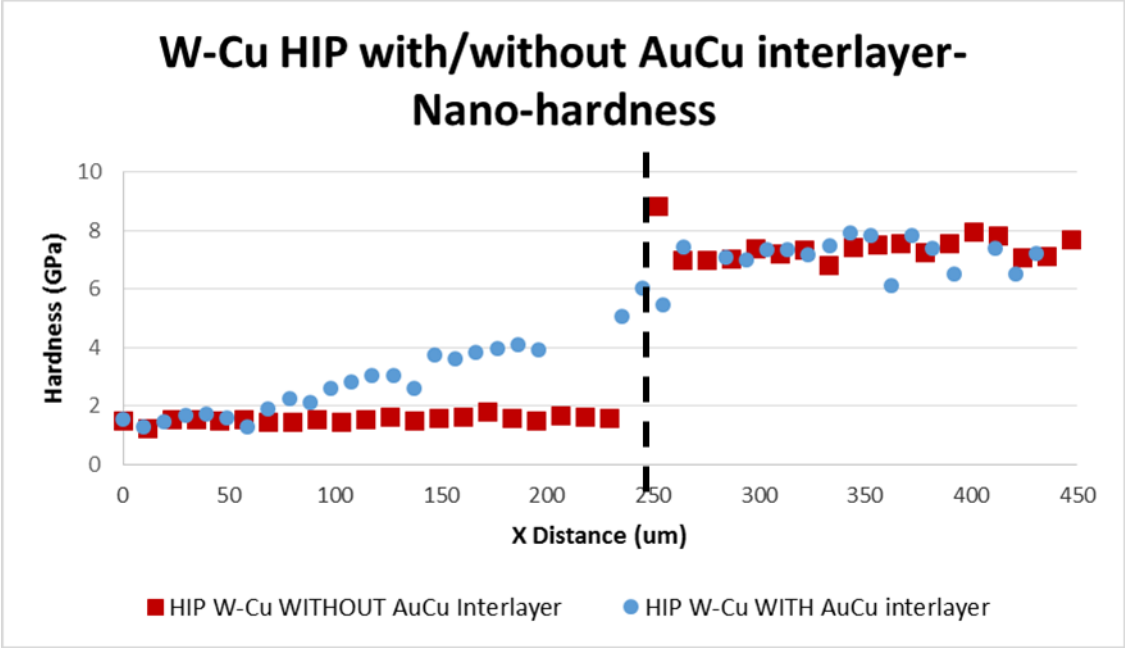

Figure 3-44 - Nano-hardness results - HIPed W-Cu with and without AuCu interlayer

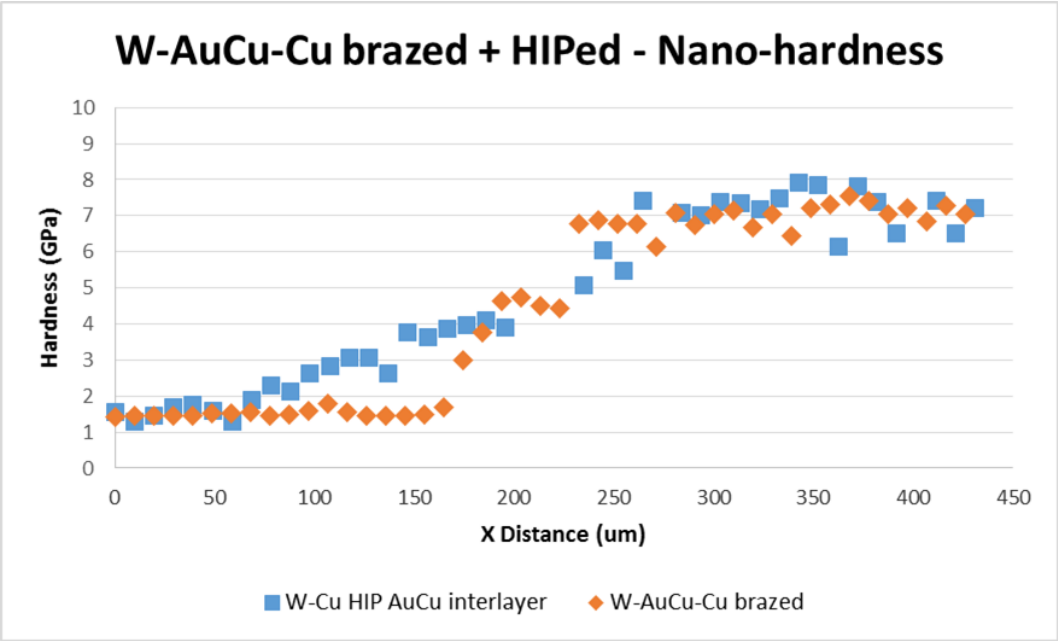

Figure 3-45 - Nano-hardness results - W-AuCu-Cu brazed and HIPed

3.5 Induction brazing

As demonstrated over the previous sections, vacuum brazing is an appropriate method of producing high quality brazed joints with the Au80Cu20 brazing alloy. However vacuum brazing is expensive and comes with a long lead time when commercial suppliers are required. Therefore it is advantageous to have a method for rapidly experimenting with different brazing parameters and materials.

Induction brazing was identified as a method of quickly and cheaply conducting brazing trials for this purpose. The advantage of induction brazing, as opposed to vacuum furnace method, was the availability of induction heating equipment within the University. This allowed the relatively speedy conduction of a large quantity of single batch trials, compared with expensive large batch vacuum brazing.

The induction brazing capability was developed by a colleague within the Fusion group at the University of Strathclyde. In addition to producing brazed specimens, this capability was developed to perform casting of brazing alloys for miniaturized mechanical testing. This capability, as well as the development process of the induction brazing, are not discussed in this thesis.

Induction brazing was performed at the University of Strathclyde using the experimental setup illustrated in Figure 3-46.

An induction heating machine with output power up to 25KW and working frequency between 30-80 KHz was used to heat the sample to the appropriate brazing temperature. An infrared temperature sensor with a range of 200-1500°C was used for temperature control. Temperature control was achieved through manual manipulation of the current by means of a foot pedal. In practice this makes it difficult to achieve accurate temperature control. Fluctuations of +/- 50°C over a short period of time were common. This compares negatively with the extremely accurate temperature control possible achievable with a vacuum furnace apparatus.

The materials to be brazed were prepared using an alcohol solvent to clean the surfaces. The samples were clamped and then placed into the vacuum vessel. The vacuum was drawn to $1x10^2$ millibar. This level of vacuum is orders of magnitude less than achieved in a designated vacuum furnace as described in section 3.2. This has the potential to result in increased levels of impurities and oxidation in the induction brazed parts.

The induction machine heated the vessel to 950°C in 110 seconds and dwelled for 2 minutes. The vessel was then left to cool down until below 200°C, with cooling taking around 100 minutes. The vacuum was retained through the whole process.

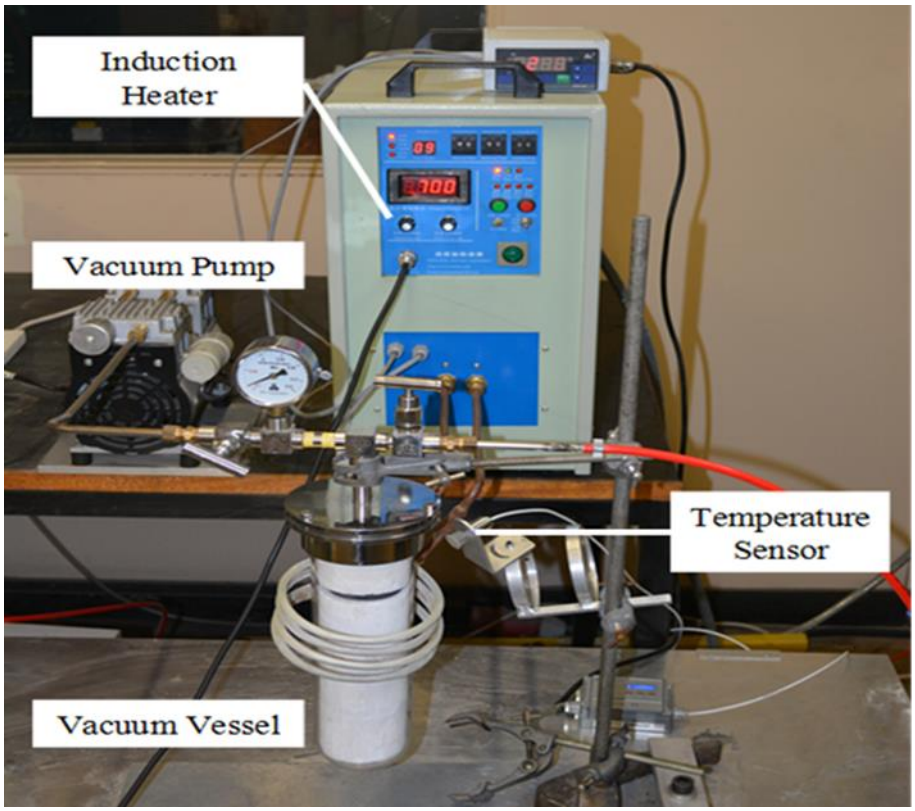

Figure 3-46 - Induction brazing apparatus

The results of induction brazing trials containing tungsten and copper are presented below.
The initial trial included the attempted brazing of tungsten with copper of grade cw-004 (99.9% purity). The results are presented in Figure 3-47.

Initially it appeared that a successful bond had been achieved, as visible in (a). However during sectioning the bond failed completely (b). Upon inspection it's clear that the entire area of the parent material surfaces were not wetted.

A purple discoloration is visible on the exterior of the specimen. This is indicative that oxidation occurred during heating. The oxidation likely prevented the capillary action required to flow the molten braze alloy.

These results would seem to confirm the conclusion that copper of grade cw-004 is not of high enough purity for brazing with AuCu filler, and that OFHC copper is required.

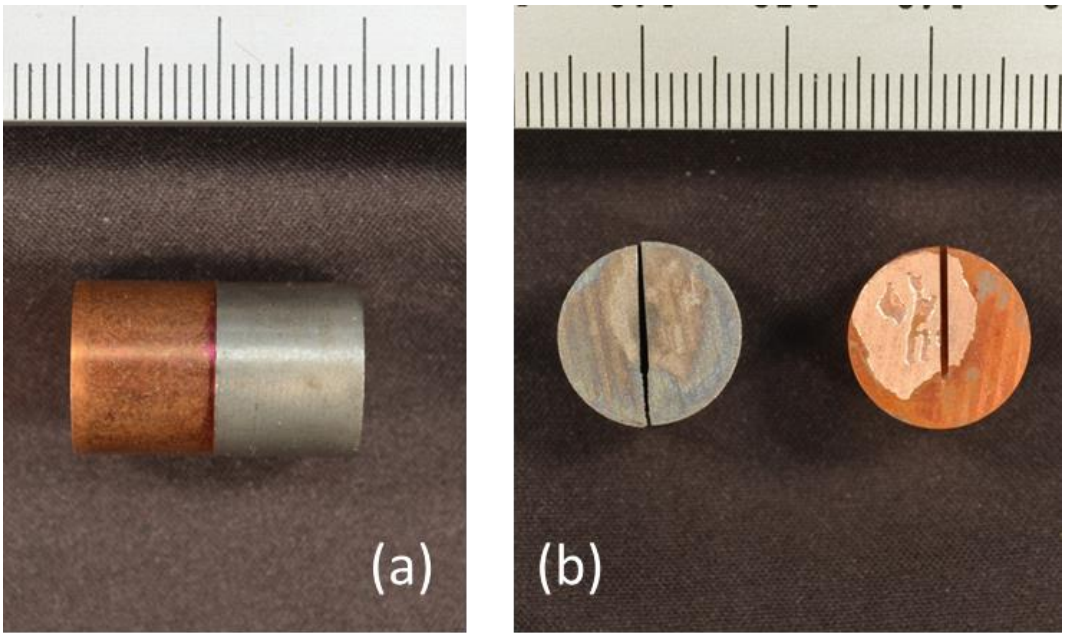

Figure 3-47 - Induction furnace brazed W-AuCu-Cu part using Cw004 grade copper. Showing (a) initially joined specimen and (b) separated part following attempted sectioning

The grade of copper was then changed to OFHC copper for the remainder of the induction brazing trials.

Figure 3-48 presents an example of a successfully bonded induction brazed W-AuCu-Cu specimen.

There is a considerable volume of brazing alloy that has pooled on the outside of the specimen as seen in (a). This is due to capillary action during the brazing process drawing the filler metal to the edge. This issue would have to be addresses should mechanical testing be planned for future research as the pooling of brazing alloy would act as a stress raiser. This would artificially influence testing outcomes, in particular for fatigue trials.

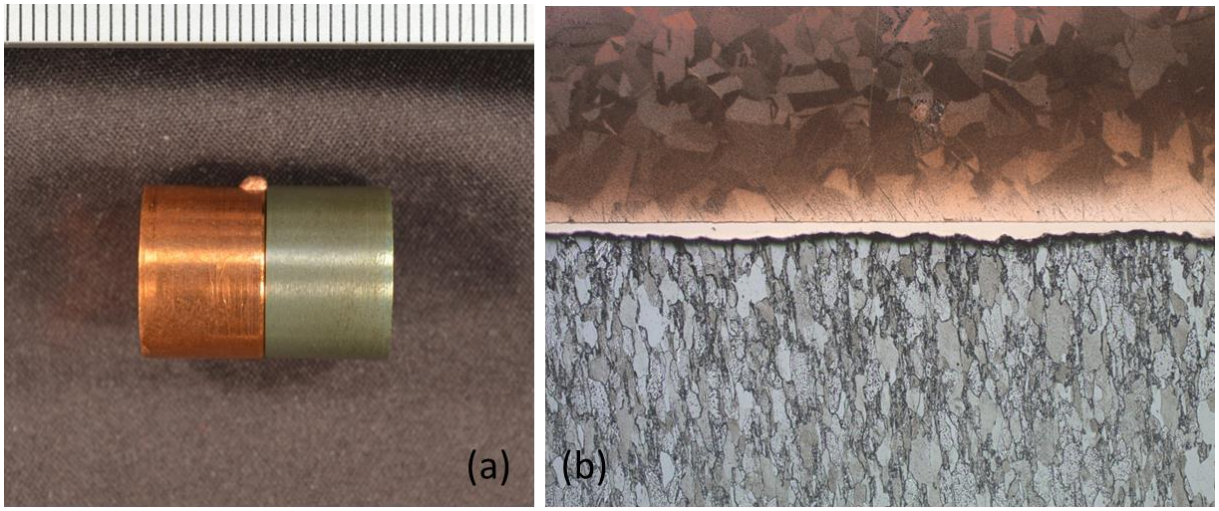

Figure 3-48 -Successfully bonded W-AuCu-Cu specimen using induction brazing. (a) Macroscopic image of bonded part and (b) micrograph of interfacial region

The microstructure of the brazed interface is presented in (b). There are no visible voids or defects. Despite reduced vacuum and temperature control induction brazing has been used to produce a specimen comparable with vacuum brazing.

Induction brazing can therefore be considered as a valid method for brazed component development with high quantity, low batch volume brazing trials.

3.6 Non-destructive evaluation

The sole method of braze quality evaluation presented in this chapter has been through sectioning, preparing and analysing metallographically. This poses several disadvantages. Firstly, this requires the destruction of the part. This is clearly not a viable method if the goal is to subject the part to mechanical or thermal testing.

Secondly, the method of sectioning the material only provides a snapshot of that particular slice through the material. In reality two cross sections are visible, with the normal distance between cross sections being equal to the width of the cutting blade. This is potentially problematic if there are voids or inclusions present in the interface, but not at that specific section. It is therefore an attractive prospect to be able to evaluate the entirety of the brazed region without the need to destroy the part.

Two methods have been investigated to achieve this goal; an ultrasonic based technique and an x-ray method.

3.6.1 Ultrasonic evaluation

Ultrasound is a commonly employed technique for evaluating the integrity of welded components [126-128]. A PVA TePla C-Sam Scanning Acoustical Microscope (SAM) was used to evaluate the interfacial region. A photograph of the equipment is shown in Figure 3-49. The SAM evaluation study was conducted at the Centre for Ultrasonic Engineering, Department of Electrical and Electronic Engineering at the University of Strathclyde.

A sound wave is propagated from a transducer by converting a high frequency electromagnetic vibration [129]. The sound wave travels through the sample until a change in acoustical impedance in the material is reached such as at a grain boundary, crack or dissimilar material interface. Based on the time-distance relationship of the wave and the acoustical impedance of the material, a 2D cross section can be mapped, known as a C-scan. Repeating this for multiple depths, i.e an X-scan, can develop a 3D representation of the part.

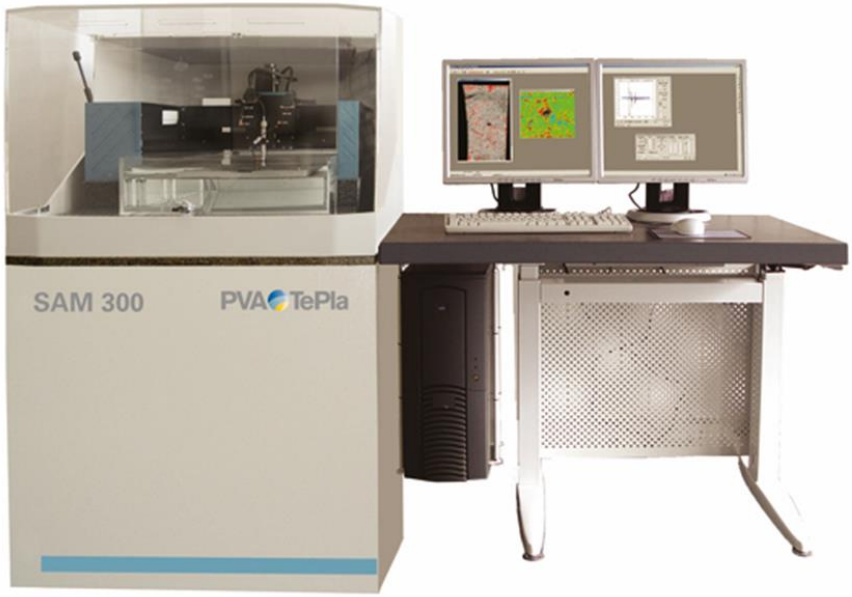

Figure 3-49 - PVA TePla Scanning Acoustical Microscope (SAM) [129]

A W-AuCu-Cu brazed specimen with overall length of approx. 20mm (10mm to interface) was evaluated using this method, presented in Figure 3-50. A 15MHz transducer was used for these measurements.

The images show from top left to bottom right the cross section at the tungsten interface transitioning through the interlayer and finally on the copper interface. Although the SAM is clearly registering aspects of the evaluated component, there is a lack of clarity sufficient to

provide information on voids and un-wetted areas. This is due to the large disparity between sample thickness (10mm for one half) and thickness of the area of interest i.e. 0.05-0.1mm.
In order to improve the resolution at the interface, a higher resolution transducer is required. However a higher frequency results in lower penetration into the sample. It was found that the braze region could not be evaluated using this method due to this limitation.

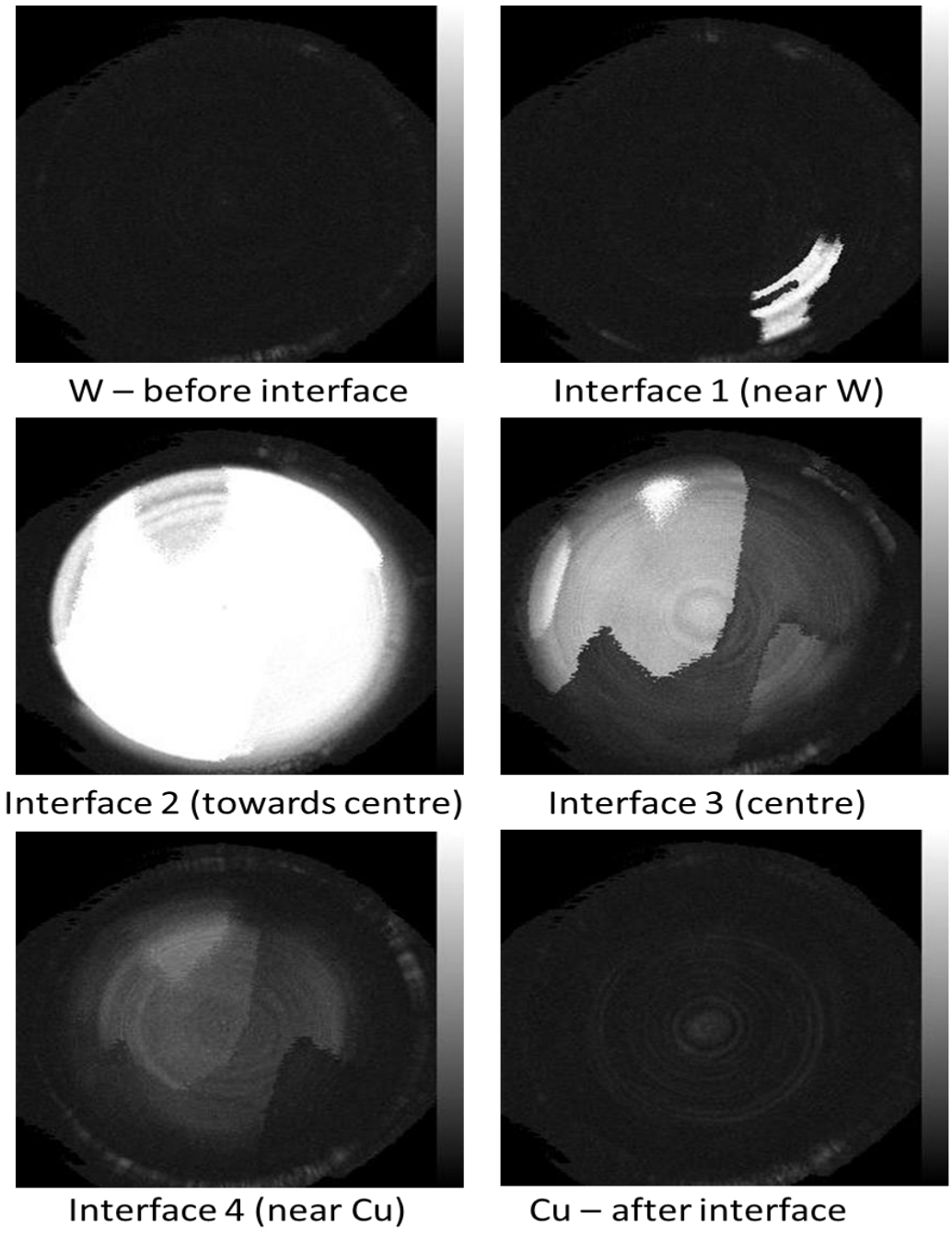

Figure 3-50 - SAM evaluation of W-AuCu-Cu brazed part

3.6.2 X-ray Tomography

X-ray computer tomography (XCT) is a non-destructive technique for assessing voids and defects in metals [130, 131] and in the earth sciences field [132]. XCT has been used for evaluating porosity in welded components [133]. For this reason XCT has been identified as a potential solution to the problem of non-destructively quantifying the quality of a dissimilar material brazed joint.

XCT experiments were performed using a Nikon XT H 225/320 LC X-ray located at the University of Strathclyde Figure 3-51.

Figure 3-51 - XCT equipment and W-AuCu-Cu brazed sample positioned for evaluation

The brazed specimens were positioned near to the x-ray emitter. The sample is then rotated whilst under x-ray irradiation, allowing for a 3D representation of the sample to be created.

The results of the scan are presented in Figure 3-52 and Figure 3-53. The sample was scanned around the full exterior of the part. A vertical cross-section of the part is shown in Figure 3-52. The XCT was not able to capture any flaws or voids in either the parent materials or the brazing interlayer. This is largely due to the fact that the x-rays were not able to fully penetrate the sample. This has resulted in vague and inconclusive scan results. This is a problem inherent with scanning both tungsten and gold due to their extremely high density (circa 19.25 g/cm^3).

A representation of the cross section of the part through the centre of the brazed region is presented in Figure 3-53. As before, although there has been a limited number of x-rays detected to generate a rough image, the resolution is not sufficient to make and conclusions on defect presence.

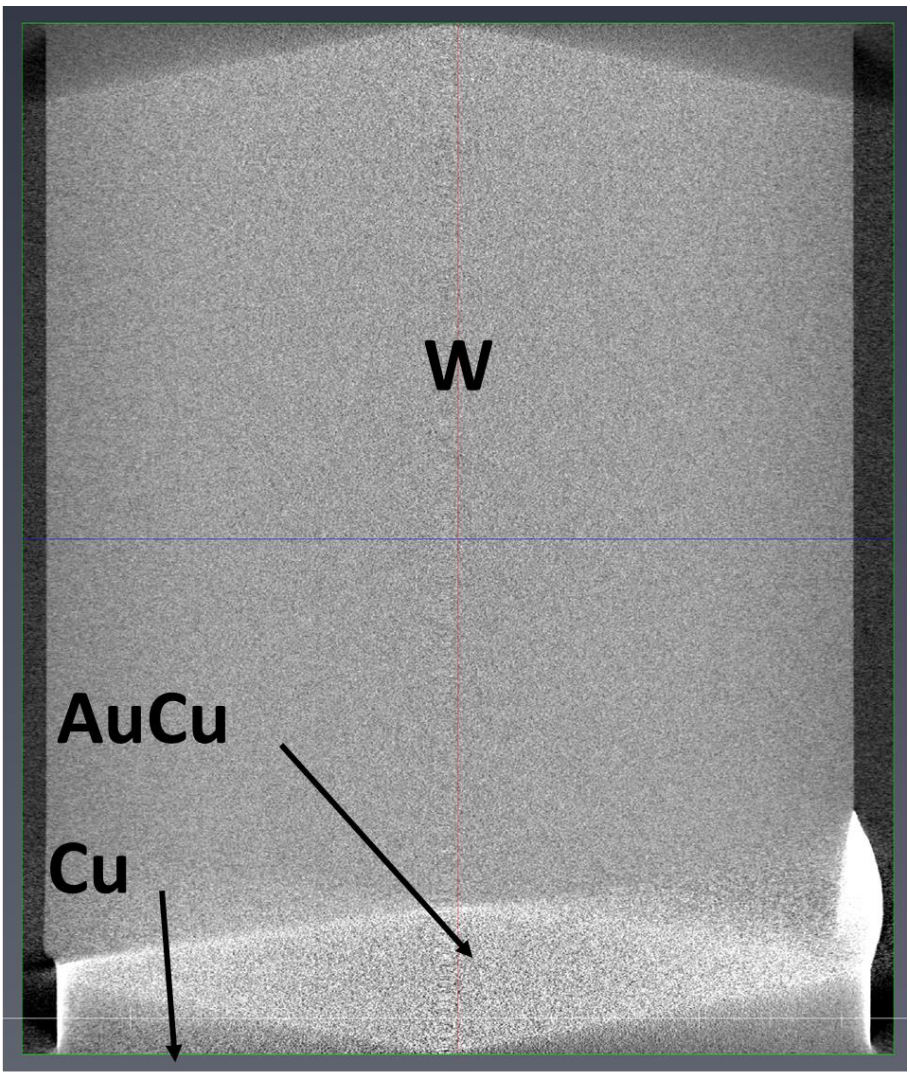

Figure 3-52 - XCT scan of brazed W-AuCu-Cu specimen

A representation of the cross section of the part through the centre of the brazed region is presented in Figure 3-53. As before, although there has been a limited number of x-rays detected to generate a rough image, the resolution is not sufficient to make and conclusions on defect presence.

The scans were conducted using the maximum available power of the XCT system. No further attempts at XCT have been trialled for this reason. A solution would be to remove the majority of the parent material, leaving only a thin sliver of tungsten and copper with the AuCu in between. However this clearly no longer could be classified as non-destructive, and would not be a suitable technique for assessing mechanical test pieces or real divertor component sized parts.

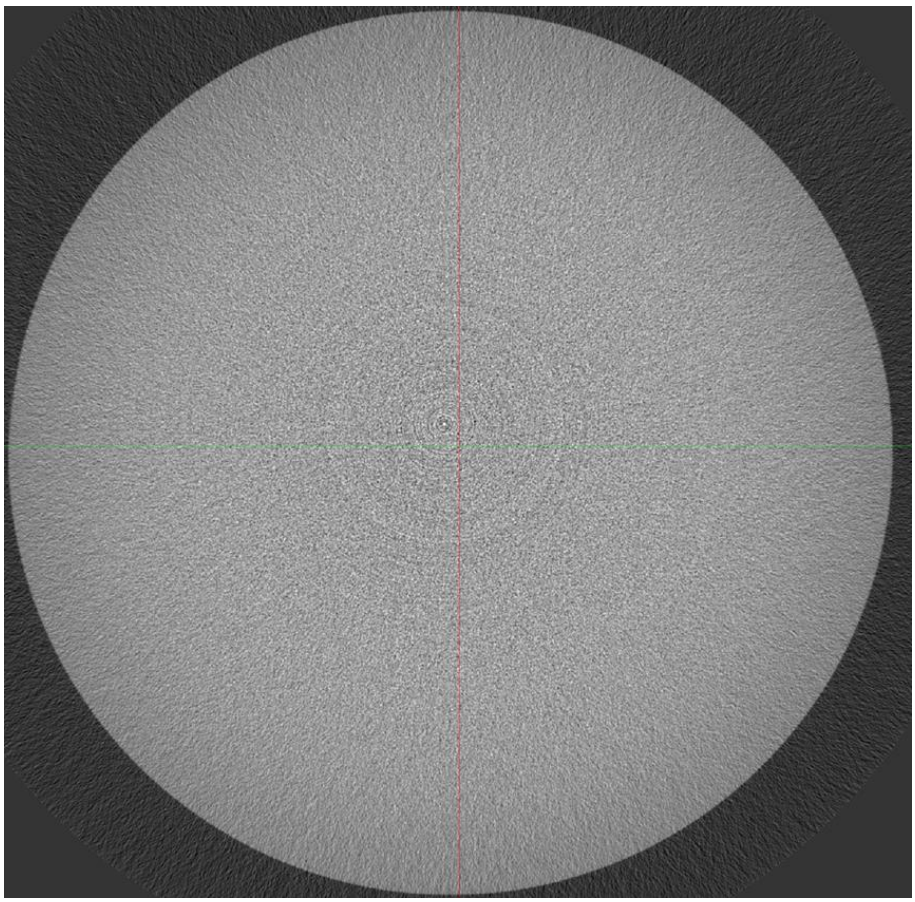

Figure 3-53 - XCT scan of cross-section of W-AuCu-Cu brazed joint

3.7 Summary

In this chapter the process of brazing of fusion relevant materials using a gold based brazing alloy has been developed. Tungsten, OFHC copper and 316L austenitic stainless steel have been bonded to create dissimilar material joints with relevance to current and future fusion divertor designs.

Successful brazing of all materials was achieved using vacuum furnace brazing with eutectic gold-copper brazing alloy at a temperature of 950°C. Brazing trials indicate that an Au80Cu20 composition brazing alloy and oxygen free high conductivity copper form the best full interfacial bond.

A high quality bond was achieved for all material combinations. In both the tungsten-copper and tungsten-316L combinations single small voids were observed, however the vast majority of the mated surfaces were fully bonded. The copper-316L combination provided a full face to face bond with no imperfections.

One concerning observation from the metallurgical inspection was the presence of interfacial defects in both the tungsten-copper and tungsten-316L combinations. Apparent delamination at the tungsten-braze interface was observed in the copper specimen. Cracks were observed nucleating at the tungsten-braze interface and propagating into tungsten for the steel parts. Both defect types have been examined optically and by SEM. These defect are highly detrimental for mechanical and thermal performance. Future brazing on mechanical test specimens and component-type designs will have to be closely monitored for such defects occurring.

The diffusion behaviour of the materials at the interfacial region has been examined by EDS analysis. It was observed on all tungsten brazed parts that there is very little diffusion between the tungsten and gold copper brazing alloy. This creates a very sharp transition in chemical composition.

Similarly there was minimal diffusion observed between the brazing alloy and 316L material. These diffusion characteristics lead to sudden changes in material properties which can have a serious impact on residual stresses and mechanical performance.

There was a much higher degree of inter diffusivity between the copper parent material and brazing alloy. This causes a much smoother transition from across the interface. Optically determining the interface between the materials is difficult due to the extent of elemental diffusion.

The variance in diffusion coefficients between materials leads to a much higher concentration of gold in the interlayer when copper is not one of the parent materials. The variability of gold content with parent materials needs to be considered in terms of effect on mechanical

performance, as gold composition will effect phase change parameters (phases, temperatures), mechanical properties and fatigue and creep performance.

The relationship between hardness and elemental composition across the brazed interfacial regions has been assessed by means of nano-indentation and micro-hardness testing.
There was a strong correlation found between nano-hardness and elemental diffusion at the interface. The tungsten-braze interface exhibited a sharp transition from high hardness tungsten to the relatively soft brazing alloy. A similar sharp transition was observed with the 316L-braze combination. This mirrors the sharp transitions in elemental composition as measured by EDS.
The hardness distribution of across the copper-braze interface was much smoother, as to be expected from EDS results.
In addition to brazed specimens, a number of HIPed tungsten-copper specimens were examined to explore the significance of the interlayer. It was observed that without the AuCu interlayer there remained a sharp transition in hardness between tungsten and copper. With the inclusion of the interlayer the HIPed tungsten-copper specimen showed an increase in smoothness of hardness distribution when compared with a brazed specimen of the same materials.

Induction brazing was used to manufacture a number of tungsten-copper specimens. This method of brazing is available within the University of Strathclyde. Induction brazing proved a successful method for joining the materials with both Au80Cu20 and Au80Cu19Fe1 brazing alloys. The quick nature and individual batch sizes of this method make it an excellent option for developing appropriate brazing conditions for new material combinations. The negative aspect of induction brazing is a lower quality of vacuum and lesser temperature control when compared with vacuum furnace brazing.

Non-destructive evaluation techniques were trialled as a way of assessing the quality of a brazed joint without the need to section the part to inspect for voids and defects. Two methods were used; ultrasonic inspection by way of scanning acoustical microscopy and x-ray tomography.
It was found that both methods failed to provide the ability to accurately resolve the brazed interface. The reasons for this being the large amount of parent material of the parts compared to the brazed region, as well as the density and acoustical impedance properties of the materials (in particular tungsten).
For future brazing trials it is recommended to use thin discs of parent material, in the region of 1mm thickness, in addition to the geometries used here in order to apply NDE techniques to assess braze quality.

4 Au80Cu20 Alloy Material Property Characterisation

4.1 Introduction

In order to perform analytical simulations of parts containing the eutectic gold-copper brazing alloy discussed in the previous chapter, it is necessary to obtain the relevant material properties to develop a material model. The material properties required for simulation such as elastic and plastic moduli, thermal expansion behaviour and heat transfer properties, are scarcely available in existing literature. It was therefore necessary to produce the data by experimental methods.

In this chapter the thermal and mechanical properties of an Au80Cu20 brazing alloy have been investigated using a range of experimental techniques. The properties required for FE simulations are elastic and plastic moduli, yield stress, thermal expansion coefficient, thermal conductivity and specific heat. A number of thermal properties; specific heat capacity, thermal conductivity and coefficient of thermal expansion, have been measured within the Advanced Materials Research Laboratory (AMRL) within the University of Strathclyde.

Mechanical properties have been assessed for both the as-received and as-brazed condition of the Au80Cu20 brazing alloy. The as-brazed properties have been assessed using two micro-mechanical testing techniques, namely nano indentation and micro-cantilever bend testing, in Chapter 3 of this thesis. This allows the mechanical properties of small areas, such as a 100μm this brazed interlayer, to be assessed that would be otherwise impossible with conventional macroscopic testing techniques. Micro-mechanical testing was performed in collaboration with Culham Centre for Fusion Energy (CCFE).
The material properties determined in this chapter are then implemented into FE simulation of the brazing and thermal autofrettage processes in Chapter 5 and Chapter 7 respectively.

The mechanical properties of the as-received brazing alloy have been investigated by means thermo-mechanical testing using miniaturised test specimens at the Advanced Forming Research Centre (AFRC), University of Strathclyde (section 4.5 and 4.6).

4.2 Thermal property testing

Thermal property characterisation has been conducted using a series of experimental techniques within the Advanced Manufacturing Research Laboratory (AMRL) at Strathclyde University. All material data has been generated upon heating only as controlled cooling rates are not a functionality of the equipment. The assumption for implementing the properties into an FE model are that there is no significant variance in properties for heating or cooling. Due to the expensive nature of the brazing alloy, a single specimen of 10mm x 10mm x 1mm was procured from the supplier of dimensions suitable for the three types of thermal testing equipment used.

The rectangular thermal property specimen has dimensions of 10 x 10mm with a thickness of 1mm. The chemical composition of 80%wt Au, 20%wt Cu is identical to the foil used for brazing throughout this thesis, and the mechanical test specimens discussed later in this chapter.

4.2.1 Thermal expansion

The co-efficient of thermal expansion (CTE) was measured using a Netzsch Dilatometer 402 [134]. The thickness of the sample is smaller than recommended by the equipment manufacturer. Due to extremely high expense of the brazing alloy, 1mm thick was the maximum that was obtainable for this study. This could potentially introduce uncertainty into the results. The smaller volume of material will increase in temperature over a shorter timescale, and expand less overall, increasing the chances of noise being introduced into the data. It is recommended that future testing be performed using a batch of specimens of larger dimensions to validate the results published here.
The results of the dilatometry test are presented in Figure 4-1.

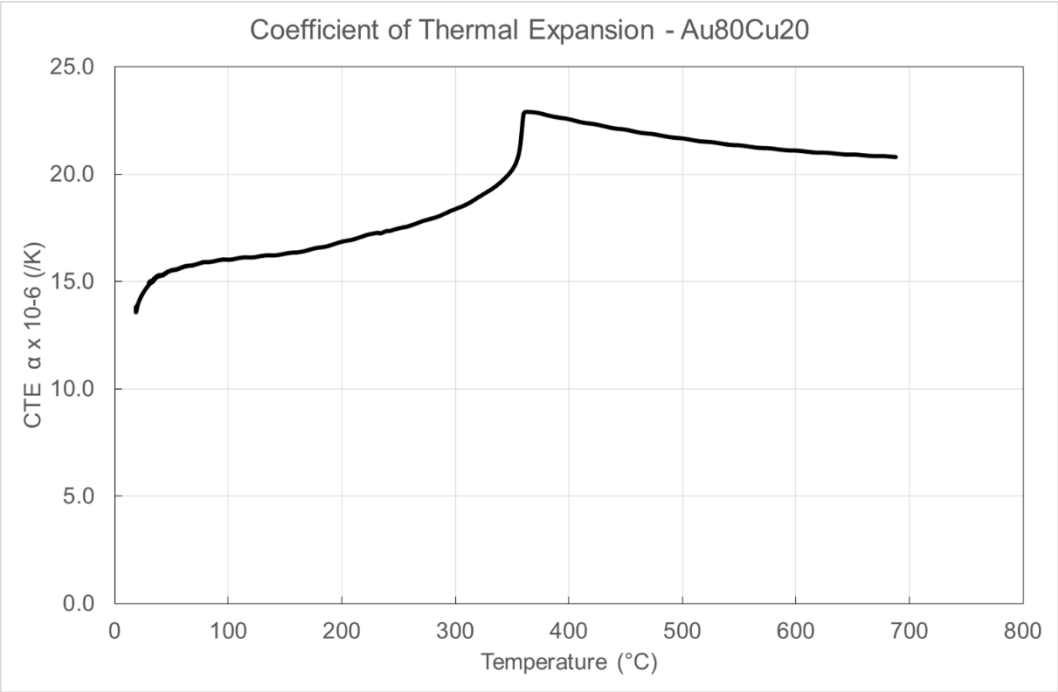

Figure 4-1 - Coefficient of thermal expansion (CTE) of Au80Cu20 in as-supplied condition

The asymptotic-like peak in thermal conductivity at circa 370°C has been observed in previous studies [96]. This coincides with the phase transformation from long-ordered AuCu II to the AuCu face centred cubic (FCC) structure [135, 136]. Further research is recommended to assess the effect of heating/cooling variation, and on sensitivity to heating/cooling rate.

Due to limitations of the equipment, it was only possible to obtain values up to c. 700°C. Beyond this, values up until the melting temperature of 910°C shall have to be estimated. Following the peak in CTE at c. 370°C, the value decreases gradually, trending towards a stable value of approximately 21 $x10^{-6}$/K.

The room temperature value of CTE experimentally measured in this study was 13.7 $x10^{-6}$/K. This is on lower than reported by a brazing alloy manufacturer for Au80Cu20 material. The manufacturer reported a value of 17.9 $x10^{-6}$/K.

As only a single sample was available for testing, it is not possible to conduct a statistical analysis of the results as would be desirable. It is therefore again recommended that future research involving the Au80Cu20 brazing alloy include a comprehensive material property testing regime.

4.2.2 Specific heat capacity

The specific heat capacity, C_p of the eutectic gold-copper brazing alloy was determined using a "Netzsch STA 449F1" Simultaneous Thermal Analysis machine which contains Differential Scanning Calorimetry (DSC) capability [137]. The same 10mm x 10mm x 1mm thermal property specimen was used as for CTE testing. The heat capacity was recorded at 0.1°C intervals from 30°C until 900°C. The results of the DSC test are presented in Figure 4-2.

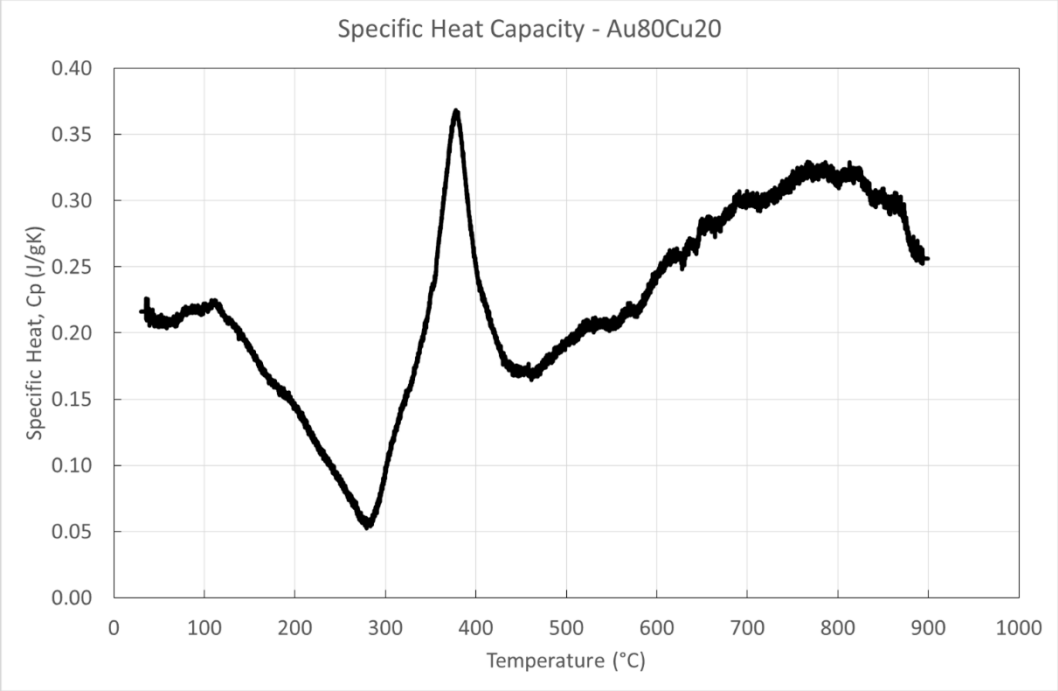

Figure 4-2 - Specific heat capacity of Au80Cu20 in as-supplied condition

As with the CTE results previously presented, there is an obvious variance in specific heat capacity over the temperature range for which the AuCu phase change is predicted. There is a decrease in heat capacity from c. 100°C until the beginning of the phase transformation occurs prior to 300°C (Figure 3-1).

The value of C_p then rises sharply until a peak value of 0.37J/gK is reached at c. 380°C. Between 450 and 800°C there is a more linear increase in C_p as the microstructure is more stable. Towards the melting temperature, i.e. 800°C+, value of C_p decreases with temperature.

The DSC test was performed up until 900°C, only 10°C lower than the liquidus temperature of the material, so no extrapolation or approximation of C_p is required.

4.2.3 Thermal conductivity

The thermal conductivity of the Au80Cu20 material was determined using a Netzsch LFA 427 laser flash analyser [138]. The same sample was used as with the formerly conducted thermal tests. The testing was conducted in accordance with the relevant ASTM standard [139].

The diffusivity/conductivity is assessed at room temperature then from 100°C to 600°C in 100°C increments. A total of three shots are performed at each temperature and the results averaged. The results of the analysis are presented in Figure 4-3.

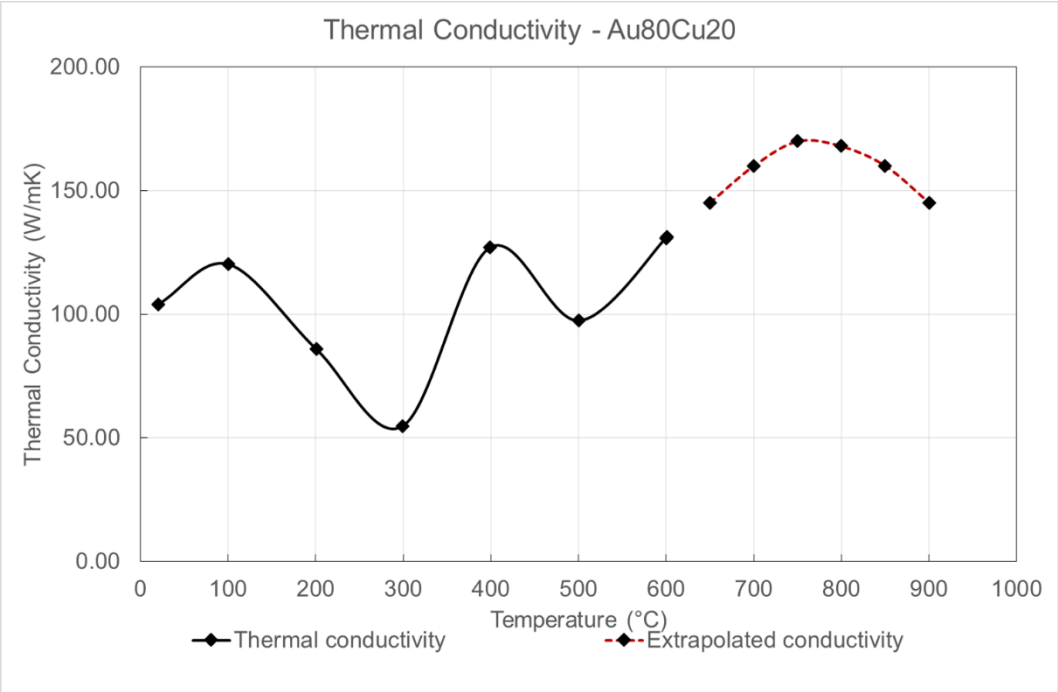

Figure 4-3 - Thermal conductivity of Au80Cu20 in as supplied condition

The variation in thermal conductivity is comparable in nature with that observed during specific heat capacity testing. Figure 4-4 presents thermal conductivity with specific heat capacity results overlain.

The values for both properties reach a minimum at c. 300°C and a peak in the region of 400°C. The profile is similar for both values up until 600°C which is the maximum temperature for which thermal conductivity data was collected. As a means of estimating the thermal conductivity values for the rest of the temperature range experienced during brazing, i.e. 910°C, it has been assumed that the profile of thermal conductivity will continue to resemble that of specific heat capacity. It

is recommended for future work that high temperature testing for thermal conductivity be performed to eliminate the need for such extrapolation, which has significant scope for error. The estimated values of thermal conductivity are represented by the red dashed profile on both plots.

At room temperature a value of approximately 100W/mK was recorded. This is higher than as published by a manufacturer of Au80Cu20 brazing alloy, which reports 52W/mK. It is clear from thermal property testing conducted for this study that discrepancies exist between published data and experimentally determined data. This further highlights the need for additional thermal property testing in future research. Ideally this would include individual samples for each test, to eliminate any effects from re-use of a single sample (including repeated microstructural changes, annealing and stress relieving of part, and dimensional changes).

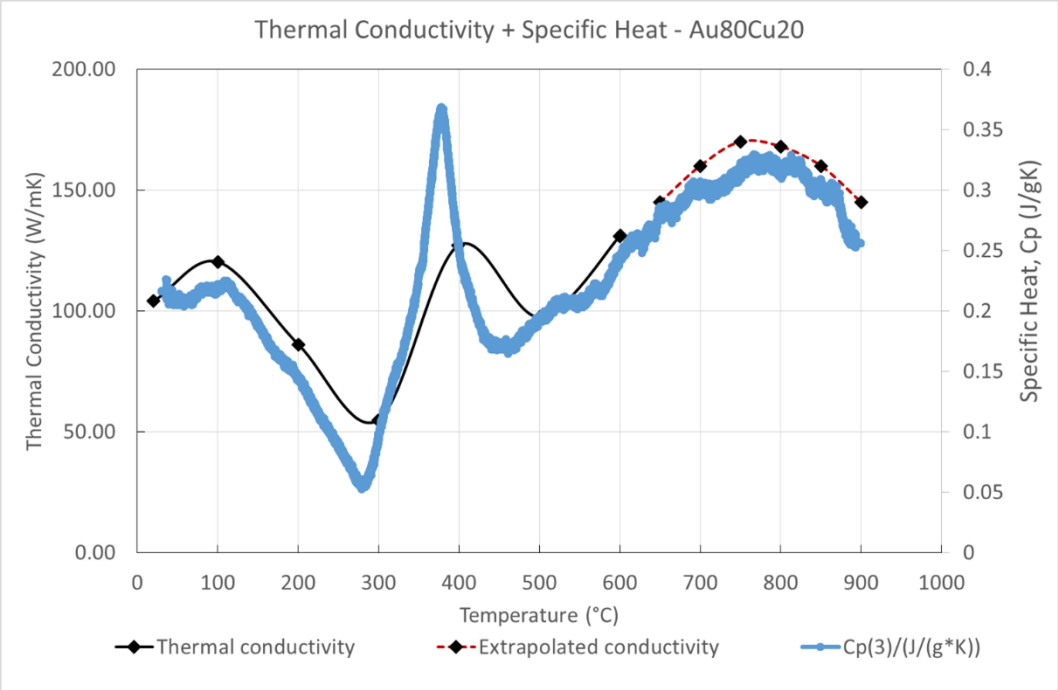

Figure 4-4 - Thermal conductivity and specific heat capacity comparison

4.3 Nano indentation- Elastic Modulus

Nano indentation is a form of micro-mechanical testing which has been used in this chapter to determine the elastic modulus of the as-brazed Au80Cu20 alloy, in addition the moduli of the parent materials within the diffusion zone in the vicinity of the braze interface. This provides information regarding elastic modulus variation with spatial variation (in respect of braze layer) at room temperature.

The technique was introduced in 1982 [140] and has been reported numerous times in literature as a reliable way of determining mechanical properties [141-144]. The technique was employed in Chapter 3 of this thesis for hardness measurements of parent and brazing materials at the dissimilar material interface.

State of the art nano indentation equipment is capable of achieving indent results with loads as low as 1μN and displacements of only 0.01nm [145, 146]. These characteristics make nano indentation an attractive proposition for assessing local elastic modulus across the brazing interface of 50-100μm.

4.3.1 Methodology

All nano indentation work presented in this thesis was performed at Culham Centre for Fusion Energy (CCFE) using an Agilent Nanoindenter G200 in accordance with ISO 14577 [146].
The continuous stiffness measurement (CSM) mode was used for all indent tests. The theory behind this method, including accounting for equipment spring stiffness and thermal drift, are reported in detail in literature [124, 145, 147] and outlined below.
The effective elastic modulus, E_{eff}, is calculated from the initial elastic unloading portion of load curve following a nano indent. This elastic gradient is termed the stiffness, S. An example of a loading-unloading curve following a nano indent is presented in Figure 4-5, showing force, P and displacement, h.

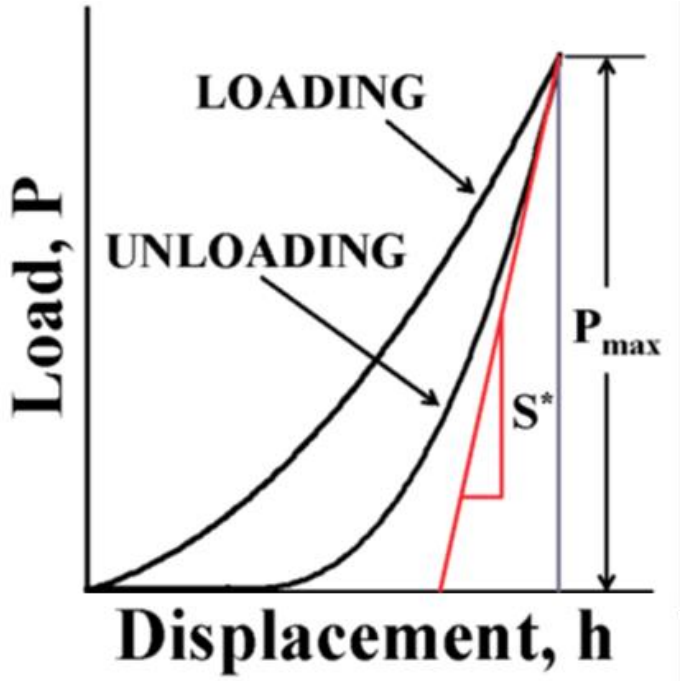

Figure 4-5 - Typical load - displacement response during loading and unloading of a nano indentation event (recreated from[145])

The relationship between E_{eff} and S is shown in Equation 1 and has been rearranged from [124].

$$E_{eff} = \frac{\sqrt{\pi}}{2}\frac{S}{\sqrt{A}}$$

Equation 1

With A, being the contact surface area between the indenter tip and indented sample volume. This effective elastic modulus accounts for elastic reactions from both the indenter and sample material. The modulus of the sample material only can be determined from Equation 2, with Poisson's ratio for the sample and indenter, ν and ν_i respectively, and elastic moduli for the sample and indenter, E and E_i [144].

$$\frac{1}{E_{eff}} = \frac{(1-\nu^2)}{E} + \frac{(1-\nu i^2)}{Ei}$$

Equation 2

The properties for the indenter tip are known as E_i=1141GPa ν_i=0.07 [124].

Two critical factors that affect the results of a nano indentation test are the size of the plastic zone and indenter sink in/pile-up. Both phenomena have been studied extensively in literature.
The effect of plastic zone size has been investigated in literature using analytical techniques [148, 149] and experimentally [150-152]. The size of the plastic zone is heavily dependent on the stress in the region. This can have a significant effect on the contact area, A. Failure to account for this

can introduce error into the results. However it was shown that for blunt indenter tips, such as the Berkovich type used in this study, the assumption of a constant relationship between hardness and contact area is valid, regardless of plastic zone size [152].

Pile-up during nano-indentation can lead to the overestimation of hardness and modulus by up to 50% [124, 153]. This is due to the contact area increasing as an elastic-plastic material is indented. Through finite element simulation this has been shown to be most likely to occur in soft materials with little potential for work hardening [153]. The degree of pile up experienced has been shown to be a function of the relationship between elastic modulus, yield stress and work hardening behaviour [153, 154].

The quantification of the effects of plastic zone size and pile-up has not been conducted in this study. However there is an appreciation from the author of the effects these can have on the results, particularly for the soft, non-work-hardening copper and Au80Cu20 material. These effects are discussed in the following section. In literature it was found that pile-up can have an effect of overestimating the elastic modulus by 10-30% [155].

Nano indentation tests were performed on a series of dissimilar material joined specimens that had been prepared using standard metallographic techniques.
The material combinations presented in the analysis section of Chapter 3, namely W-Cu, W-316L and 316L-Cu, all vacuum furnace brazed at 910°C using Au80Cu20 brazing alloy, have been assessed.

4.3.2 W-Au80Cu20-Cu

The results for the elastic modulus evaluation from nano indentation test for W-AuCu-Cu brazed sample is presented in Figure 4-6. The location for the measurements has been presented in the previous section 3.4.

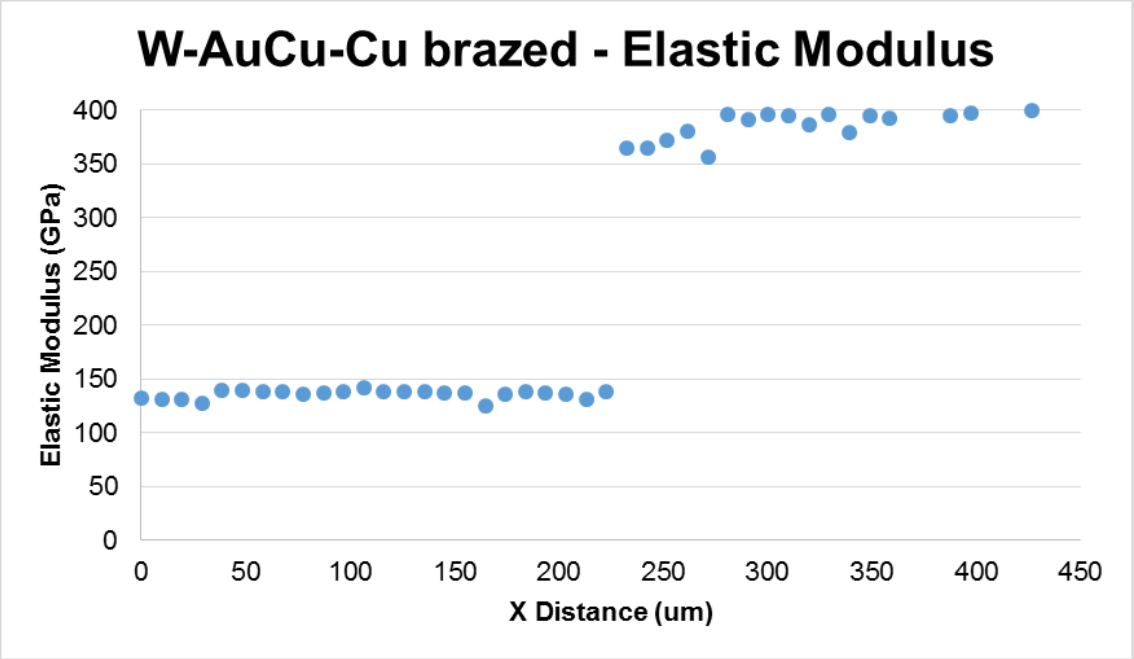

Figure 4-6 - Nano indentation Elastic Modulus results - W-AuCu-Cu

The measured elastic modulus for W was found to be approximately 400GPa which is in good agreement with literature [104]. There is a slight decrease in the vicinity of the braze interface to c. 360GPa. Although it was previously shown that interdiffusion between the brazing alloy and W parent material was minimal, there appears to be an effect on the elastic modulus. Indent size is small in relation to grain size of the parent materials and braze material. Therefore only a single grain, or small number of grains, are sampled per indent. Variations between indents in the same materials can be attributed to effects of crystal orientation of the sampled grain(s). An alternative explanation for the decrease in modulus could be an uneven surface finish of the tungsten close to the brazing material, which would be artefact of the sample preparation.

The elastic modulus of the Au80Cu20 brazing alloy is virtually identical to that of the base Cu material. A consistent value of 130-140GPa was found across the entirety of the range of indents made in the brazing alloy and Cu. This is significantly higher than the moduli for the constituent metals of pure gold, 79GPa [156], and copper 117GPa [157], at room temperature.

However it should be noted that the condition of the copper assessed in this study is not the same as reported in literature. In addition to the thermal cycle applied during the brazing process, there is the added complexity of the interdiffusion of gold and copper at the Au80Cu20-Cu interface. Due to the "soft" nature of both copper and Au80Cu20, it is believed that pile-up has resulted in artificially high elastic modulus results. If a value of 10-30% for overestimation is applicable here [155], then a true value of approx. 100-110 GPa is possible.

Figure 4-7 presents a comparison of nano indentation elastic modulus results for two W-AuCu-Cu specimens; one produced by vacuum brazing and one by HIPing. The values of E for the base metals is consistent for both methods. The results at the interfacial region show some differences. For the HIPed sample, represented in blue, there is clearly a more gradual transition in elastic modulus magnitude from W to the Au80Cu20. This finding was previously shown for hardness variation in Chapter 3.

This would suggest that the joining method and parameters have a significant effect on the material properties at the dissimilar material interface for a given combination of materials.

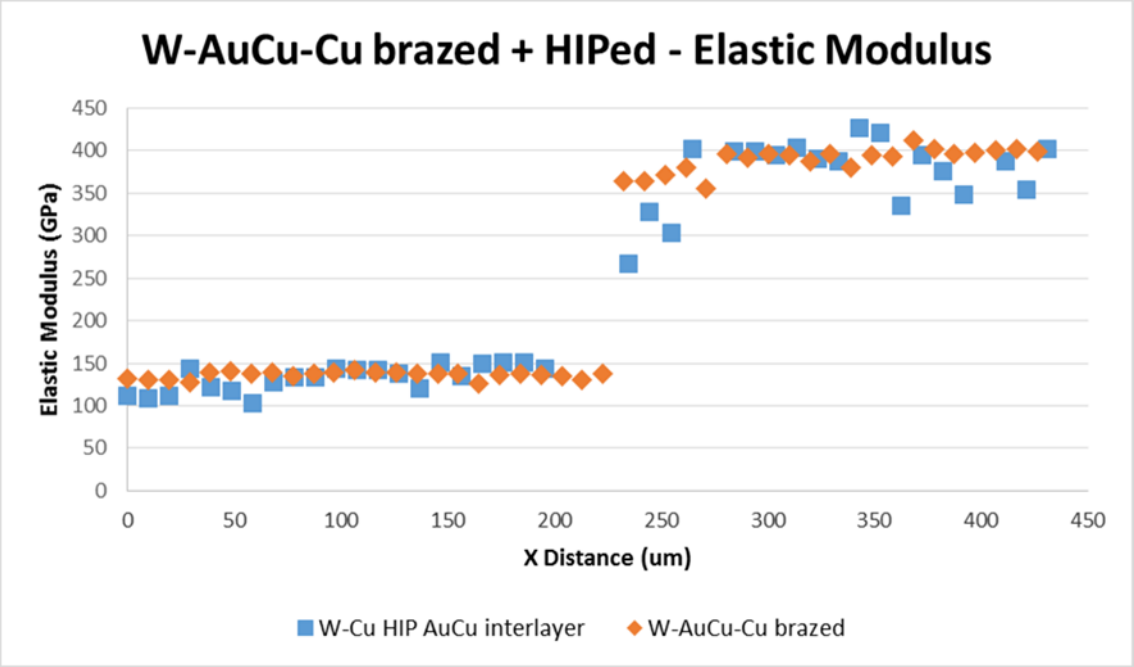

Figure 4-7 - Nano indentation Elastic Modulus results - W-AuCu-Cu brazed and HIPed comparison

4.3.3 W-Au80Cu20-316L

The nano indentation results for the W-AuCu-316L material combination are presented in Figure 4-8. With the W-AuCu-316L brazed part there is a clear distinction between both base materials and the brazing alloy, unlike with the W-AuCu-Cu combination.

The elastic modulus of the Au80Cu20 alloy was invariably 130GPa across the entire length of the braze interlayer. This suggests very little diffusion interaction between the materials that would

lead to a more gradual transition in material properties. This is in good agreement with the modulus measured for the W-Cu combination. Any influence of pile-up on the overestimation of E has been found to be consistent across both material combinations. To quantify the degree of plastic zone growth and pile-up it is recommended that future research includes Transmission Electron Microscope (TEM) and Atomic Force Microscope (AFM) analyses.

There is a sole outlier located at the Au80Cu20-W interface located at a distance of 210μm, with a value of 250GPa. This is attributed as an artefact of the measurement being performed across the interface where a change in surface height is present.

The measured value of E for the tungsten base material is less for this material combination than for the specimen brazed to copper. The value is approximately 335GPa, with some local fluctuations likely caused by surface finish and grain effects. As there has been shown to be little interaction between the base tungsten material and the brazing alloy, this decrease in E cannot be attributed to chemical or microstructural interactions between the materials. Instead, the discrepancy in results is believed to be a result of a variation in the surface preparation for each sample, which can result in varying degrees of plasticity induced by mechanical polishing. This can have a significant effect on the evaluated elastic modulus [151].

The elastic modulus values of the 316L base material as measured by nano indentation technique were shown to range from 166-181GPa across the range of points assessed. This is slightly lower than reported in literature of 193GPa. This difference can be attributed to experimental method uncertainty. Additionally, the material is in the as-brazed condition, and as such is subject to changes from chemical and microstructural evolution due to diffusion and strain induced transformations respectively (discussed in Chapter 2).

The elastic modulus of the brazing layer, Au80Cu20, is significantly smaller in magnitude than both parent materials. Considering the size of the brazing interlayer, c. 50 μm, it is possible that degree of constraint is applied on the Au80Cu20 material by the stiffer parent materials. However, as the tungsten is significantly higher than 316L in terms of stiffness, were there to be a constraining effect it would be logical to expect to observe a transition in the measured properties of the AU80Cu20 material (higher towards tungsten, lower towards 316L). As this is not observed, the effect of parent material constrain on nano indentation elastic modulus measurements of the brazing interlayer are not considered to be of importance.

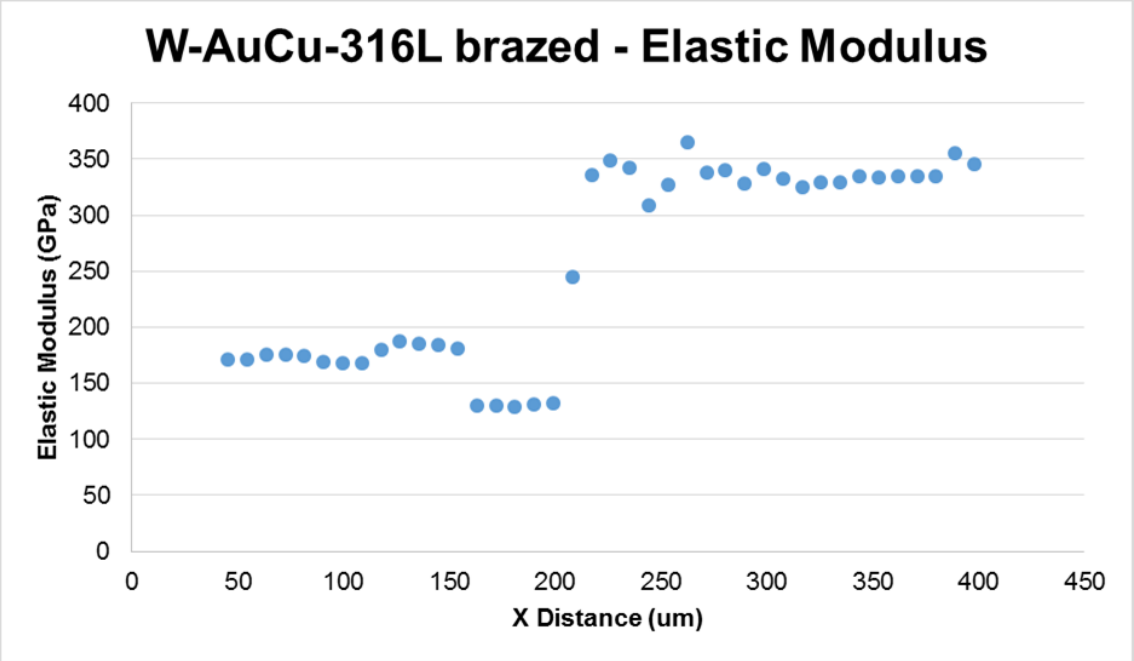

Figure 4-8 - Nano indentation Elastic Modulus results - W-AuCu-316L

4.4 Micro-cantilever bend testing

The mechanical properties of the four materials (W, Cu, 316L, Au80Cu20) considered in this brazing study have been evaluated using the micro-cantilever technique. This involves milling a prismatic cantilever beam on a polished surface using a focused ion beam (FIB) situated within an SEM. The milled cantilevers are then tested in a bending mode using the Berkovich tip of a nano indenter. The load-displacement response is then analysed using a series of MATLAB functions to determine mechanical properties of the material, described in section 4.2.2.

This micro-mechanical testing technique has been presented multiple times in literature for obtaining material properties such as elastic modulus [158-161] and yield stress [162-166]. Micro-cantilever testing has also shown promising results for assessing fracture behaviour of materials [163, 167-171], although the fracture behaviour of the materials in the interfacial region have not been considered in this study.

This type of test inherently involves micro-scale specimens. It is therefore particularly useful for assessing materials that are either impractical to handle in large quantities such as radioactive metals [147, 155] or interfacial regions that are small in nature [172-175]. It was therefore decided

that this would be an appropriate method for assessing mechanical properties of the materials in the direct vicinity of the brazing interface. This allows for testing of material in the diffused region that is not possible by conventional macro-scale test method.

Results are presented for cantilevers manufactured in two specimens; a brazed W-Au80Cu20-Cu specimen and a W-Au80Cu20-316L part. All beams were manufactured close to the brazing interface.

4.4.1 Focused ion beam milling

The FIB milling of the beams was performed at CCFE using a Helios NanoLab 600i FIB system [176]. A total of 9 complete cantilever beams were manufactured on each of the two vacuum brazed specimens, W-Au80Cu20-Cu and W-Au80Cu20-316L (termed W-Cu and W-316L samples for the purposes of this section).

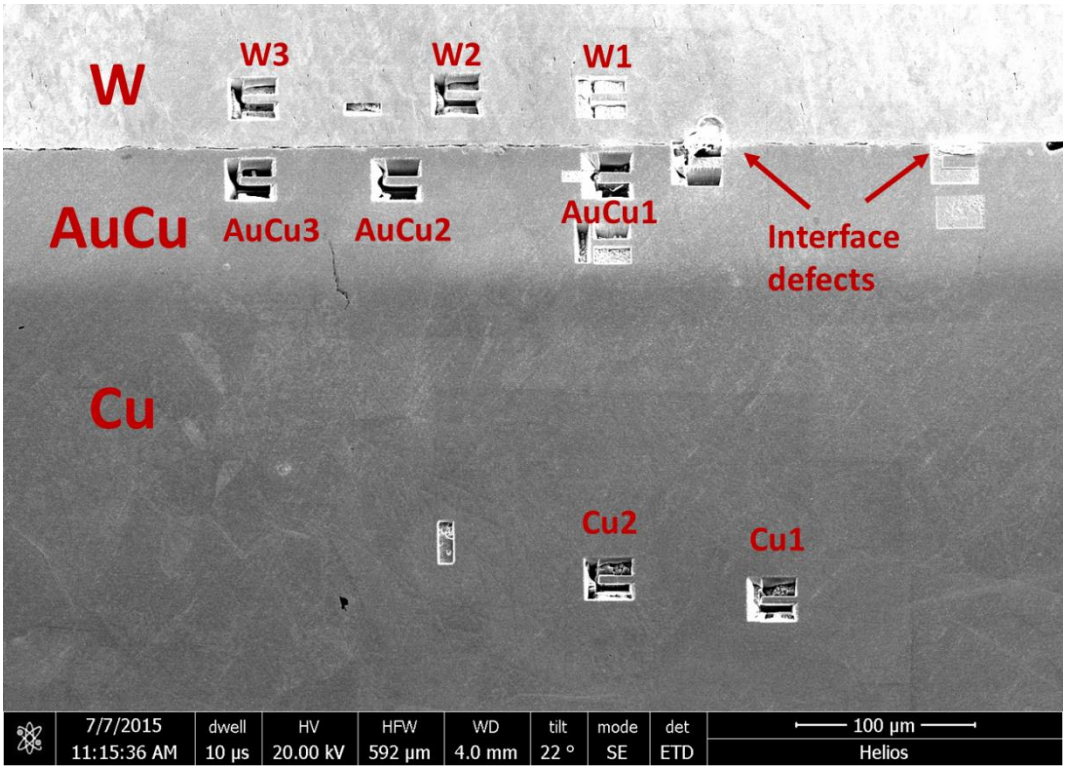

Figure 4-9 - Overview of cantilever positions created by FIB milling at W-Au80Cu20-Cu brazed interface

An overview of the FIB milling of the W-Cu sample is presented in Figure 4-9. Three micro-cantilever beams were milled on each material. The three tungsten beams, named W1, W2 and W3 were all located approximately the same distance from the interface with Au80Cu20.

The three cantilevers milled from brazing alloy, named AuCu1, AuCu2 and AuCu3 were positioned closer to the tungsten than copper. This was to ensure that it was predominately Au80Cu20 alloy that was being tested. The large degree of diffusion blurs the boundary between Au80Cu20 and Cu, making it more difficult to ensure that base copper material is not tested if the beam were to be positioned closer to the copper.

Two copper micro-cantilevers are shown in Figure 4-9, named Cu1 and Cu2.
In Figure 4-9 there are two instances of defects highlighted. These are discussed later in this section.

Figure 4-10 and Figure 4-11 present the nine micro-cantilever beam array in the W-316L specimen, with longitudinal and head-on views shown respectively.
For this material combination it was possible to locate the cantilevers for both parent materials close to the interface due to much more obvious transition between base and braze materials. To avoid confusion when discussing the beams of materials common to both samples, the three beams of each material for the W-316L sample are identified by numbers 4, 5 and 6. As such the micro-cantilevers shall be termed as W4, W5, W6, AuCu4, AuCu5, AuCu6, 316L_1, 316L_2 and 316L_3 for the remainder of this section. The beam locations and identity are shown in Figure 4-10.

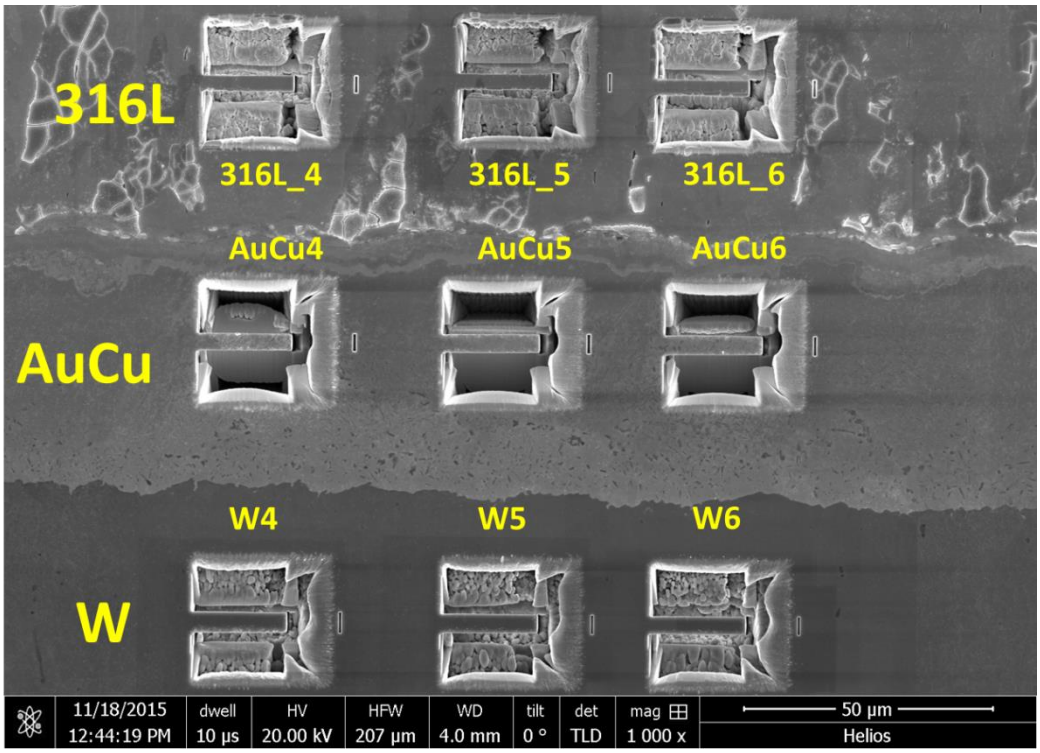

Figure 4-10 - Overview of cantilever positions created by FIB milling at W-Au80Cu20-316L brazed interface

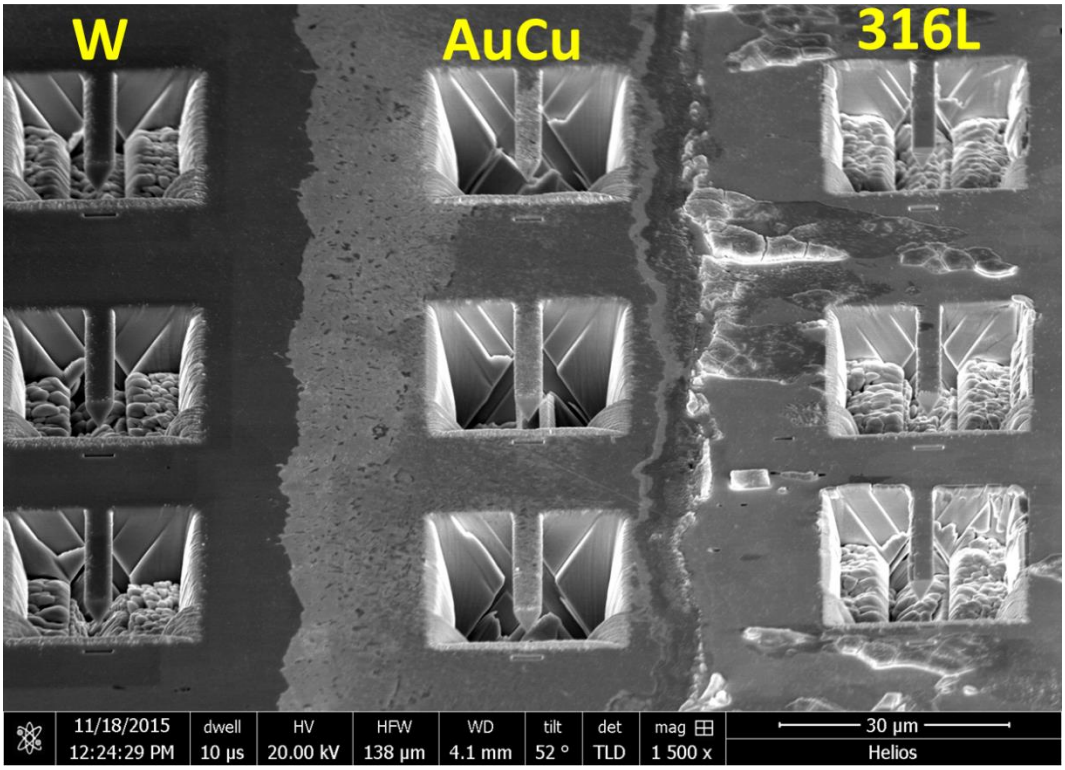

Figure 4-11 - Head-on view of FIB milled cantilevers at W-Au80Cu20-316L brazed interface

The beams were milled as part of a multi-stage process. Gallium ions with acceleration voltage of 30kV were used with decreasing current levels, resulting in a smaller collimated spot size for the FIB beam each time. This allows for large quantities of material to be removed initially, followed by finer material removal and polishing. The process used for micro-cantilever beam milling in this study was similar as previous published works [158, 177].

An initial area of 26µm x 26µm was milled, with the exception of a 20µm x 8µm section of material left un-milled. This is the material that forms the micro-cantilever beam. A beam current of 9.3nA is used for the rough trenching stage. This is shown in image a) in Figure 4-12. The area is milled to a depth of 6µm.

The stage is then tilted by 30° to one side in respect to the long axis of the beam. Rough undercutting was then performed using 9.3nA beam current. The part was then rotated by 30° to the other side to perform undercutting. The resulting profile is shown in image b) of Figure 4-12. During milling some of the material removed by interaction with the gallium ions is sputtered and redistributed on the beam as is visible in the figure. This is minimised by using ever decreasing beam currents as the final geometry is milled.

Further undercutting is performed using a reduced beam current of 0.79nA, prior to final undercutting and edge polishing using a current of 0.23nA. The final profile of the corner between beam and base is shown in image c) and the end profile of the beam shown in image d) of Figure 4-12. Although in practice it is not possible to produce a perfectly sharp corner, by using the small current beam the fillet radius has been reduced which is critical for simple beam theory assumptions.

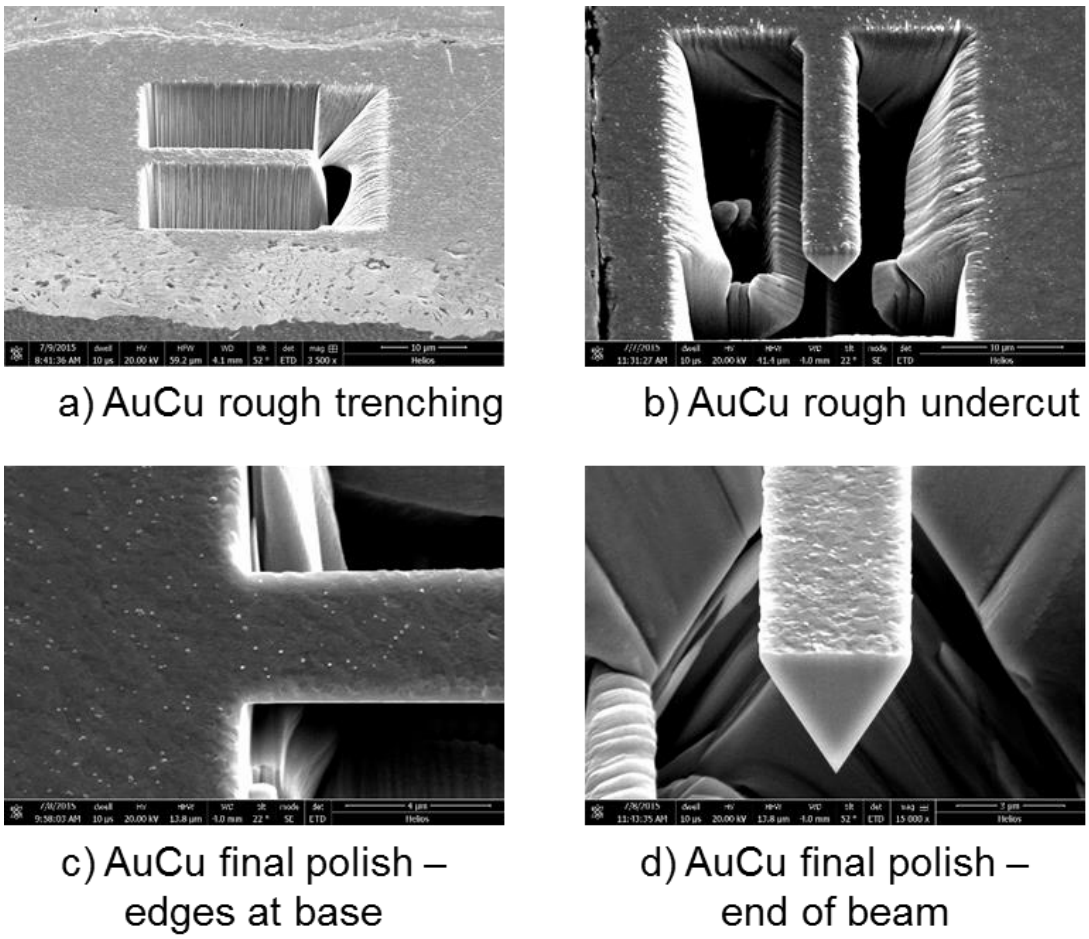

Figure 4-12 - Stages of manufacture for FIB milled cantilevers in Au80Cu20 interlayer (a) rough trenching, (b) rough undercutting at 30 tilt normal to surface, (c) final polish to achieve small fillet radius at base, (d) head on view of polish finished profile

The micro-cantilever beams were manufactured to approximate dimensions of 18μm in length with a uniform triangular cross section with 3μm edges as shown in Figure 4-13.

The dimensions were chosen to satisfy the minimum critical aspect ratio of 6 required for simple beam theory, and are in accordance with published micro-cantilever experiments in literature [158]. The internal angles of the triangular cross section are milled at an equal 60°.

However it was observed that the final dimensions of the cross section were not that of a perfect equilateral triangle. In reality the left and right hand side edges are elongated. This outcome has previously been reported in literature [158]. This could contribute to an error in the calculation for a uniform cross-section cantilever beam. It is recommended for future work to include FE calculation of load/deflection to obtain elastic modulus using the accurate geometry of the beam.

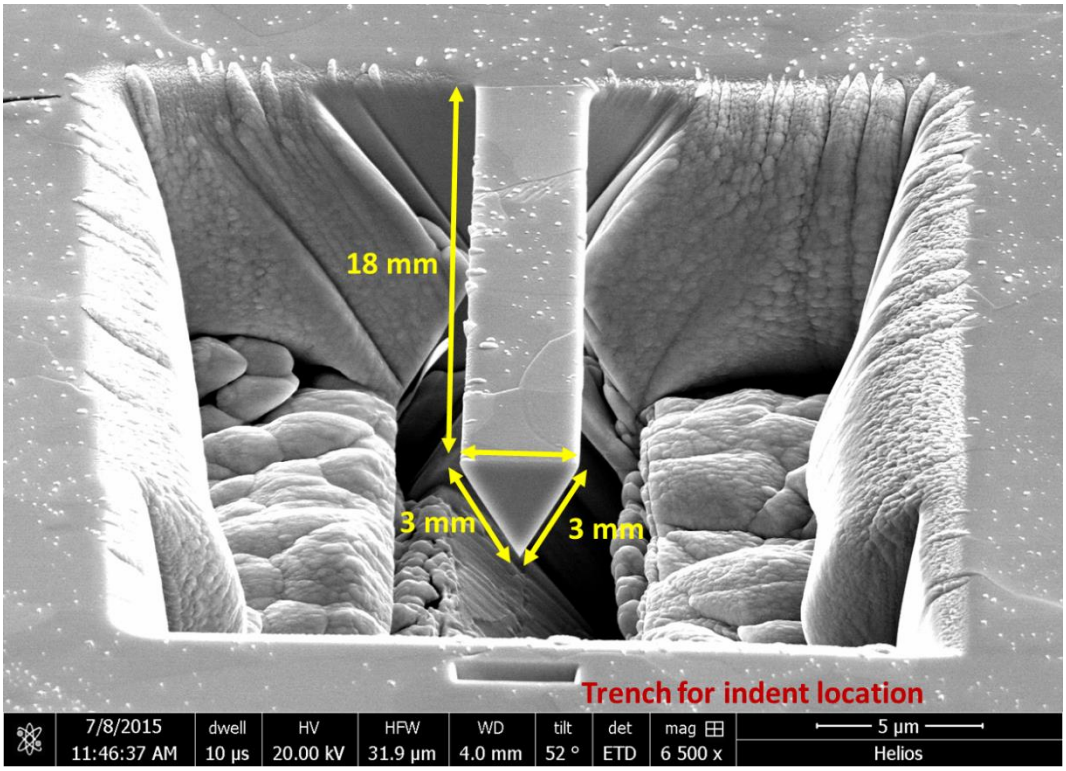

Figure 4-13 - Dimensions of FIB milled cantilever beam

An attempt was made to mill cantilevers directly across the interface between W and Au80Cu20 as shown in Figure 4-9. However during the milling process an unusual phenomenon occurred, resulting in what resembles a growth emanating from the interface. A study of existing literature has not yielded similar observations for micro-cantilever milling. The defect, or growth, that developed is presented in Figure 4-14 and in higher magnification in Figure 4-15.

As there are no reports of this behaviour occurring in other works, we can only speculate as to what the cause of the phenomenon is. It is believed that gasses and impurities not removed during heating under vacuum conditions to brazing temperature are trapped in the interfacial region. As this interface is milled, the trapped impurities are released and interact with the gallium ions, resulting in re-deposition back on the material.

Following FIB milling the micro-cantilevers were tested under bending conditions.

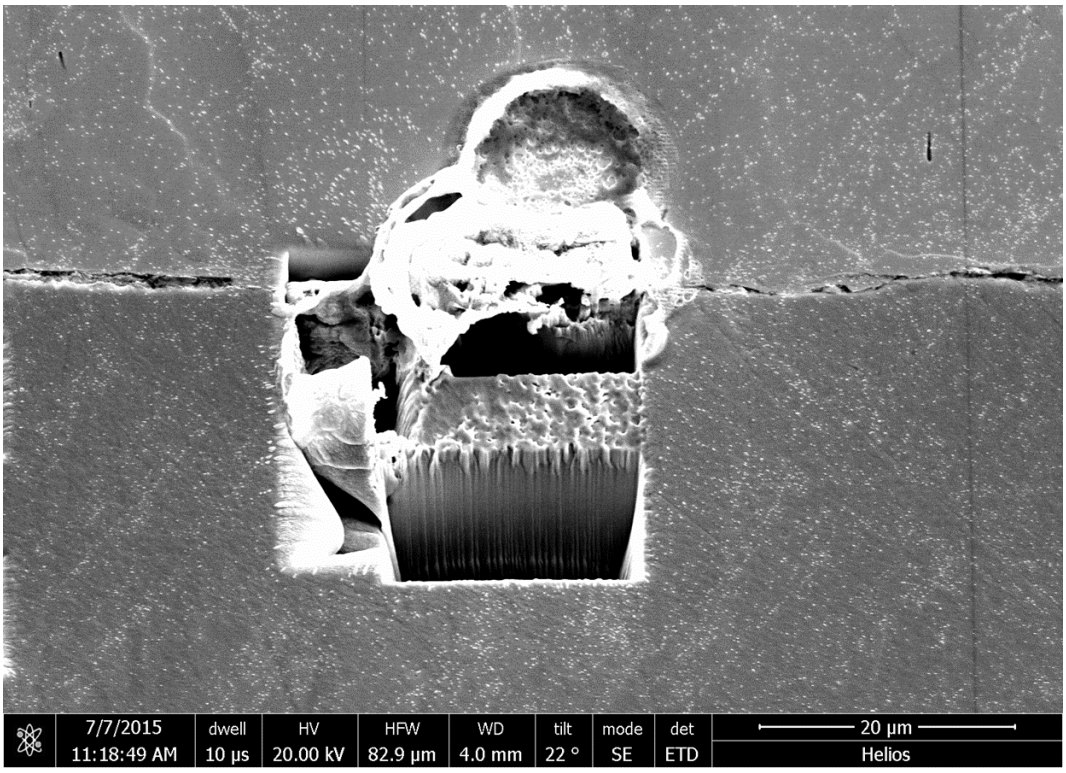

Figure 4-14 - Defect "growth" at W-Au80Cu20 interface

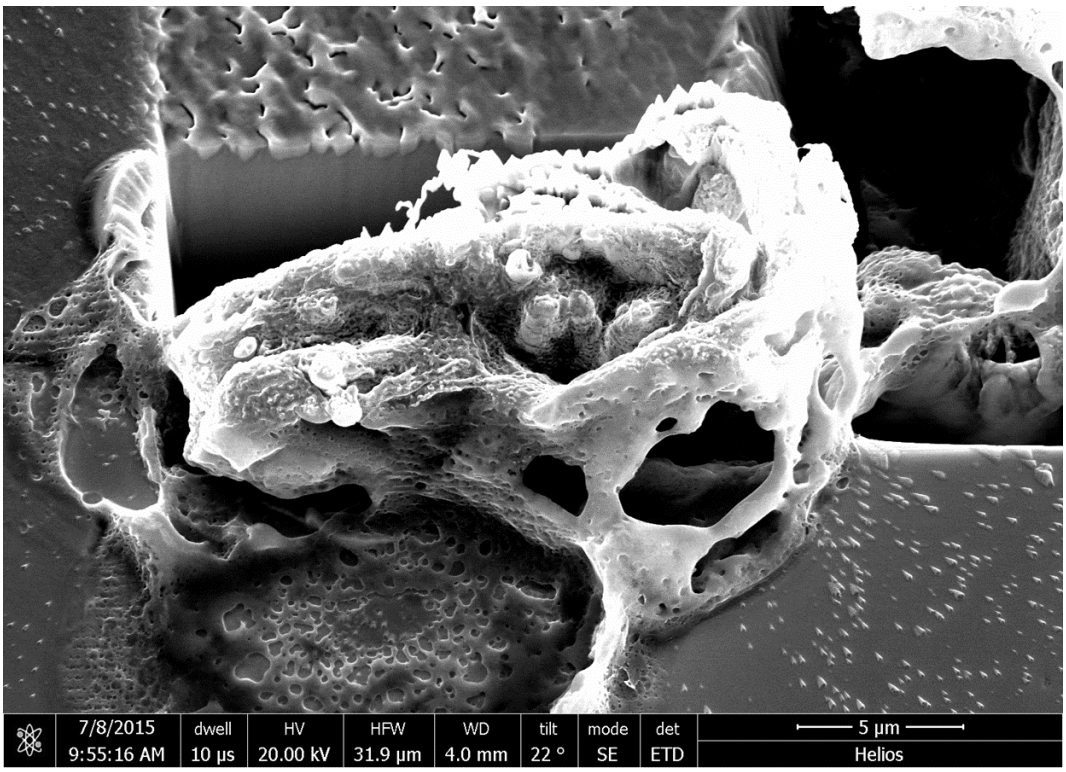

Figure 4-15 - High magnification image of defect "growth"

4.4.2 Cantilever beam testing with nano indenter

The FIB milled cantilever beams were tested using an Agilent G200 Nano Indenter. The use of nano indentation as a means of performing mechanical testing of FIB milled testing has been presented many times in literature. Initially testing was performed by milling cylinders which were deformed in a compression type mode to obtain yield characteristics [178-180].

The methodology has since been enhanced to include the testing of micro-cantilever beams of the type produced in the previous section [147, 158, 160, 177, 181]. A schematic of the cantilever beam to be tested is presented in Figure 4-16 (reproduced from [155]).

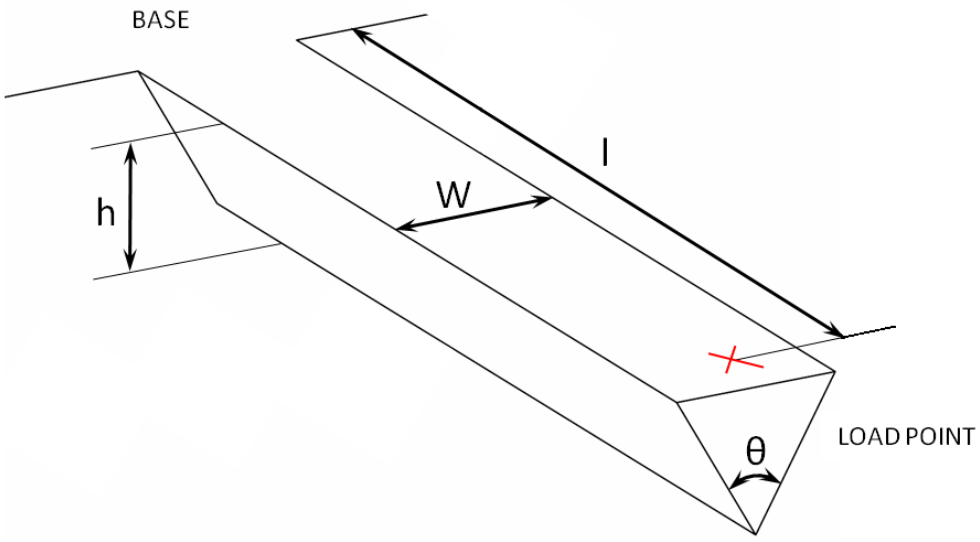

Figure 4-16 - Schematic of micro-cantilever beam [155]

The FIB milled beam can be approximated as in isosceles triangle uniform cross section cantilever beam for the purposes of simple beam theory assessment of mechanical properties. The stress, σ, and strain, ε, can be evaluated analytically using the standard relationships shown in Equation 3:

$$\frac{\sigma}{y} = \frac{M}{I} = \frac{E}{R}$$

Equation 3

With moment of inertia, I, distance from beam edge to neutral axis, y (y=2/3h) and radius of curvature to centroid of cross section, R.

The moment of inertia of the cantilever beam is given by Equation 4:

$$I = \frac{wh^3}{36}$$

Equation 4

Where the width of the sample, w, and the height of the beam, h, are known and constant.
The maximum strain and stress are obtained using Equation 5 and Equation 6 respectively:

$$\varepsilon_{max} = \frac{2\delta h}{l^2}$$

Equation 5

$$\sigma_{max} = \frac{24Pl}{wh^2}$$

Equation 6

Where *P* is the maximum load on the sample and *w* is the cross sectional area of the triangular beam. The elastic modulus can then be deduced from the stress and strain results.
The assumptions made for simple beam theory to be applicable are that there is a constant cross section, infinitely stiff base, symmetrical profile and absence of any defects or irregularities that act as stress raisers [182, 183].

In practice these assumptions do not necessarily hold exactly true. There is a small fillet radius at the corners, asymmetry from the milling process, and a base that deforms separately from the beam. However the application of simple beam theory is still considered a valid method for assessing mechanical properties of triangular cantilever beams. As stated previously, FEA could be used to improve the accuracy of the post-test determination of modulus.

The nano indenter optical imaging capabilities are not sufficient for locating the beams prior to testing. As such a method for locating beams based on AFM was utilised [155, 158]. A thin trench was milled a known distance from the edge of each cantilever beam as shown in Figure 4-13. The trench was located using AFM probe scan. Once the location of the trench was known, the indenter was translated the distance known so as to be positioned 1µm from the end of the beam.

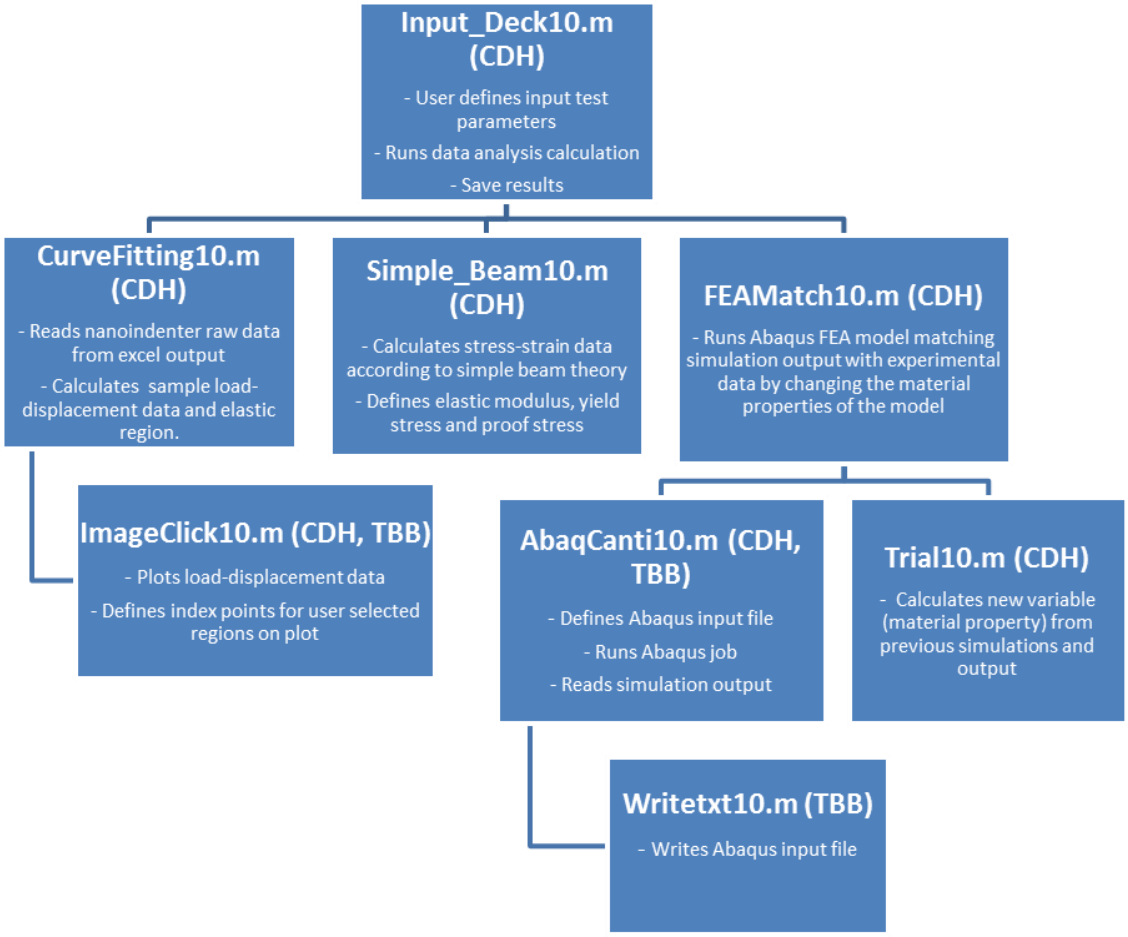

Figure 4-17 - MATLAB function flow tree for micro-cantilever analysis. Includes initials of function author (CDH - Dr CD Hardie, CCFE and TBB - Dr TB Britton, University of Oxford)

The experimental data generated during micro-cantilever testing was analysed using a series of MATLAB functions as shown in Figure 4-17, with the author of each code referenced by their initials [155]. For the work contained in this thesis only the Input_Deck, CurveFitting, ImageClick and Simple_Beam functions were used.

Figure 4-18 shows the processing steps for a typical load-displacement dataset generated during micro-cantilever testing (in this case tungsten sample W3).

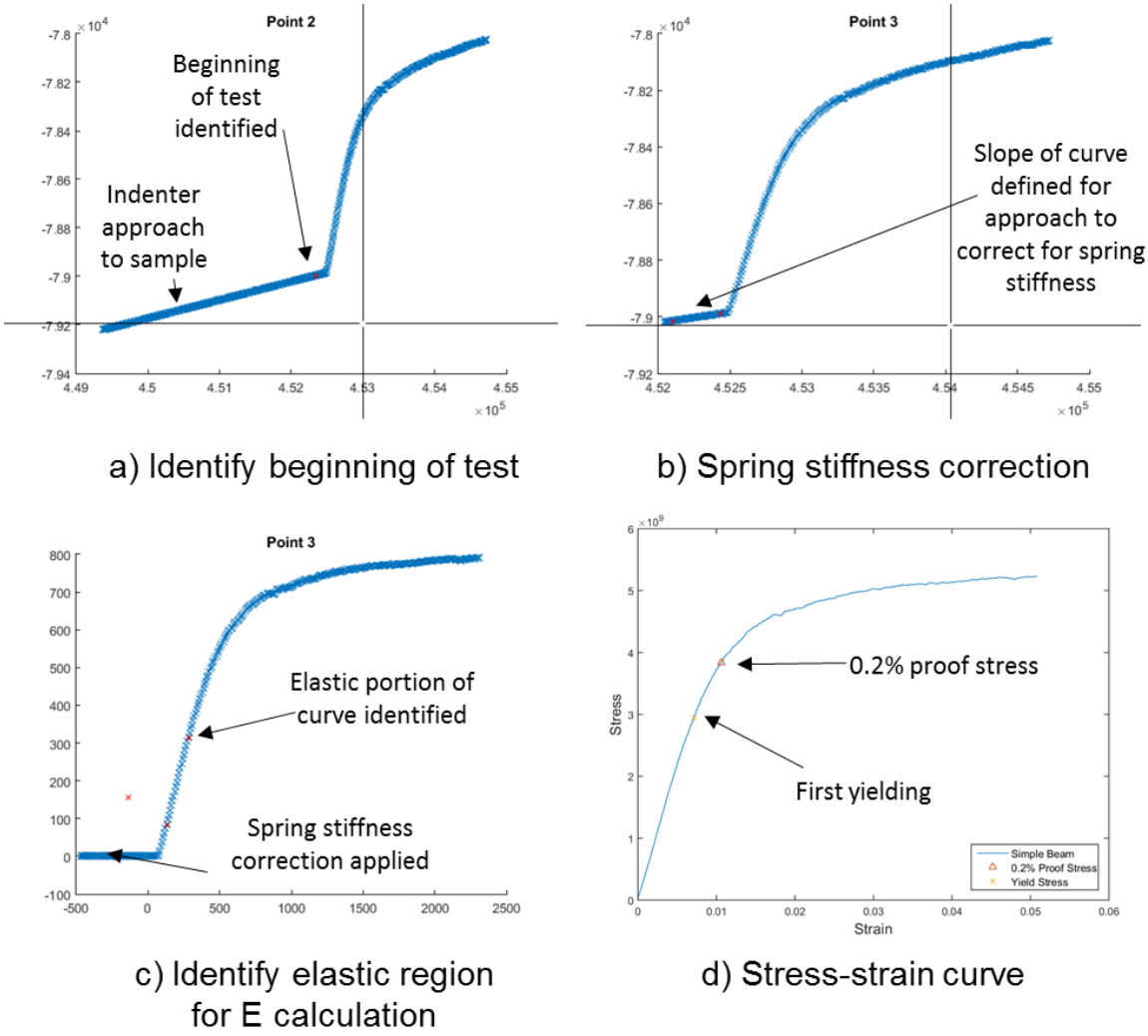

Figure 4-18 - Analysis of load-displacement data from nano indent test of W cantilever beam, (a) identify beginning of test, (b) determine stiffness gradient on approach to sample to correct for spring stiffness, (c) identify elastic region, (d) stress-strain curve

Firstly, the beginning of the test is located as shown in Figure 4-18 a). This discounts the data points collected on the approach to the sample surface. A correction for spring stiffness of the nano indenter equipment is then performed as shown in b). Finally the elastic region for which E is calculated is defined manually. The resulting output is a corrected stress-strain curve displaying E, initial yielding stress and 0.2% proof stress as shown in Figure 4-18 d).

4.4.3 Micro-cantilever results

The results of micro-cantilever testing using the nano indenter are presented in this section. Results are segregated into those beams for each material. The results for Au80Cu20 in the as-brazed with W-Cu and as-brazed with W-316L have been separated.

It should be noted that for all results presented within this section, the yield stress is shown to be far in excess of that expected from conventional, macro scale testing of similar materials. An order of magnitude difference between micro-cantilever results and conventional yield stress values is observed. This is due to the size effect, whereby the flow stress of very small specimens is increased greatly [160]. The small size and quantity of dislocation sites with a micro scale specimen are an "extrinsic size effect" which cause the drastic increase in plastic properties such as UTS and yield strength [184]. Therefore for the purposes of comparison with existing data, and for use in finite element material models, only the elastic moduli measured here are considered relevant.

4.4.3.1 Au80Cu20 cantilever – W-Cu brazed

The results for the micro-cantilever testing of Au80Cu20 brazing alloy in the as brazed with W and Cu are presented in Figure 4-19 with the results tabulated in Table 4-1.

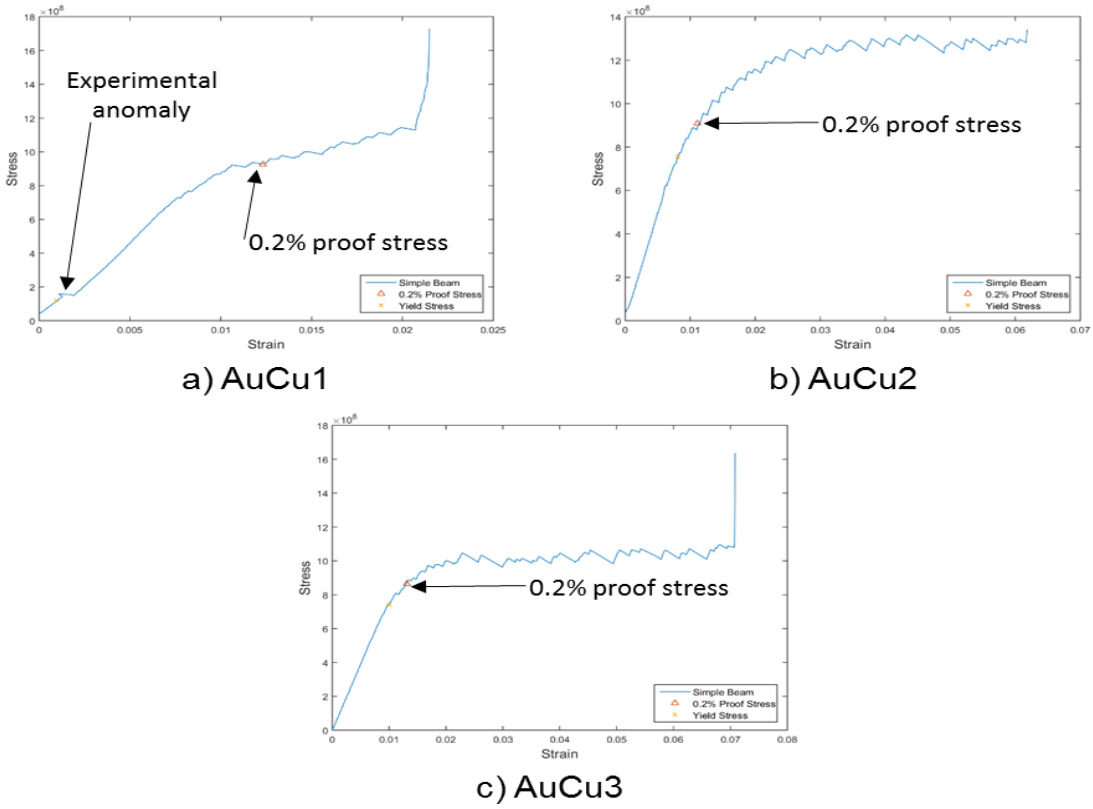

Figure 4-19 - Au80Cu20 (W-Cu brazed) cantilever results

The measured elastic moduli and 0.2% proof stress of AuCu1 and AuCu2 are in good agreement, with values of c. 95GPa for elastic modulus and 900MPa for proof stress. It is noticeable that the calculated yield point of AuCu1 is artificially low. This is due to an error in the stress-strain curve,

likely caused by experimental anomaly such as indenter tip slippage (shown in Figure 4-19). Therefore only the 0.2% proof stress is considered as a useful descriptor of yielding behaviour. Sample AuCu3 shows lower values for both E and 0.2% proof stress. The variance can be attributed to the multitude of uncertainty and error contributors that are present with this method of testing. A numerical quantification of errors associated with micro-cantilever testing is presented in literature [155].

Table 4-1 - Au80Cu20 (W-Cu brazed) cantilever results - E, yield and 0.2% proof stress

Material	Beam ID	Elastic Modulus (GPa)	Yield (GPa)	0.2% Proof Stress (Gpa)
AuCu (W brazed)	*AuCu1*	91.38	0.12	0.93
	AuCu2	98.99	0.75	0.91
	AuCu3	77.89	0.74	0.86
	Average	**89.42**	**0.54**	**0.90**
	S.D.	10.69	0.36	0.03

The average value of elastic modulus of 89GPa is significantly lower than the modulus calculated by nano indentation technique for the same material combination, of 140GPa. However if the nano-indentation results are adjusted to account for an estimated effect of pile-up, a true value of 100GPa is realistically the true value. This compares much closer to the micro-cantilever determined value of 89 GPa.

The measured proof stress of 900MPa is significantly higher than reported in literature. In macroscopic sized materials, there is a significantly higher number of dislocations sites that can accommodate crystal plasticity. Considering the micro-cantilever test is conducted over a single grain, or very small number of grains, plastic deformation does not occur at the same rate. This effect of significantly increased yield behaviour is well known and often reported in any micro-cantilever works published in literature.

It was observed during multiple tests reported in this work, including those presented in Figure 4-19 a) and Figure 4-19 c), that there is a sharp increase in load measured at the end of the test. This is due to contact between the indenter tip and the surface of the material at the edges of the milled region. For samples where this occurred, data has been discounted after the initial sharp rise.

4.4.3.2 Au80Cu20 cantilever – W-316L brazed

The results for the Au80Cu20 brazing alloy in the as brazed with W and 316L are presented in Figure 4-20 and Table 4-2.

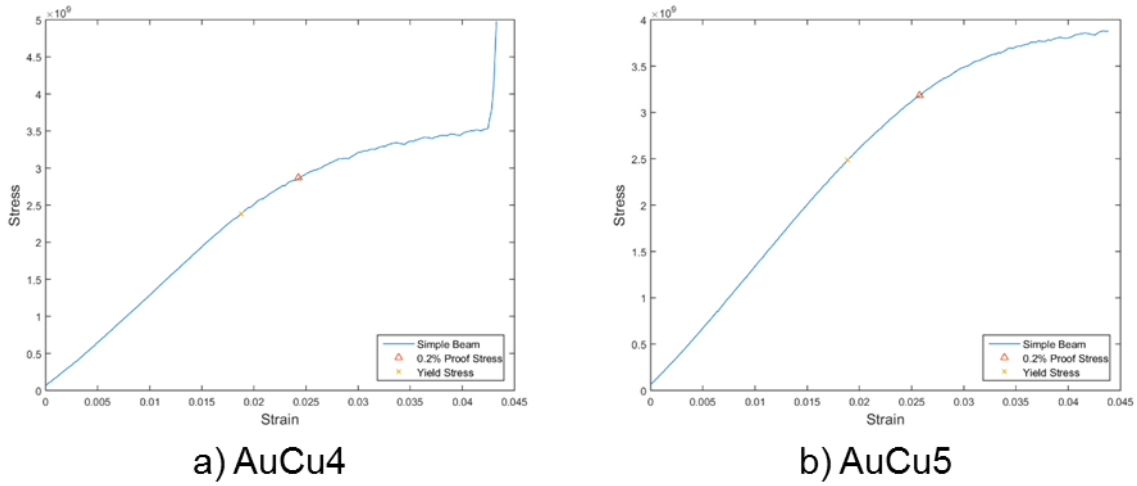

Figure 4-20 - Au80Cu20 (W-316L brazed) cantilever results

Table 4-2 - Au80Cu20 (W-316L brazed) cantilever results - E, yield and 0.2% proof stress

Material	Beam ID	Elastic Modulus (GPa)	Yield (GPa)	0.2% Proof Stress (Gpa)
AuCu (Cu brazed)	*AuCu4*	129.01	2.38	2.87
	AuCu5	134.00	2.49	3.19
	AuCu6	-	-	-
	Average	**131.50**	**2.44**	**3.03**
	S.D.	3.53	0.07	0.23

There is a significant rise in elastic modulus and yield stresses for the W-316L brazed Au80Cu20 as compared with W-Cu brazed Au80Cu20. The average E was found to be 132GPa in comparison with 89GPa. 0.2% proof stress was found to be in excess of 3GPa compared with under 1GPa previously.

This suggests that the lack of gold-copper interdiffusion in the W-316L sample has resulted in stronger elastic properties than for the case where there is a large degree of diffusion, as reported for W-Au80Cu20-Cu in Chapter 3.

Sample AuCu3 was not successfully tested due to misalignment of the indenter tip.

4.4.3.3 W cantilever

The results for W milled cantilevers are presented in Figure 4-21 and Table 4-3.

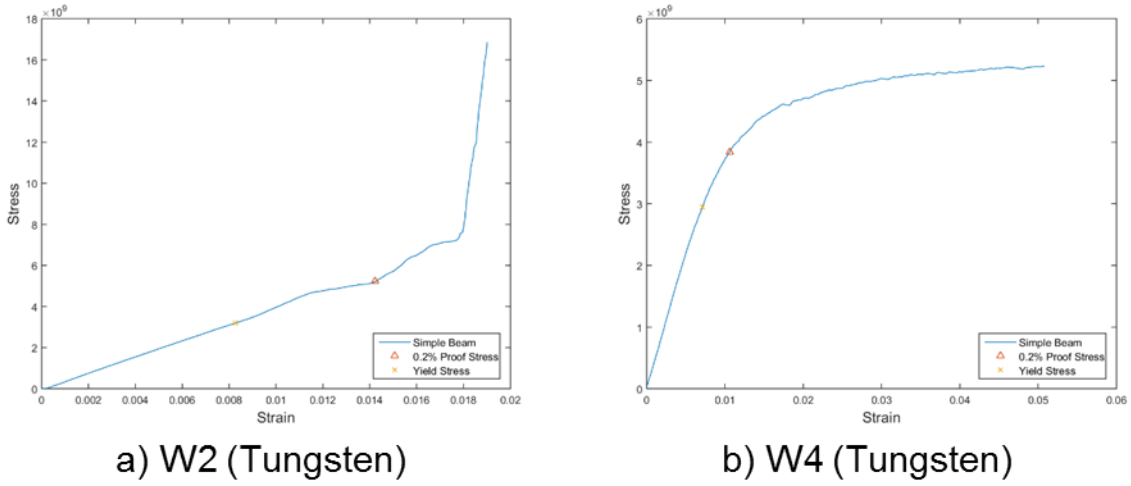

Figure 4-21 - W cantilever results

Table 4-3 - W cantilever results - E, yield stress and 0.2% proof stress

Material	Beam ID	Elastic Modulus (GPa)	Yield (GPa)	0.2% Proof Stress (Gpa)
Tungsten (W)	*W1*	-	-	-
	W2	387.13	3.20	5.24
	W3	-	-	-
	W4	442.05	2.95	3.87
	W5	-	-	-
	W6	-	-	-
	Average	**414.59**	**3.07**	**4.55**
	S.D.	38.83	0.18	0.97

It was only possible to successfully test two out of the six FIB milled W cantilevers. Samples W1, W3, W5 and W6 were not successful and did not produce valid results. Failed experiments were due to inaccurate location of the cantilever using AFM, resulting in the indenter tip either missing the cantilever or contacting the bulk material during testing.

A significant variance in elastic modulus was found between the two W samples tested (387 and 442GPa). However both are within +/- 10% of the values reported in literature of 411GPa. It is not possible to determine the statistical relevance of the results due to the low n value of the

experiment. Errors associated with beam milling and testing by nano indenter are likely to be within the +/-10% of accepted value as found by [147] for small cantilevers.
The average elastic modulus of 415 +/- 29GPa is close enough the reported value so as to increase confidence of the Au80Cu20 results for which known mechanical properties are scarce.

4.4.3.4 Cu cantilever

The Cu cantilever results are presented in Figure 4-22 and Table 4-4.

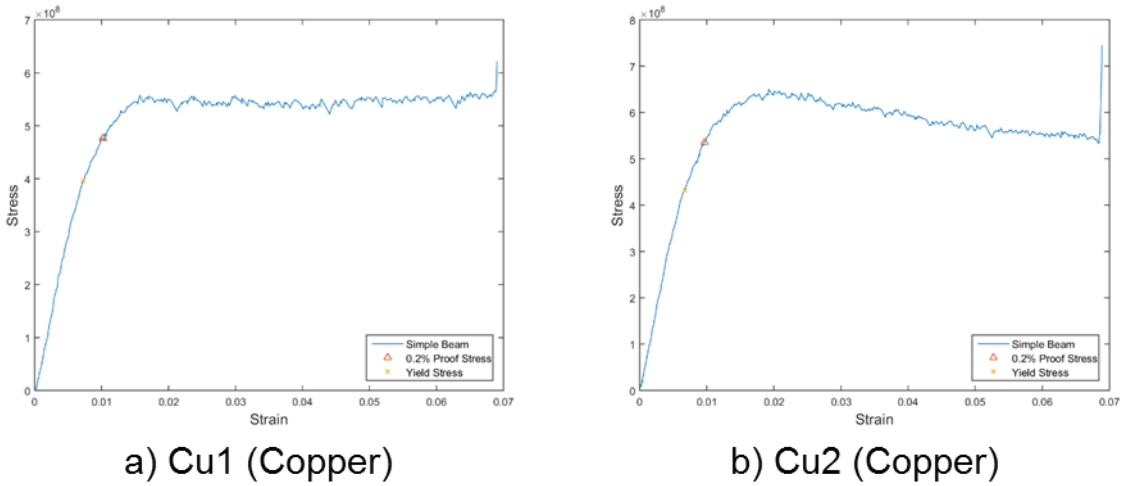

Figure 4-22 - Cu cantilever results

Table 4-4 - Cu cantilever results - E, yield stress and 0.2% proof stress

Material	Beam ID	Elastic Modulus (GPa)	Yield (GPa)	0.2% Proof Stress (Gpa)
Copper (Cu)	*Cu1*	58.30	0.40	0.48
	Cu2	69.74	0.43	0.54
	Cu3	-	-	-
	Average	**64.02**	**0.41**	**0.51**
	S.D.	8.09	0.03	0.04

The measured elastic modulus for copper in the as-brazed condition was found to be approximately 64GPa as shown in Table 4-4. This is significantly less than reported in literature for as-received oxygen free copper, 115 GPa [157, 185], and annealed copper, 110 GPa [186]. The elastic modulus as measured by nano indentation showed a higher E also of c. 140GPa. However in this case pile-up was postulated to be introducing an error into the results, thus over predicating elastic modulus.

The yield and proof stress of the Cu was found to be significantly less than the Au80Cu20 brazing alloy. The flat stress-strain response post-yield show that the copper is in an extremely soft, ductile condition.

4.4.3.5 316L cantilever

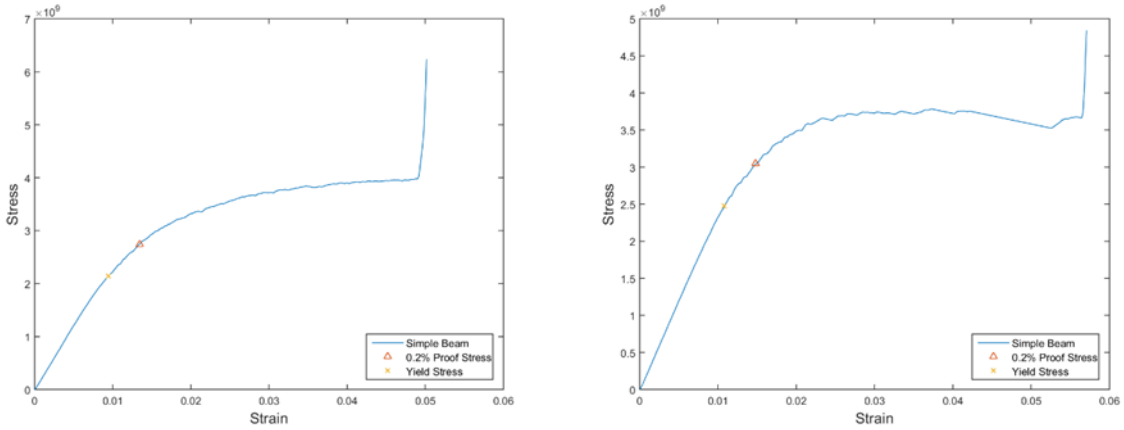

Figure 4-23 - 316L cantilever results

Table 4-5 - 316L cantilever results - E, yield stress and 0.2% proof stress

Material	Beam ID	Elastic Modulus (GPa)	Yield (GPa)	0.2% Proof Stress (Gpa)
316L	*316L_4*	239.43	2.14	2.74
	316L_5	237.67	2.48	3.05
	316L_6	-	-	-
	Average	**236.96**	**2.65**	**3.11**
	S.D.	3.49	0.72	0.52

The results of the 316L micro-cantilever tests are reported in Table 4-5 and Figure 4-23. The elastic modulus of 316L in the as-brazed condition was found to be approximately 240GPa as displayed in Table 4-5. This is significantly higher than reported for 316L in literature [187, 188]. However it must be noted that it is not pure, as-received 316L that is tested here. Instead it has essentially underwent heat treatment during brazing. The effect of thermal processing, as well as strain-induced changes due to stresses generated due to the brazing process, could result in microstructural transformations resulting in localized increases in mechanical properties. In particular deformation-induced martensitic transformation has the potential to affect mechanical properties.

4.4.4 316L-Au80Cu20-Cu

The elastic modulus nano indentation results for the 316L-Au80Cu20-Cu brazed part are presented in Figure 4-24. A number of points at the braze region were not able to be evaluated due to experimental error. This was caused by insufficient surface finish of the Au80Cu20 material. This is noticeably visible on the micrograph of the evaluated are shown in (Figure 3-34). This is an unfortunate effect of preparing a three material structure with each material exhibiting different polishing wear characteristics.

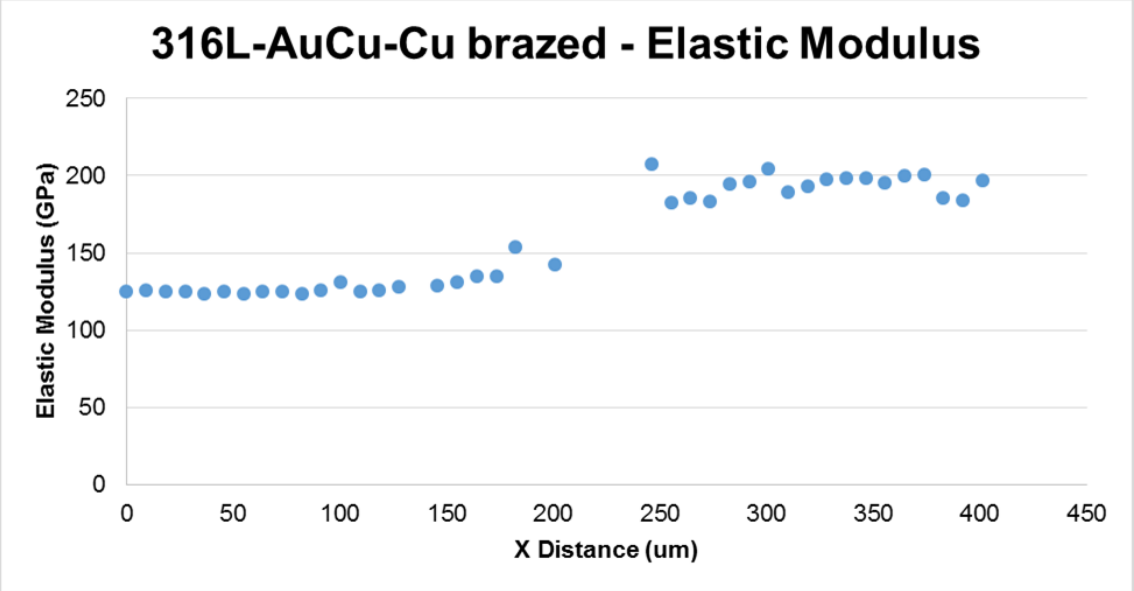

Figure 4-24 - Nano indentation Elastic Modulus results - 316L-AuCu-Cu

The elastic modulus of the brazing alloy, where valid results were produced, was found to be in the region of 140-150GPa. The copper elastic modulus was slightly lower in this instance with a value of 125GPa. This is in reasonable agreement with the W-AuCu-Cu sample, although a discernible difference between Au80Cu20 and Cu was not previously apparent.

The value of E for the 316L material ranged from 180-200GPa. This is in close agreement with values reported in literature. This suggests that the lower value of E for 316L in the W-AuCu-316L specimen was an artefact of measurement uncertainty or experimental error.

4.4.5 Micro-cantilever analysis

A summary of the elastic moduli as determined using the micro-cantilever method are shown in Figure 4-25. The results are presented for the four materials considered, with AuCu material reported separately for W-Cu and W-316L brazed specimens.

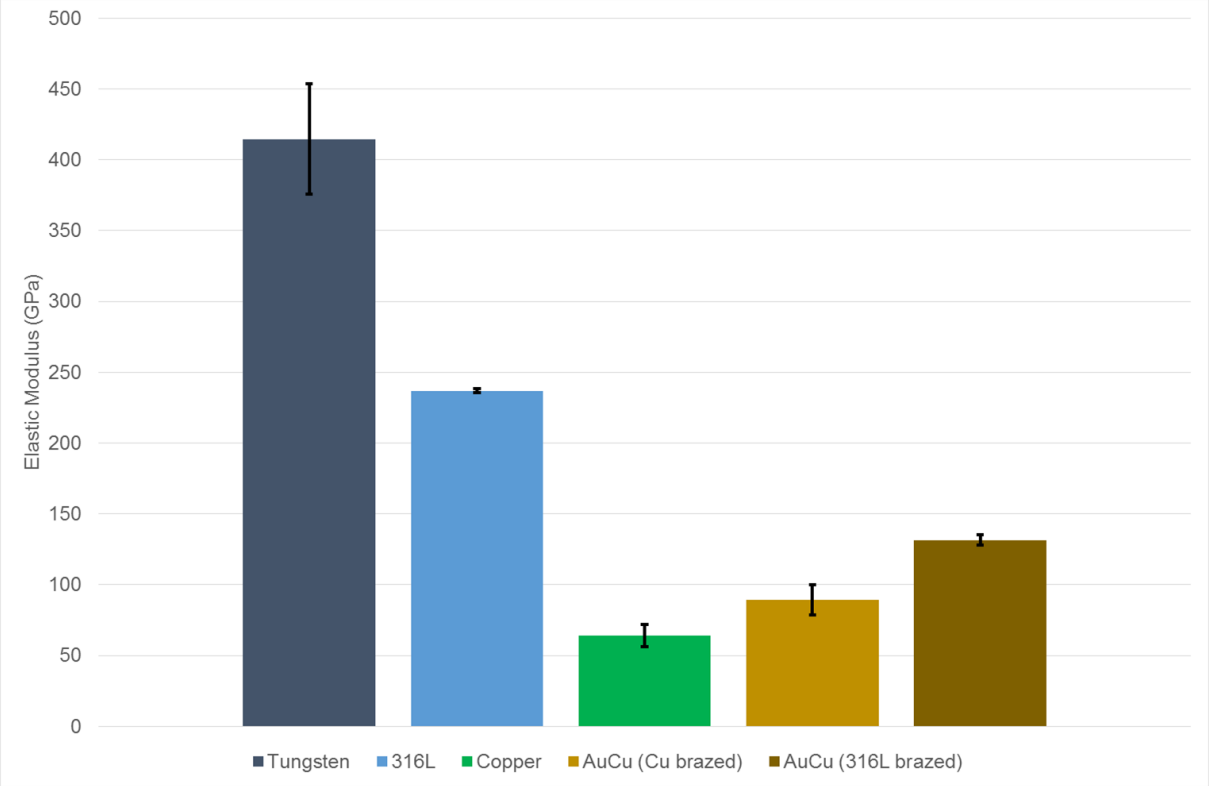

Figure 4-25 - Elastic modulus results from micro-cantilever tests

The error reported is equal to one standard deviation of measured results. In ideal circumstances a minimum of 4-10 samples per material would have been tested to obtain statistically significant measurement uncertainty indicators (such as standard deviation) [189, 190]. However due to the nature of the test it was not possible to produce a high number of samples. Access to the FIB was limited, and the success rate of obtaining useful experimental results from manufactured cantilevers was only approximately 60% (11 beams returning results out of 18 manufactured). Therefore for the purposes of this study the standard deviation is calculated using n=2 and n=3 depending on the material.

The reported error concerns only measurement variation from the results obtained. This does not include systematic experimental errors. The data available in literature for micro-cantilever testing for diffusion interfacial regions for the materials considered is virtually non-existent. It is therefore

impossible to compare experimentally achieved results with a known quantity in order to calculate and apply a correction factor to deal account for systematic errors [191]. Whilst the results obtained suggest overestimation of mechanical properties in certain cases, e.g. 316L, this has not been sufficient to develop a correction factor that can be applied across tests.

There are multiple potential sources of error in the conducting of micro-cantilever testing method that can contribute to the total experimental error. These include defects during beam manufacture, large fillet radii at the corners with the base, indenter misaligned when performing the bending test, inaccuracy of beam dimensions for calculating properties using simple beam theory, sample not perfectly normal to indenter tip and insufficient aspect ratio of length: width for beams to satisfy the simple beam calculation assumptions.

The random error, as defined by [189], experienced during a series of micro-cantilever tests has been quantified by [155]. It was found that the random error for elastic modulus and yield strength, 9.92% and 2.55% respectively. These are both smaller than the associated standard deviation of the results for tested un-irradiated Fe 12%Cr. Considering these results, standard deviation of the tested beams is an appropriate approximation of error and uncertainty from the experiment. A future study should if possible include a larger quantity of tests per condition examined in order to improve the quantification of uncertainty and improve statistical relevance.

A summary of the proof stress for all materials is presented in Figure 4-26.

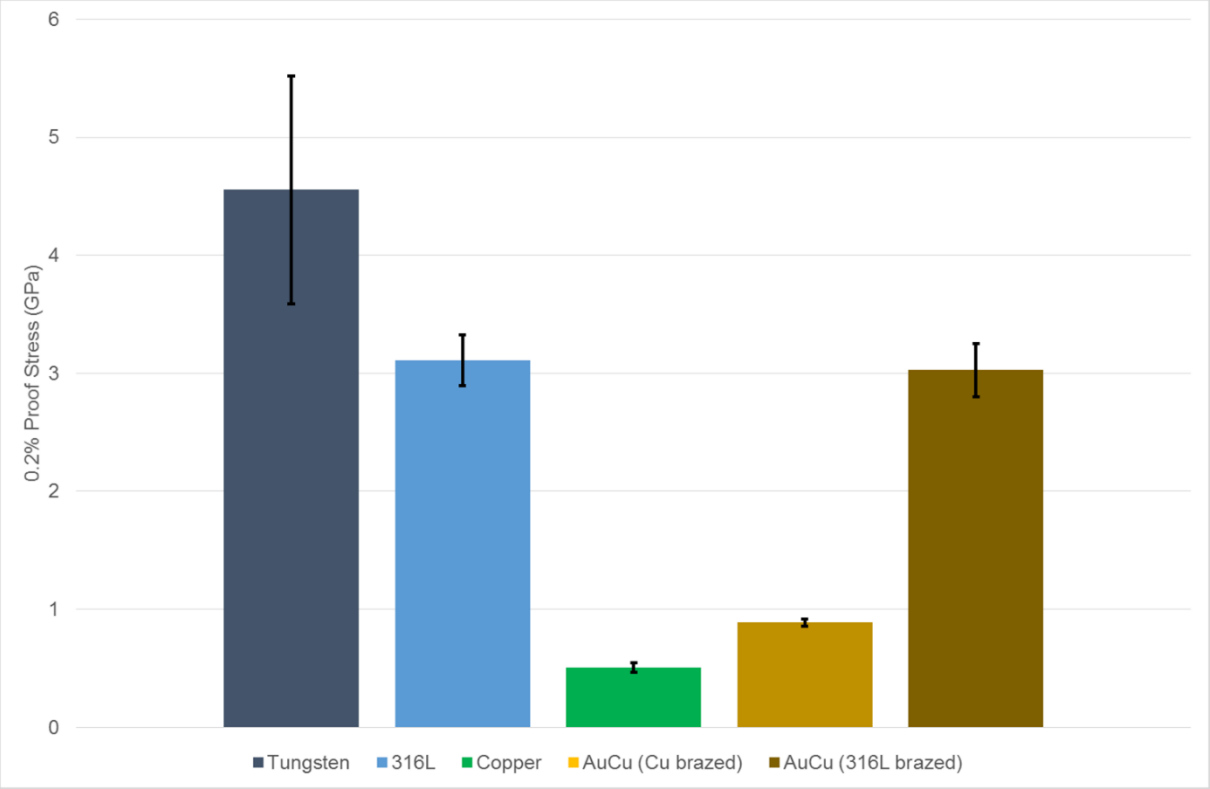

Figure 4-26 - 0.2% proof stress results from micro-cantilever tests

A comparison across all materials exhibits a similar trend as was found with elastic modulus. As would be expected, tungsten was found to be the stiffest and strongest material in terms of both E and yield stress. The austenitic stainless steel 316L showed the next highest values for both properties. Copper was has the lowest yield stress and elastic modulus of all materials tested. The initial yield stress and 0.2% proof stress for all materials is significantly higher for all materials than reported in literature for macroscopic scale tests.

The relationship between E and 0.2% proof stress is presented in Figure 4-27.

There is a clear relationship across the materials between E and proof stress. An increase in E correlates with an increase in yield point. This follows a close to linear relationship, with the exception of Au80Cu20 in the W-316L brazed condition. This material showed a proof stress closer to 316L despite a much lower elastic modulus.

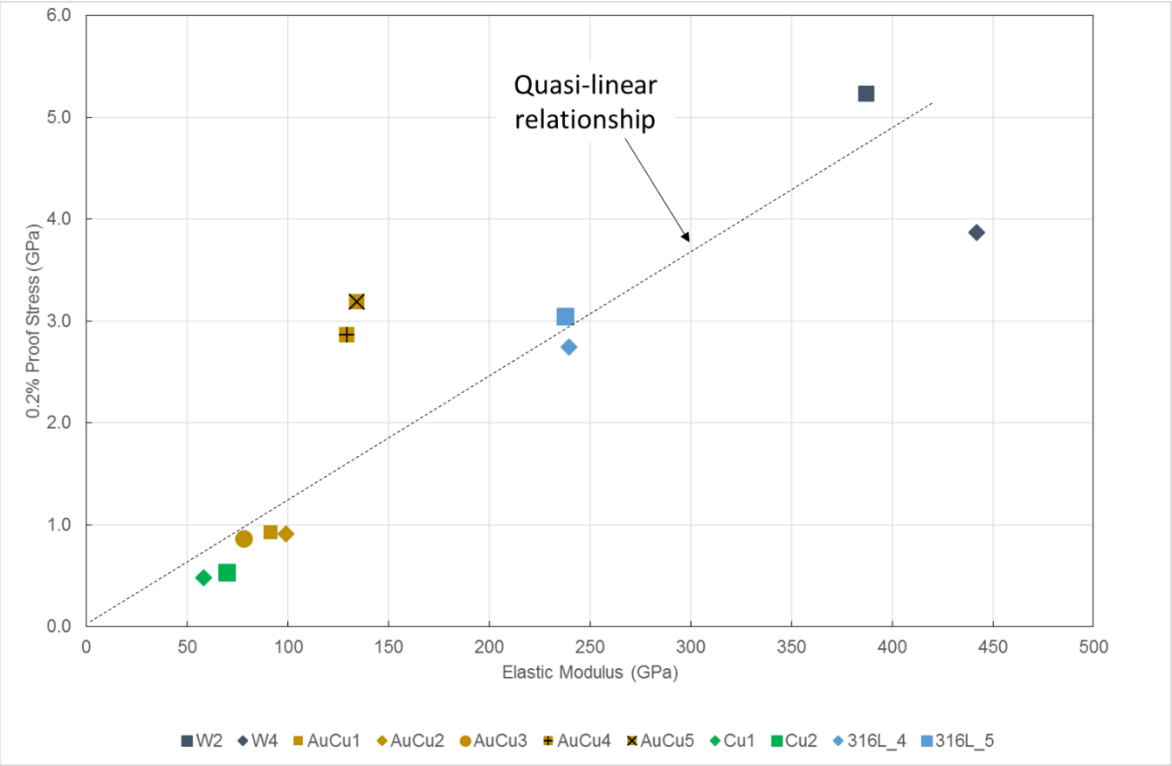

Figure 4-27 - Elastic Modulus - 0.2% proof stress relationship

It is clear that although there is reasonable agreement in certain instances between material properties published in literature and those generated by micro-mechanical testing in this thesis, there are other instances where the discrepancy is vast.

This will have a significant impact on analytical studies of the residual stress development due to the brazing process. It is also clear that the material properties vary somewhat depending on proximity to the interface and with the extent of chemical diffusion. Unless these effects are accounted for within a complex FEA material model, the nuances in deformation behaviour will not be predicted. A strength of FEA is that sensitivity studies can be performed to assess significance of material property uncertainty on simulation results. In Chapter 5 of this thesis such a study is performed for both idealised materials and elastic response of the Au80Cu20 alloy.

4.5 Electro-thermal mechanical testing

A series of axial tensile tests were performed using an Instron Electrothermal Mechanical Test System (ETMT) [192, 193]. This system uses miniature test specimens and is controlled with an Instron 8800 digital controller. Heating is performed by means of direct resistive heating. The grips are water cooled to remove heat from the sample via conduction upon cooling.

The specimens are of a simple "matchstick" design. Specimen dimensions of 50 x 3 x 1 mm were used, shown in Figure 4-28. The specimens were provided directly from the manufacturer to the dimensions required. The specimens were manufactured in accordance with ISO 17672:2010. The same material composition of 80%wt Au, 20%wt Cu (Au80Cu20) was procured.

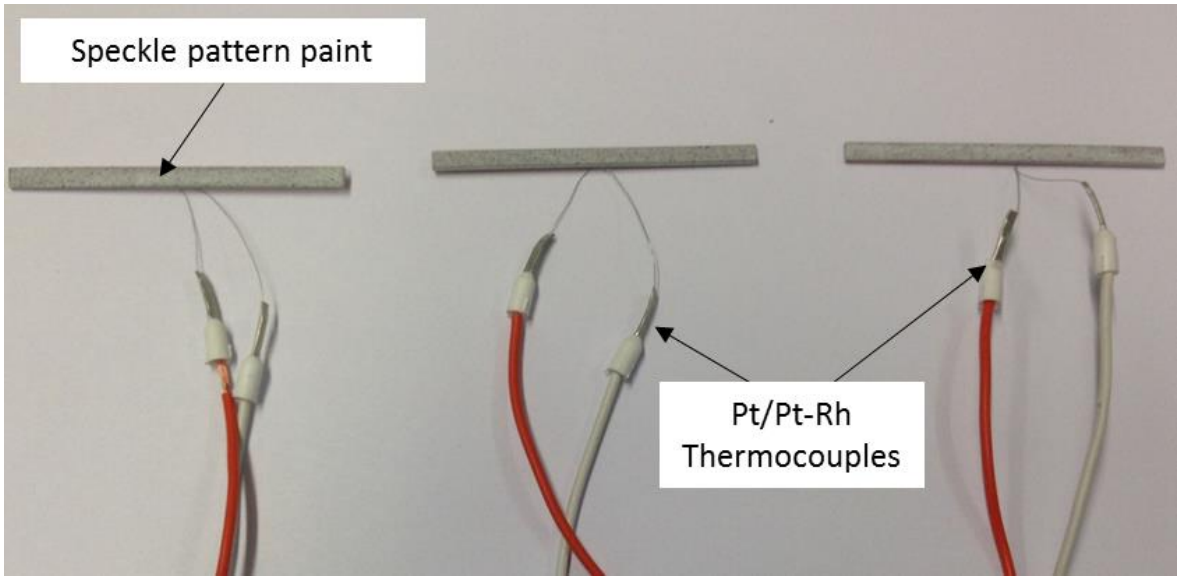

Figure 4-28 - Au80Cu20 specimens for ETMT testing with speckle pattern applied and thermocouple attached

Testing was performed at atmospheric conditions within an enclosed chamber as shown in Figure 4-29.

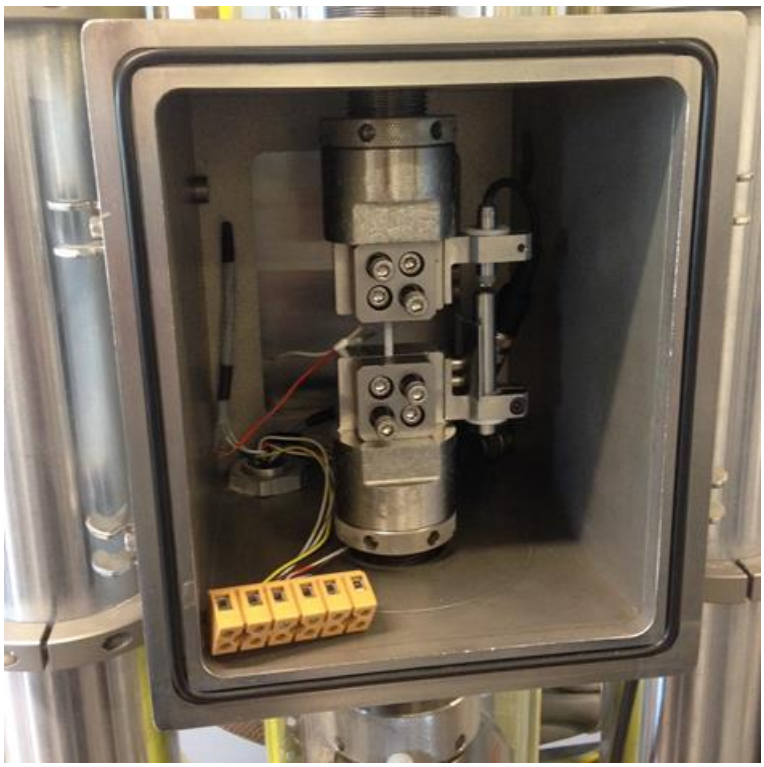

Figure 4-29 - ETMT set-up with Au80Cu20 specimen installed in between grips

As the sample is heated by water cooled grips located at the ends of the specimen, there is a non-uniform temperature profile resembling a parabolic distribution across the part [193, 194]. This is illustrated in Figure 4-30, showing the grip arrangements for a "matchstick" specimen with the parabolic temperature distribution across the part. A gauge volume comprising of a 16mm length in the centre, hottest part of the specimen is considered for strain calculations.

The temperature of the material within the gauge volume was recorded by means of thermocouple. A Type R platinum/platinum rhodium thermocouple was spot welded onto the back of each ETMT specimen. The front of the specimens were coated with high temperature paint to produce a speckle pattern that can be identified by Digital Image Correlation (DIC). The speckles allow for higher resolution of displacements/strains to be calculated, as miniscule displacements can be correlated between images.

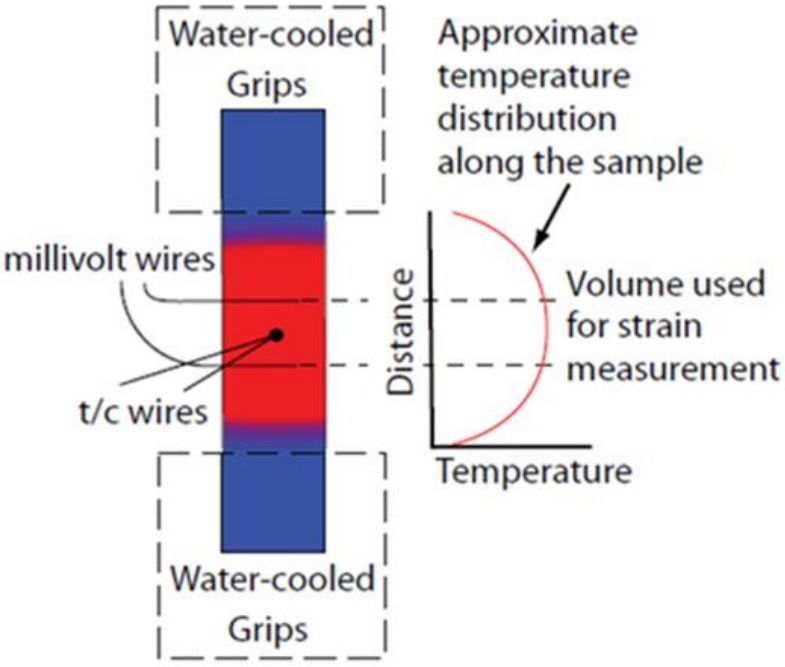

Figure 4-30 - Configuration of ETMT heating/cooling grips and parabolic temperature distribution across the sample

Strain is recorded using a linear variable displacement transformer (LVDT). To ensure that the temperature control was accurate, the proportional–integral–derivative (PID) controller was tuned. Temperature was cycled between atmospheric room temperature (c. 24°C) and 70°C. This ensures the response of the PID controller can be tested without affecting the sample thermally. The thermal cycle is illustrated in Figure 4-31. The yellow coloured profile represents the input control temperature as set within the ETMT software. The purple profile represents the true time-temperature response of the Au80Cu20 material within the gauge volume, as measured by thermocouple. PID parameters and current settings are adjusted until there is excellent agreement between input and actual temperature as shown in the figure.

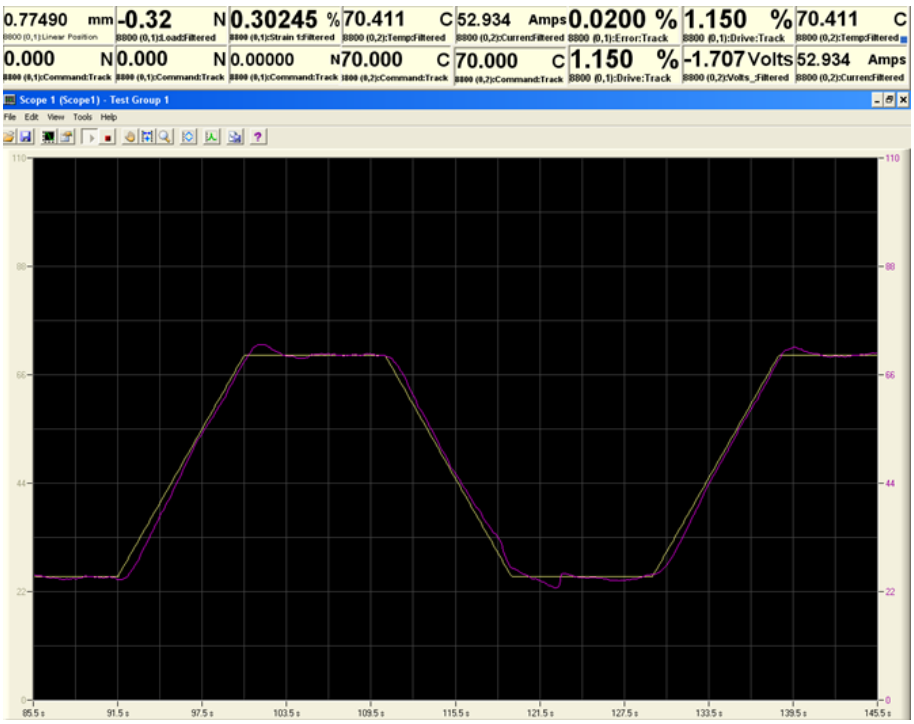

Figure 4-31 - ETMT thermal control system - time-temperature response comparison between control input temperature (yellow) and the actual sample temperature recorded by thermocouple

Due to the high balance of gold for the chosen brazing alloy, the cost of the material is extremely high. Even when using the miniature specimens suitable for ETMT testing only a small quantity could be procured within the budget available. A total of 3 samples were available for testing.
It was therefore critical that each specimen was utilised fully to obtain the maximum useful data possible. A series of axial tensile tests ranging from room temperature to 800°C was proposed.
A total of four tests were performed as detailed below:

1. Individual test at room temperature until maximum load is reached. This test used the first of three samples.
2. Stepped test ranging from 100°C to 800°C at 100°C intervals. Tests are performed to 0.14% elastic strain followed by elastic unloading. It was intended not to induce any significant plastic deformation on any load step. This ensures no strain hardening of the material. This test used the second of the three samples.
3. Individual test at 700°C. Loading is applied until maximum load or strain has been reached. This test re-used the second sample previously used for the stepped test.
4. Individual test performed at 400°C. As with the first and third tests, load was applied until the limits of the ETMT were reached (in respect to maximum travel distance of the grips). This test used the third and final sample of the three available.

4.5.1 Room Temperature

The first test performed using the ETMT was an axial tensile test at room temperature. The sample was installed in the grips and a small pre-strain was applied to ensure the part was sufficiently clamped and aligned. As the test involved no heating it was not necessary for the thermocouple response and thermal controller to be tuned.

Loading was performed under strain rate controlled conditions. The part was loaded at a rate of 0.01%/s until a maximum strain of 3% was achieved. This ensured that enough plastic strain was present to determine a tangent modulus whilst staying below the limitations of the load cell.

The results of the test are presented in Figure 4-32. Yielding began at c. 120-140MPa. The 0.2% offset proof stress, $\sigma_{0.2\%}$, was measured to be 186MPa. The $\sigma_{0.2\%}$ value shall be taken as the yield stress for the purposes of material property data in simulations later in this thesis. The 0.2% yield value of 186MPa exceeds that reported by a manufacturer of an Au80Cu20 brazing alloy of the same composition as studied here. The reported value in this case was 127MPa [195]. However as details of the testing conditions and definition of yield criteria is not present with this source, it is not possible to state whether or not the findings are in agreement.

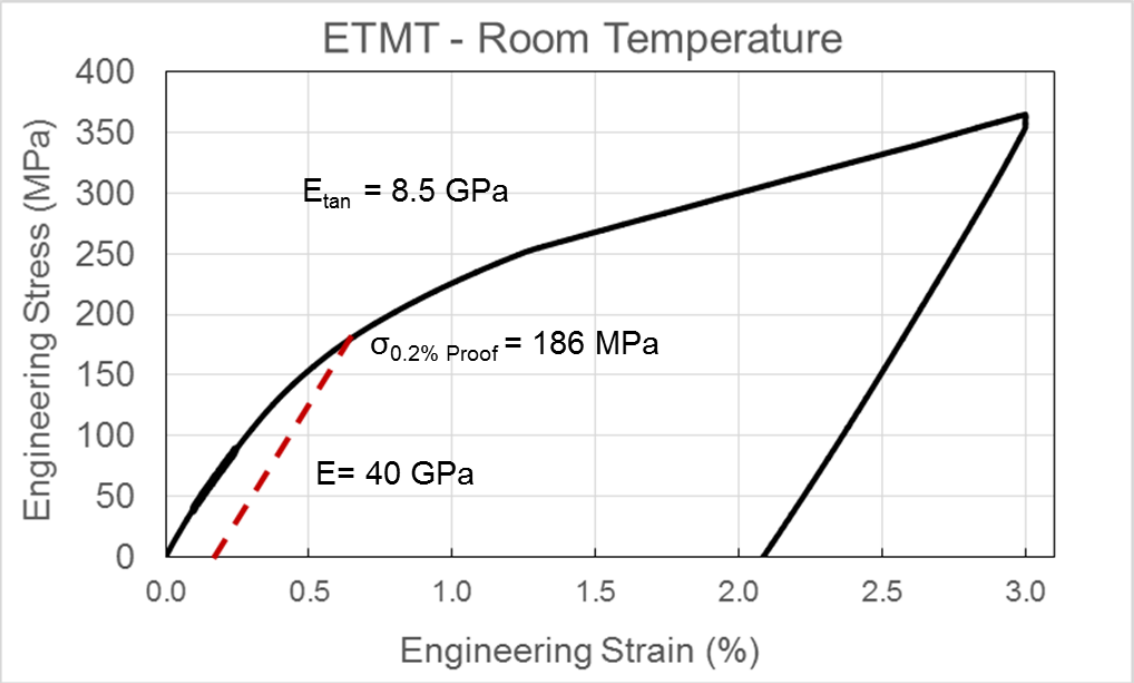

Figure 4-32 - Stress - Strain curve for ETMT tensile test of Au80Cu20 at room temperature

The elastic modulus E of the Au80Cu20 material in as-received condition at room temperature was found to be 40GPa. This value is significantly lower than experimentally determined for the as-brazed Au80Cu20 by way of micro-mechanical testing presented in the previous sections. From micro-mechanical testing the elastic was found to be in the range of 80-140GPa depending on test method and choice of brazing parent materials.

In order to better understand the discrepancy between expected modulus for Au80Cu20, a benchmarking exercise is recommended for future work. This should include ETMT testing of materials with well-established mechanical properties such as the steel, copper and tungsten considered in this thesis. Comparison between ETMT determined values for these materials with those existing in data would deepen the understanding of why the values are under predicted for Au80Cu20. It should be noted that the ETMT is calibrated on a regular basis by the manufacturer, Instron, and that the discrepancy can likely not be attributed to an equipment issue such as load cell or LVDT error.

4.5.2 Elevated temperature

In order to obtain elastic material properties for a range of temperature it was decided that a sensible approach would be to perform a stepped type test, the second test in the matrix as previously described. A single sample was heated to a given test temperature, loaded until a small % of strain had been reached, then unloaded. The temperature would then be increased and the test repeated at the higher temperature.

The temperatures selected for testing begin at 100°C and increased with 100°C increments until 800°C had been reached. It was decided not to go any higher than this temperature to reduce any risk of the Au80Cu20 material melting within the ETMT system (Au80Cu20 has a melting range of 908-910°C).

The sample was heated using resistive heating as described previously. Temperature of the part was recorded by the attached thermocouple, and this reading used to control the current power levels to match the pre-set temperature. The sample was heated under zero-load conditions, meaning the grips move to accommodate the expansion of the part due to temperature rise. Heating was performed at a constant rate of 10°C/s. Once a given test temperature was reached the part was held under zero load for 10s to allow any temperature variation within the gauge volume to equalise. It was shown in literature that variations of 10-40°C variation from the centre to the exterior can occur depending on heating rate [196]. Therefore the holding time is essential

to reduce experimental uncertainty arising from a temperature gradient across the short axes of the part.

The specimen was then loaded in strain rate control mode with a strain rate of 0.01%/s until a strain of 0.14% was reached. The load was then removed, and after a 10s delay to allow the part to settle, and the temperature increased to the next testing temperature. The time – temperature history of the stepped test can be found in Figure 4-33.

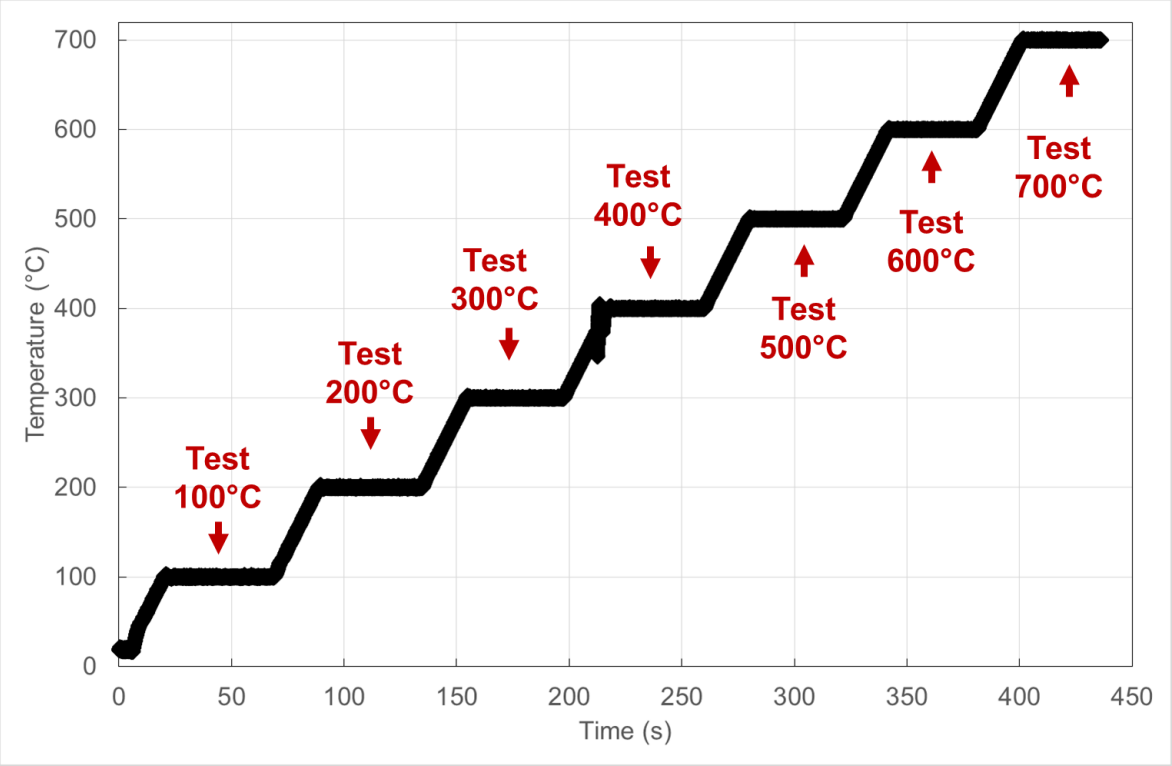

Figure 4-33 - Time-temperature history of stepped ETMT test of Au80Cu20 from 100°C to 700°C at 100°C intervals

The planned tests culminated with a test at 800°C. However during testing it was decided to abort the test following the 700°C test. At this temperature the part yielded under very low loads and deformed in essentially an elastic-perfectly plastic nature. The stress-strain curves for all of the stepped temperature tests are presented in Figure 4-34.

Due to the limited number of samples available, the experiment was designed to include the stepped temperature approach to determine elastic properties only. This was intended to avoid strain hardening of the specimen. However at elevated temperatures, unintentional yielding did occur, so yield stresses are reported for these cases.

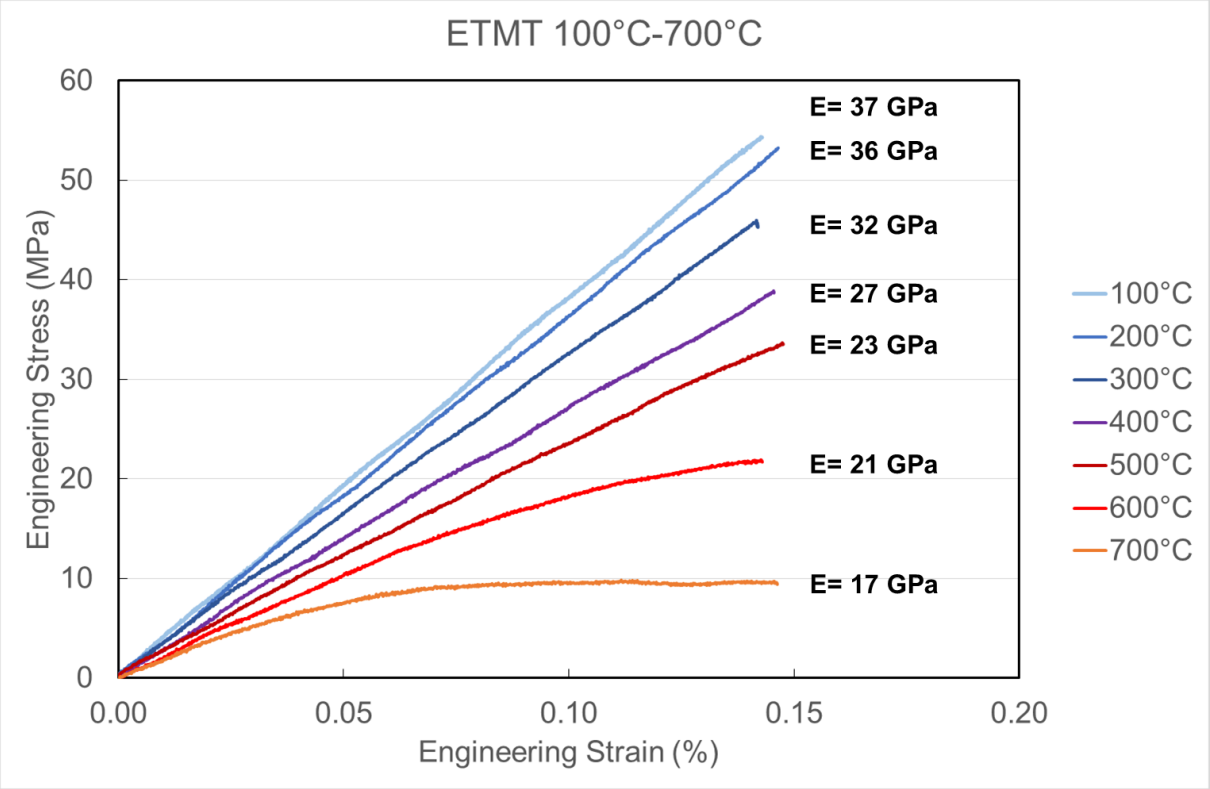

Figure 4-34 - Stress - Strain curve for stepped ETMT tensile test of Au80Cu20 from 100°C to 700°C at 100°C intervals

There is a gradual decrease in elastic modulus with increasing temperature, as well as an increasing non-linearity in stress-strain response. This is common behaviour and to be expected as the part becomes "softer" when heated towards the liquidus state at melting temperature.

The first four tests exhibit a purely linear elastic response (T=100°C to T=400°C) with elastic modulus decreasing from 37GPa to 27GPa over the temperature range.

On the fifth test, at 500°C (coloured dark red in Figure 4-34), the beginnings of plastic deformation can be observed.

This becomes more obviously noticeable with the test at 600°C (coloured bright red). The behaviour is clearly no longer fully elastic. The elastic modulus was assessed as the gradient of only the initial, linear elastic portion of the curve.

The plasticity developed during this test will have induced permanent microstructural changes within the part. Also, with an extended time at high temperature and under load, it is probable that the material experienced a degree of creep. Both of these factors contribute to uncertainty in the next test, at 700°C, with this sample. That is an unfortunate effect of having a limited number of samples.

The final completed test at 700°C is represented by the orange coloured profile in Figure 4-34. At an applied stress of less than 10MPa the sample was exhibiting purely plastic deformation. It was therefore decided that it was not worthwhile increasing the temperature any further. As with the 600°C test, only the initial linear portion of the curve was used to determine the elastic modulus. For both 600°C and 700°C it is possible to determine a yield point for the material. For 700°C in particular, although 0.2% plastic strain had not been achieved, it is assumed that 10MPa is a reasonable description of yield stress for the Au80Cu20 material at 700°C.

Determining the yield stress for the 600°C test involves a higher degree of uncertainty as the part was not observed to be fully plastic within the loading applied for this test. As the part is tending asymptotically to a horizontal profile, the stress at this point will be used as the yield, namely 22MPa. There appears to be very little strain hardening at 700°C as perfectly-plastic like deformation occurs.

For all tests at elevated temperature only engineering stress and engineering strain are considered. In reality there is likely a certain degree of necking within the gauge volume. With this considered the plastic behaviour at higher temperatures would behave in an elastic-plastic nonlinear manner as opposed to elastic-perfectly plastic. The values of elastic modulus and stresses are so low in magnitude where this is apparent. This means that the brazing material is extremely soft and providing little constraint on the parent materials during brazing at higher temperatures. The error associated with these values is therefore deemed to be of negligible consequence for finite element analysis (FEA) purposes.

Another source of error to consider with this type of testing is a variable temperature profile across the gauge volume. As is seen in Figure 4-30 there is a variation in temperature across the 16mm length of interest. However this difference is small in magnitude, and the temperature measured by the thermocouple in the centre of the gauge volume is taken to be the true temperature across the entire volume. This approach is common with ETMT testing [194, 197].

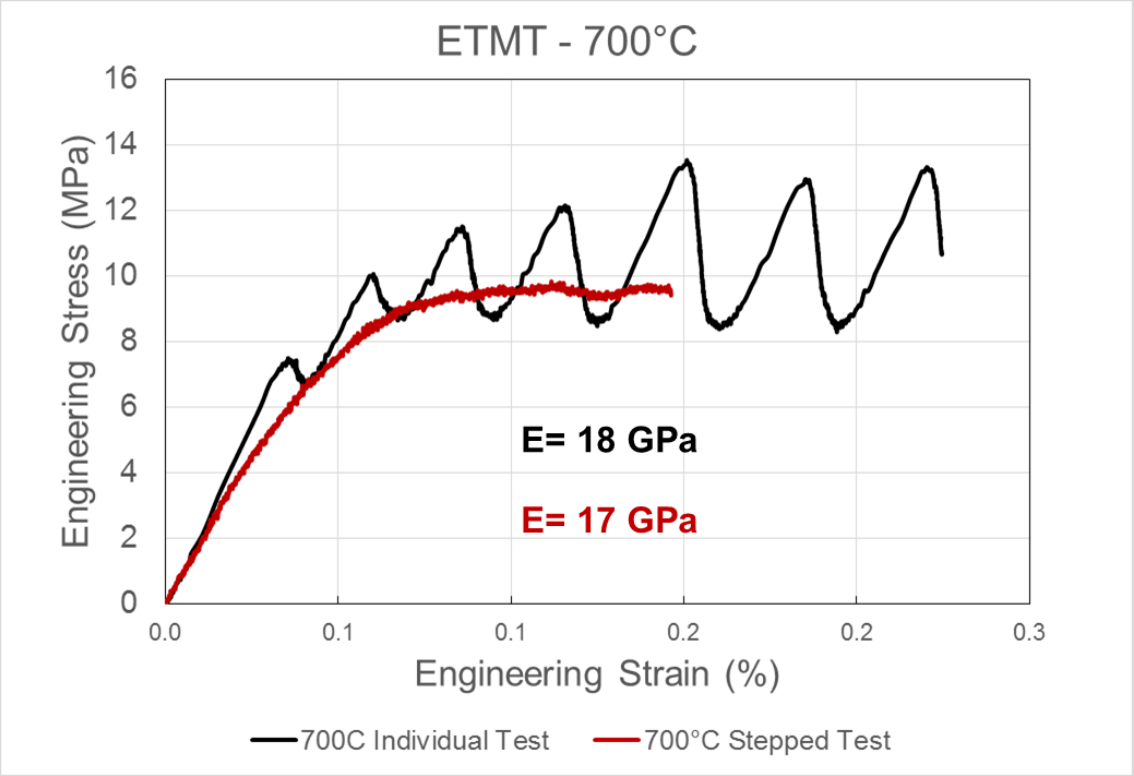

Figure 4-35 - Stress - Strain curve for ETMT tests performed at 700°C. Showing the individual test in black and stepped test in red

Following the stepped temperature test, a second tensile test was performed using the same specimen. Strain hardening and creep are expected to have affected the sample, although with a limited number of samples available the test was still conducted to at least determine the elastic behaviour. The part was removed from the ETMT and repositioned. This was done to decrease the risk of replicating any systematic experimental error that may be present during the stepped test.

Identical heating and loading parameters were used as previously described (10°C/s, 0.01%/s respectively). The testing temperature was chosen to be 700°C to provide a direct comparison with a previous test at identical temperature.

The sample was loaded until a larger degree of plastic deformation was induced. The results of this test are presented in Figure 4-35, with the previous test at 700°C as part of the stepped temperature test.

It is observed that there is good agreement between the tests, with a difference of 1GPa in elastic modulus attributable to measurement uncertainty. There is clear yielding at c. 10MPa and

essentially perfectly plastic deformation after that. This is also in excellent agreement with the previous test.

There is however a noticeable oscillation within the stress strain response. This can be attributed to an error within the PID controller. It should be noted that peak to valley magnitude of the oscillation is less than 4MPa, which can be considered of negligible importance.

A final elevated temperature test was performed at 400°C with the final remaining Au80Cu20 as-received condition sample. The stress – strain results are presented in Figure 4-36.

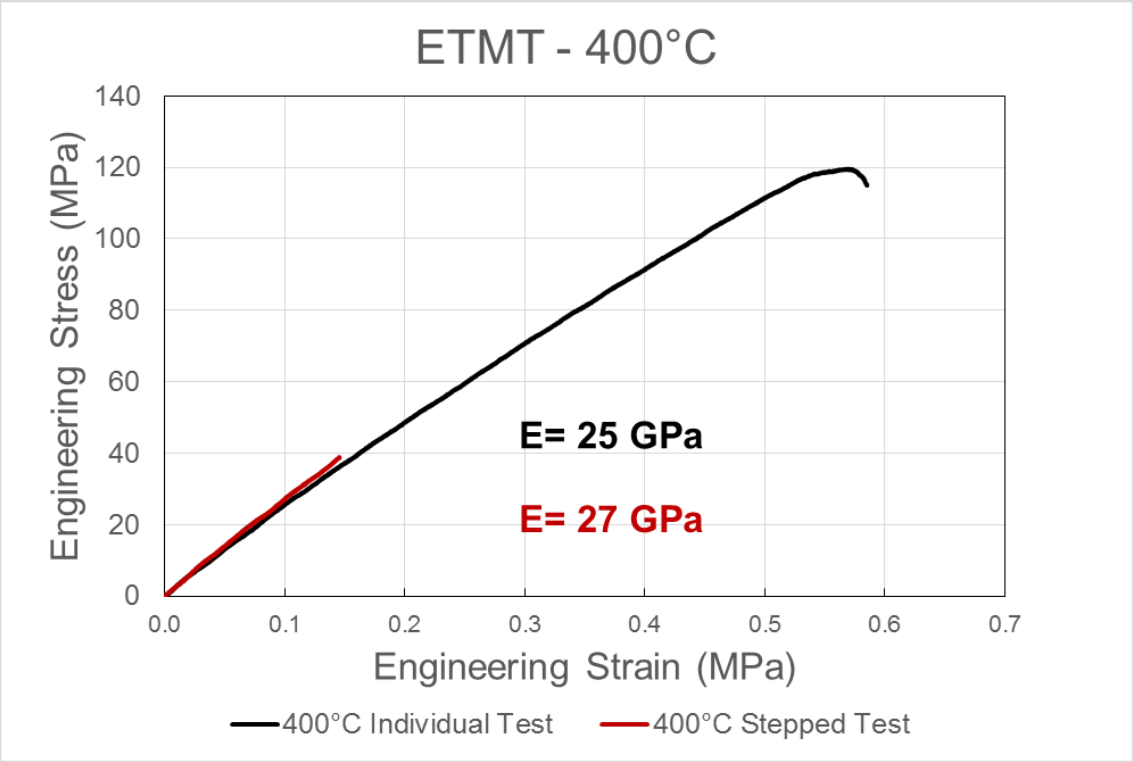

Figure 4-36 - Stress - Strain curve for ETMT tests performed at 400°C. Showing the individual test in black (fractured specimen) and stepped test in red

As with the repeated tests at 700°C, there is excellent agreement with elastic behaviour with the repeated tests at 400°C. A difference of only 2GPa was found for elastic modulus. Although there were not enough samples to repeat all temperatures for multiple repetitions, the repeatability in results for those tests that were repeated reflect positively on the repeatability of the testing regime as a whole.

For the individual test at 400°C, shown in black in Figure 4-36, it was planned to continue loading until a strain of 3% was reached. This would allow for determination of yield stress and tangent modulus. However, whilst loading in the elastic region prior any obvious yielding, a sudden and complete fracture occurred in the centre of the sample.

Figure 4-37 shows the fractured surfaces of the specimen. The fracture was observed to be fully intergranular in nature. One half of the fractured part is significantly discoloured. This is likely due to localized heating and oxidation occurring due to area through which the electrical current passed during resistive heating.

The nature of the failure is important in describing the condition of the material in the condition of elevated temperature. As is shown in Figure 3-1, there is phase transformation occurring in the 300-400C range. This is also apparent from DSC experiments previously presented. It is therefore proposed that the intergranular fracture occurred in this instance due to preferential phase precipitation at the grain boundaries [198]. A contributing factor could also be the preferential concentration of voids and micro-segregations along grain boundaries, resulting in a sudden, brittle, intergranular fracture prior to plasticity developing.

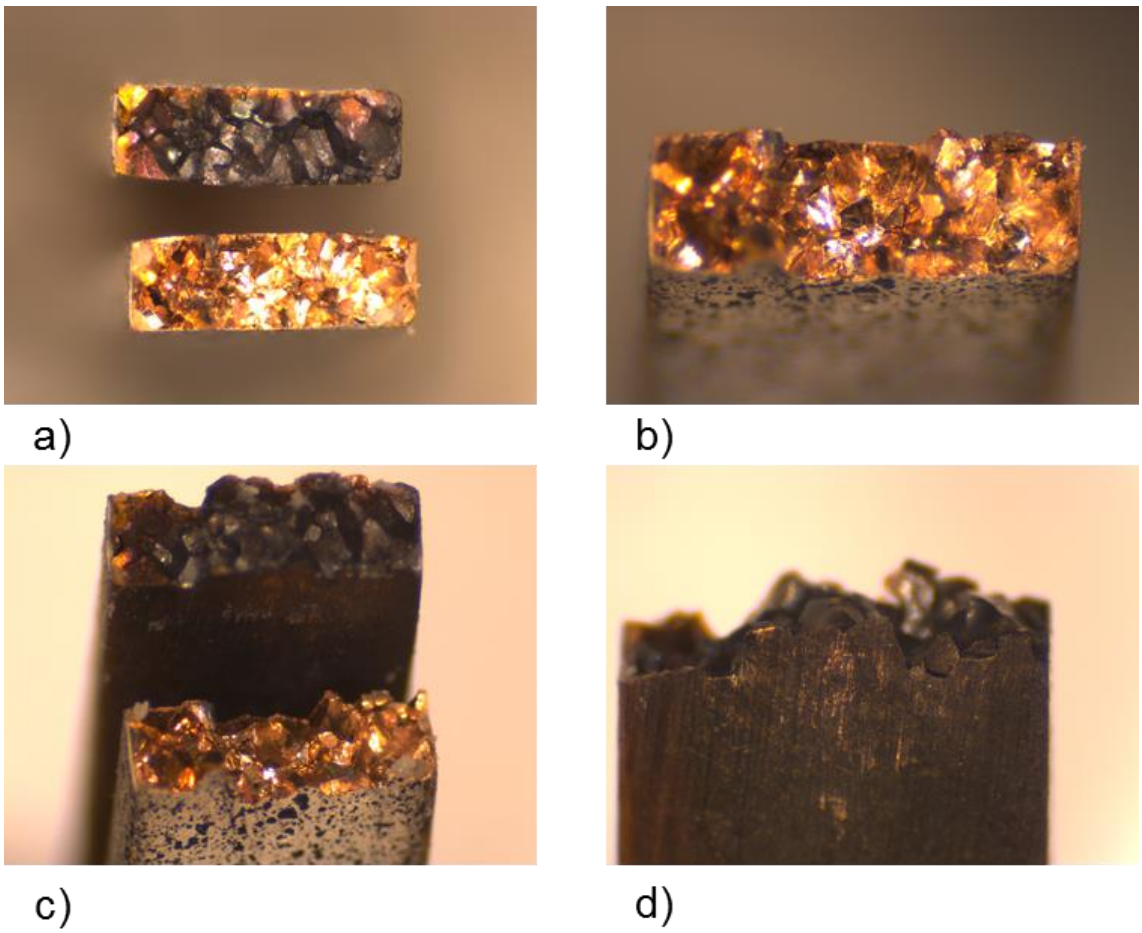

Figure 4-37 - Fracture surfaces of intergranular crack failure of Au80Cu20 ETMT test specimen. Failure occurred prior to plastic yielding at 400°C

The Au80Cu20 material used for this study is prohibitively expensive. It would be preferable to conduct a comprehensive series of ETMT tensile tests at temperature ranging from room temperature to temperatures approaching melting point, in order to better understand the evolution of material mechanical properties and plasticity and fracture behaviour throughout the range of temperatures experienced during brazing. However due to a limited budget the variation and repetition of testing conditions that is desired was not possible. Further research into the thermo-mechanical behaviour of the Au80Cu20 brazing alloy is required should the material be considered for structural applications within the divertor.

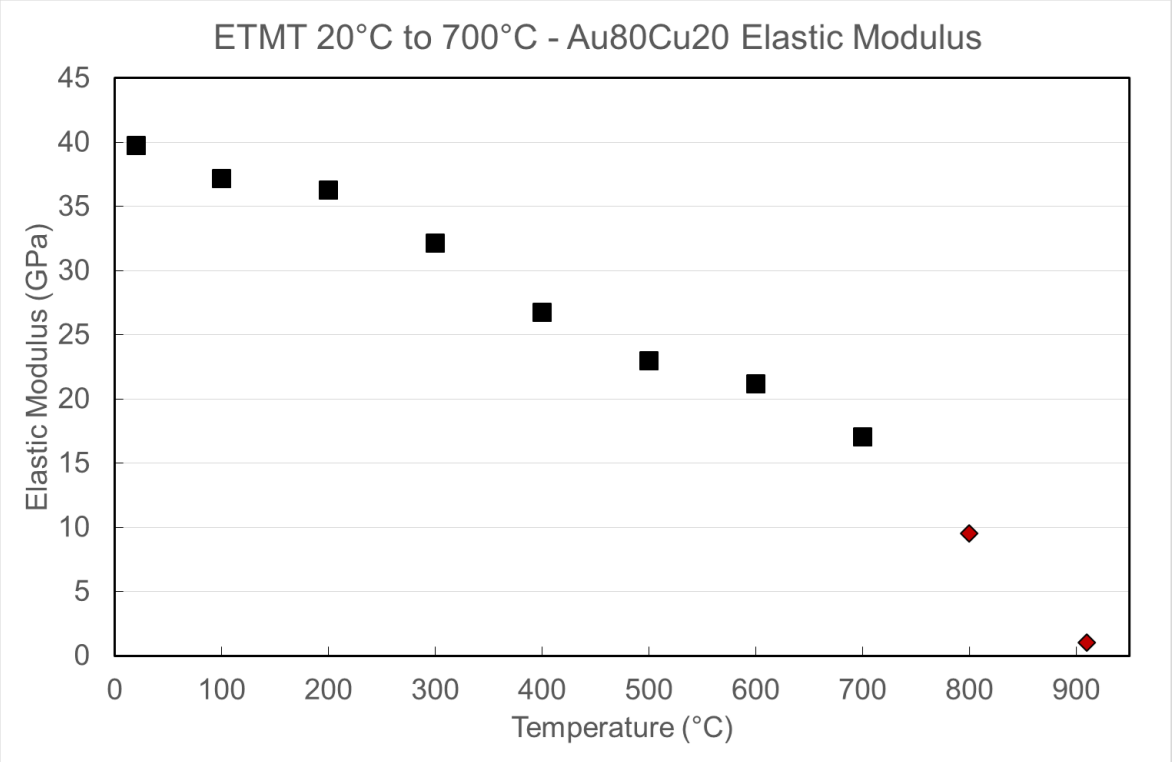

Figure 4-38 - Summary of Elastic Modulus up to 700°C obtained from ETMT testing. Interpolated values between 700°C and T_{melt} (910°C)

A summary of the temperature dependent elastic modulus for as-received Au80Cu20 brazing alloy is presented in Figure 4-38.

It has been assumed that the yield stress and elastic and plastic moduli at the melting temperature of 910°C are equal to zero. The values between those of the maximum temperature achieved during testing and the zero values at melting temperature have been approximated using linear interpolation. This approach has previously been employed for a silver based brazing alloy [100, 199]. These assumed values are coloured red in the figure above.

There is a steady decrease in elastic modulus with increasing temperature, following a close to linear relationship for the temperatures at which tests were conducted. Unlike the thermal property results, there is no relationship between the phase change at c. 300°C and the elastic properties of the material was observed.

Due to the unexpected failure of the specimen at 400°C, it has not been possible to obtain information regarding yielding and plastic behaviour at the temperatures between 20°C and 700°C. It will therefore be necessary to employ linear interpolation to obtain these values.

4.5.3 Digital Image Correlation

Digital image correlation (DIC) has been employed during ETMT testing to better understand the degree of strain localisation during axial tensile testing at room and elevated temperatures.
An LaVision DIC camera was used for the testing. The DIC was positioned close to the ETMT. The sample is visible during testing due to a clear panel in on the ETMT chamber. The experimental set-up of ETMT and DIC prior to the chamber window being attached is shown in Figure 4-39. The Au80Cu20 sample is coated with white and black high temperature paints to produce a speck pattern with enough speckle density for surface strains to be identified by DIC.

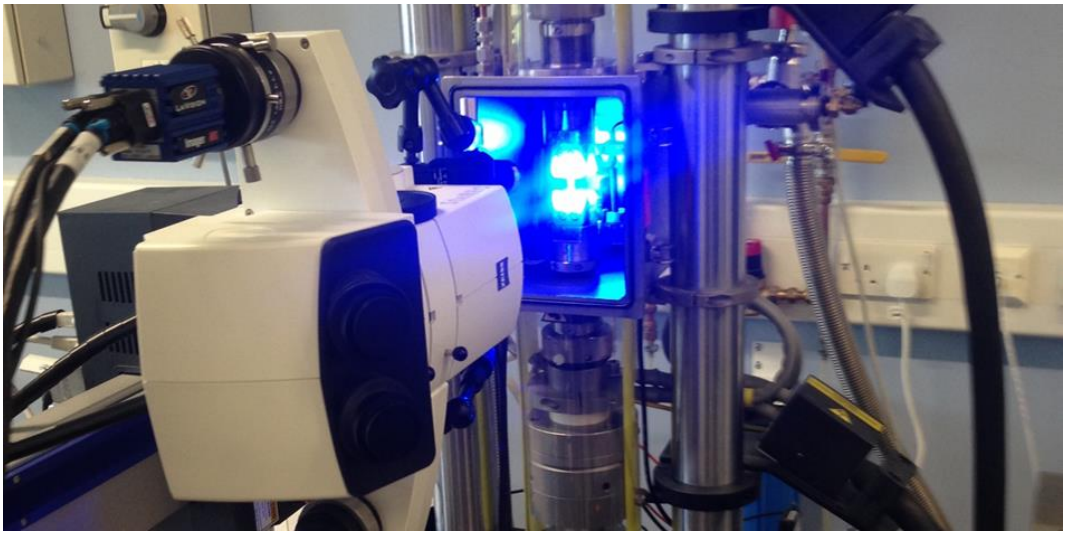

Figure 4-39 - ETMT + DIC experimental set-up

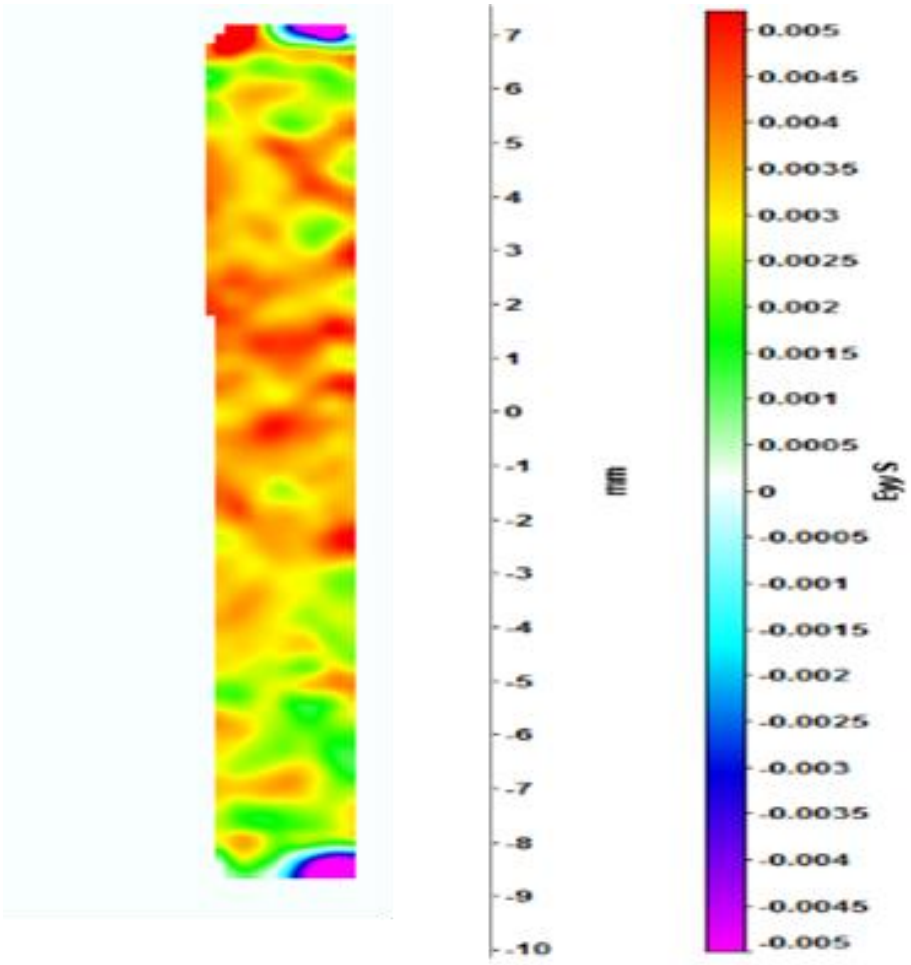

Figure 4-40 - DIC strain results for Au80Cu20 ETMT axial tensile test at room temperature

The DIC strain results for a point in time during the plastic deformation region of the room temperature ETMT test (Figure 4-32) is presented in Figure 4-40.

The ε_{yy} strain component, i.e. the strain in the direction of the uniaxial tensile loading, is presented. There is an absence of strain localisation in the specimen. This behaviour is to be expected for a test of these conditions.

The test is performed at room temperature, so there is no thermal gradient across the part that would tend to localise strain in the centre of the part. The specimens are of uniform cross section, i.e. not waisted, so there is no stress concentration as with a typical dogbone type tensile specimen. The presence of strain localisation to the gauge volume can be seen in Figure 4-41. This strain map represents the strain within the Au80Cu20 specimen tested at 700°C (Figure 4-35). As there is a parabolic temperature distribution across the part, the highest strains are expected to be in the centre which is considered as the gauge volume for LVDT strain measurement. The exception to

this behaviour would be if precipitation or ageing was occurring within the Au80Cu20 material. This has been observed to cause strain migration away from the gauge volume in certain nickel superalloys. However as this is not the case here, the approach of considering a 16mm long gauge volume in the centre of the part is shown to be a valid approach.

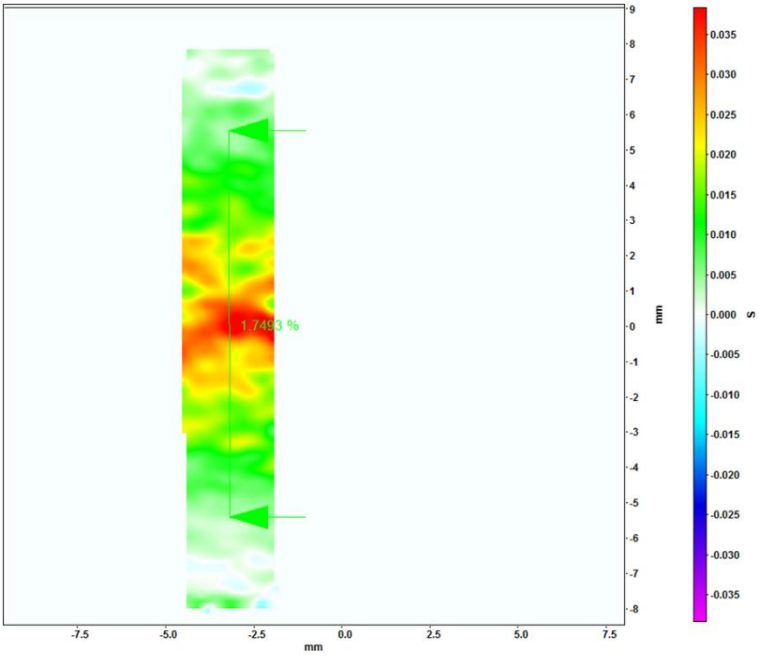

Figure 4-41 - DIC strain results for Au80Cu20 ETMT axial tensile test at 700°C

During ETMT testing an unusual and unexpected failure of the Au80Cu20 material occurred during axial tensile testing at 400°C (Figure 4-37). This fracture event has been examined using DIC images and presented in Figure 4-42. The speckle pattern applied is clearly visible in this image. The crack can be observed to evolve from non-existent (at the surface) in the top left, through the crack initiation and propagation to finally fully failed condition at the bottom right of the figure.

The associated strain mapping of the sample did not provide any useful information as to the strain state of the part prior to and during the crack event.

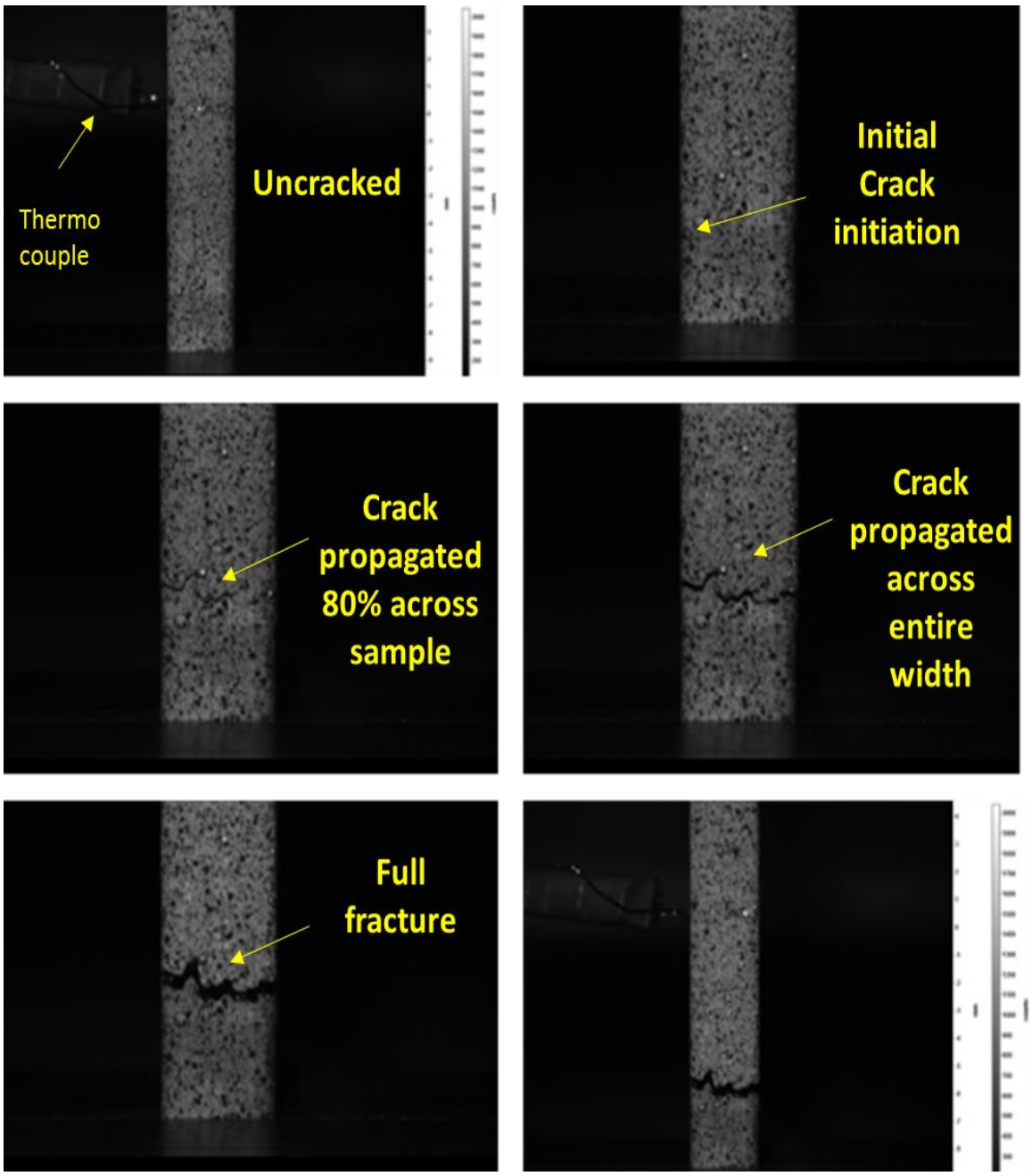

Figure 4-42 - Crack initiation and propagation as recorded by DIC during axial tensile ETMT test of Au80Cu20 at 400°C

4.6 Dynamic-mechanical thermal analysis

As a result of unexpectedly low values of elastic modulus determined from ETMT testing, an additional type of mechanical test was utilised. An existing ETMT geometry, "matchstick" type specimen was tested using a TA instruments Q800 Dynamic Mechanical Analyser (DMA) [200].

The test is performed by applying a load to a specimen in a 3 point bend configuration. The specimen from test number 1 from section 4.5, with dimensions 50mm x 3mm x 1mm, was tested. Results were obtained at 20°C, 100°C and 200°C. The resulting elastic modulus for each temperature is presented in Table 4-6. At 300°C the sample fractured mid-test, preventing any further testing for elastic modulus. This temperature is close to temperature (400°C) at which a previously discussed sample fractured during ETMT testing (section 4.5.2). Further research is required to determine if there is an embrittlement effect at this temperature range where a phase change occurs.

Table 4-6 - DMA elastic modulus results for Au80Cu20

Temp (°C)	E (GPa) - DMA	E (GPa) - ETMT
20	108	39.8
100	102	37.2
300	74	32.2

Also shown in Table 4-6 is the ETMT results discussed in section 4.5. It was found that there was an average ratio of $E_{DMA} = 2.5*E_{ETMT}$. The DMA measured moduli are relatively closer to the other measurements of E for Au8Cu20 (c. 100-100 GPa from Nanoindentation when accounting for pile up, and c. 90 GPa from micro-cantilever tests). The average differential ratio of 2.5*E was applied to the remaining temperatures for which DMA could not be assessed and is presented in Figure 4-43.

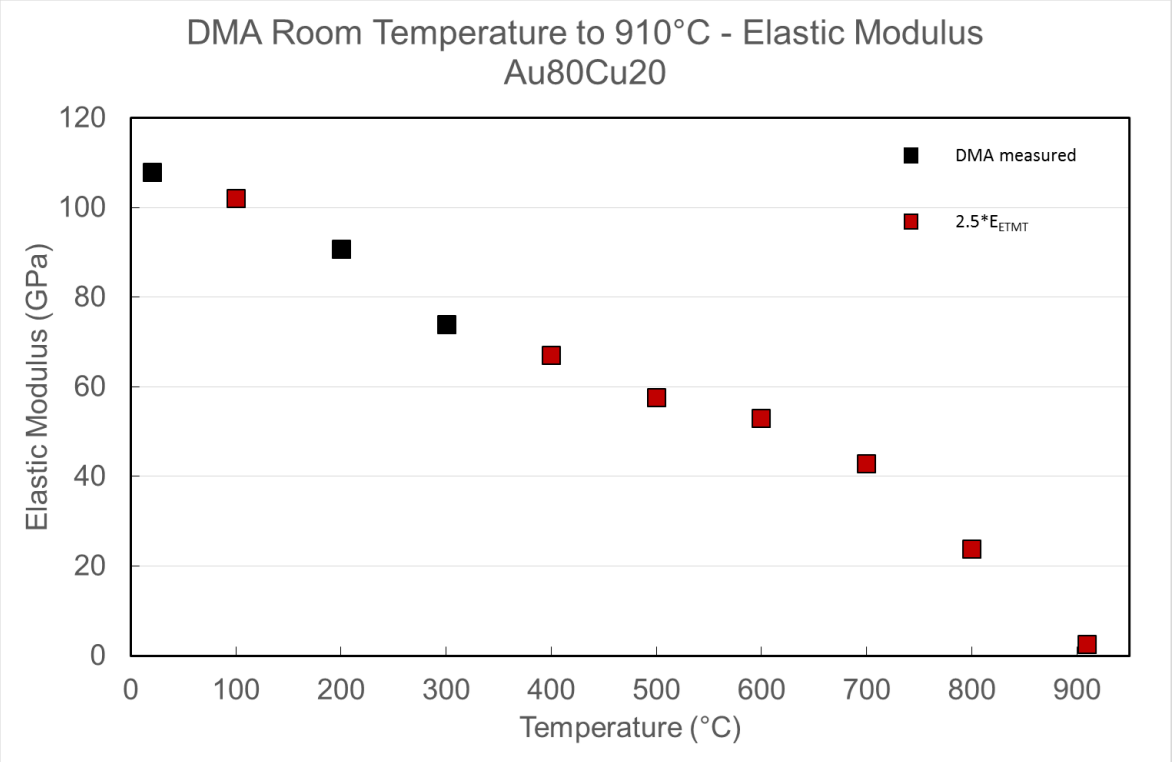

Figure 4-43 - DMA measured E and calculated E for Au80Cu20

The DMA and DMA extrapolated/calculated for correction factor set of values for elastic modulus are implemented into FE simulations of the brazing process in Chapter 5. The effects of the lower values (ETMT) or higher values (presented in this section) on the resulting residual stress predictions is examined.

4.7 Summary

In this chapter the material properties of a eutectic brazing alloy with composition 80Au20Cu have been investigated using a range of conventional and micro-mechanical techniques. The mechanical properties of the base materials, tungsten, copper and 316L austenitic stainless steel, have also been evaluated in the region of the brazing interface using micro-mechanical testing.

The thermal properties of as-received Au80Cu20 brazing alloy have been measured using STA, DSC and LFA techniques. Thermal conductivity, specific heat capacity and coefficient of thermal expansion have been measured up to temperatures close to the melting temperature of the alloy. For properties at temperatures for which experimentally determined values testing were not achievable linear interpolation has been used (for coefficient of thermal expansion) alongside educated approximations for thermal conductivity based on the similar trends between specific heat capacity.

Two micro-mechanical testing techniques have been used to determine the mechanical properties of the brazing alloy and base materials within the vicinity of the braze interlayer. Nano indentation using the CSM method was used to measure the elastic modulus of approximately 50 locations per material combination spread over the brazing interface.
The elastic modulus of the Au80Cu20 brazing alloy was found to be c. 140GPa for both the tungsten – copper brazed sample and tungsten – 316L brazed sample. However this value is thought to be an over estimation of the true elastic modulus due to pile-up, caused by the soft nature of the brazing alloy. When considering previously reported effects of up to 30% overestimation of elastic modulus when not accounting for pile up, the revised figure of 100-110 GPa for Au80Cu20 room temperature modulus is closer to the nano indentation calculated value (90 GPa) and DMA calculated value (108 GPa).
The elastic modulus of the base materials showed mixed levels of agreement with published data. Tungsten values were found to be close to those commonly reported. The 316L elastic modulus was found to be slightly lower than commonly stated (170 GPa measured compared with 200 GPa commonly reported). The elastic modulus of copper was also found to be higher than expected. For the copper at least this is thought to be attributable to pile-up during indentation.

Micro-cantilever bend testing was performed on in the region of the brazed interface for tungsten – copper and 316L brazed samples using the Au80Cu20 alloy. The elastic moduli results for Au80Cu20 were lower than those measured by nano indentation. When accounting for an

estimated over prediction of modulus due to pile-up during nano indentation, a variance of c. 20 GPa was found. For the brazing alloy in the tungsten – copper combination the modulus was measured to be 89GPa. For the brazing alloy within the tungsten – 316L system the modulus was measured at the higher value of 132GPa. The variation in elastic modulus has been attributed to the vast differences of interdiffusion of braze alloy to parent material for the two brazed specimens. The diffusion behaviour was reported in Chapter 3.

The micro-cantilever results for the elastic modulus of tungsten was in good agreement with both nano indentation results and those published in literature. There were however significant variances in the elastic moduli of copper and 316L obtained from micro-cantilever testing as were found with nano indentation. This can be attributed to grain effects, such as crystallographic orientation being tested, and a general measurement uncertainty. A larger quantity of testing is required to determine if systematic differences exist between typical values of elastic modulus and micro-cantilever calculated values.
The yield stress determined for all materials is significantly higher than reported in literature for standard sized samples of the same material. This is due to the reduced slip planes available when testing on single or a small number of grains [160].

Electrothermal mechanical testing was performed on as-received Au80Cu20 brazing alloy at temperatures ranging from 20°C to 700°C. The elastic modulus of the alloy have been obtained for all temperatures. The values for elastic modulus range from 40 GPa at room temperature to 17 GPa at 700°C. These values appear to be low compared with the modus determined using micro-mechanical techniques. Compared with DMA and micro mechanical methods, and underestimation of a factor of 2.5-3 times the value for modulus was found using ETMT. Further testing is recommended for future work to determine if the low value is a correct result for the as-received condition brazing alloy, or if a systematic experimental error caused an artificially low value. The conventional variation of elastic modulus with temperature suggest that any error was consistent across all tests.
The yield stress was determined at room temperature and 700°C. Due to an unexpected intergranular fracture of the alloy at 400°C it was not possible to obtain yield behaviour for a mid-range temperature. The failure has been analysed using optical and DIC techniques.
The plastic (tangent) modulus has been obtained at room temperature. The post-yield behaviour at high temperatures was observed to be comparable with a perfectly-plastic material.

DMA testing was performed and elastic moduli determined for 3 temperatures prior to specimen fracture. The results of DMA and ETMT were compared and found an average ratio of E_{DMA} =

2.5 * E_{ETMT} existed within the results. This factor was applied to the remaining temperatures of interest and are implemented into FEA in Chapter 5 of this thesis.

A number of the properties experimentally determined in this chapter shall be utilised in finite element simulations in the subsequent chapters of this thesis. It is clear that the material properties of materials in and around the brazing layer are not necessarily the same as reported for bulk material of the same composition. Additionally, the variable degrees of diffusion within a material result in a non-uniform profile of material properties even within a single material. These factors must be considered as possible sources for error within future analytical studies.

5 Residual stress state in dissimilar material bonded joints

5.1 Introduction

There is a large and ever growing range of applications necessitating the joining of dissimilar materials. Within a single component it is often desirable to have excellent performance of multiple properties depending on the segment of the component. For example within a divertor tile in a DEMO-like fusion reactor it is desirable to have high thermal capabilities and corrosion resistance at the plasma interface, but high heat transfer capabilities in the bulk of the structure. This is achieved through the joining of dissimilar materials. These types of operational demands are found across many engineering sectors; such as aluminium-higher strength material joints in the automotive industry, titanium alloy-steel welds in the space industry and ceramic-metal joints in high performance aerospace applications.

Whilst it is possible to optimize the performance of components through the careful selection of dissimilar materials, there is a cost associated with this. In general it is more difficult to join dissimilar materials as compared with like materials. These include solubility/wettability limitations of certain material pairs, formation of brittle intermetallic compounds, reduced fatigue performance/lifetime reduction due to joining flaws and residual stress generation due to material property dissimilarity.

The generation of residual stresses during dissimilar material joint formation shall be the focus of this chapter. The effect of material property dissimilarity in bonded structures has been extensively reported previously in literature. A study of this literature, in addition to theoretical and finite element based studies have been used to understand and predict the stress state in both idealised joint configurations and the brazed Au80Cu20 parts discussed throughout the entirety of this thesis.

5.2 Stress state of dissimilar material joints

Thermal stresses are formed at the interface of a dissimilar bonded joint upon cooling from joining due to a mismatch in thermal expansion, which restricts free contraction of the base materials [201]. Two typical dissimilar material joints are presented in Figure 5-1.

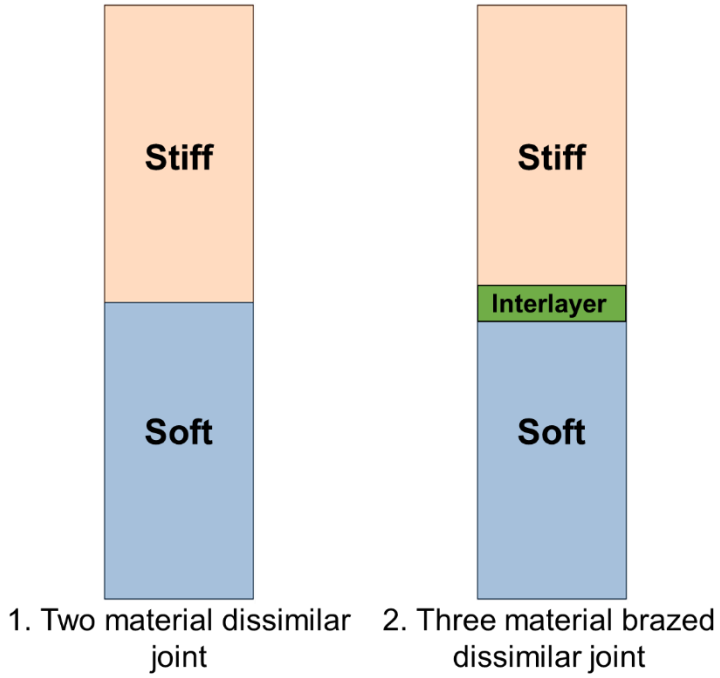

Figure 5-1 - Simple butt joint dissimilar material joints with two and three material configurations

The case on the left considers a simple butt joint configuration consisting of two dissimilar materials. The schematic on the right includes a third material, an interlayer between the two parent materials. This configuration is representative of a simple butt joint braze, such as the type used throughout this thesis.

To fully understand the stress state due to constraint on thermal contraction it is necessary to include the interlayer in any analyses [66, 68, 202, 203]. However by considering only the more simple case of a two material joint, much can still be understood about the nature of stresses due to thermal mismatch [118].

The material configuration discussed in this thesis of tungsten as one material and copper or steel as the second material can be considered analogous to a metal ceramic bond. The tungsten/ceramic has a higher E and lower CTE than the metal/ (copper or steel). This type of configuration has been evaluated many times in literature [66, 69, 201, 204-207]. For the purposes of the next few sections of this chapter where the effect of various material properties on residual stress are investigated, the following notation shall be used.

The tungsten/ceramic type material shall be designated as the stiff material due to typically higher elastic modulus, E, and yield properties. The less rigid, ductile material such as copper or steel shall be referred to as the soft material, as shown in Figure 5-1.

Figure 5-2 presents a schematic highlighting the result of differential thermal contraction of a dissimilar joint due to a difference in thermal contraction, ΔCTE. The first case shows two materials of equal starting dimensions at joining temperature. The second case shows the geometry upon cooling, where the soft material has a higher CTE than the stiff material. This results in larger thermal contraction. The third case shows a more severe case of differential thermal contraction, which could be caused by a higher difference in temperature between $T_{bonding}$ and T_{final}, (ΔT), or a higher ΔCTE between soft and stiff materials.

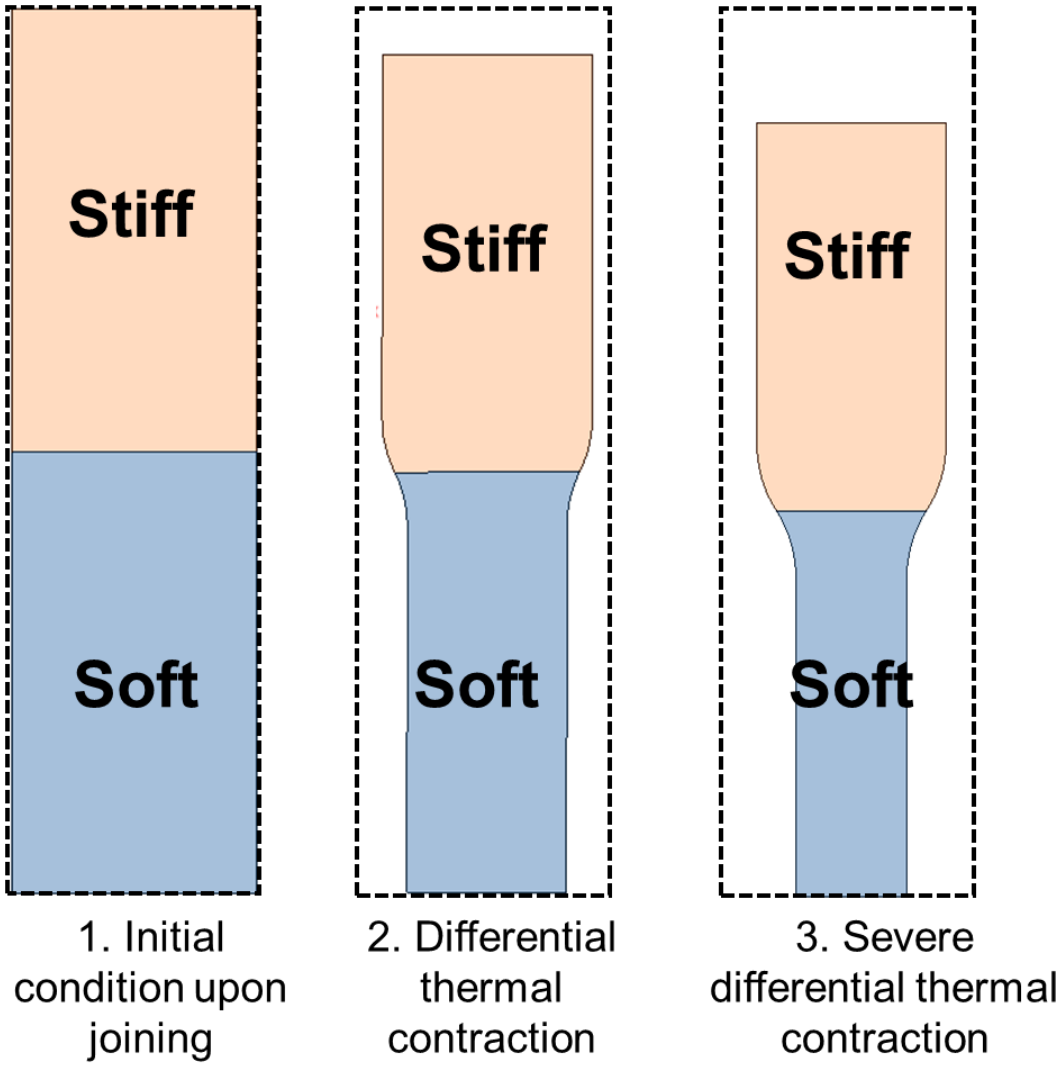

Figure 5-2 - Differential thermal contraction upon cooling due to ΔCTE

As the soft material attempts to contract more than the stiff material (as $CTE_{soft} > CTE_{stiff}$) a constraint is applied by the stiff material. The degree of this constraint is dependent on elastic material properties and thermal expansivity [66, 206]. In the case of yielding, the plastic behaviour of the soft material also becomes influential. Due to this constraining mechanism, a moment is applied at the interface as depicted in Figure 5-3. Further detail on the mechanics of constraint at the free edge has previously been presented [118, 208].

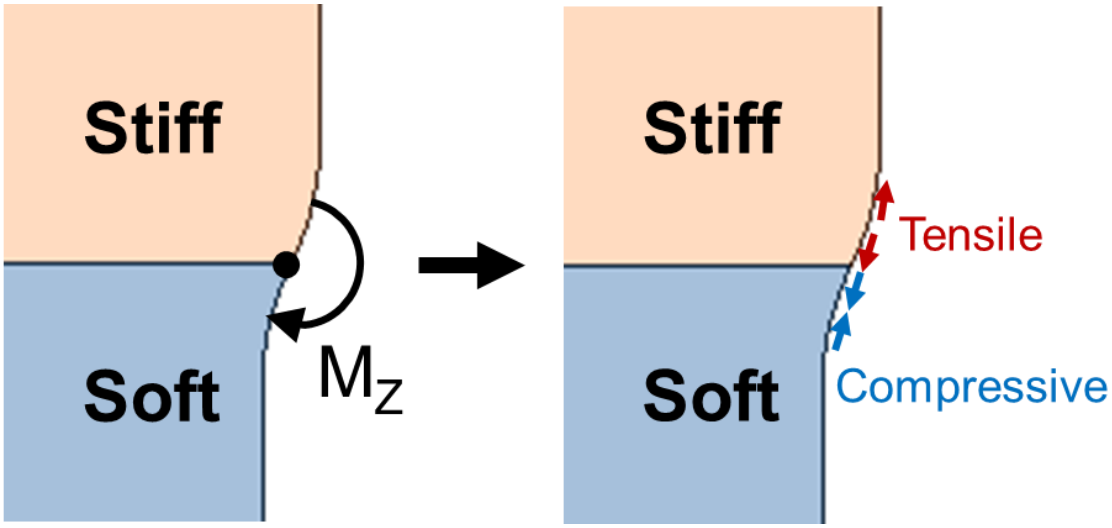

Figure 5-3 - Constraint on free contraction due to differential thermal expansion

The resulting typical stress profile long the free edge of a dissimilar joint where a singularity is present is shown in Figure 5-4 [209]. The elastic stress profile presented here is representative of that experienced at a singularity due to a dissimilar material join. Alternative sources of singularity could also provide this type of distribution such as a point load or a zero-radius re-entrant corner.

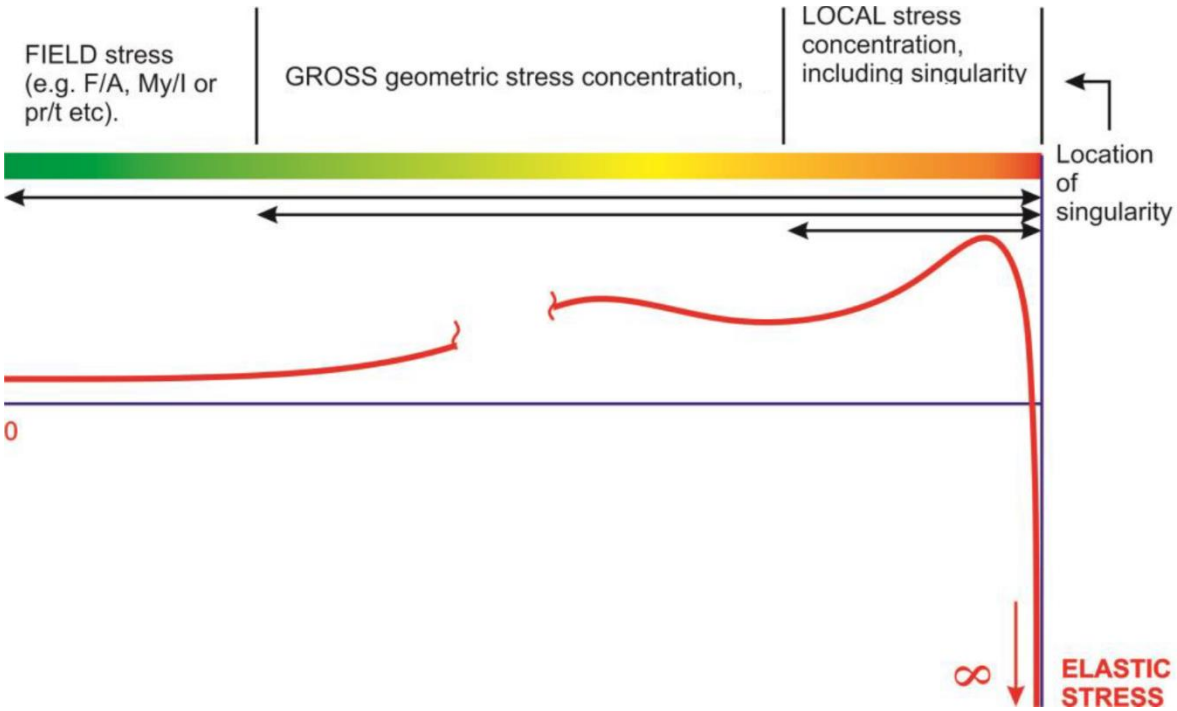

Figure 5-4 - Elastic stress distribution at the location of a singularity [209]

In a real engineering material, this elastic stress singularity will not exist in practice. Above a certain stress, dislocations within the crystal matrix in the vicinity of the interface will form. This plastic behaviour will serve to blunt the singular stress. Creep is a separate mechanism that will also serve to blunt elastic stress singularities [210]. There will remain however a local peak in stress in the region of the theoretical singularity at the local stress concentration depicted in Figure 5-4.

The presence of a singularity within a FE model has to be considered for certain analyses types. For instance, for the purposes of fatigue assessment, the stress concentration caused by the theoretical singularity would be significant, and not necessarily accurate, in predicting the lifetime performance of the dissimilar material structure. This issue has been addressed in welding codes through the use of hot-spot stress technique [209, 211]. With this method the stress at a series of distances from a singularity source, for instance a weld toe, is assessed. The stress is then extrapolated to obtain a repeatable representation of the true stress at the feature, which can then be used to calibrate the hot-spot stress method against experimentally derived failures of nominal stress [212, 213].

For the purposes of this thesis, the requirement of a hot-spot stress analysis has not been deemed necessary as fatigue has not been numerically assessed. This type of analysis is recommended for future research into brazed joints of the nature presented here.

The elastic stress singularity discussed previously has been subject to much research over the past decades. Analysis of the strength of singularities at dissimilar joints predates modern FEA techniques. Dundurs [214] and Bogy [215-218] published studies into the nature of dissimilar joint elastic singularities as far back as 1969. Following from this work, it is possible to quantify the strength of the singularity and characterize the stress at the singular location.

For a 90° butt joint, containing no interlayer, the stress at the interface which is singular in nature can be described by Equation 5-1 [201, 219]. This equation holds true only for a fully elastic response, i.e. no plastic accommodation of either material at the interface.

$$\sigma_{ij}(r,\theta) = \frac{K}{(r/L)^{\omega}} f_{ij}(\theta) + \sigma_{ij0}(\theta)$$

Equation 5-1

Where r and θ are polar coordinates, σ is the interface stress, K is the stress intensity factor, L is the characteristic length of the configuration and ω is the stress exponent. The stress exponent, ω, is generally positive and describes the stress singularity due to dissimilar materials [217]. The stress exponent can be assessed analytically using the Dundurs parameters and associated elastic material properties [214, 220].

The degree of the singular nature of thermal stresses at a bi-material joint was investigated by [221]. It was shown that the magnitude of singularity, as well as the relaxation behaviour of the singular stress over time, is heavily material dependent. This work, in addition to several others cited here, explore the mechanics and mathematics of theoretical stress singularities in much further detail, and shall not be discussed in detail in this work. For the remainder of this thesis, the focus shall be the effect of material properties on the sign and magnitude of the stress at the singularity local stress concentration.

The nature of a free edge stress perpendicular to the dissimilar joint can be determined by considering the relationship between the differences in elastic and thermal expansion properties, namely E and α. For two materials with properties E_1, α_1 (Material 1), E_2, α_2 (Material 2), the resulting sign of stress can be predicted using Figure 5-5.

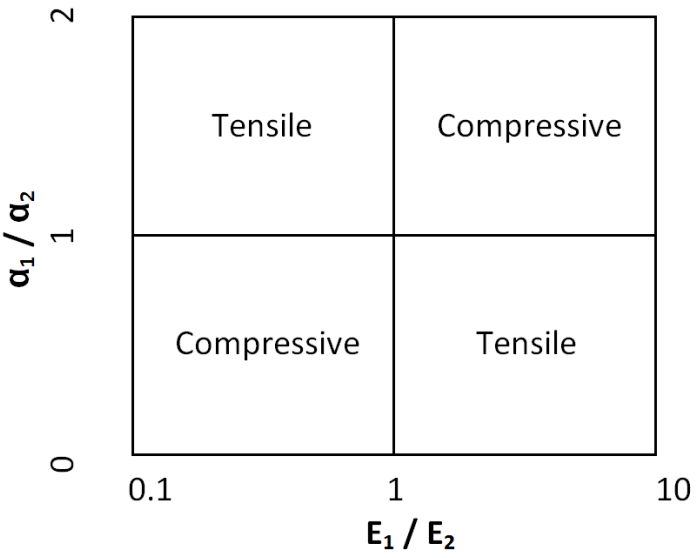

Figure 5-5 - Sign of singular interface stress upon cooling [222]

For a stiff material with high E and low α, such as tungsten or a ceramic material, the nature of the singular stress at the dissimilar material interface would be tensile in nature, as per the lower right quadrant of the diagram. Likewise, a softer metal bonded with the tungsten or ceramic, for instance steel would have a higher CTE and lower E, therefore $E_1 < E_2$ and $\alpha_1 > \alpha_2$ and the resulting stress singularity would also be tensile in nature. This however describes only the singularity component of the stress, not necessarily the stress state a short distance from the interface.

For the configuration mentioned previously this will result in tensile stresses along the free edge of the stiff material ($E_{stiff}>E_{soft}$, $\alpha_{stiff}<\alpha_{soft}$). This behaviour has been reported for multitudes of combinations including SiC-Ti and W-AlO brazed joints [66], for steel-brass joints [223], ceramic-metal joints [201, 205, 224] and titanium [199].

For an elastic approximation of dissimilar butt joint, the three material properties that significantly affect are E, α and ν [68, 206]. The effect of variations in these properties shall be evaluated using FEA in Section 5.3. It was shown that for a bi-material joint the stresses at the free edge close to the interface are always highest in the material with the higher elastic modulus E, regardless of stress exponent, ω [206]. For the purposes of work presented in this thesis, this should result in the highest stress at being present in the tungsten or "stiff" material.

Further factors that affect the singular interface stress include geometrical and plasticity effects. For the case of a simple butt joint with full contact and no misalignment the effect of contact

angle vanishes [225]. However for real parts with complex geometries it was shown that contact angle significantly affects the singular stress [225].

For a configuration including an interlayer, such as a typical brazing arrangement, the plastic properties yield and post-yield modulus are shown to be influential on the final stress state [66, 68].

Research into the stresses at a discontinuity singularity extend beyond that of brazed and diffusion bonded joints. Much research has been published on the stresses developing during bonding of ceramic-metal strips [226] and composite laminate structures.
The stress state in dissimilar material welded joints can also been considered as applicable to dissimilar brazed joints. Welded joints are similar to brazed joints in that residual stresses are generated due to a geometrical misfit caused by differential thermal contraction upon cooling from the bonding process.

However there are critical differences. Welding involves melting of both substrate and parent materials, and creates huge thermal gradients in the vicinity of welded region and heat affected zone (HAZ). Brazing on the other hand involves no melting of the parent materials, and thermal gradients are negligible in comparison to welded components.

5.3 Stress generation in bi-material dissimilar joints

In this section the effect of material properties on the subsequent stress state following the bonding of two materials at high temperature. The parameters investigated are those highlighted in Section 5.2 as being significant for the singular stress: E, α and ν.

A series of simulations were conducted taking each parameter in turn and assessing the impact of variation on resulting residual stress. Extreme conditions have been assessed in addition to more closely-matched configurations. This provides a good representation of the variations in material properties found within potential divertor materials (W, Cu, 316L and Au80Cu20 in this study).

A fully elastic model has been considered. Material properties are defined as temperature independent. The geometry and mesh parameters are kept constant. A static approach has been adopted for modelling, meaning the temperature is considered uniform throughout the entire part for a given solution step. This has been shown to be a fair approximation for the slow cooling rate of a brazed specimen within a vacuum chamber [208].

Firstly considered is a series of material property combinations representative of divertor relevance.

5.3.1 Dissimilar material combinations

The geometry for the simulations presented in this section is shown in Figure 5-6. The part has a total length of 50mm, comprised of two 25mm long parent materials, and a circumference of 12.5mm. ABAQUS CAE v6.13 [227] was used for performing brazing simulations. Quadratic axisymmetric elements were used throughout (8 noded CAX8R). Static conditions are assumed, with a ΔT applied uniformly across the part in multiple increments. An approximate element size of 10μm is used in the region of the interface. Mesh size is gradually coarsened away from the interface to aid simulation time. Convergence was assessed by performing a series of iterations of a brazing simulation, using increasingly refined mesh size at the interface. Once there was no significant change in stress profile with decreasing element size, the mesh was deemed to be converged. It was found that 10 μm was sufficient size for elements at the interface. The meshing approach and boundary conditions are discussed further in Section 5.5.2.

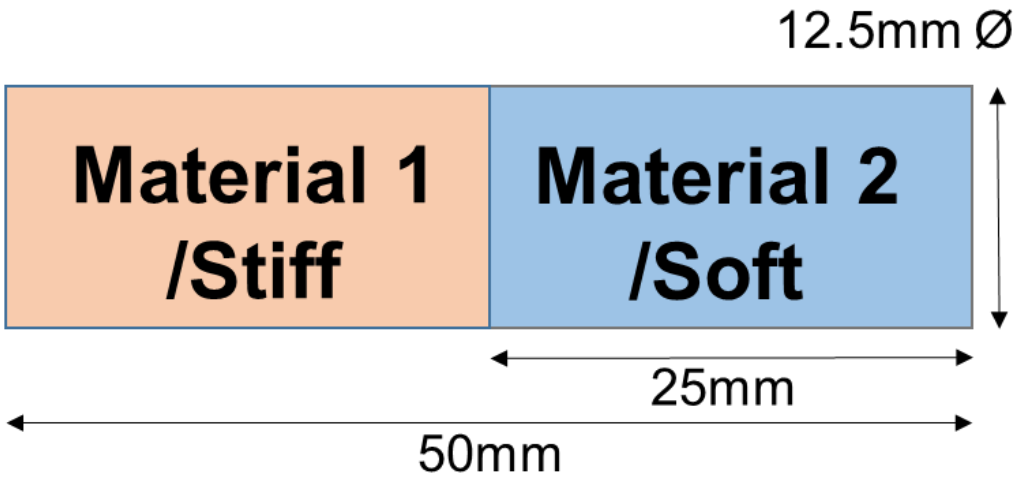

Figure 5-6 - Geometry for bi-material FEA

The first analysis looks at the case of zero and extreme degrees of material property dissimilarity. A total of four cases are considered. A summary of the properties for each case is shown in Table 5-1.

Table 5-1 - Summary of material properties for typical material combinations

Case	E (GPa)		CTE (x10-6)		v	
	Stiff	Soft	Stiff	Soft	Stiff	Soft
1	100	100	16	16	0.3	0.3
2	200	100	8	16	0.3	0.3
3	400	100	4	16	0.3	0.3
4	800	100	2	16	0.3	0.3

A ΔT of 1000°C has been applied to represent cooling from high bonding temperature. The first case consists of the two parent materials having equal properties. Each subsequent case doubles E and halves CTE, resulting in more severe dissimilarity and theoretically higher stresses. This degree of dissimilarity for each case can be described as:

1. Equal
2. Low degree of dissimilarity
3. Medium degree of dissimilarity
4. High degree of dissimilarity

The free edge axial stress results are presented in Figure 5-7.

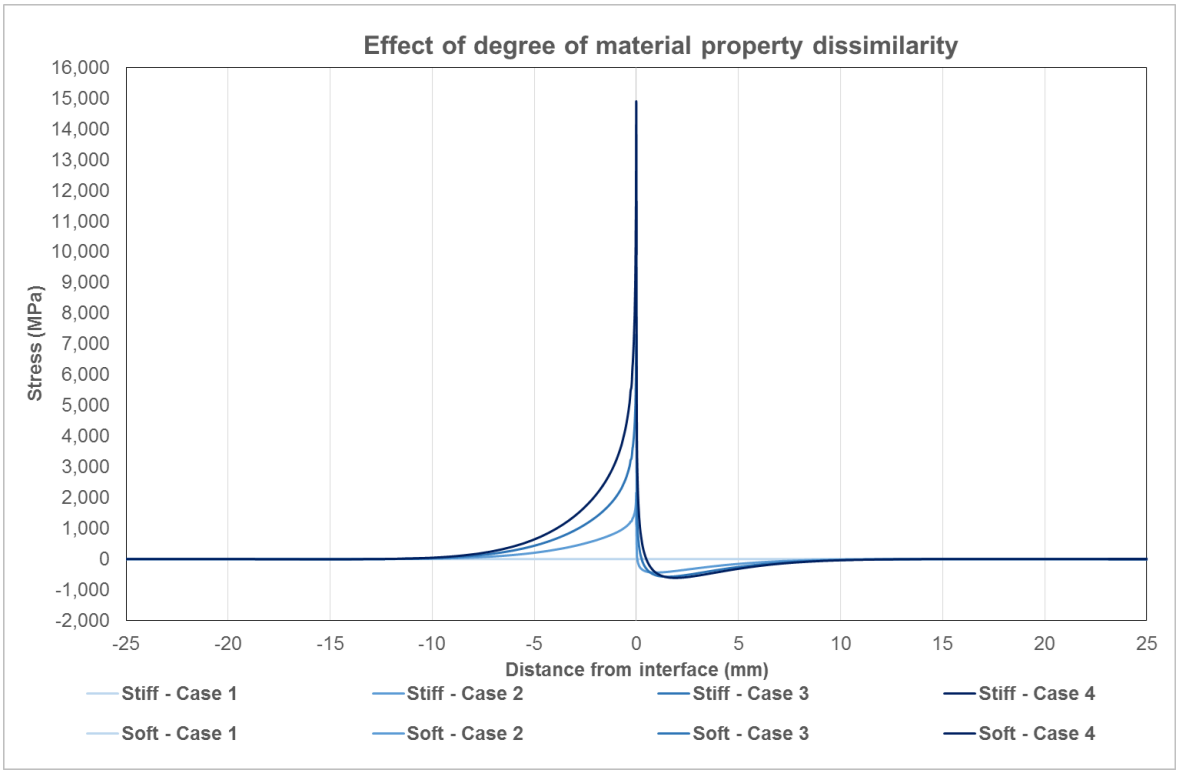

Figure 5-7 - Effect of degree of material property dissimilarity on free edge stresses

The results of the simulation presented in Figure 5-7 are intuitive and follow the principles outlined previously. Tensile stresses are expected in the stiff material, and the magnitude of stress at the region influenced by the singularity increases with increasing ΔE and $\Delta\alpha$.

In the following sections the effect of dissimilarity each property defined in this simple elastic model shall be explored.

5.3.2 Effect of CTE in bi-material joints

The first property to be varied in isolation is CTE. For this study again four cases were examined similar to Section 5.3.1. However in this case only α is varied. The two parent materials have E=100GPa and ν=0.3. The soft material has constant $\alpha=16E^{-6}/K$. The CTE of the stiff material is varied as shown below for each case:

1. Stiff CTE = $16E^{-6}/K$ (Equal properties/no dissimilarity)
2. Stiff CTE = $8E^{-6}/K$ (Low dissimilarity)
3. Stiff CTE = $4E^{-6}/K$ (Medium dissimilarity)
4. Stiff CTE = $2E^{-6}/K$ (High dissimilarity)

Results for stress dependence on CTE variation are presented in Figure 5-8. Stresses are shown for the axial direction and are unaveraged at the dissimilar interface.

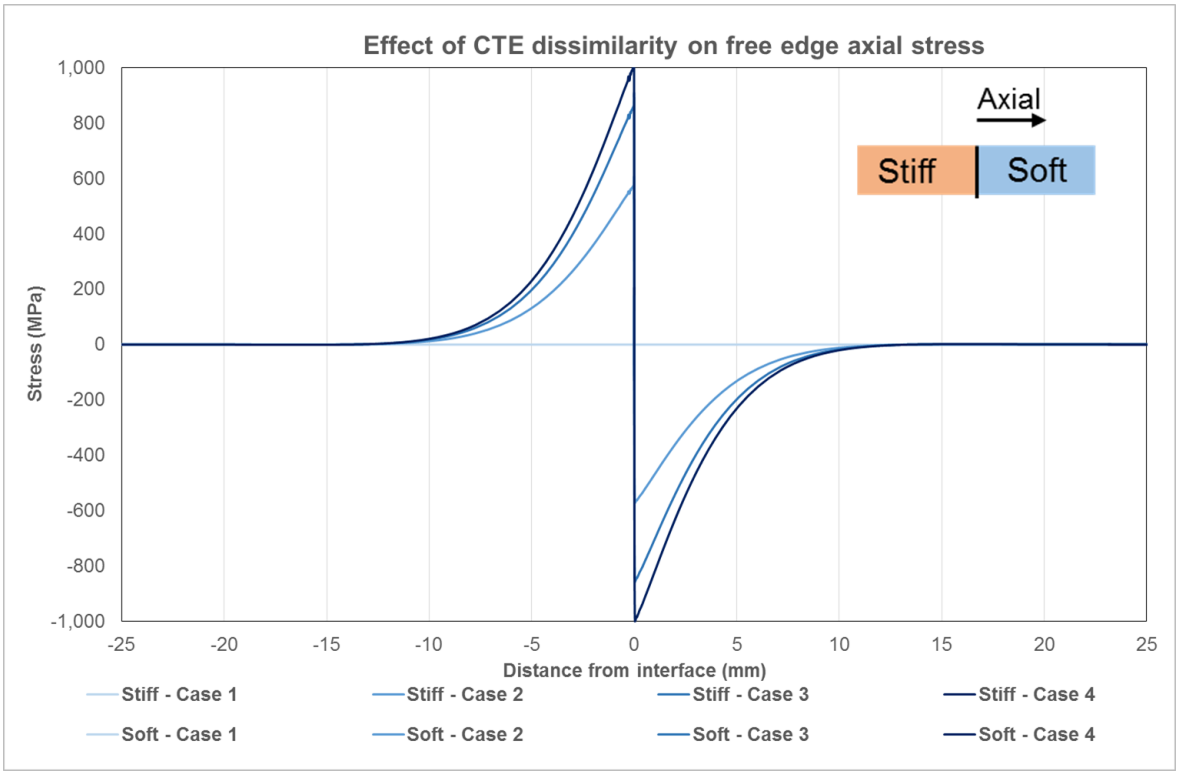

Figure 5-8 - Effect of CTE dissimilarity on free edge axial stress

The highest stress results in the case with the highest ΔCTE which is intuitive based on the theoretical understanding of the stress singularity, with a predicted higher stress singularity manifesting as large stress concentration close to the dissimilar joint. The increase in stress is not linear with increase in ΔCTE. The largest increase in interface stress is in the jump from equal CTE to CTE_{stiff}=0.5 x CTE_{soft}. For subsequent decreases in CTE_{stiff} the resulting increase in stress is less pronounced.

A further observation is that the stress does not increase as sharply in the local stress concentration region of the interface for the equal modulus, ΔCTE as compared with ΔE,CTE (Figure 5-7). For solely a difference in CTE the stress profile appears less asymptotic.

The magnitude of stresses are equal and opposite for the stiff and soft materials for any given distance from the interface. This is a function of having equal elastic properties.

5.3.3 Effect of Elastic Modulus in bi-material joints

The effect of elastic modulus dissimilarity on resulting free edge axial stress is now considered. The two parent materials are defined with equal Poisson's ratio (0.3). A constant ΔCTE is applied for all permutations of this analysis, as having equal CTE would result in no differential contraction, and hence no discontinuity stress. CTE_{stiff} is defined as 0.75 x CTE_{soft}, with values of $12E^{-6}/K$ and $16E^{-6}/K$ respectively. The soft material has constant E_{soft}=100GPa. The elastic modulus of the stiff material is varied as shown below for each case:

1. Stiff E = 100GPa (approx. equal properties/very low dissimilarity)
2. Stiff E = 200GPa (Low dissimilarity)
3. Stiff E = 400GPa (Medium dissimilarity)
4. Stiff E = 800GPa (High dissimilarity)

The results of this series of simulations are presented in Figure 5-9.

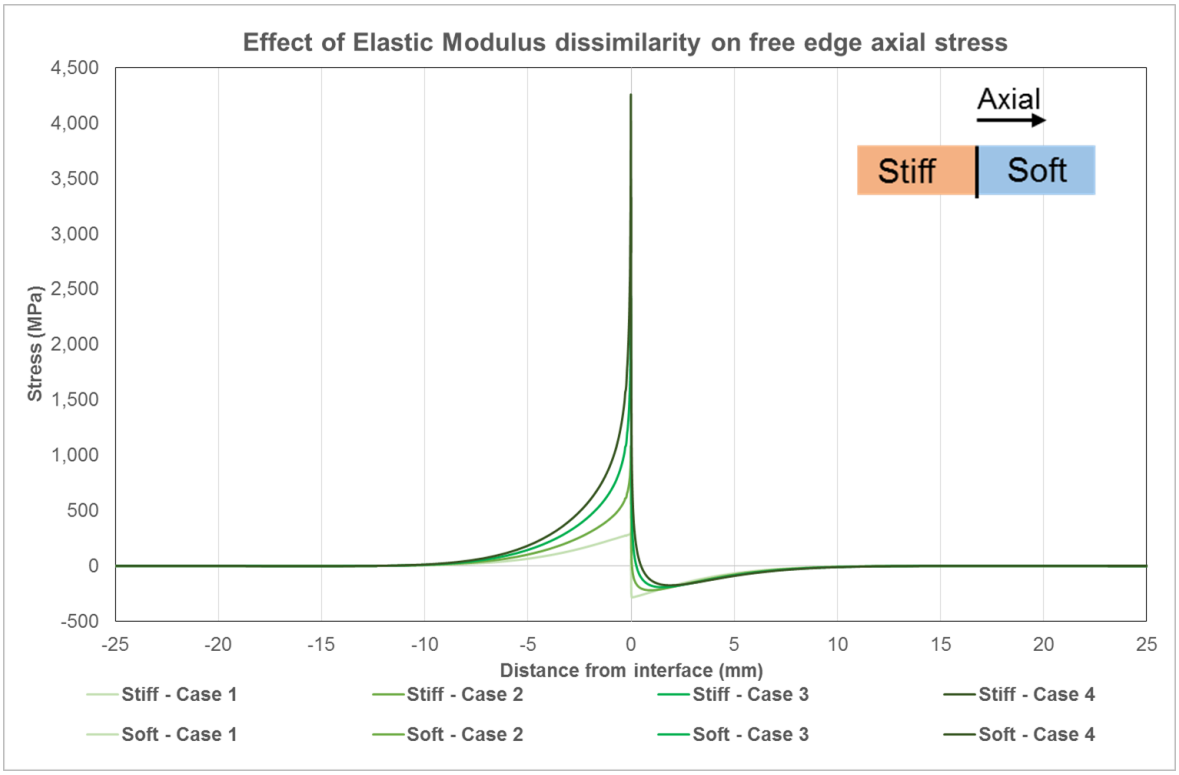

Figure 5-9 - Effect of Elastic Modulus dissimilarity on free edge axial stress

Increasing ΔE results in larger stresses for the stiff material, however the soft material is not similarly affected. The stress exponent increases with larger ΔE, so the singular behaviour of the

soft material is comparable to the stiff material. The stress in the soft material varies much less in the area a short distance remote from the interface than for the stiff material.

Increasing the dissimilarity of elastic modulus appears to have a more significant effect in a bi-material part as compared with increasing ΔCTE by a proportionally equal factor. This is true when considering the very local stress concentration region at the immediate position of the singularity, as well as the more gross stress singularity at a distance of c. 5mm from the interface albeit to a lesser degree.

5.3.4 Effect of Poisson's ratio in bi-material joints

The final material property evaluated in this section is Poisson's ratio. To evaluate the effect of a dissimilar ν_{stiff} and ν_{soft} the following approach was adopted. A set of material properties already evaluated was selected. In this instance case 2 from section 5.3.3 was selected as the control case. The material properties for each material is presented in Table 5-1 and the results presented in Figure 5-10.

Table 5-2- Material properties for Poisson's ratio analysis

Case	E (GPa)		CTE (x10-6)		v	
	Stiff	Soft	Stiff	Soft	Stiff	Soft
1	200	100	12	16	0.2	0.3
2	200	100	12	16	0.25	0.3
3	200	100	12	16	0.3	0.3
4	200	100	12	16	0.35	0.3
5	200	100	12	16	0.4	0.3

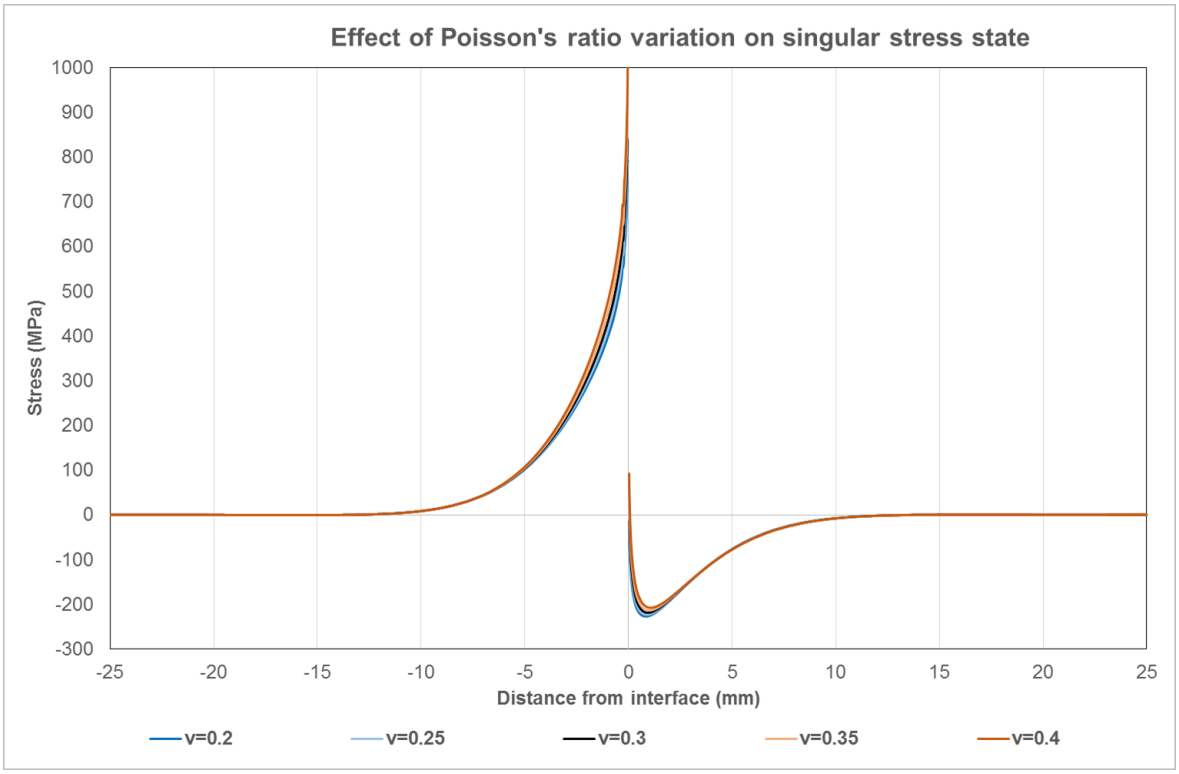

Figure 5-10 - Effect of Poisson's ratio variation on singular stress

The Poisson's ratio of the soft material was kept constant, with the stiff material Poisson's ratio increasing from 0.2 to 0.4 in 0.05 increments in order to provide a range of results with $\nu_{stiff} > \nu_{soft}$, and $\nu_{stiff} < \nu_{soft}$.

The effect of increasing ν of the stiff material results in an increase in free edge axial stress over the local stress concentration region. Reducing ν has the opposite effect. However it should be noted that the overall change to stress is small in comparison to the absolute value of stress.

The variation of stress with increasing $\Delta\nu$ can therefore be stated to be much less significant than increasing ΔE or $\Delta\alpha$.

5.4 Thermally induced stresses in three material brazed joints

In this section further material and brazing parameters are investigated using FEA. All simulations in this section contain a three-material joint identical to that presented in Figure 5-1. The geometry is consistent with Figure 5-6 with the exception of a 100μm interlayer. 10 elements are used through the thickness of the interlayer.

5.4.1 Effect of interlayer material CTE on stress state

The effect of increasing degree of dissimilarity of thermal expansion was investigated for a two material joint in Section 5.3.2. In this section the analysis is extended to include a braze layer. The material properties for the parent materials remain constant for all cases reported here, with one exception. The CTE of the interlayer is varied from 1E-^{6}/K up to 20E-^{6}/K. The material properties are presented in Table 5-3. The 16* for soft material CTE indicates a single analysis that was performed using this value in order to assess combined effect of parent material and interlayer material CTE variation.

The results of the series of simulations are presented in Figure 5-11.

Table 5-3 - Material properties for braze layer CTE analysis

Material	E (GPa)	CTE (x10-6)	v
Stiff	400	5	0.28
Interlayer	80	1,10,15,20	0.35
Soft	100	20 (16*)	0.33

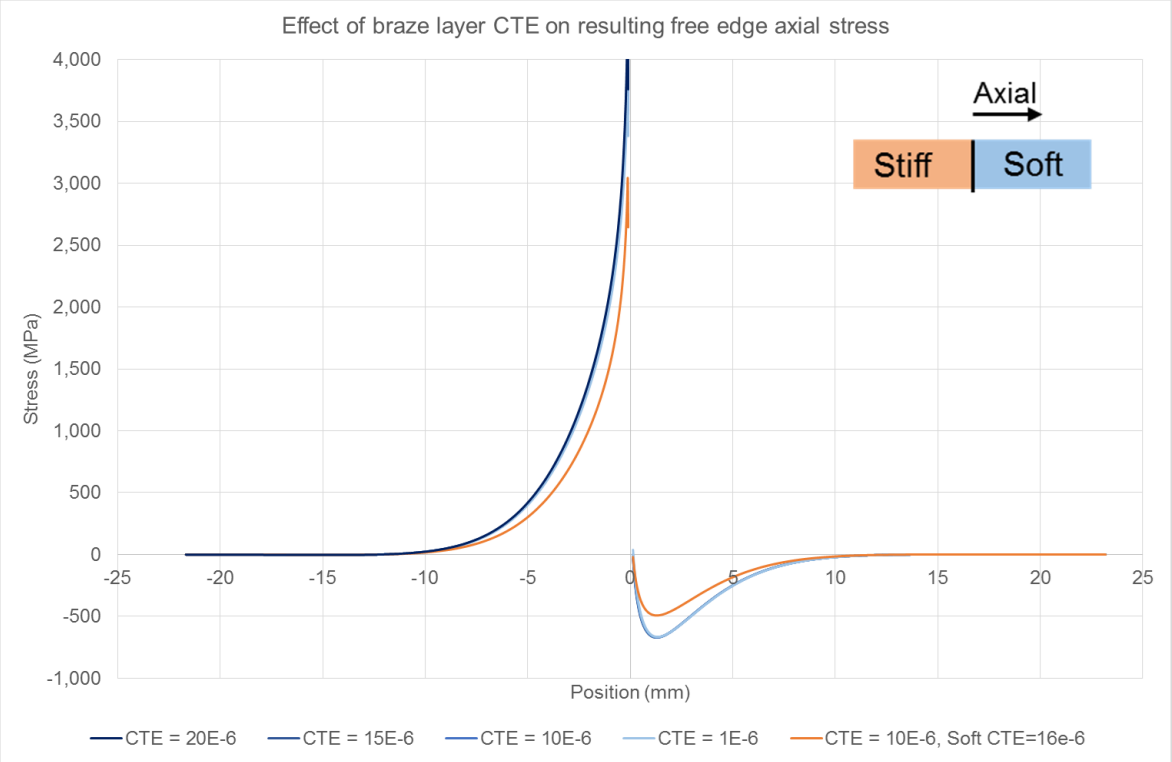

Figure 5-11 - Effect of braze layer CTE on resulting free edge axial stress

The stress profiles resulting in variation in interlayer CTE are presented in blue in Figure 5-11, with lightest to darkest shades denoting smallest to largest CTE. Further to this analysis, the CTE of the soft material was reduced for one condition, keeping all other variables constant. This plot is coloured orange.

The singular stress due to material dissimilarity does not appear to be strongly dependent on the CTE of the brazing alloy. The maximum deviation at any given point is +/-20MPa for braze layer CTE variation.

As shown in Section 5.3.2, the magnitude of the resulting stress is heavily dependent on parent material CTE. This has been further proven in this simulation, including the addition of an interlayer.

This would suggest that any uncertainties associated with material property generation in Chapter 4 for the Au80Cu20 brazing alloy are unlikely to cause a significant error in the brazing simulations presented in Section 5.5. Although the parent material properties were sown to have a larger influence on the final stress state, this only holds true to a point. For example, a zero modulus braze layer material will provide zero constraint on contraction, and that brazing induced stress will be negligible. Also, if the modulus and CTE of the braze material were to be matched with

either parent material, the system could essentially be reduced to a direct bonding of two parent materials.

5.4.2 Effect of interlayer thickness on stress state

In this section the effect of varying interlayer (i.e. braze layer) thickness on the resulting stress state has been assessed.

The effect of brazing layer thickness on maximum residual stresses at the free edge has been reported previously in literature. It was shown that for braze layer thickness has little effect for a simple butt joint configuration for thicknesses between 50μm and 700μm [91, 203]. For thicknesses below 50μm and tending towards zero braze layer thickness, it is suggested that a more significant effect on stress would be apparent.

The stress intensity factor of the interface in a three material braze configuration, K_{12}, was shown to increase as the relationship between braze layer thickness and total length decreases exponentially [202]. However as the braze layer thickness increases the stress intensity factor K_{12} becomes less significant as the influence it has on the stress field decreases [202]. Therefore the effect of increasing K_{12} may not necessarily correlate to significant increases in stress at a short distance from the dissimilar interface.

A series of FE simulations have been performed to investigate this effect. Temperature independent, fully elastic material properties have been used for both base materials and brazing layer. The properties of stiff, soft and interlayer materials are presented in Table 5-4.
The geometry of the part was kept constant with previous analyses (50mm x 12.5mm). The interlayer thickness was defined as 10μm, 50μm, 100μm and 200μm. A ΔT of 1000°C was applied. The model is fully elastic in nature. The results of the analysis are presented in Figure 5-12.

Table 5-4 - Material properties for braze layer thickness analysis

Material	E (GPa)	CTE (x10-6)	v
Stiff	400	5	0.28
Interlayer	80	15	0.35
Soft	100	20	0.33

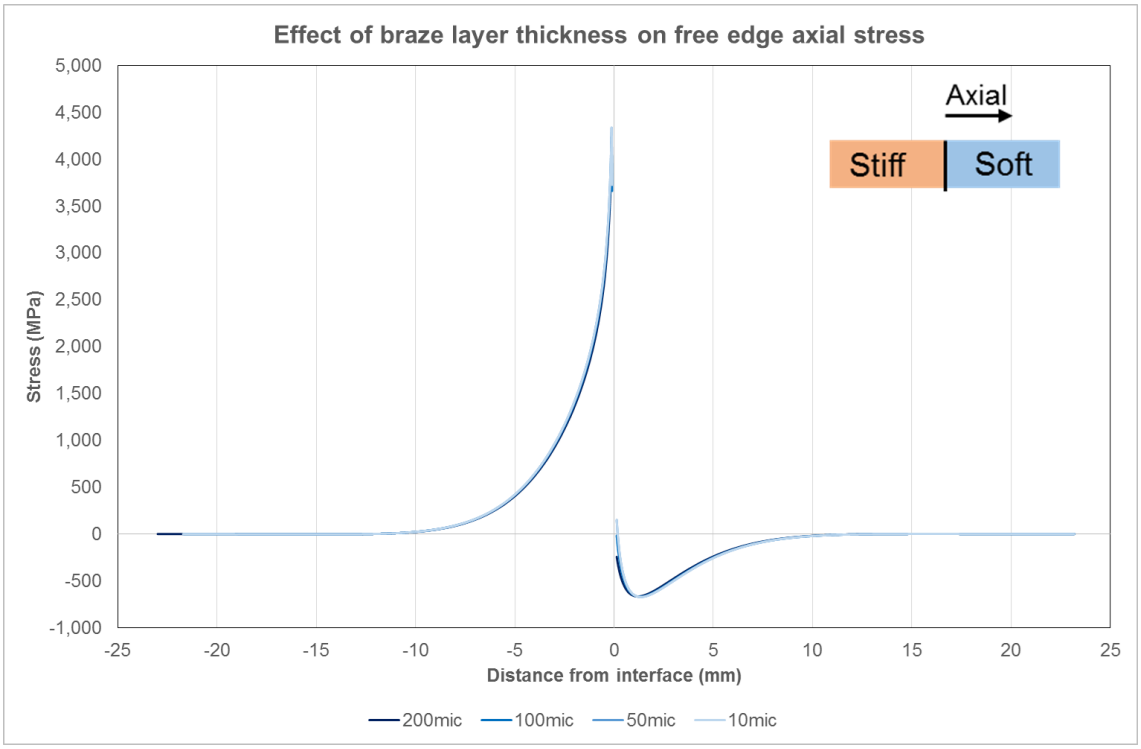

Figure 5-12- Effect of braze layer thickness on free edge axial stress

It is evident that for the range of thicknesses evaluated here, there is negligible effect on the resulting free edge stress. This is in good agreement with the works previously mentioned. This suggests that the braze thickness to be modelled for the real Au80Cu20 joints is not of significant importance. This is a beneficial result as braze thickness was found not to be equal with all parts.

The small effect that is apparent is an increase in the stress very close to the interface as braze thickness decreased towards 0μm. This variation is only apparent in the very close proximity to the braze interface (<100μm) which is strongly affected by the theoretical singularity.

5.4.3 Effect of brazing temperature on stress state

The effect of brazing temperature on the resulting stress state has been evaluated in this section. The larger the initial brazing temperature, the larger the ΔT to reach the final temperature, i.e. room temperature. Therefore it is expected that with absent of drastic changes in the relative values of material properties (i.e. each material varies by a comparable degree with ΔT), the higher the temperature the higher the resulting stress should be.

Brazing temperatures of 910°C (Au80Cu20 liquidus temperature), 700°C, 500°C, 300°C, 100°C and 50°C were investigated. The material properties used were that of the real tungsten, copper and Au80Cu20 material as shown in Table 5-5, Table 5-7 and Table 5-8 respectively. This includes elasto-plastic behaviour. The results are presented in Figure 5-13.

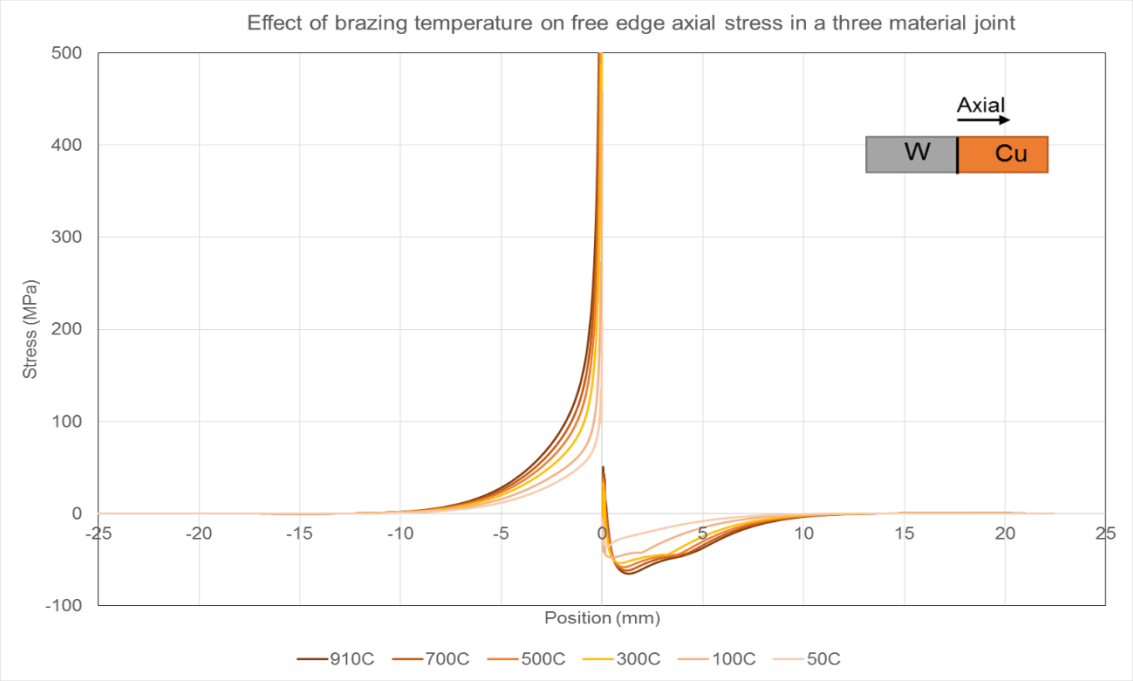

Figure 5-13 - Effect of brazing temperature on free edge axial stress in a three material joint

The results are consistent with what appears to be intuitive: increasing ΔT results in larger free edge axial stresses. The peak tensile (tungsten) and peak compressive (copper) stresses increase with increasing braze temperature. This behaviour was not previously observed when considering the effects of material property dissimilarity.

These results would suggest that in order to reduce the final residual stress profile at the free edge of a brazed joint, the filler alloy should be selected to have as low a liquidus temperature as

possible, providing all other requirements (e.g. heat transfer properties, mechanical strength) are satisfied.

5.5 FEA of tungsten, copper and steel joints brazed with Au80Cu20 alloy

5.5.1 Material properties for FEA

In this section the thermally induced stresses in brazed joints with Au80Cu20 interlayer are discussed. The temperature dependent material properties for the four materials of interest; tungsten, OFHC copper, 316L stainless steel and Au80Cu20 eutectic brazing alloy are presented in Table 5-5, Table 5-6, Table 5-7 and Table 5-8 respectively. The properties for tungsten, copper and 316L have been obtained from various literature sources which have been aggregated into the JAHM Material Property Database [228]. Experimentally determined material properties for the Au80Cu20 alloy are presented in Chapter 4.

The plastic behaviour for the three base metals has been described as a bilinear kinematic hardening relationship, with the tangent modulus E_{tan} approximated to be 0.1xE for a given temperature. This results in temperature dependent strain hardening behaviour, as temperature dependent values of E are known. Generation of temperature dependent plastic stress-strain behaviour, and implementation into the FE model, are recommended for future work.

As was discussed in the previous chapter, there was significant variation and uncertainty within the elastic mechanical properties obtained experimentally for the eutectic brazing alloy. However, as was shown in section 5.4, the final stress state of the dissimilar three material joint is less dependent on the braze alloy elastic properties and more dependent on the parent material elastic properties and CTE. Therefore the simulation results presented in this section are considered an accurate depiction of the true stress state.

Table 5-5 - Tungsten temperature dependent material properties for FEA [228]

T (°C)	E (GPa)	Yield Stress (MPa)	Plastic Tangent Modulus (GPa)	Poisson Ratio ν	Density ρ (kg/m3)	Thermal Conducivity (W/mK)	Specific Heat Capacity Cp/(J/(Kg*K))	Coeff Thermal Expansion CTE (x10-6 (/K))
20	399.3	1335.9	39.9	0.285	19300	174	132.47	4.4
100	396.1	1179.4	39.6	0.285	19300	162	135.17	4.5
200	392.0	1014.8	39.2	0.285	19300	149	138.07	4.5
300	387.7	880.9	38.8	0.285	19300	138	140.55	4.6
400	383.3	773.6	38.3	0.285	19300	131	142.73	4.6
500	378.7	689.0	37.9	0.285	19300	126	144.72	4.7
600	374.0	647.5	37.4	0.285	19300	122	146.59	4.7
700	369.1	571.9	36.9	0.285	19300	119	148.41	4.8
800	364.1	531.3	36.4	0.285	19300	116	150.25	4.8
900	358.9	497.3	35.9	0.285	19300	113	152.14	4.8
910	358.9	497.3	35.9	1.285	19300	112.78	152.14	4.8

Table 5-6 - OFHC Copper temperature dependent material properties for FEA [228]

T (°C)	E (GPa)	Yield Stress (MPa)	Plastic Tangent Modulus (GPa)	Poisson Ratio ν	Density ρ (kg/m3)	Thermal Conducivity (W/mK)	Specific Heat Capacity Cp/(J/(Kg*K))	Coeff Thermal Expansion CTE (x10-6 (/K))
20	125.4	41.3	12.5	0.33	8900	387	383.62	16.8
100	120.9	32.0	12.1	0.33	8900	385	393.29	17.2
200	115.1	23.4	11.5	0.33	8900	383	404.11	17.6
300	109.0	17.3	10.9	0.33	8900	379	413.55	17.9
400	102.6	13.0	10.3	0.33	8900	374	421.86	18.1
500	96.0	9.7	9.6	0.33	8900	368	429.59	18.3
600	89.2	6.6	8.9	0.33	8900	360	437.56	18.4
700	82.1	4.0	8.2	0.33	8900	353	446.88	18.6
800	74.7	2.0	7.5	0.33	8900	347	458.89	18.9
900	67.0	1.0	6.7	0.33	8900	340	475.24	19.2
910	67.0	1.0	6.7	0.33	8900	340.38	475.24	19.2

Table 5-7 - 316L stainless steel temperature dependent material properties for FEA [228]

T (°C)	E (GPa)	Yield Stress (MPa)	Plastic Tangent Modulus (GPa)	Poisson Ratio ν	Density ρ (kg/m3)	Thermal Conducivity (W/mK)	Specific Heat Capacity Cp/(J/(Kg*K))	Coeff Thermal Expansion CTE (x10-6 (/K))
20	194.5	302.0	19.4	0.3	7900	13	491.34	16.2
100	187.8	249.4	18.8	0.3	7900	15	525.29	16.5
200	179.4	224.0	17.9	0.3	7900	16	556.43	16.9
300	171.0	197.8	17.1	0.3	7900	18	579.2	17.2
400	162.7	185.3	16.3	0.3	7900	19	597.28	17.6
500	154.3	180.3	15.4	0.3	7900	20	613.55	18.0
600	145.9	176.0	14.6	0.3	7900	21	630.03	18.4
700	137.5	165.8	13.7	0.3	7900	23	647.96	18.8
800	129.1	142.9	12.9	0.3	7900	24	667.72	19.1
900	120.0	115.2	12.0	0.3	7900	25	688.89	19.5
910	120.0	115.2	12.0	0.3	7900	24.695	688.89	19.5

Table 5-8 - Au80Cu20 brazing alloy temperature dependent material properties for FEA

T (°C)	E (GPa)	Yield Stress (MPa)	Plastic Tangent Modulus (GPa)	Poisson Ratio v	Density ρ (kg/m3)	Thermal Conducivity (W/mK)	Specific Heat Capacity Cp/(J/(kg*K))	Coeff Thermal Expansion CTE (x10-6 (/K))
20	39.80	126.0	8.0	0.4	15200	104	216.13	13.9
100	37.20	108.7	7.0	0.4	15200	120	220.8	16.0
200	36.30	91.3	6.0	0.4	15200	86	144.82	16.9
300	32.20	74.0	5.0	0.4	15200	55	93.945	18.4
400	26.80	56.7	4.0	0.4	15200	127	253.29	22.6
500	23.00	39.4	3.0	0.4	15200	97	191.45	21.7
600	21.20	22.0	2.0	0.4	15200	131	242.34	21.1
700	17.10	10.0	1.0	0.4	15200	160	299.28	20.8
800	9.50	5.0	0.5	0.4	15200	168	314.62	20.6
900	1.00	1.0	0.1	0.4	15200	145	256.2	20.3
910	1.00	0.0	0.0	0.4	15200	145	256.2	20.3

5.5.2 FE model set up

Finite element analysis was performed using ABAQUS CAE v6.13 [227]. The part geometry is identical to that of the residual stress specimen type described in Section 3.2. A 2D axisymmetric model has been used which assumes perfect axial and angular alignment of the parent materials. The actual braze layer thickness of brazed tungsten-copper, tungsten-316L and 316L-copper parts was observed to vary depending on parent material combinations as reported in Section 3.3, with the smallest thickness being c. 50µm and the largest observed 120µm. However as braze layer thickness was shown to have negligible effect on the final stress state (at least for the thicknesses considered here), a constant thickness of 80µm has been used for all analyses presented in this section.

The initial dimensions of the parent materials were calculated by applying a ΔT of 890°C which represents heating from room temperature to the braze alloy solidus temperature of 910°C. Although in practice the brazing temperature reached 950°C, for the purposes of this model only behaviour from 910°C and below is significant. This is a result of the eutectic nature of the brazing alloy. Above 910°C the interlayer is fully liquidus and thus provides no constraint on the thermal expansion/contraction of the parent materials. Therefore the initial dimensions of the part at the instant the alloy solidifies at 910°C can be calculated solely based of the geometric expansion of each individual parent material. A representation of the W-AuCu-Cu brazed part is shown in Figure 5-14.

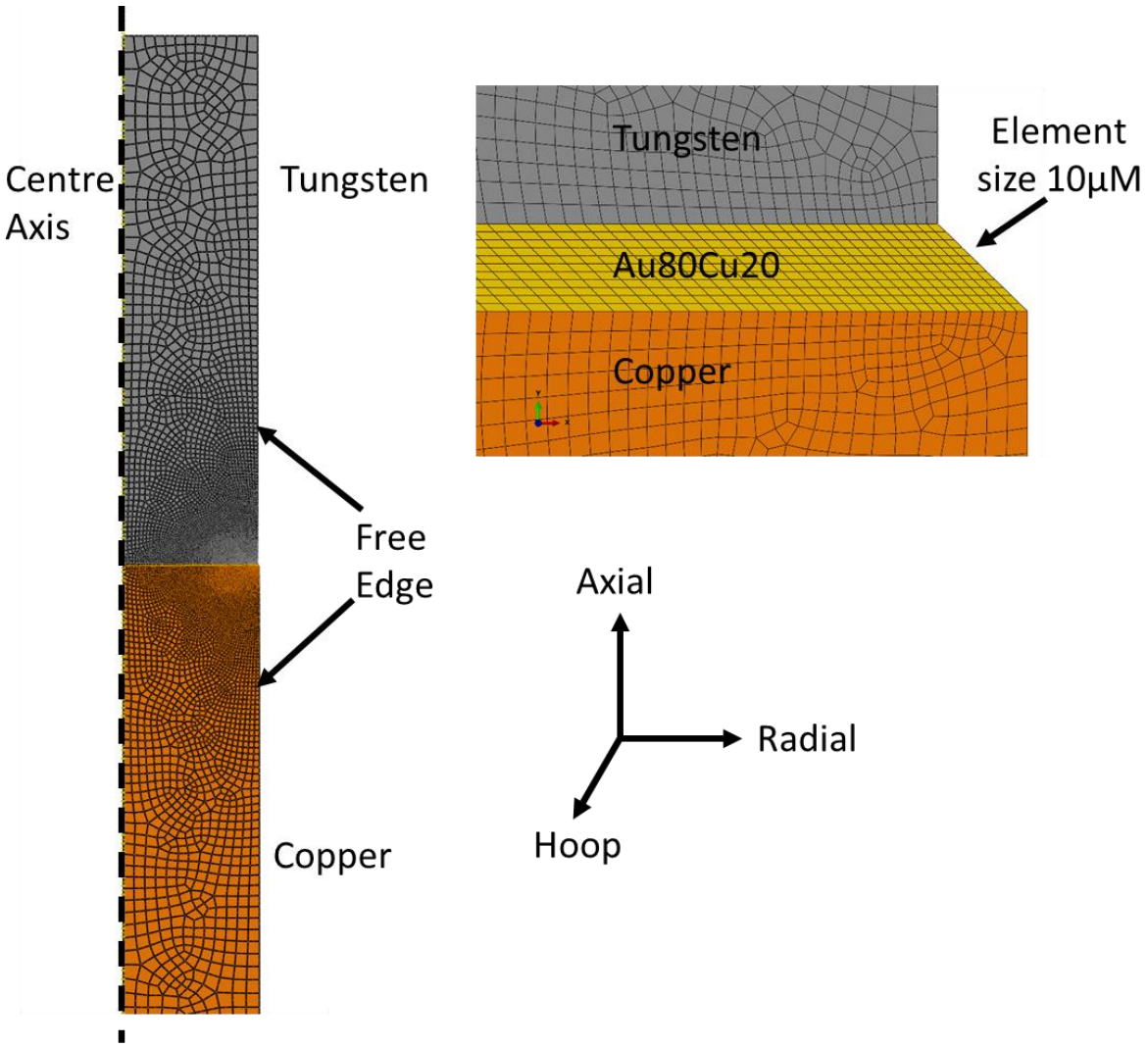

Figure 5-14 - Geometry and FE mesh of W-AuCu-Cu brazed joint

The difference in radius observed in the inset of the above figure is due to the much larger expansion of copper upon heating to brazing temperature. It is due to this CTE differential that large residual stresses are expected as discussed previously.

An extremely fine mesh was used in the vicinity of the brazing interlayer, with highest mesh density at the free edge where high singular-like stresses are expected. An approximate element size of 10µm is used at the most densely meshed region shown in Figure 5-14 which was found to be suitable resolution to provide a converged solution in the interfacial region.

The entire part is meshed with higher order quadrilateral type elements, designated CAX8R within ABAQUS. These are 8-noded, quadratic, reduced integration elements suitable for axisymmetric stress simulations.

The axis notations are shown in Figure 5-14. For the purposes of this work only the vertical and out of plane stresses pictured are considered, termed axial (σ_{axial}) and hoop (σ_{hoop}) stresses. The remaining principal stress, the radial component, is zero at the free edge. The free axial stresses are expected to be highest in magnitude [206, 219]. The hoop stresses have also been considered as this component of stress is measured experimentally in subsequent sections of this thesis.

A steady state structural simulation with ΔT applied as a predefined field has been used to simulate the brazing process. It has previously been shown that considering a transient thermal analysis for the brazing of copper and titanium resulted in negligible difference in residual stress field as compared with the method stated here [68, 208]. This approach is particularly applicable as the range of emissivity with the materials in this study (0.04 tungsten, 0.03 copper, 0.08 stainless steel and 0.025 gold) is much smaller in variation as compared with copper and titanium (0.03 and 0.19). Therefore the temperature variation as a result of differential radiative cooling shall be less for any given material combination presented in this study based on the equation for radiation heat transfer of a grey body:

$$q = \varepsilon \sigma (T_h^4 - T_c^4) A_C$$

Equation 5-2

With:

- Heat transfer coefficient, q,
- Stefan-Boltzman constant, σ
- Hot body temperature, T_h (brazed specimen in this instance)
- Cold body temperature, T_c (vacuum furnace walls)
- Area of radiating object, A_c

This assumption holds true providing the materials emissivity is equal to the absorptivity. A further assumption is that radiation is the sole heat transfer method, so negligible conduction through the base of the vacuum furnace and zero convection due to vacuum conditions.
Based on these assumptions it is thought to be appropriate to simplify the model from a transient thermal problem to a static problem.

The analysis is elasto-plastic in nature. Plasticity has been modelled using Mises yield surface criteria within ABAQUS with bilinear kinematic hardening behaviour. The hardening behaviour has been approximated for all materials to be linear in nature, given by the tangent modulus, E_{tan}, which is defined for each material and is temperature dependent (Table 5-5 to Table 5-8). The

plasticity is defined within ABAQUS by inputting a yield stress and plastic strain for the entire temperature range of the simulation. Initial yield stress, σ_{yield}, are known from literature (W, Cu, 316L) or experimentally determined (Au80Cu20). For example the stress at n% plastic strain, $\sigma_{n\%}$, is calculated by:

$$\sigma_{n\%} = (E_{tan} \cdot \varepsilon_{n\%}) + \sigma_{yield}$$

Equation 5-3

5.5.3 Tungsten – Copper brazed joint

The FE results for the brazing of W-AuCu-Cu from 910°C to 20°C are presented in Figure 5-15. The stresses presented are those averaged at nodes of each element. Due to the presence of a theoretical singularity due to material property and geometry discontinuity at each interface region the elements either side of the interface are discounted. This also removes averaging errors as at the interface the averaged nodal stress would contain stress from both materials. Stresses are presented in respect to distance from the respective braze interface for each material.

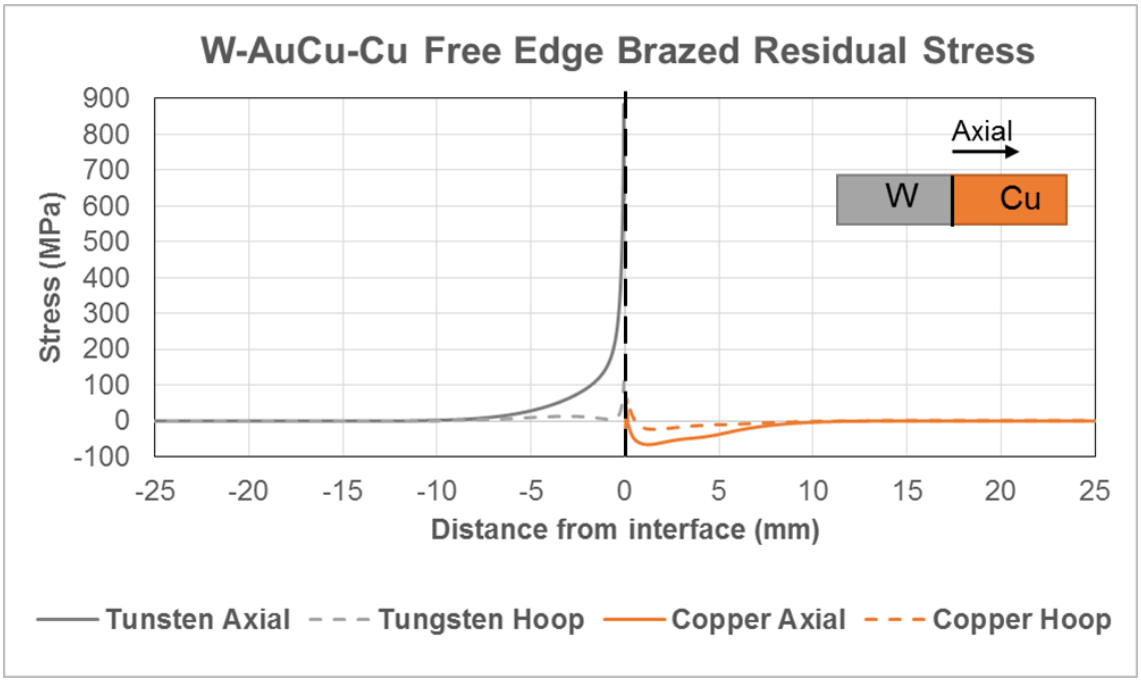

Figure 5-15- Free edge brazing residual stresses for W-AuCu-Cu configuration

From Figure 5-15 it is shown that there are high axial tensile stresses in the tungsten in the close vicinity of the braze interface. These stresses increase sharply as the proximity to the interlayer increases. The singular nature of the stresses in this region are in good agreement with both theoretical and experimental findings for dissimilar joints of this nature [68, 222, 229, 230].

The expected sign of stress based on the relationship of E and α should result in tensile stresses in the tungsten and compressive stresses in the copper since:
$E_{tungsten} > E_{copper}$ and $\alpha_{tungsten} < \alpha_{copper}$. This was found to be the result from the FE simulation (Figure 5-15).

A maximum tensile stress of approx. 1000MPa was observed for the axial component of stress in the tungsten. By considering the axial stress results for W-AuCu-Cu, the region of influence of the interface on the residual stress state is observed to be just less than 10mm in the axial direction along the free edge of the parent materials. However even for the tungsten, which exhibits the largest stresses, the residual stresses drop below a significant level ($<0.1*\sigma_{yield}$) within about 3mm. In the tungsten, at a 3mm distance from the braze, the axial stresses drop below 100MPa. Considering the high yield stress of tungsten (>1GPa) it can be stated that the free edge stresses induced by constraint on free contraction upon cooling from brazing are significant only in the vicinity of the interface and not the bulk of the material.
The hoop stresses at the free edge of the W-AuCu-Cu joint are significantly less than the axial stress. This is in good agreement with the findings of Munz et al [206, 219]. At a short distance of 1mm from the interface the tungsten was found to be in tension, and the copper in compression. The magnitudes of hoop stresses in both materials were very low, <30MPa, excluding the singular region at the interface.
The magnitude of the stress in tungsten is much higher than in copper. This should be expected due to the values of E and α, in addition to the much lower yield stress of copper.
The high axial tensile stresses in the tungsten are shown in the contour plot in Figure 5-16. The peak stresses in the tungsten are extremely high, but also localised to the free edge. Towards the bulk of the material a mild compressive state is shown. Although the peak stresses are localised to the interface, it is still considered as potentially detrimental to fatigue performance. A high tensile stress at the brittle material interface is not desirable.

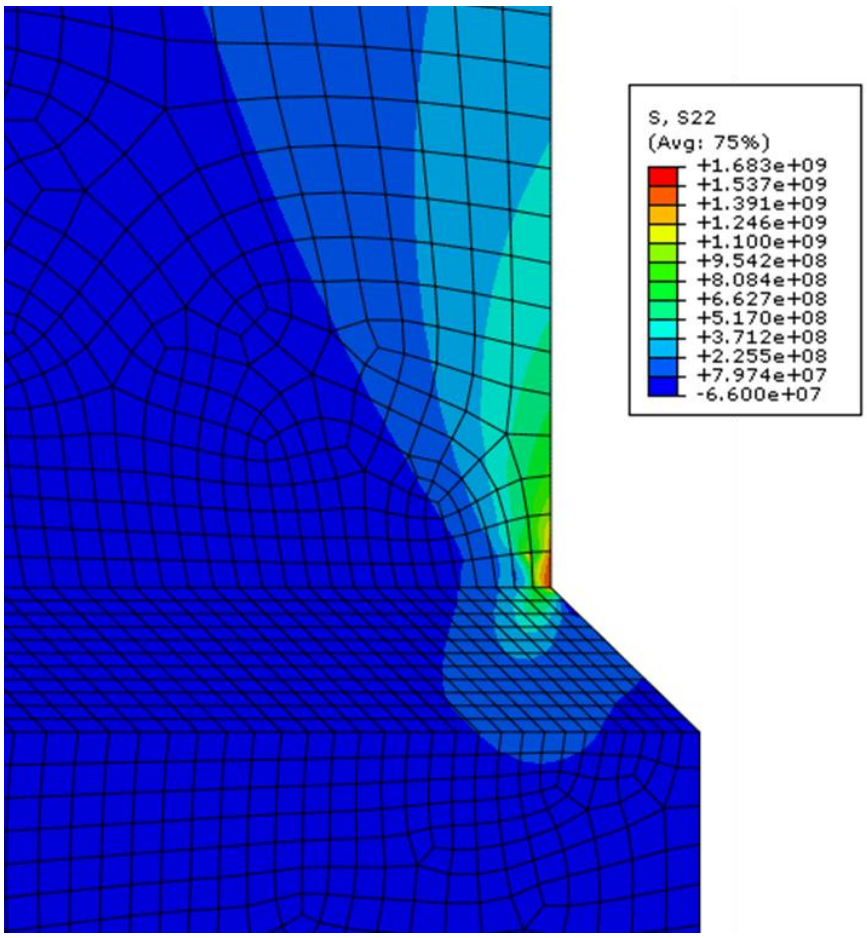

Figure 5-16 - High axial tensile stresses at W-AuCu interface

Similarly to the axial stresses presented previously, it can be observed that plastic deformation is localised to the interface in tungsten as shown in Figure 5-17. Plastic strain is limited to within 10μm of the interface in tungsten, i.e. within one element, and within the influence of the theoretical singularity. The copper material experiences plastic deformation over a much larger length scale due. This is to be expected due to the lower elastic and plastic mechanical properties of copper in relation to tungsten. With a yield stress of >1GPa, the tungsten material experiences plastic deformation only in the very close vicinity of the singularity location.

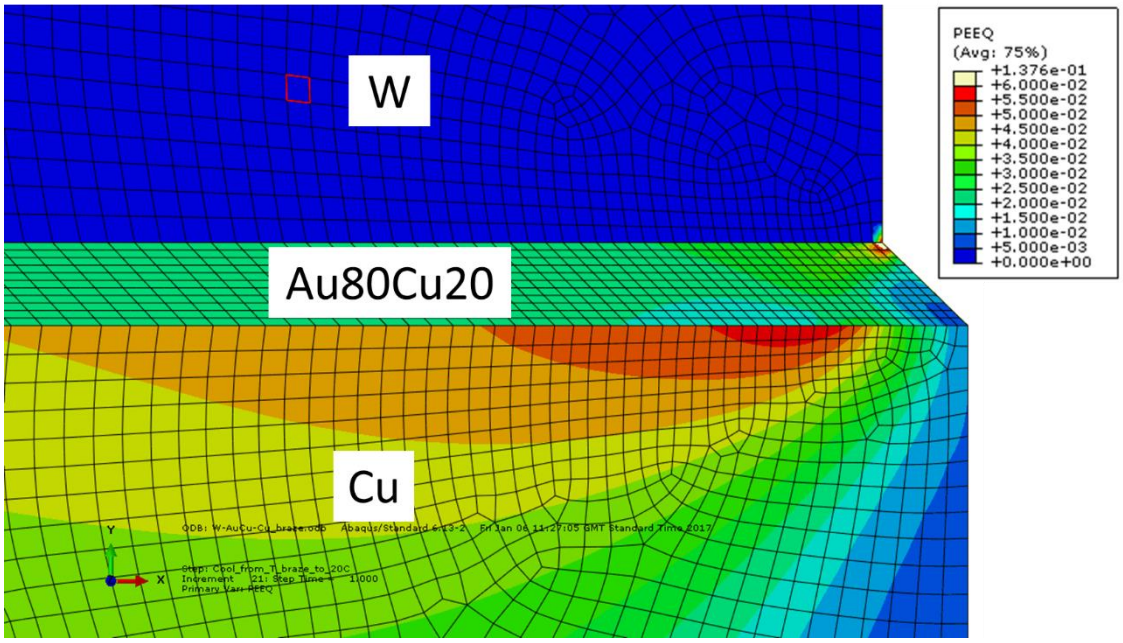

Figure 5-17 – Equivalent plastic strain distribution at W-AuCu-Cu interface following brazing simulation

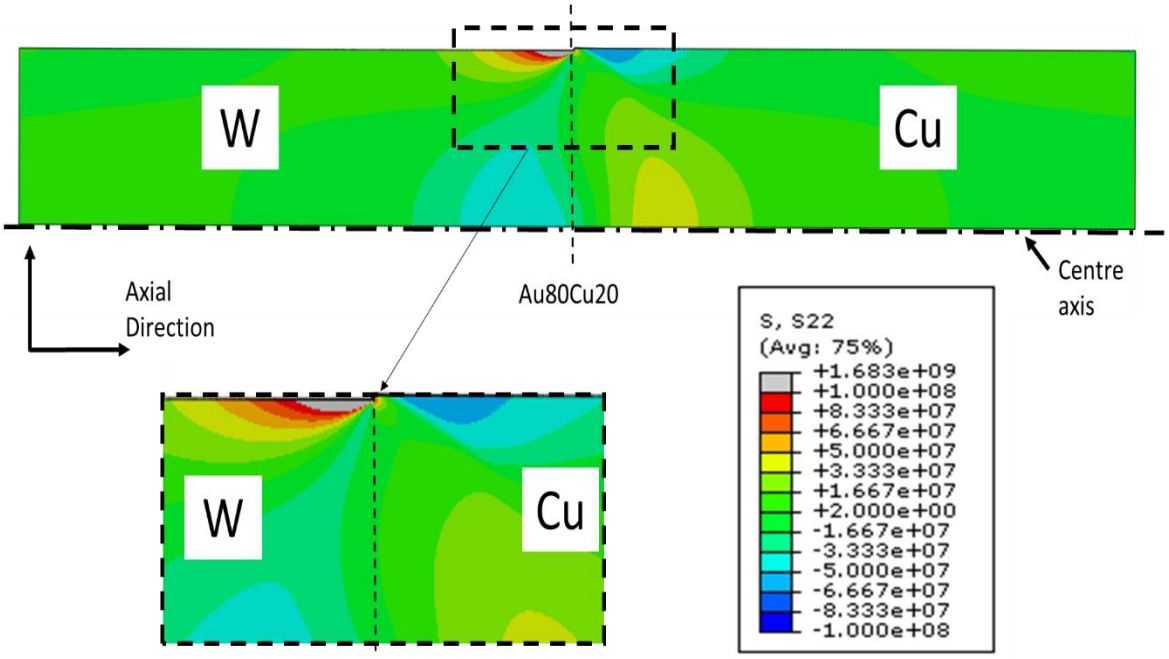

Figure 5-18 – FEA Axial stress distribution of bulk material in W-AuCu-Cu brazed part

The FE simulated axial stress distribution across the brazed W-AuCu-Cu axisymmetric joint is presented in Figure 5-18. The upper limit has been set to 100MPa in order to more easily visualise the distribution across the entirety of the part which exhibits stresses much lower than peak tungsten free edge stress. In the 5mm region of the interface in tungsten there is a relatively large compressive stress along the centre axis, with peak values of c. 70MPa. On the opposite side of the interface in copper the stresses are tensile in nature and less in magnitude, c. 40MPa.

5.5.3.1 Effect of brazing alloy properties on residual stress

The effect of brazing layer material properties was evaluated in Section 5.4. This analysis has been expanded here to assess the impact of property variation on a "real" brazed joint, using temperature dependent properties and plastic behaviour.

As was shown in Chapter 4, there was significant difference in experimentally determined elastic modulus between ETMT and DMA methods. The effect this variance has on residual stresses predicted by FE method have been explored here. The difference in E is presented in Figure 5-19. The values as calculated by ETMT are depicted in blue, and DMA values (with extrapolation/correction factor applied as detailed in section 4.6) in red.

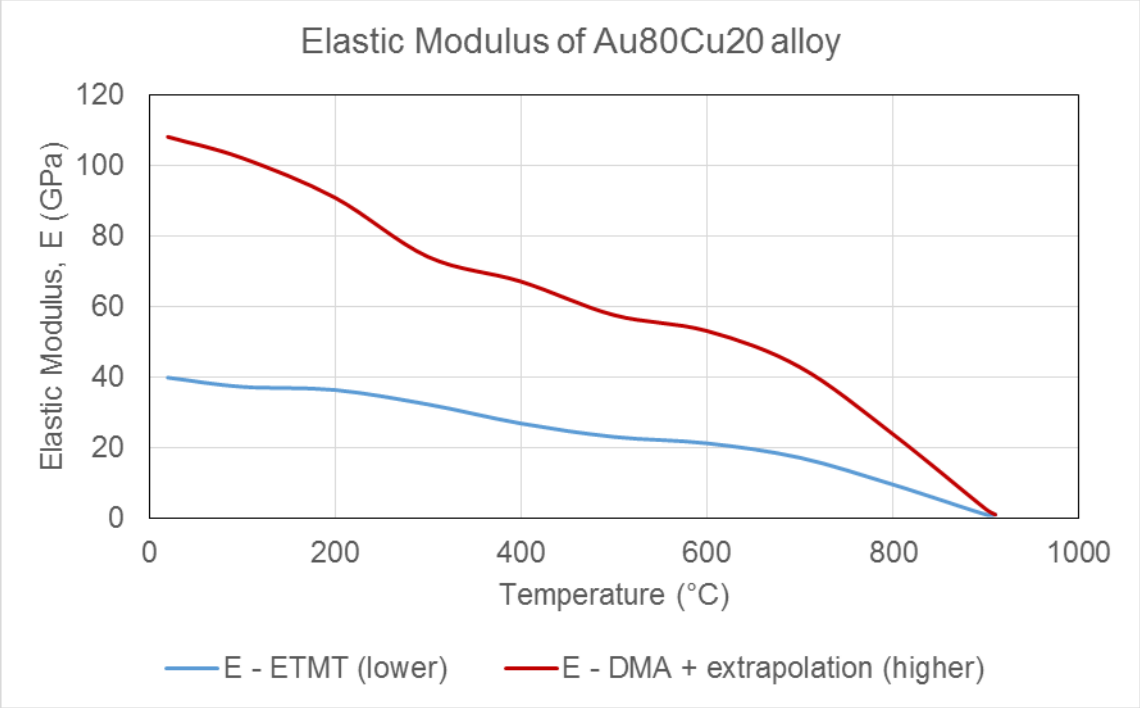

Figure 5-19 - Variance of E in AU80Cu20 brazing alloy

The brazing simulation was performed using each of the sets of E values and the results presented in Figure 5-20. It was found that variation in E did not significantly affect the stress profile at a short distance from the interface. The maximum difference in stress at any given point was found to be less than 30MPa. It would therefore be deemed a reasonable approach to use the data set generated by ETMT testing for the remainder of this chapter, however considering a minimum uncertainty at any given point of +/- 30MPa. ETMT data is used as a full temperature dependent set of data exists without excessive need for extrapolation or estimation of values. However should further testing be performed in future research to better define the material properties of Au80Cu20, the less uncertain, more accurate property values should be implemented into the FE model.

The insignificant difference in magnitude of stress with E variation is in agreement with [219]. It was shown that although variation in E can affect the strength of the singularity, as measured by curve fitting a power law to the stress profile, the magnitude of stress remote from the singularity was largely unchanged.

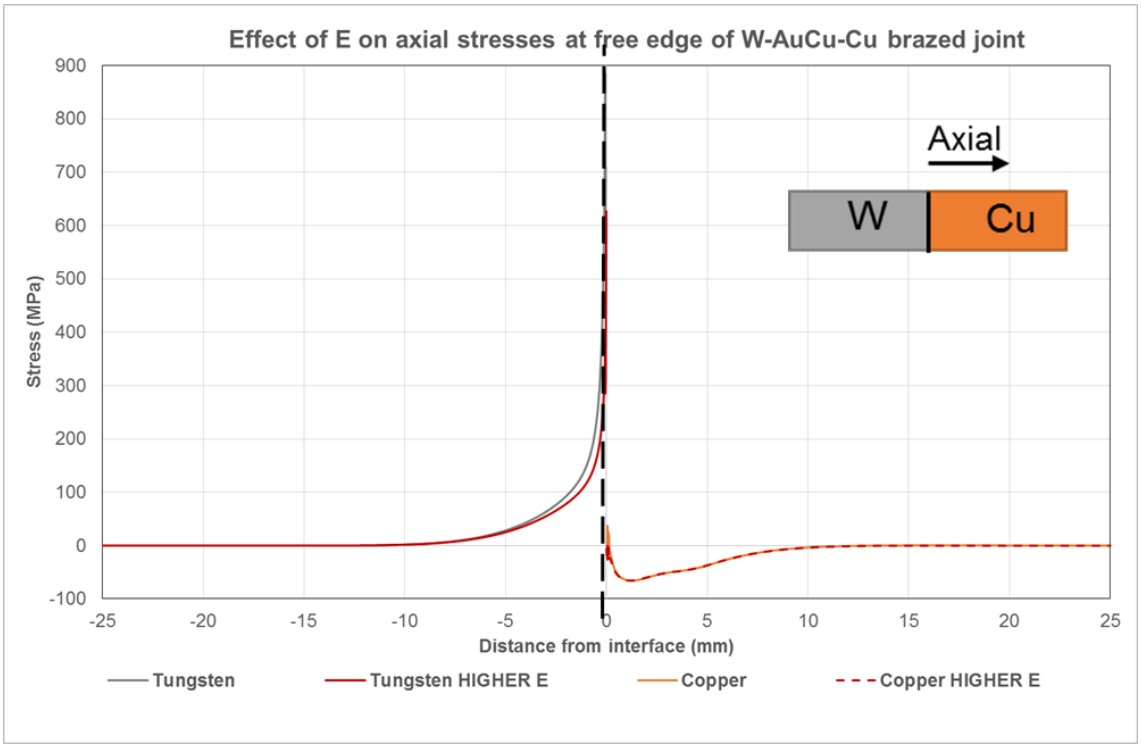

Figure 5-20 - Effect of E on axial stresses at free edge of W-AuCu-Cu brazed joint

The effect of plastic mechanical properties has also been considered for the W-AuCu-Cu brazed part. For this analysis three cases have been considered. Firstly is the control case, using the same material model and hence identical stress profile as presented in Figure 5-15. Secondly, the tangent modulus was reduced to essentially zero to model elastic perfectly plastic behaviour. The elastic properties were kept identical to the previous case. The final case considered a situation where the brazing alloy exhibited elastic perfectly plastic behaviour, and has E=1GPa. This represents a soft "compliance" type interlayer which accommodates thermal contraction. The results of the simulation are presented in Figure 5-21.

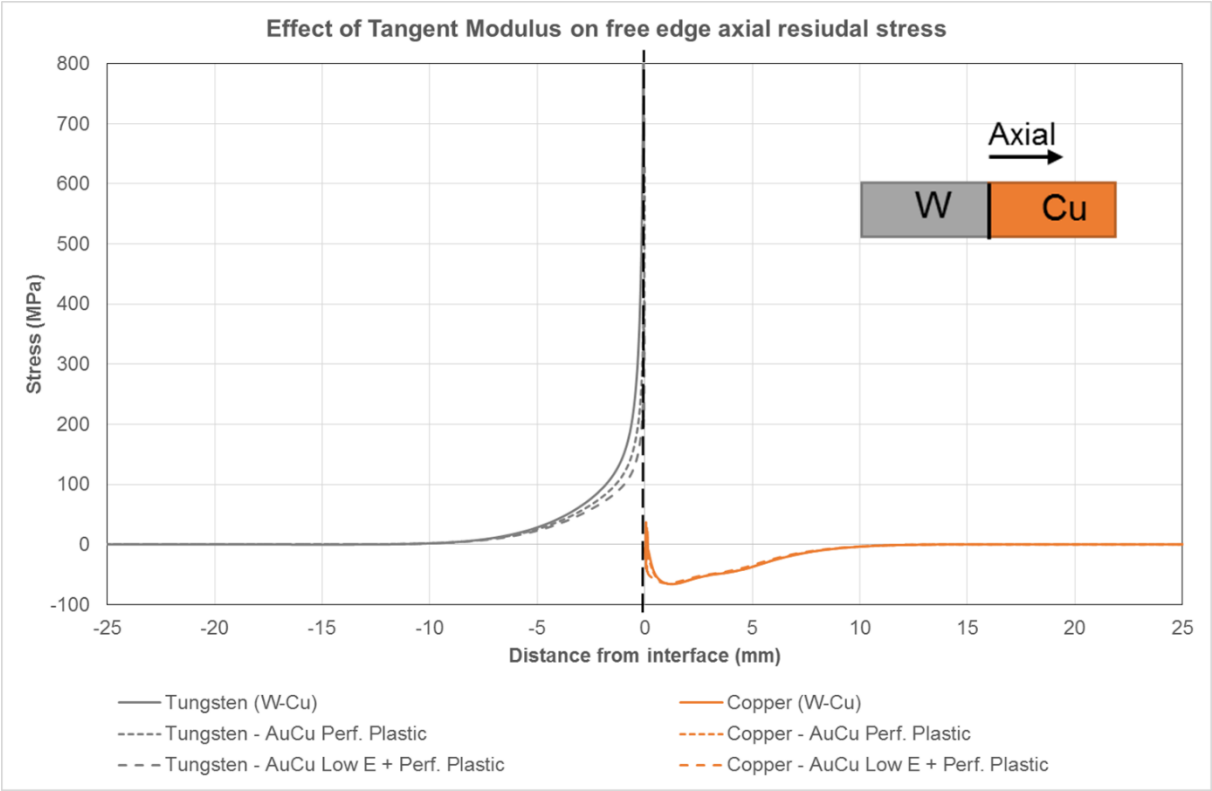

Figure 5-21 - Effect of elastic-perfectly plastic brazing alloy

The lowest stresses remote from the interlayer were found in the elastic-perfectly plastic brazing alloy material model simulations. This should be expected as the brazing layer is providing less constraint on contraction, therefore lower magnitude of stresses. A low value of E further reduces the stress magnitude.

The effect of elastic-perfectly plastic brazing alloy reducing tensile stresses in the high E, low α material is on good agreement with a similar study which considered only two-material configuration [118].

5.5.4 Tungsten – 316L brazed joint

The axial and hoop residual stresses generated during cooling from brazing for a W-AuCu-316L part are presented in Figure 5-22.

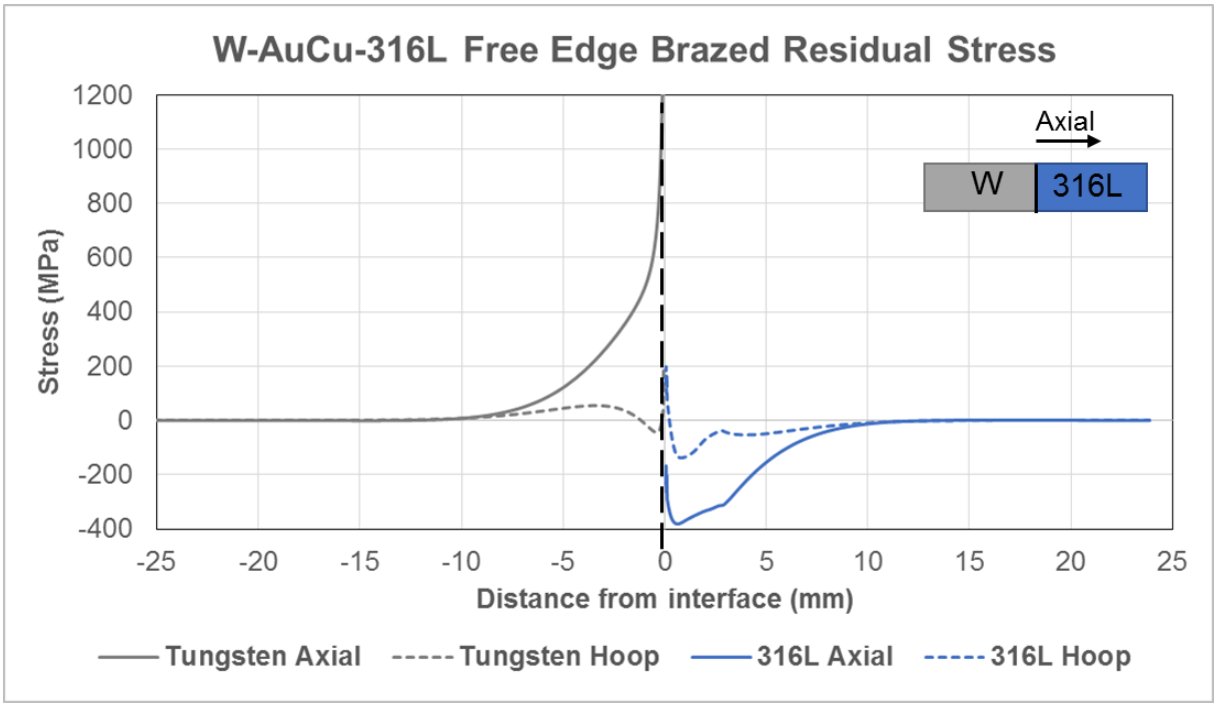

Figure 5-22 - Free edge brazing residual stresses for W-AuCu-316L configuration

The nature of residual stresses presented for W-AuCu-316L combination (Figure 5-22) is comparable to that of the W-AuCu-Cu combination (Figure 5-15).

There are high magnitude, tensile stresses in the proximity to the interface in the tungsten. The 316L material shows compressive stresses for both axial and hoop components of stress in the proximity of the braze interface. The magnitude of free edge axial stresses in 316L are less than those in tungsten.

As described previously, these trends in stress are expected due to the relationship between E and CTE for the two materials. Tungsten has a much higher E than 316L, 400GPa compared to 200GPa at room temperature, and a much lower CTE of approximately $4E^{-6}$/K compared to 16 E^{-6}/K. As shown in [206, 222], the tungsten (analogous to ceramic like material) should exhibit high tensile stresses as was the case in the simulation presented here.

The magnitude of axial stresses are considerably higher for W-AuCu-316L as compared with W-AuCu-Cu. At a distance of 3mm from the braze in tungsten, the stresses in the 316L component have 400MPa tensile compared with 100MPa tensile in the Cu component.

This is explained by considering the material properties of copper and 316L respectively. The CTE of both materials is comparable, approximately 16 E^{-6}/K. However the 316L is a much stiffer material, with higher E, yield stress and plastic tangent modulus. The results of this is a larger degree of constraint acting on the contraction of the brazed interface. This results in larger stresses in both parent materials.

The length scale of the influence from constraint of free thermal contraction is significantly increased. There are tensile axial stresses at a distance of 6mm from the braze interface. This is twice as long a distance as shown in the W-AuCu-Cu brazed part, where stresses dropped below 100MPa tensile after only 3mm.

The axial stress distribution across the entire brazed part is shown in the contour plot in Figure 5-23.

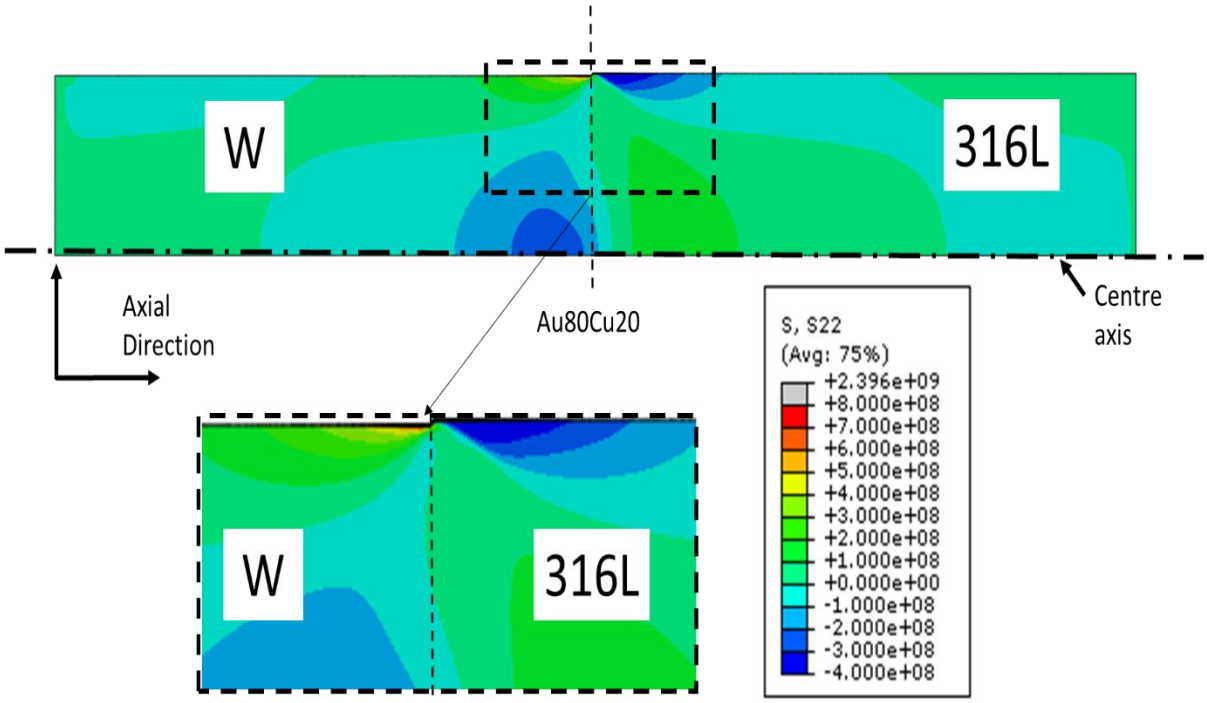

Figure 5-23 - FEA Axial stress distribution of bulk material in W-AuCu-316L brazed part

The axial stresses are significantly higher in magnitude in the bulk of the material for the 316L part (Figure 5-23) as compared with the copper brazed part (Figure 5-18). The axial stress in the

centre of the tungsten (radius=0mm) in the vicinity of the braze interface is compressive in nature with a magnitude of 400MPa.

This increased compressive stress would benefit fatigue performance should sub-surface crack initiation at the interface be an issue. However, it is known that the critical region for joint fatigue failure [158] is at the free edge. Therefore with all other factors being equal, such as misalignment and presence of crack and flaws, a reduced fatigue performance of the W-AuCu interface would be expected for the W-AuCu-316L configuration as opposed to W-AuCu-Cu.

5.5.5 316L – Copper brazed joint

The final material configuration considered is that of 316L-AuCu-Cu. The FE model is identical as to that reported in Sections 5.5.3 and 5.5.4, with the exception of the model geometry changed to reflect the initial dimensions of 316L and copper. The stress results at the free edge are presented in Figure 5-24.

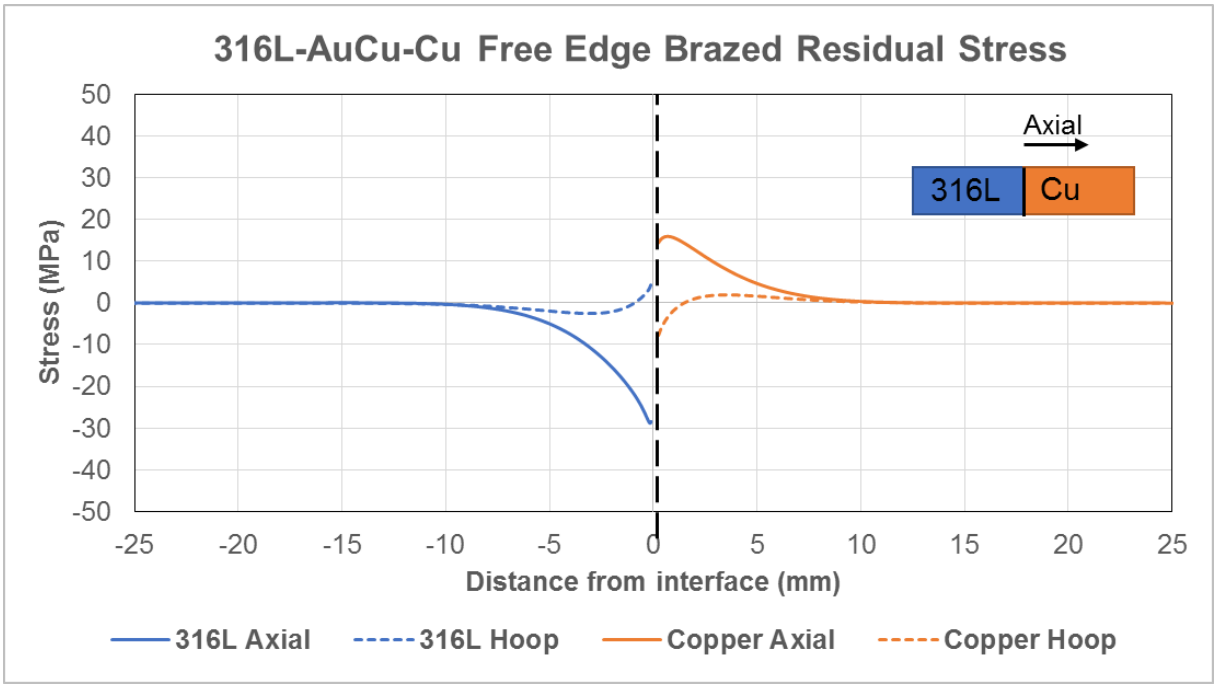

Figure 5-24 - Free edge brazing residual stresses for 316L-AuCu-Cu configuration

The stress results obtained numerically for 316L-AuCu-Cu brazed part vary significantly than the two material combinations previously discussed. It is strongly apparent that the degree of dissimilarity between 316L and copper is much lower as when compared with tungsten. The magnitude of stresses are less than 30MPa for both axial and hoop components.

By considering the relationship between E and CTE for the two materials the singular stress state at the interface during cooling can be determined from Figure 5-5. As $E_{316L} > E_{copper}$, the upper and lower left hand side quadrants are those that are relevant for determining the sign of the stress in 316L. However, the CTEs of both materials are similar throughout the temperature range, i.e $\alpha_{316L} \approx \alpha_{copper}$. Therefore the resulting sign of interface stress cannot be stated with certainty.

In Sections 5.3 and 5.4 it was shown that in addition to the sign of the stress, the magnitude of stress was predominately dependent on the severity of difference in CTE between the two parent materials. It is such unsurprising that the magnitudes determined for the 316L-AuCu-Cu part upon cooling from brazing are low and can be considered less significant when compared with tungsten dissimilar material parts. In accordance with the observation in Munz work [206], stating that the highest stress occurs in the material with highest E (due to the need for larger stresses to maintain compatibility), the 316L with higher E value does indeed experience the largest stress even when the absolute value of stress is low.

5.5.6 Summary of Au80Cu20 brazing induced residual stress

The residual stresses generated due to constraint on thermal contraction during cooling from brazing temperature have been presented for the three material combinations considered in this thesis, namely tungsten-copper, tungsten-316L and 316L-copper, all bonded using brazing with Au80Cu20 alloy.

The free edge axial component of stress for the three configurations is presented in Figure 5-25. The W-AuCu-Cu configuration exhibits the highest peak singularity stresses in both parent materials, the highest stresses a short distance from the braze layer of all combinations and has the most significant impact on stresses a larger distance from the interface, i.e. >3mm, as compared with the other combinations.

By considering the very large variations in stress with varying parent material properties, it can be concluded that the matching of parent materials is significantly more critical than selection of brazing alloy properties. This conclusion is further validated when considering the minimal impact variation of Au80Cu20 properties had on the stress distribution presented in Section 5.5.3.1, provided the properties remain applicable to a real material and not extremely soft, fully plastic behaviour with low yield stress.

It was found that the nature of stresses predicted by FEA for materials with severe dissimilarities in E and CTE were in good agreement with theoretically predicted stresses using You's rule illustrated in Figure 5-5 [222].

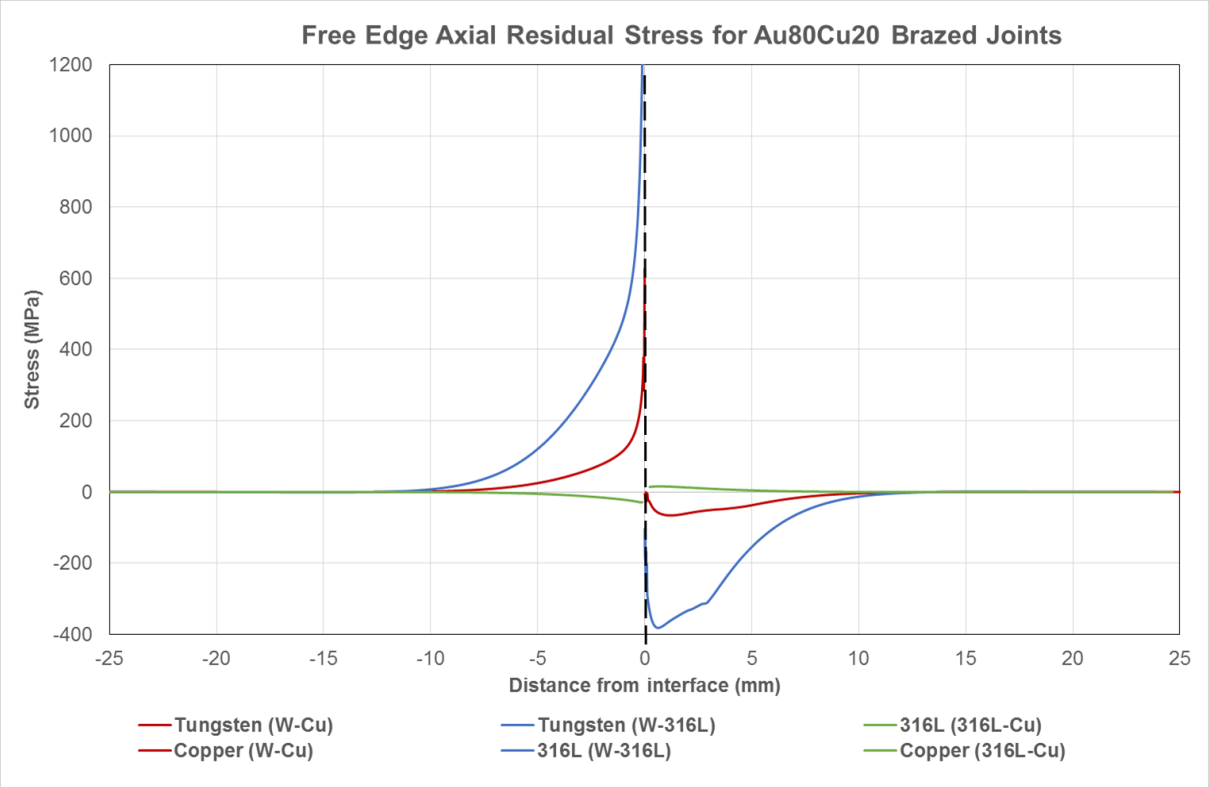

Figure 5-25 - Free edge axial residual stresses for Au80Cu20 brazed joints

The results presented in this thesis for Au80Cu20 brazed joints are in good agreement with previous work by the author [231]. This study approximated the tungsten, copper and 316L three material brazed joints using a different brazing alloy, eutectic AgCu, due to the lack of material data for Au80Cu20. The referenced study used a similar model developed in ANSYS, assuming axisymmetric conditions and identical parent material properties and geometries. The results are highly comparable for W-AuCu-Cu and W-AuCu-316L. The results are not presented here for brevity. This provides an independent check of implementation of material properties and brazing parameters with an alternative FE code with alternative methods for defining contact between materials, plastic behaviour and element types. This further suggests that for a component of similar dimensions and ratio of total thickness to braze layer thickness as presented here, the dominant factor is parent material dissimilarity.

In the following chapter the experimental measurement of residual stresses are presented, corresponding to the material combinations presented in this Chapter.

There are a number of assumptions required to model the braze simulation which depart from realistic conditions. Firstly, each three-material braze configuration is modelled as three distinct parts of homogeneous material property distribution throughout each respective part. However as was shown in Chapters 3 and 4, the assumption of homogenous chemistry and properties throughout the part is not an accurate one. Due to interdiffusion of materials at the braze layer there is a gradual change of properties and not a sudden transition as modelled here.

Similarly, the mechanical properties in the region of the braze layer shall vary as a function of chemical composition in the diffusion region, which the model presented here does not capture. A further assumption is that of perfectly aligned parent materials during the brazing process. In practice this is unlikely to be the case. It has been shown that although small degrees of angular misalignment have little effect on the interfacial stress state, axial misalignment can have a significant effect [91]. Also there is no accounting for meniscus, braze material pooling, or pre-existing brazing induced flaws considered here.

5.6 Summary

In this chapter the residual stress state in a dissimilar material joint has been evaluated both theoretically and quantitatively through the use of FEA. Idealized material models and real material data for fusion relevant tungsten, OFHC copper, 316L stainless steel and Au80Cu20 brazing alloy have been used to determine the resulting stress state in simplified and realistic dissimilar material joints.

Residual stresses are formed during dissimilar material joining primarily due to the constraint on free contraction due to differential thermal expansivity of the dissimilar materials. The singular stress state at a dissimilar material joint is well understood and much reported. This knowledge has been analysed and applied to the types of material combinations typical in a fusion environment, namely a low thermally expanding, stiff material and a less stiff (soft), highly expansive structural material. For dissimilar joints of this nature high tensile stresses are expected in the stiff material. Lower compressive stresses are expected in the softer material, albeit influenced by a positive stress singularity in the immediate vicinity of the interface.

The nature and magnitude of the free edge stress state following brazing at elevated temperature has been shown to be highly dependent on a small number of material properties. The Elastic Modulus and CTE of the base materials were shown to be the most significant factors when considering simple bi-material butt joints and more complex three material configurations including a braze material interlayer. The larger the degree of dissimilarity between the parent materials elastic moduli and CTE will result in a higher magnitude of stress in the region influenced by the theoretical (material dissimilarity) singularity. The stress concentration due to dissimilar material joining is limited to approximately 5mm distance from the interface for a 25mm long parent material. The singularity influenced stress region is limited to much closer to the interface.

The use of singular stress as a means to assess the degree of discontinuity at the interface is a useful approach [209]. In practice however the singularity does not truly exist due to material plasticity. Further to this, elemental diffusion results in the transition from one material to the next not being immediate as is assumed in the FE model.

The brazing temperature, or more specifically the brazing alloy liquidus temperature, also has a significant influence on the resulting stress state. The higher the brazing temperature, the higher the difference in thermal contraction shall be and therefore larger stresses are present in the

vicinity of the interface. The material properties of the brazing alloy were found to be less critical than those of the parent materials for the material combinations considered here.

The residual stress states following brazing of tungsten-copper, tungsten-316L and 316L-copper joints with Au80Cu20 alloy have been presented. Of primary focus is the free edge, axial (perpendicular to interface) stresses. Also considered are stresses within the bulk of material. Hoop stresses have been evaluated for the purpose of comparison with experimental measurements of stress presented in the following section. The highest stresses were found in the tungsten-316L configuration. Although the dissimilarity in elastic modulus is higher for tungsten-copper, the much higher yield stress of 316L results in a greater degree of constraint on thermal contraction. The tungsten-copper brazed part also exhibited high stresses. The magnitude of stresses in the 316L-copper joint were significantly lower in comparison.

The free-edge residual stresses presented for in this thesis are for the case of a butt joint configuration without post-joining processing. As such, the theoretical singularities, and the free edge stress concentrations attributed to said singularities, will vary for geometries other than the case of a simple butt joint. Additionally, by performing a machining operation such as edge grinding, the material containing extremely high residual stresses could be removed. This will result in redistribution of residual stresses, and a singularity theoretically still exists due to material dissimilarity, however the high magnitude damaging residual stresses could be significantly reduced. It is therefore a strong recommendation that free edge grinding be considered for the manufacture of real components. As certain divertor concepts rely on near net shape manufacture [39, 49], the presence of free edge residual stresses may not be as readily addressed through such a technique.

6 Experimental measurement of residual stresses

6.1 Introduction

In this chapter the results of a series of experiments measuring residual stresses in the tungsten, 316L and copper brazed parts (specimen manufacture described in Chapter 3 of this thesis). The results are then compared with FE predictions of residual stresses resulting from the brazing process which were presented in the previous chapter.

Three techniques were identified as being potentially suitable for measuring stresses on the cylindrical brazed specimens. X-ray diffraction (XRD) and ESPI incremental hole drilling were used for measuring stresses at the surface and a short depth into the material. Both of these techniques provide biaxial stresses at point locations.

The Contour Method was used to measure unidirectional, out of plane residual stresses on an entire cross section of the brazed parts. This provides a large quantity of stress data as well as residual stress at locations that would be difficult to access using conventional measurement techniques.

Understanding the actual stress state in the part, both at the free edge near the braze layer and in the bulk of the material, are crucial for translating findings from this work into a real component with loading and fatigue considerations. This process involves validating the FE results presented previously against the actual, experimentally determined stress state.

6.2 Surface residual stresses – X-ray diffraction

6.2.1 X-ray diffraction methodology

Measuring residual stresses by X-ray diffraction is an established technique by which the elastic strain in a material is measured based on crystal lattice spacing. Residual stress within the gauge volume is then calculated using the material specific x-ray elastic constant. XRD residual stress measurements were performed in accordance with the guidance provided in the NPL Good Practice Guide [232].

The determination of elastic strain, and therefore indirectly stress, is based on the interaction of a monochromatic X-ray beam and the crystal lattice in a polycrystalline material [233]. An illustration of X-rays being diffracted by the crystal lattice is presented in Figure 6-1. In a strain free volume of material the spacing between atoms of a given crystallographic plane is known and intrinsic to the material. If the crystallographic plane spacing is of a particular value, constructive interference occurs. This is shown in Figure 6-1, for example incident X-ray "1" is diffracted as "1' ". This phenomenon occurs only when the conditions of Bragg's law (Equation 6-1) are fulfilled [233].

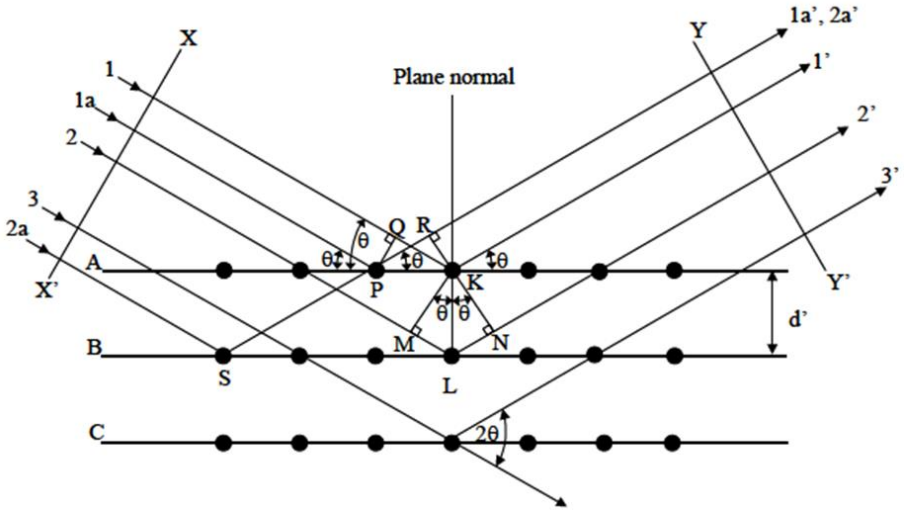

Figure 6-1 - Diffraction of X-rays by a crystal lattice [232]

$$n\lambda = 2d'sin\theta$$

Equation 6-1

Where d' is the inter-planar spacing (d-spacing), θ is the angle between incident beam and diffracted beam, λ is the X-ray wavelength and n is an integer. From Bragg's law, for constructive

interference to occur n must be a whole positive number. If a sufficient number of atoms (for instance due to a large number of grains with the correct orientation) diffract an incident X-ray then a clear diffraction peak is produced. The position of the diffraction peak is defined by θ.

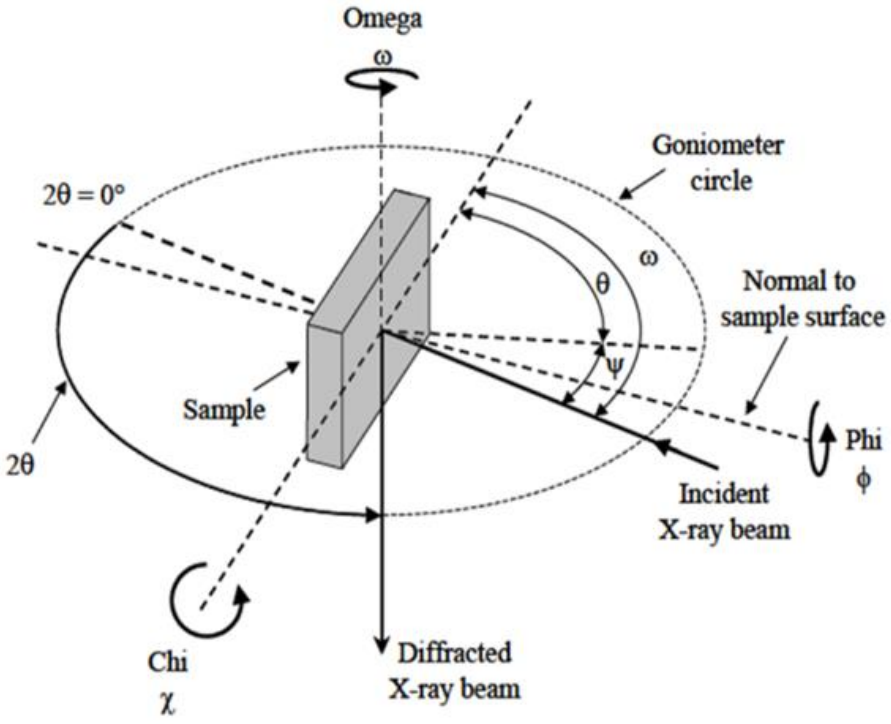

Figure 6-2 - Angles and rotations of an X-ray diffraction residual stress measurement [232]

When a strain is present in the crystal structure the lattice spacing is altered. For example the d-spacing increases under elastic tensile strain in planes perpendicular to the stress direction, and decrease for compressive strains [233].

The strain, ε, in the irradiated volume can be expressed as a function of the relationship between the unstrained lattice spacing, d_0, and the d-spacing of the strained material, d as shown in Equation 6-2.

$$\varepsilon = \frac{d - d_0}{d_0}$$

Equation 6-2

Which using Bragg's law results in:

$$\varepsilon = \frac{sin\theta_0}{sin\theta} - 1$$

Equation 6-3

The elastic strain can therefore be determined by the shift in diffraction peak from unstrained location (θ_0) to the strained position (θ).

The strains/stresses measured through this technique are macroscopic, Type I strains [103]. These are strains that are homogeneous over multiple grains. In a typical material there will also be type II and type III stresses also. Type II stresses refer to microscopic scale stresses (i.e. homogeneous across one or two grains) and Type II referring to sub-microscopic [233]. As the strain calculated by XRD is a result of interference across many grains, the micro-strains cannot be directly analysed by diffraction. The presence of these micro-strains can have an effect on the resulting diffraction peak, for instance by causing peak broadening [234].

From the measured elastic stress, the stress in a given direction can be determined from Hooke's law where:

$$\sigma = E \cdot \varepsilon$$

Equation 6-4

This relationship can be expanded to provide the solution for stress in any given direction as shown in Equation 6-5. The full derivation has been provided in literature [232].

$$\sigma_\varphi = \frac{E}{(1+\nu)sin^2\psi}\frac{d_\psi - d_n}{d_n}$$

Equation 6-5

Where σ_φ is the stress in a given phi direction, E is the elastic constant, ν is the Poisson's ratio, psi (ψ) and phi (φ) are rotation angles, d_ψ is the lattice spacing at a given psi rotation and d_n is the lattice spacing normal to the sample surface. The directions of phi and psi rotations in relation to the sample surface are defined in Figure 6-2.

The method of stress determination used in the work presented in this thesis is the $sin^2\psi$ method [64, 232, 233]. This is the most commonly employed method for determining stress using XRD. X-rays are fired at the surface a series of psi rotations as shown in Figure 6-2. The corresponding measured d-spacing is then plotted against $sin^2\psi$ for each psi rotation. For an elastic, non-textured irradiated volume the result is a linear relationship between d-spacing and $sin^2\psi$. Equation 6-5 can now be reduced to Equation 6-6, such that stress in a given phi direction is given by:

$$\sigma_{\varphi} = \frac{E}{(1+\nu)} m$$

Equation 6-6

Where m is the gradient of the d-spacing and $\sin^2\psi$ plot.

Only a certain number of planes are suitable for producing a diffraction phenomenon of sufficient intensity for strain measurement. For a suitable crystallographic plane, the wavelength is selected so as to give as high a 2-theta angle (i.e. the Bragg angle which is the angle between incident and diffracted beams) as possible. This is necessary as the shift in peak position $\Delta\theta$ is very small due to changes in d-spacing being small. As shown from the relationship in Equation 6-7, for larger 2-theta angles, a small Δd will result in a large enough change in 2-theta (although still only a fraction of a degree) to be measured experimentally. At low 2-theta angles the change is not significant enough to determine the peak shift.

$$\frac{\Delta d}{d} = -\Delta\theta cot\theta$$

Equation 6-7

The wavelength of the X-rays is determined by which radiation source is used. For residual stress measurement, the characteristic radiation $K\alpha$ is the preferred. $K\beta$ intensities are generally too low for residual stress determination.

Guidance is provided in literature on which radiation source, (hkl) plane and 2-theta angle is best suited for a given material [232, 235]. For example, stress measurements in tungsten are best evaluated on the (222) plane using Co K_α radiation source, with a wavelength of 1.7889 Å and 2-theta angle of 156.5°. A summary of the X-ray measurement parameters used for each material is presented in Table 6-1.

A 1mm diameter aperture was used to collimate the X-ray beam to give a good balance between:

- High spacial resolution required to analyse the stress profile in the proximity of the interface where the predicted stress gradient was shown to be severe
- Keeping the irradiated area smaller than 0.4 times the radius of curvature of the part in accordance with BS EN 15305:2008 [235] and within 0.25 times the radius of curvature in accordance with NPL guidance in order to achieve a residual stress measurement accuracy within 10% of the true value [232]
- Sampling a sufficient number of grains in order to achieve a strong diffraction peak and increase the accuracy of the measurement.

The total irradiated volume, or gauge volume, is a function of the X-ray spot size (0.785mm for a 1mm diameter aperture) and the depth of penetration. The depth that X-rays penetrate is dependent on the characteristics of the radiation source and the rate at which they are absorbed by the incidented material. The intensity of X-rays diffracted decreases exponentially with depth of material [232]. Therefore only very thin layer close to the surface has a significant impact on the measured residual stress. The effective penetration depth for the metals considered in this thesis is typically <20μm. As peak stresses are predicted to occur at the free edge, the measured stress will likely under-represent the peak value as part of the gauge volume contains lower stresses grains.

Table 6-1 - XRD parameters for residual stress measurement

Material	Radiation source	Wavelength, λ (Å)	{hkl}	Bragg angle (°)	S1 (1/MPa)	1/2 S2 (1/MPa)
W	Co Kα	1.79026	222	157	7.10E-07	3.20E-06
316L	Mn Kα	2.10314	311	152.8	1.20E-06	7.18E-06
Cu	Cu Kα	1.5418	420	145	2.29E-06	9.23E-06
	Mn Kα	2.10314	311	149.5	2.99E-06	1.17E-05

The elastic constants required for determining residual stress from XRD measured residual strains, termed X-ray elastic constants (XEC), S_1 and ½ S_2 are given by:

$$S_1 = \frac{-\nu}{E}$$

Equation 6-8

$$\frac{1}{2}S_2 = \frac{1+\nu}{E}$$

Equation 6-9

With E and ν being isotropic values for Young's modulus of elasticity and Poisson's ratio [236].

All XRD residual stress measurements reported in this thesis were performed at the Advanced Forming Research Centre, University of Strathclyde. XRD measurements were performed using a Proto LXRD Residual Stress Measurement System [237] shown in Figure 6-3.

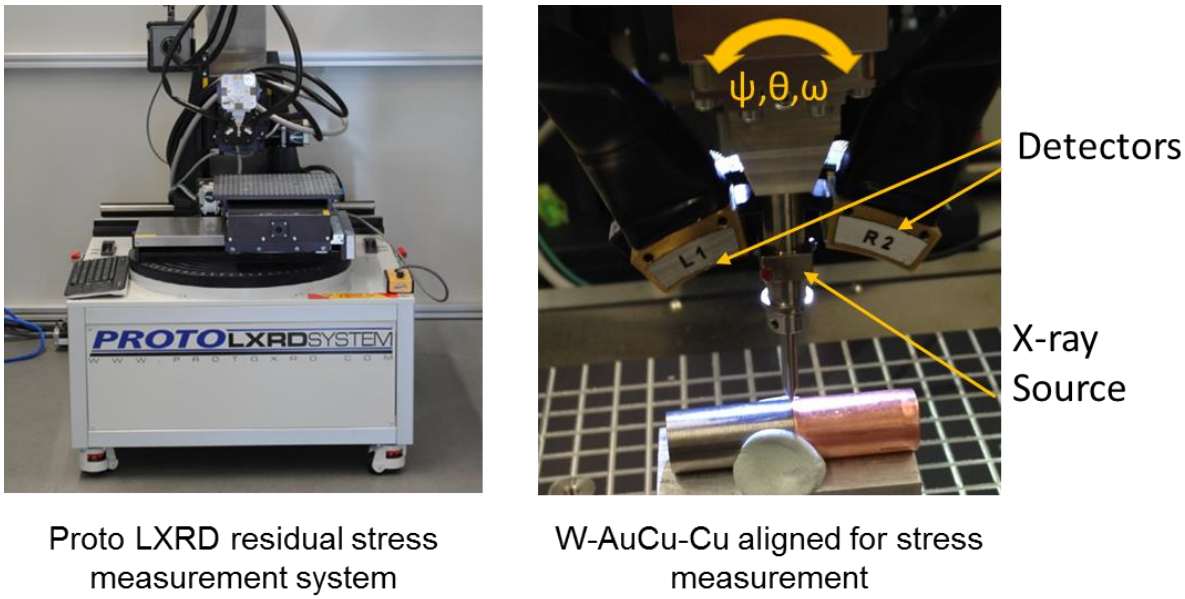

Figure 6-3- Proto LXRD System

Prior to each set of stress measurements being performed, the measurements were performed on calibrated stress standards provided by the manufacturer PROTO [237]. For each radiation anode (Mn, Co and Cu reported here) the calibration is checked against a highly stressed and nominally stress free sample. This assures accuracy of the residual stress measurements to be within +/- approximately 10MPa for any given material.

The effect of background noise, and in particular bremsstrahlung effects [238], are accounted for by careful selection of the gain voltage. To do this, a diffraction profile is collected on the surface of the target sample. A shim of a material that has no diffraction planes for the current Bragg angle is placed on top of the sample. For the materials reported here the shim was either β Ti or vanadium. A further profile is then collected, and the gain voltage set so that when the shim is removed and the sample irradiated, only the x-rays diffracted in the gauge volume are measured.

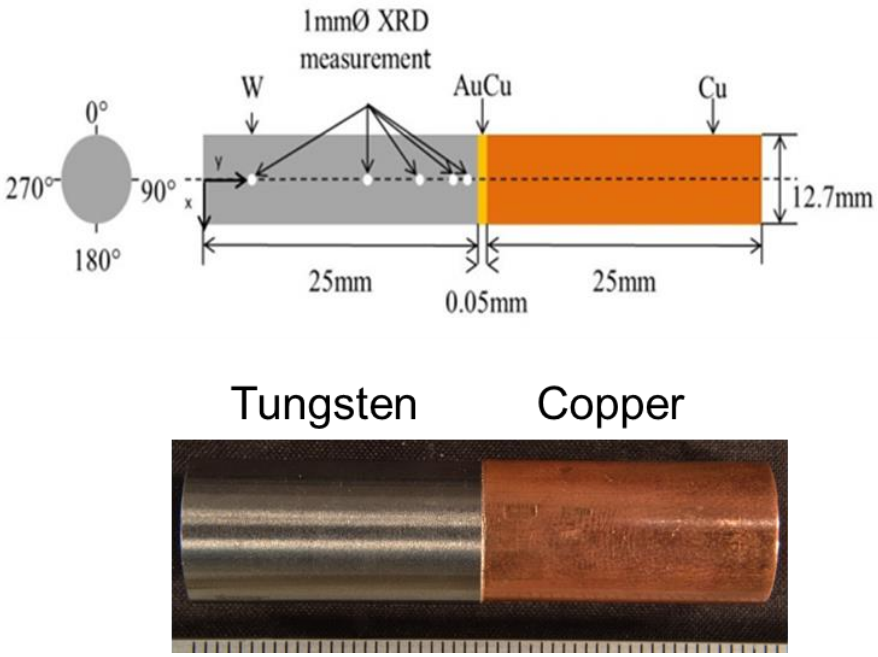

Figure 6-4 - Schematic of residual stress specimen for XRD measurement with circumferential and axial locations of measurement highlighted (above) and actual W-AuCu-Cu specimen for XRD measurements

A total of 10 samples were measured using XRD:

- W-AuCu-Cu – 6off numbered 1A-1G (sample 1E was retained for NDT trials)
- 316L-AuCu-Cu – 2off numbered 2A, 2D
- W-AuCu-316L – 2off numbered 3A, 3B

Each part was evaluated at up to 4 circumferential positions (0°, 90°, 180° and 270°) as shown in Figure 6-4. Due to limited access to experimental equipment it was not possible to evaluate all samples at all four positions. At least two circumferential positions were measured for each sample to observe any asymmetry in free edge stresses of the part.

The axial location of the measurements was weighted heavily towards the braze interface, where the local stress concentration due to constraint on free contraction upon cooling from brazing temperature is expected. Typically between 7 and 12 locations were measured per circumferential position per part. A typical distribution of measurements along the axial axis containing 10 points would be:

- 0mm (directly at the interface)
- 0.25mm (from the interface)
- 0.5mm
- 0.75mm

- 1mm
- 2mm
- 4mm
- 8mm
- 12mm
- 20mm (5mm from the edge of the 25mm long part)

The distance between axial positions close to the braze (ranging from 0.1-0.5mm depending on the part) is smaller than the spot size of the X-ray beam. This results in a degree of overlap in the results. This is unavoidable when characterising the stress profile that has a severe gradient in stress over a short distance (Δ1000Mpa over Δ1-2mm was measured in some instances). This means that for a 1mm spot size, there is a significant gradient over the irradiated volume and an averaging of the results will occur. This is still useful in characterising the stress profile, as the averaging effect will be relatively constant for a given axial position across different parts. It should be noted however that peak stresses in excess of those measured here are likely present close to the interface. With the use of a smaller aperture, for instance 0.1mm or 0.05mm it may be possible to better resolve the stress state close to the interface. This is recommended for future research as the apertures required were not currently available to the author at the time of the experiments.

Measurements were performed at two phi rotations per location. The axial stresses perpendicular to the braze interface were evaluated at the phi=0° rotation which is depicted in Figure 6-3. The stage was then rotated to phi=90° to obtain the hoop component of stress.
The total number of measurements for a part with both materials evaluated, three circumferential positions and ten axial positions per material results in a total of 120 measurements in total to characterise a single part. In practice this number varied, as it was not possible to measure both materials for many of the parts, and the number of axial and circumferential locations was not constant. Measurement of the braze layer is not possible due to the relative size of the braze layer with spot size, 0.1mm compared with 1mm. Additionally there is a lack of x-ray elastic constant data or information regarding reflection planes, Bragg angles etc. for the Au80Cu20 alloy. The number of 120 measurements however gives a good approximation of the resource associated with acquiring the data presented.

Measurement of the actual braze material was not possible with this technique. The braze layer thickness of approx. 100μm is significantly smaller than the smallest aperture available (0.5mm). In order to measure the braze layer directly it would be necessary to adopt a measurement

technique suitable for small length scales. An example of this is residual stress measurement by FIB micro machining/micro hole drilling [239] or ring-coring [240].

6.2.2 Uncertainty quantification for XRD

Measurement uncertainty from XRD measurements has been assessed considering a number of potential error sources:

- Experimental repeatability
- Stress calculation using elastic moduli and
- Statistical uncertainty from the sin2ψ fitting calculation

Experimental repeatability was calculated in accordance with NPL Good Practice Guide. No 52 [232]. Measurements of an example location were repeated 10 times, removing and replacing each time to determine instrument-operator repeatability. These measurements are performed either on a material suitable for each X-ray source considered here (Co, Mn, Cu).

XRD derived residual stresses are calculated from measured strains using an elastic constant. As such an error associated with uncertainty of the elastic constant will vary linearly with stress magnitude. In accordance with NPL guidance [232], an uncertainty of +/- 5% of X-ray elastic constant is considered for uncertainty quantification.

The final error source considered, the uncertainty due to errors in $\sin^2\psi$ fit, are calculated directly by the PROTO software. This is dependent on the average deviation from the best fit line of d-spacing for each ψ angle in the $\sin^2\psi$ – d-spacing plot.
The root sum square method is used to calculate the combined uncertainty as show in Equation 6-10.

$$u_c(\sigma) = \sqrt{\sum_{i=1}^{m} [c_i u(x_i)]^2}$$

Equation 6-10

With:

u_c = combined standard uncertainty

σ = residual stress

c_i = sensitivity coefficient

$u(x_i)$ = standard uncertainty

The standard uncertainty for each contributing source of uncertainty is given by Equation 6-11.

$$u(\sigma) = \frac{Uncertainty\ value\ \cdot\ c_i}{d_v}$$

Equation 6-11

Where d_v is the divisor used for standard uncertainty based on probability distribution and defined in NPL Good Practice Guide. No 52.

An example of the uncertainty budget calculation is shown in Table 6-2 (from NPL Good Practice Guide. No 52).

Table 6-2 - Uncertainty budget worksheet for calculating uncertainty in residual stress by XRD measurement [232]

Source of uncertainty	Value	Probability Distribution	Divisor d_v	c_i	u_σ MPa ±
Repeatability of measurement (1)	±8.6 MPa	Normal	1	$\frac{s}{\sqrt{n}}$	2.7
Modulus of elasticity (2)	±5%	Rectangular	√3	σ	15.6
$Sin^2\psi$ fit (3)	±27 MPa	Rectangular	√3	1	15.6
Combined standard uncertainty (4)		Normal			22.2
Expanded uncertainty (5)		Normal (k=2)			44.4

The combined uncertainty is calculated from Equation 6-10. In this case $u_c=\sqrt{[(2.7)^2+ (15.6)^2+ (15.6)^2]}$ resulting in uncertainty of +/- 22.2MPa.

The expanded uncertainty (U) is calculated using a coverage factor (k) as shown in Equation 6-12.

$$U = k \cdot u_c$$

Equation 6-12

A coverage factor of 1, i.e. 1 standard deviation, is used for the following results.

6.2.3 W-AuCu-Cu XRD results

The residual stress results as measured by XRD in brazed W-AuCu-Cu parts are presented in this section.

Valid results were obtainable only for the tungsten material. All attempts at measurements of the copper parts resulted in unusable results. The errors associated with curve fitting of the d-spacing/$\sin^2\psi$ plot were too great to be considered valid. There are several reasons why this occurred.

Grain sizes in the gauge volume of a material in excess of 100μm result in fewer grains contributing to the diffraction peak resulting in the quantification of peak shift due to elastic strain less accurate [232]. It was shown in Chapter 3 of this thesis that the resulting grain size of copper following brazing at 910°C was significantly larger than 100μm for large areas of the evaluated copper. The brazing temperature of 910°C is high enough that significant grain growth is expected in the copper [157, 241]. It is therefore not surprising that the grain size of copper could prohibit XRD measurements.

Measurements can be detrimentally effected due to texturing of the material during the brazing process [64]. The copper is expected to undergo significant plastic deformation in the locality of the interface as shown from the predicted stress and plastic strain distributions presented in Section 5.5. It is therefore possible that a preferential alignment of grains occurs in this region resulting in textured material. Additionally, plastic strain is a result of dislocations within the crystal lattice. The distortion of the lattice from dislocations is known to effect residual stress measurements by XRD [233]. Also, in regions with plastic deformation, the peaks from highly elastically strained grains are coincided with those from stress free grains causing deviation from Gaussian/Pearson distribution. This causes inaccuracies in measured results.

A typical axial stress profile along the free edge of the tungsten material in a brazed W-AuCu-Cu part is shown in Figure 6-5.

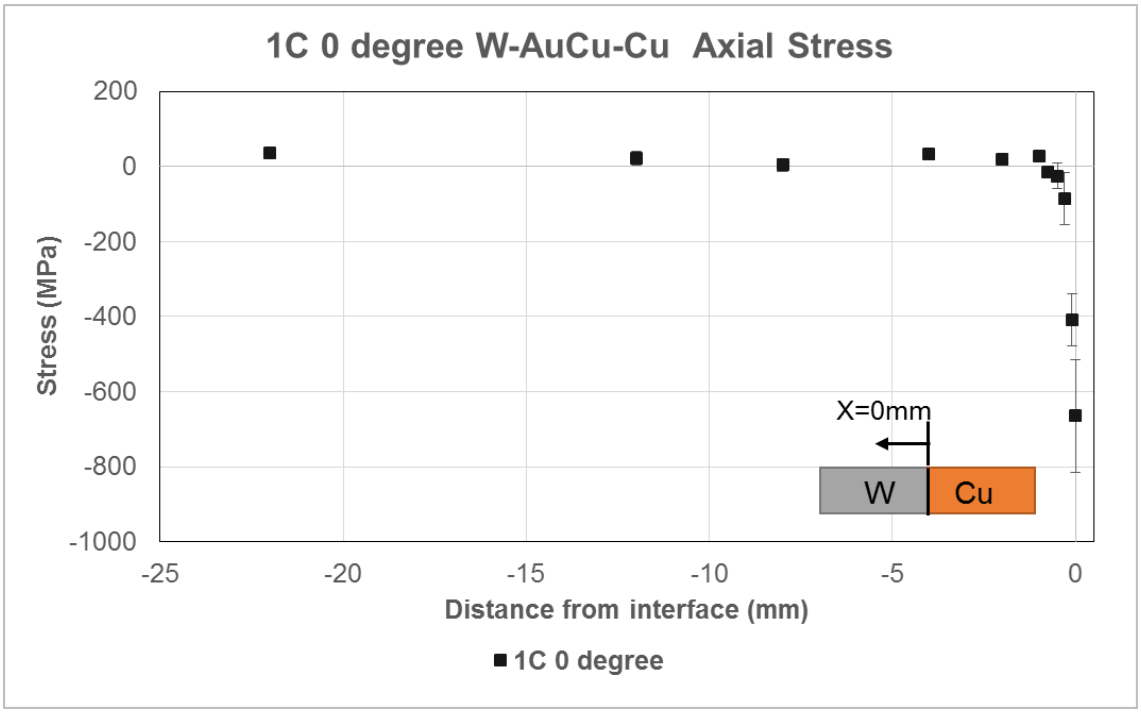

Figure 6-5 - Typical axial stress profile at free edge of tungsten in brazed W-AuCu-Cu part (part 1C circumferential position 0°)

The axial position is given as the distance from the braze interface. Errors are calculated based on the average misfit of each psi data point from the best fit line of the d-spacing/$\sin^2\psi$ plot. The uncertainty quantification is covered in section 6.2.2. In the region of the braze interface the errors are significantly higher than those of points remote from the braze layer, +/- 150MPa and +/- 15MPa respectively. This is due to interference from the Au80Cu20 and copper materials, in addition to the geometrical discontinuity at the interface. Here, due to a variation on part alignment, there are likely planes other than the (222) targeted plane that are contributing to the diffraction peak.

The magnitude and distribution with axial position of the errors are comparable for all parts measured. For the benefit of added clarity, error bars have been omitted for graphs containing multiple stress profiles provided the errors are consistent with reported errors for example in Figure 6-5.

From Figure 6-5 it is clear that a singular-like axial stress is present in the tungsten as predicted by the relationship of $E_{tungsten}/E_{copper/AuCu}$ and $CTE_{tungsten}/CTE_{copper/AuCu}$ (Chapter 5). However the theoretical stress singularity, and local stress concentration predicted by FEA, was tensile in nature. In the case of Figure 6-5 the tungsten exhibits a compressive singularity. Further analysis

of the results is presented at the end of this section and in section 6.2.5. Firstly the remainder of the W-AuCu-Cu XRD residual stress results are reported. The y-axis scale representing stress is kept consistent across stress plots in this section for easier comparison of results.

In Figure 6-6 the axial stress results, perpendicular to the interface, for all four circumferential positions (0°, 90°, 180°, 270°) of sample 1A are presented. It can be seen that the four line profiles are largely in agreement. There is a high magnitude compressive stress in the region of the interface that rapidly decreases to an essentially stress-free state after <2mm distance. A small compressive stress is measured for the 0° rotation at an axial position of 0.4mm from the interface. As this point is a clear outlier from the remainder of the plot it is likely that this results is an artefact of an experimental anomaly, for instance a surface scratch in the gauge volume. The results of this plot suggest that the stress profile of this sample is generally axisymmetric.

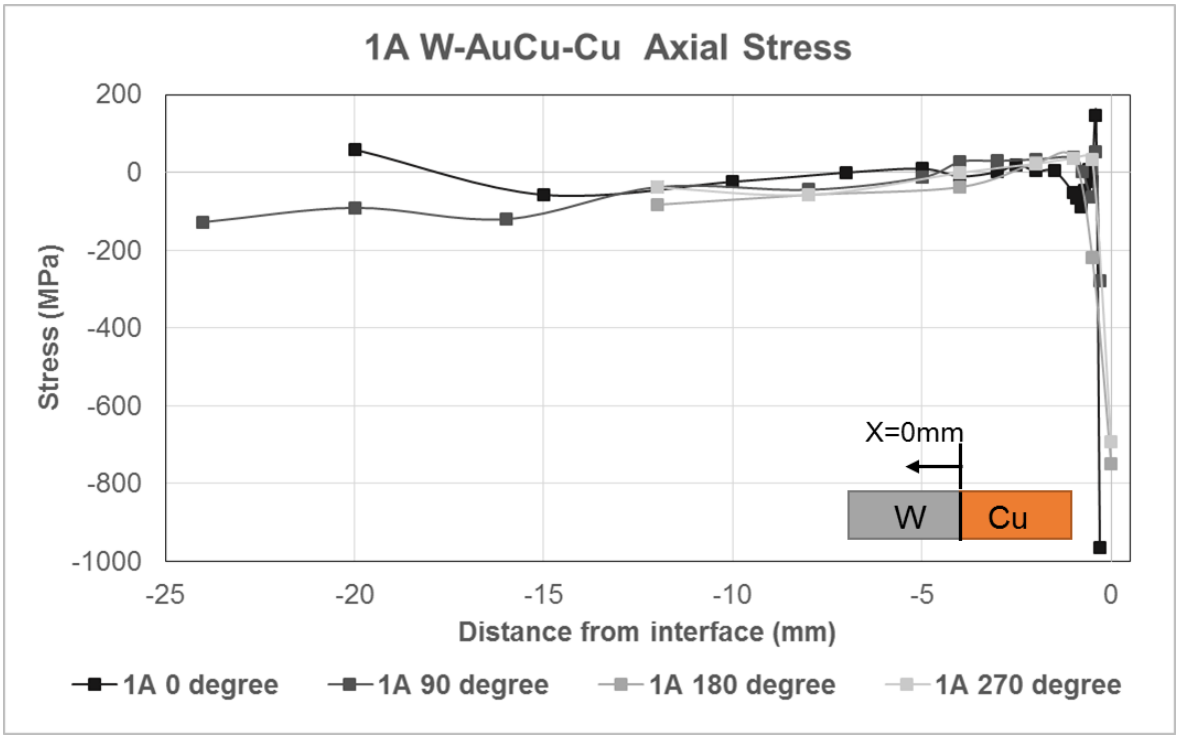

Figure 6-6 - XRD results 1A W-AuCu-Cu axial stress

The hoop component of stress for the same sample is presented in Figure 6-7. The magnitude and distribution of hoop stress is comparable to that of axial stress at the interfacial region. As with the axial stresses, the hoop stresses decrease severely over a short distance and are consistent for all circumferential positions considered.

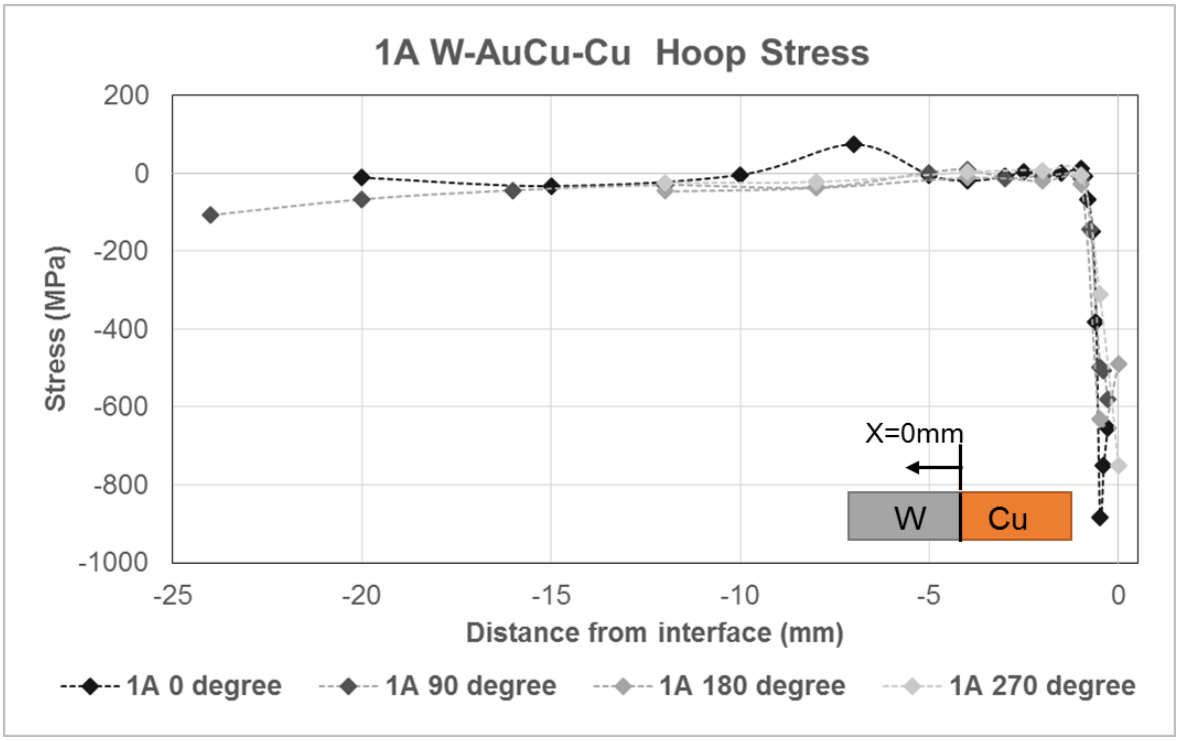

Figure 6-7 - XRD results 1A W-AuCu-Cu hoop stress

For the remaining five W-AuCu-Cu samples presented here, both axial and hoop stresses are plotted together. Axial stresses are represented by a solid line connecting data point, with hoop stresses represented by a dashed line. Both axial and hoop stress results for each circumferential rotation are assigned the same shade.

The results for the second sample of W-AuCu-Cu configuration, sample 1B, are presented in Figure 6-8. For this sample the measured hoop stresses were higher than the axial stresses. Upon examination of the sample it was discovered that axial misalignment of the base materials, tungsten and copper, was present. The effect of this has been presented previously by the author [231].

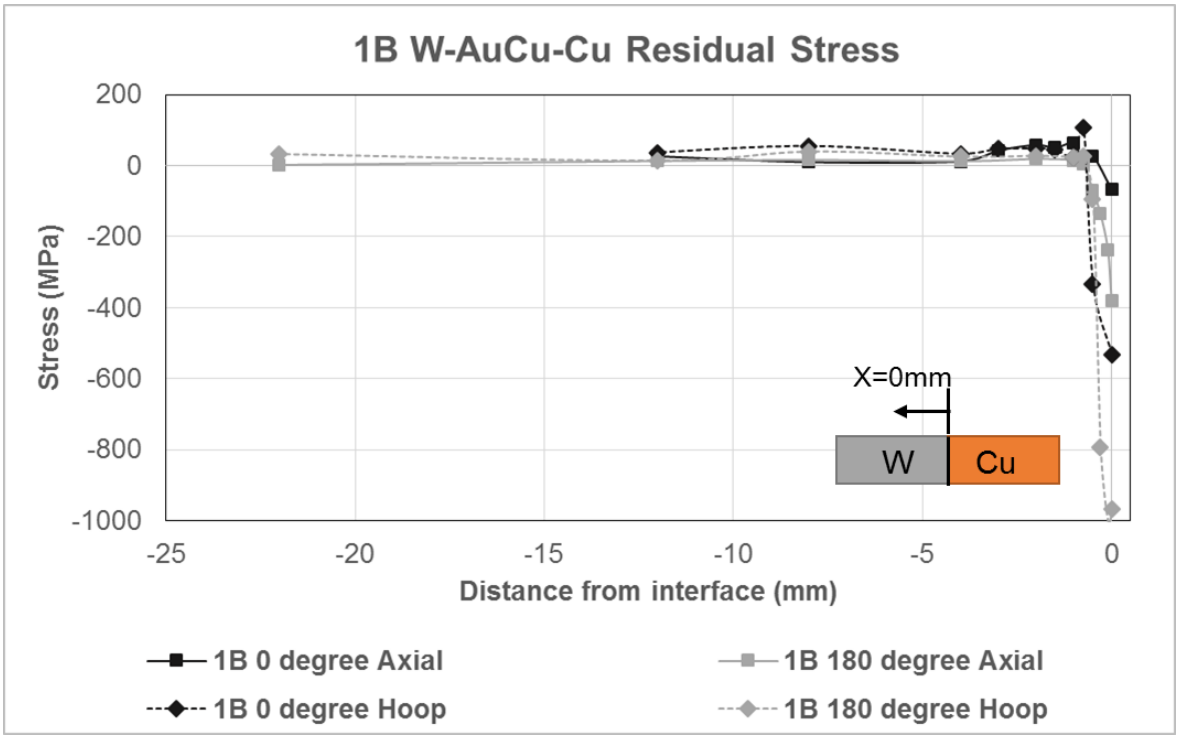

Figure 6-8 - XRD residual stress results for sample 1B W-AuCu-Cu

It can be seen from Figure 6-8 that the axial stress close to the interface is relatively high for the 180° circumferential position, with a peak of c. 400MPa compressive, compared to c. 60MPa compressive for the diametrically opposite 0° rotation. This suggests that greater constraint was applied for one segment of the part during cooling from brazing than for the other. The part was examined using optically and by SEM to analyse the extent of misalignment, presented in Figure 6-9.

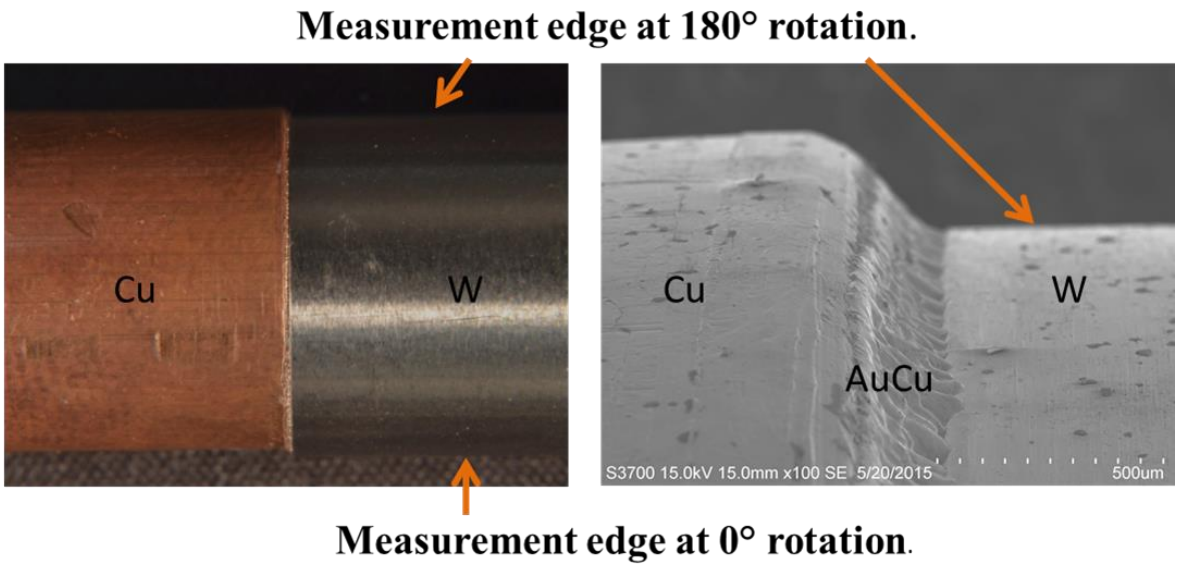

Figure 6-9 - Misalignment of sample 1B, W-AuCu-Cu brazed part

It is clear that at the 0° rotation the tungsten is aligned beyond the limits of the copper. Whilst there is still some constraint applied due to differential thermal contraction of the Au80Cu20 braze material in this position, the geometry dictates that a larger degree of constrain is applied at the 180° rotation. The opposite would be expected to hold true for the copper material had experimental measurements been possible.

The residual stresses as measured by XRD for the remaining W-AuCu-Cu parts, namely 1C, 1D, 1F and 1G are presented in Figure 6-10, Figure 6-11, Figure 6-12 and Figure 6-13 respectively.

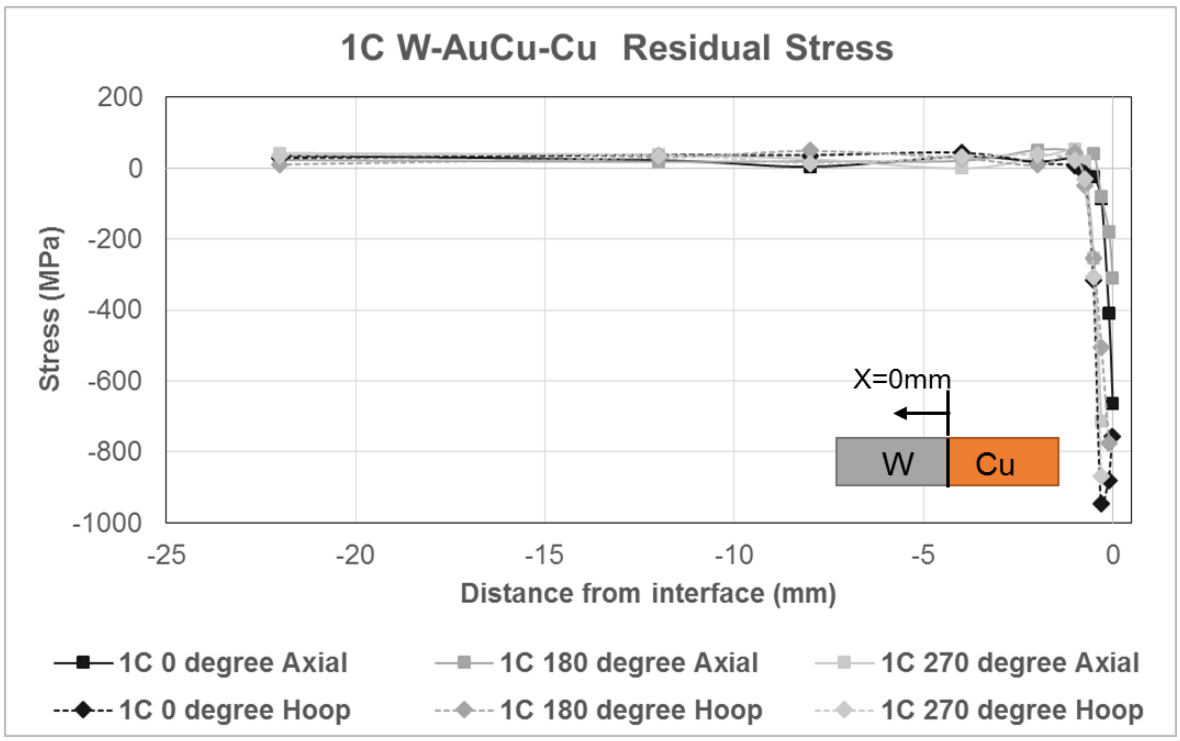

Figure 6-10 - XRD residual stress results for sample 1C W-AuCu-Cu

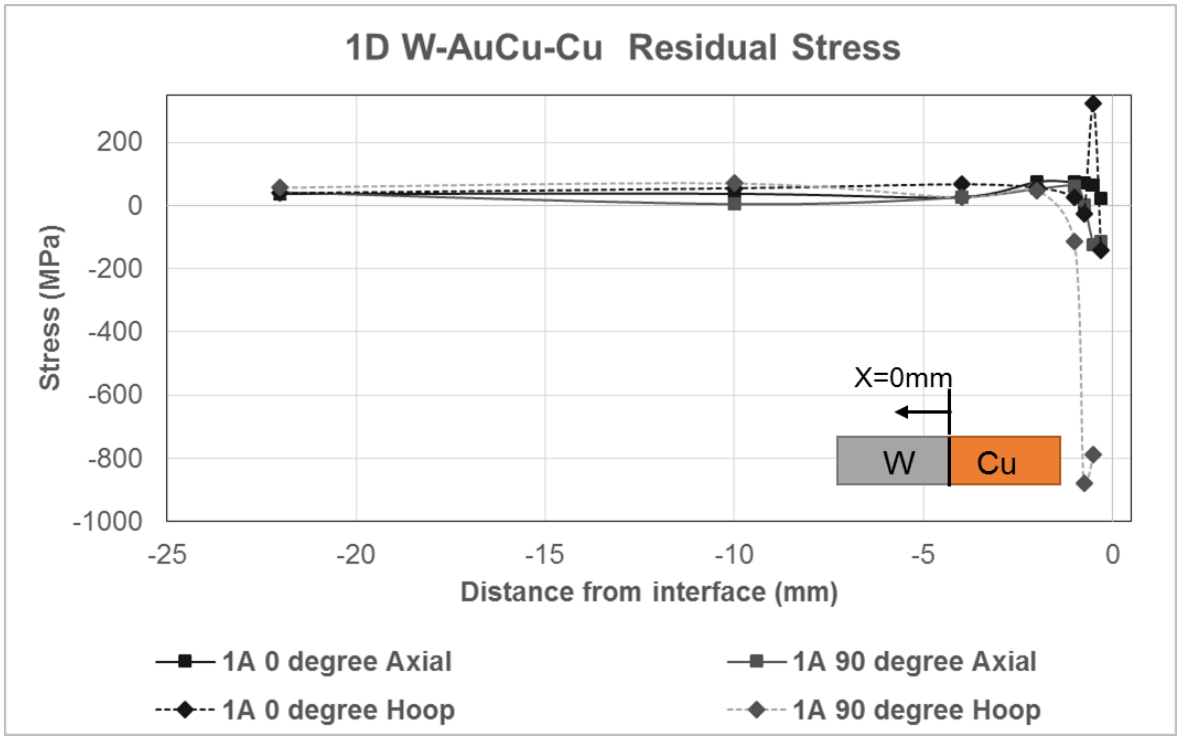

Figure 6-11 - XRD residual stress results for sample 1D W-AuCu-Cu

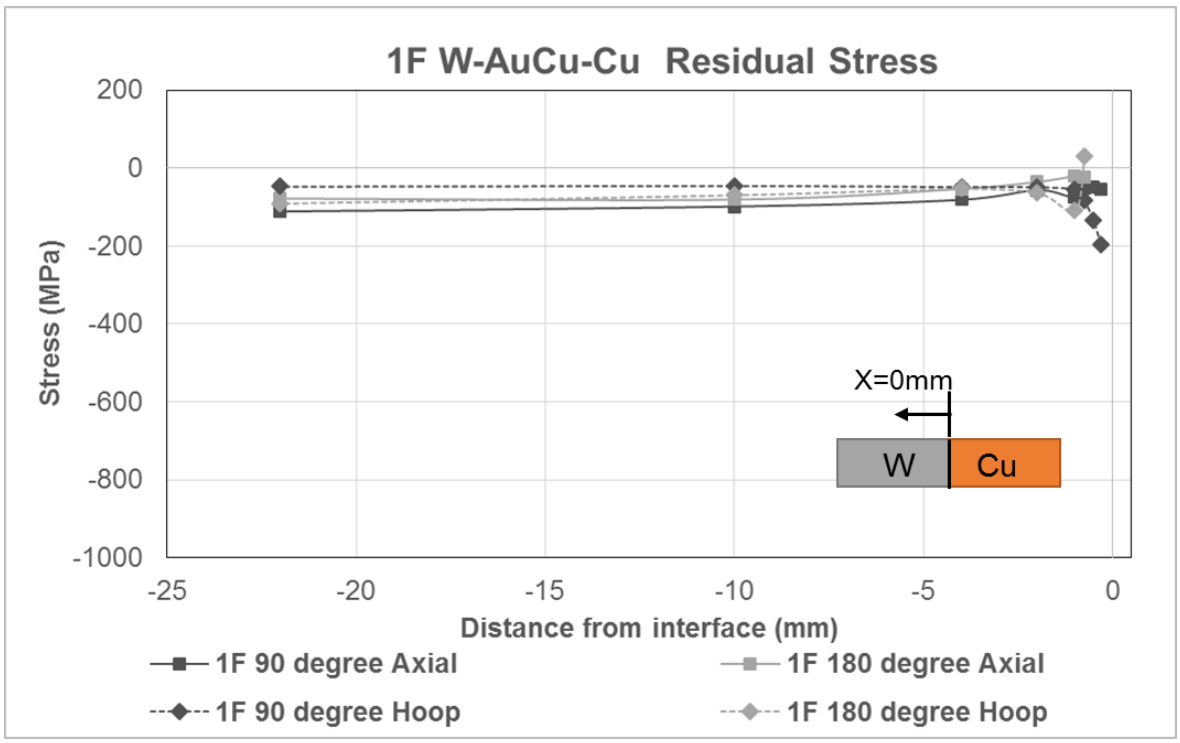

Figure 6-12 - XRD residual stress results for sample 1F W-AuCu-Cu

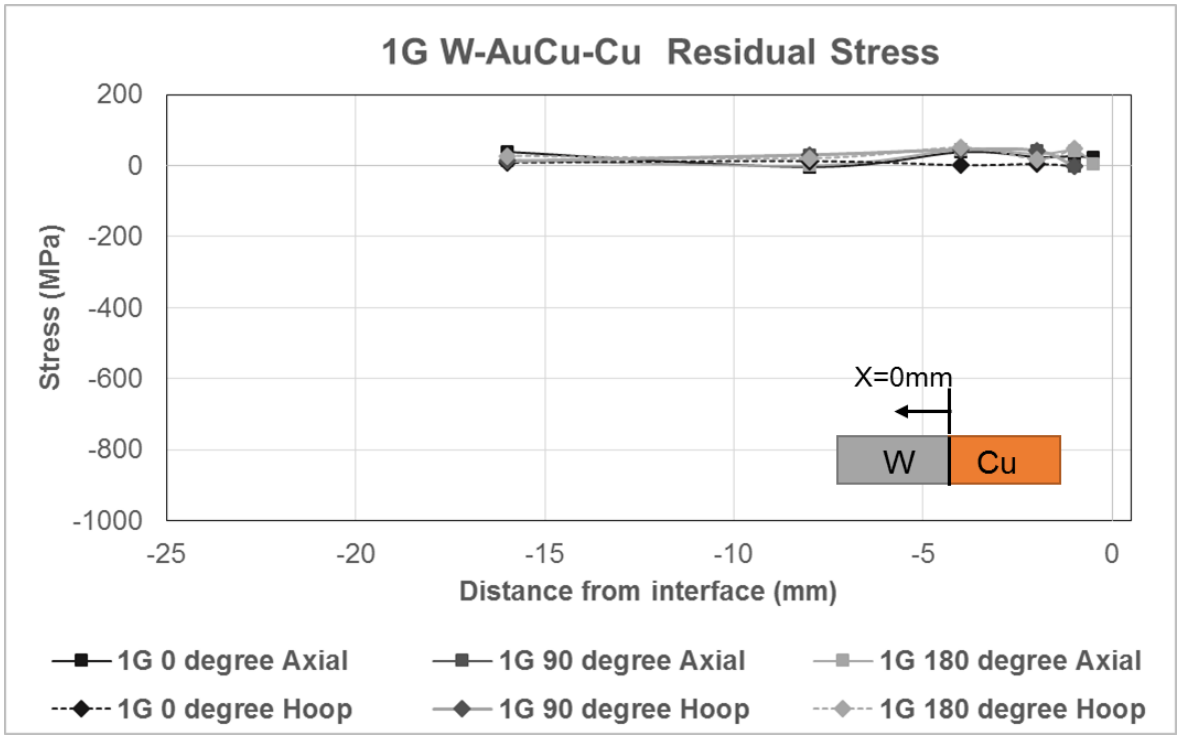

Figure 6-13 - XRD residual stress results for sample 1G W-AuCu-Cu

The axial and hoop stresses for sample 1C (Figure 6-10) are in good agreement with those previously presented of 1A (Figure 6-6 and Figure 6-7). Peak compressive stresses with a

magnitude approaching -1000MPa are present in the local stress concentration region at the dissimilar material interface. Although large in magnitude, these peak stresses are below the yield stress of the material of c. 1340MPa. The zone of influence of the interface is again less than 2mm, after which stresses drop to essentially zero.

In sample 1D, presented in Figure 6-11, there is a peak in compressive stress for both axial and hoop components, although the magnitude of the stress increase at the singular region is much less than experienced with samples 1A or 1C, or with FE predictions. As this is consistent for multiple circumferential rotations, the low magnitude of stress cannot be attributed to reduced constraint as a function of geometrical misalignment.
A similar trend in results can be seen with sample 1F (Figure 6-12). There is an upturn in the magnitude of compressive stress with increasing proximity to the interface, particularly for hoop stress.

It should be noted that the errors measured in the area close to the braze layer were highest, and therefore there is a factor of uncertainty when deducing any trends in this region. However the repletion of results in samples 1D and 1F for multiple axial positions suggests that the results are representative of the true stress state.

The different stress state in 1A, 1B and 1C compared to 1D and 1F can be explained by one of two possibilities. Firstly, the high stresses were not generated in the latter due to a variation in the brazing set up (for instance clamping arrangements). Secondly, high stresses were generated upon cooling from brazing but have since been relaxed due a mechanism such as creep or room temperature stress relaxation of copper. It is recommended that future research include microstructural examination, including plastic strain analysis using EBSD, in order to better understand the evolution and variation of the strain state in for parts of opposing results. Also, a repetition of the brazing trial and subsequent XRD measurement should be conducted.

Sample 1G, as shown in Figure 6-13, is different yet again from the previous results. Whilst 1D and 1F exhibited a small compressive peak, 1G shows negligible residual stress across the entirety of the part.
It should be noted that XRD measurements of this sample were conducted 18 months later than samples 1A-1F. Therefore any time-dependent stress relaxation is likely to be much more significant for this part. It has known that copper is capable of stress relaxation at room temperature through dislocation rearrangement [242]. Relaxation of copper occurs through grain coarsening and hardness reduction [243]. Future research should include a study whereby grain

size and hardness distribution at the interfacial free edge location of copper in a copper-tungsten joint immediately following brazing. Further populations of samples would then be analysed at a series of time intervals following brazing to identify if the mechanisms of room temperature stress relaxation are present.

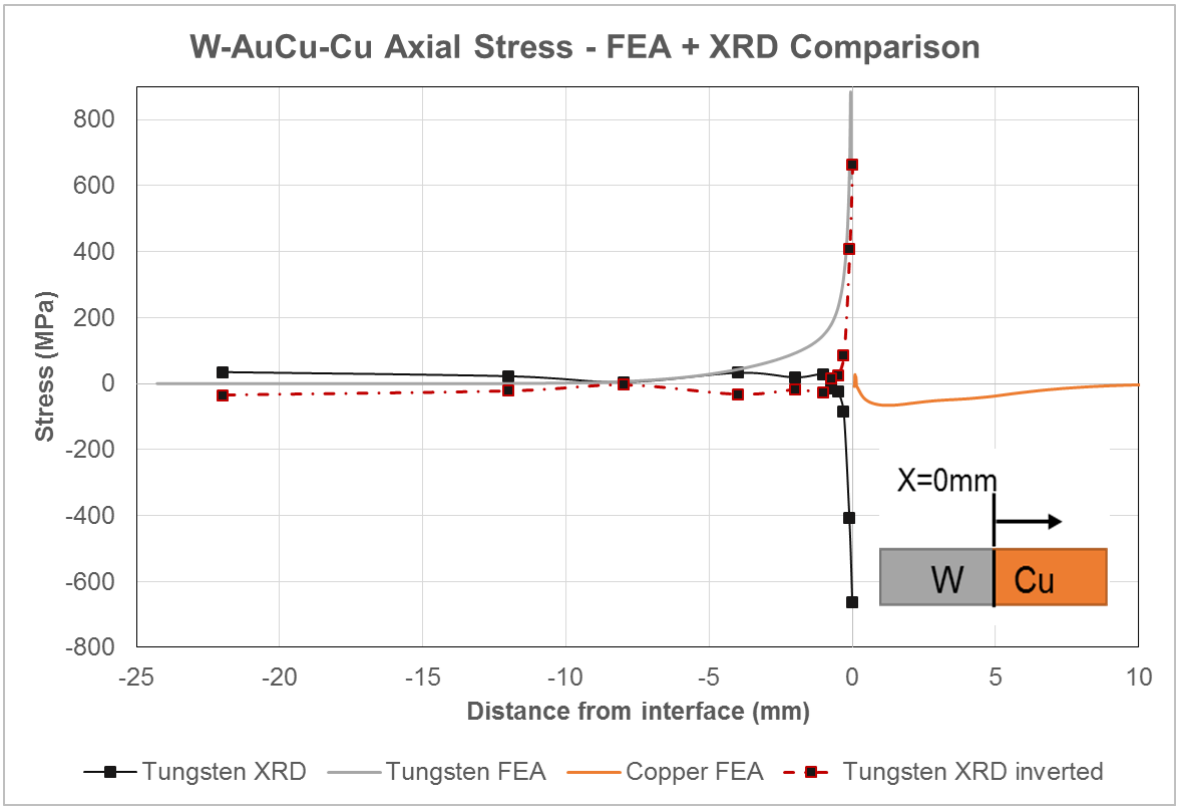

Figure 6-14 - XRD + FEA comparison of axial residual stress in W-AuCu-Cu brazed joint

A comparison of the axial stresses measured by XRD and predicted by FEA are presented in Figure 6-14. The stress profile of sample 1C at 0° rotation has been displayed as it is representative of the general profile. There is a clear disagreement of the stress singularity between the predicted and actual values. This disagreement is discussed in detail in Section 6.2.5.

In order to analyse additional characteristics of the stress profile, the XRD values have been inverted, i.e. multiplied by a factor of -1 (shown with red dashed profile). This allows for an easier comparison of the magnitude of the predicted and measured stresses.

The magnitude of the peak stresses are in agreement between predicted and actual values, with high stresses in excess of 600MPa. The high stresses as measured by XRD are much more localised to the region of the braze layer than those predicted in the ABAQUS model. Whereas

the model predicts stresses in excess of 100MPa beyond 3mm from the braze layer, the high stress state extends no more than 1mm in the real tungsten material.

This suggests that a larger proportion of the strain is being accommodated by the softer braze layer and braze/copper transition region. As discussed in section 6.2.5, composition dependent material data for the Au-Cu system and an improved material model that captures the complexity of the transition region should provide closer agreement between FEA and experimental values.

The hoop stresses as measured by XRD for a typical highly stressed W-AuCu-Cu brazed part are compared with FEA predictions in Figure 6-15. Whereas the axial stresses were in reasonable agreement in terms of magnitude, there is a clear disagreement in both magnitude and sign of the hoop stresses at the free edge in the tungsten. Compressive hoop stresses are predicted in tungsten in the vicinity of the braze interface, whereas high tensile hoop stresses are measured with XRD.

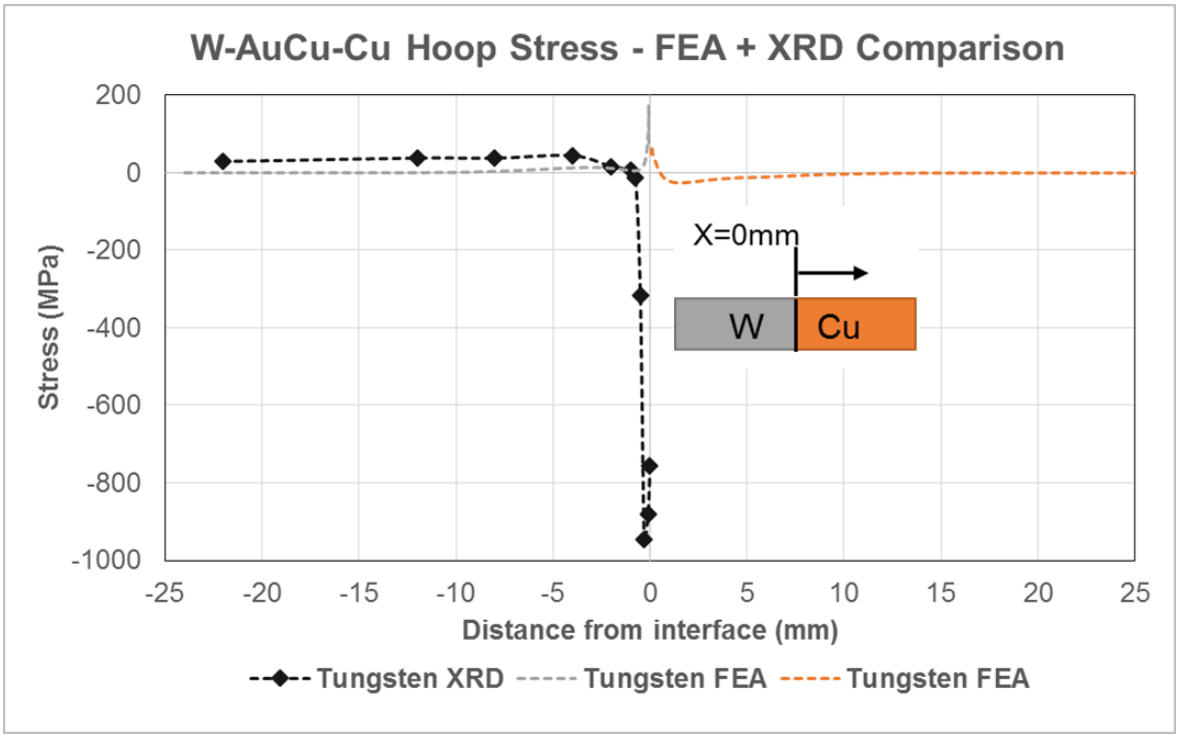

Figure 6-15 - XRD + FEA comparison of hoop stress in W-AuCu-Cu brazed joint

6.2.4 W-AuCu-316L XRD results

In this section the XRD residual stress results for tungsten – 316L brazed parts are presented. Two samples have been measured with axial and hoop stresses measured on each. Three circumferential rotations were evaluated in sample 3A and two circumferential positions for sample 3B. The axial stress results for 3A and 3B are presented in Figure 6-16 and Figure 6-17 respectively.

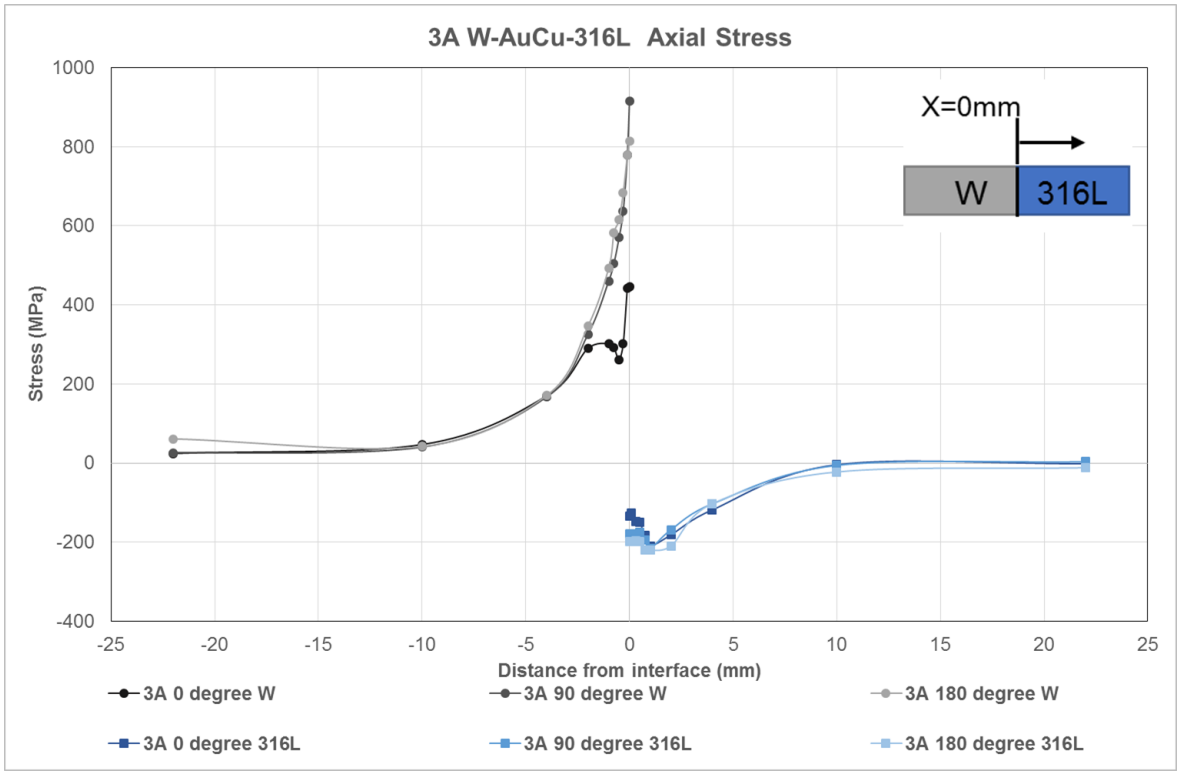

Figure 6-16 - XRD results 3A W-AuCu-316L axial stress

There is good agreement between all 316L stress profiles measured (pictured in shades of blue). Stresses are compressive in nature, with peak magnitudes of c. 200MPa compressive at a distance of 1-2mm from the dissimilar material interface. Although the stresses are compressive in nature it can be observed that there is an increase in magnitude of tensile stresses in the immediate vicinity of the interface as predicted in Section 5.5 and from the relationship of the elastic properties and CTE of the interfacial materials [206]. This manifests as a reduction in compressive stress in the vicinity of the interface.

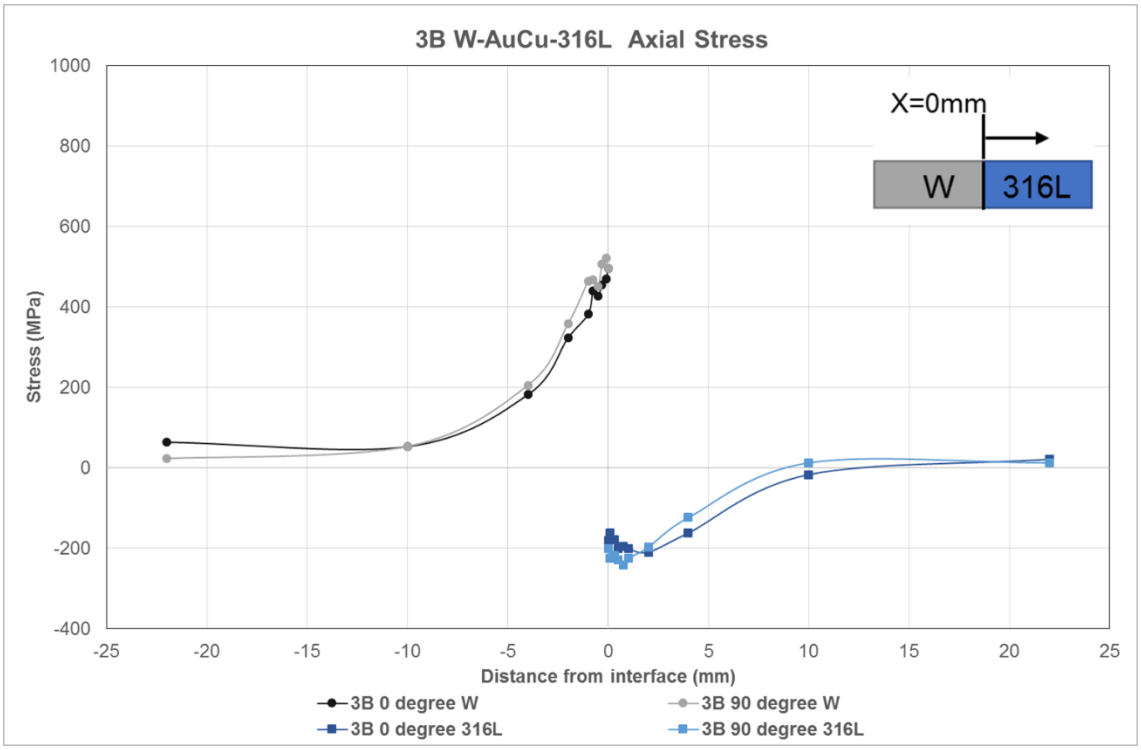

Figure 6-17 - XRD results 3B W-AuCu-316L axial stress

The stress concentration local to the dissimilar joint results in a large tensile stress in the tungsten for both 3A and 3B. At a distance of 1-2mm from the interface the magnitude is 400 MPa tensile. Part 3A exhibits a more severe increase in axial stress in the immediate vicinity to the braze layer than 3B.

The hoop stresses for W-AuCu-316L brazed parts 3A and 3B are presented in Figure 6-18 Figure 6-19 respectively. The magnitude of hoop stresses are much lower than axial stresses for the W-AuCu-316L configuration. In both the tungsten and steel material the stress remains between +/- 100 MPa, showing no significant stress concentration.

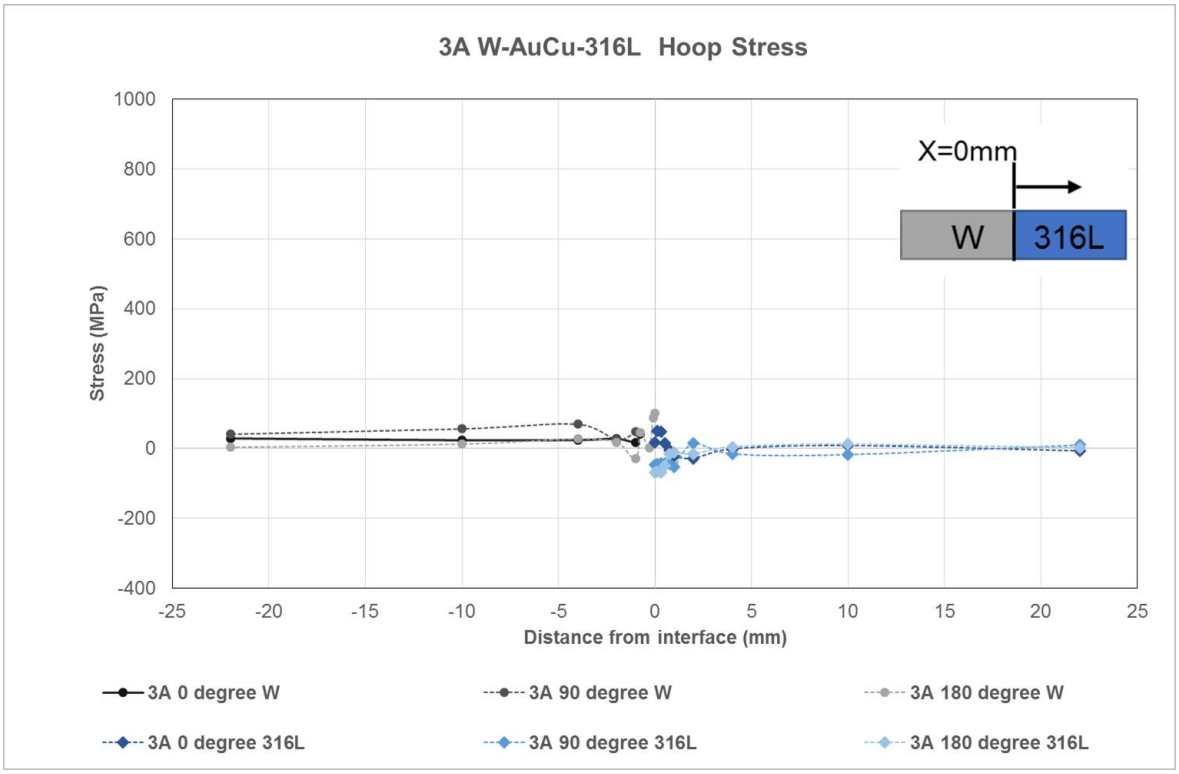

Figure 6-18 - XRD results 3A W-AuCu-316L hoop stress

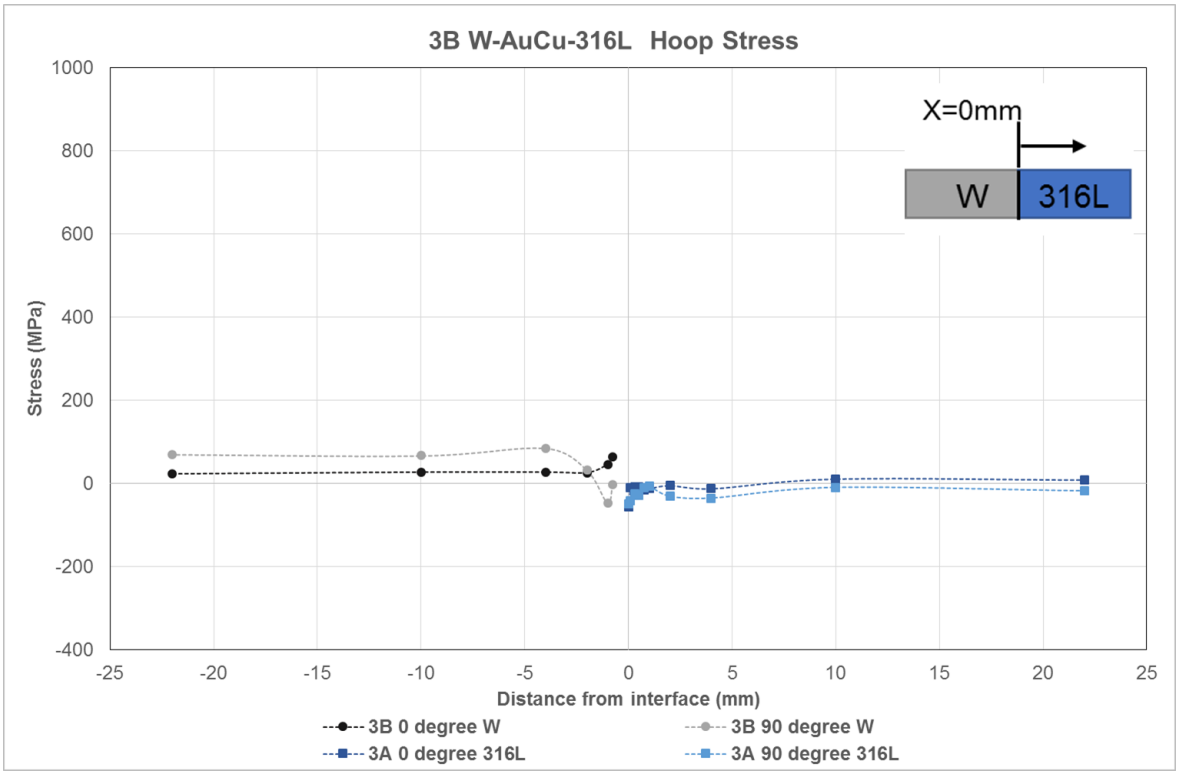

Figure 6-19 - XRD results 3B W-AuCu-316L hoop stress

A comparison of experimentally measured and FEA predicted axial stresses for the W-AuCu-316L brazed part is presented in Figure 6-20.

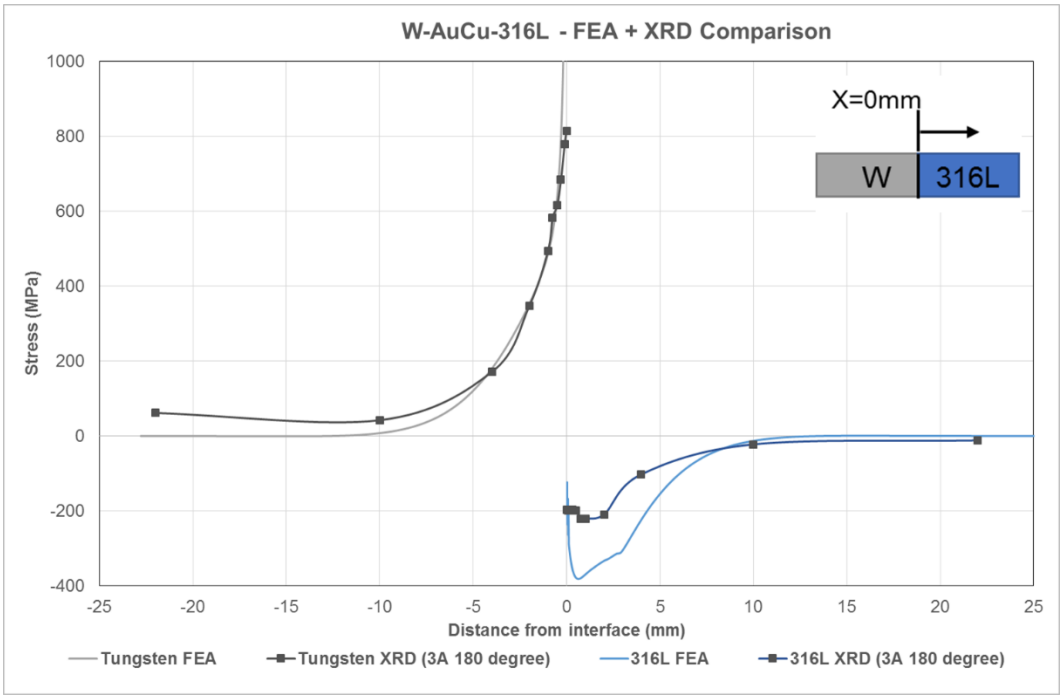

Figure 6-20 - XRD + FEA comparison of axial residual stress in W-AuCu-316L brazed joint

For the tungsten side the XRD measured free edge axial stresses are in excellent agreement with modelling predictions. The magnitude and gradient of the stress profiles are extremely comparable at both the local stress concentration region and in the tungsten remote from the interface. The agreement is likely better for tungsten as the stress/strain state is predominately elastic in tungsten material. The simple bilinear kinematic hardening model used for FEA is recommended to be improved in future work to obtain better agreement in the 316L material.

The profiles for the 316L predicted and measured axial stresses are similar in nature, however the FE predicted stresses are higher in magnitude. There is a local stress concentration due to the braze interface in both materials for a region extending 10mm from the interface. This is shown in both experimentally measured and predicted stress values.

From these results it can be concluded that the FE model presented in Chapter 5 is suitable for predicting the stress state following brazing for the W-AuCu-316L material combination.

6.2.5 316L-AuCu-Cu XRD results

The free edge axial stresses as measured by XRD for the 316L-AuCu-Cu brazed parts are presented in this section. Only stress results for the 316L side were obtainable by XRD measurement. It was not possible to obtain valid results in the copper material as discussed previously. Two parts have been evaluated, namely 2A and 2D.

The results for 316L-AuCu-Cu part 2A are presented in Figure 6-21. Stresses at two circumferential rotations were measured, 0° and 90°. Axial stress profiles are represented by a solid line and hoop stresses by a dashed line.

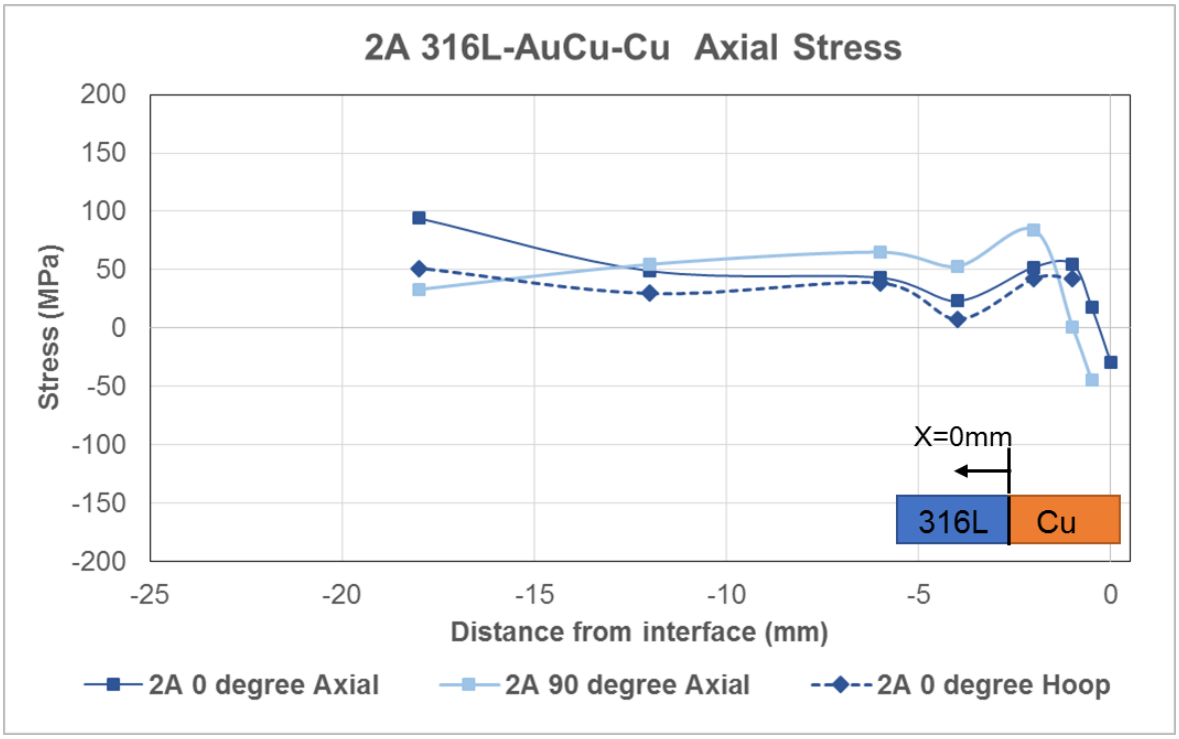

Figure 6-21 - XRD results 2A 316L-AuCu-Cu axial stress

The magnitude of the stresses for this material combination are much lower than the previous reported brazed combinations. Peak stresses in 2A were no more than 50MPa compressive for both axial and hoop directions. The small stress values are expected due to the similarity in CTE as both are approximately 17 x10^{-6}/K. Dissimilarity in CTE was shown to be the dominant factor resulting in high discontinuity stresses as discussed in the previous chapter.

The results for 316L material in part 2D (316L-copper) are presented in Figure 6-22. Only the axial component of stress was considered for this part due to limited access to the XRD equipment at the time of measurement.

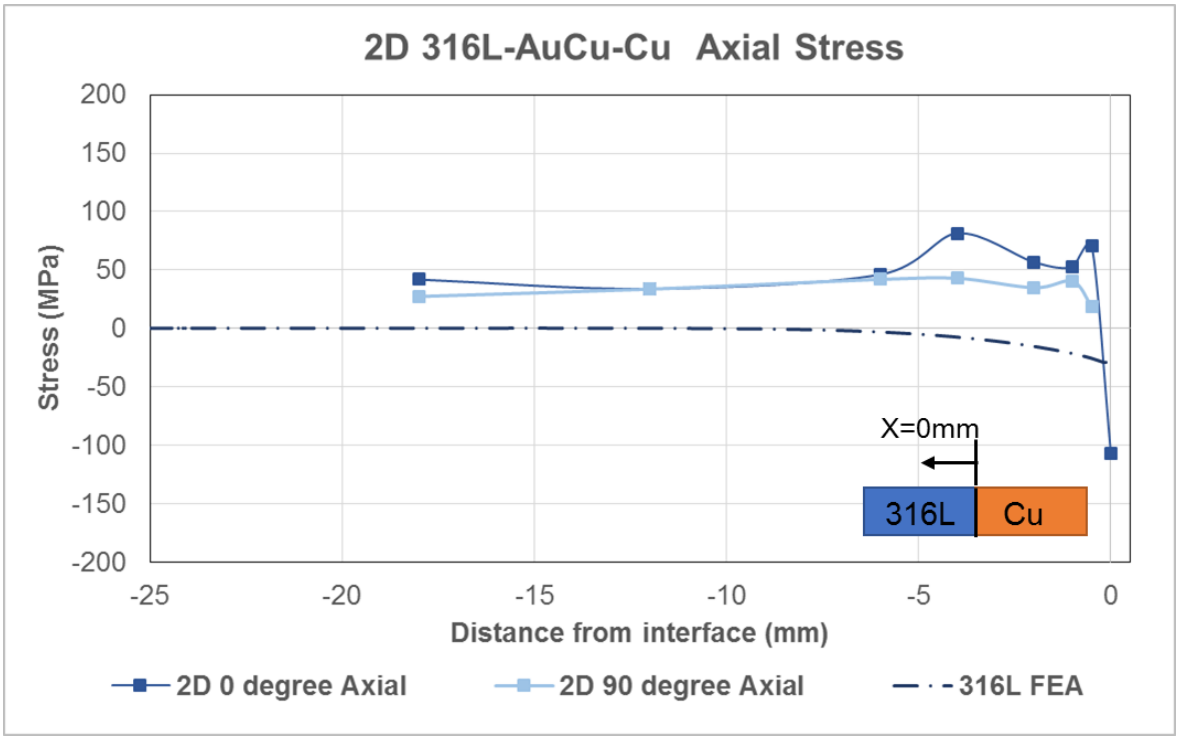

Figure 6-22 - XRD results 2D 316L-AuCu-Cu axial stress

As with part 2A (Figure 6-21), the magnitude of residual stresses in part 2D (Figure 6-22) are very small in comparison with the brazed tungsten parts. The maximum measured stress was 100MPa and compressive in nature.

The FE predicted stress profile has been plotted for the purpose of comparison here. There is reasonable agreement between XRD and FEA. The stress in the 316L remote from the material is close to stress free, with a compressive peak at the interface.

There is no strong singularity predicted by FEA, a result of the similarity in thermal expansivity. There was evidence of a sharp increase to relatively highly stressed condition for the 0° rotation close to the interface. However only a single reading showed this behaviour, and the absolute increase in stress is still low in absolute value (100MPa).

Based on both FEA and XRD results for the 316L-AuCu-Cu brazed parts it has been found that residual stresses resulting from vacuum brazing are significantly lower than dissimilar brazed joints containing tungsten.

6.2.6 Discussion of XRD results

The disagreement between modelling/theory and experimentally measured axial interface stresses for tungsten in the W-AuCu-Cu configuration was shown to be consistent across all six individual samples measured.

When considering the theory of the nature of singularities at a dissimilar interface, the sign of the singularity influenced stress concentration is dependent on the relationship between elastic moduli and CTEs for two base materials (E_1/E_2 and CTE_1/CTE_2) [222]. This relationship is discussed in detail in Chapter 5 of this thesis. As tungsten has a much higher E than copper (or Au80Cu20 alloy), and much lower CTE, the resulting singular interface stress should be tensile. This was shown in FE simulations presented in Chapter 5. However as reported in Section 6.3.1 the stresses at the interface in tungsten are compressive in nature and tend towards a compressive singularity.

Interestingly however, there is good agreement between modelling/theory and experimental results for the W-AuCu-316L combination. This would suggest that the understanding of the mechanisms of constraint during brazing, and their implementation into the FE model, is correct for at least one of the cases presented in this thesis.

It is postulated that the reason for disagreement between FEA and experimental results for the tungsten and copper brazed joint is due to a complexity in the material behaviour that is not captured by the model. Several possible mechanisms that could affect interfacial stress are discussed here.

The theoretical basis for predicting the nature of a singular stress at a dissimilar material interface is dependent on an assumption that the system is fully elastic. However for all real material systems it would be expected that some degree of plastic deformation will occur. This is particularly true for the base copper material due to the low yield stress of 40MPa at room temperature. As such significant plastic strain is expected at the interface as is presented in section 5.5. It is likely that this plastic behaviour will influence the resulting stress that isn't accounted for in the theoretical prediction.
Conversely, the 316L material has a much higher yield stress (300MPa at room temperature). It is therefore intuitive that the effects of plasticity shall be less pronounced for the tungsten and 316L brazed joint. This could be attributed as the reason why there is good agreement with tungsten-316L but not for tungsten-copper.

It is recommended that further analysis be undertaken to explore this possibility. Microstructural analysis using EBSD could be useful in comparing the severity of plastic deformation between the two material combinations.

When theoretically determining stress nature, it is assumed that the dissimilar material joint exhibits fully elastic behaviour is the assumption that the joint is comprised of only two materials. In the case of the brazed results presented here there is a third material, the braze interlayer. Whilst it is generally a fair approximation to consider the relationship between material properties of the parent materials, it is known that the added complexity of a third material can produce results that are not straightforward to predict [205].
Additional FE studies are recommended as part of future research to further evaluate the effect of interlayer material properties in an elasto-plastic model.

The FE model used for the simulations presented in Section 5.5 describes the interfacial region as being a sharp transition from one base material to the interlayer. There is a further sharp transition from the interlayer to the second base material. Due to diffusion of elements at the interface, the assumption of a sharp transition is not fully accurate. In reality there is a gradient of material properties between each parent material and the interlayer. The material properties in the diffusion region are not those of any single material. Instead they are a combination of the properties of each material, and are a function of elemental composition and distance from the interface. The influence of the theoretical singularity was shown to vary when a material gradient exists [209].

Even if the model were to be adjusted to include a transition from one region to another, there would still be a shortcoming as material data is not readily available for the diffused regions. The result is a deficiency in the FE model. Further experimentation is required to evaluate material properties of the diffused region. For example, the temperature dependent CTE of AuCu for $80\%_{wt}$ balance of Au down to almost $0\%_{wt}$ balance Au (the range in Au $\%_{wt}$ balance across a c. 200µm transition range of braze layer and diffused region).
It is postulated that the reasoning of interdiffusion of elements at the dissimilar interface being a significant contributing factor in the disagreement is valid based on the opposing nature of agreement for the two material combinations discussed here, tungsten-copper and tungsten-316L. For the tungsten-316L part it was shown in Chapter 3 that there is a negligible degree of interdiffusion between parent materials and braze interlayer. However for the tungsten-copper system, there was significant diffusion between copper base material and Au80Cu20 braze alloy.

If the material property gradient is a contributing factor to the residual stresses induced upon cooling then it would only be apparent in the tungsten-copper joint, as experienced here.

Although not as likely as the possible explanations presented previously, there are several further factors that could contribute to the disagreement in results. Due to time spent at high temperature during the brazing process it is possible that stress relaxation mechanisms and creep are significant. These are not accounted for in the model. Such effects would likely serve to blunt the peak stresses predicted.

The expected temperature gradient across the part during cooling from brazing temperature has been shown to be small [208, 222]. The possibility remains however that local temperature variations exist at the braze interface due to differential cooling rate caused by differences in thermal conductivity, heat capacity and emissivity. This behaviour is not captured by the model presented in Section 5.5 and could contribute to errors in the predicted stress state.

Stress singularities exist not only due to material dissimilarity, but also due to geometrical factors. It is possible that geometrical misalignment of the parent materials during brazing could contribute to the final stress state. The effect of axial misalignment was shown in 6.2.3. However for the majority of cases the tungsten in the tungsten-copper brazed part exhibited a compressive singularity (the only exceptions being a stress free state due to no constraint on free contraction). The real brazed parts do not contain zero-radius reentrant corners as are present in the FE model. However as there is agreement between predicted and measured axial stress for one configuration (tungsten-316L) it is unlikely this effect that causes disagreement in the tungsten-copper case.

6.3 ESPI Hole Drilling

XRD is a useful technique for evaluating residual stress at the surface/near-surface (up to a depth of approx. 20μm). To measure the stress profile with regards to depth into the sample an alternative technique is required. Electro polishing was considered as a method to remove small amount of material to allow XRD measurements at increasing depths. However the geometry of the sample resulted in this method being impractical to implement. It was therefore decided that ESPI incremental hole drilling would be a more suitable method.

Electronic speckle pattern interferometry has been used in place of the traditional strain gauge technique as a means of measuring surface displacement as a result of stress relaxation upon incremental hole drilling. This removes the necessity to mechanically prepare the surface for strain gauge attachment, in the process affecting near surface residual stresses [244-246].
The Stresstech PRISM ESPI [247] experimental set-up is shown in Figure 6-23 and a schematic of the major components shown in Figure 6-24.

Figure 6-23 – PRISM ESPI hole drilling set-up

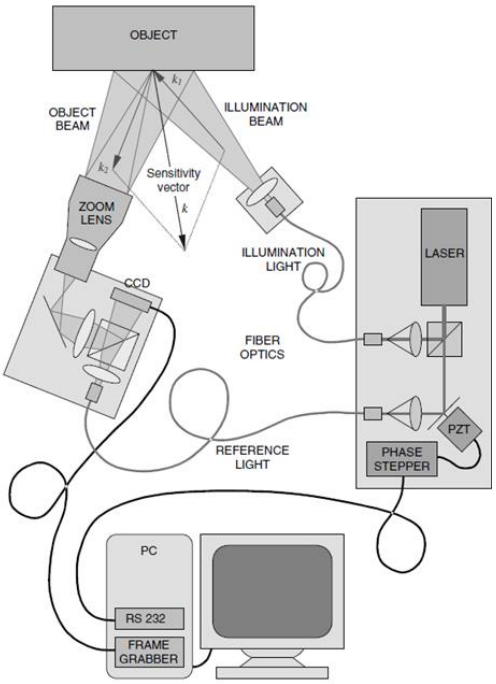

Figure 6-24 - Schematic of ESPI hole drilling equipment

The calculation of biaxial residual stresses from the holographic interference fringe pattern resulting from a shallow drilled hole was presented by Makino [248, 249].

The residual stress in the copper material is predicted to be high in relation to the yield stress of the material (60MPa) based on FE simulations presented in Section 5.5. It is known that local plastic deformation can have a significant effect on ESPI measurements of residual stress [248].

ESPI hole drilling experiments were performed on two samples, both constituting of brazed W-AuCu-Cu (part numbers 1C and 1D). The parts were clamped firmly on both sides of the braze interface.

Drilling was performed using TiALN coated 0.79mm double flute endmills. This was the smallest diameter endmill commercially available suitable for ESPI hole drilling. Due to the small diameter of the part, it was critical to use the smallest diameter drill possible in order to minimize the effect of the curved topography of the part. However, even though a small diameter drill was used, the curvature of the part was still significant and was expected to introduce errors into ESPI analysis. Whilst ESPI has successfully been applied to curved surfaces [250] it is known that the curved surface can introduce out of plane effects [251].

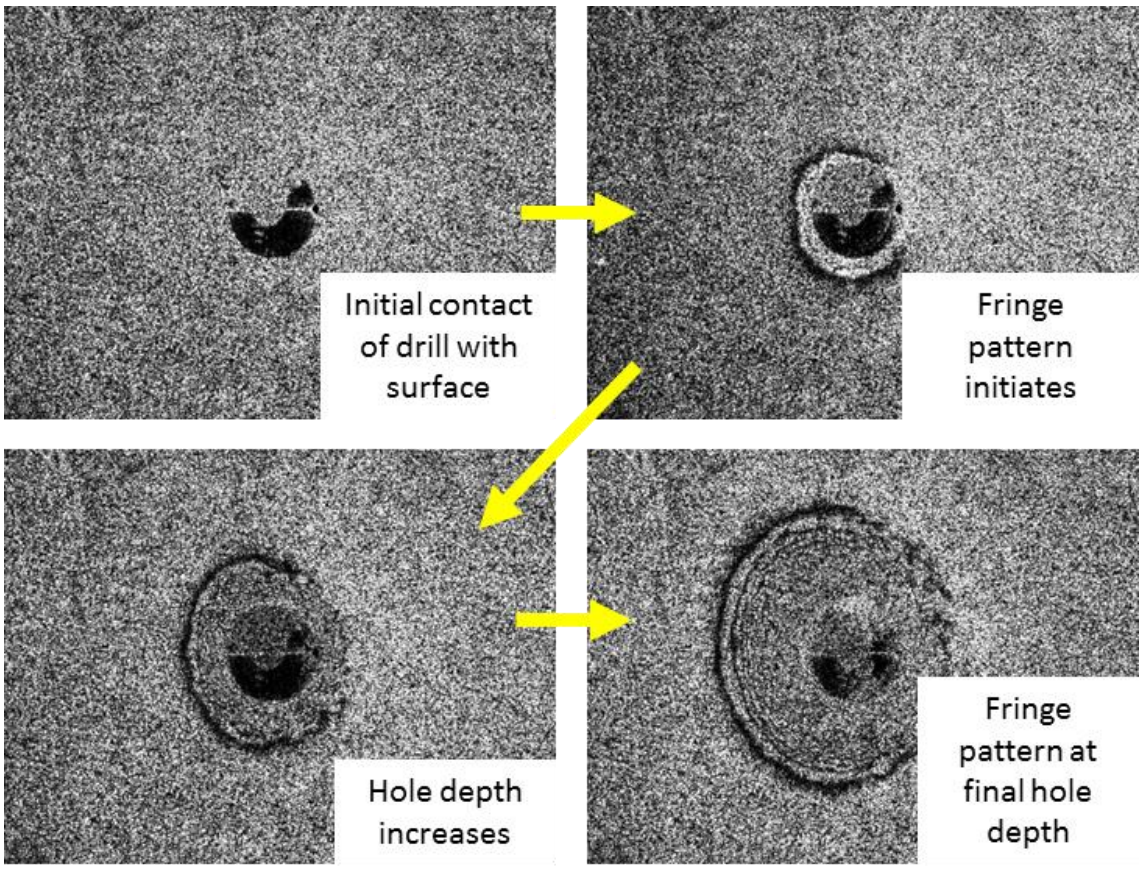

Figure 6-25 - ESPI fringe patterns during incremental drilling of Cu in W-AuCu-Cu brazed part

Figure 6-25 shows the resulting fringe pattern from an ESPI incremental hole drilling experiment on the copper side of a W-AuCu-Cu brazed part. The developing fringe pattern did not result in sensible results, with the measured stress far above the yield of the material (Figure 6-27). A number of practical limitations caused this outcome. The dimensions of the part are at the very end of the range as to what is practicably measurable. Securely clamping a small and relatively highly curved part proved to be fraught with difficulty.

The curvature of the part is large compared to the diameter of the drilled hole, and even more so when considering the area used for stress calculation (up to 5 times the diameter of the drilled hole). As can be seen in Figure 6-26, the curvature of the part is noticeable. This will introduce out of plane effects that are not considered in the stress calculation.

Additionally, it was found that residue developed on the surface during the drilling process. This was caused by difficulty achieving sufficient pressurized air flow on the curved surface to remove the residue, which can be seen in blue on the displacement map in Figure 6-26.

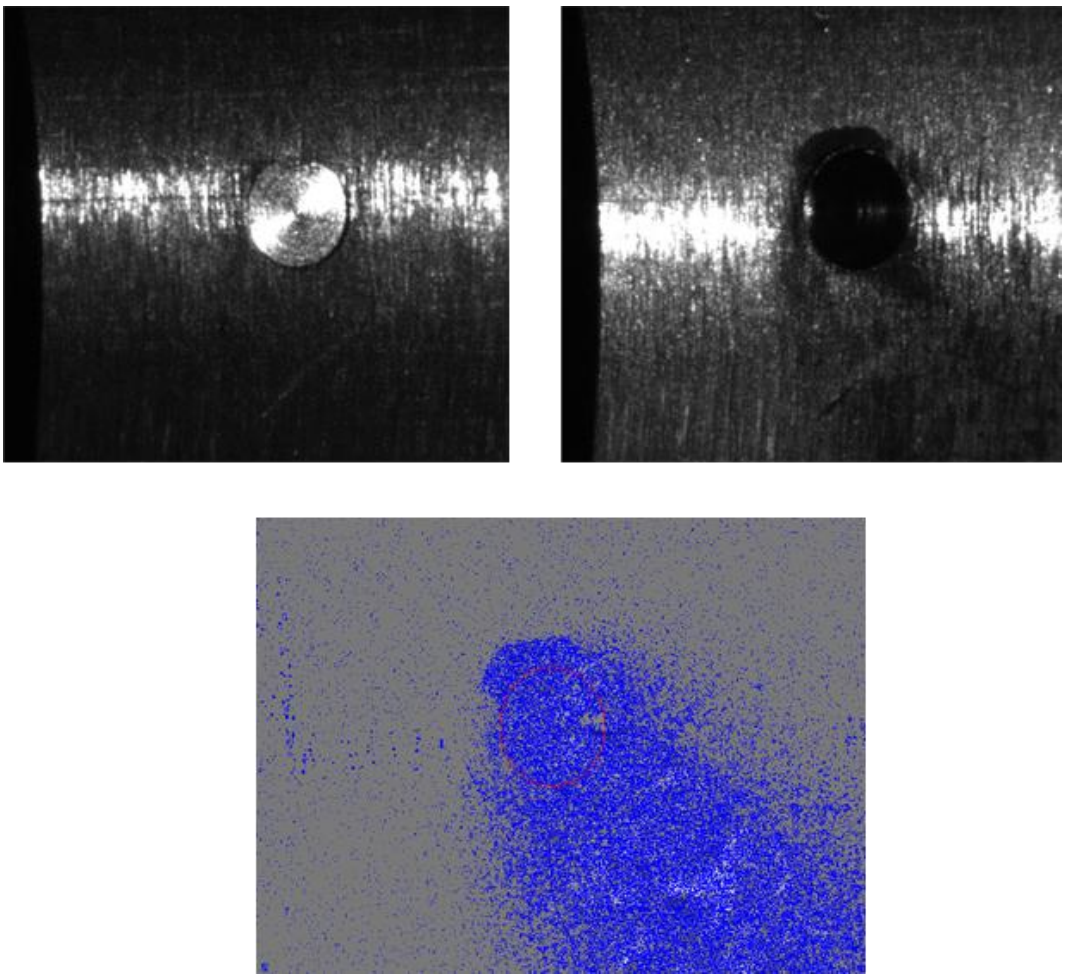

Figure 6-26 - Copper after initial drilling step (top left), after drilling to 0.5mm depth (top right), image displacement map after 0.5mm depth drilling

The results for ESPI hole drilling measurements in the copper (Figure 6-27) and tungsten (Figure 6-28) sections of a brazed W-AuCu-Cu part are shown below.

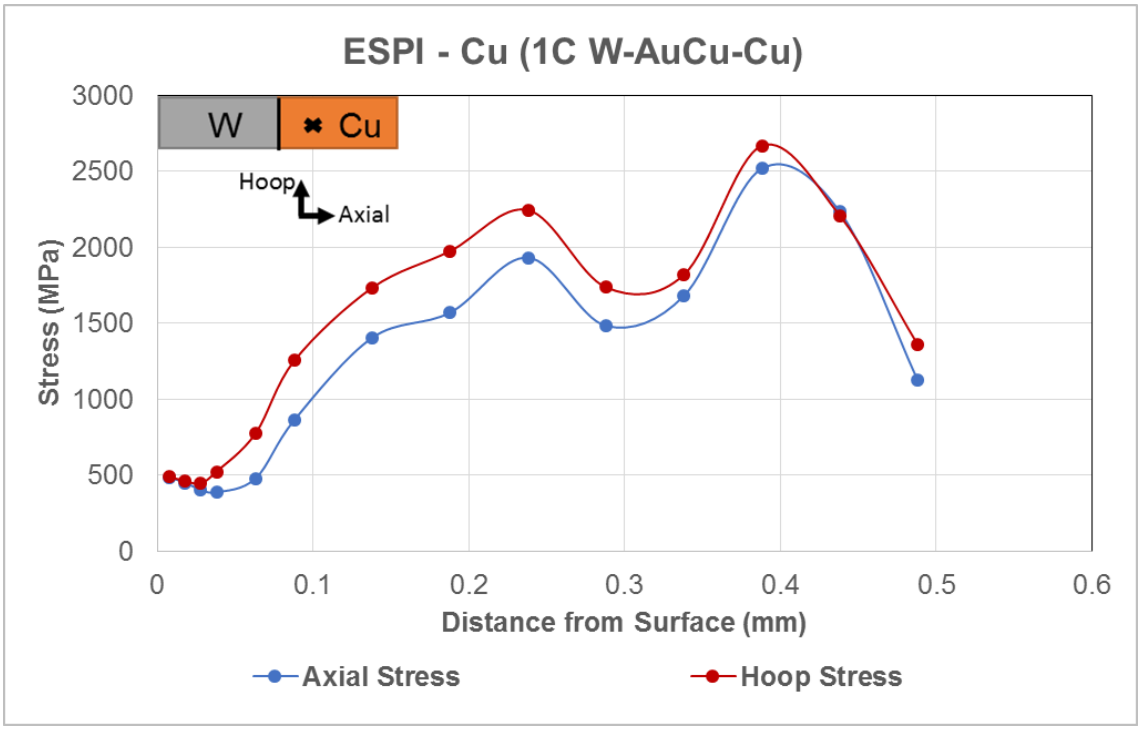

Figure 6-27 - ESPI hole drilling residual stress results in Cu (part 1C W-AuCu-Cu). Axial stress (blue) and Hoop stress (red) at position 7mm from braze interface

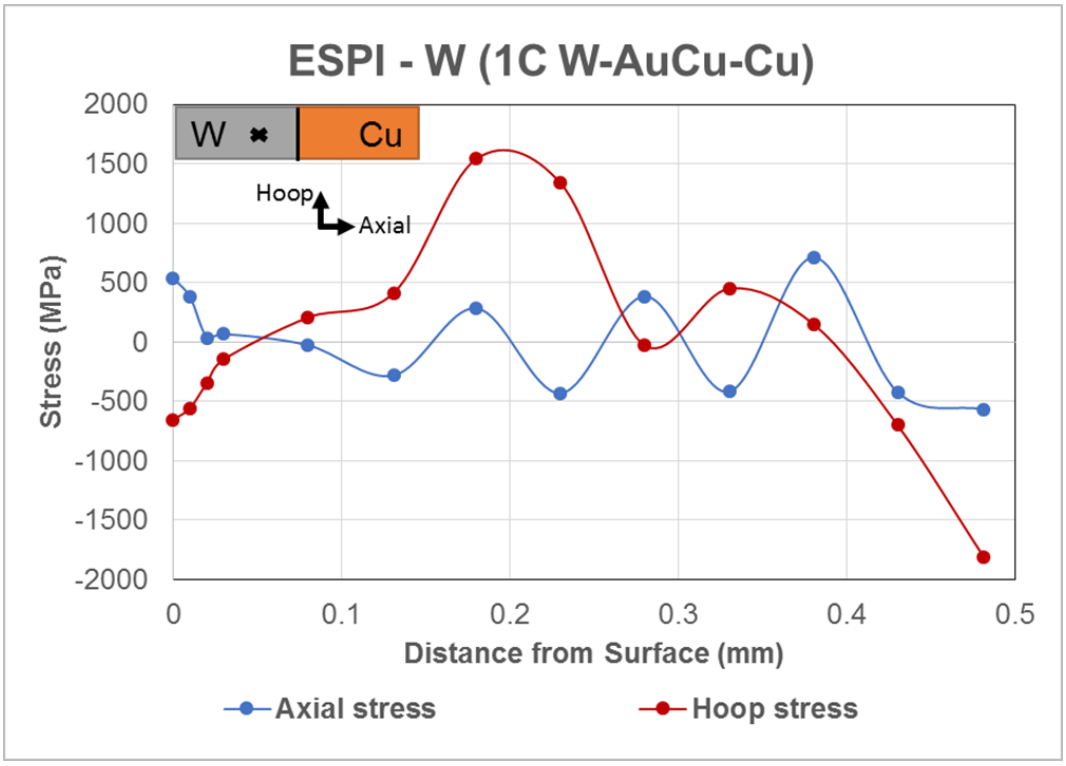

Figure 6-28 - ESPI hole drilling residual stress results exhibiting instability in W (part 1C W-AuCu-Cu). Axial stress (blue) and Hoop stress (red)

Figure 6-27 shows a typical stress profile following hole drilling, however the magnitude of the stresses are impossibly high. In addition to the practical difficulties discussed previously, this result is likely influenced by the relative similarity in residual stresses present in the copper and the yield stress. This is a known limitation of this method [67].

As the hole is drilled, stresses are released and redistributed, which as the expected stresses in copper were at or even beyond the elastic limit, plastic deformation of the copper has occurred. The large deformations experienced during plasticity, compared with small elastic displacements, have produced invalid stress results. It is recommended that in future research a larger diameter, or flat, sample is used for residual stress characterisation. This would allow for both ESPI and conventional hole drilling measurement to be performed in copper to try and alleviate issues arising with the ESPI measurement technique.

Considering Figure 6-28, the problem of clamping a small curved part securely enough for ESPI evaluation is evident. The initial stresses measured are reasonable for this material. Tensile axial stresses of c. 500MPa and compressive hoop stresses also of c. 500 MPa were measured close to the surface (20μm depth). However as drilling continues, the stress profiles are obviously unstable. This is attributed to vibration resulting in bulk movement of the part during drilling.

ESPI hole drilling has the potential to provide validation of predicted and measured near surface residual stresses at a scale comparable with XRD. However the geometry of the parts evaluated in this thesis proved to be not suitable for this method, due to degree of curvature relative to the gauge area. Future research should include a repeat of FEA and XRD for these materials, but on larger parts, perhaps with flat edges that can be more easily measured. ESPI experiments could then be performed to validate the previous findings.

6.4 Contour Method

6.4.1 Introduction to Contour Method

Whilst techniques such as XRD and Hole drilling can provide accurate residual stress data close to the surface of a part, an alternative method is required to conveniently assess the stress profile across a cross section of an engineering part. The Contour Method has been identified as a suitable method for cross sectional stress mapping of the brazed parts considered in this thesis.

The Contour Method, introduced by Prime of Los Alamos in 2001 [252], is a solid mechanics based approach that determines residual stress from the relaxation of a cut surface. This method is based on Bueckners Superposition principal [253] which states that "If a cracked body subject to external loading or prescribed displacements at the boundary has forces applied to the crack surfaces to close the crack together, these forces must be equivalent to the stress distribution in an uncracked body of the same geometry subject to the same external loading".

This principle can be applied for determining the residual stress in a body prior to sectioning by determining the "external loading", which in this case is equivalent to the residual stress released during Contour Method sectioning. Assuming fully elastic conditions, the relaxed stresses are found by measuring the surface displacement of the cut surface and analytically forcing these back to planarity.

A schematic of how the principal of Superposition can be applied for Contour Method analysis is shown in Figure 6-29, reproduced from [252]. In A, the original part containing residual stresses prior sectioning is shown. The part is then sectioned and distorts due to relaxation of stresses on the cut face as shown in B. The cut surface is then forced back to planarity, i.e. its original state as shown in C. Assuming fully elastic stress relaxation of the cut surface, the stress state normal to cut surface in C is equal to that in state A. For a truly stress free part the surface position in A would be identical to B and C, i.e. zero displacement.

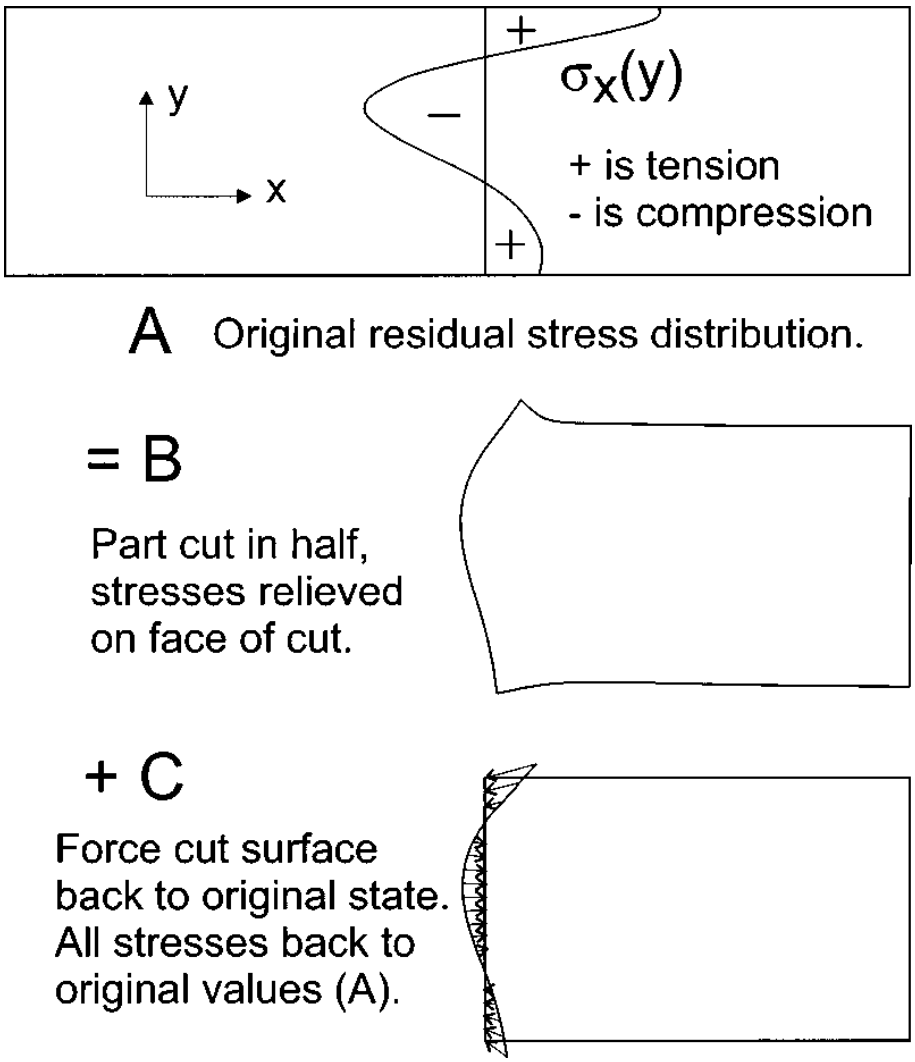

Figure 6-29 - Principle of Superposition applied for Contour Method residual stress determination [252]

The triaxial stress tensor for the part shown in Figure 6-29 is given by Equation 6-13

$$\sigma^{(A)}(x,y,z) = \sigma^{(B)}(x,y,z) + \sigma^{(C)}(x,y,z)$$

Equation 6-13

The stresses in B are only partially relaxed, however at the free surface σ_x and τ_{xy} and τ_{xz} are equal to zero [252, 254]. Considering only stresses normal to the cut plane, σ_x, Equation 6-13 can be simplified to Equation 6-14,

$$\sigma_x{}^{(A)} = \sigma_x{}^{(B)} + \sigma_x{}^{(C)}$$

Equation 6-14

And as $\sigma_x{}^{(B)}=0$, then the stresses normal to the cut plane in A can be determined solely from the relaxed stresses in C.

For the above to hold true, a series of assumptions must be satisfied [67, 252]:

1. Stress relaxation is fully elastic in nature
2. The cutting procedure introduces no additional stress to the part
3. The cutting plane remains flat relative to the original part. If the part moves during cutting, the direction of the cutting plane will change and invalidate this assumption. The part must be secured tightly enough such as to prevent this.
4. The cutting plane is a principal plane to otherwise there will exist in-plane shear stresses

Further assumptions and potential sources of uncertainty are described in the subsequent section containing a description of the experimental procedure (clamping, cutting and surface contour measurement).
Stresses in additional planes can be determined by a combination of performing additional Contour cuts and superimposing partially relaxed stresses from the initial Contour cut [254-256], although this advancement on the method has not been applied in this thesis.

A major advantage of the Contour Method is that stresses can be mapped for an entire cross section of a part with characteristics that can be problematic when applying alternative residual stress measurement techniques. For example, Contour Method has been applied for measuring parts containing material discontinuities, specifically welds, on numerous occasions [257-259]. Therefore this method appears to be a suitable approach for determining hoop stresses across a section of the AuCu brazed parts considered throughout this thesis.
The Contour Method approach has been validated multiple times by comparing Contour results with Neutron diffraction measurements, a more mature and academically/industrially accepted method [260-264]. A study conducted by Hill [265] has shown high levels of repeatability, with less than 20MPa variability for repeated measurement of a part with approx. 200MPa residual stress. Although neutron diffraction has limitations, such as the requirement to obtain the stress-free lattice parameter, it is a useful technique particularly for validation of bulk residual stresses as measured by Contour Method [67].

The Contour Method is a relatively young technique compared to more established techniques such as XRD or incremental hole drilling. As such there exists no guidance on best practice for Contour Method from establishments such as National Physical Laboratory (NPL), British Society for Strain Measurement (BSSM) or ASM (American Society for Metals) as is already in place for the aforementioned techniques. In order to ensure the best possible results were achieved for the work presented in this thesis, best practice guidelines were observed from a

document published by Open University [266] in addition to maintaining a consistent approach as that employed by experienced practitioners of Contour Method such as Prime and Hill [265, 267].

In addition to the assumptions stated previously, a further set of assumptions specific to the EDM cutting are summarised below and expanded upon in [267]:

1. Cut surfaces are not re-cut during the EDM process. This can happen to a minimal degree in compressive regions as shown in [267]. Secure clamping results in this effect largely being avoided.
2. Cutting width remains constant across the entire length of the cut. For a regular cross section, homogenous material part this effect is negligible. A change in cross section geometry or material can result in the cutting width varying, and bowing can also occur. For a part like the dissimilar material brazed specimens assessed in this thesis, this is a possible significant source of error. An uneven cut width introduces uncertainty when fitting the zero displacement plane during data analysis.
3. During EDM cutting no plasticity develops at the cut develops, idealized as a sharp crack tip. This can be largely mitigated by securely clamping the part on both sides of the cutting plane [266, 268, 269].

Due to the data analysis procedure, where both cut faces are measured and an average contour profile obtained, many potential cutting errors are canceled out. This is true for anti-symmetric (about the cutting plane) errors, but not for symmetric artefacts [267]. An example of this is shown in Figure 6-30.

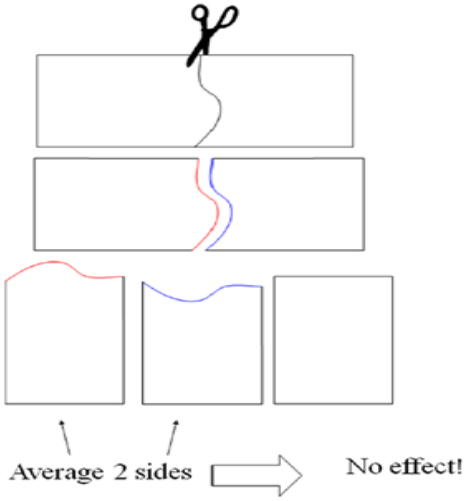

Figure 6-30 - The effect of a non-straight cut being cancelled out due to averaging of the two surfaces (recreated from [267])

The schematic shown in Figure 6-30 shows that if the cut is not straight, the result will be a straight cut following averaging of both surfaces. The surface contours due to stress relaxation will remain.

Conversely, if the error source results in a symmetric effect, the measured contour will be affected. This effect can be negligible, such as a wire breakage which can easily be removed during data cleaning and smoothing. Other errors can be more significant including change in cut width, wire vibration and bulging error. These errors are mitigated as best as possible by securely clamping that part and using appropriate cut settings on the EDM.

6.4.2 Contour Method – experimental procedures

The Contour Method experiments reported in this thesis were performed at AFRC, University of Strathclyde.

EDM sectioning was performed using an Agie Charmilles wire EDM with 0.25mm brass wire. "Skim" cut settings were used for cutting speeds, flushing parameters etc. This is in agreement with the vast majority of literature published containing Contour Method.

As discussed previously, securely clamping the part is critical to reducing errors in the experiment. In order to achieve this, it was planned to EDM drill a hole close to the end of each parent material, distant from the interface, and perform the EDM cut in three steps. This would involve cutting from hole to hole before removing the ligaments in the end. The effect of this would be self-clamping of the part during the first and most critical cut. This approach was shown to be

successful [269]. However in practice this could not be achieved. Drilling through tungsten material with the EDM drill was not possible with the equipment available. Secure clamping was therefore achieved through the configuration shown in the schematic in Figure 6-31.

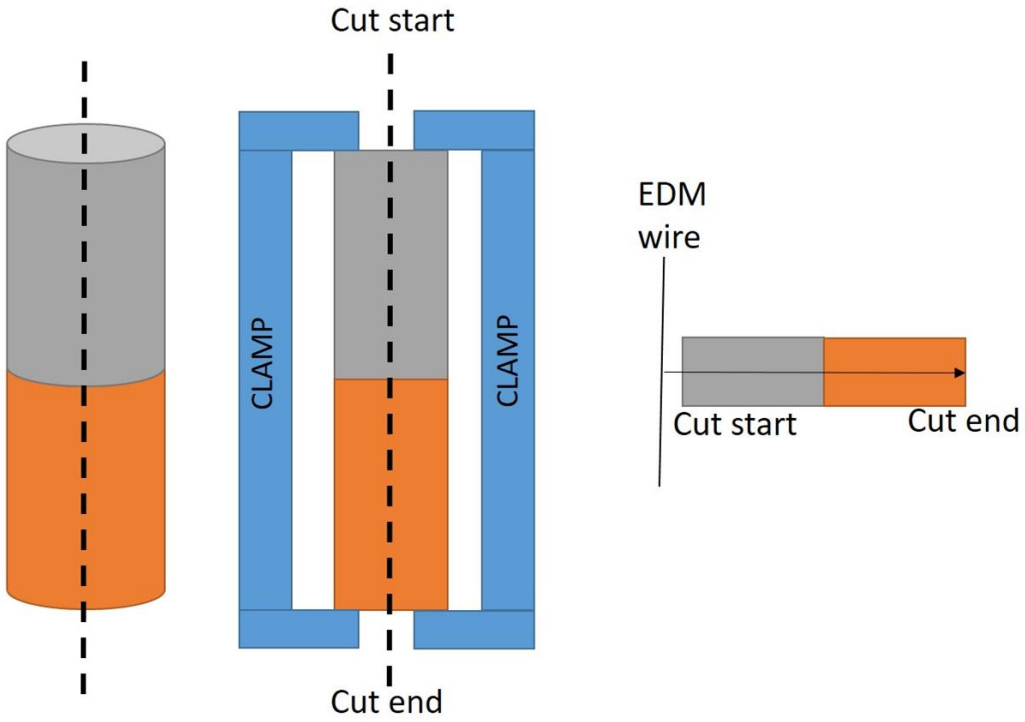

Figure 6-31 - EDM clamping arrangements for Contour Method sectioning of dissimilar material brazed parts

Following EDM sectioning each of the two cut surfaces were measured by CMM to obtain a point cloud representing the surface contours. Measurements were taken at 0.4mm spacing in both major dimensions. A Mitutoyo Crystal Apex C CMM with a 1 mm diameter Ruby attached to a Renishaw PH10T probe was used (shown in Figure 6-32). The measured point density was chosen in order to provide a rich enough dataset that short length scale stress profiles are captured, as are expected in the brazed parts from modelling and XRD surface residual stress results. The error associated with CMM measurements of the "hen peck" nature as utilised here are in the order of +/- 5µm. Individual "hen peck" measurements were used for this reason. Continuous measurements where the probe is dragged over the surface would return a denser dataset, however the experimental errors are known to be higher. For a small part which will exhibit lower magnitudes of absolute displacement, such as the brazed samples, reducing errors were identified as more important than obtaining more data.

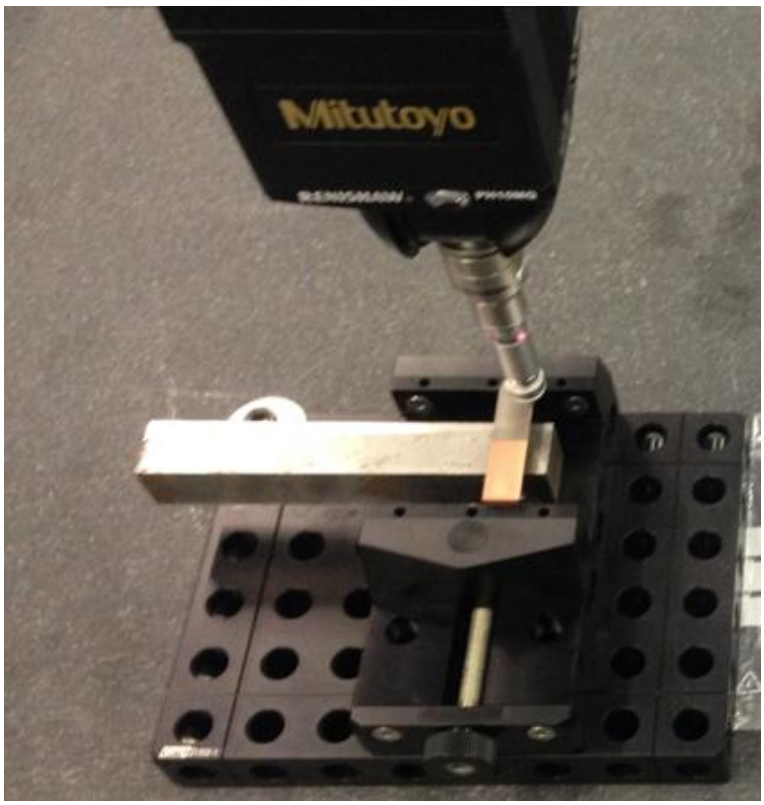

Figure 6-32 - CMM surface measurement of W-AuCu-Cu brazed part for Contour Method residual stress analysis

6.4.3 Contour Method – data analysis

The measured surface displacements are processed using a series of Matlab scripts prior to FE simulation to obtain the out of plane residual stresses. The Matlab codes used for the analysis were originally written by Greg Johnson of Manchester University [270] and are based on the principles introduced by Prime and discussed in section 6.4.1. The codes have since been added to and heavily modified by Salah Rahimi of AFRC, University of Strathclyde. The generous provision of the codes by Dr Rahimi, in addition to extensive training on the subject, were hugely appreciated by the author and crucial in obtaining the results presented here.

For each part measured using Contour Method, a multi-step data analysis process was performed. Firstly, the CMM data clouds for each two cut surfaces were plotted and cleaned (where necessary) using a Matlab script. Cleaning of the data includes removing spurious data points which can be caused by residue on the surface, a small scratch or dent, or points at the edge of the sample which were not cleanly contacted by the CMM probe.

The surface contours as measured by CMM for W-AuCu-Cu brazed part, 1A, is shown in Figure 6-33.

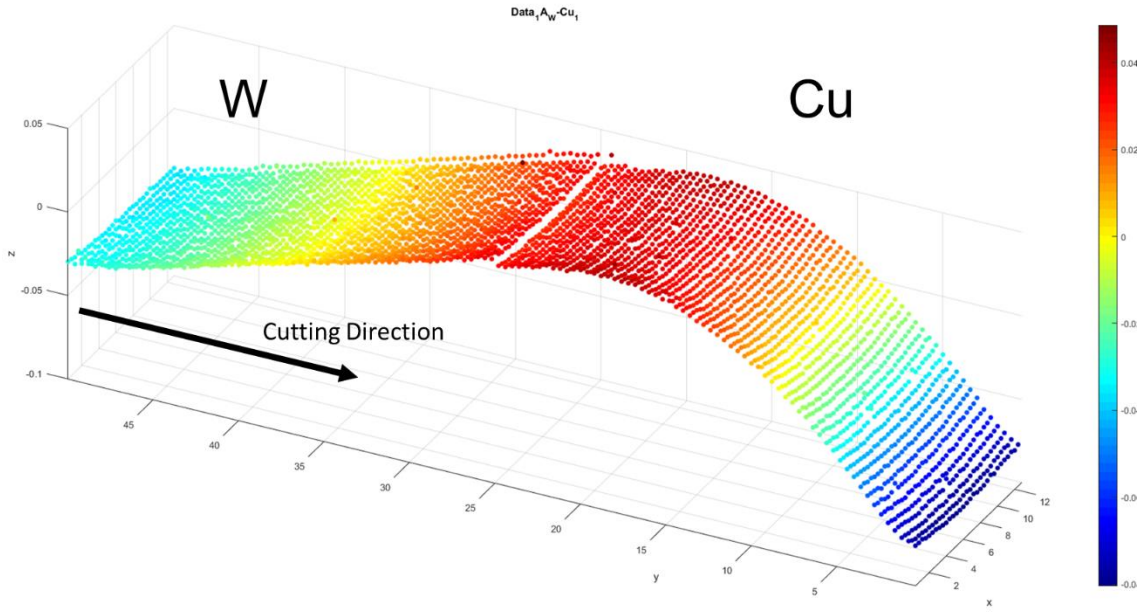

Figure 6-33 - CMM measured data cloud for surface contours of W-AuCu-Cu part (part ID 1A)

The tungsten part is shown on the left hand side of Figure 6-33, with copper on the right. The thickness of the AuCu braze interlayer is too small (<0.1μm) to be identified in the data cloud as the surface is measured in a 0.4x0.4mm grid.

It can be observed that there is large displacements of the copper towards the free end (opposite from the interface). This is likely due to the part "opening up" with respect to the cutting plane during the cutting process, introducing error into the stress calculation. The degree of opening can be seen in the sectioned tungsten-copper part shown in Figure 6-34. The two tungsten halves can be seen to be parallel as expected following a straight cut, whereas the copper halves noticeably diverge. It is recommended that the clamping strategy initially planned, described in 6.4.2, be implemented if a similar experiment were to be performed in the future.

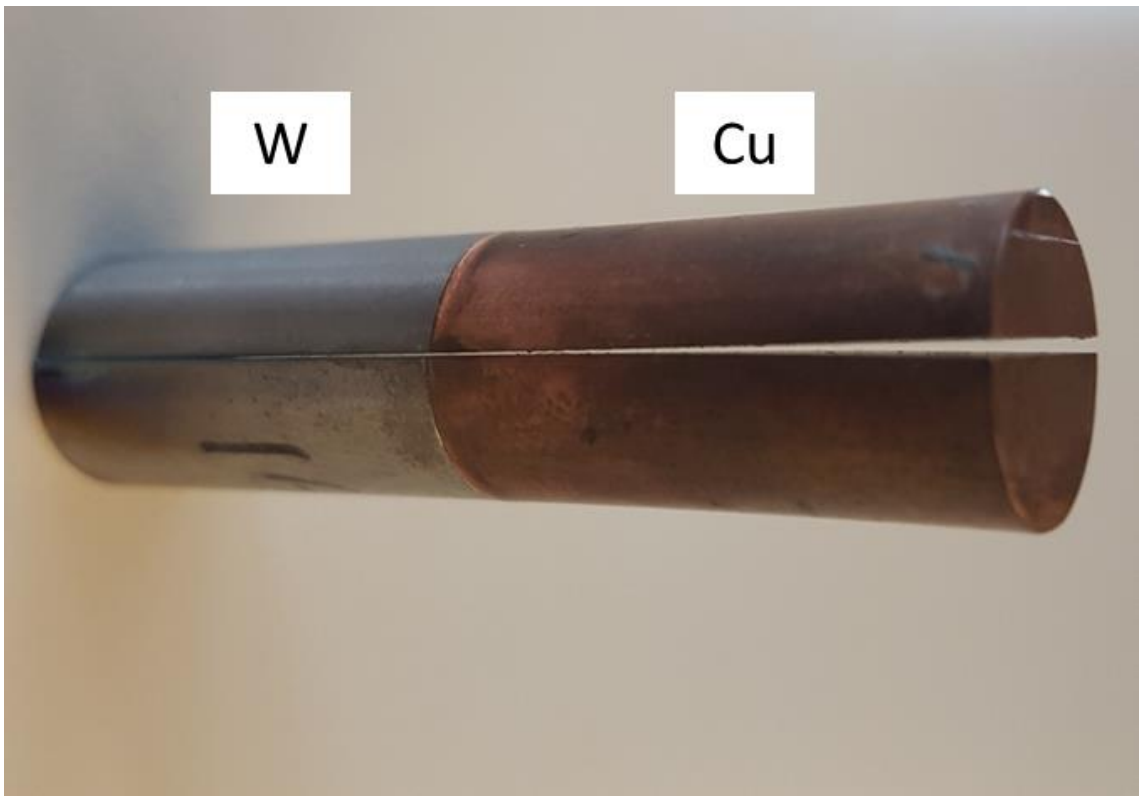

Figure 6-34 - EDM sectioned tungsten-copper part showing deflection of copper away from the cutting plane, "opening up"

A second W-AuCu-Cu part, namely 1E, was sectioned by EDM using tighter clamping. The resulting surface contours of one half is shown in Figure 6-35.

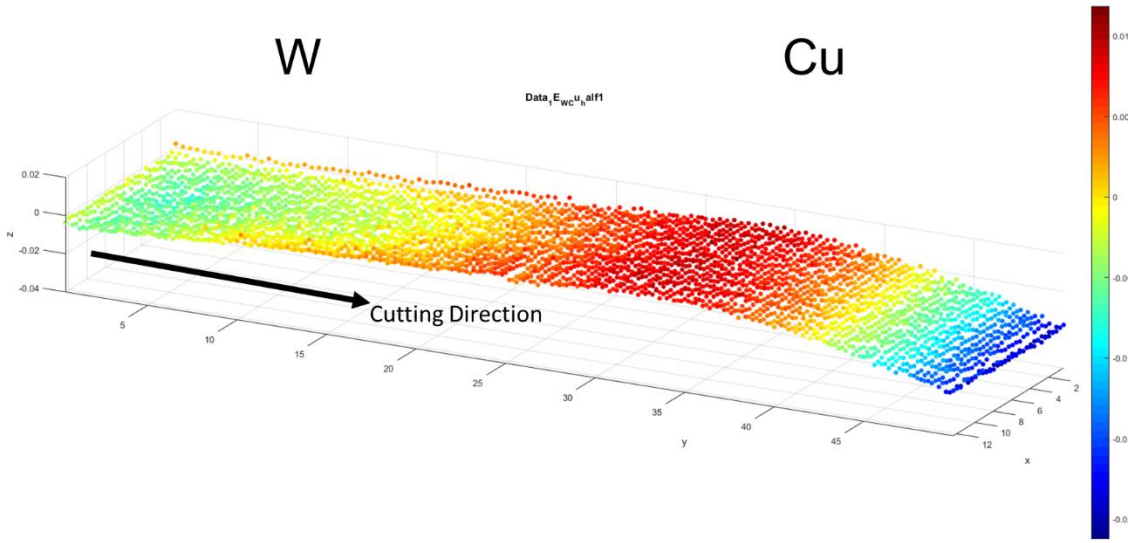

Figure 6-35 - Surface displacements of 1E (W-AuCu-Cu) showing improved clamping conditions

Improved clamping conditions for part 1E resulted in observably less plastic deformation of the copper side, which will result in a less erroneous stress result following completion of Contour Method data analysis. The maximum to minimum displacement was reduced from c. 100µm to c. 20µm which is more realistic value for a part with small dimensions.

With the data now "cleaned", the two cut surfaces are aligned to remove errors previously described and to define the zero displacement plane. The aligned surfaces for part 1E (W-AuCu-Cu) are shown in Figure 6-36.

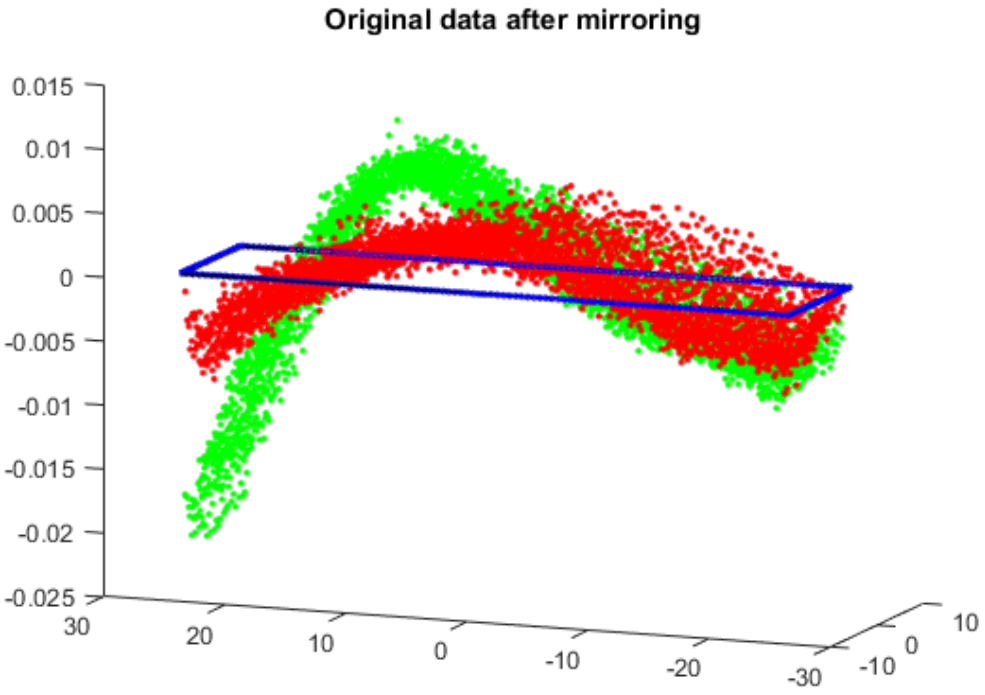

Figure 6-36 - Aligned surfaces for part 1E (W-AuCu-Cu) – dimensions of axes shown in mm

The tungsten surfaces (shown on the right hand side of Figure 6-36) show very good agreement with each other and lie on essentially the same profile. There is a difference in the measured displacements of the copper surfaces (left hand side). This is caused by insufficient clamping, with one side undergoing a degree of plastic zone developing during cutting. This could be reduced in future by employing the self-clamping using drilled holes as discussed previously.

In order to transform the displacement data clouds into a surface that can be applied as a boundary condition to an FE simulation, it is necessary to apply a surface fitting algorithm. Multiple approaches have been used for Contour Method surface fitting including Fourier transforms,

enhanced polynomials and bivariate splines. The work presented here uses a series of bivariate splines. The knot spacing of the splines is increased from very fine, 0.5mm knot, up to a relatively large 8mm knot spacing. Using a very small knot spacing results in overfitting of the data, with contours being fitted to noise within the measured data. This can produce erroneous results. Conversely, if the knot spacing is too sparse then real surface contours can go un-fitted and stress data is lost. For a small part like the one considered here a relatively dense spacing of 4.5mm per knot was found to produce the best trade-off between under and over fitting.

The result of surface fitting on the part 1E considered throughout this section is shown in for a 4.5mm bivariate spline knot spacing.

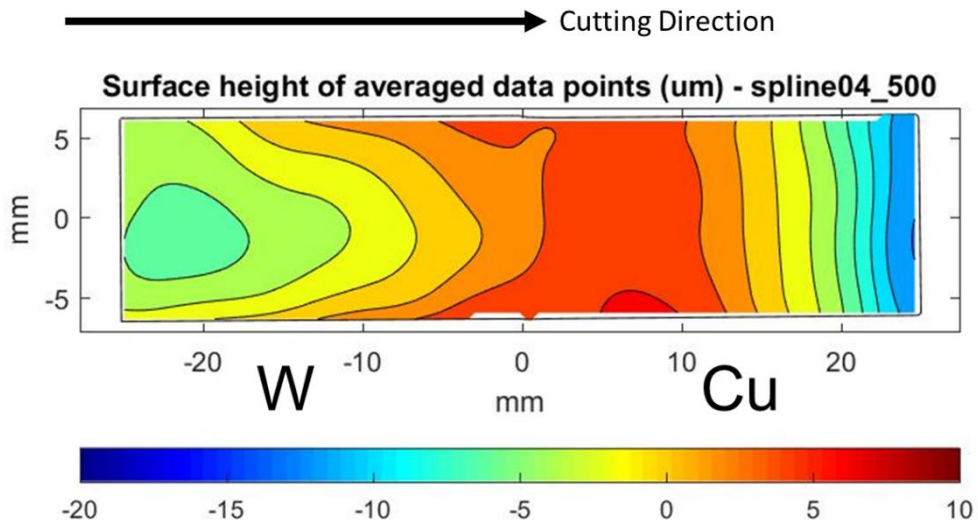

Figure 6-37 – Bivariate spline fit for surface displacement of part 1E (W-AuCu-Cu)

The AuCu braze interface can be seen at position 0mm on the x axis. Evidence of plasticity developing towards the end of the cut in Cu is apparent at the extreme right hand side of Figure 6-37, as was previously seen in Figure 6-35. Here the part has displaced away from the cutting plane on both sides of the plane. It is expected that areas in blue contour colours are very high in tensile stress, as this shows the part has distorted away from the cutting plane. Areas with red contours would therefore intuitively be compressive in nature, as a positive displacement from the zero-plane indicates that the part has closed in towards the cutting plane.

A 3D finite element model was then created that the measured surface contours could be applied to in the form of a predefined displacement in order to back-calculate the original stress state prior to sectioning.

The model was created using ABAQUS. The model was meshed with C3D20R element type. These are higher order twenty-node brick elements with reduced integration. Reduced integration was used to aid convergence considering displacements at certain locations are approaching plastic conditions where full integration would struggle to converge. This was the element type recommended by Abaqus CAE.

Mesh density is biased with a fine mesh at the cut surface and coarser mesh with increasing distance from said surface. A uniform grid of 0.4mm by 0.4mm was used on the cut surface for element size. Element depth is finest at the cut surface, 0.4mm, as shown in Figure 6-38. The elements representing the EDM cut surface are shown in red.

The mesh density was chosen to match the density of the measured CMM point cloud. From previous mesh sensitivity studies not presented here, practical experience and recommendations from literature [266], the element size should be smaller than 1/3 of the knot spacing (as cubic splines have three turning points) for first order elements. Considering quadratic elements are used here, and the knot spacings of interest are approx. 2.5mm at a minimum, then 0.4mm dimension for the element size is more than sufficiently fine to capture the displacement without losing data.

The simulation is fully elastic in nature (as dictated by Contour Method theoretical assumptions [252]). Therefore the only required material data is Elastic modulus and Poisson's ratio. For the three parent materials considered here (W, Cu, 316L) the values used are shown in Table 6-3

Table 6-3 - Material properties for Contour Method analysis

Material	Elastic Modulus	Poisson's ratio
W	400 GPa	0.28
Cu	117 GPa	0.33
316L	200 GPa	0.3

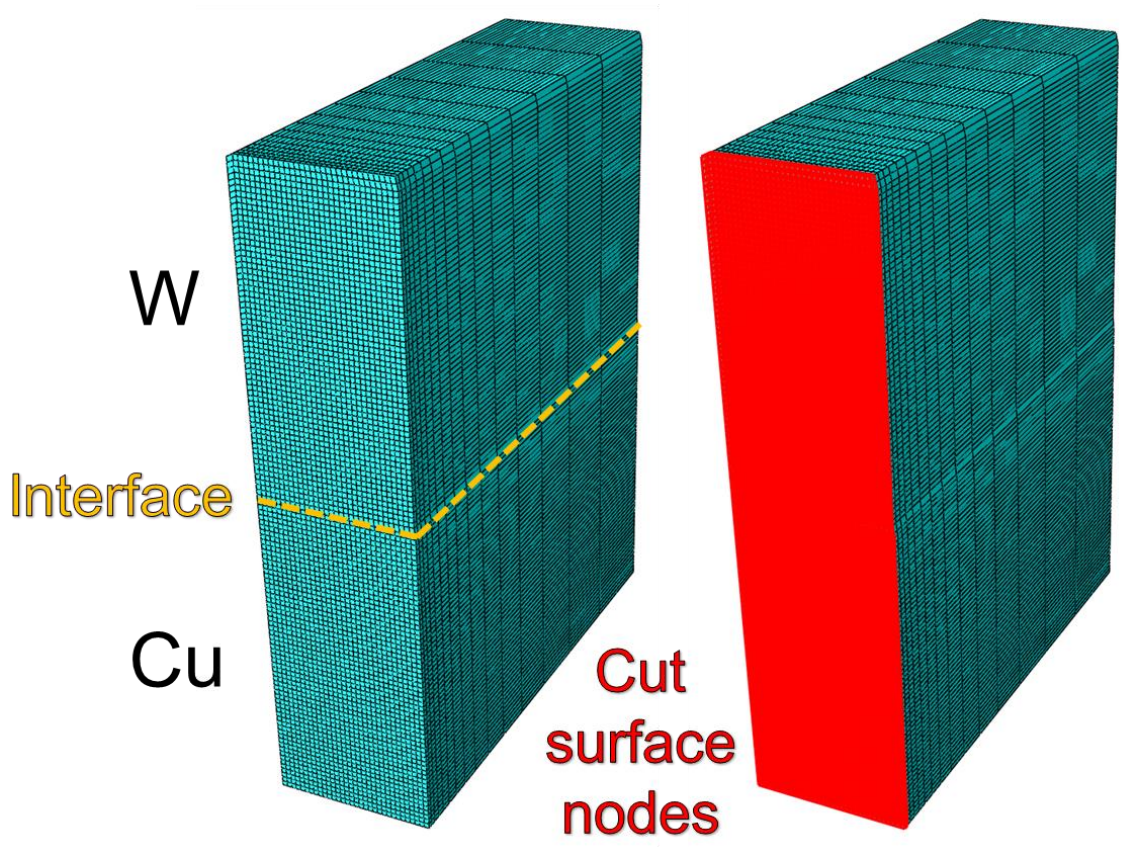

Figure 6-38 - ABAQUS 3D mesh of extruded cross section of W-AuCu-Cu brazed part for Contour Method. Showing braze interface (yellow) and cut surface nodes (red)

The cross section was extruded to a depth of 40mm. The extrusion depth was chosen so as that the stress field at the face opposite the cut face is of negligible magnitude as shown in Figure 6-39. This ensures that there is no effect from the bulk of the part on the stresses on the face of interest i.e. the stresses calculated are truly those resulting from the measured displacements with zero degree of unrelaxed stresses still in the model. This is" based on the 'die-away' length for a cosine distribution of stress applied to the edge of a semi-infinite plate" [266].

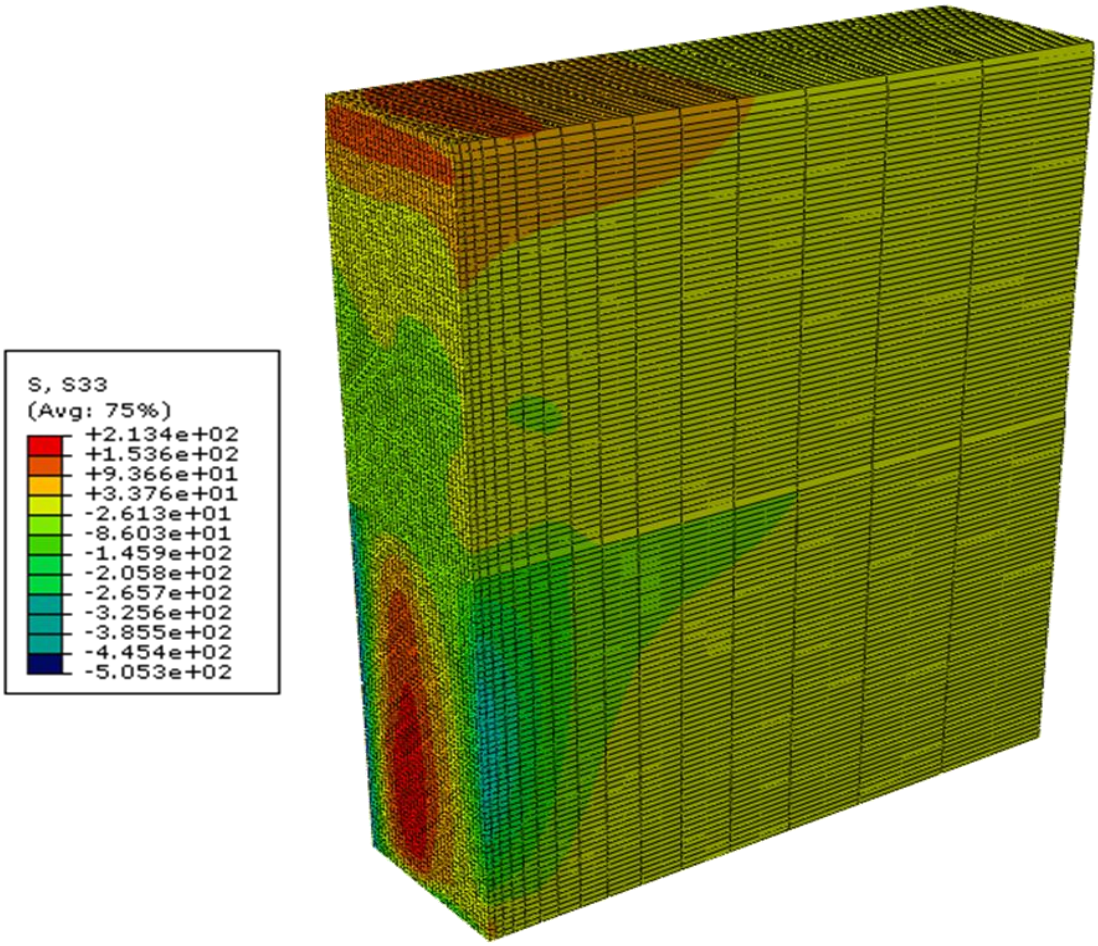

Figure 6-39 - 40mm extrusion showing depth of stress field

The boundary conditions for the model consist of fixing diagonally opposite corner nodes on the cut surface to prevent rigid body motion. Secondly, the measured surface contours are applied as fixed displacements. Instead of deforming the cut surface and forcing it back to zero-displacement, an alternative (less computationally expensive with identical results) approach is used. The measured contours are inverted, and the cut surface is deformed from flat to this inverse contour over the course of a load step, thus giving the original stress prior to relaxation. This approach is recommended by Prime who introduced Contour Method [252].

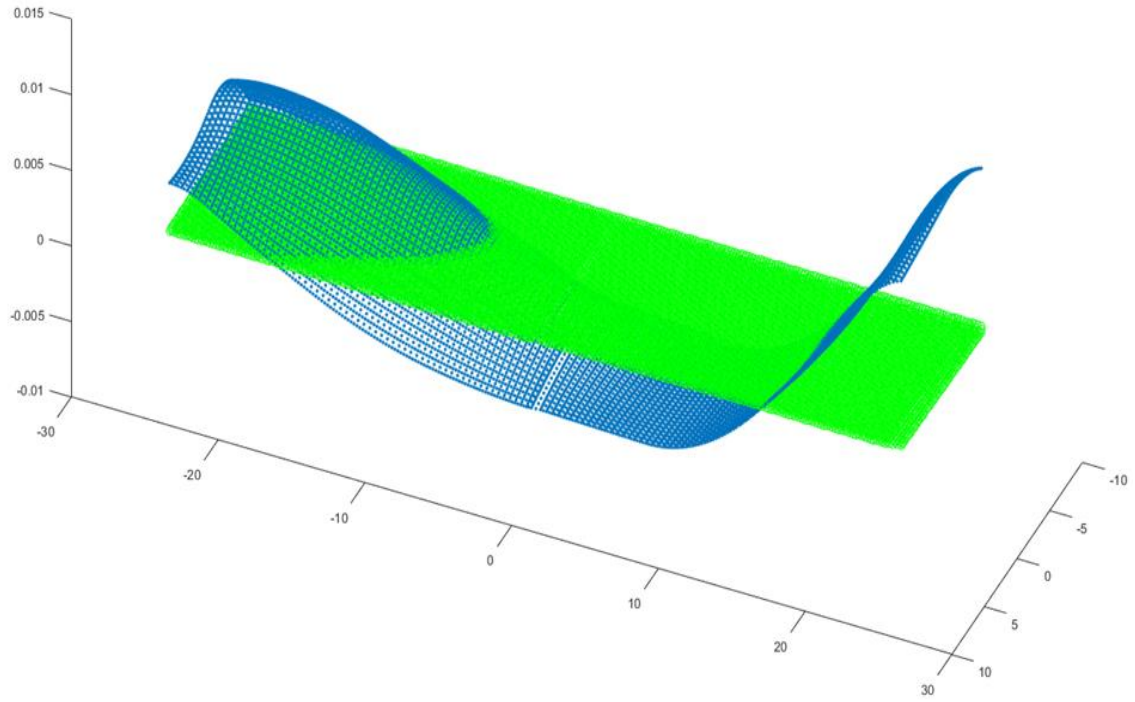

Figure 6-40 - Displacements applied to nodes representing cut surface for Contour Method. Showing undeformed nodes (green) and deformed nodes (blue) resulting from stress relaxation upon EDM sectioning

The displacements are applied by modifying an Abaqus .inp file using Matlab (codes for performing this created and provided by Rahimi, S). An example of the flat cut surface and displacement to be applied is shown in Figure 6-40.

6.4.4 Results

6.4.4.1 W-AuCu-Cu Contour Method results

The out of plane brazing induced residual stresses for a W-AuCu-Cu vacuum brazed part, specimen 1E as discussed throughout the previous section, are presented in Figure 6-41. Tungsten part is shown on the left hand side, copper on the right and the braze layer indicated by a dashed line. Residual stresses are shown in MPa. As the braze layer is not measured by CMM due to size limitations, the part is modelled with only two parent materials. As the stresses are calculated based on out of plane displacements, neglecting the braze layer will only have an effect immediately in the vicinity of the interface.

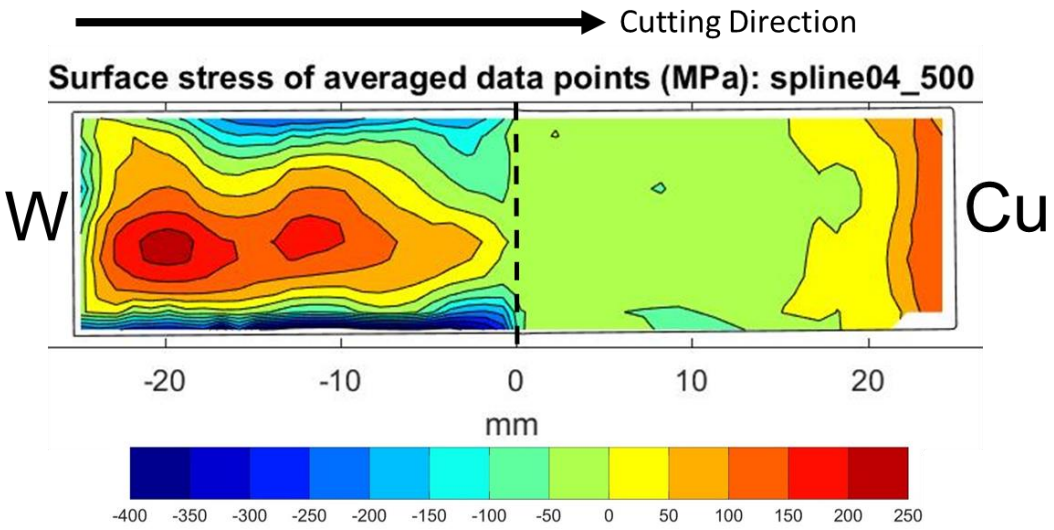

Figure 6-41 - Contour Method out of plane stress results for W-AuCu-Cu part (1E)

Figure 6-41 shows that largely speaking the highest magnitude stresses are found in the tungsten material. This is expected as tungsten has a significantly higher yield stress than copper. The copper part was found to be in mild compression close to the interface (approx. -50MPa) and mild tension towards the mid-length of the copper at 15mm from the braze interface (approx. 50MPa). Larger magnitude tensile stresses are found at the edge of the copper furthest remote from the interface. This was expected due to error introduced by plasticity developing during cutting where the part "opened up" in respect to the cutting plane. As the simulation considers only elastic conditions, the larger plastic-dominated relaxation will result in artificially high stress results in that area.

The tungsten material showed a tensile core with peak stresses approx. 250MPa. At the edges along the major axis (y-axis) high magnitude compressive regions exist.
The XRD results presented in section 6.2.3 showed high compressive hoop stresses at the free edge which would suggest reasonable agreement. However the length scale of the compressive stresses found from Contour Method (almost the entirety of the free edge) is much longer than measured by XRD (approx. 2mm) or predicted by FEA (approx. 5mm). It is therefore believed that the compressive stresses found at the free edge along the major axis are at least partially errors introduced during cutting. Bowing or cut width increasing at the centre region during EDM sectioning of the tungsten side could introduce errors of this nature.

A comparison of hoop stresses, i.e. out of plane stresses across the EDM section, as determined by FEA predictions and Contour Method measurements are presented in Figure 6-42 for the centreline through the part parallel to the major axis.

It was found that there were significant differences between FEA predictions and Contour Method results for the brazed W-AuCu-Cu part. This is similar to the comparison between FEA and surface XRD residual stress measurements (Figure 6-14). This indicates that the conclusion drawn for XRD results, that the brazing simulation FE model (Section 5.5.2) does not fully capture the complex material property and residual stress evolution for the W-AuCu-Cu system at the interface.

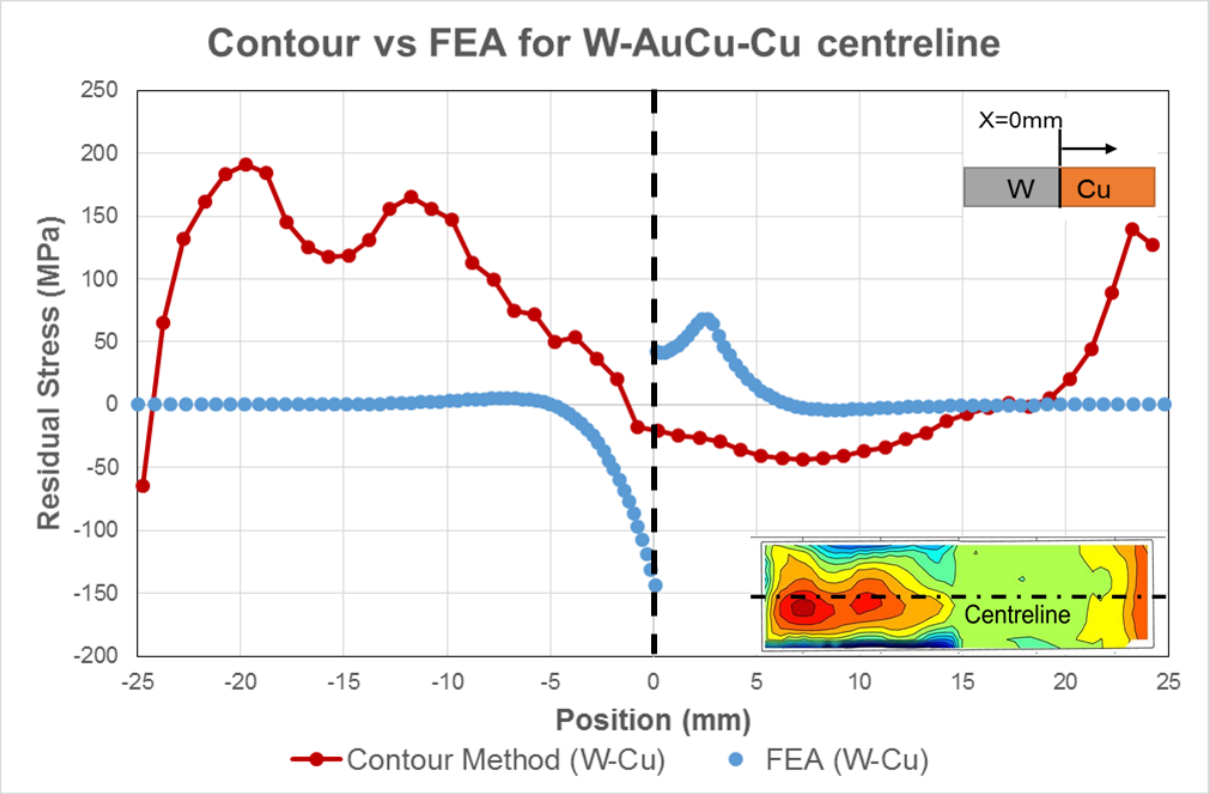

Figure 6-42 - Comparison of Contour Method and FE analyses of out of plane residual stresses through the centre of a brazed W-AuCu-Cu part (1E)

From Figure 6-42, the hoop stress measured by Contour Method in the bulk of the tungsten part is non-negligible, ranging between 50 to 200MPa. FEA predicts essentially zero stress. Although errors can be significant for Contour Method (+/-100MPa) as discussed in section 6.4.1, this still leaves the FE predictions outside of the uncertainty range from the Contour Method. This suggests that either the model contains errors or the experiment did.

Clamping was not considered during the braze simulation FEA (Chapter 5) as there was no accurate values available from the brazing process for clamping forces and conditions. The two parent materials, material of the clamps, and the phase and thickness transition of the brazing alloy means that predicting clamping conditions is a non-trivial exercise. A small clamping force was applied during earlier FE simulations but was found to have only a local effect at the clamped area. It is probable that the true clamping conditions are providing a degree of constraint not captured in the model, hence a variation in predicted and actual values.

To determine if the disagreement is down entirely to FE model, or a combination of FE and experimental errors, it is recommended that Contour Method experiments are repeated using

improved methodology not possible during this study due to resource and access to equipment. This would include performing a second, stress free cut. This would be a short distance from, and parallel to, the initial EDM cut. The out of plane stresses here should be essentially fully relaxed, and therefore the Contour Method results should be nominally zero. A deviation from this can highlight systematic errors introduced during cutting, and the errors calculated during this cut can be combined with the original cut Contour results to get closer to the true stress state. This approach is strongly recommended by the pioneers of the Contour Method, Hill [265] and Prime [267].

Additionally, a smaller diameter wire such as 0.1mm, and a bespoke clamping rig would improve the quality of the EDM cut and reduce errors in subsequent stress calculation by minimising crack tip plasticity at as cutting advances.

There is some agreement between Contour Method and FEA. Towards the interface compressive stress in the tungsten increases asymptotically. The degree of this is more severe and higher magnitude of stress in FEA than experimentally determined. The Contour Method calculation of stress is dependent on definition of an accurate zero-displacement plane. The definition of this plane is effected by the copper deforming during cutting. Were this effect to be removed, it is possible that the Contour Method profile in Figure 6-42 shifts closer to FEA predicted profile whilst retaining the a similar overall shape.

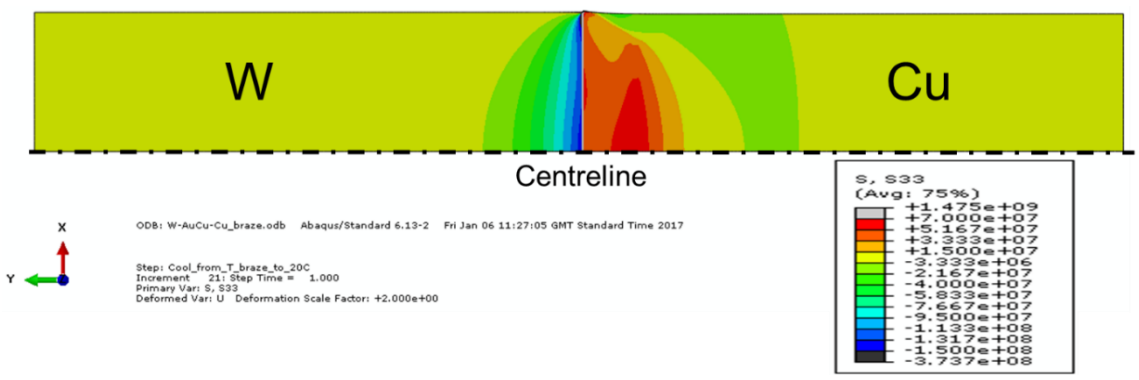

Figure 6-43 - FEA prediction of out of plane brazing induced residual stresses in W-AuCu-Cu part

The results of Contour Method for W-AuCu-Cu part are inconclusive for determining the validity of the FE model. Further work is needed to improve the assumptions included in the FE model.

6.4.4.2 W-AuCu-316L Contour Method results

The Contour Method results for the brazed W-AuCu-316L part (3B) are presented in Figure 6-45.The tungsten part is shown on the left hand side of the brazing interface, with 316L on the right hand side. The results presented are for a bivariate spline knot spacing of 3.5mm.

The data clouds generated by CMM measurement of the cut surfaces of part 3B (W-AuCu-316L) are shown in Figure 6-44. The surfaces shown have been mirrored, and for a typical case would overlay each other for a successful cut. What can be seen in Figure 6-44 is evidence of a cut that has gone off the centre plane i.e. a crooked cut. It is therefore clear that this cut was not performed under perfect conditions, either due to bulk movement of the part or difficulty of the wire erosion transitioning between materials.

This does not necessarily invalidate the measurement. The nature of the Contour Method allows for a crooked cut, as shown in Figure 6-30 and described in detail by Prime [252, 267]. As long as symmetric errors are not introduced, the asymmetry is averaged away when the surfaces are combined.

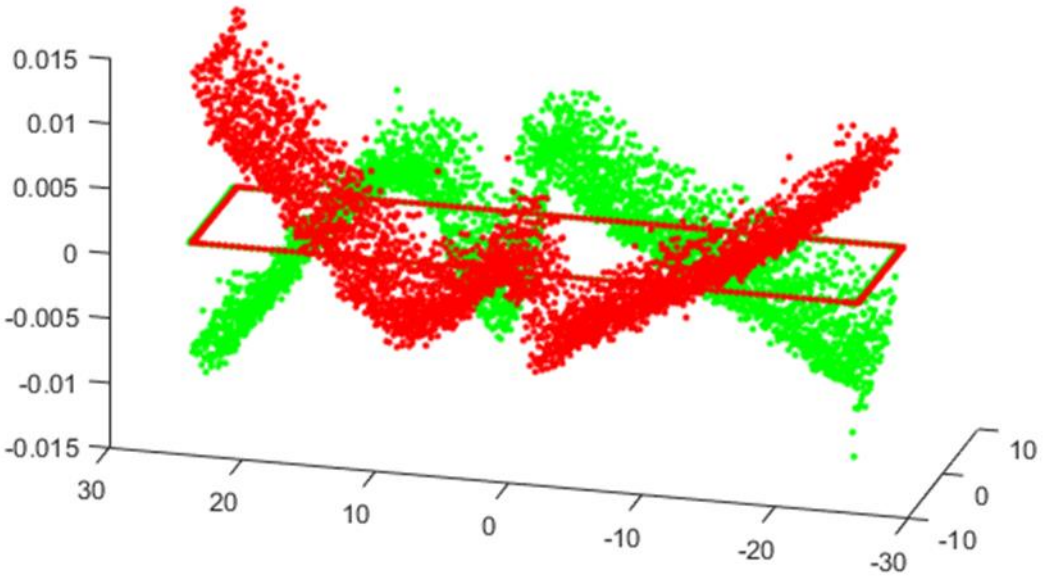

Figure 6-44 - Aligned surface profiles of sectioned part 3B (W-AuCu-316L) showing non-straight cut

In order to ensure that the surfaces shown in Figure 6-44 were indeed the true surface orientations and not a result of an error in data handling during CMM procedure, the surfaces were measured using Alicona and Atos GOM system [271]. These results, not presented here for sake of brevity, confirmed that the profiles were accurate.

The cut was then repeated at an industrial supplier on a similar part (part number 3C, W-AuCu-316L). 0.25mm wire and secure clamping on the flat ends of the part were utilised. The resulting surface profiles were similar in nature. From this it was decided that the initial part, 3B, was suitable for Contour Method. Part 3C was also assessed, although a wire breakage mid cut and difficulty restarting the cut degraded the results. As such they are not presented here.

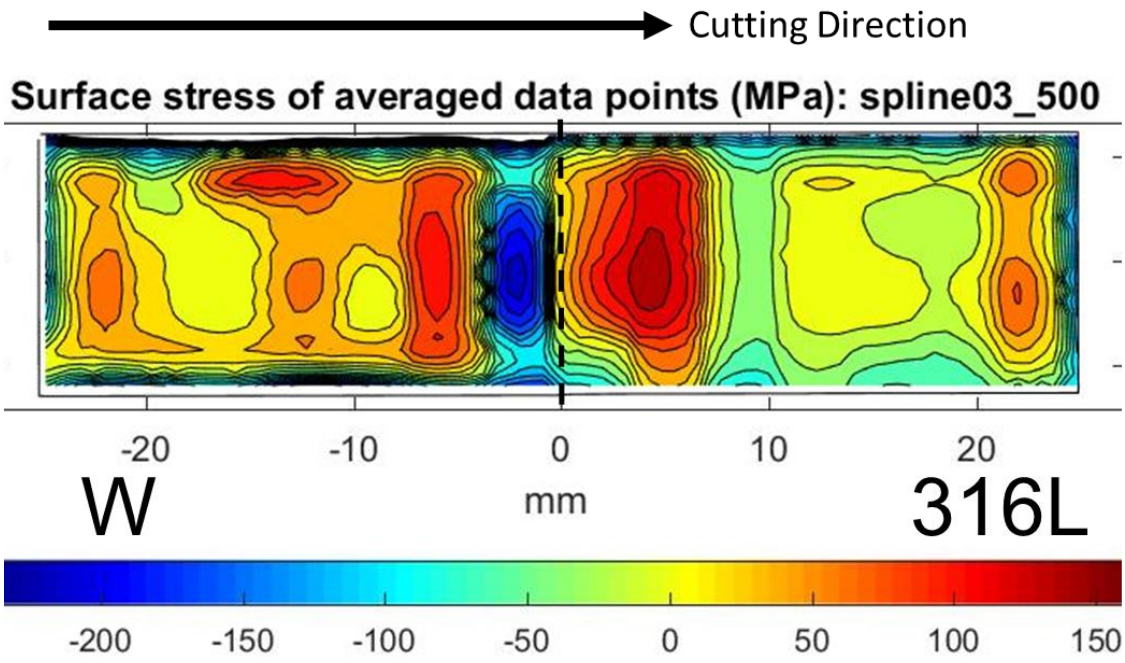

Figure 6-45 - Contour Method out of plane stress results for W-AuCu-316L part (3B)

Figure 6-45 shows a compressive region in the tungsten close to the brazing interlayer. This transitions to a tensile core in the bulk of the tungsten, although the stress values are low in comparison to the yield of the material; c. 100MPa in compared to over 1GPa. Along the free edge of the part, at both sides of the tungsten (top and bottom of the depiction) there are compressive regions. XRD results showed negligible stresses in this region, so there is an edge effect from the EDM sectioning method. This could be improved upon by using finer EDM wire diameter, improved clamping or sacrificial material.

The 316L part shows a relatively high tensile region close to the braze interlayer with 150MPa at a distance 7mm from the interface Figure 6-45. Further remote from the interface the hoop/out of plane stresses reduce to nominally 0MPa.

A comparison of FEA predicted and Contour Method measured hoop stress along the centreline for a W-AuCu-316L part are shown in Figure 6-46.

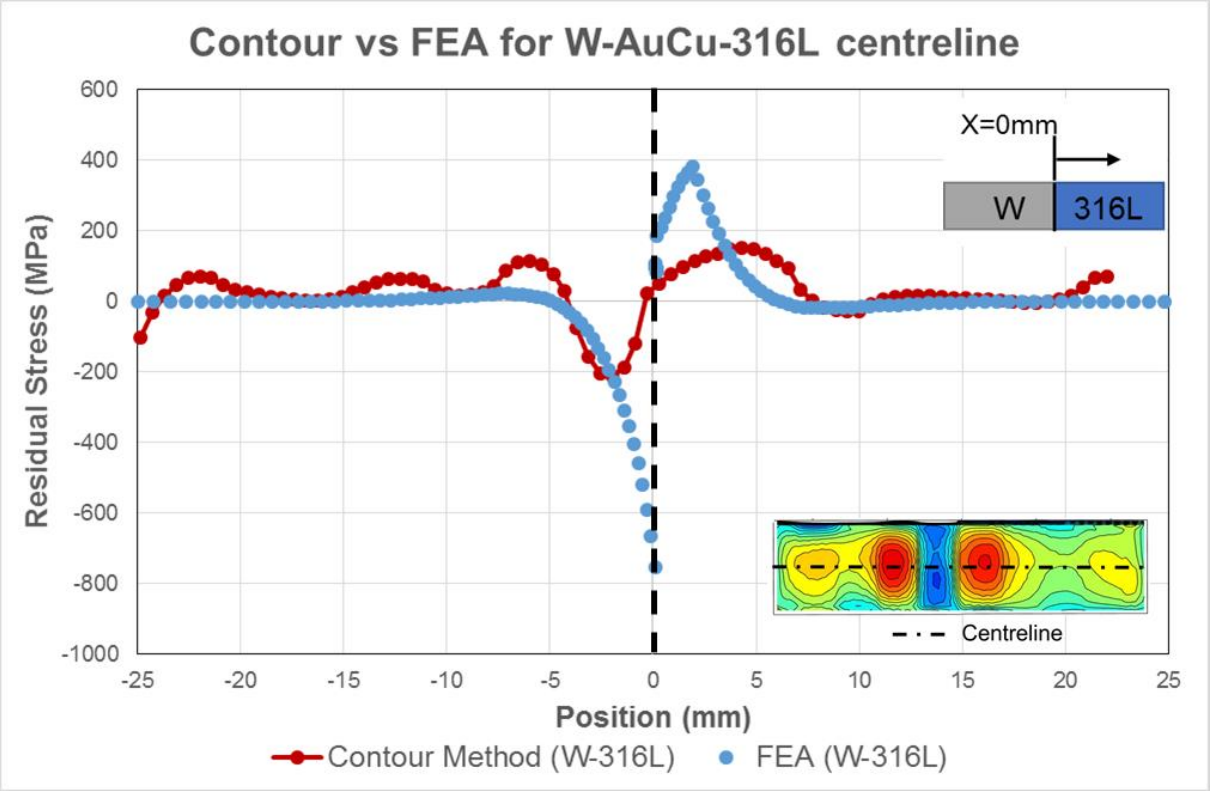

Figure 6-46 – Comparison of Contour Method and FE analyses of out of plane residual stresses through the centre of a brazed W-AuCu-316L part (3B)

In contrast to the W-AuCu-Cu comparison, the W-AuCu-316L comparison between FEA and Contour Method shows better agreement than the WAuCu-Cu configuration. The tungsten material is largely stress free until approx. 5mm from the braze layer where stresses increase and are compressive in nature. The predicted stresses are higher and do not peak and return to zero stress, unlike the measured stress. This indicates that stress relaxation occurs at the interface region that is not captured in the FEA model (Chapter 5). The overall trend in stresses in tungsten are generally closely matching.

In the 316L part there is also good agreement in the stress profile (Figure 6-46). The 316L material is nominally stress free until approx. 6-7mm distant from the braze layer. As the braze layer is approached, tensile stresses develop before a turning point is reached and stress returns to zero at the braze layer. There are differences in the profiles however; the profile of the curves are different and as with the tungsten, the peak tensile stresses measured are less than predicted (150MPa compared with 400MPa).

It can be concluded that the FE model is sufficiently accurate to predict the hoop stress distributions in the bulk of a brazed W-AuCu-316L part. Further efforts are required to optimize

the model, including better understanding of the material behaviour and properties, in order to more accurately predict magnitudes of residual stress.

6.4.4.3 316L-AuCu-Cu Contour Method results

The Contour Method results for the brazed 316L-AuCu-Cu part (part number 2C) is shown in Figure 6-47.

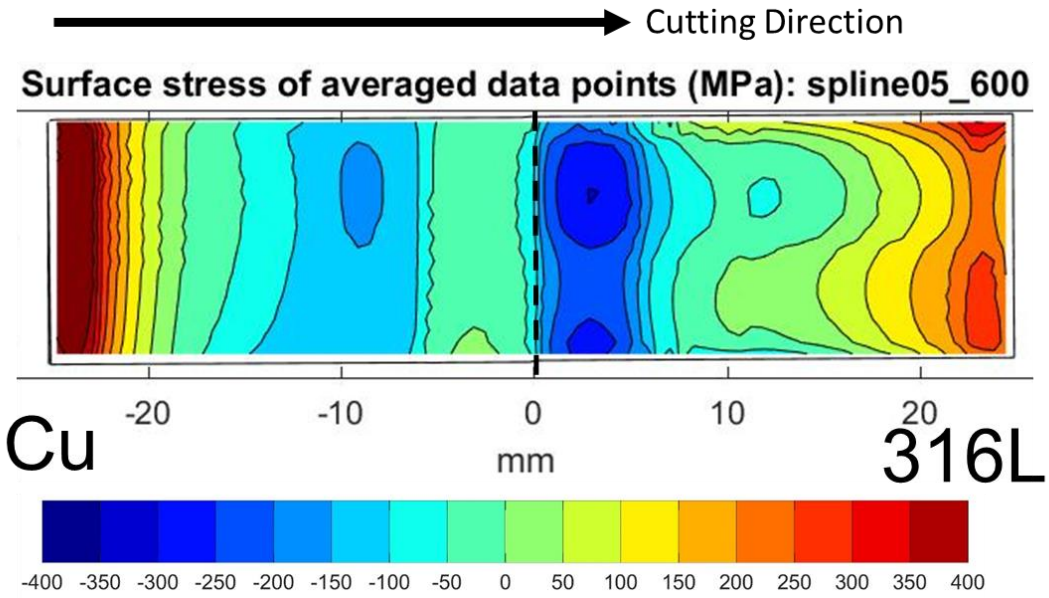

Figure 6-47 - Contour Method out of plane stress results for 316L-AuCu-Cu part (2C)

It is evident that similar to the W-AuCu-Cu Contour Method experiments, large degrees of plasticity develop during EDM sectioning in the copper material. This is shown by the excessive stresses calculated of 400MPa, whilst the yield strength is closer to 70MPa. The excessive deformation with regards to the cutting plane is similar to that shown in Figure 6-34. This distortion is likely to introduce errors into the stress calculation for the entire part, as determining the reference (zero displacement) plane will be negatively affected.

The results show a high compressive region in the 316L material close to the braze interface. Stresses in the copper are reasonable and compressive in nature close to the braze layer, in the range of -20 to -70MPa. However for the final 10mm closest to the end of the copper part (position -15mm to -25mm) there is clear influence from the cutting induced plastic deformation. There also appears to be some evidence of "opening" at the far end of the 316L part.

A comparison of FEA and measured Contour Method results for the 316L-AuCu-Cu part is shown in Figure 6-48.

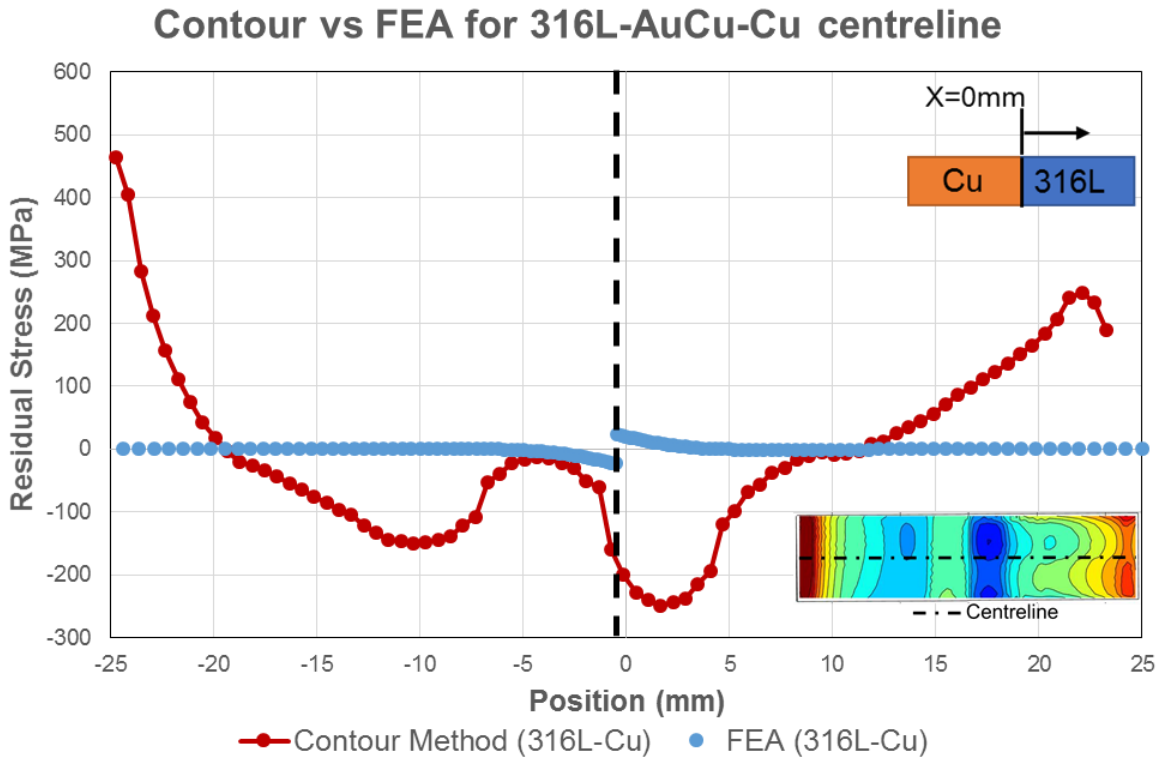

Figure 6-48 - Comparison of Contour Method and FE analyses of out of plane residual stresses through the centre of a brazed 316L-AuCu-Cu part (2C)

The FE model predicts negligible magnitude of stresses across the entire centerline of the part due to the similar thermal expansion properties of 316L and copper. This was found not to be the case when measured experimentally. However the magnitude of stresses calculated by Contour Method are over predicting the true values due to the effect of the copper deforming during sectioning.

Discounting the magnitude of the stresses, there is still poor agreement in the profile of the residual stress across the centerline. Further research, including improved clamping and cutting is required to better assess the validity of the FE model.

There is agreement at the free edge on the major axis of the 316L material for XRD measured hoop stress (Figure 6-21) and Contour Method measured stress (Figure 6-47). The magnitude of stress calculated by Contour Method is known to be erroneous, however both techniques show tensile hoop stresses distant from the braze layer.

6.5 Summary

Brazing induced residual stresses have been measured using three experimental techniques. XRD and ESPI incremental hole drilling have been used determine biaxial stresses at, and at a small depth from, the surface of the brazed parts. The Contour Method was utilised to measure the uniaxial, out of plane stress state across the entire cross section of the parts. Brazed parts consisting of the three material combinations discussed throughout this thesis have been evaluated, namely tungsten to copper, tungsten to 316L stainless steel and 316L to copper (all with Au80Cu20 eutectic brazing interlayer). Results have been compared with FEA predictions reported in the previous chapter of this thesis.

For brazed parts containing tungsten parent material, two contrasting outcomes were found for the two material combinations. Tungsten to 316L parts (W-AuCu-316L) showed good agreement for both surface residual stresses (XRD) and cross sectional hoop stresses (Contour Method) when compared with FEA results.
Conversely, tungsten to copper brazed parts (W-AuCu-Cu) showed poor agreement for free edge surface residual stresses close to the braze interface. Cross sectional hoop stresses measured also showed large areas of disagreement between predicted and measured values.

It was expected that high tensile stresses, increasing exponentially as the braze layer was approached, would be present in the tungsten for a tungsten to copper part. This was predicted by FEA and from literature when considering the resulting free edge residual stress given the relative values of elastic modulus and CTE.
When measured by XRD, the tungsten was found to have the high magnitude stresses, with asymptotic like increase towards the interface, however the nature of the stress was opposite than predicted. High compressive stresses were found at multiple angular rotations on a number of W-AuCu-Cu samples.
A number of explanations for this variation have been put forward in Section 6.2.6. These include:

- FE model not sufficiently capturing the plastic behaviour that develops during brazing. A bilinear kinematic hardening model is adopted in FEA which may not sufficiently describe the complex behaviour in the interfacial region. Presently strain hardening material data does not exist for the brazing alloy.

- Theoretical predictions from literature are based on a two material structure. The added complexity of a brazing layer with vastly varying properties at different temperatures is likely causing deviation from the predicted stress state.
- The FE model consists of three distinct materials (two base materials and an interlayer). In reality, interdiffusion of elements at the interface results in a more graded type structure as shown in chapter 3 of this thesis. In this region the elemental composition of the materials is varying and not readily available for implementing into a model. Future research into the effect of material property variation due to interfacial region diffusion, and the effect this has on bonding induced stresses, could help to shed light on the disparity between predicted and real stress values encountered here.

For the tungsten to 316L brazed parts the FEA and XRD results were in very close agreement in terms of the nature and magnitude of the brazing induced residual stresses. This suggests that the model is capable at predicting the resulting stress state following brazing for this material combination. Further research is required to improve the model for the tungsten to copper pairing.

Contour method results also showed high levels of agreement between the predicted and actual values for W-AuCu-316L brazed parts. The distribution of stresses were closely matching, however FEA over predicts the magnitude of the stresses. This is likely due to plasticity developing and subsequent relaxation of stresses that the FE model is not fully capturing.

Experimental measurement of stresses in the final material combination, 316L to copper, was not as successful as previous combinations. The results achieved from Contour Method were heavily influenced by deformation that occurred in the copper during EDM sectioning. However there was some agreement between predicted and measured cross sectional hoop stresses, with tensile stresses in the 316L transitioning to compressive stress as the interface is approached.

Determining a level of agreement between XRD and FEA results was inconclusive for this material combination. Measuring surface stresses by XRD was not possible in copper due to the nature of the material (grain size particularly) following brazing.

At the free edge of the 316L to copper parts there was good agreement between XRD, Contour Method and FEA results for the hoop component of stress. A compressive peak stress was found by all methods.

The final measurement technique utilised was ESPI hole drilling. Unfortunately the dimensions of the brazed parts, in addition to difficulties securely clamping the part and stresses too close to yield stress in copper, resulted in invalid measurements. For future trials an alternative geometry, both larger and flatter surface, is recommended for the purposes of ESPI hole drilling measurements. This would allow experimental validation of XRD results in the near surface region.

The results presented here show that the stress state in tungsten-Au80Cu20-316L brazed parts is well understood and can be both predicted and accurately measured. This knowledge can be used when designing components, such as divertor tiles, where this material combination is likely. A thorough knowledge of the residual stress state is critical when predicting loading and lifing conditions.

7 Residual stress modification by thermal autofrettage

7.1 Introduction

It is a well-known fact that residual stresses have a significant influence on the lifetime of a component, particularly in regards to fatigue performance in brittle materials [272]. It therefore stands that the lifetime of a component subjected to cyclic loading can potentially be improved by careful control of residual stresses in critical areas [273].

In the preceding sections of this thesis the residual stress state in brazed dissimilar material joints was predicted and measured. The material combinations investigated herein: tungsten-copper and tungsten-316L stainless steel, are relevant for the divertor component of a future fusion reactor such as DEMO [26]. A key performance requirement of the divertor is good fatigue performance in order to minimize plant downtime [29, 72]. Therefore if the residual stress distribution at the dissimilar material joint could be improved, it is likely that the performance of the divertor can be enhanced.

In this chapter the residual stress state within Au80Cu20 brazed tungsten-copper, tungsten-316L and 316L-copper parts have been modified through a process called thermal autofrettage [199, 274]. Following vacuum furnace brazing, the dissimilar material parts are cooled cryogenically in a liquid Ni cask. Constraint provided by the differential thermal expansion/contraction of the parts results in plasticity developing at the interface. Upon returning to ambient temperatures, the plastic deformation followed by elastic unloading causes a permanent change to the residual stress distribution.

The thermal autofrettage (TAF) process of the brazed parts has been simulated using FEA (section 7.4). The real residual stresses have been measured experimentally using XRD and the Contour Method (section 7.5 and 7.6 respectively).

The significance of the residual stress modification and the potential application of these results for improving the performance of a divertor tile are then discussed.

7.2 Thermal autofrettage background

There are many methods of beneficially modifying residual stresses through a loading/un-loading, i.e. autofrettage, process. Traditionally the most common approach was through mechanically yielding the material on the inner bore of a thick-walled cylinder by applying a hydrostatic pressure. This process was introduced in 1907 by Col. L. Jacob of the French Artillery [275]. The inner bore of gun barrels were over pressurized in an attempt to improve the firing range of the artillery [276]. It was found that these guns lasted significantly longer than untreated parts, as cracks were suppressed and hence delaying fracture. As such the idea of mechanically overloading a structure to introduce beneficial compressive residual stress.

This process has many uses including pipes, thick walled cylinders and pressure vessels for petrochemical and nuclear applications [277-280]. In addition to pressurizing cylinders and pressure vessels, a number of alternative autofrettage techniques have been developed. Thermal autofrettage utilises a geometrical incompatibility upon heating/cooling caused by differential thermal contraction, and as such upon removal of the ΔT, existing residual stresses as a result of previous processing have been modified. This technique has been explored for both thick-walled cylinders [274, 281-283] and solid dissimilar material cylinders [199].

Similarly, the effect of differential thermal contraction upon application of a ΔT to autofrettage a component has been utilised through weld cladding of hollow cylinders [284] and by combining both weld cladding and traditional pressurization of a cylinder [285].

The autofrettage principles, namely loading, material yielding and subsequent unloading have applied using rotational velocity to achieve rotational autofrettage [286].

The method of residual stress modification that has been applied in this work is thermal autofrettage. An overview of the theory of thermal autofrettage is given below. A more detailed discussion on the mechanics of constraint during the process is presented in previous works published by Hamilton et. al. [199, 208].

The process of thermal autofrettage is performed in this instance by subjecting the entire part to a temperature below ambient conditions. Liquid Ni is suitable for this purpose. Due to the difference in CTE and elastic moduli of both parent materials and brazing alloy, there is additional constraint applied at the interfacial region.

During this process, the stress at the braze region exceeds the yield of the material due to the local stress concentration provided by the geometrical and material discontinuity at the interface. When the part is returned to room temperature, elastic unloading of the material occurs. The result is a change in the residual stress prior to plastic deformation. This process is shown in Figure 7-1 for the more simple case of a beam in bending, with a bending moment of 1.5 x yield applied Figure 7-1.

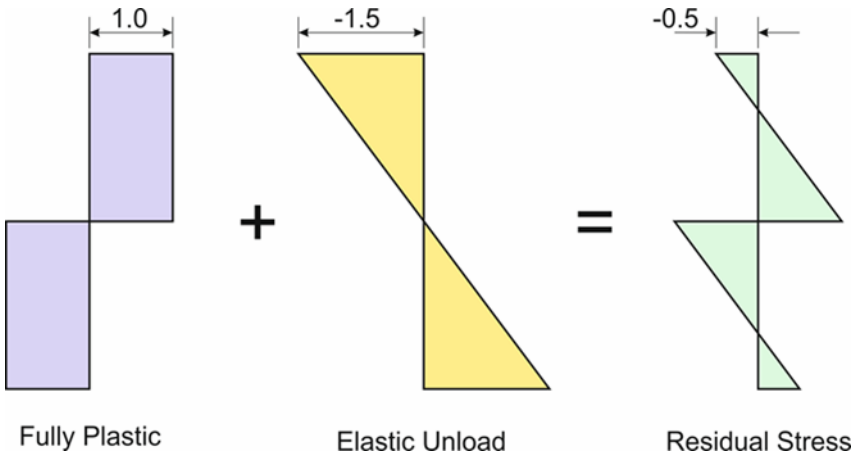

Figure 7-1 - Stress distribution across a beam in bending with applied moment of 1.5 x Myield [199]

Figure 7-2 shows a schematic of the change in geometry due to different CTE values for each material for a W-AuCu-Cu brazed part. Also shown is the temperature history throughout the autofrettage process.

At condition (a) the part is bonded by vacuum brazing at the eutectic temperature of the brazing alloy. The parts are considered stress free. The diameter of the copper is larger than tungsten due to a larger CTE. The parts are then cooled to room temperature at (b). Due to restriction of thermal contraction of the larger CTE copper, the free edge of the copper becomes compressively stressed, with tensile stress developing in the tungsten. A small plastically strained region develops at the interface. This is shown in Figure 7-3 (recreated from [199] where tungsten is analogous to material 2 and copper is analogous to material 1).

When cooled to -196°C in (c), the stress in the region increases. Tungsten becomes more tensile in nature, and compressive stresses in copper increase also. Due to the higher magnitude of stresses, further plasticity is developed. This is equivalent to the over loading moment applied in Figure 7-1 which also causes plasticity.

The part is then returned to room temperature in (d), effectively unloading the materials. Due to elastic unloading, the magnitude of stresses are at worst reduced. At best it is possible to reverse the sign of the stress such that the tungsten material is in compression.

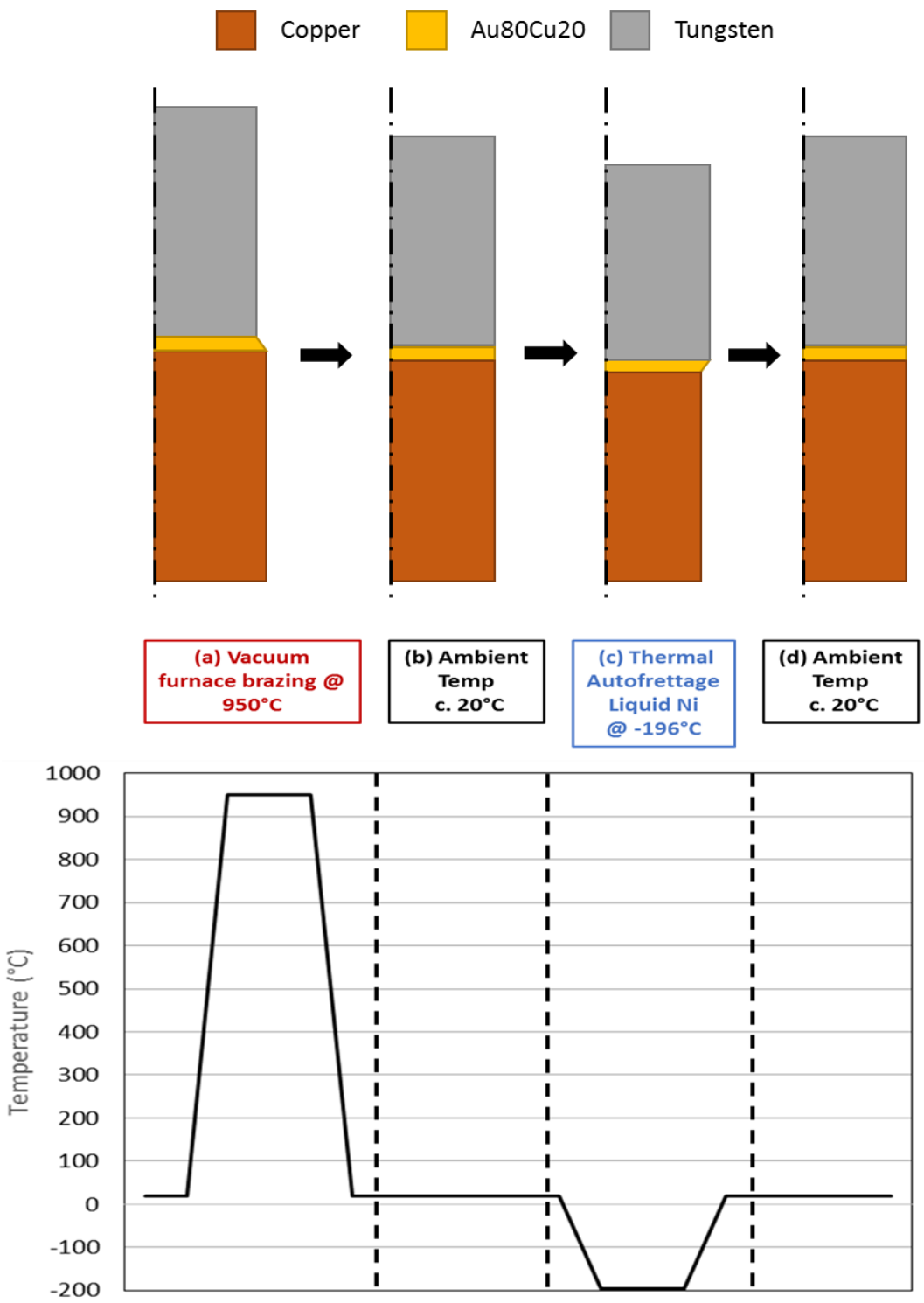

Figure 7-2 - Temperature profile and geometry evolution during brazing and thermal autofrettage of W-AuCu-Cu part

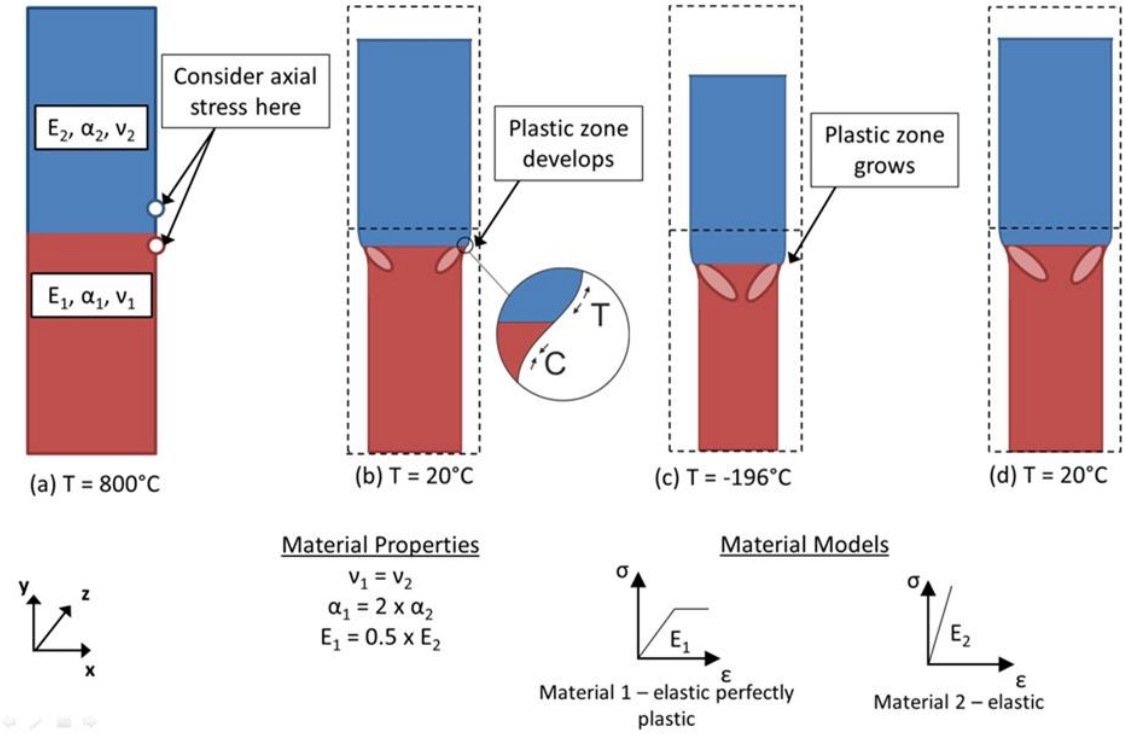

Figure 7-3 - Development of plastic region during thermal autofrettage process [199]

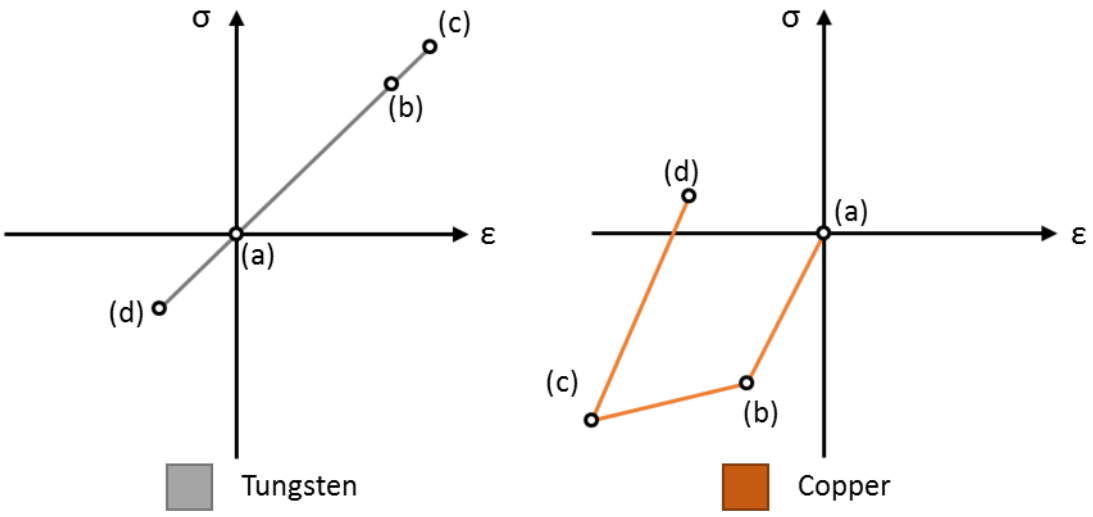

Figure 7-4 - Stress-strain history during brazing and thermal autofrettage at the free edge of a tungsten-copper dissimilar joint

The theoretical strain history of tungsten and copper throughout the thermal autofrettage process is depicted in Figure 7-4. Considering first the tungsten (grey). At initial bonding (a) with $T=T_{Braze}$, the free edge axial stress is zero. Upon cooling from brazing at (b) T=20°C there is a tensile stress developed. At cryogenic conditions (c) T=-196°C there is an increase in tensile stress. This

is followed by a reduction in stress magnitude, or in this case change to small compressive state, during unloading and returning to room temperature (d) with T=20°C.

The copper material was shown to be at yield stress following brazing, at (b), in section 6.2.2. The copper then deforms plastically from (b) to (c). Upon unloading the compressive stress is reduced in copper, and in this case to the extent that a small tensile stress exists.

The degree of plasticity developing, and therefore the effectiveness of the thermal autofrettage process was investigated in an FEA study in [208]. It was found that should the braze layer exhibit an elastic-perfectly plastic response, that theoretically full removal of the free edge residual stresses could be achieved. Of course in practice a real braze alloy will exhibit some degree of strain hardening. However by using a brazing alloy with as close to elastic-perfectly plastic behaviour as possible, the effect of thermal autofrettage can be enhanced.

7.3 Experimental procedures

7.3.1 Cryogenic soaking

Thermal autofrettage was performed by soaking the brazed parts in liquid Ni at -196°C. This acts as the loading phase of the autofrettage process. After sufficient time at cryogenic temperatures, i.e. the brazed specimen reaches a uniform temperature equal to that of the media, the parts are removed and warm to room temperature. This acts as the unloading phase of the autofrettage process.

Previous work utilizing this method developed the procedures for performing the cryogenic treatment [199, 208]. The parts were encased in an insulating foam block with a hole removed to make room for the sample (Figure 7-5). The insulated block and part were then protected by PVC wrap to protect the sample from direct contact with the liquid Ni. This was done to minimize the risk of thermal shock, which could initiate micro cracks or propagate existing micro cracks further if there was damage from previous processing.

The parts were then submerged in a canister containing Ni at -196°C. A tungsten rod was secured to the outside of the insulated part to ensure full submersion in the liquid (Figure 7-5).

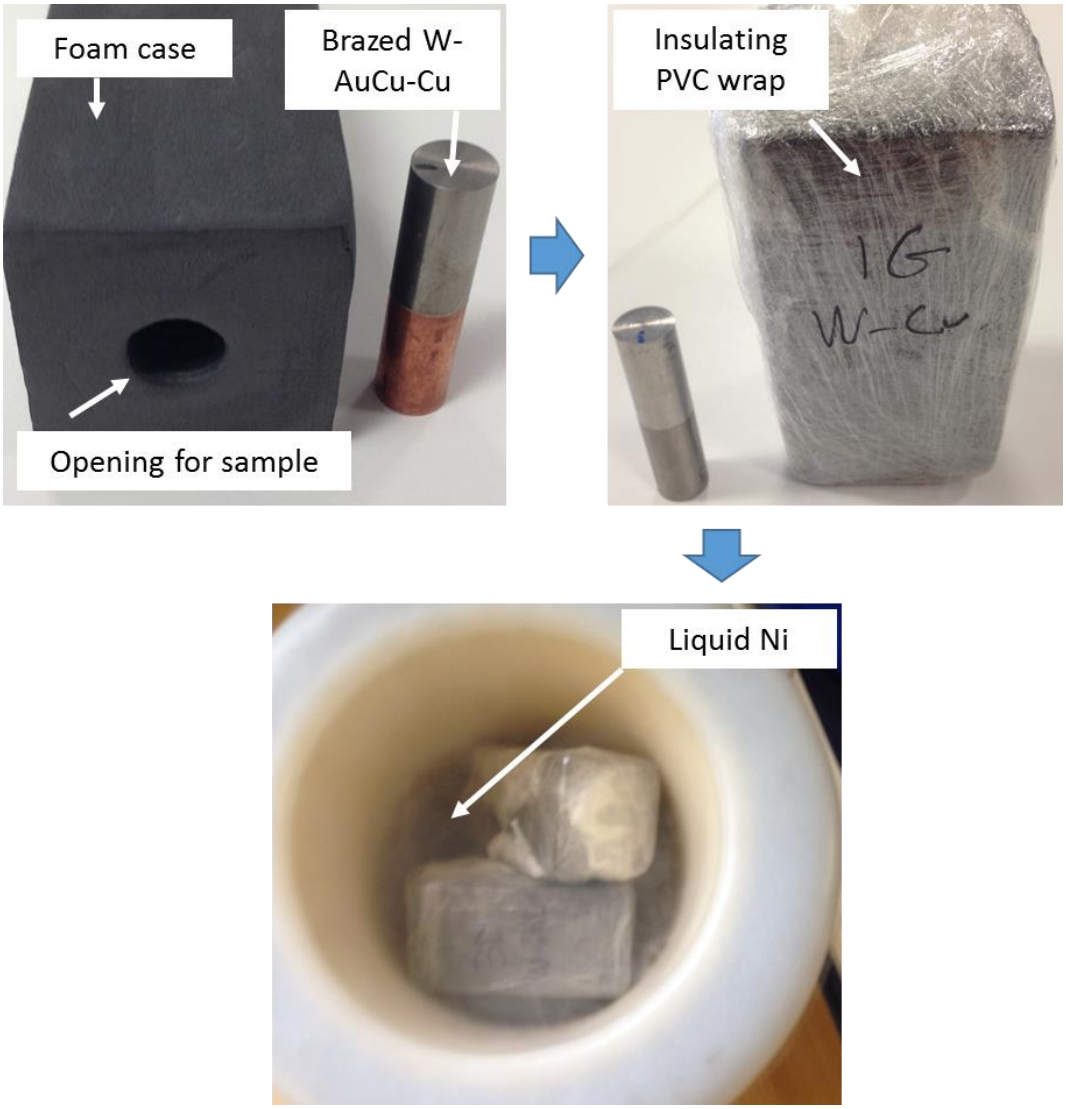

Figure 7-5 - Experimental set-up for thermal autofrettage through cryogenic cooling. Showing opening for sample in insulating polyethylene foam (top left), PVC wrap to protect sample from direct liquid Ni contact (top right), insulated samples submerged in Ni

In order to ensure a uniform temperature of -196°C was reached within the part, the cryogenic storage was performed for a minimum of 8 hours. A previous transient thermal FE analysis [208] showed that for ideal conditions, namely perfect contact between cooling media, insulation material and the brazed part, a cooling rate of 12°C would ensure a uniform temperature of -196°C after c. 1 hour. However when accounting for the possibility of retarding factors to cooling rate, such as air pockets within the insulation set-up, would prolong uniform temperature distribution being achieved. Assuming a worst case scenario of 1mm air gap around the entire sample the required soaking time raises to c. 8 hours [199]. Therefore an experimental cooling

time of 8 hours was deemed to be a conservative approach and removes the risk of not achieving the desired uniform temperature.

7.3.2 Sample inspection

The samples were inspected for thermal autofrettage induced damage upon removal from the liquid Ni. It is known that large thermal gradients imposed on dissimilar material metallic and ceramic parts can cause thermal shock induced cracks [287-289]. Studies have further shown that tungsten is susceptible to thermal shock induced cracking [290]. Therefore it was necessary to ensure the measures described previously taken to avoid a sharp cooling rate, and possible thermal shock, had indeed been sufficient.

The inspection procedure consisted of an initial macroscopic examination immediately upon removal from the cryogenic cask. No samples that were treated with the thermal autofrettage process were found to exhibit obvious signs of damage.

A more detailed inspection was performed using stereo microscopy. The results of this analysis are shown in Figure 7-6, with W-AuCu-Cu shown in (a) and W-AuCu-316L in (b).

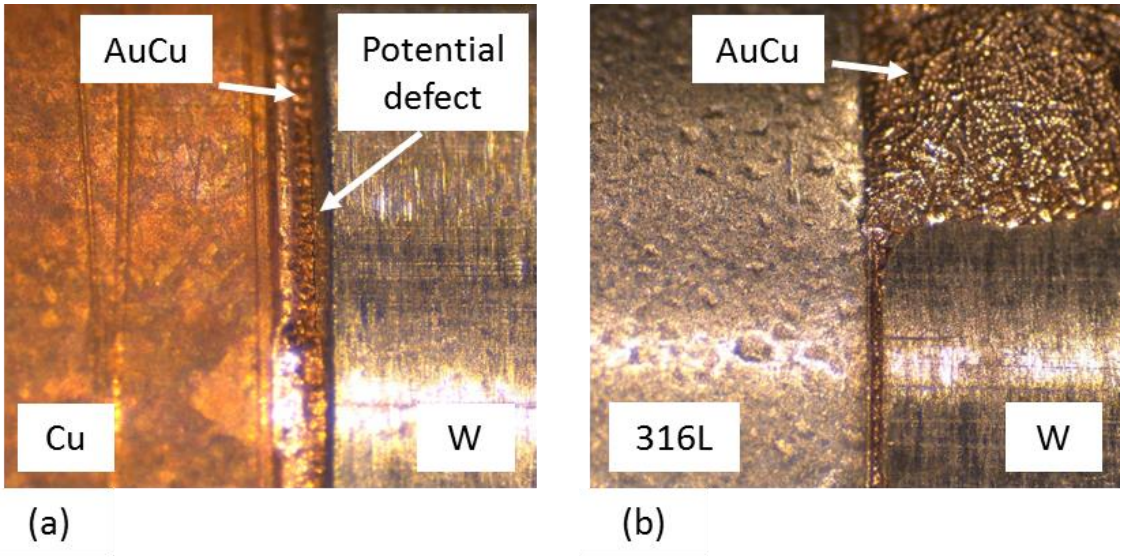

Figure 7-6 - Stereo microscope inspection of as-thermal autofrettaged (a) W-AuCu-Cu and (b) W-AuCu-316L

Making a conclusive determination of whether thermal autofrettage induced cracking occurred proved to be difficult. At the interfacial region, there is a geometrical discontinuity, uneven braze

material surface and existing imperfections on both parent materials. The need for accurate NDE is as such further highlighted and is recommended in for future work.

There are noticeable imperfections at the braze interfaces in (a), although it is not clear if they are cracks. In (b) there was no noticeable cracks at the either the tungsten-Au80Cu20 or 316L-Au80Cu20 interfaces. However at a later date (approx. 6 months) following thermal autofrettage, a tungsten-316L sample fractured completely. The part was awaiting EDM sectioning for Contour Method residual stress measurement when it was found to be fractured, as shown in Figure 7-7.

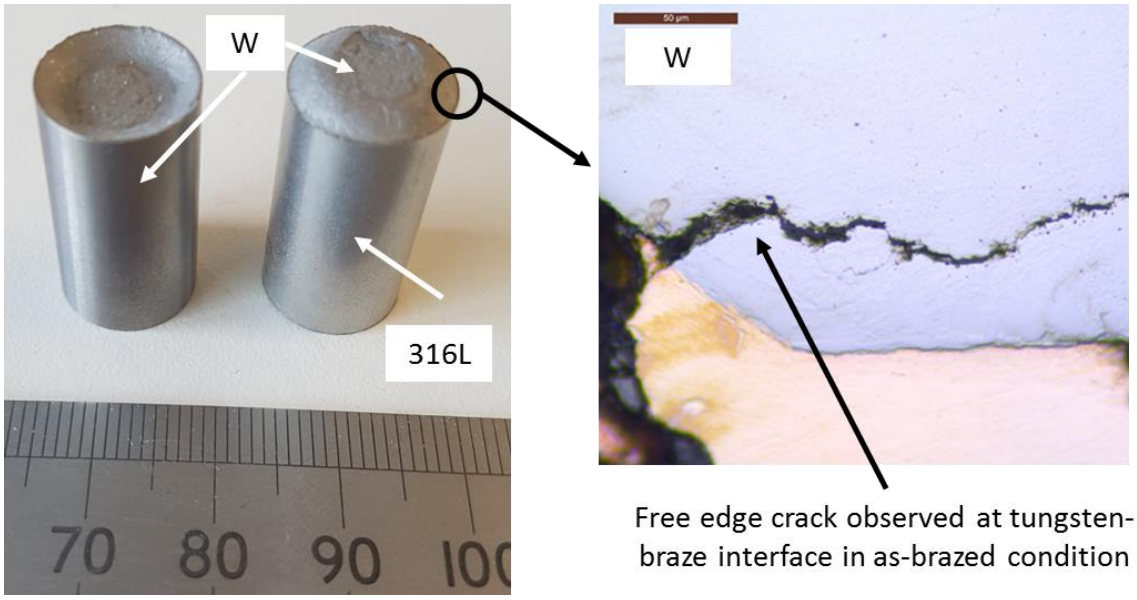

Figure 7-7 - Fracture of W-AuCu-316L thermal autofrettaged part and previously observed crack in similar part

The crack originates at the tungsten side of the brazed interface. This location was previously observed to contain cracks in Chapter 3 of this thesis, and is also shown in Figure 7-7. It is postulated that the crack grew during thermal autofrettage process. Residual stresses within the part then caused the crack to propagate whilst the part was stored, prior to a critical crack length being reached whereupon full failure occurs in the bulk tungsten material.

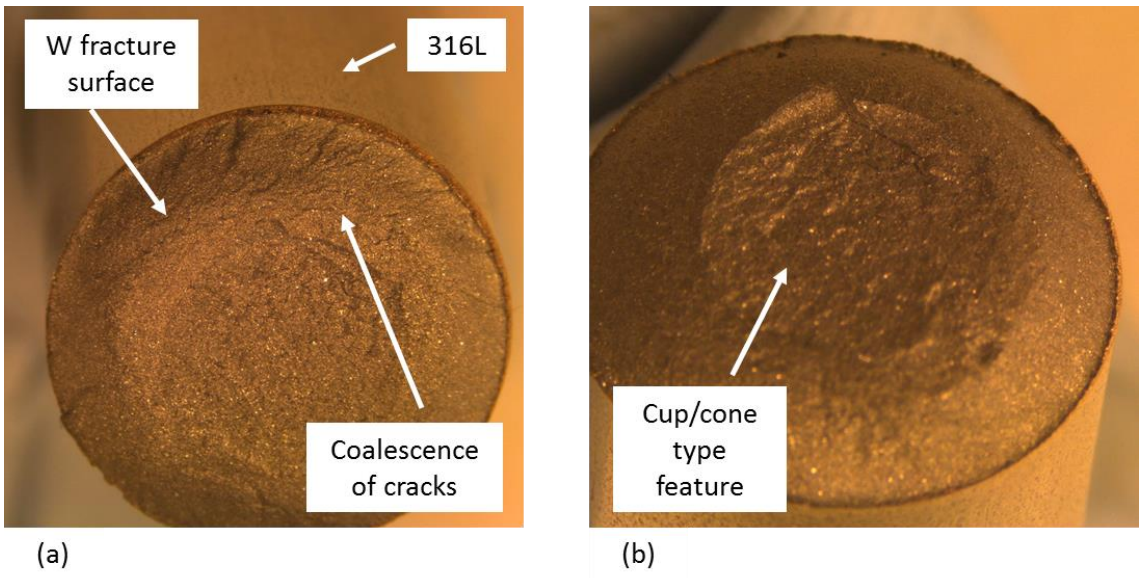

Figure 7-8 - Fracture surface of W-AuCu-316L failed part following thermal autofrettage

The fracture surface was inspected using stereo microscope (Figure 7-8). There is no single initiation site. Upon inspection of the surface multiple crack like features can be seen beginning at the outer diameter (the free edge where cracks were previously observed) and continue until a position about half way to the centre. It appears these multiple, small cracks coalesced to the point where a sudden failure occurs.

The shape of the fracture surfaces resemble a cup/cone fracture characteristic of ductile failure. This is not expected to be a likely occurrence in highly brittle tungsten [290]. Further investigation via SEM fractography is required and is recommended for future work.

The presence of cracks at the edge of the W-AuCu-316L specimen, coupled with the fracture discussed here, are clear issues of concern. Such defects are not acceptable for divertor components. Due to the small quantity of samples treated using the thermal autofrettage process, it is not possible to determine whether cracks and brittle fractures are likely to be a common occurrence for brazed tungsten joints. So whilst thermal autofrettage has potentially useful effects, it must be demonstrated to not induce such defects during future research. A beneficial modification of residual stresses is not meaningful if large cracks are developing.

The issue of cracking during thermal autofrettage should be strongly considered for future research. By more carefully controlling the processing temperature, for example -100°C compared with -200°C, such issues may be avoided. Similarly, by performing a light grinding operation to

remove the material at the free edge of a dissimilar material joint, including the areas where cracks have been observed, then thermal autofrettage could again be a useful process.

7.4 FEA of thermal autofrettage of brazed joints

7.4.1 Model set-up

The thermal autofrettage process was modelled using ABAQUS v6.3 [227]. The model set-up is identical to that presented for brazing simulation in Chapter 5. Previously the simulation included one load step, with an initial T=910°C and final T=20°C. An elasto-plastic model with minimum element size of 10μm (0.1 times braze thickness) was used.

For the thermal autofrettage simulation presented here, two additional load steps were added. The sequence of load steps is shown below:

1. Initial step – Brazing temperature, T=910°C
2. 1st load step – Cool from braze T to ambient conditions, T=20°C
3. 2nd load step – Cryogenic cooling (thermal autofrettage), T=-196°C
4. 3rd load step – Heating to ambient conditions, T=20°C

The initial, 1st, 2nd and 3rd load steps correspond with configurations (a), (b), (c) and (d) respectively (from Figure 7-2).

As with the brazing simulation in Chapter 5 a static structural model is utilised as thermal gradients were shown to be insignificant [208]. Therefore uniform temperature distribution inherent with the static structural model is deemed sufficient to model the process.

Table 7-1 - Low temperature material properties for FE simulation of thermal autofrettage

Material	Temp (°C)	α (x10^{-6} /K)	E (GPa)	σ_{yield} (MPa)	E_{tan} (GPa)
Au80Cu20	-100	11.8	42.3	143	9.0
	-200	9.7	44.7	161	10.0
W	-100	4.2	404	1340	0.1 x E
	-200	3.65	407	1340	0.1 x E
Cu	-100	15.7	133	79.2	0.1 x E
	-200	13.6	136	87.1	0.1 x E
316L	-100	15.0	202	393	0.1 x E
	-200	13.2	208	505	0.1 x E

The material properties for temperatures below 20°C used for FEA are shown in Table 7-1. Material properties for 20°C and above are presented in Section 5.5.1. Low temperature material properties were not fully available for 316L within the JAHM material database [228]. Properties for standard 316 were used in their place. Properties for copper and tungsten were sourced from [228].

Low temperature material properties were not generated for Au80Cu20 brazing alloy during the project. Therefore it was necessary to extrapolate data from room temperature to -196°C. Linear extrapolation from room temperature data was used, and as such there is a degree of uncertainty in the values. Future work to further characterise properties of Au80Cu20 material should include low temperature testing. This would improve the significance of simulation results by reducing uncertainty from material property data.

7.4.2 Tungsten-copper thermal autofrettage FEA

The FEA simulation results for the thermal autofrettage of a brazed W-AuCu-Cu part are presented in Figure 7-9. Residual stresses are shown for the free edge location of the tungsten and copper parts. The axial component of stress is plotted as this is the most significant component of stress when considering dissimilar material interfaces. Stresses in step (d) following thermal autofrettage are donated TAF.

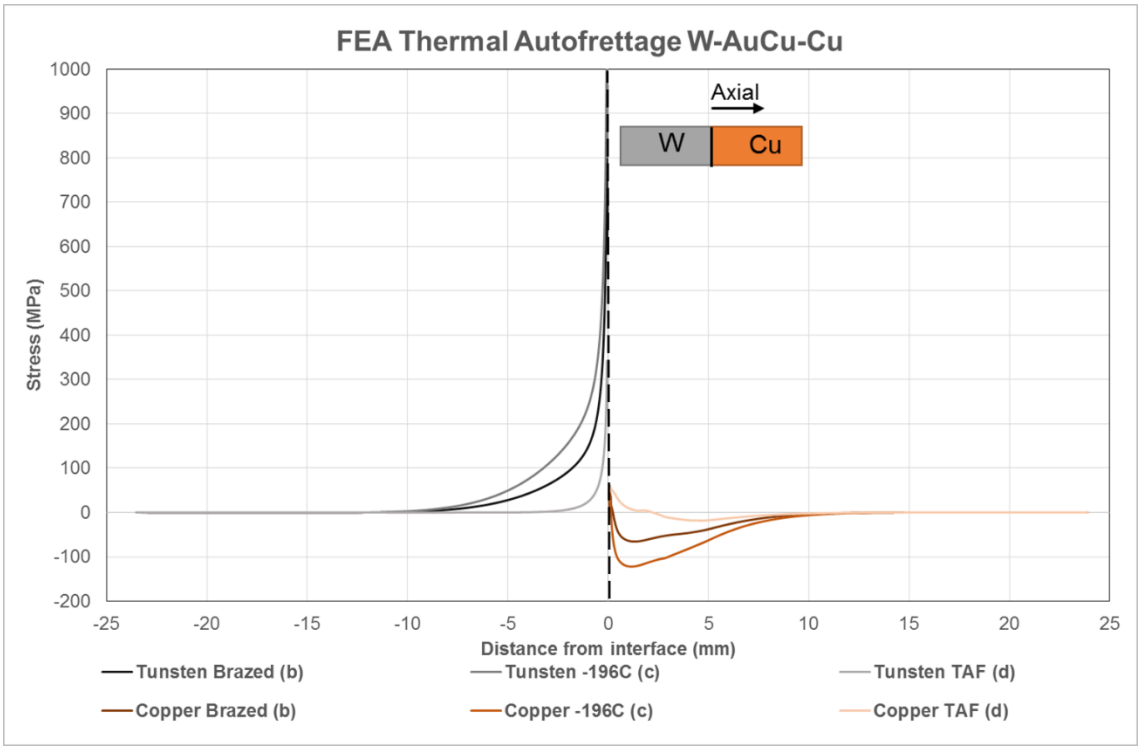

Figure 7-9 - FE simulation of thermal autofrettage (TAF) process for brazed W-AuCu-Cu part

The stresses at (b) represent the residual stress profile upon cooling from brazing temperature to room temperature, as previously reported in Chapter 5. High tensile stresses are present in tungsten and lower magnitude compressive stress is exhibited in copper.

During cryogenic cooling, (c), there is an increase in tensile stresses in tungsten in the local stress concentration region of the braze interface. This is a logical outcome as the constraint mechanism present during cooling from brazing applies, and the effective ΔT becomes c. 1100°C in (c) compared with c. 900°C in (b).

Upon returning to room temperature in (d) there is a significant reduction in tensile stresses close to the interface in tungsten. This is evidence that that theoretical application of thermal autofrettage (TAF) to reduce brazing induced tensile stresses is possible.

7.4.3 Tungsten-316L thermal autofrettage FEA

Axial residual stresses at the free edge of a brazed W-AuCu-316L part subjected to thermal autofrettage process are presented in Figure 7-10.

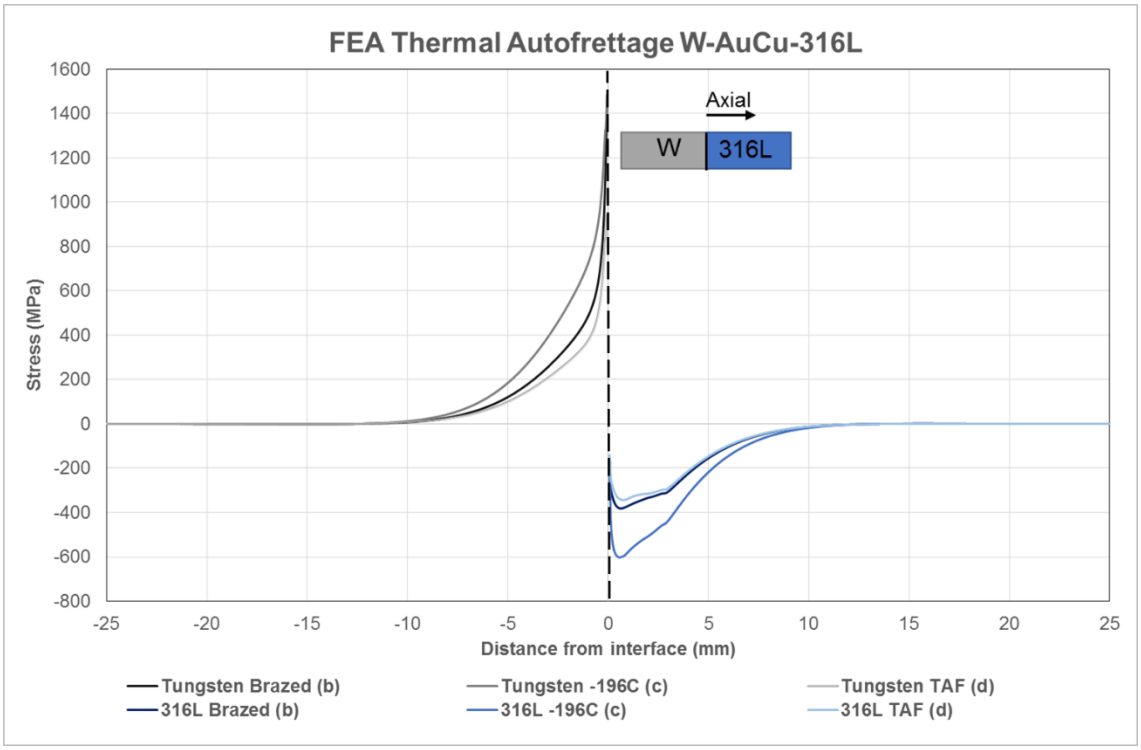

Figure 7-10 - FE simulation of thermal autofrettage process for brazed W-AuCu-316L part

As with the tungsten-copper configuration, the stresses in tungsten in the tungsten-316L combination are tensile in nature at the interfacial region following brazing (b). The stresses are higher in magnitude for tungsten-316L (Figure 7-10) than for tungsten-copper (Figure 7-9). As the difference in CTE is comparable between the two cases, it follows that the greater constraint on contraction/expansion provided by 316L would result in higher stresses compared with the less stiff copper (lower elastic and plastic moduli and yield stresses).

At -196°C, (c), the tensile stresses in tungsten increase. Following the unloading phase, i.e. returning to ambient temperature in (d), there is a reduction in magnitude of tensile stresses in the brittle tungsten material. At a distance of 2-3mm from the braze interface this results in a c. 100 MPa reduction in stress.

In 316L, initial moderate compressive stresses increase in magnitude (from a peak stress of c. 400 MPa compressive to 600 MPa compressive). Upon returning to room temperature (d) there is a slight reduction in compressive stress when compared with brazing induced stresses (b).

7.4.4 316L-copper thermal autofrettage FEA

The free edge, axial residual stress profile for a brazed 316L-AuCu-316L thermally autofrettaged part is shown in Figure 7-11.

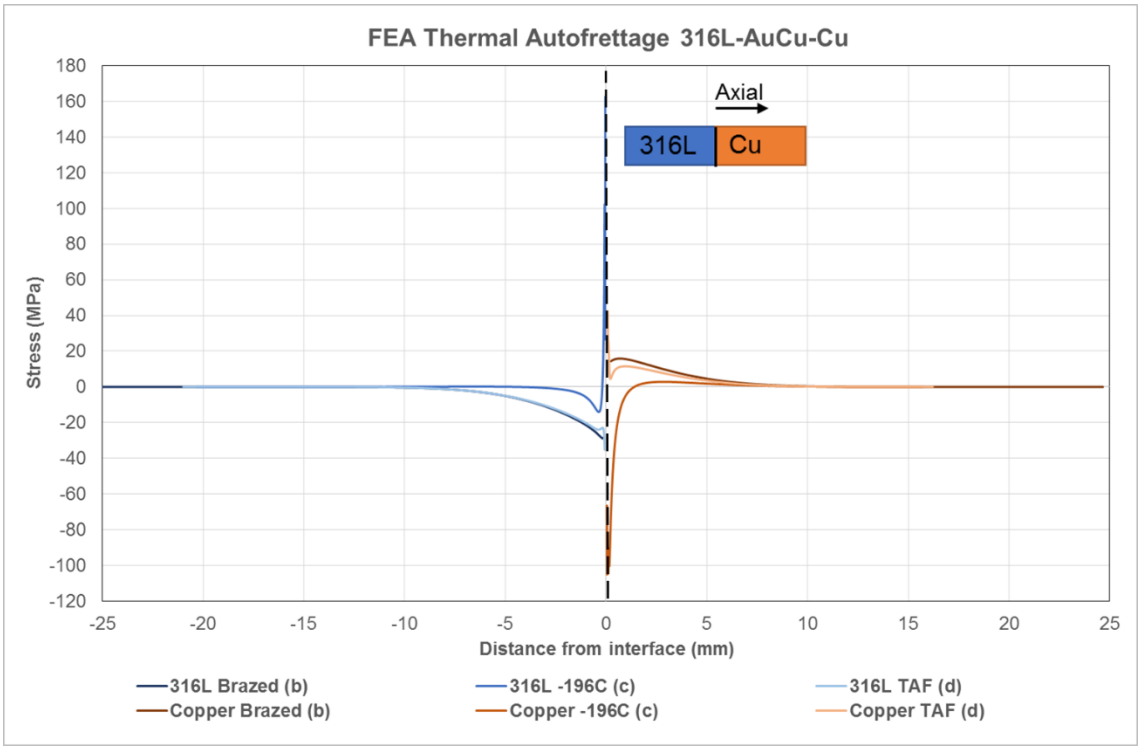

Figure 7-11 - FE simulation of thermal autofrettage process for brazed 316L-AuCu-Cu part

There is minimal effect of stress reduction in either 316L or copper following thermal autofrettage of the 316L-copper brazed part. Initial brazing stresses (b) are not significantly high enough to require stress reduction in any case. This is due to the close similarity in the material properties that dictate dissimilarity-type stresses, namely CTE and elastic modulus.

The focus of measurement of residual stresses shall therefore be on the two material combinations with tungsten as a parent material.

7.5 Surface Residual stress measurement of thermal autofrettaged brazed joints

The surface, axial residual stresses in brazed parts following thermal autofrettage have been measured using XRD. Measurement procedures, including material constants, radiation sources and Bragg angles, are as described in section 6.2.

Measurement uncertainty has been quantified as in section 6.2.2. A root of sum of the squares approach was utilised, accounting for repeatability uncertainty, material x-ray elastic constant uncertainty, and the error as calculated by PROTO software based on the average deviation from best fit line of the $\sin^2\psi$ plot [232].

All XRD residual stress measurements presented here were performed at AFRC, University of Strathclyde, with a PROTO LXRD system.

Tungsten-316L and tungsten-copper were identified as the most interesting and potentially useful combinations, both from a fusion relevance and thermal autofrettage perspective. Therefore in order to maximize the limited time available with measurement apparatus, only these two combinations have been assessed.

7.5.1 Tungsten-copper free edge residual stress

Two individual W-AuCu-Cu parts were measured by XRD. As with the brazed-only specimens presented in Chapter 6, the thermal autofrettage induced surface residual stresses could only be measured in tungsten. Measurement in copper material was not possible as discussed in section 6.2.3.

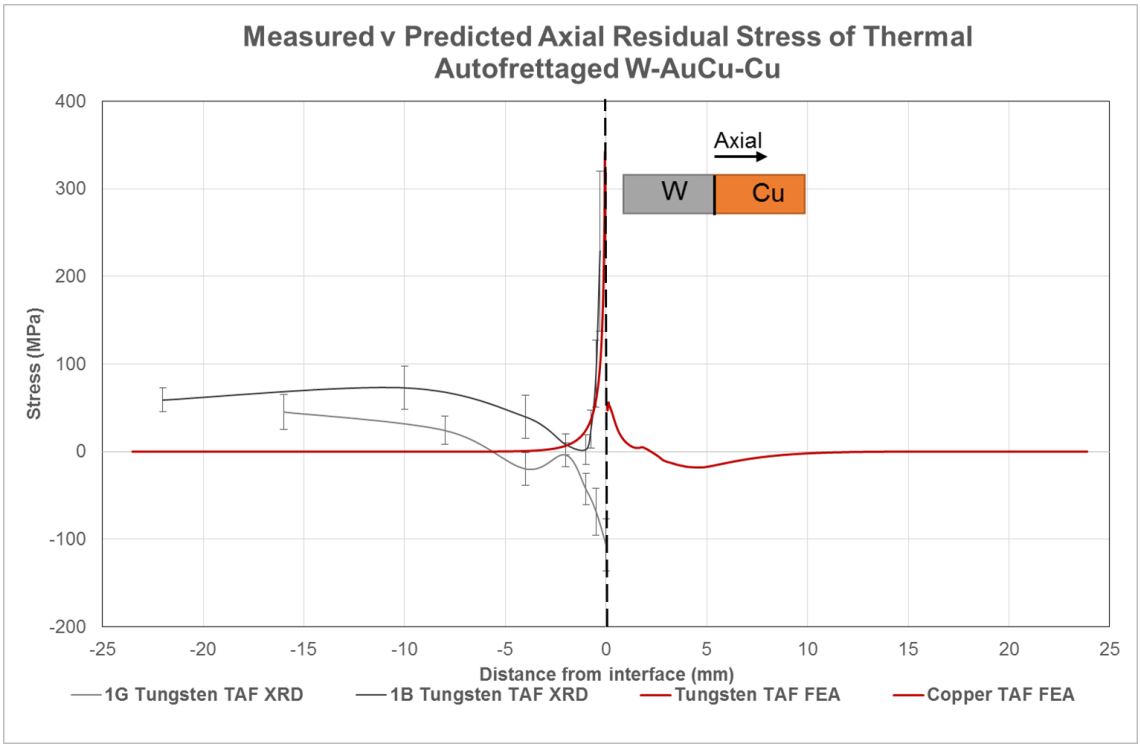

Figure 7-12 – Surface axial residual stress profile as measured by XRD for W-AuCu-Cu brazed and TAF joint, and comparison with FEA prediction

A comparison of FEA predicted and XRD measured free edge axial residual stresses for thermal autofrettaged tungsten-copper part are shown in Figure 7-12.

There is an observable difference between the two measured residual stress profiles in tungsten, part 1G (light grey) and part 1B (dark grey). Part 1G shows a compressive stress concentration, which is in contradiction to FE predictions. This was the expected outcome based on the findings in Chapter 6. Part 1B shows an opposite trend in stress as the distance to the interface tends to 0mm when compared with FE predictions (red). There was a clear disagreement between FE predicted (and determined theoretically) and actual measured stresses in tungsten for the tungsten-copper configuration. This is likely due to the FE model not fully capturing the;

- Significantly diffused region at the interface, resulting in a deviation from the simple 3 material model simulated in Abaqus
- Material property data for the diffused region at the braze interface which will differ than that of Au80Cu20.

This disagreement would be expected to continue as the thermal autofrettage process is simply a reverse of the cooling from braze process, in terms of constraint mechanisms. It is unexpected therefore that part 1B is in fact in reasonably good agreement with the FE prediction. However there are only a couple of data points in the vicinity of the interface, and measurement uncertainty is high, so this may be an artefact of measurement uncertainty. Errors are higher in the vicinity of the interface as the 1mm spot size used for XRD measurements includes parts of the braze layer and other parent material. The geometry of the braze layer, and possible interference from reflection planes of Au80Cu20 and copper, serve to increase the error in the $\sin^2\psi$ fitting error.

A comparison of surface residual stresses in tungsten-copper part 1G before and after thermal autofrettage is presented in Figure 7-13.

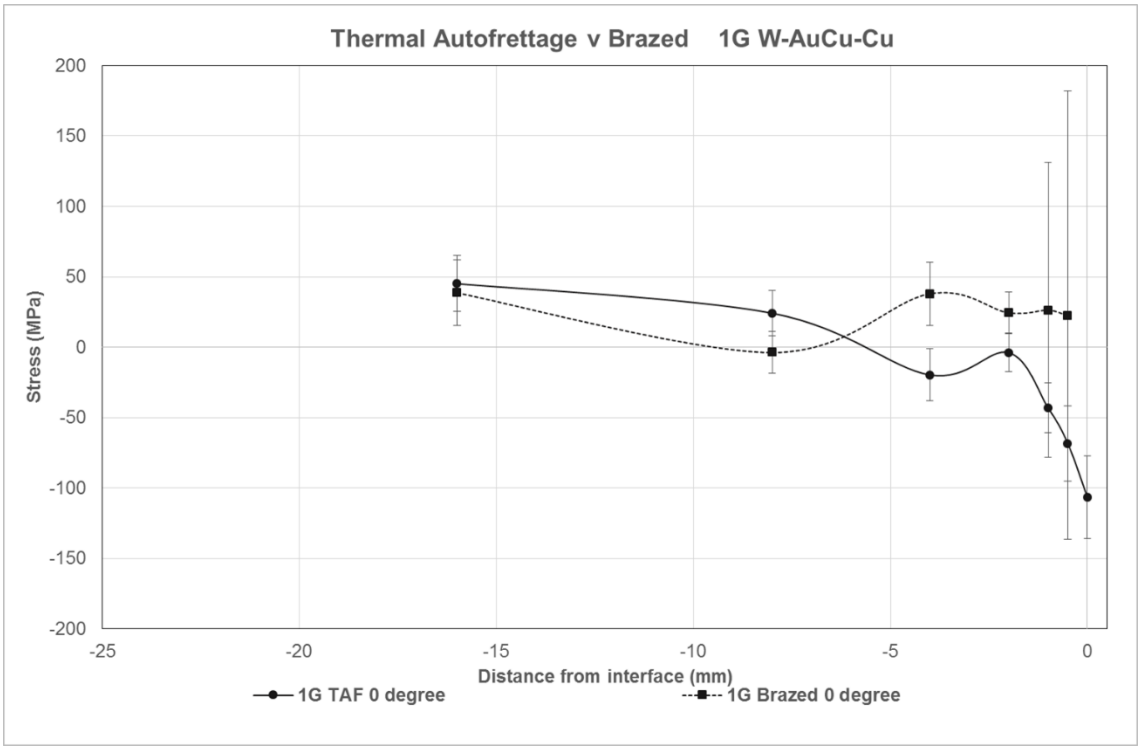

Figure 7-13 – Comparison of XRD measured axial residual stress before and after thermal autofrettage for W-AuCu-Cu part

The solid grey profile representing the as-autofrettaged condition shows an increase in compressive stress in the tungsten in the vicinity of the braze interface. An increase in compressive stress can be thought of as comparable to a reduction in tensile stress, as described for the stiff material in Section 7.2.

The assumption that the stress distribution prior to autofrettage is tensile for the stiff material (from theory and FEA) is of course not the case for the as-brazed tungsten-copper presented in this thesis. The fact that an increase in compressive stress in the brittle tungsten has occurred does

suggest that the reason for applying thermal autofrettage to this material combination is potentially useful.

However further research is required to determine the cause of the disagreement between the as-brazed predicted and measured stresses. If this is achieved, the best approach for modifying tungsten-copper using a technique such as autofrettage could be determined.

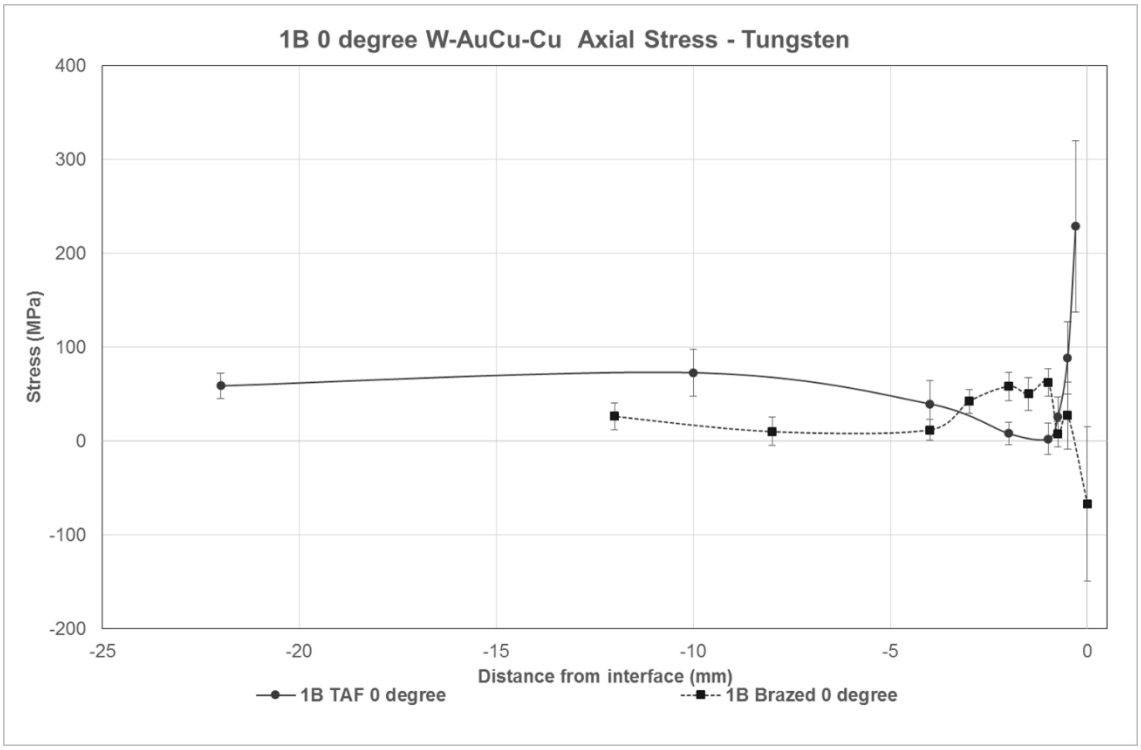

Figure 7-14 - XRD measured residual stress in thermal autofrettaged W-AuCu-Cu part 1B

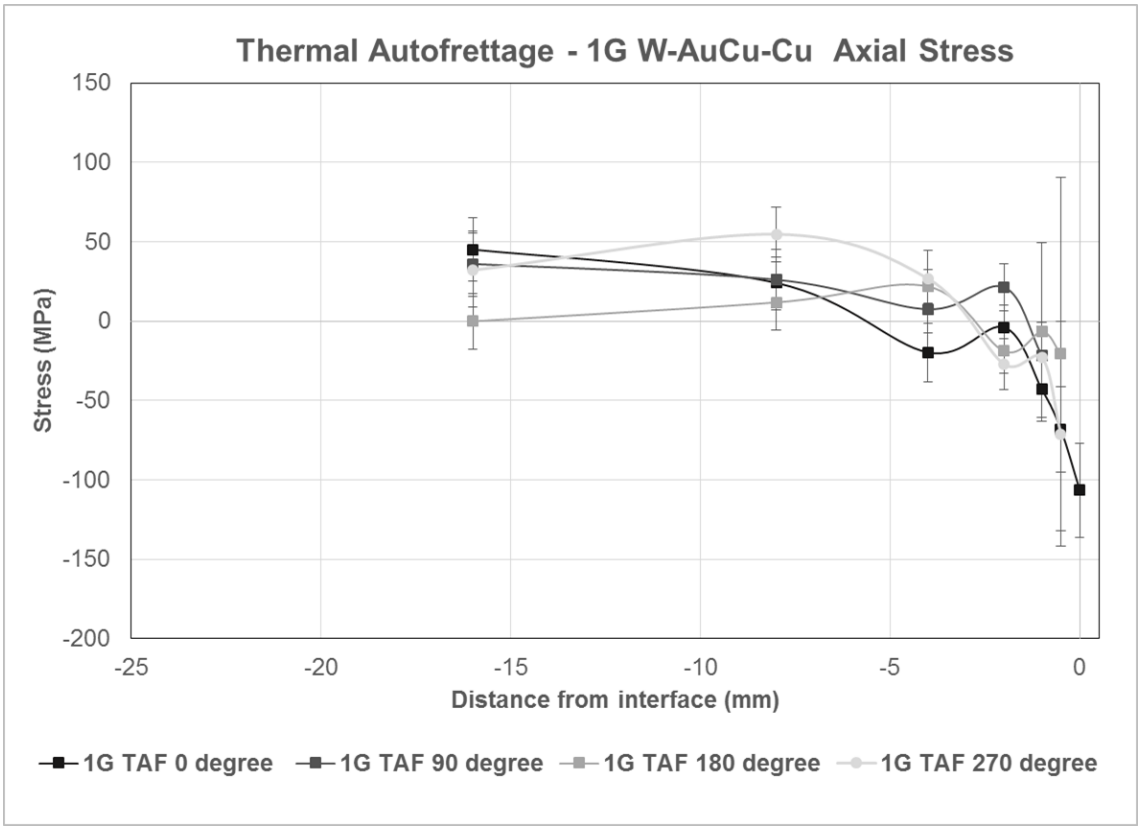

Figure 7-15 - XRD measured residual stress in thermal autofrettaged W-AuCu-Cu part 1G

A comparison between as-brazed and as-autofrettaged free edge axial residual stresses in W-AuCu-Cu par 1B are shown in Figure 7-14. Initial compressive stresses following brazing are transformed to tensile stresses following thermal autofrettage.

In Figure 7-15 the as-autofrettaged residual stress at 4 circumferential positions (0°, 90°, 180° and 270°) for part 1G are presented. There is good agreement for all four angular positions considered.

It can be stated that whilst stress profiles are consistent for a given part, namely 1G, there is variability between different tungsten-copper parts, namely 1G and 1B.

7.5.2 Tungsten-316L free edge residual stress

In this section the results for W-AuCu-316L brazed and thermally autofrettaged parts are considered.

A comparison of FE predicted and XRD measured stresses are presented in Figure 7-16 for the as-autofrettaged condition of a tungsten-316L part.

When compared with the tungsten-copper combination, there is much better agreement between predicted and measured stresses for autofrettaged tungsten-316L brazed part. From both FEA and XRD there are tensile stresses in tungsten at the local stress concentration region of the braze interface. Compressive stresses are found in 316L in both cases, with the peak stress approx. 1-2mm from the interface predicted and measured.

Where the FE predictions and real measured stresses differ is in the magnitude of the axial residual stresses. The measured stresses were found to be lower than predicted stresses, indicating that the autofrettage process was more effective than estimated by FEA. A similar outcome was found for titanium-copper brazed parts [199].

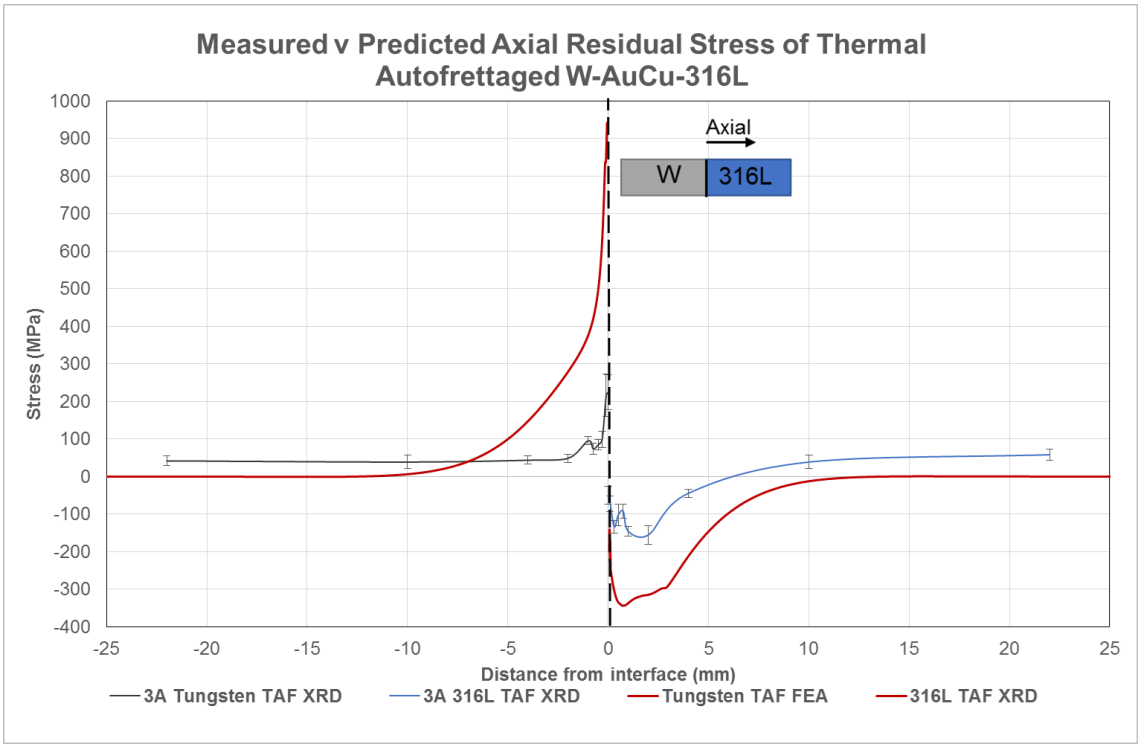

Figure 7-16 - Surface axial residual stress profile as measured by XRD for W-AuCu-316L part 3A in as-brazed and thermally autofrettaged condition, and comparison with FEA prediction

This indicates that the FE model may not be capturing the full extent of the plastic region that grows and develops during cryogenic cooling. The larger the degree of plasticity developing, the more potential there is for modifying the residual stresses using autofrettage [274]. Therefore if the model is improved to better capture the plastic behaviour, more accurate prediction of the thermal autofrettage process could be achieved.

This improvement could be brought about by improving the material data used, including low temperature data for the Au80Cu20 braze material and for the 316L steel. Also, by incorporating complex hardening behaviour, more accurate predictions of autofrettage can be achieved [291].

In order to directly measure the degree of the plastically strained region in the vicinity of the interface, EBSD plastic strain mapping is recommended for future work [292-294].

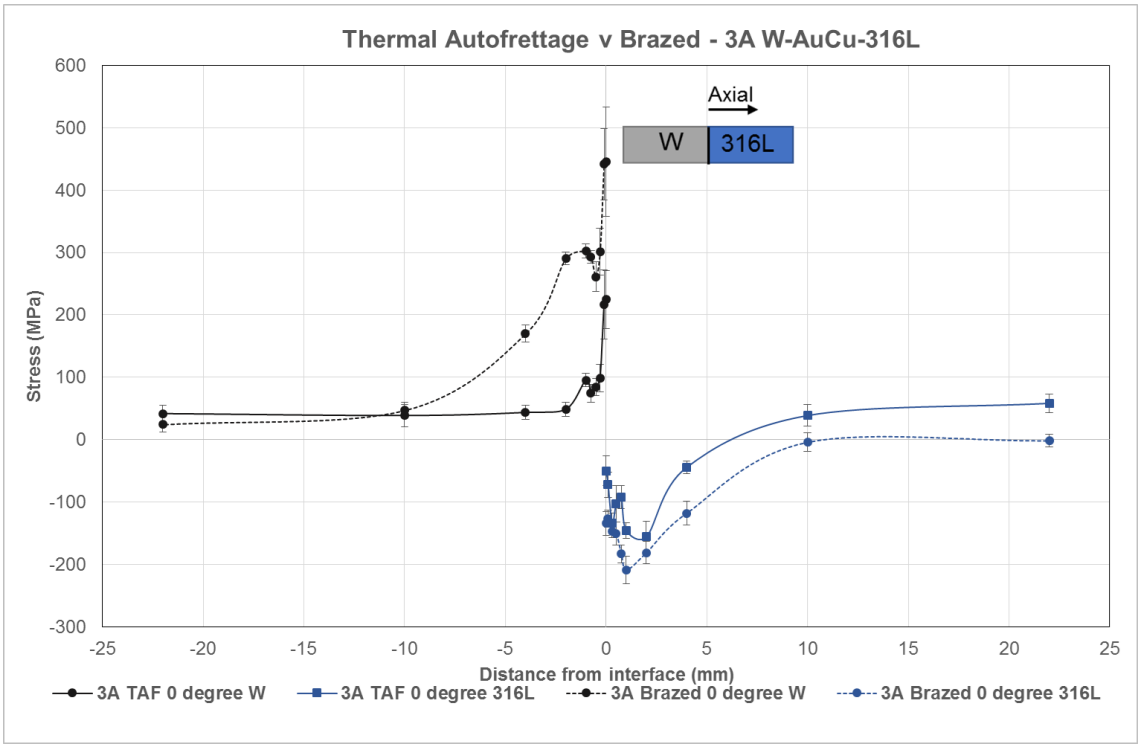

Figure 7-17 - Comparison of XRD measured axial residual stress before and after thermal autofrettage for tungsten-316L part

The effect thermal autofrettage on the free edge axial residual stress in brazed tungsten-316L parts can be seen in Figure 7-17. The as-brazed stresses are represented in dashed profiles for tungsten (grey) and 316L (blue), with as-autofrettaged stresses shown with a solid line profile.

The initial, as-brazed high tensile stresses in tungsten, c. 300-500 MPa close to the braze interface, are reduced significantly. In the immediate locality of the braze interface a peak tensile stress of 200 MPa was experimentally found in tungsten, with a smaller peak at 1-2mm from the braze interface of 100 MPa. Considering the high yield stress of the material (excess of 1 GPa) it can be stated that the potentially damaging tensile residual stresses have been significantly reduced.

As an additional benefit, the vast reduction in tungsten tensile stress was achieved without significantly reducing the potentially helpful compressive residual stress in 316L.

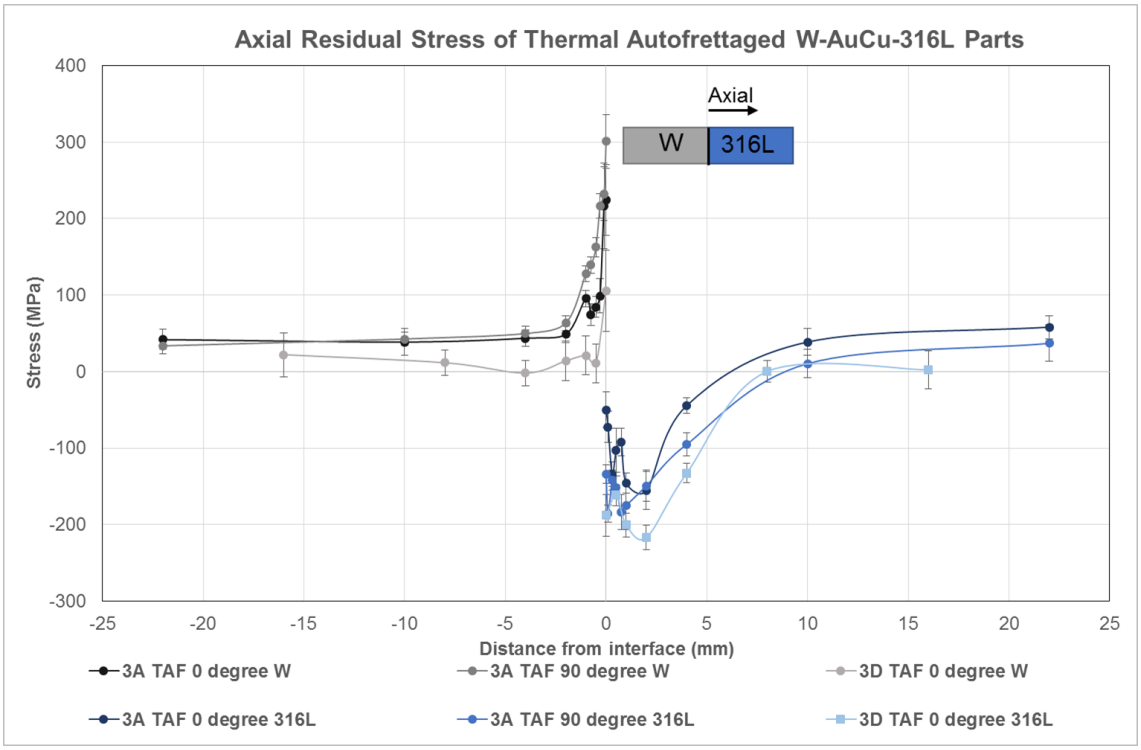

Figure 7-18 - Summary of as-thermally autofrettaged free edge axial residual stresses in brazed tungsten-316L part

A summary of all measurements performed on as-autofrettaged W-AuCu-316L is presented in Figure 7-18.

There is a high degree of repeatability in the measured stress profiles for the thermally autofrettaged tungsten-316L parts. The shape of the free edge axial stress profile was found to be consistent.

Stresses in tungsten are exclusively tensile, with all 316L parts showing compressive stresses close to the interface. This is an encouraging sign if the thermal autofrettage process utilized here were to be applied to a real component, such as a divertor tile, where repeatable performance is required.

7.6 Contour Method analysis of thermal autofrettaged brazed joints

Contour Method residual stress measurement has been used to measure the hoop stresses across a complete axial cross section of brazed and thermally autofrettaged tungsten-copper and tungsten-316L parts.

The experimental procedures for performing Contour Method are described in section 6.4.2. It was originally planned to perform analysis of two parts per material combination (tungsten-copper and tungsten-316L). However the second tungsten-316L designated for Contour Method assessment suffered from tabletop failure (the fractured part discussed in section 7.3.2). Therefore the cross sectional stress map for only one W-AuCu-316L part is presented here.

7.6.1 Autofrettaged Tungsten-copper Contour Method

The Contour Method was performed on two thermally autofrettaged brazed tungsten-copper parts. The results for the two parts, namely 1D and 1G, are presented in Figure 7-19 and Figure 7-20 respectively.

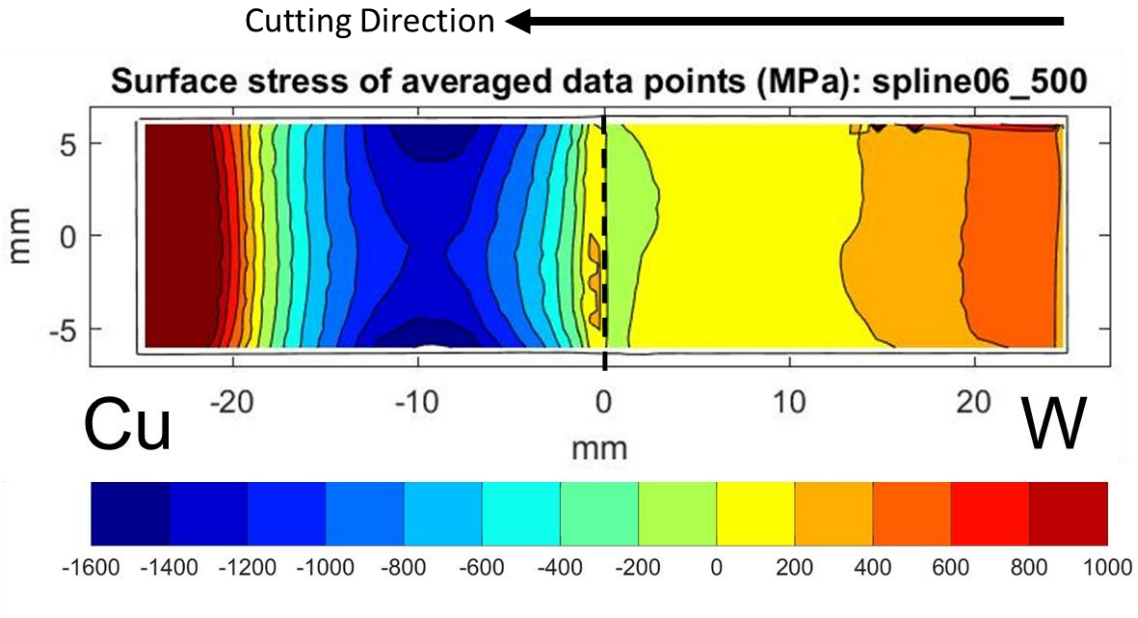

Figure 7-19 - Contour Method out of plane stress results for thermal autofrettaged W-AuCu-Cu part (1D)

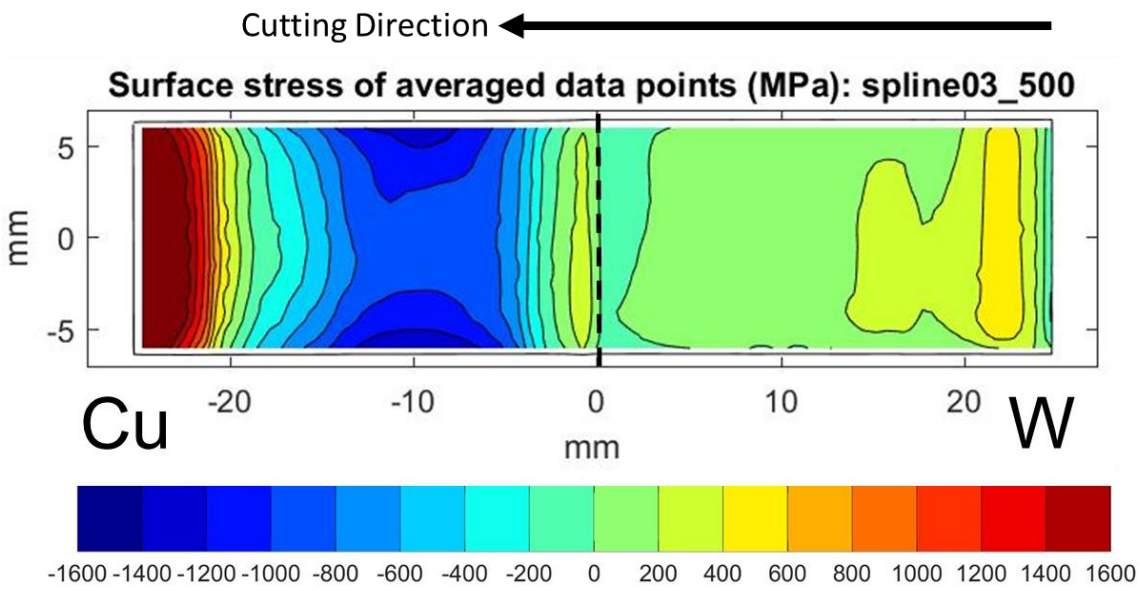

Figure 7-20 - Contour Method out of plane stress results for thermal autofrettaged W-AuCu-Cu part (1G)

The results for copper are shown in the left side of each map for both 1D and 1G. It is clear that an error has occurred during EDM sectioning of the parts resulting in impossibly high residual stresses. The same type of erroneous result was found for tungsten-copper in section 6.4.3 for the as-brazed parts.

During sectioning the copper has undergone significant plastic deformation, opening up in respect to the cutting plane as the cut progresses. As the Contour Method analysis is based on fully linear elastic conditions, when applying large surface displacements (such as those caused here by plasticity) the stress magnitudes are grossly over predicted. Although this can occur any part, based on the results in this chapter and the subsequent chapter, it is concluded that simple end clamping of a stressed copper component is not sufficient for Contour Method analysis.

It is therefore recommended that a bespoke clamping arrangement is considered for any further EDM sectioning of similar copper parts for residual stress analysis.

As the large deformations in copper significantly affect the fitting of a zero-displacement plane, a crucial step in the analysis process, it is not possible to derive meaningful stress results for either of the parts presented in Figure 7-19 or Figure 7-20.

7.6.2 Autofrettaged Tungsten-316L Contour Method

The Contour Method results for thermally autofrettaged W-AuCu-316L part 3D are presented in this section. The part was sectioned by EDM wire cutting and measured using a CMM as per procedures outlined in Chapter 6. The CMM measured surface data cloud for one of two surfaces and the subsequent alignment of both surfaces are shown in (a) and (b) of Figure 7-21 respectively.

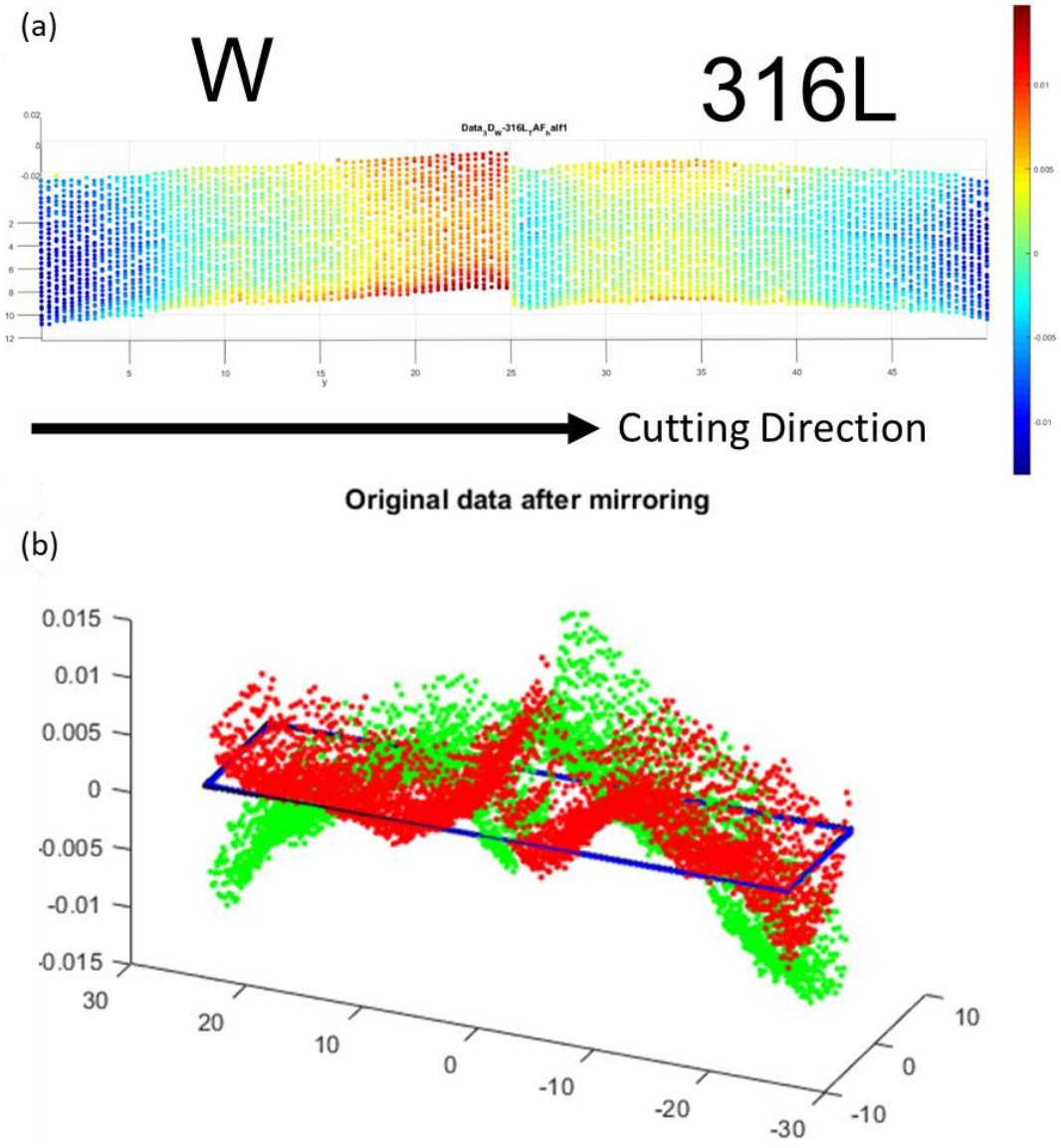

Figure 7-21 - CMM measured surface data cloud (a) following data cleaning and (b) following data alignment

As with the brazed, non-autofrettaged part considered in 6.4.4, there is evidence of a non-straight cut in the W-AuCu-316L part. This is evident in both parts investigated in Chapter 6 and the autofrettaged part here, indicating that it is intrinsic when sectioning tungsten-316L using the set-

up employed here. This is likely an effect of the particular clamping arrangement and relative difficulty the EDM machine experiences when cutting tungsten. However as described before, the resulting surface profiles are still very much suitable for residual stress analysis. This is because asymmetric errors, like a non-straight cut experienced here, are averaged away during the analysis process [252].

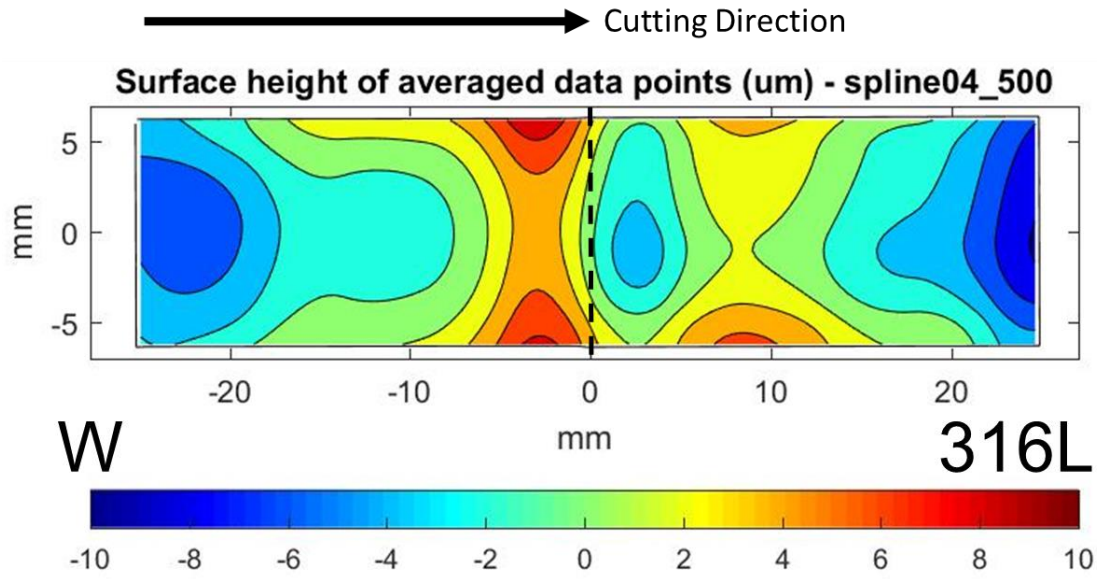

Figure 7-22 - Surface displacement of autofrettaged W-AuCu-316L part 3D following bivariate spline surface fitting

The averaged surface data cloud was then fitted using a bivariate spline fit in Matlab (codes courtesy of S. Rahimi of AFRC, University of Strathclyde). The surface displacement map for a knot spacing of 4.5mm is presented in Figure 7-22 for autofrettaged tungsten-316L part 3D.

The surface displacements are again applied to an FE model to calculate the residual stress profile. The hoop stress cross sectional map for part 3D is shown in Figure 7-23.

The stresses in tungsten were found to be compressive in nature close to the braze interface following thermal autofrettage. There is change in nature in the immediate vicinity of the interface, with tensile stresses being measured. The peak magnitude of compressive stresses is c. -700 MPa. More remote from the interface there are tensile regions of stress within the tungsten.

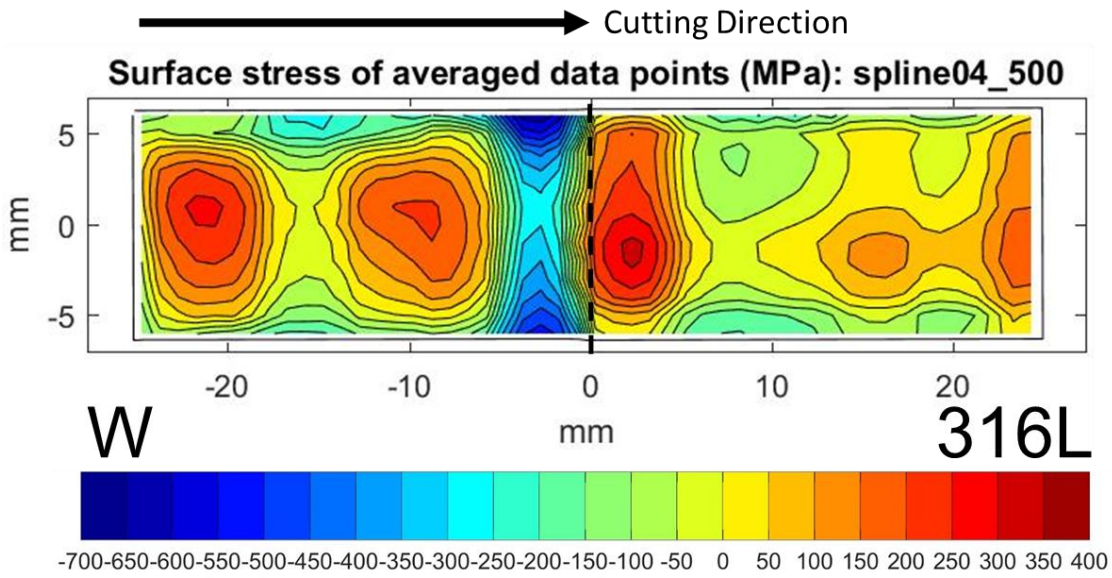

Figure 7-23 - Contour Method measured residual hoop stress results for thermal autofrettaged W-AuCu-316L part (3D)

Tensile hoop stresses were measured in 316L in the interfacial region, with a maximum tensile stress of c. 350 MPa. As with the tungsten material, the peak stress does not occur immediately at the interface. This is observed for axial surface stresses also (Figure 7-18) where the peak stress is found 1-2mm from the respective braze interface.

The stress profile at the centerline of the autofrettaged tungsten-316L part as measured by Contour Method is compared with FEA predictions at the same location, shown in Figure 7-24.

There was found to be excellent agreement between FEA predictions for residual stress in the 316L part of the tungsten-316L autofrettaged part. In the vicinity of the braze interface the predicted and measured profiles are essentially collinear. The magnitude and location of the peak stress is consistent in both predicted and measured profiles.

In the tungsten half there is also relatively good agreement in results in the interfacial region. The presence of high compressive stresses predicted by FEA is confirmed by Contour Method analysis. The FE model does not predict the location of the peak stress in tungsten being remote from the braze interface. This is consistent with the prediction for axial free-edge stresses in tungsten (Figure 7-10).

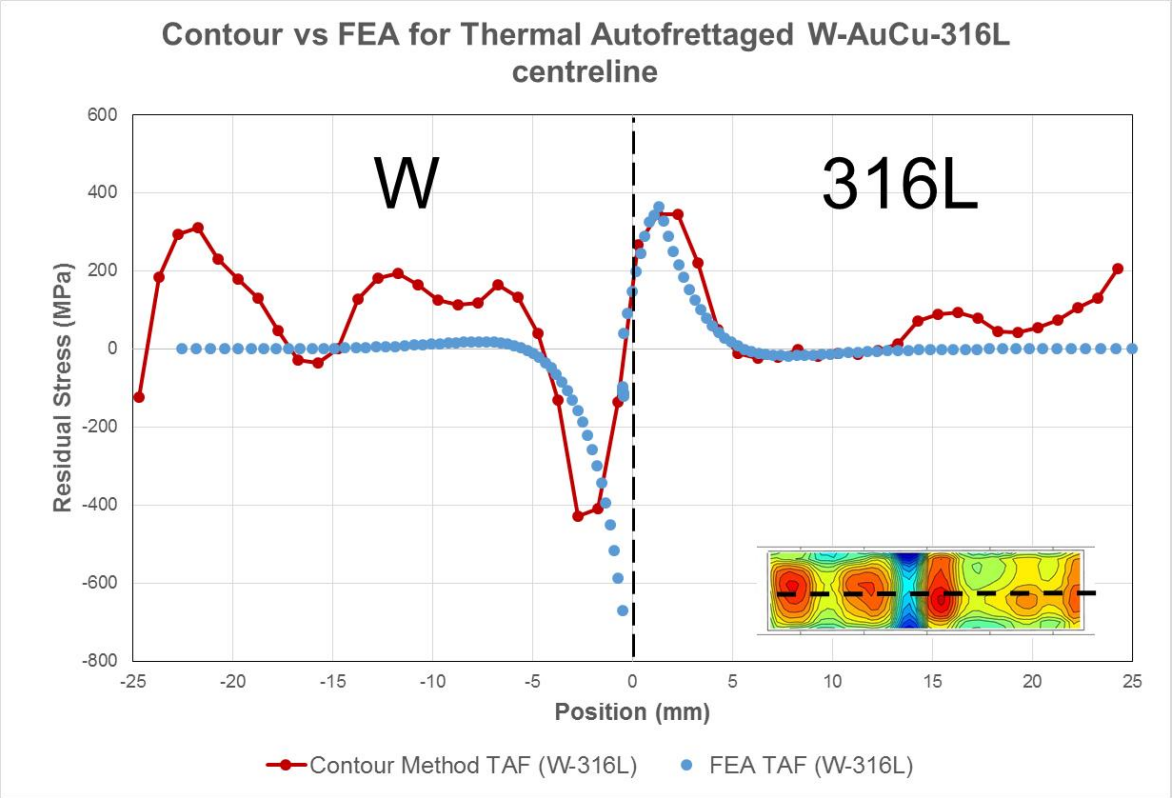

Figure 7-24 - Comparison of Contour Method and FE analyses of out of plane residual stresses through the centre of as-thermal autofrettaged W-AuCu-316L part (3D)

The variation in measured stresses for tungsten away from the interface can be explained by a combination of experimental uncertainty and pre-existing stresses not considered in the FE model. The total difference of magnitudes for surface displacement in tungsten as measured by CMM was approx. 20µm. Considering an uncertainty from CMM measurement in the order of 1-2µm, coupled with non-optimal clamping and cutting conditions, it is proposed that improvement of both measurement and sectioning could bring the measured results closer to those predicted in Abaqus.

7.7 Discussion

In this chapter thermal autofrettage by means of cryogenic soaking was performed on dissimilar material brazed parts. Two parts per material combination (tungsten-copper, tungsten-316l) were assessed. The residual stresses in the autofrettaged parts were measured on the surface and across an axial cross section of the parts, using XRD and Contour Method respectively. The results were then compared with FEA predictions of residual stresses for the two material combinations focused on, tungsten-copper and tungsten-316L bonded using vacuum brazing and a eutectic Au80Cu20 brazing alloy.

By comparing both the XRD results from section 7.5 and Contour Method results in section 7.6 with FEA predictions in section 7.4, there is a clear contrast in how comparable predictions and measured results are for the two material combinations.

The tungsten-copper combination showed relatively poor agreement between modelling and experimental results. This is a similar result to the as-brazed findings in Chapter 6. This is not surprising considering. The modelling results from Chapter 6, whereby the nature of the free edge axial residual stress in tungsten was opposite from what was measured experimentally, mean that the from the outset of modelling the thermal autofrettage process there is a discrepancy between model input and real material condition.
In order to resolve this, further research is required to determine exactly why the experimentally determined stresses in tungsten are highly compressive in nature. Based on FE simulations and theoretical predictions considering the relationship between CTE and E of elastically dissimilar materials [220, 222], the tungsten "should" be in a highly tensile condition. Discussion on this disagreement was presented in section 6.2.5, with the complexity of the interfacial region and %Au material property dependence attributed as the likely source of disagreement.

In contrast to the tungsten-copper results, a relatively high level of agreement was obtained for predicted and measured stresses in the thermal autofrettaged tungsten-316L brazed part.

The surface stress profiles for both tungsten and 316L in 7.5.2 were comparable in terms of the overall shape and position of peak stresses compared with modelling results. However the magnitude of experimentally measured stresses were lower than predicted.
It is postulated that this is caused by an insufficiency of the model to fully capture the plastic deformation occurring during the autofrettage process. An improvement to the model to include

specific, strain dependent plastic deformation behaviour is recommended to try and improve the modelling and get closer to reality.
Also, it is recommended that plastic strain analysis be performed using EBSD maps and subsequent MATLAB analysis [295]. This will allow for a better understanding of the true extent of plasticity in the region of the braze interface resulting both brazing and thermal autofrettage. Although the strains could not be mapped directly at the surface, by analysing an area on a cross section similar to those presented in section 3.3 at a distance of c. 20μm from the free edge a useful comparison could be made between brazed and autofrettaged conditions.

There was also good agreement between FE predicted hoop stresses and Contour Method results for tungsten-316L. In particular the 316L part showed excellent agreement.
The free edge axial stresses are considered most critical for the type of application these dissimilar joints could have, such as a tungsten/316L or tungsten/copper alloy divertor tile subjected to cyclic thermal loading. Therefore obtaining good agreement between XRD surface stresses and FE predictions could be deemed most critical. Further to this, verification of measured residual stresses using a second experimental method is required. However the assessment of cross sectional maps of residual stress by Contour Method give an insight into the bulk stresses of the part, and whether the model is capable of predicting them. This is vital for validating any FE model used to design such part.

Perhaps most importantly it was shown that for the tungsten-316L combination, potentially damaging high tensile stresses in tungsten can be significantly reduced by applying the thermal autofrettage process.
The peak free edge axial stresses were reduced by 100-200 MPa in the tungsten material at the braze interface. This significant reduction could lead to an improved fatigue life of the part by reducing the effective mean stress. For a component such as the divertor where minimizing downtime for servicing is critical for maintaining economic viability [6, 10], a potential fatigue performance increase is significant.

The observed failure of the tungsten-316L part in section 7.3.2 however must be considered when assessing whether thermal autofrettage is a suitable stress modification tool for critical components such as fusion reactor divertor tiles.
The potential for failure of thermally autofrettaged tungsten-316L parts is furthered by the repeated observation of cracks at the tungsten-braze interface reported in Chapter 3. If cracks are already present in the brittle tungsten material, then it is no surprise that subjecting the material to increased tensile stresses whilst submerged in liquid Ni at -196°C will result in propagation of

said cracks and subsequent failure of the part. Improvement of the joining procedure is required to eliminate edge cracking from the outset. Alternatively a technique such as edge grinding could be applied to remove the cracked region.

In practice, the thermal autofrettage process will only truly be an effective means of mitigating damaging residual stresses if the cracks can be avoided. It is therefore a strong recommendation to further investigate the initiation of thermal autofrettage induced cracks. Optimisation of the thermal autofrettage process itself should be considered not only to better modify the residual stress state, but also to avoid conditions where cracking is observed to occur.

In order to optimize the effect of thermal autofrettage on reducing the tensile residual stress in brazed tungsten dissimilar material joints, further research investigating alternative brazing alloys is recommended. With all other factors being equal, a low yield stress, quasi elastic-perfectly plastic brazing alloy would be the ideal candidate for reducing damaging tensile stresses. However there are a multitude of other factors to consider, including microstructural features, wetting ability, neutron embrittlement and activation performance to name only a few.
A preliminary study whereby a number of significantly different brazing alloys (in terms of yield and plastic behaviour) are used for the tungsten-316L joint is recommended. A comparison of FEA and experimental results after brazing and again after thermal autofrettage would give an idea for whether the autofrettage process can be improved further for a real tungsten-316L part. If successful, the other associated studies could be performed (such as microstructural evolution).

The reduction of tensile residual stress in a brazed tungsten dissimilar material part is only truly useful if it translates into a performance benefit. Therefore it is recommended that a program of fatigue testing be conducted to determine if there is a marked increase in fatigue life following thermal autofrettage when compared with brazing alone. This could consist of either uniaxial fatigue loading or rotating bend type fatigue test. Both of these methods were investigated for fusion relevant material combinations [91]. This type of study could therefore be extended to include thermal autofrettage of a population of parts.

7.8 Summary

The residual stress state in brazed, fusion relevant dissimilar material parts (tungsten-copper, tungsten-316L, 316L-copper) have been modified using a variation of thermal autofrettage. The

as-brazed parts were soaked in liquid Ni at -196°C before being returned to ambient conditions. Due to a difference in CTE and elastic modulus, constraint is applied during this process, replicating a loading-unloading cycle. Upon returning to room temperature, plastic deformation coupled with elastic unloading resulted in a modification of the residual stress state.

The thermal autofrettage process was modelled using commercial FEA software. The simulation results were compared with experimentally measured residual stresses.

Good agreement was achieved for the tungsten-316L thermally autofrettaged part when comparing FE results with free edge stresses (XRD) and bulk residual hoop stresses (Contour Method).
The tungsten-copper combination did not exhibit such agreement. This is closely comparable with the conclusions from Chapter 6, whereby similar levels of agreement and disagreement were found for tungsten-316L and tungsten-copper respectively.

The thermal autofrettage process was successful in significantly reducing the potentially damaging tensile stresses at the free edge interface in tungsten. This is potentially of high value for the design of tungsten based divertor tiles for a future nuclear fusion reactor. The presence of small cracks at the interface between tungsten and Au80Cu20, in addition to an observed full failure of a tungsten-316L autofrettaged part, indicate that careful attention must be paid to the condition of the part after each processing stage.

8 Conclusions

8.1 Summary

Dissimilar material parts with relevance to a future fusion reactor divertor have been produced and characterised. A vacuum brazing methodology was developed to join tungsten, copper and 316L using a eutectic Au80Cu20 brazing alloy. The dissimilar joints were characterised using a number of techniques including optical microscopy, SEM, EDS elemental analysis, and micro and nano-hardness testing. Mechanical properties of the as-brazed materials in the interfacial region were investigated using a combination of nano indentation and FIB milled micro-cantilever testing.

Temperature dependent thermal and mechanical property data for the Au80Cu20 alloy was produced through a number of experimental means including DMA and ETMT. The experimentally generated material properties were then implemented into FEA of the brazing and thermal autofrettage processes.

FEA was used to investigate the effect of varying parent material and brazing alloy properties on the resulting residual stress state of the dissimilar parts due to constraint on free thermal contraction. Brazing induced residual stress distributions for the three brazed combinations considered here (tungsten-copper, tungsten-316L and 316L-copper) were then predicted using FEA.

The residual stresses in the dissimilar material brazed parts were then evaluated on real parts using XRD and Contour Method measurement techniques. The measured residual stress distributions were then compared with FEA predicted values.

The thermal autofrettage process was used to modify the residual stresses, with a view to increasing the mechanical performance of the part. Using the thermal autofrettage process, the brazed parts underwent plastic deformation and subsequent elastic unloading, resulting in modification of the residual stress state. The aim was to increase the level of compressive stress (or reduce existing tensile stresses) in tungsten, such that when tensile operational stresses are applied there is an enhancement of fatigue life.

The key outcomes of the work presented in this thesis are listed below, followed by detailed discussion in the following section:

1. Vacuum furnace brazing using eutectic gold-copper alloy (Au80Cu20) has been used to manufacture dissimilar material parts for metallurgical and residual stress characterisation. Tungsten-copper, tungsten-316L stainless steel and 316L-copper joints were manufactured.
2. An almost full face bond was achieved for all material combinations. Only small voids were detected. No significant un-wetted areas were found at the interface. Small cracks were however detected at the tungsten-braze interface for tungsten-316L parts.
3. Tungsten-316L interfacial regions show a very sharp transition in chemical composition and mechanical properties (nano + micro hardness, elastic modulus) at the braze interfaces. For brazed configurations including copper there is a large degree of diffusion between copper and Au80Cu20 alloy. This is evident optically from micrographs, from EDS chemical composition profiles and from mechanical properties.
4. Temperature dependent thermal and mechanical property data were generated experimentally for the Au80Cu20 brazing alloy for the purpose of FE modelling of the brazing and thermal autofrettage process.
5. Variation in elastic properties for the brazing alloy were found depending on test method used. The effect of the different values mechanical properties of the braze layer measured were investigated using FEA.
6. Micro-cantilever testing was used to assess the elastic modulus of the braze alloy and parent materials in the as-brazed condition, in the vicinity of the interface.
7. Due to variable levels of braze material to parent material interdiffusion, a significant difference in braze layer stiffness was found for tungsten-copper compared with tungsten-316L parts.
8. FEA was used to predict the stress state in the three material combinations considered. The effects of braze material properties on the resulting residual stresses was investigated.
9. FEA predictions of residual stresses in the brazed parts were compared with experimentally measured stresses. Surface residual stress was assessed using X-ray diffraction. 2D cross sectional mapping of stress was achieved using the Contour Method.
10. Good agreement was found between predicted and measured values for the tungsten-316L brazed configuration. At the free edge, high tensile axial stresses were observed in tungsten. This is a potentially detrimental stress distribution when considering fatigue performance. Lower magnitude compressive stresses were found in the 316L steel.

11. Poor agreement was reached between FE predicted (also theoretically predicted based on a simplified two material elastic joint) and experimentally determined residual stress for tungsten-copper brazed configuration. High tensile residual stresses were measured in tungsten, whereas FEA and theoretical predictions were expected to result in tensile residual stress state. Verification of XRD results through an alternative experimental measurement technique is recommended for future research.
12. Similarly to X-ray diffraction results, Contour Method had mixed success in replicating FE predictions for tungsten-copper and tungsten-316L. Due to excessive plastic deformation during EDM sectioning of copper in the tungsten-copper part, a reliable 2D stress map could not be determined. For tungsten-316L however good agreement was found between actual and predicted stress.
13. Thermal autofrettage was successfully applied to tungsten-316L brazed parts to beneficially modify residual stress.
14. High tensile stresses in tungsten at the braze interface were shown to be reduced significantly using FEA and experimentally. The reduction in stress was found to be larger in reality than predicted by the model.
15. A reduction in tensile residual stress in the brittle tungsten section of a component, such as the divertor tile considered in this thesis, will result in improved fatigue performance under tensile operational loads.
16. Free edge residual stresses as result of dissimilar joining can be mitigated by a finishing operation such as edge grinding or turning. Residual stress modification techniques could then be applied to the as-machined part.

8.2 Discussion

The primary aim of this project was to beneficially modify the free edge residual stress in a vacuum brazed tungsten dissimilar joint. This has been achieved for tungsten-316L parts brazed with Au80Cu20 eutectic alloy through the use of thermal autofrettage. Large tensile residual stresses in tungsten following brazing were significantly reduced after application of thermal autofrettage process. The materials considered are relevant to the divertor tile of a future fusion reactor, a component subject to high cyclic loading. Therefore a beneficial modification of residual stress in a critical area such as the interface is of significant importance. Alternative residual stress modification techniques are discussed in Future Work section.

In Chapter 3 of this thesis the development of the vacuum brazing process and microstructural evaluation of the manufactured dissimilar material parts were presented. A eutectic Au80Cu20

brazing alloy was selected based on its compatibility with the parent materials (tungsten, copper, 316L austenitic stainless steel) and its viability in regards to acceptable neutron activation characteristics. A vacuum furnace brazing temperature of 950°C was found to be successful. Oxygen free high conductivity copper (>99.99% purity) was found to be required to avoid oxidation at the interface which acts as a barrier to bonding.

For this thesis simple butt joint configuration parts were manufactured for the purposes of characterisation and residual stress analysis. Based on the success of the brazing process, more complex geometries could now be manufactured for the materials discussed here. These include dissimilar material waisted mechanical specimens suitable for tensile, axial fatigue, thermal fatigue and creep testing, cylindrical dogbone specimens for rotating bend fatigue tests, fracture test specimens, and small scale component geometries. Away from the free edge of the interface, analysis of wetted area through destructive sectioning of the brazed parts showed promising results for all three material combinations. Only small voids were observed in the braze layer. The need for NDE of braze interfaces became apparent and is discussed in recommendations for future work. There was some evidence of cracking occurring in the tungsten-316L parts at the junction between tungsten and Au80Cu20 at the free edge. These cracks were observed on sectioned tungsten-316L parts during optical and electron microscopy, with typical crack lengths of 100-200μm. Further brazing trials using alternative geometries, temperatures and clamping conditions would be required to definitively conclude whether free edge cracks are likely a problem when manufacturing component-like parts.

When analysing dissimilar material joints, whether for FEA purposes or theoretical prediction of singular stresses, it is essential to treat the part as containing three distinct materials. In Chapter 3 this was shown to be a fair assumption for the tungsten-316L brazed configuration. From EDX analysis there was shown to be a sharp transition between the braze material and each of the parent materials, with minimal interdiffusion of elements. This was further evident from nano-hardness and elastic modulus profiles taken across the braze layer. In practice, brazed layers are often omitted from FE analyses and instead an idealised two material joint implemented here. Based on the findings presented here, not only should a braze layer be included in FEA, but implementing a graded layer with transitioning material properties could be required for certain cases (such as tungsten-copper discussed in conclusion 11). A recommendation for including a graded braze interface is discussed in the Future Work section.

For the two material configurations containing copper (tungsten-copper, 316L-copper) the assumption of three distinct materials was shown to be inaccurate. Large degrees of diffusion between gold and copper was observed. This diffusion results in a much more gradual transition

of properties between copper parent material and the braze layer (c. 50μm), whereas tungsten-AuCu and 316L-AuCu exhibits a much sharper transition (c. 5μm).

In Chapter 4 the temperature dependent material properties of Au80Cu20 alloy required for FEA simulations of brazing and autofrettage were generated experimentally. There was found to be a large variance in elastic modulus for two different experimental methods, DMA and ETMT, with room temperature values of c.100 GPa and c. 40 GPa respectively. To further complicate the material model, measurement of the as-brazed Au80Cu20 alloy was performed using micro-cantilever testing. This showed that there is a large variation in braze alloy elastic modulus depending on diffusion of elements in the braze interface. Although micro-mechanical tests are subject to grain size and orientation effects, there was a consistently lower elastic modulus found in the Au80Cu20 material in the tungsten-copper combination than tungsten-316L. Due to the highly expensive nature of the brazing alloy it was not possible to perform further experiments. This is strongly recommended for future research.

FEA predictions of residual stresses induced by constraint on contraction upon cooling from brazing were presented in Chapter 5. An investigation into the effect of parent material properties shows that elastic modulus and CTE are the most significant factors when determining the resulting stress state. The effect of braze layer properties proved to be less influential on brazing induced residual stress (within reasonable limits, as a zero modulus braze would provide zero constraint and as such no residual stress would form). Therefore the risk of high uncertainty of the Au80Cu20 elastic modulus degrading FE predictive capability was somewhat mitigated.

The FE modelling presented in Chapter 5 predicts high tensile stresses in the tungsten part of both tungsten-copper and tungsten-316L Au80Cu20 brazed parts. This is intuitive as the elastic modulus of tungsten is much larger than both copper and 316L, and the CTE is likewise much smaller than both copper and 316L. This relationship results in a tensile stress concentration in tungsten (as per Kelly [220] and Munz [219] when considering two dissimilar material elastic joints). Brazing induced residual stresses in 316L-copper were shown to be significantly lower due to the similarity in thermal expansion behaviour.

The prediction of high free edge tensile stress in tungsten for a tungsten-316L brazed part was verified through XRD in Chapter 6. Good agreement was also found for residual stress within the bulk of the dissimilar part through Contour Method and FEA comparison.
High tensile stress in the tungsten material, the brittle part of the joint, are not attractive from a fatigue life perspective. However the ability to accurately predict the formation of tensile stress

will allow designs to either account for the detrimental effect, or beneficially modify the stress as achieved in Chapter 7.

Although the ability of the FE model to predict the stress state in tungsten-316L brazed parts was demonstrated, there remains the problem of contradiction in nature of stress for tungsten-copper brazed parts. High tensile stresses were expected, and yet high compressive stresses exist in actuality. This disparity can be attributed to an insufficiency in the FE model to capture the complex microstructural state, and therefore material property distribution, at the tungsten-Au80Cu20-coppper brazed interfacial region. As was shown in Chapters 3 and 4, there is a significant degree of elemental diffusion for tungsten-copper part. It is therefore over simplistic to describe the system as three distinct materials with immediate transitions between parents and braze materials. Instead the properties are shown to vary with chemical composition, and are dependent on the degree of interdiffusion of elements between parent and braze materials. This was shown for elastic modulus, ranging from 90GPa to 130GPa for Au80Cu20 from micro-cantilever tests for tungsten-copper (high diffusion) and tungsten-316L (low diffusion) respectively. Such variation in properties based on composition is likely for other properties such as thermal expansion, although that could not be investigated in this work.
The Au80Cu20 alloy composition considered here does not in actuality exist across the braze region due to diffusion of gold into base copper material. To accurately model the region, a gradual transition is required containing a material model with properties for gold %wt values of 80% to 0%. At present this data is not readily available. A FE based sensitivity study investigation graded braze interlayer with varying properties for the tungsten brazed joints here is recommended for future work
As the residual stress in tungsten-316L (minimal interdiffusion) is accurately predicted, yet stress in tungsten-copper (significant interdiffusion) is not, the role of capturing the diffusion behaviour in the model is recommended as a key topic for future work. An additional key recommendation for future work is the need for a second experimental method of surface residual stress measurement to verify XRD results.

Contour Method was shown to be a valid approach for determining cross-sectional stress maps in dissimilar material brazed parts. The EDM sectioning strategy of simple end-face clamping, 0.25mm wire and one single cut from end to end produced good results for the tungsten-316L parts, both in the brazed and thermal autofrettaged condition. As with XRD, the magnitude of stresses are lower when measured experimentally with Contour Method as compared with FE predictions. The bilinear kinematic hardening model used for plastic behaviour in the model could be improved to better capture the blunting effect plastic deformation has in reality.

The cutting/clamping strategy utilized for Contour Method was found not to be sufficient for the soft copper material. Excessive deformation during EDM sectioning occurred repeatedly in copper. A bespoke clamping arrangement, with self-clamping and finer wire could all improve the results of future studies with similar parts.

The thermal autofrettage process was successfully applied to reduce brazing induced tensile stresses in the tungsten part of a tungsten-316L brazed part. The brazed dissimilar material part was treated by submerging in liquid Ni, whereupon plasticity develops due to constraint on thermal contraction. Once returned to ambient conditions, elastic unloading occurs and the tensile stress in tungsten was significantly reduced at the region of the braze interface. Reasonable agreement was found between FE predicted stress following autofrettage and experimentally measured surface (XRD) and bulk (Contour Method) modified stresses.

The primary material combinations considered in this thesis, tungsten-copper and tungsten—316L, are required to be bonded in a number of future fusion reactor divertor designs. As this is a critical component subjected to cyclic loading, requiring as long a lifetime as possible to minimize plant downtime, any reduction in detrimental residual stress is of significant importance. By applying the thermal autofrettage process presented here, or some variation thereof, the fatigue performance of a real divertor tile could be improved.

9 Recommendations for future work

Considering the successes and challenges encountered throughout this thesis, a number of areas for future research have been recommended.

9.1 Joining technologies and materials

The primary focus of the work presented in this thesis utilized vacuum furnace brazing as the joining technology. Alternative diffusion bonding technologies show promising applicability for fusion reactor components, including hot isostatic pressing (HIP) [58, 296] and hot radial pressing (HRP) [297]. HRP is a particularly promising technology for bonding a structural/heat sink material pipe within a tungsten monoblock type divertor component [34, 297]. The constraint on thermal contraction present in vacuum brazing is also present in HIP/HRP, along with additional hydrostatic loading.

As part of an undergraduate final year project performed in conjunction with this thesis, HIPing was investigated as a means of bonding tungsten to copper and tungsten to 316L, with and without an Au80Cu20 interlayer [125]. Successful bonding was achieved in both cases. An example of HIPed tungsten-copper with and without an Au80Cu20 interlayer, in (a) and (b) respectively, is shown in Figure 9-1.

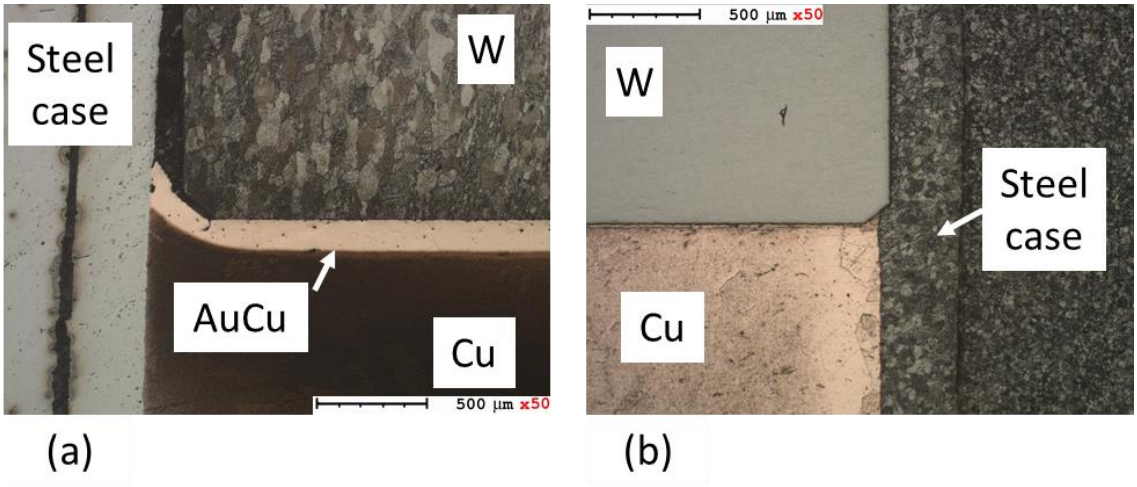

Figure 9-1 - (a) HIP tungsten-copper with Au80Cu20 compliance interlayer, and (b) HIP tungsten-copper direct bond

With the viability of HIPing as a joining process for tungsten to copper and 316L, further research is required to determine the suitability of the joined parts for divertor applications. This should include FE modelling and residual stress studies similar to those presented in this thesis. Following this thermal autofrettage, or an alternative autofrettage process, should be applied to modify stresses beneficially as per Chapter 7 of this thesis.

In addition to diffusion bonding of armour and heat sink materials, functionally grading tungsten and copper has been investigated in literature [60, 298-300]. By using functionally graded materials (FGM) as an interlayer, the high discontinuity stresses between tungsten and copper due to CTE and E dissimilarity can be essentially eliminated [298, 301]. The functionally graded tungsten-copper material can be bonded using a diffusion method or plasma spark sintering.

An alternative to using an FGM as a compliance interlayer between bulk tungsten and copper, is to create a graded structure using powder metallurgy. Multiple layers, transitioning from pure tungsten to pure copper, are deposited prior to ultra-high pressure sintering as shown in [299].

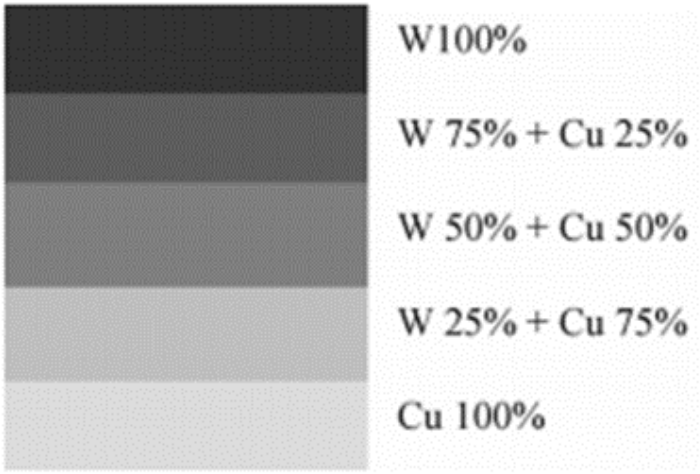

Figure 9-2 - Functionally graded tungsten-copper structure (recreated from [299])

It is recommended that this technique be utilized to produce cylindrical samples for metallurgical and residual stress characterisation purposes. This would allow for a direct comparison between vacuum brazed and FGM materials, in order to assess the perceived benefit of lower stresses in the FGM part. High resolution residual stress measurement techniques, such as micro hole drilling or slotting, should be used to determine if high stress concentrations exist locally to the graded layers.

A previous theoretical study [91] showed that multiple graded layers reduces the overall stress singularity between two dissimilar joined materials. By performing a study on FGM tungsten-copper and either vacuum brazed or direct-bond HIPed samples, the findings of this study could be verified experimentally.

Further research is required to optimize the vacuum furnace brazing process to produce joint quality suitable for a fusion reactor component. As currently stands, there is no direct guidance as to the requirement for quality of brazed joint in the ITER SDC [102]. However due to the extremely high thermal loads of 10-20 MW/m^2 it is reasonable to assume that voids cannot be tolerated due to the risk of localized melting due to air resistance. Increasing the wetted area at the braze interface, and reducing voids, was discussed in Chapter 3 and in other works [90, 91]. Continued work in improving the quality of the joint by surface modification prior to brazing, surface coating, part geometry and clamping conditions are required to reduce the quantity of bonding flaws.

Assessing the quality of the joint required destructive examination of brazed parts in this thesis. This is not a practical method for inspecting real dissimilarly joined components. In section 3.6 of this thesis non-destructive evaluation techniques such as x-ray tomography and ultrasonic imaging were examined. Although satisfactory results were not obtained here, this is an important area for future work.

Infrared thermography was successfully used to detect calibrated flaws in W-WL_{10} tiles [302], shown in Figure 9-3. This method would provide an excellent means by which to evaluate the brazed parts manufactured as part of work presented in this thesis. The thermography method, or ultrasonic measurements optimized for the brazed joints [302-304] would be well suited for detecting the presence of interfacial cracks found in the tungsten-316L parts in section 3.3.

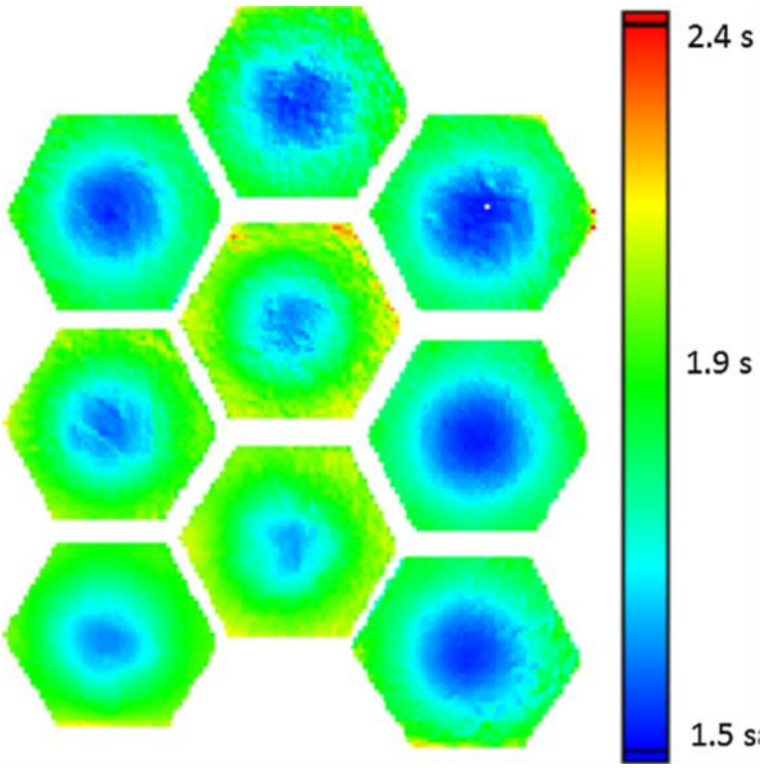

Figure 9-3 - Infrared thermography of DEMO like tungsten tiles [302]

The work contained in this thesis focused on conventional materials, namely pure tungsten, OFHC copper and 316L stainless steel. Current designs for a potential DEMO divertor often include more exotic, less-researched materials. Focusing on the pure tungsten, copper and 316L was required due to cost and availability of materials and material data. Going forward it is recommended to study the vacuum brazing process for materials such as tungsten alloys (lanthanum, rhenium), copper-chrome-zirconium alloy, oxygen dispersion strengthened copper and steels, and reduced activation ferritic martensitic steels, all of which feature in proposed divertor concepts [25, 51, 73, 77, 305].

9.2 Micro-mechanical testing

Micro-mechanical testing was identified and utilised in chapters 3 and 4 of this thesis as a useful means to assess material properties in close vicinity to the brazed interface. Micro-cantilever testing was used to determine elastic modulus in the braze layer and parent materials in the diffusion region of the interface. This concept is recommended to be further expanded to further characterise the properties in the interfacial region. By using a large array of small cantilevers, property variation can be determined with high spatial resolution to the braze layer. A similar study was conducted on irradiated and non-irradiated materials for fusion applications, (Figure 9-4, [155]).

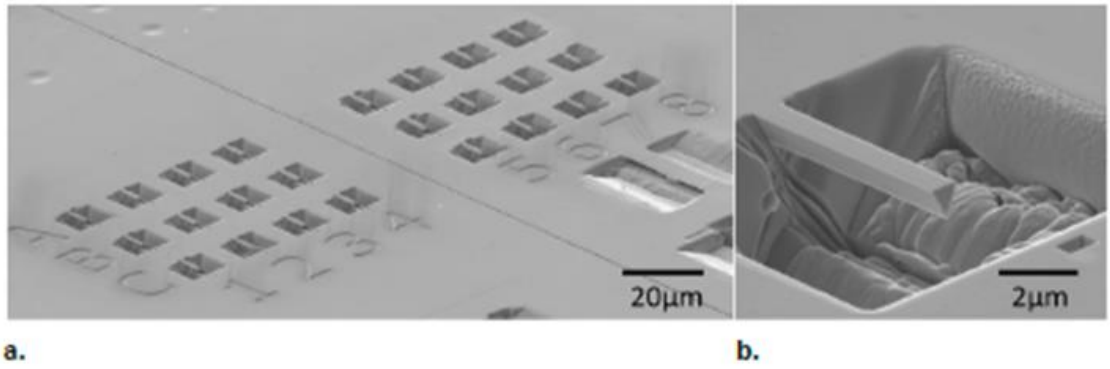

Figure 9-4 - Micro-cantilever array [155]

Micron-scale testing is recommended for residual stress measurement of the brazed materials parts presented in this thesis. As has been shown throughout this work, there is a complex microstructural and residual stress state close to, and directly in, the braze interface. By using SEM and FIB scale testing techniques, residual stresses could be measured in in these regions.

Surface relief techniques such as ring coring or slotting are identified as particularly suitable [306-309]. One of the underlying questions remaining from this thesis is the unexpected compressive stress in the tungsten material of the tungsten-copper brazed joint. Using a micron scale technique such as discussed here, residual stresses close to the surface could be mapped to better understand the stress field in these parts. For example, the slot milling technique with DIC measurement of surface relaxation of peened material shown in Figure 9-5 (recreated from [309]) would provide sufficient resolution to measure stress in the AuCu braze layer itself, in addition to the tungsten material.

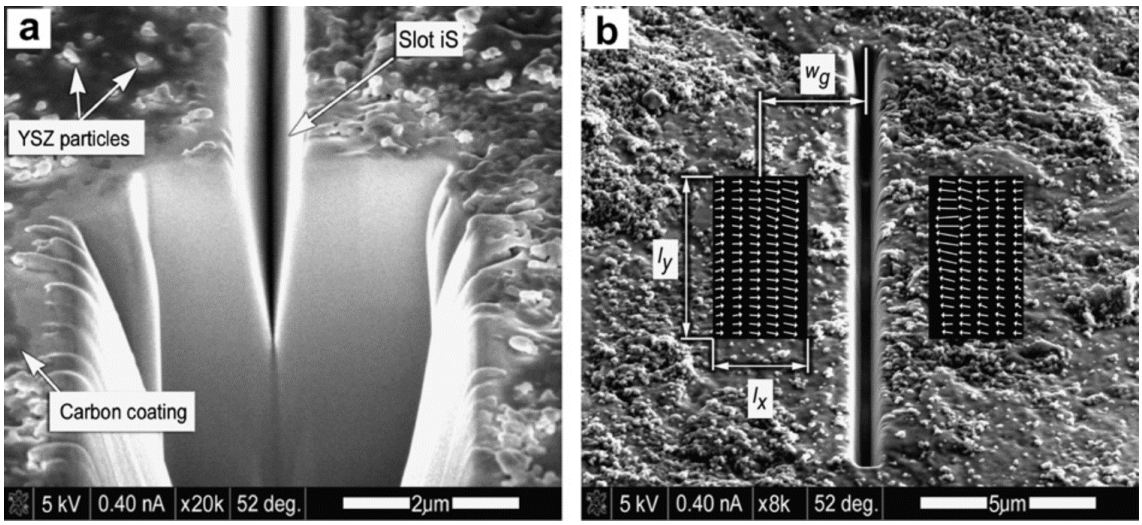

Figure 9-5 – FIB milled slot for surface relaxation residual stress measurement [309]

By using this technique, residual stress could be measured in both the Au80Cu20 braze material and copper material, neither of which were possible using conventional techniques such as XRD or hole drilling. These measurements could also provide a second experimental method for the tungsten-316L XRD measurements to validate the findings of the work.

Further to micron-scale residual stress measurements, plastic strain mapping by way of EBSD is recommended to investigate the plastic deformation behaviour in the Au80Cu20 brazed parts [292, 293]. This would be useful in furthering understanding of two key questions arising from this thesis.

Firstly, the magnitude of stresses measured in chapters 6 and 7 were generally lower than predicted. This is attributed to additional plastic strain developing than is predicted by the FE model. A combination of further FE studies with alternative hardening models, in addition to direct measurement of plastic strains in the interface area, would help answer this question definitively.

Secondly, there was a contradiction between predicted and measured residual stress in the brazed tungsten-copper parts. Conventional measurements of residual stress were not sufficient to fully understand the stress state at the interface. By combining micron-scale measurements, plastic strain mapping at the interface, and further modelling efforts, it should be possible to resolve the discrepancy.

An additional application for EBSD plastic strain mapping is recommended to be understanding of the plastic region during cooling brazing and thermal autofrettage modification. The development of plasticity is a requirement for residual stress induced from brazing. In order to reduce tensile stresses by elastic unloading in the autofrettage process, it is first necessary to grow

the plastic region at the interface. EBSD mapping would allow the visualization of this in real parts to compliment the theoretical understanding of the process.

9.3 Development of residual stress prediction of dissimilar material joints

A key recommendation arising from this thesis is to further optimize the residual stress modification of brazed (or otherwise bonded) tungsten joints for divertor applications. FE modelling is a critical part of this to select optimal parameters for brazing and autofrettage modification. To improve the accuracy of the modelling, improved material data for Au80Cu20 brazing alloy is required.

Large variations in temperature dependent elastic properties were found in Chapter 4 and 5 for the brazing alloy. Further experimental generation of data was not possible due to the restrictive cost of the material. If the Au80Cu20 material is to be considered for real, structural components then a large testing program is required to generate temperature dependent elastic and strain-rate dependent deformation behaviour. This should be achieved by miniaturized testing, such as ETMT/DIC or DMA, due to the expensive nature of the material. Additionally, sub-zero temperature material properties are required to improve the accuracy of thermal autofrettage modelling.

In practice, the material that exists in the braze region is not necessarily the Au80Cu20 composition that exists in the un-brazed condition. This is due to interdiffusion of braze alloy and parent material during brazing (or a process such as HIPing). It is therefore recommended to characterise Au %wt dependent properties. In practice this is not a trivial process. An initial study using nano indentation as in Chapter 3 and 4 to gather composition dependent properties is recommended.

Additionally, an FE study exploring the effect of changes in properties of brazing alloy on resulting residual stress should be performed. Simulations of this nature were presented in Chapter 5. Extending this type of study to include drastic changes in material properties in the temperature range of the AuCu phase change should help to improve the model to replicate the compressive stresses found in tungsten (for tungsten-copper brazed part). The effect of a transitional region of material property variation, as opposed to a sharp transition, is also recommended.

Validating FE results with experimental measurements of residual stress is required in order to have confidence in the models predictive abilities. XRD was successfully used in this thesis to measure residual stress and should be considered for any future studies. Contour Method was used to a lesser degree of success. For certain parts the cutting and clamping strategy applied was not suitable. For future research, the use of bespoke clamping should be considered to minimize bulk movement of the part during cutting. This also serves to reduce plasticity developing at the cutting zone which will improve results. This should include self-contained clamping using drilled holes and multiple cutting steps [267, 269, 310]. The use of techniques to improve the quality of the cut, particularly at edge locations, is recommended when considering small parts such as the brazed components here. Recommendations include finer cutting wire and the use of sacrificial material bonded to the outer surface of the cutting plane.

It is recommended in future studies that larger diameter parts than the 12.7mm utilized here, or alternatively prismatic parts, are used to further enable the use of conventional residual stress measurement techniques. ESPI and conventional hole-drilling residual stress measurements could be used in addition to XRD on such parts. Measurement of surface residual stresses by an alternative technique to XRD would provide a means of verifying experimental results presented in Chapter 6 and Chapter 7 of this thesis.

Further verification of the measured residual stresses presented in this thesis is recommend for future work, by way of neutron diffraction. Neutron diffraction is a technique often used for characterising residual stresses in joined interfaces, in particular for welded joints [311-313]. This technique would allow for triaxial stress measurements which could be used to verify FE predictions and to provide a second experimental measurement to compliment Contour Method measurements.

9.4 Other considerations

In this thesis the residual stress of a tungsten brazed part was modified to give a potentially improved fatigue performance. The next logical step in that path is to quantify what, if any, performance enhancement can be gained through thermal autofrettage of dissimilar material brazed parts.

The first step in this process is to manufacture and test parts in the as brazed condition. Beginnings of this work were conducted using axial fatigue testing of simple butt joints and

rotating bend fatigue testing [91]. These techniques would therefore be appropriate for quantifying the performance benefit of thermal autofrettage. By reducing the tensile residual stress in the brittle tungsten material, where fatigue failure is expected, the mean stress during testing is effectively reduced and the finite life and endurance limit of the brazed part should increase. Generation of an S-N curve for each of tungsten-copper and tungsten-316L is recommended. Following this, thermal autofrettage should be applied to the parts, and additional fatigue testing commence. Should an increase in fatigue performance be significant enough, then the thermal autofrettage process would be recommended for treating actual divertor components.

In addition to thermal autofrettage, alternative stress modification techniques could be investigated to through both residual stress characterisation and mechanical testing. These include mechanical autofrettage through either hydrostatic pressure, or applied compressive loading. Surface engineering techniques such as shot and laser peening, or edge grinding, are also recommended to be considered.

The entirety of work in this thesis considers conventional material properties and conditions (vacuum brazed, room temperature, liquid Ni). An additional complexity that exists in reality for plasma facing components is the effect of neutron irradiation. Neutron irradiation is known to have a significant effect on material mechanical properties [147, 314, 315]. Elastic properties are known to degrade and embrittlement occurs. The effect of neutron irradiation on dissimilar material brazed joints is very scarcely reported in literature [316].

A metallurgical and residual stress characterisation of the brazed parts considered here, in either ion or neutron irradiated condition, would be a highly useful and strongly recommend avenue for future research. This would allow understanding of material and mechanical behaviour in the condition the dissimilar part would actually be in as part of a plasma facing component in a DEMO-like reactor.

List of References

[1] C. L. Smith, "The need for fusion," *Fusion Engineering and Design,* vol. 74, pp. 3-8, 2005.

[2] H. C. J. Godfray, J. R. Beddington, I. R. Crute, L. Haddad, D. Lawrence, J. F. Muir*, et al.*, "Food Security: The Challenge of Feeding 9 Billion People," *Science,* vol. 327, pp. 812-818, 2010.

[3] N. S. Lewis and D. G. Nocera, "Powering the planet: Chemical challenges in solar energy utilization," *Proceedings of the National Academy of Sciences of the United States of America,* vol. 103, pp. 15729-15735, 2006.

[4] *http://www.who.int/mediacentre/factsheets World Health Organistation, WHO Website (accessed 24/05/2017).*

[5] D. Maisonnier, D. Campbell, I. Cook, L. Di Pace, L. Giancarli, J. Hayward*, et al.*, "Power plant conceptual studies in Europe," *Nuclear Fusion,* vol. 47, pp. 1524-1532, 2007.

[6] K. Lackner, R. Andreani, D. Campbell, M. Gasparotto, D. Maisonnier, and M. A. Pick, "Long-term fusion strategy in Europe," *Journal of Nuclear Materials,* vol. 307–311, Part 1, pp. 10-20, 2002.

[7] D. J. Ward, N. P. Taylor, and I. Cook, "Economically acceptable fusion power stations with safety and environmental advantages," *Fusion Engineering and Design,* vol. 58–59, pp. 1033-1036, 2001.

[8] I. Cook, "Economic, safety and environmental characteristics of commercial fusion power," *IAEA First Generation of Fusion Power Plants: Design and Technology,* 2005.

[9] D. J. Ward and S. L. Dudarev, "Economically competitive fusion," *Materials Today,* vol. 11, pp. 46-53, 2008.

[10] D. Maisonnier, I. Cook, S. Pierre, B. Lorenzo, B. Edgar, B. Karin*, et al.*, "The European power plant conceptual study," *Fusion Engineering and Design,* vol. 75-79, pp. 1173-1179, 2005.

[11] I. Cook, R. L. Miller, and D. J. Ward, "Prospects for economic fusion electricity," *Fusion Engineering and Design,* vol. 63–64, pp. 25-33, 2002.

[12] C. A. Haynam, P. J. Wegner, J. M. Auerbach, M. W. Bowers, S. N. Dixit, G. V. Erbert*, et al.*, "National ignition facility laser performance status," *Applied Optics,* vol. 46, pp. 3276-3303, 2007.

[13] *https://www.euro-fusion.org/jet/ (accessed 24/05/2017).*

[14] *https://www.ipp.mpg.de/w7x (accessed 24/05/2017).*

[15] *www.iter.org ITER Organisation Website (accessed 24/05/17)*

[16] Y. Shimomura, "The present status and future prospects of the ITER project," *Journal of Nuclear Materials,* vol. 329–333, Part A, pp. 5-11, 2004.

[17] D. Maisonnier, I. Cook, S. Pierre, B. Lorenzo, D. P. Luigi, G. Luciano*, et al.*, "DEMO and fusion power plant conceptual studies in Europe," *Fusion Engineering and Design,* vol. 81, pp. 1123-1130, 2006.

[18] G. Federici, C. Bachmann, W. Biel, L. Boccaccini, F. Cismondi, S. Ciattaglia*, et al.*, "Overview of the design approach and prioritization of R&D activities towards an EU DEMO," *Fusion Engineering and Design,* 2015.

[19] S. Ichimaru, "Nuclear fusion in dense plasmas," *Reviews of Modern Physics,* vol. 65, pp. 255-299, 1993.

[20] *European Nuclear Society, ENS Website (www.euronuclear.org).*

[21] V. P. Smirnov, "Tokamak foundation in USSR/Russia 1950-1990," *Nuclear Fusion,* vol. 50, 2010.

[22] F. Najmabadi, A. Abdou, L. Bromberg, T. Brown, V. C. Chan, M. C. Chu*, et al.*, "The ARIES-AT advanced tokamak, Advanced technology fusion power plant," *Fusion Engineering and Design,* vol. 80, pp. 3-23, 2006.

[23] N. Mitchell, A. Devred, P. Libeyre, B. Lim, and F. Savary, "The ITER magnets: Design and construction status," *IEEE Transactions on Applied Superconductivity,* vol. 22, 2012.
[24] G. Federici, C. H. Skinner, J. N. Brooks, J. P. Coad, C. Grisolia, A. A. Haasz*, et al.*, "Plasma-material interactions in current tokamaks and their implications for next step fusion reactors," *Nuclear Fusion,* vol. 41, pp. 1967-2137, 2001.
[25] P. Norajitra, S. I. Abdel-Khalik, L. M. Giancarli, T. Ihli, G. Janeschitz, S. Malang*, et al.*, "Divertor conceptual designs for a fusion power plant," *Fusion Engineering and Design,* vol. 83, pp. 893-902, 2008.
[26] J. Reiser and M. Rieth, "Optimization and limitations of known DEMO divertor concepts," *Fusion Engineering and Design,* vol. 87, pp. 718-721, 2012.
[27] V. Barabash, M. Akiba, A. Cardella, I. Mazul, B. C. Odegard Jr, L. Plöchl*, et al.*, "Armor and heat sink materials joining technologies development for ITER plasma facing components," *Journal of Nuclear Materials,* vol. 283–287, Part 2, pp. 1248-1252, 2000.
[28] A. R. Raffray, R. Nygren, D. G. Whyte, S. Abdel-Khalik, R. Doerner, F. Escourbiac*, et al.*, "High heat flux components—Readiness to proceed from near term fusion systems to power plants," *Fusion Engineering and Design,* vol. 85, pp. 93-108, 2010.
[29] M. Merola, W. Dänner, and M. Pick, "EU R&D on divertor components," *Fusion Engineering and Design,* vol. 75-79, pp. 325-331, 2005.
[30] G. Janeschitz, L. Boccaccini, W. H. Fietz, W. Goldacker, T. Ihli, R. Meyder*, et al.*, "Development of fusion technology for DEMO in Forschungszentrum Karlsruhe," *Fusion Engineering and Design,* vol. 81, pp. 2661-2671, 2006.
[31] S. Wurster, N. Baluc, M. Battabyal, T. Crosby, J. Du, C. García-Rosales*, et al.*, "Recent progress in R&D on tungsten alloys for divertor structural and plasma facing materials," *Journal of Nuclear Materials,* vol. 442, pp. S181-S189, 2013.
[32] M. Rieth and e. al, "Recent progress in research on tungsten materials for nuclear fusion applications in Europe," *Journal of Nuclear Materials,* vol. 432, pp. 482-500, 2013.
[33] Y. Patil, S. S. Khirwadkar, and D. Krishnan, "Thermal response of actively cooled tungsten monoblocks to inhomogeneous surface heat loading," *Journal of Physics: Conference Series,* vol. 823, 2017.
[34] M. Roedig, W. Kuehnlein, J. Linke, M. Merola, E. Rigal, B. Schedler*, et al.*, "Investigation of tungsten alloys as plasma facing materials for the ITER divertor," *Fusion Engineering and Design,* vol. 61–62, pp. 135-140, 2002.
[35] A. Li-Puma, M. Richou, P. Magaud, M. Missirlian, E. Visca, and V. P. Ridolfini, "Potential and limits of water cooled divertor concepts based on monoblock design as possible candidates for a DEMO reactor," *Fusion Engineering and Design,* vol. 88, pp. 1836-1843, 2013.
[36] K. Tobita, S. Nishio, M. Enoeda, M. Sato, T. Isono, S. Sakurai*, et al.*, "Design study of fusion DEMO plant at JAERI," *Fusion Engineering and Design,* vol. 81, pp. 1151-1158, 2// 2006.
[37] P. J. Withers, "Residual stress and its role in failure," *Reports on Progress in Physics,* vol. 70, p. 2211, 2007.
[38] K. Ezato, S. Suzuki, Y. Seki, H. Yamada, T. Hirayama, K. Yokoyama*, et al.*, "Progress of ITER full tungsten divertor technology qualification in Japan: Manufacturing full-scale plasma-facing unit prototypes," *Fusion Engineering and Design,* vol. 109–111, Part B, pp. 1256-1260, 2016.
[39] J. B. Weathers, L. Crosatti, R. Kruessmann, D. L. Sadowski, and S. I. Abdel-Khalik, "Development of modular helium-cooled divertor for DEMO based on the multi-jet impingement (HEMJ) concept: Experimental validation of thermal performance," *Fusion Engineering and Design,* vol. 83, pp. 1120-1125, 2008.
[40] E. Visca, "KIT Fusion Summer School course notes," Karsruhe Institute of Technology, Germany, 2013.
[41] R. A. Pitts, S. Carpentier, F. Escourbiac, T. Hirai, V. Komarov, S. Lisgo*, et al.*, "A full tungsten divertor for ITER: Physics issues and design status," *Journal of Nuclear Materials,* vol. 438, Supplement, pp. S48-S56, 2013.

[42] K. Ezato, S. Suzuki, Y. Seki, K. Mohri, K. Yokoyama, F. Escourbiac*, et al.*, "Progress of ITER full tungsten divertor technology qualification in Japan," *Fusion Engineering and Design,* vol. 98–99, pp. 1281-1284, 2015.

[43] P. Gavila, B. Riccardi, S. Constans, J. L. Jouvelot, I. B. Vastra, M. Missirlian*, et al.*, "High heat flux testing of mock-ups for a full tungsten ITER divertor," *Fusion Engineering and Design,* vol. 86, pp. 1652-1655, 2011.

[44] E. Visca, E. Cacciotti, A. Komarov, S. Libera, N. Litunovsky, A. Makhankov*, et al.*, "Manufacturing, testing and post-test examination of ITER divertor vertical target W small scale mock-ups," *Fusion Engineering and Design,* vol. 86, pp. 1591-1594, 2011.

[45] Y. G. Prokofiev, V. R. Barabash, V. F. Khorunov, S. V. Maksimova, A. A. Gervash, S. A. Fabritsiev*, et al.*, "Some problems of brazing technology for the divertor plate manufacturing," *Journal of Nuclear Materials,* vol. 191–194, Part A, pp. 483-487, 1992.

[46] S. Suzuki, K. Ezato, T. Hirose, K. Sato, H. Yoshida, M. Enoeda*, et al.*, "First wall and divertor engineering research for power plant in JAERI," *Fusion Engineering and Design,* vol. 81, pp. 93-103, 2006.

[47] P. Norajitra, R. Giniyatulin, T. Ihli, G. Janeschitz, W. Krauss, R. Kruessmann*, et al.*, "He-cooled divertor development for DEMO," *Fusion Engineering and Design,* vol. 82, pp. 2740-2744, 2007.

[48] P. Norajitra, R. Giniyatulin, T. Hirai, W. Krauss, V. Kuznetsov, I. Mazul*, et al.*, "Current status of He-cooled divertor development for DEMO," *Fusion Engineering and Design,* vol. 84, pp. 1429-1433, 2009.

[49] P. Norajitra, S. Antusch, L. V. Boccaccini, M. Kuzmic, I. Maione, and L. Spatafora, "He-cooled demo divertor: Design verification testing against mechanical impact loads," *Fusion Engineering and Design,* vol. 87, pp. 932-934, 2012.

[50] P. Norajitra, S. Antusch, R. Giniyatulin, I. Mazul, G. Ritz, H. J. Ritzhaupt-Kleissl*, et al.*, "Current state-of-the-art manufacturing technology for He-cooled divertor finger," *Journal of Nuclear Materials,* vol. 417, pp. 468-471, 2011.

[51] R. Lässer, N. Baluc, J. L. Boutard, E. Diegele, S. Dudarev, M. Gasparotto*, et al.*, "Structural materials for DEMO: The EU development, strategy, testing and modelling," *Fusion Engineering and Design,* vol. 82, pp. 511-520, 2007.

[52] J. Reiser, M. Rieth, B. Dafferner, and A. Hoffmann, "Tungsten foil laminate for structural divertor applications – Basics and outlook," *Journal of Nuclear Materials,* vol. 423, pp. 1-8, 2012.

[53] J. Reiser, M. Rieth, A. Möslang, B. Dafferner, A. Hoffmann, X. Yi*, et al.*, "Tungsten foil laminate for structural divertor applications – Tensile test properties of tungsten foil," *Journal of Nuclear Materials,* vol. 434, pp. 357-366, 2013.

[54] J. Reiser, J. Hoffmann, U. Jäntsch, M. Klimenkov, S. Bonk, C. Bonnekoh*, et al.*, "Ductilisation of tungsten (W): On the shift of the brittle-to-ductile transition (BDT) to lower temperatures through cold rolling," *International Journal of Refractory Metals and Hard Materials,* vol. 54, pp. 351-369, 2016.

[55] A. Pizzuto, P. J. Karditsas, C. Nardi, and S. Papastergiou, "HETS performances in He cooled power plant divertor," *Fusion Engineering and Design,* vol. 75–79, pp. 481-484, 2005.

[56] J. R. Nicholas, P. Ireland, D. Hancock, and D. Robertson, "Development of a high-heat flux cooling element with potential application in a near-term fusion power plant divertor," *Fusion Engineering and Design,* vol. 96–97, pp. 136-141, 2015.

[57] S. Wang, Y. Ling, P. Zhao, N. Zang, J. Wang, S. Guo*, et al.*, "Bonding tungsten, W–Cu-alloy and copper with amorphous Fe–W alloy transition," *Fusion Engineering and Design,* vol. 88, pp. 248-252, 2013.

[58] H. Noto, T. Yamada, Y. Hishinuma, and T. Muroga, "Development of high strength W/V/Au/ODS-Cu joint using HIP process," *Nuclear Materials and Energy*.

[59] J. Reiser, P. Norajitra, and R. Ruprecht, "Numerical investigation of a brazed joint between W-1%La2O3 and ODS EUROFER components," *Fusion Engineering and Design,* vol. 83, pp. 1126-1130, 2008.

[60] R. Mitteau, J. M. Missiaen, P. Brustolin, O. Ozer, A. Durocher, C. Ruset*, et al.*, "Recent developments toward the use of tungsten as armour material in plasma facing components," *Fusion Engineering and Design,* vol. 82, pp. 1700-1705, 2007.
[61] B. A. Kalin, V. T. Fedotov, O. N. Sevrjukov, A. N. Kalashnikov, A. N. Suchkov, A. Moeslang*, et al.*, "Development of brazing foils to join monocrystalline tungsten alloys with ODS-EUROFER steel," *Journal of Nuclear Materials,* vol. 367-370, pp. 1218-1222, 2007.
[62] T. Chehtov, J. Aktaa, and O. Kraft, "Mechanical characterization and modeling of brazed EUROFER-tungsten-joints," *Journal of Nuclear Materials,* vol. 367-370, pp. 1228-1232, 2007.
[63] Z. Zhong, H.-c. Jung, T. Hinoki, and A. Kohyama, "Effect of joining temperature on the microstructure and strength of tungsten/ferritic steel joints diffusion bonded with a nickel interlayer," *Journal of Materials Processing Technology,* vol. 210, pp. 1805-1810, 2010.
[64] G. E. Totten, M. A. H. Howes, and T. Inoue, "Handbook of residual stress and deformation of steel," ed. Materials Park, OH :: ASM International, 2002.
[65] P. J. Withers and H. K. D. H. Bhadeshia, "Residual Stress Part 2, Natrue and Origins," *Materials Science and Technology,* vol. 17, p. 366, 2001.
[66] A. Levy, "Thermal Residual Stresses in Ceramic-to-Metal Brazed Joints," *Journal of the American Ceramic Society,* vol. 74, pp. 2141-2147, 1991.
[67] G. S. Schajer, *Practical residual stress measurement methods*: Wiley, 2013.
[68] M. Galli, J. Botsis, J. Janczak-Rusch, G. Maier, and U. Welzel, "Characterization of the Residual Stresses and Strength of Ceramic-Metal Braze Joints," *Journal of Engineering Materials and Technology,* vol. 131, p. 021004, 2009.
[69] Y. Nemoto, "Analysis and measurement of residual stress distribution of vanadium/ceramics joints for fusion reactor applications," *Journal of Nuclear Materials,* vol. 258-263, 1998.
[70] C. T. Chang and R. K. Shiue, "Infrared brazing Ti–6Al–4V and Mo using the Ti–15Cu–15Ni braze alloy," *International Journal of Refractory Metals and Hard Materials,* vol. 23, pp. 161-170, 2005.
[71] J. H. You and G. Breitbach, "Deformation of ductile braze layer in a joint element under cyclic thermal loads," *Fusion Engineering and Design,* vol. 38, pp. 307-317, 1998.
[72] T. Hirai, K. Ezato, and P. Majerus, "ITER Relevant High Heat Flux Testing on Plasma Facing Surfaces," *MATERIALS TRANSACTIONS,* vol. 46, pp. 412-424, 2005.
[73] D. Stork, P. Agostini, J. L. Boutard, D. Buckthorpe, E. Diegele, S. L. Dudarev*, et al.*, "Developing structural, high-heat flux and plasma facing materials for a near-term DEMO fusion power plant: The EU assessment," *Journal of Nuclear Materials,* vol. 455, pp. 277-291, 2014.
[74] P. Norajitra, A. Gervash, R. Giniyatulin, T. Ihli, W. Krauss, R. Kruessmann*, et al.*, "He-cooled divertor for DEMO: Experimental verification of the conceptual modular design," *Fusion Engineering and Design,* vol. 81, pp. 341-346, 2006.
[75] M. Rieth, J. L. Boutard, S. L. Dudarev, T. Ahlgren, S. Antusch, N. Baluc*, et al.*, "Review on the EFDA programme on tungsten materials technology and science," *Journal of Nuclear Materials,* vol. 417, pp. 463-467, 2011.
[76] D. Easton, J. Wood, A. Galloway, Y. Zhang, M. B. O. Robbie, and C. Hardie, "Brazing Development and Interfacial Metallurgy Study of Tungsten and Copper Joints with Eutectic Gold Copper Brazing Alloy," *Fusion Engineering and Design,* vol. 98–99, pp. 1956–1959, 2015.
[77] H. Bolt, V. Barabash, W. Krauss, J. Linke, R. Neu, S. Suzuki*, et al.*, "Materials for the plasma-facing components of fusion reactors," *Journal of Nuclear Materials,* vol. 329-333, pp. 66-73, 2004.
[78] A. Herrmann, H. Greuner, N. Jaksic, B. Böswirth, F. Reimold, A. Scarabosio*, et al.*, "Design and concept validation of the new solid tungsten divertor for ASDEX Upgrade," *Fusion Engineering and Design,* vol. 88, pp. 577-580, 2013.

[79] R. J. Kurtz, K. Abe, V. M. Chernov, D. T. Hoelzer, H. Matsui, T. Muroga, *et al.*, "Recent progress on development of vanadium alloys for fusion," *Journal of Nuclear Materials,* vol. 329–333, Part A, pp. 47-55, 2004.
[80] H. Bolt, V. Barabash, G. Federici, J. Linke, A. Loarte, J. Roth, *et al.*, "Plasma facing and high heat flux materials – needs for ITER and beyond," *Journal of Nuclear Materials,* vol. 307–311, Part 1, pp. 43-52, 2002.
[81] L. V. Boccaccini, L. Giancarli, G. Janeschitz, S. Hermsmeyer, Y. Poitevin, A. Cardella, *et al.*, "Materials and design of the European DEMO blankets," *Journal of Nuclear Materials,* vol. 329-333, pp. 148-155, 2004.
[82] M. Gasparotto, G. Federici, and F. R. Casci, "Design and technical status of the EU contribution to ITER," *Fusion Engineering and Design,* vol. 84, pp. 143-149, 2009.
[83] K. Ioki, M. Akiba, P. Barabaschi, V. Barabash, S. Chiocchio, W. Daenner, *et al.*, "ITER nuclear components, preparing for the construction and R&D results," *Journal of Nuclear Materials,* vol. 329–333, Part A, pp. 31-38, 2004.
[84] G. Janeschitz, "Plasma–wall interaction issues in ITER," *Journal of Nuclear Materials,* vol. 290–293, pp. 1-11, 2001.
[85] L. V. Boccaccini, L. Giancarli, G. Janeschitz, S. Hermsmeyer, Y. Poitevin, A. Cardella, *et al.*, "Materials and design of the European DEMO blankets," *Journal of Nuclear Materials,* vol. 329–333, Part A, pp. 148-155, 2004.
[86] M. Gasparotto, L. V. Boccaccini, L. Giancarli, S. Malang, and Y. Poitevin, "Demo blanket technology R&D results in EU," *Fusion Engineering and Design,* vol. 61–62, pp. 263-271, 2002.
[87] P. Norajitra, S. Antusch, R. Giniyatulin, V. Kuznetsov, I. Mazul, H. J. Ritzhaupt-Kleissl, *et al.*, "Progress of He-cooled divertor development for DEMO," *Fusion Engineering and Design,* vol. 86, pp. 1656-1659, 2011.
[88] T. Weber, M. Härtelt, and J. Aktaa, "Considering brittleness of tungsten in failure analysis of helium-cooled divertor components with functionally graded tungsten/EUROFER97 joints," *Engineering Fracture Mechanics,* vol. 100, pp. 63-75, 2013.
[89] S. Jitsukawa, A. Kimura, A. Kohyama, R. L. Klueh, A. A. Tavassoli, B. van der Schaaf, *et al.*, "Recent results of the reduced activation ferritic/martensitic steel development," *Journal of Nuclear Materials,* vol. 329–333, Part A, pp. 39-46, 2004.
[90] Y. Zhang, A. Galloway, J. Wood, M. B. O. Robbie, D. Easton, and W. Zhu, "Interfacial metallurgy study of brazed joints between tungsten and fusion related materials for divertor design," *Journal of Nuclear Materials,* vol. 454, pp. 207-216, 2014.
[91] M. B. O. Robbie, "A Study of Joints between Dissimilar Materials with a View to Fatigue Performance in Fusion Reactor Applications," PhD, Mechanical and Aerospace Engineering, University of Strathclyde, 2016.
[92] D. Jacobson and G. Humpston, *Principles Of Brazing*, 2005.
[93] M. Schwartz, "Brazing," *ASM International,* 2003.
[94] "Volume 6 - Welding, Brazing, and Soldering," *ASM Metals Handbook,* 2001.
[95] http://www.ccfe.ac.uk/special_techniques.aspx *(accessed 24/05/2017).*
[96] T. Anraku, I. Sakaihara, T. Hoshikawa, and M. Taniwaki, "Phase Transitions and Thermal Expansion Behavior in AuCu Alloy," *Materials Transactions,* vol. 50, pp. 683-688, 2009.
[97] I. M. Wolff and M. B. Cortie, "The development of Spangold," *Gold Bulletin,* vol. 27, pp. 44-54, 1994.
[98] "Volume 3 - Alloy Phase Diagrams.pdf," *ASM Metals Handbook,* 2001.
[99] J. Wood and e. al, "Theoretical elastic stress singularities...much maligned and misunderstood," *NAFEMS World Congress 2015,* 2015.
[100] N. Hamilton, "Niall Hamilton Thesis," PhD, Mechanical and Aerospace Engineering, University of Strathclyde, 2013.
[101] http://www.bodycote.com/en/services/metal-joining/furnace-brazing.aspx *(accessed 24/05/2017).*
[102] "ITER Structural design criteria for in-vessell components," 2001.
[103] "Volume 10 Materials Characterization," *ASM Metals Handbook,* 2001.

[104] Erik Lassner and W.-D. Schubert, *Tungsten- Properties, Chemistry, Technology of the Element, Alloys, and Chemical Compounds* 1999.
[105] S. Cronje, R. E. Kroon, W. D. Roos, and J. H. Neethling, "Twinning in copper deformed at high strain rates," *Bulletin of Materials Science,* vol. 36, pp. 157-162, 2013.
[106] C. X. Huang, K. Wang, S. D. Wu, Z. F. Zhang, G. Y. Li, and S. X. Li, "Deformation twinning in polycrystalline copper at room temperature and low strain rate," *Acta Materialia,* vol. 54, pp. 655-665, 2// 2006.
[107] V. Slugen, J. Kuriplach, P. Ballo, P. Domonkos, G. Kögel, P. Sperr*, et al.*, "Positron annihilation Investigations of defects in copper alloys selected for nuclear fusion technology," *Fusion Engineering and Design,* vol. 70, pp. 141-153, 2004.
[108] C. Lundin and W. Delong, "Ferrite-Fissuring Relationship in austenitic stainless steel weld metals," *Welding Research Supplement,* 1975.
[109] S. Y. Kim, H. S. Kwon, and H. S. Kim, "Effect of Delta Ferrite on Corrosion Resistance of Type 316L Stainless Steel in Acidic Chloride Solution by Micro-Droplet Cell," *Solid State Phenomena,* vol. 124-126, pp. 1533-1536, 2007.
[110] A. F. Padilha, C. F. Tavares, and M. A. Martorano, "Delta Ferrite Formation in Austenitic Stainless Steel Castings," *Materials Science Forum,* vol. 730-732, pp. 733-738, 2012.
[111] S. R. Moturu, "Characterization of Stress and Plastic Residual Strain In Austenitic Stainless Steel Weldments " PhD, Department of Engineering Innovation, Open University, 2015.
[112] *http://www.alicona.com/products/infinitefocus (accessed 24/05/2017).*
[113] I. Langmuir, "Thoriated tungsten filaments," *Journal of the Franklin Institute,* vol. 217, pp. 543-569, 1934.
[114] T. Watanabe, "Approach to grain boundary design for strong and ductile polycrystals," *Res Mechanica: International Journal of Structural Mechanics and Materials Science,* vol. 11, pp. 47-84, 1984.
[115] J. W. Hutchinson and A. G. Evans, "On the delamination of thermal barrier coatings in a thermal gradient," *Surface and Coatings Technology,* vol. 149, pp. 179-184, 2002.
[116] L. Suominen, M. Khurshid, and J. Parantainen, "Residual Stresses in Welded Components Following Post-weld Treatment Methods," *Procedia Engineering,* vol. 66, pp. 181-191, 2013.
[117] Y. Matsumoto, F. Hashimoto, and G. Lahoti, "Surface Integrity Generated by Precision Hard Turning," *CIRP Annals - Manufacturing Technology,* vol. 48, pp. 59-62, 1999.
[118] N. R. Hamilton, J. Wood, A. Galloway, M. B. Olsson Robbie, and Y. Zhang, "The metallurgy, mechanics, modelling and assessment of dissimilar material brazed joints," *Journal of Nuclear Materials,* vol. 432, pp. 42-51, 2013.
[119] S. Chen and B. A. Chin, "Low activation braze joint of dispersion-strengthened copper," *Journal of Nuclear Materials,* vol. 225, pp. 132-136, 1995.
[120] M. K. Ghovanlou, H. Jahed, and A. Khajepour, "Mechanical reliability characterization of low carbon steel brazed joints with copper filler metal," *Materials Science and Engineering: A,* vol. 528, pp. 6146-6156, 2011.
[121] *http://www.hitachi-hightech.com/eu/product_detail/?pn=em-su8200&version= (accessed 24/05/2017).*
[122] N. Stoloff, "Physical Metallurgy and processing of Intermetallic Compounds," 1995.
[123] C. A. Schuh, "Nanoindentation studies of materials," *Materials Today,* vol. 9, pp. 32-40, 2006.
[124] W. C. Oliver and G. M. Pharr, "Measurement of hardness and elastic modulus by instrumented indentation: Advances in understanding and refinements to methodology," *Journal of Materials Research,* vol. 19, pp. 3-20, 2004.
[125] K. Johnston, "A Viability Study for the use of Hot Isostatic Press (HIP) Joining for Nuclear Fusion-Relevant Materials," Bachelor of Engineering, Mechanical and Aerospace Engineering, University of Strathclyde, 2015.
[126] T. W. Institute. (www.twi-global.com (accessed 11/10/17)).

[127] J. Lee, J. Park, and Y. Cho, "A novel ultrasonic NDE for shrink fit welded structures using interface waves," *Ultrasonics,* vol. 68, pp. 1-7, 2016.
[128] G. H. Kim, C. K. Park, S. W. Jin, H. S. Kim, K. H. Hong, Y. J. Lee*, et al.*, "Qualification of phased array ultrasonic examination on T-joint weld of austenitic stainless steel for ITER vacuum vessel," *Fusion Engineering and Design,* vol. 109–111, Part B, pp. 1099-1103, 2016.
[129] P. T. S. http://www.pva-analyticalsystems.com/en/products/sam-line/pva/sam-line/sam-300.
[130] J. Mathew, A. Mandal, J. Warnett, M. A. Williams, M. Chakraborty, and P. Srirangam, "X-ray tomography studies on porosity and particle size distribution in cast in-situ Al-Cu-TiB2 semi-solid forged composites," *Materials Characterization,* vol. 118, pp. 57-64, 2016.
[131] S. Tammas-Williams, H. Zhao, F. Léonard, F. Derguti, I. Todd, and P. B. Prangnell, "XCT analysis of the influence of melt strategies on defect population in Ti–6Al–4V components manufactured by Selective Electron Beam Melting," *Materials Characterization,* vol. 102, pp. 47-61, 2015.
[132] Z. Yang, W. Ren, R. Sharma, S. McDonald, M. Mostafavi, Y. Vertyagina*, et al.*, "In-situ X-ray computed tomography characterisation of 3D fracture evolution and image-based numerical homogenisation of concrete," *Cement and Concrete Composites,* 2017.
[133] S. K. Dinda, J. M. Warnett, M. A. Williams, G. G. Roy, and P. Srirangam, "3D imaging and quantification of porosity in electron beam welded dissimilar steel to Fe-Al alloy joints by X-ray tomography," *Materials & Design,* vol. 96, pp. 224-231, 2016.
[134] *https://www.netzsch-thermal-analysis.com/en/products-solutions/dilatometer/ (accessed 24/05/2017).*
[135] J. Bonneaux and M. Guymont, "Study of the order–disorder transition series in AuCu by in-situ temperature electron microscopy," *Intermetallics,* vol. 7, pp. 797-805, 1999.
[136] K. I. Udoh, A. M. El Araby, Y. Tanaka, K. Hisatsune, K. Yasuda, G. Van Tendeloo*, et al.*, "Structural aspects of AuCu I or AuCu II and a cuboidal block configuration of f.c.c. disordered phase in AuCu ▪ Pt and AuCu ▪ Ag pseudobinary alloys," *Materials Science and Engineering: A,* vol. 203, pp. 154-164, 1995.
[137] *https://www.netzsch-thermal-analysis.com/en/products-solutions/simultaneous-thermogravimetry-differential-scanning-calorimetry/sta-449-f1-jupiter/ (accessed 24/05/2017).*
[138] *https://www.netzsch-thermal-analysis.com/en/products-solutions/thermal-diffusivity-conductivity/lfa-427/ (accessed 24/05/2017).*
[139] "ASTM Standard Test Method for Thermal Diffusivity by the Flash Method," in *e1461-13*, ed. ASTM International, West Conshohocken, PA, USA, 2013.
[140] J. B. Pethica, "Microhardness tests with penetration depths less than ion implanted layer thickness," in *Ion Implantation Into Metals*, W. A. Grant and R. P. M. Procter, Eds., ed: Pergamon, 1982, pp. 147-156.
[141] H. Ichimura and I. Ando, "Mechanical properties of arc-evaporated CrN coatings: Part I — nanoindentation hardness and elastic modulus," *Surface and Coatings Technology,* vol. 145, pp. 88-93, 2001.
[142] L. Shen, P. Septiwerdani, and Z. Chen, "Elastic modulus, hardness and creep performance of SnBi alloys using nanoindentation," *Materials Science and Engineering: A,* vol. 558, pp. 253-258, 2012.
[143] C. Tromas, J. C. Stinville, C. Templier, and P. Villechaise, "Hardness and elastic modulus gradients in plasma-nitrided 316L polycrystalline stainless steel investigated by nanoindentation tomography," *Acta Materialia,* vol. 60, pp. 1965-1973, 2012.
[144] C. D. Hardie, S. G. Roberts, and A. J. Bushby, "Understanding the effects of ion irradiation using nanoindentation techniques," *Journal of Nuclear Materials,* vol. 462, pp. 391-401, 2015.
[145] M. R. VanLandingham, "Review of Instrumented Indentation," *Journal of Research of the National Institute of Standards and Technology,* vol. 108, pp. 249-265, 2003.

[146] http://www.keysight.com/en/pd-1675520-pn-U9820A/agilent-nano-indenter-g200?cc=GB&lc=eng *(accesed on 29/11/2016).*
[147] C. D. Hardie, G. R. Odette, Y. Wu, S. Akhmadaliev, and S. G. Roberts, "Mechanical properties and plasticity size effect of Fe-6%Cr irradiated by Fe ions and by neutrons," *Journal of Nuclear Materials,* vol. 482, pp. 236-247, 2016.
[148] A. Bolshakov, W. C. Oliver, and G. M. Pharr, "Influences of stress on the measurement of mechanical properties using nanoindentation: Part II. Finite element simulations," *Journal of Materials Research,* vol. 11, pp. 760-768, 1996.
[149] M. Mata, O. Casals, and J. Alcalá, "The plastic zone size in indentation experiments: The analogy with the expansion of a spherical cavity," *International Journal of Solids and Structures,* vol. 43, pp. 5994-6013, 2006.
[150] C. K. Dolph, D. J. da Silva, M. J. Swenson, and J. P. Wharry, "Plastic zone size for nanoindentation of irradiated Fe–9%Cr ODS," *Journal of Nuclear Materials,* vol. 481, pp. 33-45, 2016.
[151] K. Durst, B. Backes, and M. Göken, "Indentation size effect in metallic materials: Correcting for the size of the plastic zone," *Scripta Materialia,* vol. 52, pp. 1093-1097, 2005.
[152] C. L. Woodcock and D. F. Bahr, "Plastic zone evolution around small scale indentations," *Scripta Materialia,* vol. 43, pp. 783-788, 2000.
[153] A. Bolshakov and G. M. Pharr, "Influences of pileup on the measurement of mechanical properties by load and depth sensing indentation techniques," *Journal of Materials Research,* vol. 13, pp. 1049-1058, 1998.
[154] A. C. Fischer-Cripps, "Factors Affecting Nanoindentation Test Data," in *Nanoindentation*, ed New York, NY: Springer New York, 2002, pp. 61-82.
[155] C. Hardie, "Micro-Mechanics of Irradiated Fe-Cr Alloys for Fusion Reactors," PhD, University of Oxford, 2013.
[156] W. Martinson and H. Warlimont, *Springer Handbook of Condensed Matter and Materials Data*, 2005.
[157] J. R. Davis, "ASM Specialty Handbook: Copper and Copper Alloys," 2001.
[158] D. E. J. Armstrong, A. J. Wilkinson, and S. G. Roberts, "Measuring anisotropy in Young's modulus of copper using microcantilever testing," *Journal of Materials Research,* vol. 24, pp. 3268-3276, 2009.
[159] J. Gong and A. Wilkinson, "Investigation of elastic properties of single-crystal α-Ti using microcantilever beams," *Philosophical Magazine Letters,* vol. 90, 2010/07/01 2010.
[160] D. E. J. Armstrong, C. D. Hardie, J. S. K. L. Gibson, A. J. Bushby, P. D. Edmondson, and S. G. Roberts, "Small-scale characterisation of irradiated nuclear materials: Part II nanoindentation and micro-cantilever testing of ion irradiated nuclear materials," *Journal of Nuclear Materials,* vol. 462, pp. 374-381, 2015.
[161] D. Kiener, C. Motz, G. Dehm, and R. Pippan, "Overview on established and novel FIB based miniaturized mechanical testing using in-situ SEM," *International Journal of Materials Research,* vol. 100, pp. 1074-1087, 2009.
[162] J. Gong and A. J. Wilkinson, "Anisotropy in the plastic flow properties of single-crystal α titanium determined from micro-cantilever beams," *Acta Materialia,* vol. 57, pp. 5693-5705, 2009.
[163] K. Matoy, H. Schönherr, T. Detzel, T. Schöberl, R. Pippan, C. Motz*, et al.*, "A comparative micro-cantilever study of the mechanical behavior of silicon based passivation films," *Thin Solid Films,* vol. 518, pp. 247-256, 2009.
[164] G. Otieno, A. Koos, F. Dillon, N. A. Yahya, C. E. J. Dancer, G. M. Hughes*, et al.*, "Stiffness, strength and interwall sliding in aligned and continuous multi-walled carbon nanotube/glass composite microcantilevers," *Acta Materialia,* vol. 100, pp. 118-125, 2015.
[165] J. Gong and A. J. Wilkinson, "A microcantilever investigation of size effect, solid-solution strengthening and second-phase strengthening for 〈a〉 prism slip in alpha-Ti," *Acta Materialia,* vol. 59, pp. 5970-5981, 2011.

[166] E. Tarleton, D. S. Balint, J. Gong, and A. J. Wilkinson, "A discrete dislocation plasticity study of the micro-cantilever size effect," *Acta Materialia,* vol. 88, pp. 271-282, 2015.
[167] C. Bohnert, N. J. Schmitt, S. M. Weygand, O. Kraft, and R. Schwaiger, "Fracture toughness characterization of single-crystalline tungsten using notched micro-cantilever specimens," *International Journal of Plasticity,* vol. 81, pp. 1-17, 2016.
[168] F. Iqbal, J. Ast, M. Göken, and K. Durst, "In situ micro-cantilever tests to study fracture properties of NiAl single crystals," *Acta Materialia,* vol. 60, pp. 1193-1200, 2012.
[169] L. Liu, Z. Chen, C. Liu, Y. Wu, and B. An, "Micro-mechanical and fracture characteristics of Cu6Sn5 and Cu3Sn intermetallic compounds under micro-cantilever bending," *Intermetallics,* vol. 76, pp. 10-17, 2016.
[170] J. J. Roa, R. Rodríguez, V. Lamelas, R. Martínez, E. Jiménez-Piqué, and L. Llanes, "Small scale fracture behaviour of multilayer TiN/CrN systems: Assessment of bilayer thickness effects by means of ex-situ tests on FIB-milled micro-cantilevers," *Surface and Coatings Technology,* 2016.
[171] Y. Zou, P. Okle, H. Yu, T. Sumigawa, T. Kitamura, S. Maiti*, et al.*, "Fracture properties of a refractory high-entropy alloy: In situ micro-cantilever and atom probe tomography studies," *Scripta Materialia,* vol. 128, pp. 95-99, 2017.
[172] J. Schaufler, C. Schmid, K. Durst, and M. Göken, "Determination of the interfacial strength and fracture toughness of a-C:H coatings by in-situ microcantilever bending," *Thin Solid Films,* vol. 522, pp. 480-484, 2012.
[173] R. Daniel, M. Meindlhumer, W. Baumegger, J. Zalesak, B. Sartory, M. Burghammer*, et al.*, "Grain boundary design of thin films: Using tilted brittle interfaces for multiple crack deflection toughening," *Acta Materialia,* vol. 122, pp. 130-137, 2017.
[174] K. Gall, N. West, K. Spark, M. L. Dunn, and D. S. Finch, "Creep of thin film Au on bimaterial Au/Si microcantilevers," *Acta Materialia,* vol. 52, pp. 2133-2146, 2004.
[175] J. Zechner, G. Mohanty, C. Frantz, H. Cebeci, L. Philippe, and J. Michler, "Mechanical properties and interface toughness of metal filled nanoporous anodic aluminum oxide coatings on aluminum," *Surface and Coatings Technology,* vol. 260, pp. 246-250, 2014.
[176] *https://cemas.osu.edu/fei-helios-nanolabtm-600-dualbeam-fibsem (accessed 24/05/2017).*
[177] D. Di Maio and S. G. Roberts, "Measuring fracture toughness of coatings using focused-ion-beam-machined microbeams," *Journal of Materials Research,* vol. 20, pp. 299-302, 2005.
[178] M. D. Uchic, D. M. Dimiduk, J. N. Florando, and W. D. Nix, "Sample Dimensions Influence Strength and Crystal Plasticity," *Science,* vol. 305, pp. 986-989, 2004.
[179] J. R. Greer and W. D. Nix, "Size dependence of mechanical properties of gold at the sub-micron scale," *Applied Physics A,* vol. 80, pp. 1625-1629, 2005.
[180] D. Kiener, C. Motz, and G. Dehm, "Dislocation-induced crystal rotations in micro-compressed single crystal copper columns," *Journal of Materials Science,* vol. 43 (7), pp. 2503-2506, 2008.
[181] C. E. Coleman and D. Hardie, "The hydrogen embrittlement of zirconium in slow-bend tests," *Journal of Nuclear Materials,* vol. 19, pp. 1-8, 1966.
[182] J. Sharpe, "Springer Handbook of Experimental Solid Mechanics," 2008.
[183] J. Gere, *Mechanics of Materials, 6th Edition*, 4th ed., 2004.
[184] J. R. Greer and J. T. M. De Hosson, "Plasticity in small-sized metallic systems: Intrinsic versus extrinsic size effect," *Progress in Materials Science,* vol. 56, pp. 654-724, 2011.
[185] "Volume 2 - Properties and Selection Nonferrous Alloys and Special Purpose Materials," *ASM Metals Handbook,* 2001.
[186] *www.matweb.com Annealed Cu, accessed on 20/11/2016.*
[187] F. Dalle, M. Blat-Yrieix, S. Dubiez-Le Goff, C. Cabet, and P. Dubuisson, "17 - Conventional austenitic steels as out-of-core materials for Generation IV nuclear reactors A2 - Yvon, Pascal," in *Structural Materials for Generation IV Nuclear Reactors*, ed: Woodhead Publishing, 2017, pp. 595-633.
[188] "Volume 1 - Properties and Selection Irons Steels and High Performance Alloys," *ASM Metals Handbook,* 2001.

[189] S. A. Bell, "NPL Good Practice Guide 11 - A beginner's guide to uncertainty of measurement," *National Measurement Conference (NMC) 1999, 2-4 November 1999, Brighton. UK, Paper 2,* 1999.
[190] K. Birch, "NPL Good Practice Guide 36 - Estimating uncertainties in testing," *NPL Measurement Good Practice Guide No. 36,* 2001.
[191] JCGM, "Evaluation of measurementdata — Guide to the expression of uncertainty in measurement," *Joint Committee for Guides in Metrology Working Group 1,* vol. JCGM 100:2008, 2008.
[192] *http://www.instron.co.uk/en-gb/products/testing-systems/dynamic-and-fatigue-systems/high-temp-fatigue-testing-systems/etmt (accessed 23/11/2016).*
[193] B. Roebuck, D. Cox, and R. Reed, "An innovative device for the mechanical testing of miniature specimens of the superalloys," presented at the Seven Springs Superalloy Conference, , 2004.
[194] A. Nemeth, D. Crudden, and D. Collins, "Novel Techniques to Assess Environmentally-Assisted Cracking in a Nickel-based Superalloy," presented at the Proceedings of the 13th Intenational Symposium of Superalloys, 2016.
[195] *http://www.wesgometals.com/resources/mechanical-physical-properties/ (accessed 24/05/2017).*
[196] H. Andersson and E. Sjostrom, "Thermal gradients in round TMF specimens," *International Journal of Fatigue,* vol. 30, pp. 391-396, 2008.
[197] S. Pahlavanyali, A. Rayment, B. Roebuck, G. Drew, and C. M. F. Rae, "Thermo-mechanical fatigue testing of superalloys using miniature specimens," *International Journal of Fatigue,* vol. 30, pp. 397-403, 2008.
[198] "Volume 11 - Failure Analysis And Prevention," *ASM Metals Handbook,* 2001.
[199] N. R. Hamilton, J. Wood, D. Easton, M. B. O. Robbie, Y. Zhang, and A. Galloway, "Thermal autofrettage of dissimilar material brazed joints," *Materials & Design,* vol. 67, pp. 405-412, 2015.
[200] *http://www.tainstruments.com/q800/ (accessed 24/05/2017).*
[201] K. Mizuno, "Characterization of thermal stresses in ceramic metal joint," *Journal of the Faculty of Engineering, University of Tokyo,* 1988.
[202] M. Heinzelmann, "Singular thermal stress fields in brazed three-layer joints," *Engineering Fracture Mechanics,* vol. 55, pp. 647-655, 1996.
[203] P. Dadras, J. M. Ting, and M. L. Lake, "Brazing residual stresses in Glidcop-All2Si-Be," *Journal of Nuclear Materials,* vol. 230, pp. 164-172, 1996.
[204] J. E. Inge and J. E. Swanson, "Experimental investigation of stresses in a ceramic-to-metal brazed joint," *Experimental Mechanics,* vol. 2, pp. 289-295, 1992.
[205] D. Munz, M. A. Sckuhr, and Y. Yang, "Thermal Stresses in Ceramic-Metal Joints with an Interlayer," *Journal of the American Ceramic Society,* vol. 78, pp. 285-290, 1995.
[206] D. Munz and Y. Y. Yang, "Stresses near the free edge of the interface in ceramic-to-metal joints," *Journal of the European Ceramic Society,* vol. 13, pp. 453-460, 1994.
[207] K. Suganuma, T. Okamoto, M. Koizumi, and K. Kamachi, "Influence of shape and size on residual stress in ceramic/metal joining," *Journal of Materials Science,* vol. 22, pp. 3561-3565, 1987.
[208] N. Hamilton, "A Study of the Residual Stresses in Dissimilar Material Brazed Joints," PhD, University of Strathclyde, 2013.
[209] J. Wood, M. B. O. Robbie, N. Hamilton, D. Easton, and Y. Zhang, "Theoretical elastic stress singularities much maligned and misunderstood," presented at the NAFEMS World Congress, San Diego, United States, 2015.
[210] W. Jiang, J. Gong, H. Chen, and S. T. Tu, "The effect of filler metal thickness on residual stress and creep for stainless-steel plate–fin structure," *International Journal of Pressure Vessels and Piping,* vol. 85, pp. 569-574, 2008.
[211] "BS EN 13445 Unfired Pressure Vessels – Part 3 Design. BSI,," ed, 2009 with corrigendum August 2010.

[212] A. M. van Wingerde, J. A. Packer, and J. Wardenier, "Criteria for the fatigue assessment of hollow structural section connections," *Journal of Constructional Steel Research,* vol. 35, pp. 71-115, 1995.
[213] W. Fricke, "Fatigue analysis of welded joints: state of development," *Marine Structures,* vol. 16, pp. 185-200, 2003.
[214] J. Dundurs, "Discussion: "Edge-Bonded Dissimilar Orthogonal Elastic Wedges Under Normal and Shear Loading" (Bogy, D. B., 1968, ASME J. Appl. Mech., 35, pp. 460–466)," *Journal of Applied Mechanics,* vol. 36, pp. 650-652, 1969.
[215] D. B. Bogy, "Two Edge-Bonded Elastic Wedges of Different Materials and Wedge Angles Under Surface Tractions," *Journal of Applied Mechanics,* vol. 38, pp. 377-386, 1971.
[216] D. B. Bogy, "On the problem of edge-bonded elastic quarter-planes loaded at the boundary," *International Journal of Solids and Structures,* vol. 6, pp. 1287-1313, 1970.
[217] D. B. Bogy, "Edge-Bonded Dissimilar Orthogonal Elastic Wedges Under Normal and Shear Loading," *Journal of Applied Mechanics,* vol. 35, pp. 460-466, 1968.
[218] D. B. Bogy and K. C. Wang, "Stress singularities at interface corners in bonded dissimilar isotropic elastic materials," *International Journal of Solids and Structures,* vol. 7, pp. 993-1005, 1971.
[219] D. Munz and Y. Y. Yang, "Stress Singularities at the Interface in Bonded Dissimilar Materials Under Mechanical and Thermal Loading," *Journal of Applied Mechanics,* vol. 59, pp. 857-861, 1992.
[220] P. Kelly, "The design of joints between elastically dissimilar components," *Journal of Strain Analysis,* vol. 27, pp. 15-20, 1992.
[221] J. P. Blanchard and N. M. Ghoniem, "Relaxation of Thermal Stress Singularities in Bonded Viscoelastic Quarter Planes," *Journal of Applied Mechanics,* vol. 56, pp. 756-762, 1989.
[222] J. H. You and H. Bolt, "Analysis of singular interface stresses in dissimilar material joints for plasma facing components," *Journal of Nuclear Materials,* vol. 299, pp. 1-8, 2001.
[223] D. Post, J. D. Wood, B. Han, V. J. Parks, and J. F. P. Gerstle, "Thermal Stresses in a Bimaterial Joint: An Experimental Analysis," *Journal of Applied Mechanics,* vol. 61, pp. 192-198, 1994.
[224] M. Wittmer, C. R. Boer, P. Gudmundson, and J. Carlsson, "Mechanical Properties of Liquid-Phase-Bonded Copper-Ceramic Substrates," *Journal of the American Ceramic Society,* vol. 65, pp. 149-152, 1982.
[225] D. Munz and Y. Y. Yang, "Stresses near the edge of bonded dissimilar materials described by two stress intensity factors," *International Journal of Fracture,* vol. 60, pp. 169-177, 1993.
[226] C. H. Hsueh and A. G. Evans, "Residual Stresses in Meta/Ceramic Bonded Strips," *Journal of the American Ceramic Society,* vol. 68, pp. 241-248, 1985.
[227] *http://www.3ds.com/products-services/simulia/products/abaqus/abaquscae/ accessed 09/01/2017.*
[228] J. Software", "Material Property Database (MPDB)," ed, 2015.
[229] M. Fränkle, D. Munz, and Y. Y. Yang, "Stress singularities in a bimaterial joint with inhomogeneous temperature distribution," *International Journal of Solids and Structures,* vol. 33, pp. 2039-2054, 1996.
[230] D. Munz, T. Fett, and Y. Y. Yang, "The regular stress term in bonded dissimilar materials after a change in temperature," *Engineering Fracture Mechanics,* vol. 44, pp. 185-194, 1993.
[231] D. Easton, J. Wood, N. Hamilton, C. Hardie, S. Rahimi, and Y. Zhang, "Residual stress generation in brazed tungsten dissimilar joints," *Transactions on Plasma Science,* vol. Volume 44, pp. 1625-1630, 2016.
[232] M. Fitzpatrick, A. Fry, T. Holdway, and F. Kandil, "Determination of Residual Stresses by X-ray Diffraction," *NPL Measurement Good Practice Guide No 52,* 2005.
[233] J. Lu, *Handbook of measurement of residual stress*. Society for Experimental Mechanics, 1996.

[234] P. Prevey, "X-Ray diffraction residual stress techniques," *Metals Handbook. 10. American Society for Metals,* pp. 380-392, 1986.
[235] "BS EN 15305:2008 Non-destructive testing. Test method for residual stress analysis by X-ray diffraction," ed, 2008.
[236] A. C. Vermuelen, "An elastic constants database and XEC calculator for use in residual stress analysis," *Advances in X-ray Analysis,* vol. 44, pp. 128-133, 2001.
[237] *http://www.protoxrd.com/lxrd-laboratory.html (accessed 24/05/2017).*
[238] I. Noyan and J. Cohen, *Residual Stress: Measurement by Diffraction and Interpretation*: Springer-Verlag, 1987.
[239] X. Song, K. B. Yeap, J. Zhu, J. Belnoue, M. Sebastiani, E. Bemporad*, et al.*, "Residual stress measurement in thin films using the semi-destructive ring-core drilling method using Focused Ion Beam," *Procedia Engineering,* vol. 10, pp. 2190-2195, 2011.
[240] E. Salvati, T. Sui, and A. M. Korsunsky, "Uncertainty quantification of residual stress evaluation by the FIB–DIC ring-core method due to elastic anisotropy effects," *International Journal of Solids and Structures,* vol. 87, pp. 61-69, 2016.
[241] "Volume 4 - Heat Treating," *ASM Metals Handbook,* 2001.
[242] P. Parikh and E. Shapiro, *"A Phenomenology of Room-Temperature Stress Relaxation in Cold-Rolled Copper Alloys", Stress Relaxation Testing*, 1979.
[243] Y. Huang, S. Sabbaghianrad, A. I. Almazrouee, K. J. Al-Fadhalah, S. N. Alhajeri, and T. G. Langdon, "The significance of self-annealing at room temperature in high purity copper processed by high-pressure torsion," *Materials Science and Engineering: A,* vol. 656, pp. 55-66, 2016.
[244] J. N. Butters and J. A. Leendertz, "Holographic and Video Techniques Applied to Engineering Measurement," *Measurement and Control,* vol. 4, pp. 349-354, 1971.
[245] J. A. Leendertz, "Interferometric displacement measurement on scattering surfaces utilizing speckle effect," *Journal of Physics E: Scientific Instruments,* vol. 3, p. 214, 1970.
[246] G. S. Schajer and M. Steinzig, "Full-field calculation of hole drilling residual stresses from electronic speckle pattern interferometry data," *Experimental Mechanics,* vol. 45, p. 526, 2005.
[247] *http://ast.stresstechgroup.com/content/94567/en/1034/1460/1460.html (accessed 24/01/2017).*
[248] A. Makino, D. V. Nelson, E. A. Fuchs, and D. R. Williams, "Determination of Biaxial Residual Stresses by a Holographic-Hole Drilling Technique," *Journal of Engineering Materials and Technology,* vol. 118, pp. 583-588, 1996.
[249] A. Makino and D. Nelson, "Residual-stress determination by single-axis holographic interferometry and hole drilling—Part I: Theory," *Experimental Mechanics,* vol. 34, pp. 66-78, 1994.
[250] D. e. a. Kennedy, "Application of ESPI-Method for Strain Analysis in Thin Wall Cylinders," *Optics and Lasers in Engineering,* vol. vol 41, pp. 585-594, 2004.
[251] J. N. Butters and J. A. Leendertz, "A double exposure technique for speckle pattern interferometry," *Journal of Physics E: Scientific Instruments,* vol. 4, p. 277, 1971.
[252] M. B. Prime, "Cross-Sectional Mapping of Residual Stresses by Measuring the Surface Contour After a Cut," *Journal of Engineering Materials and Technology,* vol. 123, pp. 162-168, 2001.
[253] H. Bueckner, "The Propagation of Cracks and the Energy of Elastic Deformation," *Transactions of the American Society of Mechanical Engineers,* vol. 80, pp. 1225-1230, 1958.
[254] P. Pagliaro, M. B. Prime, H. Swenson, and B. Zuccarello, "Measuring Multiple Residual-Stress Components using the Contour Method and Multiple Cuts," *Experimental Mechanics,* vol. 50, pp. 187-194, 2010.
[255] A. T. DeWald and M. R. Hill, "Multi-Axial Contour Method for Mapping Residual Stresses in Continuously Processed Bodies," *Experimental Mechanics,* vol. 46, pp. 473-490, 2006.
[256] P. Pagliaro, "Mapping Multiple Residual Stress Components Using the Contour Method and Superposition," PhD Thesis, 2008.

[257] A. T. DeWald, M. R. Hill, and M. B. Prime, "Residual stress in a thick steel weld determined using the contour method," 2001.
[258] M. B. Prime, T. Gnäupel-Herold, J. A. Baumann, R. J. Lederich, D. M. Bowden, and R. J. Sebring, "Residual stress measurements in a thick, dissimilar aluminum alloy friction stir weld," *Acta Materialia,* vol. 54, pp. 4013-4021, 2006.
[259] D. W. Brown, T. M. Holden, B. Clausen, M. B. Prime, T. A. Sisneros, H. Swenson*, et al.*, "Critical comparison of two independent measurements of residual stress in an electron-beam welded uranium cylinder: Neutron diffraction and the contour method," *Acta Materialia,* vol. 59, pp. 864-873, 2011.
[260] M. B. Prime, R. J. Sebring, J. M. Edwards, D. J. Hughes, and P. J. Webster, "Laser surface-contouring and spline data-smoothing for residual stress measurement," *Experimental Mechanics,* vol. 44, pp. 176-184, 2004.
[261] P. Rangaswamy, M. L. Griffith, M. B. Prime, T. M. Holden, R. B. Rogge, J. M. Edwards*, et al.*, "Residual stresses in LENS® components using neutron diffraction and contour method," *Materials Science and Engineering: A,* vol. 399, pp. 72-83, 2005.
[262] D. Thibault, P. Bocher, M. Thomas, M. Gharghouri, and M. Côté, "Residual stress characterization in low transformation temperature 13%Cr–4%Ni stainless steel weld by neutron diffraction and the contour method," *Materials Science and Engineering: A,* vol. 527, pp. 6205-6210, 2010.
[263] W. Woo, G. B. An, E. J. Kingston, A. T. DeWald, D. J. Smith, and M. R. Hill, "Through-thickness distributions of residual stresses in two extreme heat-input thick welds: A neutron diffraction, contour method and deep hole drilling study," *Acta Materialia,* vol. 61, pp. 3564-3574, 2013.
[264] M. Kerr, M. B. Prime, H. Swenson, M. A. Buechler, M. Steinzig, B. Clausen*, et al.*, "Residual Stress Characterization in a Dissimilar Metal Weld Nuclear Reactor Piping System Mock Up," *Journal of Pressure Vessel Technology,* vol. 135, pp. 041205-041205, 2013.
[265] M. R. Hill and M. D. Olson, "Repeatability of the Contour Method for Residual Stress Measurement," *Experimental Mechanics,* vol. 54, pp. 1269-1277, 2014.
[266] F. Hosseinzadeh, J. Kowal, and P. J. Bouchard, "Towards good practice guidelines for the contour method of residual stress measurement," *Journal of Engineering (online only),* 2014.
[267] M. B. Prime and A. L. Kastengren, "The Contour Method Cutting Assumption: Error Minimization and Correction," in *Experimental and Applied Mechanics, Volume 6: Proceedings of the 2010 Annual Conference on Experimental and Applied Mechanics*, T. Proulx, Ed., ed New York, NY: Springer New York, 2011, pp. 233-250.
[268] Y. Traoré, F. Hosseinzadeh, and P. J. Bouchard, "Plasticity in the Contour Method of Residual Stress Measurement," *Advanced Materials Research,* vol. 996, pp. 337-342, 2014.
[269] F. Hosseinzadeh, Y. Traore, P. J. Bouchard, and O. Muránsky, "Mitigating cutting-induced plasticity in the contour method, part 1: Experimental," *International Journal of Solids and Structures,* vol. 94–95, pp. 247-253, 2016.
[270] G. Johnson, "Residual stress measurements using the contour method," PhD, Faculty of Engineering and Physical Sciences, University of Manchester, 2008.
[271] *http://www.gom.com/metrology-systems/atos.html (accessed 24/05/2017).*
[272] S. Suresh, "Fatigue of materials," *Advanced Materials,* vol. 5, pp. 309-309, 1993.
[273] G. A. Webster and A. N. Ezeilo, "Residual stress distributions and their influence on fatigue lifetimes," *International Journal of Fatigue,* vol. 23, Supplement 1, pp. 375-383, 2001.
[274] S. M. Kamal and U. S. Dixit, "Feasibility Study of Thermal Autofrettage Process," in *Advances in Material Forming and Joining: 5th International and 26th All India Manufacturing Technology, Design and Research Conference, AIMTDR 2014*, R. G. Narayanan and U. S. Dixit, Eds., ed New Delhi: Springer India, 2015, pp. 81-107.
[275] A. Malik and S. Khushnood, "A review of swage - autofrettage process," in *Proceedings of the 11th international conference on nuclear engineering*, Japan, 2003, p. 3610.

[276] M. Perl and M. Steiner, "The beneficial effect of full or partial autofrettage on the combined 3-D stress intensity factor for an inner radial lunular or crescentic crack in a spherical pressure vessel," *Engineering Fracture Mechanics,* vol. 156, pp. 124-140, 2016.
[277] A. P. Parker, "Autofrettage of open-end tubes - Pressures, stresses, strains, and code comparisons," *Journal of Pressure Vessel Technology, Transactions of the ASME,* vol. 123, pp. 271-281, 2001.
[278] R. Zhu and J. Yang, "Autofrettage of thick cylinders," *International Journal of Pressure Vessels and Piping,* vol. 75, pp. 443-446, 1998.
[279] M. M. Megahed and A. T. Abbas, "Influence of reverse yielding on residual stresses induced by autofrettage," *International Journal of Mechanical Sciences,* vol. 33, pp. 139-150, 1991.
[280] M. Perl and M. Steiner, "The beneficial effect of full or partial autofrettage on the combined 3-D stress intensity factors for inner radial crack arrays in a spherical pressure vessel," *Engineering Fracture Mechanics,* vol. 175, pp. 46-56, 2017.
[281] S. M. Kamal and U. S. Dixit, "A comparative study of thermal and hydraulic autofrettage," *Journal of Mechanical Science and Technology,* vol. 30, pp. 2483-2496, 2016.
[282] M. A. Hussain, S. L. Pu, J. D. Vasilakis, and P. O'Hara, "Simulation of partial autofrettage by thermal loads," *Journal of Pressure Vessel Technology, Transactions of the ASME,* vol. 102, pp. 314-323, 1980.
[283] C. Levy, M. Perl, and Q. Ma, "Erosions and their effect on the fatigue life of thick walled, autofrettaged, pressurized vessels," *Journal of Pressure Vessel Technology, Transactions of the ASME,* vol. 125, pp. 242-247, 2003.
[284] G. Schnier, J. Wood, and A. Galloway, "Investigating the effects of process variables on the residual stresses of weld and laser cladding," *Advanced Materials Research,* vol. 996, pp. 481-487, 2014.
[285] G. Benghalia and J. Wood, "Material and residual stress considerations associated with the autofrettage of weld clad components," *International Journal of Pressure Vessels and Piping,* vol. 139–140, pp. 146-158, 2016.
[286] H. R. Zare and H. Darijani, "A novel autofrettage method for strengthening and design of thick-walled cylinders," *Materials & Design,* vol. 105, pp. 366-374, 2016.
[287] D. Sherman and D. Schlumm, "Mechanical behavior of ceramic-metal laminate under thermal shock," *Journal of Materials Research,* vol. 14, pp. 3544-3551, 1999.
[288] A. Kawasaki and R. Watanabe, "Thermal fracture behavior of metal/ceramic functionally graded materials," *Engineering Fracture Mechanics,* vol. 69, pp. 1713-1728, 2002.
[289] Z.-H. Jin and R. C. Batra, "Stress intensity relaxation at the tip of an edge crack in a functionally graded material subjected to a thermal shock," *Journal of Thermal Stresses,* vol. 19, pp. 317-339, 1996.
[290] M. Wirtz, G. Cempura, J. Linke, G. Pintsuk, and I. Uytdenhouwen, "Thermal shock response of deformed and recrystallised tungsten," *Fusion Engineering and Design,* vol. 88, pp. 1768-1772, 2013.
[291] D. W. A. Rees, "A theory of autofrettage with applications to creep and fatigue," *International Journal of Pressure Vessels and Piping,* vol. 30, pp. 57-76, 1987.
[292] S. I. Wright, M. M. Nowell, and D. P. Field, "A review of strain analysis using electron backscatter diffraction," *Microsc Microanal,* vol. 17, pp. 316-29, 2011.
[293] M. Kamaya, A. J. Wilkinson, and J. M. Titchmarsh, "Measurement of plastic strain of polycrystalline material by electron backscatter diffraction," *Nuclear Engineering and Design,* vol. 235, pp. 713-725, 2005.
[294] A. Gholinia, P. B. Prangnell, and M. V. Markushev, "The effect of strain path on the development of deformation structures in severely deformed aluminium alloys processed by ECAE," *Acta Materialia,* vol. 48, pp. 1115-1130, 2000.
[295] S. I. Wright, M. M. Nowell, and D. P. Field, "A Review of Strain Analysis Using Electron Backscatter Diffraction," *Microscopy and Microanalysis,* vol. 17, pp. 316-329, 2011.

[296] S. Saito, K. Fukaya, S. Ishiyama, and K. Sato, "Mechanical properties of HIP bonded W and Cu-alloys joint for plasma facing components," *Journal of Nuclear Materials,* vol. 307–311, Part 2, pp. 1542-1546, 2002.
[297] E. Visca, S. Libera, A. Mancini, G. Mazzone, A. Pizzuto, and C. Testani, "Hot radial pressing: An alternative technique for the manufacturing of plasma-facing components," *Fusion Engineering and Design,* vol. 75–79, pp. 485-489, 2005.
[298] G. Pintsuk, S. E. Brünings, J. E. Döring, J. Linke, I. Smid, and L. Xue, "Development of W/Cu—functionally graded materials," *Fusion Engineering and Design,* vol. 66–68, pp. 237-240, 2003.
[299] Z.-J. Zhou, J. Du, S.-X. Song, Z.-H. Zhong, and C.-C. Ge, "Microstructural characterization of W/Cu functionally graded materials produced by a one-step resistance sintering method," *Journal of Alloys and Compounds,* vol. 428, pp. 146-150, 2007.
[300] Y. Itoh, M. Takahashi, and H. Takano, "Design of tungsten/copper graded composite for high heat flux components," *Fusion Engineering and Design,* vol. 31, pp. 279-289, 1996.
[301] J. H. You, A. Brendel, S. Nawka, T. Schubert, and B. Kieback, "Thermal and mechanical properties of infiltrated W/CuCrZr composite materials for functionally graded heat sink application," *Journal of Nuclear Materials,* vol. 438, pp. 1-6, 2013.
[302] M. Richou, M. Missirlian, N. Vignal, V. Cantone, C. Hernandez, P. Norajitra*, et al.*, "Non-destructive examination of the bonding interface in DEMO divertor fingers," *Fusion Engineering and Design,* vol. 88, pp. 1753-1757, 2013.
[303] S. Roccella, E. Cacciotti, F. Escourbiac, A. Pizzuto, B. Riccardi, A. Tatì*, et al.*, "Development of an ultrasonic test method for the non-destructive examination of ITER divertor components," *Fusion Engineering and Design,* vol. 84, pp. 1639-1644, 2009.
[304] I. Šmid, E. Kny, M. Scheerer, P. A. Hahn, G. Korb, J. Linke*, et al.*, "Non-destructive characterization of plasma-sprayed tungsten and braze-joints for fusion by ultra-sonic examination," *Fusion Engineering and Design,* vol. 42, pp. 511-517, 1998.
[305] M. Kaufmann and R. Neu, "Tungsten as first wall material in fusion devices," *Fusion Engineering and Design,* vol. 82, pp. 521-527, 2007.
[306] B. Winiarski and P. J. Withers, "Mapping residual stress profiles at the micron scale using FIB micro-hole drilling," in *Applied Mechanics and Materials* vol. 24-25, ed, 2010, pp. 267-272.
[307] B. Winiarski and P. J. Withers, "Novel implementations of relaxation methods for measuring residual stresses at the micron scale," *The Journal of Strain Analysis for Engineering Design,* vol. 50, pp. 412-425, 2015.
[308] B. Winiarski, R. M. Langford, J. Tian, Y. Yokoyama, P. K. Liaw, and P. J. Withers, "Mapping residual stress distributions at the micron scale in amorphous materials," *Metallurgical and Materials Transactions A: Physical Metallurgy and Materials Science,* vol. 41, pp. 1743-1751, 2010.
[309] B. Winiarski, A. Gholinia, J. Tian, Y. Yokoyama, P. K. Liaw, and P. J. Withers, "Submicron-scale depth profiling of residual stress in amorphous materials by incremental focused ion beam slotting," *Acta Materialia,* vol. 60, pp. 2337-2349, 2012.
[310] A. H. Mahmoudi, "Plasticity Effect on Residual Stresses Measurement using Contour Method," *International Journal of Engineering,* vol. 26, 2013.
[311] J. A. Francis, M. Turski, and P. J. Withers, "Measured residual stress distributions for low and high heat input single weld beads deposited on to SA508 steel," *Materials Science and Technology,* vol. 25, pp. 325-334, 2009.
[312] J. A. Francis, A. F. Mark, M. Turski, S. K. Bate, M. Hofmann, and P. J. Withers, "A comparison of residual stresses in single-pass and multipass SA508 steel welds," in *American Society of Mechanical Engineers, Pressure Vessels and Piping Division (Publication) PVP*, 2010, pp. 1415-1423.
[313] J. A. Francis, H. K. D. H. Bhadeshia, and P. J. Withers, "Welding residual stresses in ferritic power plant steels," *Materials Science and Technology,* vol. 23, pp. 1009-1020, 2007.

[314] C. Heintze, F. Bergner, S. Akhmadaliev, and E. Altstadt, "Ion irradiation combined with nanoindentation as a screening test procedure for irradiation hardening," *Journal of Nuclear Materials,* vol. 472, pp. 196-205, 2016.
[315] J. I. Cole and T. R. Allen, "Microstructural changes induced by post-irradiation annealing of neutron-irradiated austenitic stainless steels," *Journal of Nuclear Materials,* vol. 283–287, Part 1, pp. 329-333, 2000.
[316] D. J. Edwards, M. L. Hamilton, F. A. Garner, P. Samal, and J. D. Troxell, "Brazed dispersion strengthened copper: the effect of neutron irradiation and transmutation on bond integrity," in *ASTM Special Technical Publication*, 1999, pp. 973-990.

Previous Publications

D. Easton, J. Wood, A. Galloway, Y. Zhang, M. B. O. Robbie, and C. Hardie, "Brazing Development and Interfacial Metallurgy Study of Tungsten and Copper Joints with Eutectic Gold Copper Brazing Alloy," Fusion Engineering and Design, vol. In Press, 2014

D. Easton, J. Wood, N. Hamilton, C. Hardie, S. Rahimi, and Y. Zhang, "Residual stress generation in brazed tungsten dissimilar joints," Transactions on Plasma Science, vol. Volume 44, pp. 1625-1630, 2016.

D. Easton, J. Wood, S. Rahimi, A. Galloway, Y. Zhang and C. Hardie, "Residual stress generation in tungsten-copper brazed joint using brazing alloy," 2015 IEEE 26th Symposium on Fusion Engineering (SOFE), Austin, TX, 2015, pp. 1-6.

Y. Zhang, A. Galloway, J. Wood, M. B. O. Robbie, D. Easton, and W. Zhu, "Interfacial metallurgy study of brazed joints between tungsten and fusion related materials for divertor design," *Journal of Nuclear Materials,* vol. 454, pp. 207-216, 2014

N. R. Hamilton, J. Wood, D. Easton, M. B. O. Robbie, Y. Zhang, and A. Galloway, "Thermal autofrettage of dissimilar material brazed joints," *Materials & Design,* vol. 67, pp. 405-412, 2015

J. Wood, M. B. O. Robbie, N. Hamilton, D. Easton, and Y. Zhang, "Theoretical elastic stress singularities much maligned and misunderstood," presented at the NAFEMS World Congress, San Diego, United States, 2015

Appendix A – Material Certificates

This information has been removed by the author of this thesis for commercial reasons

This information has been removed by the author of this thesis for commercial reasons

This information has been removed by the author of this thesis for commercial reasons